Multiscale Multimodal Imaging of Nanoporous Catalyst

A thesis submitted to the University of Nottingham
for the degree of Doctor of Philosophy
Department of Chemical Engineering

July 2022

S. A. Mousa
Department of Chemical Engineering
University of Nottingham
Nottingham
NG7 2TQ

This thesis was typeset using LaTeX typesetting system originally developed by Leslie Lamport, based on TeX created by Donald Knuth. The body text uses Bitstream Charter, TeX Gyre Heros and TeX Computer Modern font types. The thesis contains 7 chapters, 250 pages, 119 figures and 25 tables. The figures were prepared in OriginPro® and the sketches were drawn in MS Visio (All final figures to PDF).

© 2022 Suleiman Mousa.

Abstract

This thesis is dedicated to the study of the structure-transport relationship in disordered porous materials such as heterogeneous catalyst systems. Integrated mercury porosimetry and gas adsorption experiments, including the gas overcondensation method, have been applied to probe the relative importance of particular sub-sets of pores to mass transport rates within various disordered catalyst pellets. This was achieved by examining the relative rates of low-pressure gas uptake into a network before and after a known set of pores was filled with frozen, entrapped mercury. The multi-scale data from porosimetry was combined with multi-modal imaging, including low and high-resolution CXT and FIB-SEM, to spatially locate the specific pore sizes that entrapped mercury and study their impact on the mass transport in the pellets.

The first part of this thesis investigates fresh, reduced, and spent methanol synthesis catalyst pellets made using spray-dried (SD) or roll compacted (RC) feed materials. It examined how the different pellet fabrication processes affected the pore structure of the fresh catalyst by studying both the starting feed particles and the finished tablets. The impact on mass transfer of the controlled modifications to the void space, achieved through mercury porosimetry, was modelled with a random pore-bond network using characteristic parameters obtained from percolation analysis of the overcondensation data. This revealed the differential importance to mass transfer of particular sets of pores associated with certain pellet structural features and the impact on tortuosity of pellet fabrication parameters such as particle feed size. The effectiveness of the reduced and spent methanol synthesis pellets, and the impacts of cracks on the random pore-bond model, were also investigated. It was found that a random pore-bond percolation model accurately captures the macroscopic structure of the reduced and spent SD pellets but not the reduced and spent RC pellets.

In the second part of this thesis, i) the entrapment of non-wetting fluids in high-temperature shift catalyst pellets made via precipitation was investigated using the combined indirect characterisation and X-ray imaging methods. This technique was used to identify the specific pore sizes that entrapped mercury and their impact on the mass transport rates, ii) A novel thermoporometry by DSC method was introduced that uses three separate probe liquids (nitrogen, water and mercury) to validate pore space characterisations obtained through indirect methods. This hybrid experiment permits the comparison of data from multiple techniques for the same sample, allowing parameter calibration and phase transition mode selection to be performed. It was found that the dual-probe experiment overcomes the critical drawbacks and assumptions made when applying the indirect pore characterisation methods to disordered porous materials.

List of Publications and Presentations

1. **S. MOUSA**, V. NOVAK, R. FLETCHER, M. GARCIA, N. MACLEOD, M. CORFIELD and S. RIGBY. Integration of multi-scale porosimetry and multi-modal imaging in the study of structure-transport relationships in porous catalyst pellets. In: Chemical Engineering Journal **452** (2022), p. 139122. DOI: 10.1016/j.cej.2022.139122.

2. **S. MOUSA**, K. BARON, R. FLETCHER, and S. RIGBY. Triangulation of pore structural characterisation of disordered mesoporous silica using novel hybrid methods involving dual-probe porosimetries. In: *Colloids and Surface A: Physicochemical and Engineering Aspects* **653** (2022), p.130026. DOI: 10.1016/j.colsurfa.2022.130026.

3. **S. MOUSA**, R. FLETCHER, M. GARCIA, N. MACLEOD, and S. RIGBY. Studies on the effectiveness of freshly reduced and spent methanol synthesis catalyst pellets. Chemical Engineering Science. 2023. (*in preparation*)

4. **S. MOUSA**, N. MACLEOD, and S. RIGBY. Multi-scale, Multi-modal imaging of Nanoporous Catalyst. *Presentation*. Johnson Matthey Academic Conference (JMAC2022), Warwick University, UK, 5-6 April 2022.

5. **S. MOUSA**, N. MACLEOD, and S. RIGBY. Multi-scale, Multi-modal imaging of Nanoporous Catalyst. *Poster presentation*. Johnson Matthey Academic Conference (JMAC2019), Warwick University, UK, 9-10 April 2019.

Acknowledgements

This thesis would not have been possible without the support, ideas, friendship, and assistance of numerous people. Foremost among them is Professor Sean Rigby, my academic supervisor at Nottingham University, who is a constant source of ideas and inspiration, and I consider myself extremely fortunate and privileged to have him as my PhD supervisor. Your guidance and frequent availability for brain picking have been invaluable throughout the years. Our weekly meetings over the years are a fond memory of mine, despite my spending much of the time in a state of confusion.

Thanks to Johnson Matthey and EPSRC for providing funding for this iCASE studentship project. I owe much to Rob Fletcher who showed me how to use the gas adsorption equipment from my first visit to JM. Rob produced most of the overcondensation data for the methanol catalyst pellets during the Covid-19 lockdowns when I could not visit JM site. He then put up with my demands for ever more data, which he was able to provide even if it sometimes proved inconvenient for his outstanding work. I am also very thankful to Emma Softley, who showed me how to use the mercury porosimetry kit and generated some of the mercury porosimetry data. Thank you for letting me loose in your labs and showing me how your equipment works.

A big thank you to Monica Garcia and Norman Macleod, my industrial supervisors at JM. Thank you for the many useful discussions and for being extremely helpful on all the methanol characterisation matters. I hope you have found the results from this research project as valuable as your guidance has been to my development. I would also like to thank the HTS team (Katie, Toby and Emily) for the samples and many useful conversations.

I would like to thank Dr Martin and Dr Vlad for generating the low-and-high resolution CXT images. I also thank Dr Chris for allowing me to use his FIB-SEM machine and then producing most of the SEM images for the methanol samples. Thank you to Jason and Kieran in the characterisation labs for all your help and setting up the Hg + DSC experiments.

I would also like to thank my experimental and gym buddy Kyro Baron. Kyro was the first person to show me how to analyse the rate of adsorption data and how to bench press properly in the gym too! Thank you for being a good source of friendship and a good collaborator. I thank my good friend Eisah Al-Ghanim for proofreading my entire thesis in under three days. I really appreciated this!!

Finally, I would like to thank my family, particularly my mother, for her continuous prayers and my brother Ali's support and encouragement during the 8+ years I was at university.

Contents

Abstract i

List of Publications and Presentations ii

Acknowledgements iii

Nomenclature viii

List of Figures xiv

List of Tables xv

1 Introduction and Thesis Outline 1
- 1.1 Introduction . . . 1
- 1.2 Methanol Synthesis Catalyst: A General Overview . . . 4
- 1.3 High-Temperature Water-Gas-Shift Catalyst . . . 7
- 1.4 Outline of thesis . . . 8

2 Porous Material Characterisation Techniques 10
- 2.1 Introduction . . . 10
- 2.2 Gas Adsorption . . . 11
  - 2.2.1 Adsorption Phenomena . . . 11
  - 2.2.2 Adsorption Isotherms and their Classifications . . . 12
  - 2.2.3 Gas Overcondensation . . . 14
  - 2.2.4 BET Surface Area Measurement . . . 15
  - 2.2.5 Gas Adsorption and Capillary Condensation . . . 16
  - 2.2.6 Hysteresis . . . 17
  - 2.2.7 The Adsorption or Desorption Isotherm . . . 18
  - 2.2.8 Mesoporous and Macroporous Pore Volume . . . 20
- 2.3 Mercury Porosimetry . . . 21
  - 2.3.1 Basic Theoretical Background . . . 21
  - 2.3.2 Pore Size Calculations from MIP . . . 22
  - 2.3.3 Hysteresis in Mercury Data . . . 23
  - 2.3.4 Mercury Entrapment . . . 26

2.3.5 Limitations of Mercury Porosimetry . . . 28
2.4 Integrated Mercury Porosimetry and Gas Sorption . . . 29
2.4.1 Introduction . . . 29
2.4.2 Previous Studies using Integrated Gas-Mercury Method . . . 30
2.5 Computerised X-ray Tomography (CXT) . . . 32
2.5.1 Background Theory . . . 32
2.5.2 Synchrotron CT and Linear Accelerators . . . 34
2.5.3 Workflow, Reconstruction and Image Processing . . . 34
2.5.4 CXT Applications . . . 35
2.5.5 Representative Elementary Volume . . . 38
2.6 Scanning Electron Microscopy (SEM) . . . 40
2.6.1 SEM Concept and Brief History . . . 40
2.6.2 FIB-SEM Lift-outs and Serial Sectioning . . . 42
2.7 Thermoporometry by Differential Scanning Calorimetry . . . 45
2.7.1 Background to Thermoporometry . . . 45
2.7.2 Determining the Gibbs-Thomson constant . . . 47
2.7.3 Selecting the Probe Liquid . . . 48
2.7.4 Hysteresis in Thermoporometry . . . 49
2.8 Conclusions . . . 51

3 Integration of multi-scale porosimetry and multi-modal imaging in the study of structure-transport relationships in porous catalyst pellets 52
3.1 Abstract . . . 52
3.2 Introduction . . . 53
3.3 Theory . . . 56
3.4 Materials and Method . . . 59
3.4.1 Samples studied . . . 59
3.4.2 Experimental Procedure . . . 59
3.4.3 Integrated Mercury Porosimetry and Gas Sorption . . . 59
3.4.4 Rate of Adsorption procedure . . . 61
3.4.5 Overcondensation gas sorption procedure . . . 62
3.4.6 Computerised X-ray tomography and dual-beam electron microscopy . . . 62
3.4.7 Low resolution computerised X-ray tomography (CXT) . . . 62
3.4.8 High resolution computerised X-ray tomography (CXT) . . . 63
3.4.9 Focussed ion beam-scanning electron microscopy (FIB-SEM) . . . 63
3.5 Results . . . 64
3.5.1 Imaging of empty spray-dried (SD) feed pellets . . . 64
3.5.2 Low resolution CXT . . . 64
3.5.3 High resolution CXT . . . 64
3.5.4 FIB-SEM imaging . . . 65
3.5.5 Imaging of empty roll-compacted (RC) feed pellets . . . 67
3.5.6 Low resolution CXT . . . 67
3.5.7 High Resolution CXT . . . 67

3.5.8 FIB-SEM imaging . . . 69
3.5.9 Mercury porosimetry . . . 69
3.5.10 Low resolution CXT imaging of pellets following mercury entrapment . . . 73
3.5.11 Gas Sorption and Overcondensation Isotherms . . . 73
3.5.12 Fragmented Pellets . . . 76
3.5.13 Serial Sorption of Nitrogen and Water . . . 81
3.5.14 Pore Size Distributions . . . 85
3.5.15 Rate of Adsorption . . . 85
3.6 Discussion . . . 91
3.7 Conclusion . . . 98

4 Automated Segmentation of X-ray and FIB-SEM Images of Methanol Synthesis Catalyst using Deep Learning Neural Networks 99
4.1 Introduction . . . 99
4.2 Materials and Image Acquisitions . . . 104
4.2.1 Samples Studied . . . 104
4.2.2 Integrated Mercury Porosimetry and CXT Imaging . . . 105
4.2.3 Low resolution computerised X-ray tomography (CXT) . . . 106
4.2.4 Focussed ion beam-scanning electron microscopy (FIB-SEM) . . . 106
4.3 Background on Artificial Neural Networks . . . 107
4.3.1 Deep Learning Neural Network Architecture . . . 107
4.3.2 Convolutional Neural Networks (CNNs) Architecture . . . 110
4.4 Deep Learning Image Segmentation Strategy . . . 112
4.4.1 Image Preprocessing . . . 112
4.4.2 Training Deep Learning CNNs . . . 114
4.5 Results and Discussion . . . 116
4.5.1 Fresh Pellets CXT Segmentation . . . 116
4.5.2 Reduced Pellets CXT Segmentation . . . 119
4.5.3 Segmentation of Mercury in Cracks . . . 119
4.5.4 Spent Pellet CXT Segmentation . . . 122
4.5.5 FIB-SEM Imaging Results . . . 124
4.5.6 Fresh SD FIB-SEM . . . 124
4.5.7 Fresh RC FIB-SEM . . . 125
4.5.8 Post-segmentation Quantification and Model Validations . . . 126
4.6 Conclusion . . . 127

5 Studies on the Effectiveness of Reduced and Spent Methanol Synthesis Catalyst 128
5.1 Introduction . . . 128
5.2 Materials and Methods . . . 129
5.2.1 Samples studied . . . 129
5.2.2 Integrated mercury porosimetry and gas sorption . . . 129
5.2.3 Rate of Adsorption (ROA) procedure . . . 130
5.2.4 Overcondensation gas sorption procedure . . . 130

5.2.5 Imaging using CXT and SEM . . . 130
5.3 Results . . . 131
5.3.1 CXT Imaging . . . 131
5.3.2 Imaging Empty Reduced SD and RC . . . 131
5.3.3 Imaging Empty Spent SD and RC . . . 132
5.3.4 FIB-SEM Imaging . . . 133
5.3.5 Mercury Porosimetry Data . . . 134
5.3.6 CXT imaging of pellets following mercury entrapment . . . 136
5.3.7 Gas Sorption Data . . . 139
5.3.8 Gas sorption scanning curve isotherms . . . 139
5.3.9 Overcondensation . . . 140
5.3.10 Pore Size Distribution . . . 142
5.3.11 Rate of Adsorption . . . 143
5.4 Discussion . . . 147
5.5 Conclusion . . . 151

6 Triangulation of Pore Structural Characterisation of Disordered Mesoporous Silica Using Novel Hybrid Methods Involving Dual-Probe Porosimetries 152
6.1 Abstract . . . 152
6.2 Introduction . . . 153
6.3 Theory . . . 157
6.3.1 Gas Sorption . . . 157
6.3.2 Adsorbed Films on Fractally Rough Surfaces . . . 157
6.3.3 Capillary Condensation . . . 157
6.3.4 Thermoporometry . . . 158
6.3.5 Small Angle X-ray Scattering (SAXS) . . . 159
6.4 Material and Methods . . . 160
6.4.1 Silica Materials . . . 160
6.4.2 Serial Water Pre-adsorption, Mercury Porosimetry, and Nitrogen Adsorption 160
6.4.3 Serial Adsorption of Nitrogen-Water-Nitrogen . . . 161
6.4.4 Dual Liquid DSC Thermoporometry using Water and Mercury . . . 162
6.4.5 Integrated Nitrogen Sorption and Mercury Porosimetry . . . 163
6.5 Results . . . 164
6.5.1 Adsorbent Characteristics . . . 164
6.5.2 Serial Nitrogen-Water-Nitrogen Adsorption . . . 164
6.5.3 Serial Water Pre-adsorption, Mercury Porosimetry, and Nitrogen Adsorption 170
6.5.4 Dual Liquid Mercury-Water DSC Thermoporometry . . . 172
6.5.5 Integrated Nitrogen Sorption and Mercury Porosimetry . . . 174
6.6 Discussion . . . 176
6.7 Conclusion . . . 179

7 Study of the Entrapment of Non-wetting Fluid in High Temperature Shift Catalyst 180
7.1 Introduction . . . 180

7.2 Materials and Method . . . 181
7.2.1 Samples studied . . . 181
7.2.2 Integrated mercury porosimetry and gas sorption . . . 182
7.2.3 Rate of Adsorption (ROA) procedure . . . 183
7.2.4 Imaging using CXT . . . 183
7.3 Results . . . 184
7.3.1 Imaging Empty Samples . . . 184
7.3.2 Mercury Porosimetry Data . . . 185
7.3.3 Mercury porosimetry Pore Size Distribution . . . 189
7.3.4 CXT Images of Pellets Following Mercury Porosimetry . . . 190
7.3.5 Gas Sorption . . . 195
7.3.6 Incremental Pore Volume . . . 197
7.3.7 Gas Sorption Pore Size Distribution . . . 199
7.3.8 Rate of Adsorption . . . 200
7.4 Discussion . . . 203
7.5 Conclusion . . . 204

Conclusion **205**
7.6 Conclusion . . . 205
7.7 Future Work . . . 209

Appendix A: Fresh Methanol Catalyst **210**

Appendix B: Triangulation of Pore Structural Characterisation **212**

Bibliography **216**

Nomenclature

Abbreviations

AFM	Atomic force microscopy
ANN	Artificial neural network
BET	Brunauer-Emmett-Teller
BJH	Barrett-Joyner-Halenda
CNN	Convolutional neural network
CPG	Controlled pore glass
CXT	Computerised X-ray tomography
DSC	Differential scanning calorimetry
FBP	Filtered back projection
FHH	Frenkel-Halsey-Hill
FIB-SEM	Focussed ion beam-scanning electron microscopy
HTS	High temperature shift
LDF	Linear driving force
MIP	Mercury intrusion porosimetry
MTC	Mass transfer coefficient
PSD	Pore size distribution
PUI	Pore utility index
RC	Roll compacted
REV	Representative elementary volume
ROA	Rate of adsorption
SAXS	Small angle X-ray scattering
SD	Spray dried
TEM	Transmission electron microscopy

Symbols

α	Constant
β	Exponent in universal scaling function=0.41
ΔH_f	Bulk enthalpy of fusion (J/g)
ΔP	Change in pressure (Psia)
ΔT_m	Melting point depression (K)
ϵ	Voidage fraction(porosity)

γ	Surface tension (N/m)
κ	Geometry parameter for pore meniscus
Λ	Effective network size
λ	Wavelength of radiation (Å)
μ	Linear attenuation coefficient
ν	Exponent in universal scaling function=0.88
ω	Feed particle size (μm)
ρ	Density (g/cc)
σ	Thickness of a monolayer (nm)
τ	Tortuosity
θ	Contact angle in degrees
φ	Scattering angle in degrees
ξ	Characteristic length-scale for the structure creating the scattering
A	Surface area of an adsorbed film (nm^2)
a	Diffusion penetration depth
B	Empirical constant related to heat of adsorption
C	Constant in the BET equation
D	Fractal dimension
d	Pore diameter (nm)
D_A	Diffusivity
G	Universal scaling function
I_0	X-ray beam energy (mA)
K	Mass transfer coefficient
K_{GT}	Gibbs-Thomson parameter
L	Lattice sizes
l_i	Pore length
M_0	Total adsorbed amount of gas for the adsorption pressure point
P	Pressure (Psia)
P_0	Saturated vapour pressure (Psia)
R	Universal gas constant
r_p	Pore radius (nm)
S	Surface area of the pellet (m^2)
t	Multilayer film thickness (nm)
T	Temperature (K)
T_m	Melting point (K)
T_m^∞	Bulk melting temperature (K)
V	Molar volume of adsorbate (cc/mol)
V_m	Monolayer capacity (cc/g)
V_p	Gurvitsch volume (cc)
W	Weight on artificial neural network connection
X^A	Accessibility
Z	Connectivity

List of Figures

1.1 World consumption of methanol 2016 4

2.1 Classification of IUPAC isotherms 12
2.2 Example of conventional and overcondensation desorption isotherms 14
2.3 Formal classification of hysteresis loops by IUPAC 17
2.4 Wardlaw and McKellar diagram showing MIP on glass micromdels 26
2.5 Mercury intrusion and extrusion according to ink-bottle theory 27
2.6 Schematic diagram showing integrated mercury porosimetry and gas sorption 29
2.7 Principles of computerised X-ray tomography. 32
2.8 Typical CXT scan workflow and image analysis procedure. 34
2.9 Electron-matter interactions signals generated 40
2.10 SEM and TEM schematic comparisons 41
2.11 FIB-SEM serial sectioning method 42
2.12 Example of FIB-SEM lift out stages for methanol pellet 43
2.13 Frozen and non-frozen probe liquid inside a pore. 46
2.14 Example of DSC melting endotherm for a dual-liquid probe. 48

3.1 A schematic representation of the gas-mercury-gas-imaging technique 60
3.2 2D radial cross-section slice CXT image of SD pellet 64
3.3 2D and 3D reconstruction and segmentation of SD 65
3.4 2D and 3D reconstruction of high resolution SD images 66
3.5 2D and 3D reconstructed grayscale FIB-SEM images and segmentation of SD 67
3.6 2D radial cross-section slice CXT image of RC pellet 68
3.7 2D and 3D reconstruction of high resolution RC images 68
3.8 2D and 3D reconstructed grayscale FIB-SEM images and segmentation of RC 69
3.9 Mercury intrusion and extrusion data for SD and RC feed particles 70
3.10 Mercury scanning curves for a whole SD and RC 71
3.11 2D and 3D reconstruction for whole SD post mercury intrusion 72
3.12 2D and 3D reconstruction for whole RC post mercury intrusion 74
3.13 Fresh SD isotherm and OC pre and post mercury intrusion 77
3.14 Fresh RC isotherm and OC pre and post 10,800 psia 78
3.15 Fresh RC isotherm and OC pre and post 14,700 psia 79
3.16 Fresh RC isotherm and OC pre and post 30,000 psia 80

3.17 Fresh SD isotherm and scanning curve up to 0.85 . . . 80
3.18 Fresh SD isotherm and OC post 21,000 and 30,000 . . . 81
3.19 Powdered sample isotherm and overcondensation . . . 82
3.20 Nitrogen sorption scanning loops for SD and RC . . . 83
3.21 Comparison of BJH PSDs for whole fresh SD and RC . . . 83
3.22 Conventional isotherms pre and post water adsorption . . . 84
3.23 BJH pore size distribution for scanning curves post Hg . . . 86
3.24 BJH pore size distribution for scanning curves post H2O . . . 87
3.25 MTC fractional decline comparisons for fresh SD . . . 89
3.26 MTC fractional decline comparisons for fresh RC . . . 90
3.27 Schematic showing interpretation of the Hg, CXT and OC data . . . 92
3.28 Pore utility index for the fresh SD and RC . . . 94
3.29 Fresh SD and RC tortuosity ratio against L . . . 95
3.30 Observed vs predicted tortuosity for the fresh SD and RC . . . 96

4.1 Traditional vs deep learning image segmentation . . . 101
4.2 CXT and FIB-SEM images of methanol synthesis catalyst pellet . . . 102
4.3 Flowchart of methanol synthesis samples studied . . . 104
4.4 Relationship between AI, ML, ANN and DL . . . 107
4.5 Schematic representation of an Artificial Neural Network (ANN) . . . 108
4.6 An example of activation functions . . . 109
4.7 An Example of a fully connected CNN architecture . . . 110
4.8 An Example of convolution operation in CNN . . . 111
4.9 Examples of max and average pooling operation in CNN . . . 112
4.10 A flowchart showing the overall image processing steps . . . 113
4.11 2D FIB-SEM image of fresh RC sample pre and post stripe removal . . . 114
4.12 Segmentation results and raw CXT images of an empty fresh SD sample . . . 116
4.13 Segmentation and raw CXT images of fresh SD with Hg up to 8,600 psia . . . 117
4.14 Raw CXT images and segmentation for fresh RC with Hg up to 8,600 psia . . . 118
4.15 Raw and segmented CXT images of an empty reduced SD sample . . . 120
4.16 Fracture mesh for measuring crack thickness . . . 121
4.17 Raw images and segmentation for reduced RC with Hg 3,800 psia . . . 122
4.18 Raw images and segmentation for spent RC with Hg up to 2,860 psia . . . 123
4.19 Raw images and segmentation for spent RC with Hg up to 2,860 psia . . . 124
4.20 Reconstructed FIB-SEM images and segmentation for fresh SD . . . 125
4.21 Reconstructed FIB-SEM images and segmentation for fresh RC . . . 126

5.1 Integrated mercury porosimetry and gas sorption sifting strategy. . . . 130
5.2 2D slice and 3D reconstruction for reduced SD and RC. . . . 131
5.3 2D slice and 3D reconstruction for spent SD and RC. . . . 132
5.4 2D and 3D reconstructed FIB-SEM of reduced SD and RC . . . 133
5.5 2D and 3D reconstructed FIB-SEM of spent SD and RC . . . 134
5.6 Mercury scanning curve for the reduced and spent pellets . . . 135

5.7 Kloubek scanning curves for the reduced and spent pellets . . . 136
5.8 Raw CXT images of the reduced SD and RC post 3800 psia . . . 137
5.9 Raw CXT images of the spent SD and RC post 2860 psia . . . 138
5.10 Nitrogen isotherms pre and post Hg for reduced and spent pellets. . . . 139
5.11 OC isotherms pre-post Hg for the reduced-spent pellets . . . 141
5.12 Change in incremental BJH PSD for the reduced and spent . . . 143
5.13 Rate of adsorption plots for the reduced and spent pellets . . . 144
5.14 Experiment observed MTC compared with Prager model MTC . . . 145
5.15 Mercury locations in pellets and MTC variation . . . 148
5.16 Reduced and spent SD and RC PUI plots . . . 148
5.17 Tortuosity ratio vs percolation lattice size for reduced and spent . . . 149
5.18 Experimental vs predicted tortuosity for methanol pellets . . . 150
5.19 Spent RC sample (2860 psia) with grid overlay measuring crack size . . . 151

6.1 Schematic diagram illustrating triangulation analysis . . . 156
6.2 Serial water pre-adsorption, mercury and nitrogen adsorption . . . 160
6.3 A schematic representation of integrated nitrogen and water . . . 161
6.4 Sketch showing dual-liquid DSC-thermoporometry procedure . . . 162
6.5 Silica C10 AFM images . . . 164
6.6 Silica C10 nitrogen isotherm before and after water adsorption . . . 165
6.7 Silica C10 water adsorption and desorption isotherms . . . 166
6.8 Plot of logarithm of monolayer capacity for water and others . . . 167
6.9 Fractal film plots for the nitrogen side and water . . . 169
6.10 Cumulative BJH PSD before and after water 0.914 . . . 170
6.11 Fractal film plots for the nitrogen side and water . . . 171
6.12 Silica C10 cumulative BJH and differential plot . . . 172
6.13 DSC melting curves for mercury and water for C10 . . . 173
6.14 Comparison of BJH PSD and DSC Hg contribution . . . 174
6.15 Silica C10 cumulative BJH and differential plot . . . 175
6.16 Comparison of DSC Hg contribution and BJH PSD (pre-post) . . . 175

7.1 CXT image of empty H1 and H2 pellets . . . 184
7.2 CXT image of empty H1 and H2 pellets . . . 185
7.3 Mercury porosimetry curves for the HTS pellets . . . 186
7.4 Kloubek scanning curves for the HTS pellets . . . 187
7.5 Whole and powdered HTS pellets mercury curves . . . 188
7.6 Whole and powdered HTS pellets mercury curves . . . 189
7.7 HTS pellet mercury PSDs for 5336 and 60000 psia. . . . 190
7.8 Raw images and segmentation result for H1 with Hg 1200 psia . . . 191
7.9 Raw images and segmentation result for H2 with Hg 1200 psia . . . 192
7.10 Raw images and segmentation result for H3 with Hg 1200 psia . . . 193
7.11 Raw images and segmentation result for H4 with Hg 1200 psia . . . 194
7.12 HTS pellets gas sorption isotherms before and after mercury . . . 196

7.13 Change in incremental pore volume plots for HTS pellets 198
7.14 HTS BJH PSD before and after mercury5336 psia 199
7.15 Rate of adsorption plots for the HTS pellets 200
7.16 Observed and expected MTC variation for the HTS pellets 201
7.17 HTS pellet pore network structure representations. 203

List of Tables

2.1 Parameters for Kloubek correlation 24

3.1 Fresh SD and RC whole sample characteristics 59
3.2 Fresh SD and RC whole sample pore size and volume 59
3.3 Fresh SD FIB-SEM volume fractions for 3 phases. 66
3.4 Fresh SD and RC percolation parameters, Z and L 75
3.5 Fresh SD MTC variations with increasing mercury saturations 88
3.6 Fresh RC MTC variations with increasing mercury saturations 88

4.1 Properties of samples studied SD and RC 104
4.2 Mercury porosimetry scanning curve pressure 105
4.3 Deep learning segmentation models used for CXT and SEM images 115

5.1 Freshly reduced and spent samples properties 129
5.2 Freshly reduced and spent samples pore sizes and volumes 129
5.3 Connectivity and lattice sizes for reduced SD and RC 142
5.4 Connectivity and lattice sizes for spent SD and RC 142
5.5 Variation in adsorption-corrected MTC for reduced and spent 146
5.6 Variation in adsorption-corrected MTC for reduced and spent 147

6.1 Fits of the fractal Porod law to SAXS 164
6.2 Fractal dimensions values for different adsorbent 167
6.3 Fractal dimensions before and after water adsorption 168
6.4 Relative pressures for serial water adsorption experiments 169

7.1 Process steps, reactions and catalysts for steam reforming 181
7.2 High temperature shift catalyst sample properties 181
7.3 High temperature shift pore sizes and volumes 182
7.4 Pore volumes lost due to mercury entrapment for HTS 196
7.5 Variation in adsorption-corrected MTC for H1-H3 202

Chapter 1

Introduction and Thesis Outline

1.1 Introduction 1
1.2 Methanol Synthesis Catalyst: A General Overview 4
1.3 High-Temperature Water-Gas-Shift Catalyst 7
1.4 Outline of thesis 8

1.1 Introduction

Heterogeneous catalysis is a fascinating but complex multidisciplinary science that is crucial to the energy, chemical, automotive, and pharmaceutical industries, as more than 90% of the chemical manufacturing processes involve catalysts at one stage or another.[1] Although advances in understanding of the working principles and dynamics of catalytic materials have been made, their origin and mechanistic functioning under realistic reaction settings remain significant research challenges for both academic and industrial scientists. The potential of intelligently designing pellets with specific active sites to selectively catalyse a chemical reaction with a high yield is quite appealing. First and foremost, it represents the most cost-effective and environmentally friendly method of producing the transportation fuels, materials, and chemicals we use every day. However, it is also critical to understand the interfacial chemistry between the gas or liquid phase and the catalytic surface at elevated temperatures and pressures.[2,3]

Modern heterogeneous catalysts are usually supported on microporous or mesoporous materials such as alumina or silica. These new support materials are selected or designed to have specific surface areas and pore sizes to control the delivery of reactant molecules to the active site and regulate local reactant concentrations.[4] For a chemical reaction to occur, the reactants and products must be transferred between the catalyst surface and the catalytically active sites inside the pellet. This diffusion process of the reactants and products can influence both the apparent activity of the catalyst and its deactivation behaviour. For many of the chemical reactions involv-

[1] G. Q. Lu and X. S. Zhao. *Nanoporous materials: science and engineering*. World Scientific, 2004.
[2] J. N. Armor. *Appl. Catal., A*, **222**: 407–426, 2001.
[3] J.M. Thomas and W.J. Thomas. *Appl. Catal., A*, 686, 1997.
[4] I. Chorkendorff and J. Niemantsverdriet. *Concepts of modern catalysis and kinetics*. Wiley, 2003.

ing heterogeneous catalysts, the effectiveness factor of the pellet is typically only ∼50 to 60% due to diffusion limitations.[5] This poor effectiveness factor is caused by high diffusional resistance, reducing the mass transfer rates. Many industrial processes operate under conditions such that the pore diffusion occurs in the Knudsen regime, and one way to lower the diffusional resistance in such cases is to introduce large pores into the pellet structure to provide better access to the centre of the pellet where smaller pores are located. However, an increased number of pervasive networks of large pores within the pellet might negatively impact pellet strength. Furthermore, the presence of large pores will lead to a decline in the catalyst specific activity as larger pores have a lower surface-to-volume ratio than smaller pores. Hence, there is often an optimum level and distribution of macroporosity, but this is a challenge that is currently facing the catalyst designer.[6]

Deep structural insight into the principles of heterogeneous catalysis and understanding of their performances can only be obtained by employing modern characterisation methods and appropriate *in-situ* reaction cells and measurement techniques.[7–10] Hence, pore structural characterisation is an important stage in designing new, more efficient catalysts. A careful understanding of the pore size distribution is critical for understanding the structure-transport relationship for highly complex porous catalysts. Determining an optimum combination of large and small pores for a particular reaction has led many workers to use computer simulations and various imaging modalities to understand catalyst performance.[11–13] However, no single imaging modality or simulation can visualise pores across all size scales, from nanopores to micron-sized macropores, in pellets exhibiting hierarchical or multi-scale porosity.[7,14] Additionally, the current computer powers are a long way from the levels necessary to employ full 3D reconstructions of a typical mesoporous catalyst pellet or run simulations of diffusion and reaction processes within the pellet, as a typical catalyst pellet has more than 10^{10} pores (or image volumes), each of which may have varied intrinsic characteristics and some type and degree of spatial correlation.[7] Therefore, there is a problem in establishing the specific influence that a particular aspect of the pore structure has on the overall mass transport within the pellet. The vast range of options means that purely empirical methods of process design are likely to be time-intensive and expensive for finding optimal conditions and parameters, and thus a more efficient, systematic approach is required.

The approach taken in this thesis is to develop an experimental method to directly 'filter out' certain pore sizes within the catalyst pellets and then study how important those pores were to the rate of mass transport before and after their removal. This technique uses mercury porosimetry scanning curves to progressively eliminate particular, chosen pore sizes from the transport network by filling them with mercury and then studying their importance to mass transport with nitrogen

[5] M. V. Twigg. *Catalyst handbook*. CRC Press, 2018.
[6] A. Nepryahin et al. *Chem. Eng. Sci.*, **152**: 663–673, 2016.
[7] S. P. Rigby. *Structural characterisation of natural and industrial porous materials: A manual*. Springer Nature, 2020.
[8] S. J. Gregg and K. S. Sing. *Adsorption, surface area and porosity.* 2nd. Academic Press, London, 1982.
[9] F. Rouquerol et al. *Adsorption by powders and porous solids.* Academic Press, London, 1999.
[10] S. Lowell et al. *Characterization of porous solids and powders: surface area, pore size, and density.* Springer, 2005.
[11] S. Prachayawarakorn and R. Mann. *Catal. Today*, **128**: 88–99, 2007.
[12] C. Rieckmann and F. Keil. *Chem. Eng. Sci.*, **54**: 3485–3493, 1999.
[13] S. Gheorghiu and M. Coppens. *AlChE J.*, **50**: 812–820, 2004.
[14] B. Bukowski et al. *Adsorption (Boston)*, **27**: 683–760, 2021.

gas sorption. The mercury porosimetry and nitrogen gas sorption experiment is combined with multi-modal imaging, employing both high and low-resolution CXT, together with FIB-SEM to visualise the spatial distribution of the blocked-out void space under study because the entrapped mercury is clearly visible in the images. The multi-modal imaging techniques could be used to improve interpretation of each other, as well as of the indirect pore characterisation methods, in addition to providing spatially-resolved information. This combined characterisation technique is called 'integrated mercury porosimetry & nitrogen gas sorption', and is an experimental method, in contrast to modelling efforts that use computer simulations on model structures to determine the importance of specific aspects of the pore structure to mass transport.[6] Using this technique, the key features of the void-space that control gas-phase uptake into the porous pellets can be determined, and their relationship to, for example, the fabrication process and raw materials, can be identified. Hence, this method could be used to inform the design and optimisation of the pellet manufacturing process.

The 'sifting' strategy used in this thesis was previously[6] applied to tabletted methanol synthesis catalyst pellets, made using roll compacted (RC) feed, and compacted to two different densities. It was found that cracks across the pellet and voids generated by the splintering of feed particle edges during compaction dominated mass transport. However, the pore structural characterisation was limited due to the use of solely conventional gas sorption procedures to investigate the void space left accessible following mercury entrapment and the limitations of the CXT imaging used. In this thesis, however, the gas overcondensation technique will be employed to expand the range of pore sizes that can be evaluated up to very large macropores. The gas overcondensation method used in this thesis thus overcomes previous failings[6] with missing the largest macropores within the methanol catalyst pellets using both conventional nitrogen gas adsorption and mercury porosimetry. As a result of gas overcondensation, the whole boundary desorption isotherm has become available for use in percolation modelling, which would not have been feasible with conventional adsorption isotherms. Additionally, the gas overcondensation allows us to model the macroscopic structure of the catalyst pellets studied by using three-dimensional, random pore bond networks. This is achieved by determining two characteristic parameters for the structure: connectivity, Z and lattice sizes, L. The parameters Z and L can be obtained from percolation analysis of gas sorption data using a method based on that developed by Seaton.[15]

The complexity that can arise from the application of indirect pore characterisation methods to disordered materials, such as pore-to-pore co-operative effects and the assumptions made to probe a pore size, has led, in recent years, to the study of other characterisation methods, such as thermoporometry by differential scanning calorimetry (DSC). The thermoporometry characterisation method is significantly less developed than gas sorption and mercury porosimetry. However, it is possible to conduct a novel thermoporometry experiment with multiple, immiscible probe liquids within the same sample simultaneously, e.g., mercury and water. This hybrid experiment enables the confrontation of data from multiple techniques for the same sample, allowing parameter calibration and phase transition mode selection to be performed. Thermoporometry also offers a range of advantages over gas sorption and mercury porosimetry that are currently not being

[15] N. A. Seaton. *Chem. Eng. Sci.*, **46**: 1895–1909, 1991.

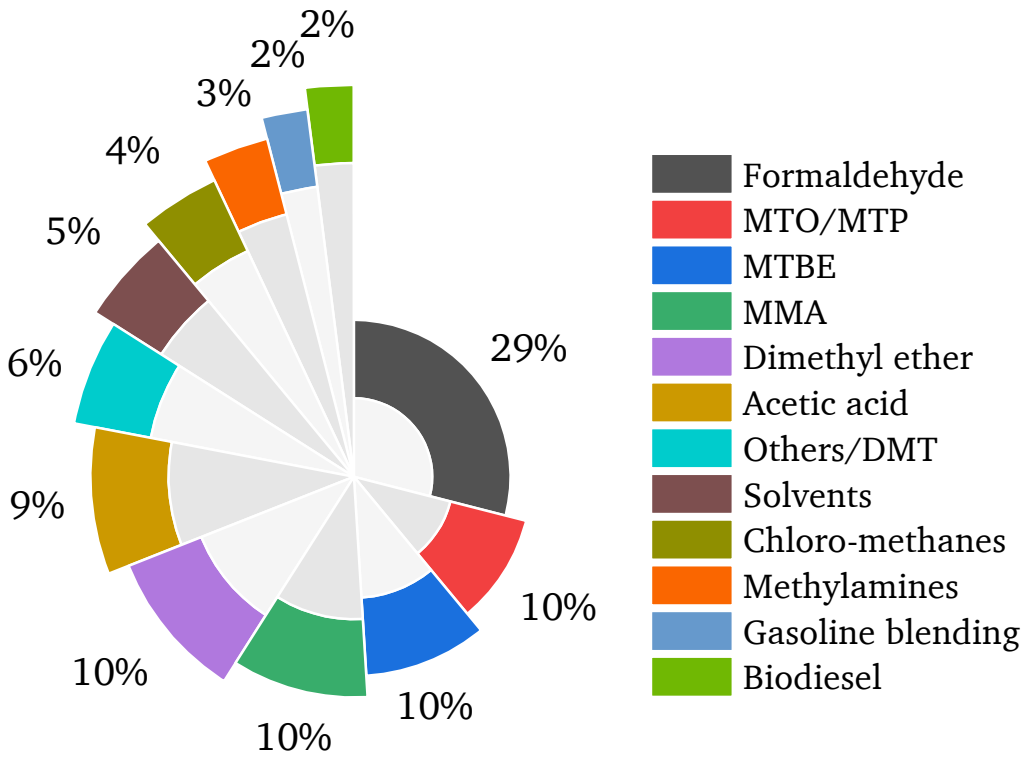


Figure 1.1: World 2016 consumption of methanol by end use (IHS, 2016).

exploited. When compared to porosimetry or gas sorption, thermoporometry requires less time for sample preparation, which might possibly improve high-throughput pore characterisation.[7]

This thesis will examine a range of catalyst pellets and catalyst-support materials, including methanol synthesis catalysts, high-temperature shift pellets, and silica catalyst support (C10) made by the sol-gel method. It will focus on improving the fundamental understanding of the structure-transport relationship of the catalyst pellets and validating the pore space characterisation from the different indirect methods.

1.2 Methanol Synthesis Catalyst: A General Overview

Catalyst processes based on hydrogen or synthesis gas (H_2 and CO) are among the most basic and vital processes in providing food, fuel, and chemical resources for the people of this planet. Methanol and ammonia synthesis were among the first and arguably most important large-scale catalytic processes created in the early twentieth century. These were among the first high-volume, high-pressure catalytic processes.[5] Methanol, in particular, is one of the top ten most important bulk synthetic organic chemicals manufactured worldwide.[16] It is a colourless, flammable, and volatile polar liquid at ambient conditions (298.15 K, 101.325 kPa), with a freezing point of -97.6°C and boiling point of 64.6°C. The largest fraction (∼25 to 35%) is used in the manufacture

[16] Z. Zhong, U. Etim, and Y. Song. *Front. Energy Res.*, 239, 2020.

of formaldehyde. Other established applications are shown in Figure 1.1 and include the synthesis of chloromethanes, methanol-to-olefins (MTO), tert-Butylmethylether (MTBE) as a fuel additive to enhance antiknock properties of gasoline, dimethyl ether (DME), acetic acid, as well as use as a solvent.[16,17] Furthermore, the use of methanol as a fuel, either pure or in combination with gasoline, is becoming increasingly widespread. Methanol can be utilised in direct methanol fuel cells (DMFC) or steam-reformed, and the released hydrogen functions as the fuel in reformed methanol fuel cells (RMFC).[18–20]

Until the early 1900s, methanol was produced by the destructive distillation of wood. However, in 1923 BASF(Germany) produced the first synthetic methanol on a large scale.[21] Their catalytic process, a high-pressure synthesis on a Zn/Cr_2O_3 catalyst at 300-400°C and about 300 atm, was only the second large-scale application of catalyst and high-pressure technology. The Zn/Cr_2O_3 catalyst and the high-pressure process were the most effective available technology for the next 40 years until the 1966 development by Imperial Chemical Industries (ICI) of the substantially more active Cu/ZnO alumina catalyst, which enabled methanol to be synthesized at much lower temperatures and pressure, (i.e. 220-300°C and 50-100 atm).[22] The new low-pressure process featured the following advantages: (1) reduced compression power, (2) longer catalyst life, (3) larger capacity, single-train converter designs, and (4) an improvement in the productivity from 770 to 1120 tons of methanol per million cubic meters of natural gas.[23] Currently, most of the methanol plants in the world use the more active low-temperature Cu catalyst while operating at an optimum pressure of 80-100 atm.[17] In 2020, over 90 methanol plants were operating worldwide with a combined production capacity of about approximately 110 million metric tons per year (almost 138 billion litres).[24] According to IHS, global methanol demand reached 75 million metric tons in 2015 (91 billion litres), driven mainly by emerging energy applications for methanol which now account for 40% of methanol consumption.

Methanol synthesis reaction is a combination of two exothermic equilibrium reactions: conversion of CO to CO_2 via the water-gas-shift process, followed by hydrogenation of CO_2 to CH_3OH[25–27]:

$$\begin{aligned} &\mathrm{CO} + \mathrm{H_2O} \rightarrow \mathrm{H_2} + \mathrm{CO_2}; && \Delta H_{298\ \mathrm{K}} = -41.2\ \mathrm{kJ/mol} \\ &\mathrm{CO_2} + 3\mathrm{H_2} \rightarrow \mathrm{CH_3OH} + \mathrm{H_2O}; && \Delta H_{298\ \mathrm{K}} = -49.5\ \mathrm{kJ/mol} \end{aligned} \tag{1.1}$$

When these reactions are added, one obtains a net stoichiometric equation for reaction of CO to

[17] M. Bertau et al. *Methanol: the basic chemical and energy feedstock of the future*. vol. 1 Springer, 2014.
[18] A. Sonthalia et al. *Clean Technol. Environ. Policy*, 1–25, 2021.
[19] T. Veziroğlu and S. Şahi. *Energy Convers. Manage.*, **49**: 1820–1831, 2008.
[20] S. Verhelst et al. *Prog. Energy Combust. Sci.*, **70**: 43–88, 2019.
[21] A. Mittasch, M. Pier, and K. Winkler. *Germany Patent DE415686*, **24**: , 1923.
[22] D. Sheldon. *Johnson Matthey Technol. Rev.*, **61**: 172–182, 2017.
[23] L. Wade et al. *Kirk-Othmer Encycl. Chem. Technol.*, 16, 1981.
[24] M. Alvarado. *IHS Chem. Bull.*, **3**: 10–11, 2016.
[25] K. Klier. *Adv. Catal.*, **31**: 243–313, 1982.
[26] J. Yoshihara et al. *Catal. Lett.*, **31**: 313–324, 1995.
[27] G.C. Chinchen et al. *Appl. Catal.*, **30**: 333–338, 1987.

CH_3OH:

$$CO + 2H_2 \rightarrow CH_3OH; \quad \Delta H_{298\ K} = -90.6\ kJ/mol \tag{1.2}$$

It is observed that under typical commercial conditions, methanol synthesis reactions occur at near equilibrium and that conversion in methanol synthesis increases with decreasing temperature and increasing pressure. The reverse water-gas shift process is a reaction that is closely related to the synthesis of methanol from carbon dioxide and hydrogen. This reaction is an integral part of the methanol synthesis reaction, but it is also promising in carbon dioxide recycling via syngas creation, allowing the manufacture of valuable chemicals whilst reducing our dependence on fossil resources.[28]

The first-generation methanol synthesis catalyst, Zn/Cr_2O_3, was developed by BASF[21] in 1923, and because of its relatively low activity, it required commercial operation at 300 atm and about 300-400°C. Blasiak[22] invented a significantly more active Cu/ZnO alumina catalyst in 1947, which was successfully used in high-pressure methanol synthesis plants in Poland throughout the 1950s and 1960s. In the 1960s, ICI research led to the development of a low-pressure, low-temperature synthesis based on a similar Cu/ZnO alumina catalyst,[22,29] which allowed operation at 230-260°C and 50-100 atm, thereby favouring higher CO/CO_2 conversions. This catalyst has an optimal yield at a composition of around 75% Cu (relative to Cu + Zn)[30]; hence a typical commercial catalyst may comprise 60-70 wt% CuO, 20-30 wt% ZnO, and 5-10 wt% alumina. The typical commercial catalyst is a complex multiphase material, and its properties are affected by preparation method, pre-treatment, and operating conditions. ZnO is a textural and chemical promoter in the form of small crystallites. It facilitates the formation of small Cu crystallites at its surface and thermally stabilises Cu against sintering. In addition, ZnO scavenges sulphur and chlorides, thereby limiting the poisoning of Cu. ZnO may also neutralise acidic sites in the alumina phase, reducing dimethyl ether formation. The alumina stabilises ZnO and Cu crystallites against sintering. The Cu/ZnO alumina catalyst has a very high selectivity for methanol (> 99.5%).[30] Cu-containing catalysts on other supports may have substantially lower selectivity; for example, the yield for Cu/Cr_2O_2 is around 96-97%, 2% CH_4, 0.5% higher alcohols, and 0.5-1% dimethyl ether.[31]

The Cu/ZnO/ alumina catalyst is commonly produced by controlled-pH precipitation from an aqueous solution comprising Cu, Zn, and Al salts, and the preparation of an active, selective methanol catalyst requires careful choice of materials and precise control of precipitation, calcination and activation conditions.[31] Commercial catalysts are charged to the reactor as cylindrical pellets with diameters ranging from 5-8 mm. Cu/Zn alumina catalysts typically have bulk densities of 2.0-2.4 g/cm^3.

[28] J. Yao et al. *Front. Chem.*, 442, 2018.
[29] P. Davies et al. *UK Patent*, , 1965.
[30] G. Ertl, H. Knözinger, and J. Weitkamp. *Handbook of heterogeneous catalysis*. Wiley-VCH, 2008.
[31] C. H. Bartholomew and R. J. Farrauto. *Fundamentals of industrial catalytic processes*. John Wiley & Sons, 2011.

1.3 High-Temperature Water-Gas-Shift Catalyst

Hydrogen can be produced using electrolysis, but on a large industrial scale, it is more cost-effective to liberate it from water using a chemical reducing agent or to generate it through partial oxidation of hydrocarbons in the presence of steam and oxygen. The most common method is steam reforming, in which a hydrocarbon fuel is used as a reducing agent for the steam.[31] In modern plants, natural gas composed mainly of methane (CH_4) is most commonly used. Alternatively, petroleum naphtha could also be used depending on feedstock availability. Steam reforming of hydrocarbons involves six different catalytic process steps, including desulphurisation, primary steam reforming, secondary steam reforming, high-temperature water-gas-shift, low-temperature water-gas-shift and methanation.[5] In this section, however, we will mainly focus on the high-temperature water-gas-shift process and the associated catalyst.

$$\mathrm{CO} + \mathrm{H_2O} \rightarrow \mathrm{H_2} + \mathrm{CO_2}; \quad \Delta H_{298\ \mathrm{K}} = -41.2\ \mathrm{kJ/mol} \tag{1.3}$$

The high-temperature water-gas-shift (HT-WGS) reaction in Equation (1.3) is a reversible exothermic chemical process with significant technological implications for decreasing carbon monoxide concentration during natural gas or liquid hydrocarbon to hydrogen conversion.[32] The high-temperature WGS reaction increases the hydrogen concentration while lowering the CO concentration from 10-13% to 2-3% in the exiting gas from the secondary reformer.[5] The reaction occurs in an adiabatic fixed-bed water-gas-shift reactor operating at 350-500°C and 20-30 atm. The equilibrium conversion of CO and H_2O to CO_2 and H_2 increases sharply with decreasing temperature and therefore, the feed gas is cooled to 350-400°C before it is passed through the HTS catalyst which is composed of Fe_3O_4 and Cr_2O_3.[31] BASF originally developed this catalyst in 1915 as part of the ammonia synthesis process.[21]

The HTS catalyst is relatively inexpensive and resistant to sintering (Cr_2O_3 acts as a stabiliser to minimise the sintering of the active iron oxides).[33] The catalyst also offers protection for the low-temperature shift catalyst by adsorbing residual sulphur-or-chlorine-containing compounds which have passed through the pre-purification step. A typical freshly prepared catalyst comprises 90% Fe_2O_3 and 10% Cr_2O_3.[34] The Fe-Cr oxide catalyst can be prepared by precipitation or co-precipitation of the mixed iron and chromium nitrates with ammonia hydroxides. Alternatively, iron hydroxide gel is prepared and then impregnated with chromium nitrate solution using the impregnation method.[31,35] Since the high temperature WGS reaction experiences high-pore-diffusional resistance at temperatures 350°C and 30 atm, relatively small (8 x 4 mm, diameter x length) catalyst tablets with a surface area of 60-80 $\mathrm{m^2\,g^{-1}}$ are used to maximise reaction rates.[34] The active form of the catalyst is magnetite Fe_3O_4, produced by the reduction of hematite with hydrogen and carbon monoxide from the process gas stream.[31] Although the HT-WGS catalytic process based on iron-chromium oxides is widely known in the industry, some Cr^{3+} is converted to Cr^{6+} during manufacturing. This hexavalent chromium is highly toxic and harmful to both hu-

[32] C. Rhodes, G. Hutchings, and A. Ward. *Catal.*, **23**: 43–58, 1995.
[33] R. Keiski and T. Salmi. *Appl. Catal. A-Gen.*, **87**: 185–203, 1992.
[34] F Domka, A Basinska, and R Fiedorow. *Surf. Technol.*, **18**: 275–282, 1983.
[35] A. Pereira et al. *J Mol. Catal. A Chem.*, **281**: 66–72, 2008.

mans and the environment. Therefore, Cr^{6+} is classified as a Class I carcinogen, and its presence is restricted under the UK and EU regulations.

1.4 Outline of thesis

This section aims to outline the thesis structure so that the readers know how to navigate through the chapters. The central theme of the entire thesis is to help improve the understanding of the structure-transport relationship of porous materials and porous material characterisation. The work in the thesis was partly sponsored by Johnson Matthey (JM), a leading chemicals and catalyst manufacturer. As a part of the detailed investigation of the methanol synthesis catalyst pellets, an extensive array of experiments were performed both at the University of Nottingham and JM laboratories in Billingham, Teesside. The work in this thesis will focus on the issues raised in the introduction section and is divided into eight chapters:

- **Chapter 1: Introduction**
- **Chapter 2: Porous material characterisation techniques**
  This chapter will explore the literature on the porous material characterisation methods used in this thesis. The theoretical concepts underpinning each characterisation method and the benefits and drawbacks of mercury porosimetry, gas sorption, thermoporometry, scanning electron microscopy, and computerised X-ray tomography will be covered in the literature review portion.
- **Chapter 3: Integration of multi-scale porosimetry and multi-modal imaging**
  This chapter will look at fresh methanol synthesis pellets made from two different types of feed material, spray-drying and roll-compaction. It will investigate how the various pelleting fabrication methods affect the finished pellet properties. The starting feed particles, as well as the finished tablets, will be examined. The gas overcondensation method will also be employed in this work to expand the range of pore sizes that can be examined up to very large macropores. Furthermore, multi-modal imaging using both high and low-resolution CXT, as well as FIB-SEM, will be employed to improve interpretation of each other, as well as of the indirect pore characterisation techniques.
- **Chapter 4: Automated segmentation of X-ray and FIB-SEM images of methanol synthesis catalyst using deep learning neural networks**
  This chapter discusses an image segmentation approach based on a deep learning neural network that can automatically segment both CXT and FIB-SEM images of methanol synthesis catalyst pellets. The automated segmentation approach used in this chapter is based on a software called Dragonfly ORS, which employs the popular TensorFlow deep learning engine in a user-friendly image processing environment.
- **Chapter 5: Studies on the effectiveness of reduced and spent methanol catalyst pellets**
  This chapter will focus on freshly reduced and spent methanol synthesis pellets made from two different types of feed material, spray-drying and roll-compaction. It will first investigate

how the various pellet fabrication methods affect the finished pellet properties and then the effects of the cracks on pellet performance, diffusion, and percolation. The gas overcondensation method will also be employed to expand the range of pore sizes that can be examined up to very large macropores. Similarly, multi-modal imaging using low-resolution CXT, as well as FIB-SEM, will be used to improve the interpretation of each other, as well as of the indirect pore characterisation techniques.

- **Chapter 6: Triangulation of pore structural characterisation of disordered mesoporous silica using novel hybrid methods involving dual-probe porosimetries**
  This chapter will present a novel thermoporometry by DSC method that uses three separate probe liquids (nitrogen, water and mercury) to validate pore space characterisations obtained through various indirect methods. This hybrid experiment allows us to compare data from multiple techniques for the same sample, allowing parameter calibration and phase transition mode selection to be performed.

- **Chapter 7: Study of the entrapment of non-wetting fluid in HTS catalyst pellets**
  This chapter uses the integrated nitrogen-mercury-nitrogen experiment to study the pores that entrap mercury in high-temperature shift catalyst pellets. The mercury-containing samples will also be imaged using X-ray tomography to understand the spatial distribution of mercury within the void spaces. The chapter will also present the sample preparation and data analysis from each characterisation technique.

- **Section 7.5: Conclusion**
  The final section will give a general conclusion to the thesis and will propose any future work recommendations.

Chapter 2

Porous Material Characterisation Techniques

2.1 Introduction 10
2.2 Gas Adsorption 11
2.3 Mercury Porosimetry 21
2.4 Integrated Mercury Porosimetry and Gas Sorption 29
2.5 Computerised X-ray Tomography (CXT) 32
2.6 Scanning Electron Microscopy (SEM) 40
2.7 Thermoporometry by Differential Scanning Calorimetry 45
2.8 Conclusions 51

2.1 Introduction

The structure-transport properties of porous materials are strongly affected by how the pores of various sizes are distributed within the material. Hence, the use of characterisation methods to probe porous media is a critical step in obtaining information on pore sizes and pore structures. This has long been recognised in the catalysis field and will be the focus of the literature review sections of this thesis. An essential aspect of the characterisation methods is to understand how the geometry and interfacial confinement due to the pore structure affect a variety of phenomena, including effective diffusivity, adsorption/desorption, capillary condensation and tortuosity. When it comes to understanding porous materials, the key areas of interest include porosity, pore sizes, pore-to-throat size ratio, pore connectivity, and pore volumes. Obtaining accurate measurements for all these features requires more statistically representative and accurate characterisation methods.

This chapter will review the literature on the characterisation methods for porous materials used throughout this thesis. New characterisation approaches and new models of interpretations of the findings are constantly being developed with new applications. However, this chapter will mainly focus on the pore-structure characterisation techniques that have been established and are widely utilised in catalysis science. It begins by looking at gas adsorption, one of the most widely used methods for studying pore-structure in materials containing micro-and-mesopores.

Gas adsorption provides a wide range of information, including surface area, pore-volume, pore sizes and porosity. The gas adsorption section will look at the fundamentals of gas adsorption phenomena, the different types of isotherms, and their classification. This section will also present the causes of hysteresis between the adsorption and desorption branches and the different theories proposed to explain the presence of hysteresis in gas sorption.

The second technique discussed is mercury porosimetry, which has been shown to be an effective method for characterising a wide range of porous materials with pore diameters spanning over several orders of magnitude (i.e. 3 to 500 nm). In mercury porosimetry, the entrapment of the non-wetting fluid is observed after the intrusion and extrusion cycles. The entrapped mercury can be imaged using computerised X-ray tomography (CXT) to study the spatial distribution of mercury within the void spaces of the material.

Each characterisation method has its own set of benefits and drawbacks, which may or may not be complementary. A crucial part of this chapter is the section on integrated methods, which outlines attempts to carefully integrate different techniques together, force a confrontation between their conclusions, and generate a comprehensive, self-consistent interpretation of all data from each method. The integrated method discussed here will mainly focus on gas adsorption and mercury porosimetry. However, other hybrid methods can also be found in other thesis chapters.

Other characterisation methods discussed in this chapter include scanning electron microscopy (SEM) and thermoporometry, which can be performed either by differential scanning calorimetry (DSC) or nuclear magnetic resonance (NMR). In each method, the basic principles, as well as their applications and limitations, are mentioned.

2.2 Gas Adsorption

2.2.1 Adsorption Phenomena

Adsorption is a surface phenomenon brought about by the interaction between molecules from a fluid phase (the adsorbate) and solid (the adsorbent). Hence, adsorption can be defined as the enrichment of atoms, ions or molecules in the vicinity of an interface.[9] The molecule enrichment is due to the binding interaction between the adsorbate and adsorbent. The adsorption process is a dynamic equilibrium process since the molecules are both arriving on the surface and escaping to the gaseous phase at all times. The return of molecules to the gaseous phase due to the breakage of the adsorption bond is known as desorption. There are two kinds of forces involved in an adsorption process, which give rise to either physical adsorption (physisorption) or chemical adsorption (chemisorption).[9] Physisorption occurs by the formation of London-van der Waals[9] forces between the adsorbate and adsorbent, whereas chemisorption is relatively irreversible process that leads to the formation of chemical compounds. The distinction between chemisorption and physisorption, however, is not always sharp. This thesis will largely focus on physical adsorption processes, and therefore, any details of chemical adsorption are omitted.

[9] F. Rouquerol et al. *Adsorption by powders and porous solids.* Academic Press, London, 1999.

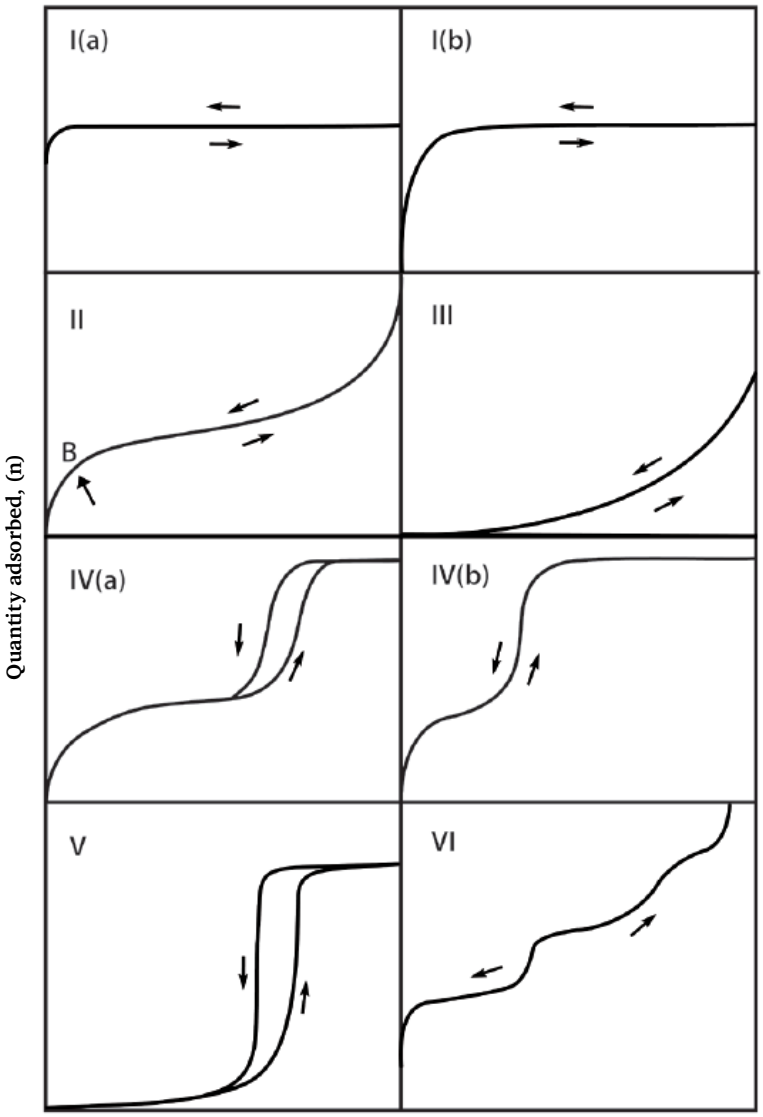


Figure 2.1: Classification of IUPAC isotherms [8].

2.2.2 Adsorption Isotherms and their Classifications

When investigating the porous material's pore structure and surface area using gas adsorption, the first step is to determine what is known as the adsorption (or desorption) isotherm.[8,9] Adsorption isotherm is a measure of the molar quantity of gas taken up, or released, at a constant temperature by an initially clean solid surface as a function of gas pressure.[8] The isotherm measurement experiment for nitrogen is usually conducted at a cryogenic temperature, e.g. Liquid nitrogen at $77.35\,\mathrm{K}$ and $1\,\mathrm{atm}$. The quantity of gas adsorbed is conventionally expressed as its volume at standard temperature and pressure ($0\,^{\circ}\mathrm{C}$ and $760\,\mathrm{mmHg}$ STP). In contrast, the pressure is expressed as a relative pressure, which is the actual gas pressure over the saturated vapour pressure of the

[8] S. J. Gregg and K. S. Sing. *Adsorption, surface area and porosity.* 2nd. Academic Press, London, 1982.

adsorbing gas at the experiment's temperature. A graph of the quantity of gas adsorbed against the corresponding relative pressure constitutes an adsorption (or desorption) isotherm, and the shape of the plot reveals much about the structure of the material studied. The quantity of gas adsorbed by solid mass is a function of equilibrium temperature, pressure, and the solid-gas interaction's nature. As gas molecules are adsorbed onto the solid, the surface of the solid becomes more densely populated until a monomolecular layer (monolayer) of gas is formed. The monolayer extends the solid surface and will attract additional gas molecules by van der Waal's interactions. This process of the gas molecules continually adsorbing, with increasing pressure, is known as the multimolecular (multilayer) adsorption.[9]

Experimentally observed adsorption isotherms can be classified into six different types (I-VI) according to the International Union of Pure and Applied Chemistry (IUPAC) definitions. A schematic representation of these types is shown in Figure 2.1. Some subclasses of these adsorption isotherms have been introduced recently, but they are not discussed in this thesis.[9]

Types I isotherms are also referred to as Langmuir isotherms. These isotherms are characteristic for microporous material showing micropore filling but no multilayer adsorption. At low pressures, the quantity of gas adsorbed increases rapidly, corresponding to the micropores filling. However, the isotherm displays a horizontal plateau at higher pressures, which means all the pores are filled with adsorbed gas.

Type II isotherms are characterised by the formation of a monolayer coverage at low pressures and multilayer coverage at high pressures, but no hysteresis. These isotherms are observed in disperse, non-porous or only in macroporous solids, and the BET equation or its generalisations usually describe them.

Type III isotherms are typically obtained when the interaction between adsorbent and adsorbate on a non-porous or macroporous adsorbent is weak, e.g. mercury adsorption on charcoal. At low pressures, the adsorption is not favourable because of the charcoal surface's non-polar (hydrophobic) nature. At high pressures, the adsorption is due to capillary condensation in the mesopores. A true Type III isotherms are not common.[9]

Type IV isotherms display a similar shape to type II isotherms in the lower regions that correspond to the formation of a monolayer and subsequent multilayer of adsorbate molecules. However, the quantity of gas adsorbed increases sharply at higher relative pressures. This sharp increase corresponds to capillary condensation filling the mesopores. The isotherm then levels off at high pressures indicating a complete pore filling. Type IV exhibits a hysteresis between the adsorption and desorption branches when the pressure is reduced. More details on *hysteresis* are discussed in the following sections.

Type V isotherms are similar to type III isotherms as they display weak interactions between the adsorbent and adsorbate. These isotherms exhibit a sharp gas uptake with increasing relative pressure associated with capillary condensation. As with type IV, the presence of capillary condensation causes the formation of a hysteresis loop between the adsorption and desorption branches

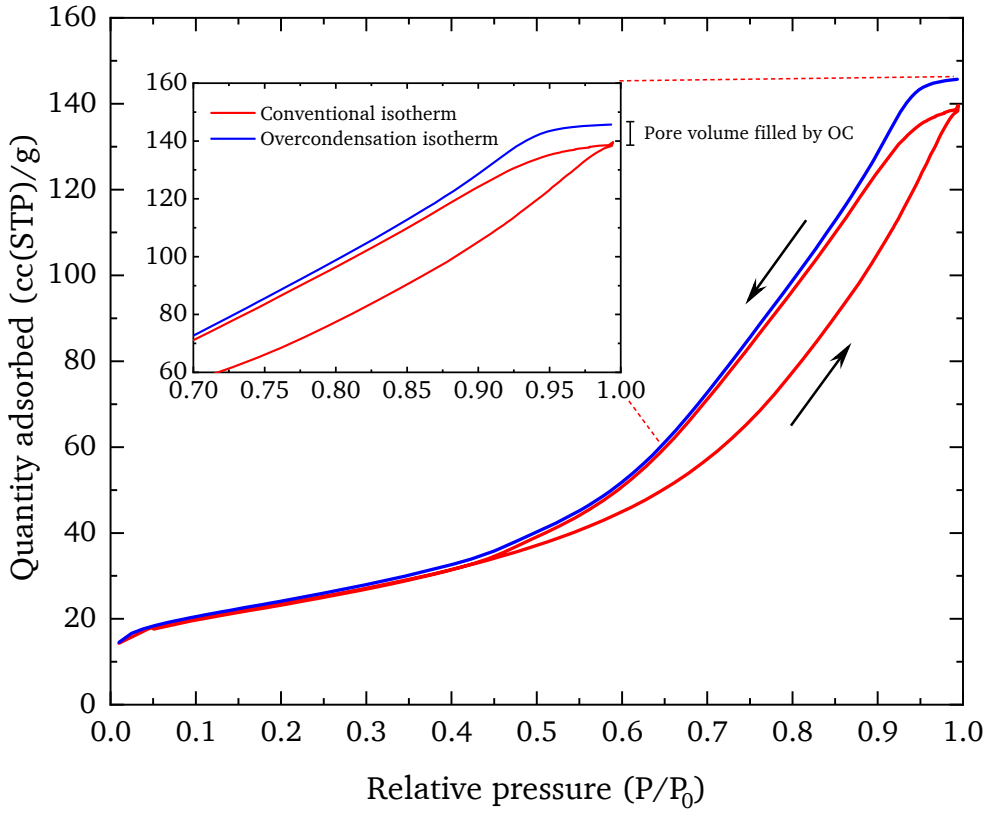


Figure 2.2: A typical example of conventional and overcondensation desorption isotherm for the fresh methanol synthesis catalyst. The inset shows zoomed version of the same graph to highlight the pore volume filled by overcondensation.

when the pressure is reduced.

Type VI isotherms are typical of multilayer adsorption on a uniform non-porous surface. These isotherms are commonly referred to as *stepped isotherms* because of the layered build-up of gas where each layer is completed before the next one starts. Type VI isotherms produced with argon or krypton on graphitised carbon blacks at liquid nitrogen temperatures (77 K) are among the best examples.[36]

2.2.3 Gas Overcondensation

Conventional gas sorption machines are designed to stop the adsorption isotherms before the sample chamber completely floods with liquid nitrogen. Because of this limitation, the isotherm can terminate before pore filling occurs for samples with large pores, making conventional gas sorption experiments unsuitable for the complete characterisation of samples with larger macropores. To overcome this limitation and determine the true pore-volume of a sample using gas sorption experiment, the overcondensation (OC) method can be used. This method was first introduced by

[36] M. Thommes et al. *Pure Appl. Chem.*, **87**: 1051–1069, 2015.

Aukett and Jessop,[37] and a similar method were later adopted by Murray.[38] The OC experiment involves "flooding" the sample chamber and submerging the sample under liquid nitrogen to investigate any porosity beyond the instrument upper limit for the conventional isotherm ($P/P_o > 0.995$). Once the sample is fully submerged in liquid nitrogen and total pore filling is achieved, pressure in the tube is lowered to just below the saturated vapour pressure of nitrogen such that the bulk condensate vapourises completely while all the sample internal porosity is liquid-filled. Once this step has been achieved, the first data point on the overcondensation desorption isotherm can be measured. This point corresponds to the total pore volume of the sample. Figure 2.2 shows a typical example of a conventional and overcondensation isotherms for a fresh methanol pellet.

2.2.4 BET Surface Area Measurement

Data from the gas adsorption experiment can be used to obtain the surface area of porous media using a model for monolayer or multi-layer. Two commonly used models are the Langmuir[39] and Brauneur–Emmett–Teller[40] (BET) equations. For completeness, the BET surface area measurements will be quoted for all samples tested in this research project; however, the work of this thesis will not study surface areas in depth. The Langmuir isotherm equation is given by:

$$\frac{V}{V_m} = \frac{BP}{1 + BP} \tag{2.1}$$

and it assumes that adsorption only arises in a monolayer, where all molecules are in contact with the adsorbent surface.Where V is the amount adsorbed, V_m is the monolayer capacity, P is the pressure, and B is an empirical constant related to heat of adsorption. The monolayer capacity is obtained by linearising the Langmuir isotherm equation in the form of:

$$\frac{1}{v} = \frac{1}{v_m B}\frac{1}{P} + \frac{1}{v_m} \tag{2.2}$$

If a data obeys the Langmuir model, a plot of $^1/_V$ against $^1/_P$ should be a straight line. The monolayer capacity is then reciprocal of the y-intercept. The specific surface can be obtained by multiplying the monolayer capacity by the effective cross-sectional area of a single gas molecule, in this case, nitrogen, which is $0.162\,\mathrm{nm}^2$. A second method to characterise the surface area of porous materials has been described by Brauner, Emmett and Teller (BET) and is commonly referred to as the BET method.[40] The BET model expands on the Langmuir[39] model by allowing for multi-layer adsorption, where the adsorbate can adsorb upon itself, as well as on the adsorbent surface. The BET equation in its most general form is given by:

$$\frac{P/P_0}{V\,(1 - P/P_0)} = \frac{1}{V_m C} + \frac{C - 1}{V_m C}\frac{P}{P_0} \tag{2.3}$$

[37] P. N. Aukett and C. A. Jessop. *Fundamentals Ads.*, 59–66, 1996.
[38] K. L. Murray, N. A. Seaton, and M. A. Day. *Langmuir*, **15**: 6728–6737, 1999.
[39] I. Langmuir. *J. Am. Chemi. Soc.*, **40**: 1361–1403, 1918.
[40] S. Brunauer, P. Emmet, and E. Teller. *J. Am. Chemi. Soc.*, **60**: 309, 1938.

where C is an empirical constant related to the heat of adsorption of the gas onto the solid. If the gas sorption data obeys the BET model, a plot of $P/P_0/V(1-P/P_0)$ against P/P_0 should be linear. The BET monolayer is then obtained from the reciprocal of the slope and y-intercept of this plot. To calculate the BET surface area, the monolayer capacity is then multiplied by the cross-sectional area of one molecule, similar to Langmuir calculation. The typical range of relative pressure fittings recommended for the BET equation is 0.05–0.3, which is the region that is typically linear. The BET model, thus, does not apply to microporous solids because the surface potentials of the two opposite walls of a micropore overlap, making it less easy to distinguish between the adsorbed phase and the bulk gas.[7]

2.2.5 Gas Adsorption and Capillary Condensation

The catalyst pellets studied in this thesis have mesopores and display type IV isotherms. For this reason, the region of the isotherm most interest is the capillary condensation and evaporation region. The capillary condensation and evaporation regions are associated with gas condensing in the pores to become a liquid-like state or the liquid in the pores evaporating, respectively. The pressure at which these processes happen can be related to a pore size by the Kelvin equation,[8] which is given by:

$$\ln\left(\frac{P}{P_0}\right) = -\frac{2\gamma V_m \cos\theta}{RT\,(r_p)} \tag{2.4}$$

where P is the equilibrium vapour pressure, P_0 is the saturation vapour pressure, r_p is the pore radius, and V_m is the molar volume of the adsorbate. The Kelvin equation predicts that for increasing pore sizes, the pressure necessary for condensation increases.[10] The contact angle in Equation (2.4) depends on the adsorbate-adsorbent interaction and can vary between $0°$ and $180°$. If the adsorbate fully wets the surface, the contact angle is assumed to be $0°$, which means the $cos\theta$ term becomes 1. When the Kelvin equation is used to calculate the pore sizes, the multilayer adsorption thickness must be accounted for correctly, as this could contribute as much 18% of the pore diameter for a cylindrical pore that fills at relative pressure 0.8. The thickness of the layer can be found from the following Equation (2.5)[9]:

$$t = \sigma_m \frac{n}{n_m} \tag{2.5}$$

Where n is the amount adsorbed, n_m is the amount adsorbed for a monolayer, and σ_m is the thickness of a monolayer.

A change to the Kelvin equation may be made to account for the multilayer adsorption thickness, t, and is given by:

$$\ln\left(\frac{P}{P_0}\right) = -\frac{2\gamma V_m \cos\theta}{RT\,(r_p - t)} \tag{2.6}$$

[7] S. P. Rigby. *Structural characterisation of natural and industrial porous materials: A manual*. Springer Nature, 2020.
[10] S. Lowell et al. *Characterization of porous solids and powders: surface area, pore size, and density.* Springer, 2005.

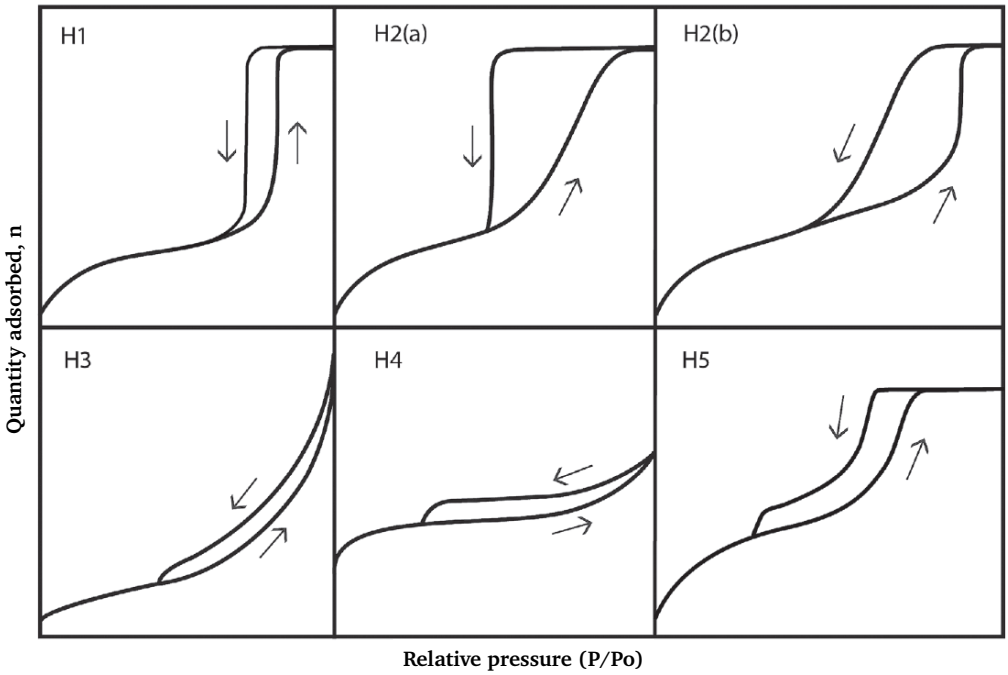


Figure 2.3: Formal classification of hysteresis loops by IUPAC [8].

In gas adsorption, nitrogen at 77 K is commonly used as an adsorbate for the characterisation of porous materials, in which case universal *t*-layer thickness equations have been proposed by different workers, including that of Halsey,[41] Harkins-Jura,[42] and de Boer.[43] However, these equations were obtained based on the adsorption on non-porous materials with a flat surface, and therefore the thickness layer will not be the same in a mesoporous solid that have walls with severe curvature. The impact of the surface curvature on the film thickness at a given pressure was addressed in the analysis of Barrett, Joyner and Halenda.[44] The algorithm proposed by Barrett, Joyner and Halenda, commonly known as BJH, is used to calculate pore size distribution in gas adsorption.

2.2.6 Hysteresis

Experimental gas sorption data for Type IV isotherms are characterised by the presence of a hysteresis loop, as was mentioned earlier in Section 2.2.2. The desorption branch of a Type IV isotherm does not necessarily follow the same path as the adsorption branch, and a gap forms between the two branches. This gap is known as 'hysteresis', and it denotes the presence of a non-equilibrium process.[7] The points on the isotherm plot where the adsorption and desorption curves first meet at either edge of the hysteresis regions are referred to as the hysteresis closure points, and the relative pressure at which the loop closes depends on the adsorbate type and temperature. When nitrogen is used as the adsorbate, the lower hysteresis closure point is approximately $P/P_o = 0.40$,

[41] G. Halsey. *J. Chem. Phys.*, **16**: 931–937, 1948.
[42] W. Harkins and G. Jura. *J. Am. Chem. Soc.*, **66**: 1362–1366, 1944.
[43] J. C. P. Broekhoff and J. H. de Boer. *J. Catal.*, **10**: 377–390, 1968.
[44] E. P. Barrett, L. G. Joyner, and P. P. Halenda. *J. Am. Chem. Soc.*, **73**: 373–380, 1951.

and it is rare to have a hysteresis loop that has not closed at the lower end by $P/P_o = 0.30$.[45]

For Type IV isotherms, there are several forms of hysteresis loops that may be divided into different categories, including the de Boer[46] and IUPAC[36] classifications. De Boer presented five fundamentally different types of hysteresis loops based on the steepness of the adsorption and desorption branches. Types A, B, and E are the most common in practice, whereas Types C and D are not frequently encountered. De Boer argued that the hysteresis process during physical adsorption occurs almost exclusively in mesopores rather than macropores or micropores and that experimental hysteresis loops may result from the combination of two or more types of pores.

The International Union of Pure and Applied Chemistry (IUPAC) has proposed a new classification of hysteresis loops, which is seen in Figure 2.3. The IUPAC classification contains de Boer's suggested hysteresis Types A, B, and E, corresponding to the new hysteresis Types H1, H3, and H2, respectively. H1 loops are frequently formed from materials with cylindrical pores, or spheroidal particles, of relatively homogeneous pore sizes, such as MCM-41 and SBA-15. Materials with ink-bottle-shaped pores tend to produce H2 loops; however, pore size and shape distribution are not well defined. Types H3 and H4 loops are associated with adsorbent having slit-shaped pores.[8]

The extensive research on adsorption hysteresis by Everett[8] and colleagues has indicated that the phenomenon is temperature-dependent.[8] As a result, most hysteresis loops shrink in size as the temperature rises for adsorption experiments on mesoporous controlled-pore glass,[47] and MCM silica.[48,49] The following section will discuss the literature work on the origins and causes of hysteresis that have been presented over the past century.

2.2.7 The Adsorption or Desorption Isotherm

When it comes to pore analysis calculations, the presence of the hysteresis loop in Type IV isotherms adds a layer of complexity. This is because there are two relative pressures corresponding to a given quantity of gas adsorbed within the hysteresis loop, with the lesser value always sitting on the desorption isotherm. Therefore, the fundamental concern is whether to use the hysteresis loop's adsorption or desorption branch for pore size determination. It has been suggested that the desorption branch should, with certain exceptions, be used for pore size calculations as the relative pressures on the desorption isotherm correspond to the more stable adsorbate conditions. Many researchers have used the desorption branches of nitrogen isotherms for pore structure analysis, and the agreement between the cumulative surface area of the pore walls and the surface area calculated using the BET method has been proposed as the primary basis for the correctness of their analysis.[8,10] Cranston and Inkley,[50] on the other hand, employed both the adsorption and desorption branches in their analysis and discovered that for the majority of the adsorbents they

[45] K. K. Aligizaki. *Pore structure of cement-based materials*. Taylor & Francis, 2006.
[46] J. H. de Boer, A. V. Heuvel, and B. G. Linsen. *J. Catal.*, **3**: 268–273, 1964.
[47] G. H. Findenegg. *Adv Chromatogr*, **383**: , 1992.
[48] M. Thommes, R. Köhn, and M. Fröba. *App. Surf. Sci.*, **196**: 239–249, 2002.
[49] K. Morishige and Y. Nakamura. *Langmuir*, **20**: 4503–4506, 2004.
[50] W. Cranston and A. Inkley. *Determination of pore structures from nitrogen adsorption isotherms.* 1957. 143–154

examined, the adsorption branch produced surface areas that were more consistent with the BET surface area than the desorption branch.

Several different theories have been proposed to explain the causes of hysteresis and the differences between the state of the adsorbate during adsorption and desorption. Most of the older, classic theories made use of the Kelvin equation[8–10,51] to explain the causes of hysteresis, including that of Zsigmondy,[9] who was the first to suggest that hysteresis was due to a difference in the contact angles of the condensing and evaporating liquid. The 'ink-bottle theory' first proposed by Kraemer[52] and later modified by McBain[53] was another early theory that gained a great deal of attention. McBain's[53] model is based upon the concept of pore blocking, commonly known as the ink bottle pore model. According to McBain's model, the larger pore body is filled at high relative pressures during adsorption, but it cannot empty during desorption until the narrow neck of the pore empties at low relative pressures first. However, once the narrow pore neck has been filled at low relative pressure, his model cannot explain how condensation might occur inside the wider pore body.

The mechanism of meniscus formation has also been used to provide more general explanations of hysteresis in both the adsorption and desorption processes.[46,47,54–60] Foster[54] suggested that hysteresis is caused by a delay in meniscus formation. According to this theory, pores do not always contain dead ends from which condensation might begin, unlike the ink-bottle pore studied by McBain.[53] Instead, the pores might be through pores that are open on both ends. Because there is no flat surface for a hemispherical meniscus to develop in such a pore, the condensation process is 'delayed'. However, as the pressure increases, the adsorbate forms a multilayer on the pore wall that becomes bigger. The multilayer eventually bridges the pore gap, and a meniscus with a hemispherical shape forms and spreads through the pore. On the other hand, the desorption is not delayed since a hemispherical meniscus has already developed at the pore's end, and as a result of this, Foster concluded that the desorption process was in equilibrium.

Foster's idea was later expanded by Cohan[55] who quantified the pressure at which adsorption would occur in an open-end cylindrical pore using Equation (2.7). Cohan proposed that a difference in meniscus formation is involved in the condensation and evaporation processes in an open-ended pore. According to this theory, condensation is governed by the initial formation of a cylindrical meniscus, which is followed by the development of two hemispherical menisci once the pore has been filled. As a result of the different meniscus geometries, the adsorption and desorption processes occur at different relative pressures, causing hysteresis. This explanation

[51] T. William. *Philos. Mag.*, **42**: 448–452, 1871.
[52] E. O. Kraemer. *Tran. on Phys. Chem.*, **42**: 1661, 1931.
[53] J. W. McBain. *J. Am. Chem. Soc.*, **57**: 699–700, 1935.
[54] A. G. Foster. *Trans. Faraday Soc.*, **28**: 645, 1932.
[55] L. H. Cohan. *J. Am. Chem. Soc.*, **60**: 433–435, 1938.
[56] J. H. De Boer, Van D. H., and B. G. Linsen. *J. Catal.*, **3**: 268–273, 1964.
[57] D. H. Everett and W. I. Whitton. *Trans. Faraday Soc.*, **48**: 749–757, 1952.
[58] D. H. Everett and F. W. Smith. *Trans. Faraday Soc.*, **50**: 187–197, 1954.
[59] D. H. Everett. *Trans. Faraday Soc.*, **50**: 1077–1096, 1954.
[60] D. H. Everett. *Trans. Faraday Soc.*, **51**: 1551–1557, 1955.

of hysteresis, where the adsorption and desorption processes have a different meniscus geometry, is referred to as single pore hysteresis. The Cohan theory was widely accepted until Everett and Haynes[58] demonstrated that the process is oversimplified since a long cylindrical film is less stable than an analogous unduloid with uniform mean curvature and the same quantity of material.

$$\ln\left(\frac{P}{P_0}\right) = -\frac{\gamma V_m \cos\theta}{RT\,(r_p - t_c)} \tag{2.7}$$

2.2.8 Mesoporous and Macroporous Pore Volume

Gas adsorption data can also be used to obtain the specific pore volume of porous media. The adsorption isotherm can have a flat plateau at the top of the isotherm plot for certain materials. In these cases, the ultimate amount adsorbed can then be converted to specific pore volume by using the Gurvitsch rule:

$$V_P = 1.547^{-3} V_a \tag{2.8}$$

where V_p is the volume of liquid adsorbate in cm^3 and V_a the volume of adsorbed gas in cm^3(STP). The V_p value is typically known as the *Gurvitsch volume*.[61,62]

However, for some materials, the isotherm plot does not create a plateau at the top of the curve, and the adsorption isotherm branch is still rising vertically at the highest relative pressures achieved by the conventional experiments. For these materials, the over-condensation experiment can be used to determine the pore-filling volume of the condensed phase. Further details on the over-condensation experiment are described in detail elsewhere in Chapter 3 in the thesis.

[61] L. Sliwinska and H. Davis. *Ambix*, **34**: 81–88, 1987.
[62] J. C. Broekhoff. *Stud. Surf. Sci. Catal.*, **3**: 663–684, 1979.

2.3 Mercury Porosimetry

2.3.1 Basic Theoretical Background

While conventional gas adsorption may be used to evaluate the pore network properties of materials with micro-and mesopores, a different characterisation method must be used for macropores because of the limitations on the upper pore size that can be probed with conventional gas sorption machines.[7] The International Union of Pure and Applied Chemistry (IUPAC)[63,64] provided an overview of several techniques that may be used for macropore analysis, including liquid intrusion methods such as contact porosimetry, capillary flow porosimetry, and mercury porosimetry. Among these techniques, mercury porosimetry[65–70] is still regarded as the state of the art method for characterisation of macroporous materials and is frequently used for pore size analysis of various materials, including catalysts. The main advantage of this technique is that it allows pore size analysis to be performed in a quick and reproducible manner across an extensive range of mesopore and macropore sizes (from 3.6 nm to 500 um).[65] Unlike gas sorption, where the adsorbate wets the adsorbent, liquid metals such as mercury do not wet most porous materials. Hence, a droplet of mercury on a solid flat surface will form a ball with a contact angle greater than $90°$, and hydraulic pressure is required to force it into pores. Washburn[71] derived a simple relationship, better known as the Washburn equation, that relates the pores sizes and the pressure required to enter the pores.

Drake and Ritter[72] built the first mercury intrusion porosimetry (MIP) instrument in 1945, where they tested a variety of porous materials by penetration of mercury into pores. Their device was initially capable of penetrating pores as small as $20\,\mathrm{nm}$ in radius, and then $2\,\mathrm{nm}$ a few years later. The availability of pressurised hydraulic instruments in 1960 has made the development of the mercury porosimetry technique easier to the extent that it is now possible to determine a wide variety of pore structure parameters such as pore size distribution, specific surface area, total pore volume and density. Despite the variety of modifications, most of the current porosimetry instruments still use a similar concept as the first one built by Drake and Ritter.

The pressure required to force mercury into pores is calculated from a special case of the Young-Laplace[9] equation shown below:

$$\Delta P = -\gamma \left(\frac{1}{r_1} + \frac{1}{r_2} \right) \tag{2.9}$$

[63] J. Rouquerol et al. *Pure Appl. Chem.*, **84**: 107–136, 2011.
[64] J. Rouquerol et al. *Microporous Mesoporous Mater.*, **154**: 2–6, 2012.
[65] H. Giesche. *Part. Part. Syst. Charact.*, **23**: 9–19, 2006.
[66] J. Van Brakel, S. Modrý, and M. Svatá. *Powder Technol.*, **29**: 1–12, 1981.
[67] N. Wardlaw and M. McKellar. *Powder Technol.*, **29**: 127–143, 1981.
[68] L. Moscou and S. Lub. *Powder Technol.*, **29**: 45–52, 1981.
[69] J. Kloubek. *Powder Technol.*, **29**: 89–97, 1981.
[70] S. Rigby et al. *J. Colloid Interface Sci.*, **240**: 190–210, 2001.
[71] W. E. Washburn. *Phys. Rev.*, **18**: 206–209, 1921.
[72] L. C. Drake and H. L. Ritter. *J. Ind. Eng. Chem.*, **17**: 787–791, 1945.

Where r_1 and r_2 are the radii of the curvature of the mercury-gas meniscus and γ is the surface tension between the pore wall and mercury. Cylindrical pores are a common pore geometry assumption in mercury porosimetry. When mercury is forced into a cylindrical pore, it creates a spherical interface and, hence both radii, r_1 and r_2, are equal and Equation (2.9) can now be simplified to:

$$\Delta P = \frac{2\gamma}{r} \tag{2.10}$$

Introducing the contact angle, θ between mercury and the pore walls (defined as $>90^\circ$ for non-wetting fluids), the final equation becomes:

$$\Delta p = \frac{-2\gamma \cos\theta}{r_p} \tag{2.11}$$

Equation (2.11) is commonly referred to as the 'Washburn equation' after Edward W. Washburn, who was the first to use this expression to measure pore sizes. The Washburn equation provides a simple relationship to convert the mercury pressure into a pore size. The Washburn equation assumes that mercury's contact angle and surface tension are independent of the pressure applied to intrude mercury into the pores. The value of surface tension of mercury depends on several factors, including temperature. Drake and Ritter[72] initially used a surface tension value of $0.485\,\mathrm{N/m}$, which is the value commonly accepted by most researchers at $25\,^\circ\mathrm{C}$. Any larger variation of the surface tension is usually due to mercury contamination, and therefore, it is recommended to use fresh (triple distilled) mercury for all the measurements.

The contact angle value used in the Washburn equation directly influences the calculated pore size; hence, the appropriate contact angle values for a given sample must be obtained.[73] The value of the contact angle typically depends upon surface chemistry and roughness.[74] Drake and Ritter measured the contact angle for a variety of materials and found it to be between 130° and 140°. For this reason, values between 130° and 140° are commonly used. The contact angle could also be measured directly for each sample by using either mercury contact anglo-meter or sessile drop test experiment.[7] In a sessile drop test, the sample is first turned into powder and compacted into a flat surface. A drop of mercury is then placed on top of the compacted powder, and the shape is examined under a microscope. The image of the mercury drop on a flat surface is then digitised, and the contact angle is measured as the tangent at the point of contact. Despite these direct measurements, it is important to note that the contact angle varies greatly. For example, contact angles of 122° to 148° have been found for 'identical' system of mercury on a glass sample.[65]

2.3.2 Pore Size Calculations from MIP

Pore sizes and pore volumes are the two most prominent results from a mercury porosimetry analysis. Pore sizes are directly obtained from the Washburn[71] equation by using the appropriate

[73] J. G. Robert and S. M. Raouf. *Powder Technol.*, **29**: 53–62, 1981.
[74] R. N. Wenzel. *J. Phys. Colloid Chem.*, **53**: 1466–1467, 1949.

values for the mercury's contact angle and surface tension. However, pores sizes obtained from basic mercury porosimetry should not be interpreted as the cavity sizes but rather as the biggest entry or throat opening into the pores. As a result, the pore sizes obtained by mercury porosimetry are always smaller than the comparable pore sizes reported by micrographs.[65]

2.3.3 Hysteresis in Mercury Data

The MIP instrument records data as the volume of mercury that penetrates the sample against the corresponding pressure. This plot is commonly known as the cumulative intrusion volume curve. Drake and Ritter[72] observed that the volume-pressure relationship obtained during intrusion is different from the volume-pressure relationship during extrusion. Additionally, a certain amount of mercury remains trapped in the sample after the pressure is reduced to atmospheric pressure at the end of the experiment. The retraction of mercury from the sample when the pressure is lowered to atmospheric pressure reveals two phenomena: hysteresis between intrusion and extrusion and entrapment of mercury inside the pores. Hysteresis is observed where the intrusion branch of the plot does not follow the same route as the extrusion branch, and there is a gap between the two branches.[7]

The appearance of hysteresis between the cumulative intrusion-extrusion curves is a universal feature observed in nearly all samples tested during the MIP experiment.[9,73,75–82] There are at least two known causes of hysteresis between mercury intrusion and extrusion branches. The first one is *contact angle hysteresis*, which occurs when the values of the product $\gamma \cdot \cos\theta$ differ for advancing and retreating menisci. The second one is *structural hysteresis*, where different aspects of the pore structure control the pressures at which intrusion and retraction processes occur.[7] Different theories have been proposed to explain the presence of hysteresis between the two MIP branches; however, no single theory can provide a definite explanation of all the experimentally observed effects.

Contact angle hysteresis arises due to the differences between the advancing and receding contact angles of mercury.[80,83] A substantial amount of work detailed in the literature has shown that surface tension and contact angle values can change depending on pore size,[75] the nature of the surface,[68] or whether the mercury is advancing or retreating.[66,75,79,80,83] Liabastre et al.[84] were some of the earliest researchers to investigate the causes of contact angle hysteresis, where they studied the intrusion of mercury into controlled pore glass (CPG). These researchers used microscopy to get values for the diameters of the pores in the glasses and compared their results

[75] J. Kloubek. *Powder Technol.*, **29**: 89–97, 1981.
[76] J. Kloubek. *Powder Technol.*, **29**: 63–73, 1981.
[77] L. S. Merrick. *J. Pharm. Sci.*, **80**: 376–379, 1991.
[78] N. Wardlaw, M. McKellar, and L. Yu. *Carbonates Evaporites*, **3**: 1, 1988.
[79] S. Lowell and J. Shields. *Powder Technol.*, **38**: 121–124, 1984.
[80] S. Lowell and S. Joan. *J. Colloid Interface Sci.*, **80**: 192–196, 1981.
[81] R. W. Smithwick and E. L. Fuller. *Powder Technol.*, **38**: 165–173, 1984.
[82] S. P. Rigby and P. I. Chigada. *Langmuir*, **26**: 241–248, 2010.
[83] I. Chatzis and F. Dullien. *Powder Technol.*, **29**: 117–125, 1981.
[84] A. Liabastre and C. Orr. *J. Colloid Interface Sci.*, **64**: 1–18, 1978.

Table 2.1: Parameters for the advancing and retreating meniscus for Kloubek correlation in Equation (2.13).

	A	B	Range of validity (nm)
Intrusion	-302.533	-0.739	6-99.75
Extrusion	-68.366	-235.561	4-68.5

to those obtained via the Washburn equation by assuming fixed values for the surface tension and contact angle. In order to retrieve information about a porous medium from mercury intrusion and extrusion curves, it is essential to deconvolve the two types of hysteresis. This may be accomplished by analysing the raw mercury porosimetry data using semi-empirical alternatives to the Washburn Equation, known as Kloubek correlation, which has been proposed by Kloubek.[75] Kloubek used the data from the work by Liabastre and Orr[84] to determine the relationships for the variation of the contact angle and surface tension, as a function of pore radius, and obtained the expression below:

$$\gamma \cos\theta = A + \frac{B}{r} \tag{2.12}$$

where A and B are constants whose values are determined by whether the mercury meniscus is advancing or retreating. Table 2.1 lists the values of these constants obtained for the controlled pore glasses, as well as their pore size ranges of application.

Rigby et al.[85,86] derived an empirical relationship between intrusion pressure (in MPa) and the pore radius (nm) for mercury intrusion and retraction by inserting Equation (2.12) into the Washburn equation (Equation (2.11)), and obtained the following relationship for intrusion and extrusion, respectively.

$$r = \frac{302.533 + \sqrt{91526.216 + 1.478p}}{p} \tag{2.13}$$

$$r = \frac{68.366 + \sqrt{4673.91 + 471.122p}}{p} \tag{2.14}$$

The above expressions have the advantage of taking into account the changes in the contact angle and surface tension as the mercury meniscus radius is reduced. However, these equations are empirical in origin, and their use leads to experimental errors in the pore size estimation of around ∼4-5%.[86] The Kloubek correlation has been used to analyse the raw mercury porosimetry data for both a whole and a fragmented sample of several different batches of sol-gel silica spheres by Rigby et al.[85–90] It was found that, for the whole pellet samples, the Kloubek method leads to a partial superposition of the intrusion and extrusion curves at smaller pore sizes, but no superposi-

[85] S. P. Rigby. *Stud. Surf. Sci. Catal.*, **144**: 185–192, 2002.
[86] S. Rigby et al. *Appl. Catal., A*, **238**: 303–318, 2003.
[87] S. Rigby and K. Edler. *J. Colloid Interface Sci.*, **250**: 175–190, 2002.
[88] S. Rigby, R. Fletcher, and S. Riley. *Appl. Catal., A*, **247**: 27–39, 2003.
[89] S. Rigby, R. Fletcher, and S. Riley. *Chem. Eng. Sci.*, **59**: 41–51, 2004.
[90] S. Rigby et al. *Chem. Eng. Sci.*, **61**: 7579–7592, 2006.

tion was observed in the larger pore sizes, and both hysteresis and entrapment were still present at larger pore sizes. Rigby et al.[87] interpreted the findings as to the complete deconvolution of the contact angle, leaving the intrusion and extrusion curves entirely driven by structural hysteresis. On the other hand, the Kloubek[85] correlations showed a complete superposition of the intrusion and retraction curves when samples of the sol-gel spheres were broken into fragments with a particle size of $\sim$30-40 μm. This indicated that the contact angle hysteresis had been entirely removed using the Kloubek correlation. Additionally, it showed that no structural hysteresis or mercury entrapment was now taking place either. A pore structure where it is possible to remove structural hysteresis by fragmentation of the sample is a macroscopically heterogeneous pore structure, where long-range pore size correlations are present.[87]

Rigby et al.[86,90] established that Kloubek correlation could be used without any modifications for some sol-gel silica materials with the same surface fractal dimension as the CPG material used by Liabastre[84] and obtain superposition of the intrusion and extrusion curves. However, if no superposition is achieved, the values of A and B can be adjusted until it is possible to obtain a complete superposition of the intrusion and extrusion curves within the experimental errors. If a complete superposition is achieved, the values of A and B employed to achieve the superposition are assumed to be valid for that particular sample.[87,90]

Lowell[91] proposed a different theory to explain the causes of hysteresis. This theory treats pores as wells of potential energy. Mercury atoms are larger than nitrogen and argon atoms, and once inside a pore, they interact with the pore walls and is trapped in a potential well of energy. The pore potential theory, which is also referred to as the *energy barrier theory*, explains mercury entrapment and hysteresis independent of the pore shape. During the extrusion stage, the mercury column is under tension because of pore potential and can snap off if the pore radius is very small and the pore potential is very high. Smaller pores require less energy to break the mercury column than larger ones, as they act as deep potential wells due to their smaller cross-sectional area and proximity to the pore walls.[79]

[91] S. Lowell and S. Joan. *J. Colloid Interface Sci.*, **90**: 203–211, 1982.

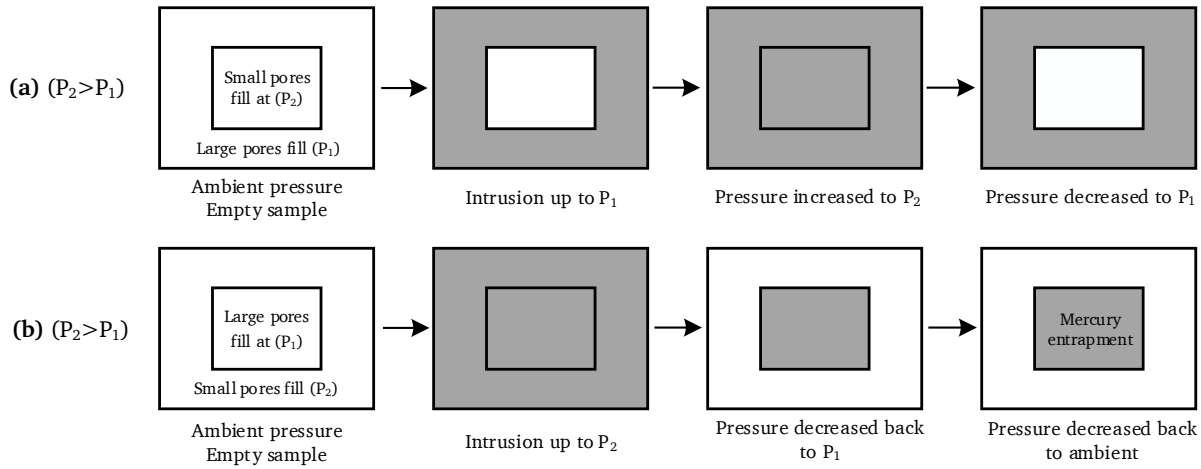


Figure 2.4: A schematic diagram showing the results of mercury porosimetry experiment on glass micromodels by Wardlaw and McKellar [67].

2.3.4 Mercury Entrapment

Many workers[67,79,80,88,90,92–95] have conducted a wide range of experiments to explain the causes of mercury entrapment, which can easily be recognised when the retraction curve does not give a zero volume. Wardlaw and McKellar[67] carried out detailed experimental work to determine the source of mercury entrapment. These workers conducted mercury porosimetry experiments on different micromodels consisting of a network of capillaries etched in a glass. In one micromodel, the network was a non-random system composed of smaller pores that occurred within isolated larger pores, as shown in Figure 2.4a. Wardlaw and McKellar observed that mercury preferentially filled the larger pores first when mercury was introduced into the empty model, and as the pressure was raised higher, mercury then entered the clusters of smaller pores next. Once the pressure was reduced, it was observed that mercury extruded from the smaller pores first. The mercury retreated from the rest of the network when the mercury pressure was reduced further. In a second glass micromodel, which was made up of isolated clusters of larger pore elements within a continuous network of smaller pores, no mercury entered the structure until the pressure reached the level needed to penetrate the smaller pore elements. In this second micromodel, shown in Figure 2.4b, the sample became saturated once mercury was introduced into the model. When the mercury pressure was subsequently reduced, the mercury first withdrew from just the smaller pore elements. However, by the time the pressure was decreased below the threshold for emptying the clusters of bigger pore elements, the mercury had already been disconnected by the snap-off effect, and significant residual mercury was retained in the bigger pores. These results demonstrated that mercury entrapment levels in porous materials are controlled by non-random structural heterogeneity.

[92]S. Lowell and S. Joan. *J. Colloid Interface Sci.*, **83**: 273–278, 1981.
[93]R. L. Portsmouth and L. F. Gladden. *Chem. Eng. Sci.*, **46**: 3023–3036, 1991.
[94]C. D. Tsakiroglou and A. C. Payatakes. *J. Colloid Interface Sci.*, **137**: 315–339, 1990.
[95]C. Salmas and G. Androutsopoulos. *J. Colloid Interface Sci.*, **239**: 178–189, 2001.

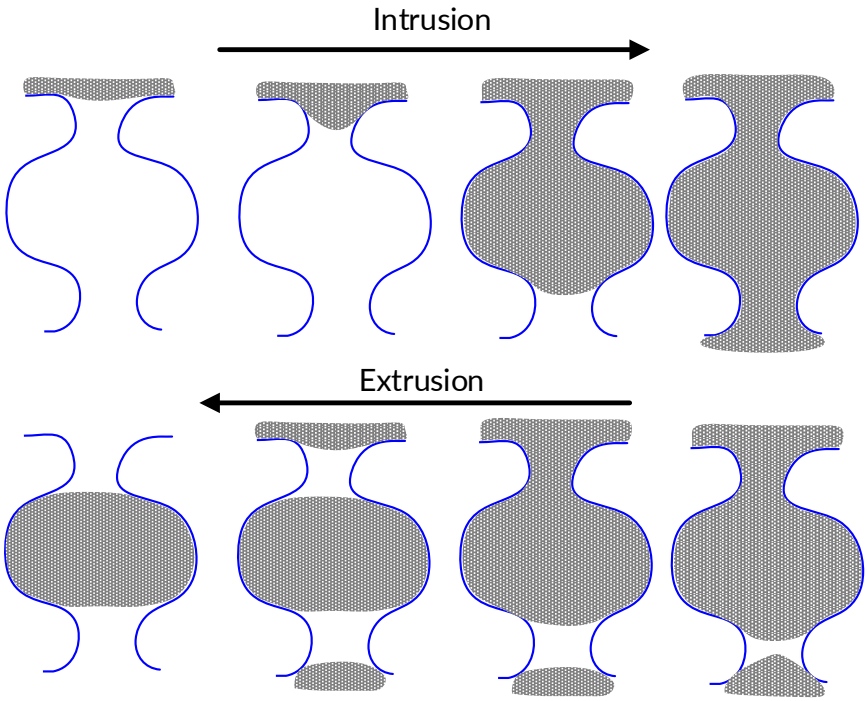


Figure 2.5: Mercury intrusion and extrusion according to ink-bottle theory[45].

Wardlaw and McKellar[67] also built other glass micromodels with rows of large pore bodies separated by narrow pore throats. In this micromodel, the quantity of mercury entrapment was observed to rise when the ratio of pore-body to pore-throat size increased. As a result, it was also demonstrated that 'snap-off', in which the mercury thread breaks as it tries to retreat from a relatively large pore body through a narrow neck, leads to mercury entrapment. In this scenario, Matthews et al.[96] found that the required ratio to cause a snap-off in a larger pore-body adjacent smaller pore-neck size is ∼6. In further glass micromodel, Wardlaw and McKellar discovered that, for a large void space nestled in a continuous network of smaller pores, when mercury leaves the surrounding smaller pores, it will get trapped in the larger pores.

Mercury entrapment has also been attributed to the presence of *ink-bottle*[8,9,64–68] shaped pores in the sample. The ink-bottle pore theory is where a bigger diameter pore-body is connected to a smaller diameter neck, and therefore higher pressure is required for mercury to penetrate the smaller neck and hence, the pore-body. Mercury will enter to fill the pore body at a pressure determined by the size of the neck and not by the actual pore cavity size. However, upon depressurisation, the pore-body cannot empty until a lower pressure is reached, leaving mercury entrapped in the wide inner portion of the pore-body.

Tsakiroglou et al.[67] used a model porous media consisting of throats and chambers, which accounted for the effects of network topology and pore aspect ratio to develop a mathematical relationship for the critical pressure for the retraction and snap-off of mercury menisci. The re-

[96]G. P. Matthews, C. J. Ridgway, and M. C. Spearing. *J. Colloid Interface Sci.*, **171**: 8–27, 1995.

searchers have compared results from their expression with actual experimental data and have found a satisfactory agreement between the two. However, their studies have been limited to porous materials with regular pore structures, whereas a typical heterogeneous catalyst has complex and random pore structures.

Another notable study was conducted by Portsmouth et al.[93] where they have investigated the effects of pore size distribution and pore connectivity on a three dimensional, spherical random network. Their results have revealed that mercury entrapment is a function of both the pore network connectivity and the width of the volume-weighted pore size probability density function. A more recent study by Rigby et al.[90] have looked at mercury entrapment in a nanoporous silica material using a combination of magnetic resonance imaging (MRI) and micro-computed X-ray tomography (micro-CXT). Their investigation revealed that the level of mercury entrapment was determined by the close interaction between the pellet macroscopic structure and the microscopic mercury retraction mechanism. Additionally, it has been determined that mercury entrapment is confined to only the larger pores in the materials. Further investigation on sol-gel silica by Rigby et al.[97] has concluded that the mercury retraction curves of particular sol-gel silica material are independent of equilibration time and thus probably results in the breaking of mercury ganglia at the boundaries of the region of smallest pores within the material.

2.3.5 Limitations of Mercury Porosimetry

One of the drawbacks of mercury porosimetry is that it only measures the smallest entrance of a pore and not the actual inner cavity size. This means that the data obtained from mercury porosimetry is only one-dimensional and thus does not contain any information on the spatial distribution of pores size. As a result, mercury is susceptible to the pore 'shadowing' or 'shielding' effects. Because mercury enters pores in decreasing size as pressure increases, a bigger pore externally accessible only via a smaller pore will be viewed as a volume of the smaller pores.[7]

Another limitation of mercury porosimetry is the assumption of cylindrical pore geometry in the Washburn[71] equation, even though actual pores are rarely cylindrical. This makes mercury porosimetry an indirect characterisation method,[7] in which a model of interpretation representing the porous medium is required to obtain a de-shielded pore size distribution. The most common models implicitly assume that the void space may be represented as a collection of parallel, straight cylinders,[71,82,85–90] and for many porous mediums, this assumption in models is likely to be highly inaccurate. However, in recent times, more direct three-dimensional reconstructions of pore spaces have been obtained by imaging techniques such as scanning electron microscopy (SEM), demonstrating that many sol-gel silica and alumina samples seem to have cylindrical or packed spherical pores shapes.[82]

[97] S. Rigby et al. *Chem. Eng. Sci.*, **63**: 5771–5788, 2008.

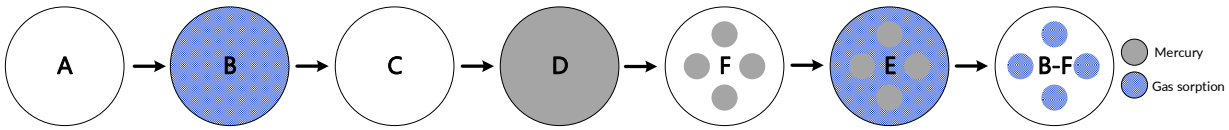


Figure 2.6: Schematic diagram showing integrated mercury porosimetry and gas sorption. The experiment stages are: **(a)** Empty sample, **(b)** First gas sorption experiment, **(c)** Empty sample, **(d)** Mercury porosimetry, **(e)** Mercury entrapment, **(f)** Second gas sorption experiment.

2.4 Integrated Mercury Porosimetry and Gas Sorption

2.4.1 Introduction

Both mercury porosimetry and gas sorption are indirect characterisation techniques and require a model to interpret the raw data. Commonly used models assume that the void spaces may be modelled as a bundle of parallel, straight cylinders.[71,82,85–90] However, as mentioned above, this assumption is likely to be highly inaccurate for many porous media. Furthermore, the underlying physical processes in mercury and gas sorption methods can be complicated with co-operative effects connected to the structural heterogeneity of typically disordered material.[98] In gas sorption, these unique effects include advanced adsorption and delayed condensation, and in porosimetry, mercury snap-off and entrapment.[99] In most cases, many of the shortcomings of individual characterisation techniques can be solved by serially combining them to deliver a much better fundamental understanding of the porous material than the individual techniques alone could, even when these methods are used in parallel. An example of the combined techniques is the integrated mercury porosimetry and gas sorption, which consists of a series of sorption and porosimetry experiments conducted in series on the same sample each time, as shown in Figure 2.6. In this method, any entrapped mercury is frozen *in situ* after the porosimetry stage before a subsequent gas sorption experiment is performed. The integrated technique allows one to block a particular portion of the pore structure selectively and determine the transport properties before and after their removal.[99] This section will describe integrated mercury porosimetry and gas sorption methods and examine previous studies utilising them.

[98] S. Rigby et al. *Colloids Surf., A*, **517**: 33–44, 2017.
[99] S. P. Rigby. *JM Techno. Review*, **62**: 296–312, 2018.

2.4.2 Previous Studies using Integrated Gas-Mercury Method

The integrated gas sorption and mercury porosimetry method has been utilised by Rigby and co-workers in several publications.[89,100–111] The method has been used to test the presence of pore to pore co-operative effects such as pore-blocking,[98,102] characterise the spatial distribution of different pore sizes,[101] validate the semi-empirical alternative to Washburn equation,[102] as well as for determining the distribution of average pore length with pore diameter for mesoporous solids.[104] The integrated method was further used in combination with CXT imaging to reveal the differences in entrapment mechanism and macroscopic spatial distribution of mercury in sample pore network.[6,99,100,110,112]

Early works employing integrated mercury porosimetry and gas sorption revealed the presence of pore-blocking effects during the desorption of nitrogen from a sol-gel silica sample with a modal pore size of $10\,\mathrm{nm}$.[102] The study compared the gas sorption isotherms of a sol-gel silica sample from the same batch before and after mercury porosimetry and found that the two isotherms superimposed in the hysteresis regions below $\sim 600\,\mathrm{cc(STP)/g}$. Additionally, it was observed that both isotherms plateaued, but the isotherm after mercury porosimetry plateaued at a lower amount adsorbed. The difference in total quantity adsorbed before and after mercury porosimetry equalled the amount of mercury entrapped in the sample pores. This discrepancy between the isotherms at higher relative pressures indicated that the mercury became entrapped in the biggest pores. Furthermore, it was observed that capillary evaporation began at the same relative pressure before and after mercury porosimetry, which was 0.85. This indicated that the big pores that entrap mercury could only be emptied after the surrounding smaller necks were emptied at relative pressure 0.85. In order to further validate their findings, Rigby et al. fragmented the sol-gel silica sample to separate the large pore bodies from the necks. The fragmented sample's ensuing desorption isotherm began at a higher relative pressure. This was because the large pore bodies were no longer obstructed by narrow necks and could therefore be empty at the same relative pressure for a retreating meniscus in the pore neck. The results of this investigation revealed that sol-gel silica samples display a pore-blocking mechanism.[102]

The integrated mercury porosimetry and gas sorption method was also used to detect the loca-

[100] S. P. Rigby et al. *Phys. Chem. Chem. Phys.*, **4**: 3467–3481, 2002.
[101] S. P. Rigby. *J. Colloid Interface Sci.*, **224**: 382–396, 2000.
[102] S. P. Rigby and R. S. Fletcher. *J. Phys. Chem. B*, **108**: 4690–4695, 2004.
[103] S. P. Rigby and R. S. Fletcher. *Part. Part. Syst. Char.*, **21**: 138–148, 2004.
[104] S. P. Rigby, M. J. Watt-Smith, and R. S. Fletcher. *J. Catal.*, **227**: 68–76, 2004.
[105] S. P. Rigby, M. J. Watt-Smith, and R. S. Fletcher. *Adsorption (Boston)*, **11**: 201–206, 2005.
[106] S. P. Rigby et al. *Part. Part. Syst. Char.*, **23**: 82–93, 2006.
[107] S. P. Rigby et al. *Adsorption (Boston)*, **14**: 289–307, 2008.
[108] S. P. Rigby and P. I. Chigada. *Adsorption (Boston)*, **15**: 31–41, 2009.
[109] B. Bafarawa et al. *J. Colloid Interface Sci.*, **426**: 72–79, 2014.
[110] I. Hitchcock et al. *J. Phys. Chem. A.*, **118**: 20627–20638, 2014.
[111] I. Hitchcock et al. *J. Colloid Interface Sci.*, **417**: 88–99, 2014.
[6] A. Nepryahin et al. *Chem. Eng. Sci.*, **152**: 663–673, 2016.
[112] A. Nepryahin et al. *Adsorption (Boston)*, **22**: 993–1000, 2016.

tion of the pores that entrap mercury after the end of the mercury intrusion experiment.[89,98,102,113] Nitrogen sorption isotherms have been conducted both before and after a mercury porosimetry experiment on a sol-gel silica catalyst support pellets (of nominal diameter 3 mm). The results of their experiment revealed that, for this particular type of sol-gel silica catalyst, the entrapped mercury is confined to only the largest pores and that the presence of macroscopic heterogeneities in the spatial distribution of pore size is the most likely source of mercury entrapment in this material. These findings were further consistent with the results of the analysis of the raw porosimetry data using the Kloubek correlation,[75] which is a semi-empirical alternative to the traditional Washburn equation.[71]

The integrated method was used to study whether entrapped mercury moves around between the end of the MIP experiment and the beginning of the second gas sorption experiment or thermoporometry.[105] To confirm this, gas sorption studies were carried out immediately after porosimetry and a week later, and while some materials showed no significant changes in isotherm shape during this period, others showed considerable changes. These studies have demonstrated that mercury entrapped using shorter equilibration times in porosimetry experiments is more unstable and likely to migrate than mercury entrapped after longer equilibration times.

The presence of advanced adsorption has also been observed for a spherical sol-gel silica sample using integrated gas sorption and mercury porosimetry.[107,108] It was found that the spatial arrangement of large and small pores within the region of the sol-gel silica sample where mercury is trapped is similar to a through ink bottle, and when mercury is trapped in the larger pores, it creates dead-end pores in the smaller pores. It was also found that the relative pressure of condensation in the region of interest in an empty sample was found to be the square root of the reduced condensation that occurs in that region after mercury entrapment. These findings were consistent with the presence of advanced condensation, similar to what is expected from the Cohan-Kelvin equation for a through ink bottle pores.[55]

More recently, the advantage of the integrated method over the two individual techniques applied separately was demonstrated by using scanning curves experiments conducted in series before and after mercury porosimetry.[111] This work revealed that crossing scanning curves are obtained for some disordered porous material with through ink-bottle pores. Furthermore, the integrated experiments have enabled the relationship between pore structure and mass transport to be studied directly without requiring intermediate pore network modelling techniques. Nepryahin et al.[6,112] studied tabletted methanol synthesis pellets, made using roll compacted feed, and compacted to two different densities. It was found that cracks dominated mass transport through the pellet, and voids formed via splintering of the feed particles during compaction. However, the comprehensiveness of the pore characterisation was limited due to the use of only conventional gas sorption experiments to probe the void space left accessible following mercury entrapment and the limitations on the resolution of the CXT imaging employed.

[113] S. Rigby et al. *Ind. Eng. Chem. Res.*, **56**: 14822–14831, 2017.

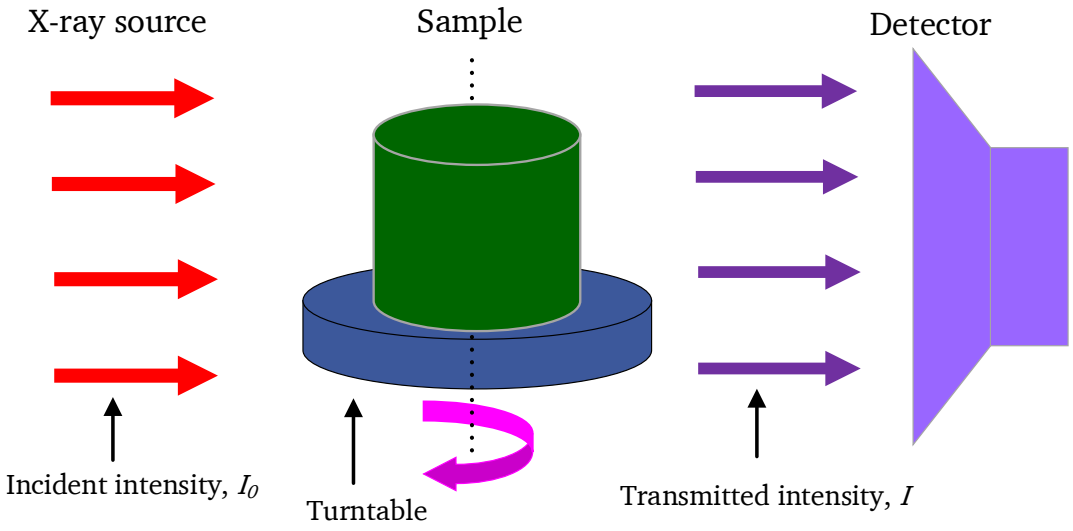


Figure 2.7: Schematic depiction of the principles of computerised X-ray tomography [114].

2.5 Computerised X-ray Tomography (CXT)

2.5.1 Background Theory

X-rays were discovered in 1895 by Wilhelm Röntgen[115] while testing whether cathode rays could pass through glass. Röntgen's investigations focused on light phenomena produced by passing a high voltage current through so-called 'Crookes tube,' a glass bulb with positive and negative electrodes that shine fluorescently when a high voltage current is run through them. Röntgen noticed that when he shielded the tube with heavy black cardboard, the incandescent green light caused a fluorescent screen to glow. Röntgen established that the fluorescence was generated by invisible rays emitted by the Crookes tube he was using to examine cathode rays (later identified as electrons), which pierced the thick black paper wrapping around the tube. Through further experimentation, Wilhelm discovered that the new type of rays could pass through most things, including the body's soft tissues, but left bones and metals visible. Since this discovery, X-rays have been used extensively in many research fields, including medical imaging.[116] material analysis.[117] and dimensionless metrology.[118]

A major drawback of older X-rays was the loss of depth information due to radiography projecting a 3D object onto a 2D plane. However, a new technique called computerised X-ray tomography (CXT) was developed in the 1970s to overcome this drawback.[116,119,120] The newly developed CXT method is non-destructive and allows the reconstruction of a 3D volume of objects by acquiring projection images from different directions. The new technique also enabled the visualisation of

[115] A. Hessenbruch. *Endeavour*, **26**: 137–141, 2002.
[116] J. Ambrose. *Br. J. Radiol.*, **46**: 1023–1047, 1973.
[117] D. Chioibasu et al. *Metals*, **10**: , 2020.
[118] J. Kruth et al. *CIRP Annals*, **60**: 821–842, 2011.
[119] G. N. Hounsfield. *Br. J. Radiol.*, **46**: 1016–1022, 1973.
[120] G. N. Hounsfield. *Can. Assoc. Radiol. J.*, **27**: 135–142, 1976.

materials' internal features and digital information about their 3D geometry and properties from the metres down to tens of nanometres length scales. Each CXT image is called a *slice*, and each slice is composed of *voxels* (volume elements) and corresponds to what the object being scanned would look like if it were sliced open along a plane. The X-ray source and the detector remain stationary while the sample under investigation rotates during the scanning process. This set-up achieves better mechanical stability required at high resolutions.[121]

A key feature of X-ray radiation is its ability to penetrate different materials in varying degrees to obtain a series of radiographs of the sample viewed from different directions. The change in X-ray intensity as it passes through the material is described by Lambert-Beer's law,[122–124] which describes intensity reduction as a function of X-ray energy, path length, and material linear attenuation coefficient:

$$I = I_0 e^{-\int \mu(s) ds} \tag{2.15}$$

The Lambert-Beer law describes the reduction in the intensity of monochromatic X-ray beam as a function of initial X-ray energy, I_o path length, s and material linear attenuation coefficient, μ. The intensity of X-ray beams attenuates as it penetrates matter as each material atom removes an X-ray photon, decreasing its intensity. The amount of decrease in intensity of the X-ray beam depends on two factors: (1) The thickness of the material and (2) a characteristic of the material called linear attenuation coefficient, μ. When X-rays pass through an object, some of the energy is transmitted, some are scattered, and some are absorbed. A detector on the opposite side of the sample detects the transmitted photons, yielding a single 2D attenuation map (shadow projection). The shadow projection image is collected from a variety of angles since the sample is rotated in 360° on a turn-table (see Figure 2.7). With the aid of image reconstruction algorithms, the complete 3D structure of the samples can be reconstructed from the projections. After reconstruction, an image post-processing step, including segmentation, is usually necessary to analyse the X-ray images.[114]

The X-ray resolution, R depends on the geometric magnification M, which is determined by distance between X-ray source and the sample.[125]

$$R = \frac{d}{M} + \left(1 - \frac{1}{M}\right) s \tag{2.16}$$

Where d is the pixel size and s is the spot size (focus spot) at the X-ray source. The magnification is given by:

$$M = (\text{ total source } - \text{ detector distance })/ (\text{total source } - \text{ object distance }). \tag{2.17}$$

[121] V. Cnudde and M. Boone. *Earth Sci. Rev.*, **123**: 1–17, 2013.
[122] R. A. Geise. *Computed tomography: physical principles, clinical applications, and quality control*. Elsevier, 1995.
[123] A. Thompson and R. Leach. *Industrial X-Ray computed tomography*. Springer International Publishing, 2018.
[124] J. Hsieh. *Computed tomography: principles, design, artifacts, and recent advances*. SPIE PRESS, 2015.
[114] A. Miguelez-Moran et al. *Eur. J. Pharm. Biopharm.*, **72**: 173–182, 2009.
[125] V. Cnudde et al. *Appl. Geochem.*, **21**: 826–832, 2006.

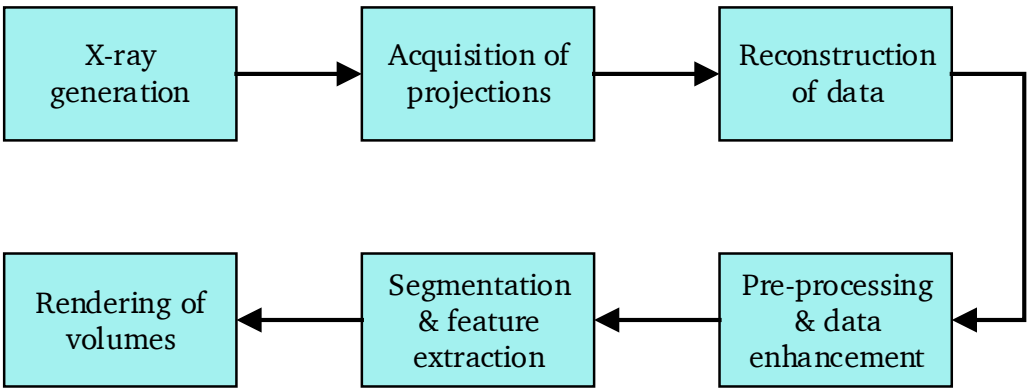


Figure 2.8: Generalised CXT scan workflow and image analysis procedure [123].

2.5.2 Synchrotron CT and Linear Accelerators

Although electron guns are the most frequent X-ray generators, there are alternative ways to accelerate electrons against a target to create X-rays. Linear accelerators and synchrotrons, in particular, have distinct benefits over conventional electron guns. Linear accelerators (LINAC) accelerate electrons or other charged particles by subjecting them to a sequence of fluctuating electric potentials along a linear beamline.[123] Due to their tremendous energy, linear accelerators can penetrate very thick and high absorbing materials, for example, up to meters of concrete or metal. X-rays can also be produced using synchrotrons, which are unique particle accelerators located in extensive facilities. Synchrotrons are also of interest because they can produce highly collimated, monochromatic X-ray beams that are also coherent, bright, and easily tuneable.[126] On the other hand, Synchrotrons have the problem of having an enormous footprint, typically requiring massive facilities of hundreds of meters in diameter and high associated costs.[126]

2.5.3 Workflow, Reconstruction and Image Processing

In a CXT scan, the collection of projection data is merely the first step towards producing a tomogram and deriving meaningful insights from it. However, the 2D projections must be reconstructed into a 3D stack of slices to quantity or visualise specific sample regions. The reconstruction method recovers the spatial distribution of the attenuation coefficient μ(x,y) slice by slice to form a greyscale image of the object from the set of projections. The Radon[127] transform mathematically describes the relationship between slices and projections, and it forms the basis for the two primary types of reconstruction algorithms, analytic and iterative methods. Filtered back projection (FBP)[128] and the Feldkamp–Davis–Kress (FDK)[129] technique are the two most common analytical methods used in modern times. These two methods rely on Fourier-space filtering of the projection data and object reconstruction using a discretised version of the Radon transformation.[128,129]

[126] L. De Chiffre et al. *CIRP Annals*, **63**: 655–677, 2014.
[127] J. Radon. *Modern Diagno. Radiol.*, **5**: 21, 2005.
[128] G. N. Ramachandran and A. V. Lakshminarayanan. *PNAS*, **68**: 2236–2240, 1971.
[129] L. A. Feldkamp, L. C. Davis, and J. W. Kress. *J. Opt. Soc. Am. A*, **1**: 612–619, 1984.

After obtaining a reconstructed volume, the data must be handled properly in order to extract the maximum amount of information from the images without adding operator bias or any additional artefacts. This stage usually involves noise reduction filters and the segmentation of the phases present in the volume. The purpose of the filtering procedure is to smooth homogenous areas while maintaining edges.[130] Examples are the median,[131] anisotropic,[132] and non-local means filters.[133] On the other hand, segmentation can be accomplished on a global or a local scale, employing a vast range of methodologies, such as histogram shape analysis, clustering analysis, or thresholding. Following segmentation, it is sometimes required to apply additional image post-processing procedures to account for any segmentation errors. In general, morphological procedures like erosion and dilation and size-dependent operations like the removal of tiny spots are utilised here.[134]

In recent times, machine learning (ML)[135] and deep learning[136] methods are rapidly developing an alternative to traditional image reconstruction of tomographic data sets, which are most used in medical CT image analysis. For example, in situations where high temporal resolution is required, which requires shortened detector integration times and a reduction in the number of projections, machine learning methods can yield significantly better reconstructions than the traditional analytic or iterative methods. More details on machine learning and artificial neural networks (ANN) can be found in the image analysis chapter (Chapter 4).

2.5.4 CXT Applications

X-ray CT as a non-destructive testing technique has become essential for doctors, material scientists, and geologists who work with materials where the delicate internal structure or changes are critical to understanding the material's behaviour. X-ray CT is now widely used in these areas and sub-micron material characterisation facilities. This section will look at the various CXT application fields to demonstrate how micro and nano-CT scans have been used as a non-destructive tool for porous material characterisation, quality control, and manufacturing and optimisation.

Soon after CXTs were commercially available in 1975, researchers in petroleum engineering and soil science began using the technology to study multi-phase flow problems in their respective areas. Some of the early papers in the subject of soil science employed medical CT scanners to quickly measure soil bulk density;[137] map temporal changes in spatial soil moisture distribution,[138] and follow percolating moisture front in a soil sample in 3D.[139,140] After these publications, Wang

[130] S. Schlüter et al. *Water Resour. Res.*, **50**: 3615–3639, 2014.
[131] T. Huang, G. Yang, and G. Tang. *IEEE Trans.*, **27**: 13–18, 1979.
[132] P. Perona and J. Malik. *IEEE Trans.*, **12**: 629–639, 1990.
[133] A. Buades, B. Coll, and J.-M. Morel. *IEEE Comput. Appl. Power*, **2**: 60–65, 2005.
[134] R. M. Haralick, S. R. Sternberg, and X. Zhuang. *IEEE Trans.*, **PAMI-9**: 532–550, 1987.
[135] G. Litjens et al. *Med. Image Anal.*, **42**: 60–88, 2017.
[136] S. Flenner et al. *J. Synchrotron Radiat.*, **27**: , 2020.
[137] A. M. Petrovic, J. E. Siebert, and P. E. Rieke. *Soil Sci. Soc. Am. J.*, **46**: 445–450, 1982.
[138] J. M. Hainsworth and L. A. Aylmore. *Soil Res.*, **21**: 435–443, 1983.
[139] W. J. Anton et al. *Geoderma*, **64**: 183–196, 1995.
[140] S. H. Anderson et al. *Soil Sci. Soc. Am. J.*, **52**: 35–40, 1988.

et al.[141] presented the first study in the field of petroleum engineering to employ CT to map oil saturation distribution in a Berea sandstone core. A number of similar studies by Wellington[142] and Vinegar as well as Hunt et al.[143] followed shortly after, with the first truly quantitative study coming in 1987 when Vinegar and Wellington[144] used CT to study three-phase flow experiments and implemented the use of multiple doped silicon to separate the different fluid saturations. This was followed by the work of Withjack[145] in 1988, who utilised CXT to determine the saturation necessary to produce relative permeability curves for Berea sandstone and dolomite cores.

The resolution of the studies mentioned above was restricted to hundreds of micrometres to millimetres due to the usage of medical CT scanners. As a result, imaging individual grains, pores or fluid-fluid interfaces proved impossible. However, by the early 1990s, lab-scale X-ray equipment had advanced to the point that micro-tomographic imaging could be completed more quickly. Jasti et al.[146] produced the first genuinely pore-scale images of porous media (glass beads and Berea sandstone samples) and fluid distributions of oil and water using a lab-scale system. Clausnitzer and Hopmans[147] went a step further in 2000 by conducting a quantitative study of pore-scale solute escape in sand packs. However, they concluded that X-ray synchrotron sources were required to obtain truly pore-scale measurements. Laboratory and industrial CXTs have advanced rapidly since then and are currently on a level with synchrotron-based systems in terms of spatial resolution and image quality, although scan times for lab-scale systems are still much longer.

With the introduction of synchrotron X-ray tomography, it is now possible to characterise individual pores and extract high-resolution three-dimensional information on the pore network morphology and connectivity of natural porous media. The synchrotron imaging has enhanced understanding of the relationship between pore-scale properties and continuum-scale measurements, including porosity,[148,149] pore-size distribution,[150] surface area,[151] tortuosity,[152] and permeability.[153] Synchrotron studies have been carried out on both unconsolidated (e.g., glass bead, soil)[154–160]

[141] S. Y. Wang, S. F. Ayral, and C. C. Gryte. *AIChE J.*, **30**: 642–646, 1984.
[142] S. L. Wellington and H. J. Vinegar. *Pet. Technol.*, **39**: 885–898, 1987.
[143] P. Hunt, P. Engler, and C. Bajsarowicz. *Pet. Technol.*, **40**: 1203–1210, 1988.
[144] H. J. Vinegar and S. L. Wellington. *Rev. Sci. Instrum.*, **58**: 96–107, 1987.
[145] E. M. Withjack. *SPE Form. Eval.*, **3**: 696–704, 1988.
[146] K. Jasti, G. Jesion, and L. Feldkamp. *SPE Form. Eval.*, **8**: 189–193, 1993.
[147] V. Clausnitzer and J. Hopmans. *Water Resour. Res.*, **36**: 2067–2079, 2000.
[148] M. Betson et al. *Transp. Porous Media*, **57**: 203–214, 2004.
[149] C. Milena and V. Jana. *J. Hydrol.*, **267**: 186–200, 2002.
[150] L. M. Schwartz et al. *Physica A*, **207**: 28–36, 1994.
[151] M. Schmitt et al. *Solid Earth*, **7**: 285–300, 2016.
[152] L. Decker, D. Jeulin, and I. Tovena. *Acta Stereol.*, , 1998.
[153] J. Arns et al. *J. Petro. Techno.*, **39**: 247–259, 2003.
[154] F. Auzerais et al. *Geophys. Res. Lett.*, **23**: 705–708, 1996.
[155] D. Coker, S. Torquato, and J. Dunsmuir. *J. Geophys. Res.*, **101**: 17497–17506, 1996.
[156] S. Song et al. *Bull. Volcanol.*, **63**: 252–263, 2001.
[157] M. Prodanovic, W. Lindquist, and R. Seright. *Adv. Water Resour.*, **30**: 214–226, 2007.
[158] Y. Nakashima et al. *J. Contam. Hydrol.*, **74**: 253–264, 2004.
[159] C. H. Arns et al. *SPE J.*, **10**: 475–484, 2005.
[160] P. Lehmann et al. *Vadose Zone J.*, **5**: 80–97, 2006.

and consolidated media (e.g., sandstone and carbonate rock).[161–163] Additionally, synchrotron-generated pore-network data has been utilised to assist in the design and implementation of a lattice-Boltzmann simulators[164–169] and a pore network simulations, such as 3DMA software.[170,171] Furthermore, Synchrotron CXT has also been used to quantify the pore-network topology of porous media, with algorithms extracting information on the 3D spatial distribution of pore-bodies and pore-throats, as well as pore connectivity.[152]

CT scans can also be used in hydrocarbon reservoir characterisation, where a 3D image of reservoir rocks is obtained in a non-destructive way. The pores could then be segmented from the solid materials by carrying out image analysis to understand better the reservoir system's specific petrophysical properties, such as permeability, tortuosity, and acoustics. The quantification of these properties is essential in monitoring reservoir fluid flow, such as wormhole formation and carbon dioxide sequestration. There is comprehensive literature on the application of X-ray tomography to geosciences, particularly in reservoir geology,[172] reservoir rock characterisation,[173] complex porosity and pore geometry of carbonate reservoirs,[174] and the performance of sandstones.[144]

Computerised X-ray Tomography has also been used to map the spatial distribution of contrast agents in the porous network for heterogeneous catalyst.[6,90,99,112,113,175–177] Rigby et al.[90] studied the entrapment of non-wetting fluids within nanoporous sol-gel silica sphere, with a typical pellet diameters of $\sim 3\,\mathrm{mm}$, by using micro-CXT Skyscan 1072. The samples were first intruded with mercury to act as a contrast agent and imaged to obtain 3D constructed volume. Using the experimental data from the X-ray images and simulations, Rigby et al.[90] constructed a model for the microscopic mercury retractions. The results of their investigation suggested that the level and spatial distribution of mercury entrapment in the sol-gel silica material studied arises because of an interaction between the macroscopic structure of the pellet and the microscopic mechanism of mercury snap-off. In another study, Rigby et al.[175] have utilised CXT and mean-field density functional theory (MF-DFT) to study the pore potential theory of hysteresis, entrapment and the percolation properties of commercially available silica and alumina blank catalyst support. Rigby et al. observed from the CXT scan that the pore potential effects can be seen directly as mercury

[161] M. Redwan and D. Rammlmair. *Soil Sci. Soc. Am. J.*, **74**: 1457–1468, 2010.
[162] R. Al-Raoush, K. Thompson, and C. Willson. *Soil Sci. Soc. Am. J.*, **67**: 1687–1700, 2003.
[163] R. I. Al-Raoush and C. S. Willson. *J. Hydrol.*, **300**: 44–64, 2005.
[164] X. Shan and H. Chen. *Phys. Rev. E.*, **47**: 1815–1819, 1993.
[165] B. Ferreol and D. Rothman. *Multiphase flow in porous media*. Springer, 1995. 3–20
[166] R. D. Hazlett, S. Y. Chen, and W. E. Soll. *Petro. Sci. Eng.*, **20**: 167–175, 1998.
[167] H. Vogel et al. *Vadose Zone J.*, **4**: 380–388, 2005.
[168] B. Ahrenholz et al. *Adv. Water Resour.*, **31**: 1151–1173, 2008.
[169] M. Porter, M. Schaap, and D. Wildenschild. *Adv. Water Resour.*, **32**: 1632–1640, 2009.
[170] W. Lindquist et al. *J. Geophys. Res.*, **105**: 21509–21527, 2000.
[171] M. Prodanović, W. Lindquist, and R. Seright. *J. Colloid Interface Sci.*, **298**: 282–297, 2006.
[172] W. D. Carlson. *Earth Planet. Sci. Lett.*, **249**: 133–147, 2006.
[173] J. Dewanckele et al. *Sci. Total Environ.*, **416**: 436–448, 2012.
[174] C. Purcell et al. *Energy Procedia*, **1**: 2323–2331, 2009.
[175] S. Rigby et al. *Chem. Eng. Sci.*, **66**: 2328–2339, 2011.
[176] S. Rigby et al. *Mar. Pet. Geol.*, **112**: 104058, 2020.
[177] E. P. Pitcher et al. *Mar. Pet. Geol.*, **134**: 105348, 2021.

entrapment preferentially arose within the regions of high pore potential due to the presence of mercury-wetting materials. Furthermore, it has been shown that CXT can be used to detect percolation pathways in macro-porous alumina directly and study the spatial configurations of entrapped mercury ganglia within such an amorphous material. More recently, Nepryahin[6,112] used CXT to map the spatial distribution of entrapped mercury in a copper/zinc oxide alumina roll compacted feed catalyst (high density and low-density cylindrical tablets). Their study has revealed that the relative importance of the sub-sets of pores is related to their pervasiveness across the pellet and whether they percolate to the centre of pellet.

Other notable areas where CT is used include, building material characterisation (e.g, bricks, mortar and concrete).[178] fibre reinforced composites (e.g. foams),[179] Metrology e.g., edge detection,[118] biomaterials (e.g., Bone TE scaffolds),[180] dental implants (e.g., root canal morphology),[181] and paleoradiology (e.g., Egyptian mummies).[182]

2.5.5 Representative Elementary Volume

Understanding macroscopic characteristics of a porous media requires knowledge at the microscopic pore scale; thus, prior to performing upscaling exercises of physical properties, accurate characterisation of the porous media at the pore scale is critical for quantifying the heterogeneity of a large system.[183] In order to address the heterogeneity of a porous media from X-ray CT images, the concept of a representative elementary volume (REV) is used. REV is an important parameter and was first introduced in 1972 by Bear.[184] REV describes the smallest value that can be taken as a representation for the entire sample area/volume that does not respond to small changes in volume or location.[184] The size of a REV varies from a minimal bound, which represents the transition from the microscale to the macroscale level, to a maximum bound, which represents the shift from a homogeneous to a heterogeneous condition.

There are two ways to determine the REV of a given sample to predict and study effective macroscale parameters. The first technique, popular in soil science and hydrology literature, determines a REV based on porosity regardless of the macroscale parameter of concern (i.e., a sample is considered a REV if its porosity is consistent across different sizes of the sample). Clausnitzer and Hopmans[147] utilised this method as a primary basis to estimate the REV of ideal systems (i.e., glass beads packs). Other researchers[163,185–187] used a similar approach by determining porosity to calculate REVs of natural soil systems. The second method, which determines a REV based on macroscale factors without first determining microscale sample properties (e.g., porosity), is

[178] A. Plessis and W. Boshoff. *Constr. Build. Mater.*, **199**: 637–651, 2019.
[179] J. Summerscales. *Microstructural characterisation of fibre-reinforced composites*. CRC Press, 1998.
[180] A. Jones et al. *Biomater. Adv.*, **25**: 4947–4954, 2004.
[181] C. Massaro et al. *J. Mater. Sci.: Mater. Med.*, **13**: 535–548, 2002.
[182] E. Rönkkö, T. Terpstra, and M. Walton. *scientific studies of Egyptian mummy*. Block Museum of Art, 2019.
[183] R. Al-Raoush and A. Papadopoulos. *Powder Technol.*, **200**: 69–77, 2010.
[184] J. Bear. *Dynamics of fluids in porous media*. Courier Corporation, 1988.
[185] G. O. Brown, H. T. Hsieh, and D. A. Lucero. *Water Resour. Res.*, **36**: 1199–1207, 2000.
[186] P. Baveye et al. *Meas. Sci. Technol.*, **13**: 775, 2002.
[187] M. Razavi, B. Muhunthan, and O. Hattamleh. *Geotech. Test. J.*, **30**: 212–219, 2007.

widely utilised in engineering mechanics literature. In this second method, the size of REV is commonly determined by macroscale characteristics, and when the macroscale under consideration remains consistent throughout various volumes, the sample is considered a REV. Determining the REV size is by no means a simple process because it depends on the nature of the material under consideration and microscale characteristics that influence the effective macroscale parameters. Furthermore, the complexity of microscale characterisation of natural porous media systems makes determining REV from microscale factors considerably more difficult. The first method, porosity vs cube size, was used to determine the REV for the scanning electron microscopy images of the methanol synthesis catalyst pellets studied in this thesis.

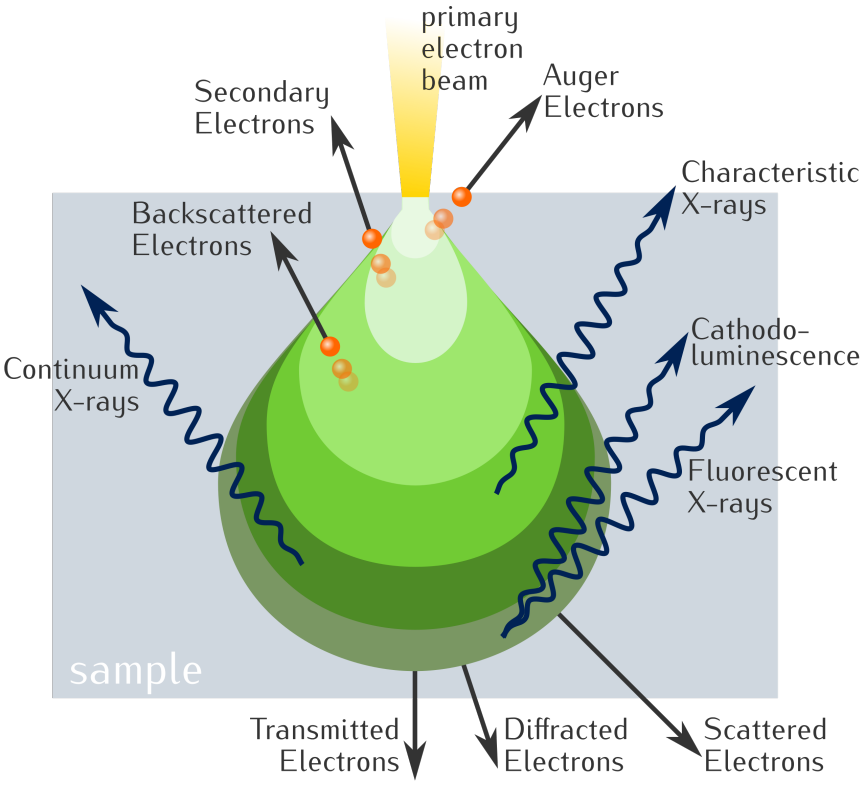


Figure 2.9: Electron-matter interactions - the different types of signals which are generated [188].

2.6 Scanning Electron Microscopy (SEM)

2.6.1 SEM Concept and Brief History

Electron microscope (EM), as the name indicates, uses a high-energy electron beam to generate a variety of signals at the surface of samples and were developed due to the limitations of light microscopes.[188] EMs are capable of much higher magnifications and have a greater resolving power than a light microscope, allowing them to see much smaller objects at a subcellular, molecular and atomic level. The signals produced by the interactions between electron and sample provides information about the sample's external morphology, chemical composition, and crystalline structure. In standard imaging mode, EMs probe only the sample's surface and provide a 2D image that shows spatial variations in these properties. Max Knoll and Ernst Ruska[189] created the first electron microscope in 1931 with a resolution of 100 µm, which was later improved to 0.05 µm by adding electromagnetic lenses, and EMs has since evolved to be an incredibly versatile instrument. The field of electron microscopy is divided into scanning electron microscopy (SEM) and transmission electron microscopy (TEM), and while both instruments can measure many signals coming from electron and matter interactions, the two imaging modes have generally been treated as independent fields due to differences in equipment designs, sample preparation, and information acquired.[188] SEMs are often more user-friendly and easier to operate than TEMs, making them

[188] A. Bogner et al. *J. Micron*, **38**: 390–401, 2007.
[189] M. Knoll and E. Ruska. *J. Für Phys.*, **78**: 318–339, 1932.

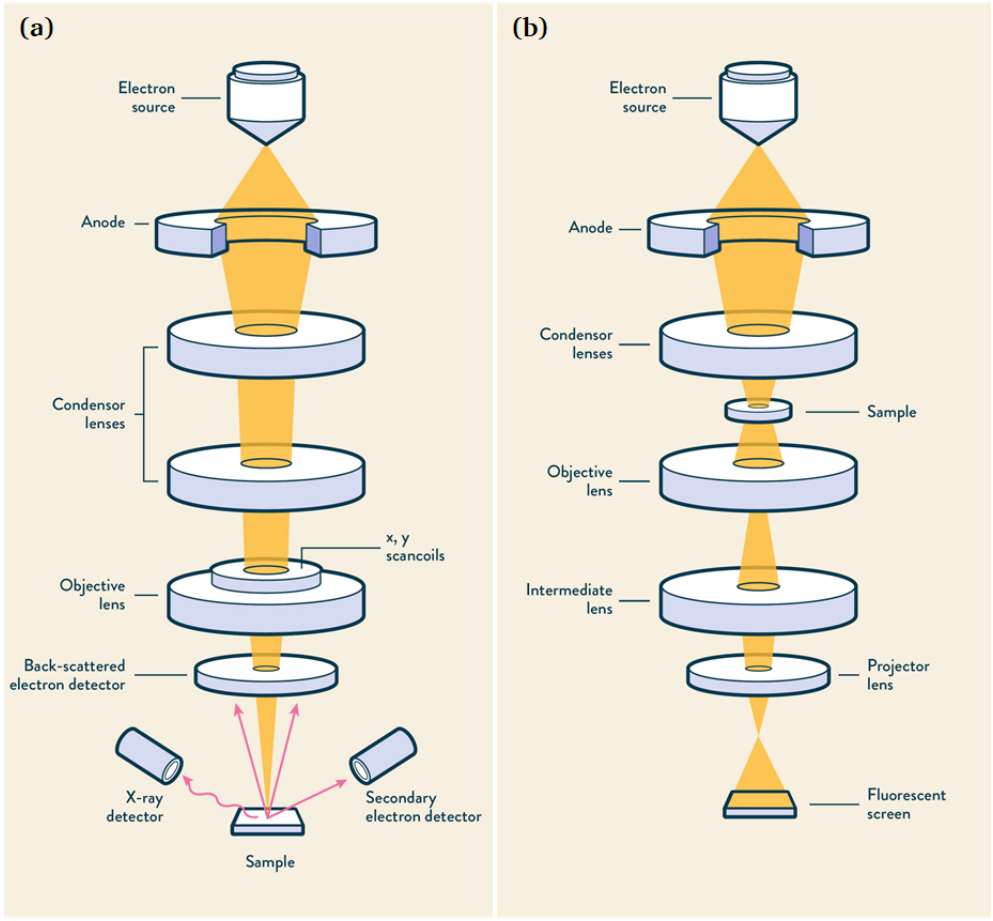


Figure 2.10: Comparisons of closer look of **(a)** SEM, and **(b)** TEM.

more accessible to non-experts looking for a microstructure and analysis tool. Additionally, many current SEMs enable low−voltage viewing of samples, allowing for the non−destructive study of beam sensitive materials. In recent times, scanning transmission electron microscopy (STEM) has revolutionised electron microscopy's capabilities, with many transmission experiments now being done in SEMs and scanning coils becoming more common in classic TEM designs.[188]

In SEM, the electron source forms a beam of electrons and accelerates toward the sample using a positive electrical potential. The beam travels through electromagnetic fields and lenses in the vacuum column, focusing the beam down toward the sample. A mechanism of deflection coils enables to guide the beam so that it scans the surface of the sample in a raster pattern. When the primary electron beam interacts with the sample, the electrons lose energy by repeated random scattering and absorption inside the interaction region, which is a 'teardrop-shaped ' section of the sample that ranges from less than 100 nm to nearly 10 nm under the surface (see Figure 2.9). The size of the interaction volume is determined by the electron's landing energy and the sample's atomic number and density. The kinetic energy of the accelerated electron is dispersed as various signals that are generated during electron-sample interactions. These signals include secondary electrons (SE), backscattered electrons (BSE), diffracted backscattered

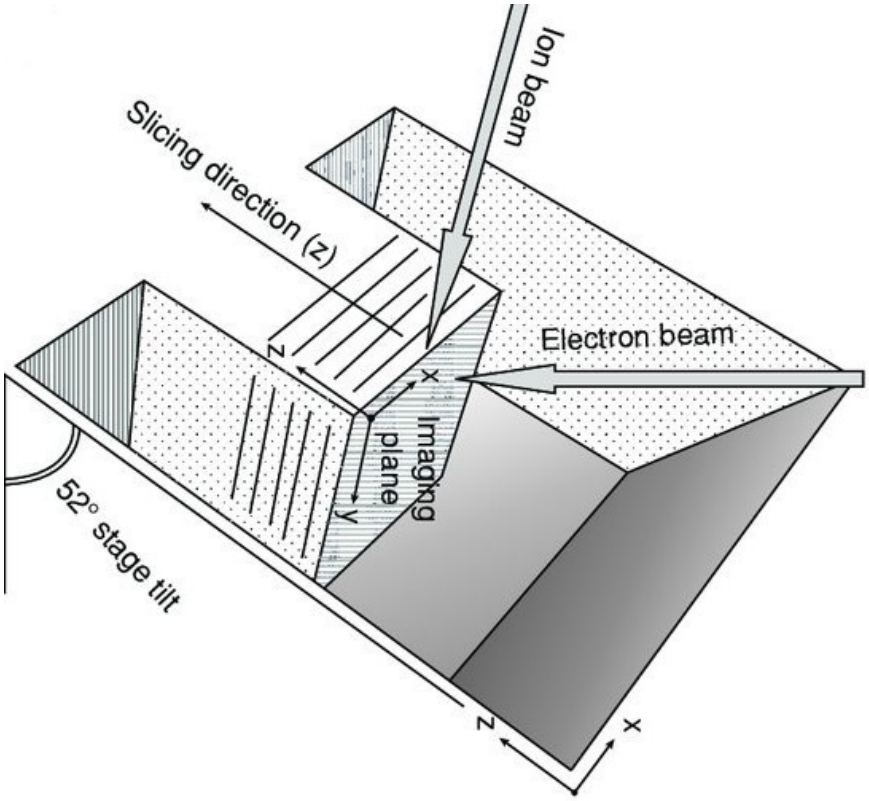


Figure 2.11: Schematic representation of dual beam FIB-SEM serial milling [190].

electrons, photons (characteristic X-rays used for elemental mapping and continuum X-rays) and visible light (cathodoluminescence-CL), each of which can be detected by respective detectors.[7] Both secondary and backscattered electrons are often used for imaging the samples; however, secondary electrons are best for demonstrating morphology and topography on samples, while backscattered electrons are best for illustrating compositional differences in multiphase samples (i.e., for rapid phase discrimination). Electronic amplifiers are employed to amplify the signals, and electronic detectors convert the signals into digital pictures shown on computer screens. SEM analysis is considered non-destructive, which means that the X-rays produced by electron interactions do not cause volume loss in the sample, allowing it to be used to analyse the same materials repeatedly.[190]

2.6.2 FIB-SEM Lift-outs and Serial Sectioning

A focused ion beam (FIB) instrument is similar to a scanning electron microscope (SEM) and typically consists of a vacuum system, ion column, detectors, gas injectors, and a sample stage.[191] The FIB instrument may be used as a standalone or incorporated into other systems, such as SEM, TEM or secondary ion mass spectrometry (SIMS), the most common of which is a FIB-SEM dual-

[190] I. Utke, S. Moshkalev, and P. Russell. *Nanofabrication using focused ion and electron beams: principles and applications*. Oxford University Press, 2012.

[191] R. Langford and C. Clinton. *J. Micron*, **35**: 607–611, 2004.

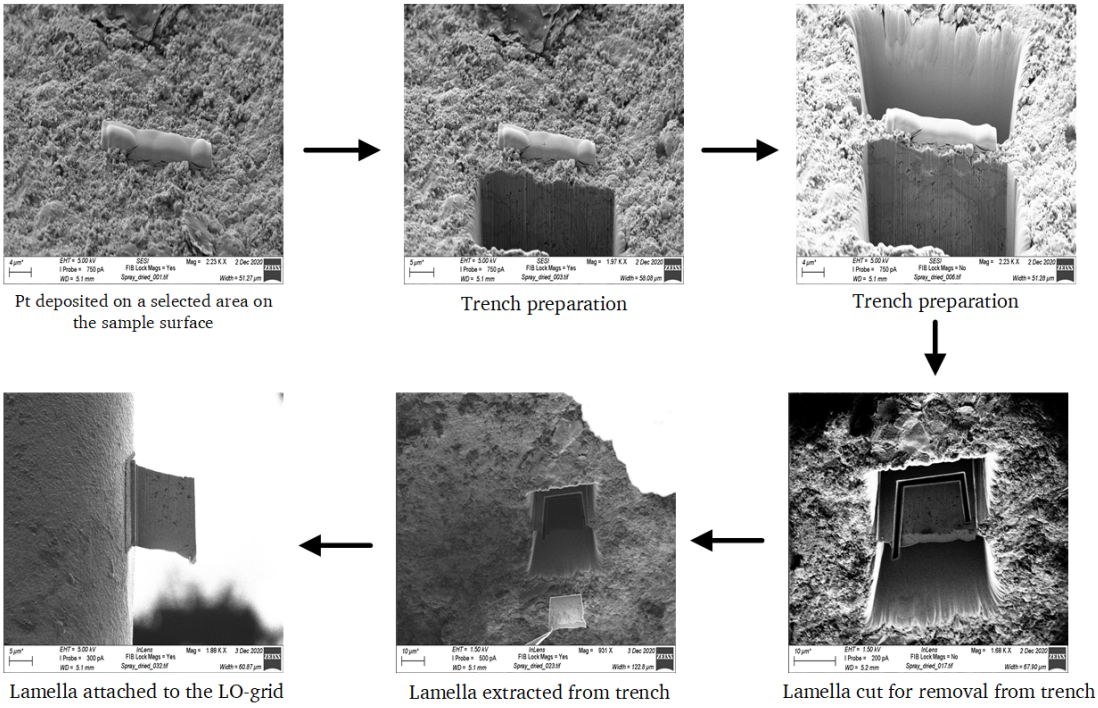


Figure 2.12: Example of FIB-SEM lift out stages for a fresh spra-dried methanol catalyst pellet.

platform instrument.[190] The ion column in the standalone system is typically mounted vertically; however, the dual-platform instruments usually have the FIB mounted at some angle. The stage in the FIB-SEM instrument is set up so that FIB and the SEM are looking at the same spot on the sample, and the SEM continually monitors the FIB operations. The stage is typically inclined (52°) to ensure that the sample's surface is perpendicular to the FIB (see Figure 2.11).

FIB has become a standard instrument for preparing samples for subsequent analysis by several other analytical tools. The versatility of the FIB makes it advantageous for numerous applications, including FIB-SEM 'serial sectioning' and 'lift-out' techniques, which are generally rapid. In addition, because of the tiny probe size and a broad range of beam currents achievable by new FIB instruments, FIB sample preparation techniques currently offer the best spatial resolution where site-specificity is required. FIB lift-outs and grid mounting processes can be accomplished inside the FIB instrument (i.e., in-situ) or outside (i.e., ex-situ).[192] The ex-situ grid mounting method is very swift compared to in-situ; however, no further thinning or artefact removal is possible on the prepared lamella. The in-situ method is newly developed and combines all of the advantages of the ex-situ method but offers the possibility of further ion milling of the lamella, thinning it and removing any artefacts.[192]

The lift-out procedure was first reported by Overwijk et al.[193] where they have used a FIB to prepare a thin electron transparent membrane from a larger bulk sample. Many Workers have

[192] L. Giannuzzi et al. Springer, 2005.
[193] M. Overwijk, F. Heuvel, and C. Bulle-Lieuwma. *J. Vac. Sci. Technol., A*, **11**: 2021–2024, 1993.

since utilised the method. Leslie et al.[194] used a similar removal procedure as Overwijk et al.[193] and noted some practical problems and artefacts of the technique; however, little details were provided on using the tungsten needle probes to remove the thinned sample. In 1997, Giannuzzi[195] and co-workers documented a routine FIB lift-out technique to prepare site-specific TEM specimens. This technique was first developed specifically for applications in the microelectronics industry; however, the FIB LO technique has been routinely used by other authors with slight variations for numerous material systems and geometrical configurations. On the other hand, the in-situ lift-out procedure was first pioneered by Yaguchi et al.[196–198] where they have performed the lift-out within the FIB instrument. The in-situ method is similar to the ex-situ method but allows a larger sample size extraction. When running an in-situ operation, the Omni-probe is positioned to touch the milled piece of the sample, then welded to the sample using platinum metal, and the sample is lifted out of the bulk material.

Most modern FIB-SEM instruments could also be used for 'serial sectioning ' to generate a regular stack of images, which can be transformed into a voxel-based data volume. Serial-sectioning is an alternating process of sectioning and imaging, in which the ion beam is used to erode thin layers ($\sim$10 nm) of the sample in the y-direction sequentially, and the electron beam is used to scan them.[190] The serial sectioning method could generate 3D volumes of up to $\sim$50x50x50 $\mu\mathrm{m}$, with typical slice thicknesses of around 30 nm. The complete serial sectioning operation is divided into three stages: (1) cube preparation and parameter optimisation, (2) serial sectioning, and (3) data processing.[199]

FIB-SEM is frequently used to characterise porous materials and granular microstructures. The structure-transport properties of porous material are governed by topological aspects such as connectivity, percolation, and pore neck diameters, and some of these features can be accurately quantified using adequate 3D imaging of the corresponding sample. Hence, FIB-SEM serial sectioning opens up new possibilities for analysing pore structures with sub-micron dimensions, as demonstrated for hydrated cement,[200–202] porous rocks and clays,[203,204] crack growth in metals,[205] fuel cell layers,[206] and catalyst pellets.[207]

[194] A. Leslie et al. *TEM sample preparation using FIB: Practical problems and artifacts*. ASM International, 1995.
[195] L. Giannuzzi et al. *MRS Online Proceed.*, **480**: , 1997.
[196] T. Yaguchi et al. *Microsc. Microanal.*, **5**: 365–370, 1999.
[197] T. Yaguchi et al. *Microsc. Microanal.*, **6**: 218–223, 2000.
[198] T. Yaguchi et al. *MRS Online Proceed.*, **636**: D9.35.1, 2000.
[199] S. Zaefferer, S. Wright, and D. Raabe. *Metall. Mater. Trans. A*, **39**: 374–389, 2008.
[200] L. Vandewalle. *Measuring, monitoring and modeling concrete properties*. Springer, 2006.
[201] L. Holzer and B. Muench. *Advances in concrete through science and engineering*. RILEM, 2006.
[202] P. Trtik et al. *J. Microsc.*, **232**: 200–206, 2008.
[203] L. Holzer et al. *Appl. Clay Sci.*, **47**: 330–342, 2010.
[204] G. Desbois, J. Urai, and P. Kukla. *Earth Discuss.*, **4**: 1–19, 2009.
[205] C. Holzapfel et al. *Scr. Mater.*, **56**: 697–700, 2007.
[206] J. Wilson et al. *Nat. Mater.*, **5**: 541–544, 2006.
[207] N. Duyckaerts et al. *FIB-SEM tomography imaging and 3D structure quantification of supported metal catalysts*. Wiley, 2016.

2.7 Thermoporometry by Differential Scanning Calorimetry

2.7.1 Background to Thermoporometry

Thermoporometry (or thermoporosimetry) is a calorimetric method for determining pore sizes using the melting or freezing point depression of a liquid confined in pores based on the observation of the solid-liquid phase transition.[208] There are several techniques for detecting the solid-liquid phase transition in pores as a function of temperature, including differential scanning calorimetry (DSC),[209] nuclear magnetic resonance (NMR),[210] and X-ray diffraction.[211] This part of the literature review will mainly focus on differential scanning calorimetry methods.

A differential scanning calorimeter (DSC) is well suited for detecting tiny temperature fluctuations due to its sensitivity to exothermic freezing and endothermic melting transitions. The physical explanation for the shift is that the equilibrium temperature for a solid-liquid phase transition is determined by the radius of curvature of the solid-liquid phase interface. Because a liquid confined inside a porous material is finely divided, the radius of curvature is directly related to the pore size.[209] The development of this technique is more recent and, hence not well recognised compared to mercury porosimetry and gas sorption. DSC measures the change in the heat flow rate to the sample pan and an empty reference pan, and can be used to characterise a wide variety of porous materials such as controlled pore glass (CPG),[209] sol-gel silica,[212] and ordered mesoporous materials such as MCM-41.[213–215] The technique has the advantage of being simple, easy to use, and measurements can be performed very quickly. Furthermore, no time-consuming sample preparation is required, and sample volumes required are in the milligramme range.

Brun et al.[216] pioneered the thermoporometry technique by developing the thermodynamic foundation for calculating pore size distribution from freezing liquid inside the pores. The confinement of material into microscopic pores is known to produce a decrease in melting point, as indicated by the Gibbs–Thomson[217] equation. Gibbs[218] demonstrated that the melting point of small crystals confined to small pores depends on the surface area of the pores. This idea was further developed by Thomson,[219] who proposed the crystal curvature theory and related it to liquid droplets. When a crystal confined within a cylindrical pore is melting, the relevant form of the

[208] J. Riikonen, J. Salonen, and V. Lehto. *J. Therm. Anal. Calorim.*, **105**: 811–821, 2011.
[209] M. R. Landry. *Thermochim. Acta*, **433**: 27–50, 2005.
[210] R. Valckenborg, L. Pel, and K. Kopinga. *J. Appl. Phys.*, **35**: 249–256, 2002.
[211] G. P. Johari. *J. Chem. Phys.*, **107**: 10154–10165, 1997.
[212] K. Ishikiriyama and M. Todoki. *J. Colloid Interface Sci.*, **171**: 103–111, 1995.
[213] A. Schreiber, I. Ketelsen, and H. Findenegg. *Phys. Chem. Chem. Phys.*, **3**: 1185–1195, 2001.
[214] K. Kloetstra et al. *Cataly. Lett.*, **33**: 145–156, 1995.
[215] T. Yamamoto et al. *J. Colloid Interface Sci.*, **284**: 614–620, 2005.
[216] M. Brun et al. *Thermochim. Acta.*, **21**: 59–88, 1977.
[217] C. A. Johnson. *Surf. Sci.*, **3**: 429–444, 1965.
[218] J. W. Gibbs. *Am. J. Sci.*, **16**: 441, 1869.
[219] W. Thomson. *Proc. R. Soc. Edinb.*, **7**: 63–68, 1875.

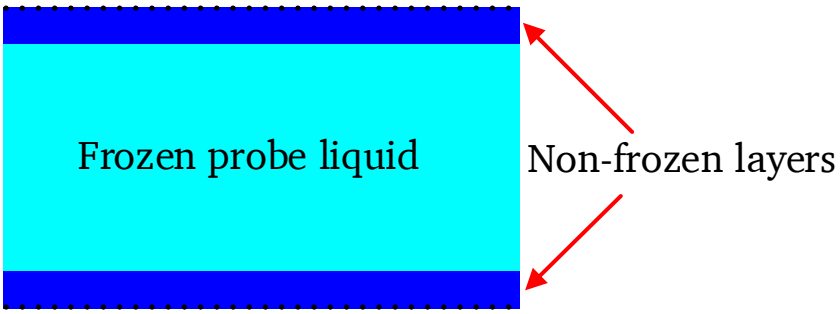


Figure 2.13: Schematic representation of frozen probe fluid and non-frozen liquid like layers inside a pore.

Gibbs-Thomson equation suggests that the melting point depression ΔT_m will be given by:

$$\Delta T_m = T_m^{\infty} - T_m(x) = -\frac{4\delta_{sl}T_m^{\infty}}{x\Delta H_{f\rho s}}\cos(\theta) \tag{2.18}$$

where $T_m(x)$ is the melting point in a pore of diameter x, T_m^{∞} is the bulk melting temperature, ΔH_f is the bulk enthalpy of fusion, δ_{sl} is the solid-liquid surface tension, ρ_s is the solid phase density, and θ is the contact angle between the frozen crystal and pore wall.

Equation (2.18) is referred to as the Gibbs-Thomson equation. The interaction between the pore wall and the imbibed fluid is assumed to be weak, and therefore, the contact angle is typically taken to be $180°$.[220] This assumption implies that the frozen crystal and the pore wall are not in contact with one another, but instead, there is a non-frozen liquid layer between the pore wall and the solid crystal.[213,220] The existence of the non-frozen layer was confirmed experimentally by Overloop and Vangerven.[221] Using NMR, these workers discovered that even after the imbibed liquid became frozen in the pore system, there was still a noticeable magnetisation. This magnetisation reduced gradually when the temperature was lowered, and it was not linked with hysteresis when the temperature was increased. From this, Overloop and Vangerven deduced that the shift in magnetisation could not be due to the imbibed fluid freezing or melting but must be due to a liquid layer that does not freeze. This non-frozen layer is comparable to the *t*-layer in gas sorption analysis, which is described elsewhere in the gas sorption sections.

Many of the parameters in the above equation are constants for a particular system, hence Strange et al.[222] suggested combining the parameters in the Gibbs-Thomson equation and deriving them experimentally. Therefore, the Gibbs-Thomson equation can be simplified as:

$$\Delta T_m = K_{GT}/X \tag{2.19}$$

In the above expression, K_{GT} is known as the Gibbs-Thomson constant. The K_{GT}-value is found experimentally, and usually a liquid with a large value of K_{GT} is preferred as this will make it

[220] C. L. Jackson and G. B. McKenna. *Chem. Mater.*, **8**: 2128–2137, 1996.
[221] K. Overloop and L. Vangerven. *J. Magn. Reson.*, **101**: 179–187, 1993.
[222] J. Strange, M. Rahman, and E. Smith. *Phys. Rev. Lett.*, **71**: 3589, 1993.

easier to observe when a given pore has frozen or molten. A Gibbs-Thomson values of $52\,\mathrm{nm\,K}$ has been suggested for mercury experiment on CPG silica.[213] However, Bafarawa et al.[109] found that for a mercury meniscus, melting hemispherically, the Gibbs-Thomson value was $90\,\mathrm{nm\,K}$.

Schreiber et al.[213] proposed a simple adjustment to the Gibbs-Thomson equation that accounts for the non-frozen layer of thickness t between the ice crystal and the pore wall. Thus, Equation (2.19) can be modified as:

$$\Delta T_m = \frac{K_{GT}}{x - 2t} \tag{2.20}$$

Equation (2.20) can be used to calculate a pore size distribution from the DSC thermograms since the pore size depends on the phase transition temperature, and the pore volume is proportional to the melting enthalpy of the phase transition.

2.7.2 Determining the Gibbs-Thomson constant

The Gibbs-Thomson constant is usually determined empirically using a sample with a known pore size such as SBA-15 or CPG materials. A plot of the melting point depression and the inverse median pore size should give a linear relationship according to Equation (2.19) for the portions that correspond to the Gibbs-Thomson constant. However, non-linear relationships have also been reported.[223] The validity of this method relies on the accuracy of calculating the known pore size distribution of the SBA-15 or the CPG samples, which is commonly obtained from electron microscopy and gas sorption analysis.[224] As a result, any errors in the pore size distribution from these methods will be reflected in the Gibbs-Thomson constant. The Gibbs-Thomson constant is still calculated using the technique described above despite these issues. Thus, there is a need for a more precise technique to determine the Gibbs-Thomson parameter, which would enable an accurate pore size to be found from thermoporometry. An alternative method was proposed by Perkins,[225] that compared the freezing curves of fragmented sol-gel silica with the corresponding water intrusion curves, analysed with the Kloubek relation. Perkins found that the Gibbs-Thomson parameter and the non-frozen layer thickness to be $48\,\mathrm{nm\,K}$ and $0.4\,\mathrm{nm}$, respectively, which are similar to the previously published values found by Petro and Furo.[226] The technique proposed by Perkins,[225] which accounts for the possibility of pore-pore interaction from water porosimetry data, is more accurate compared to the other methods as the other workers have ignored these effects.

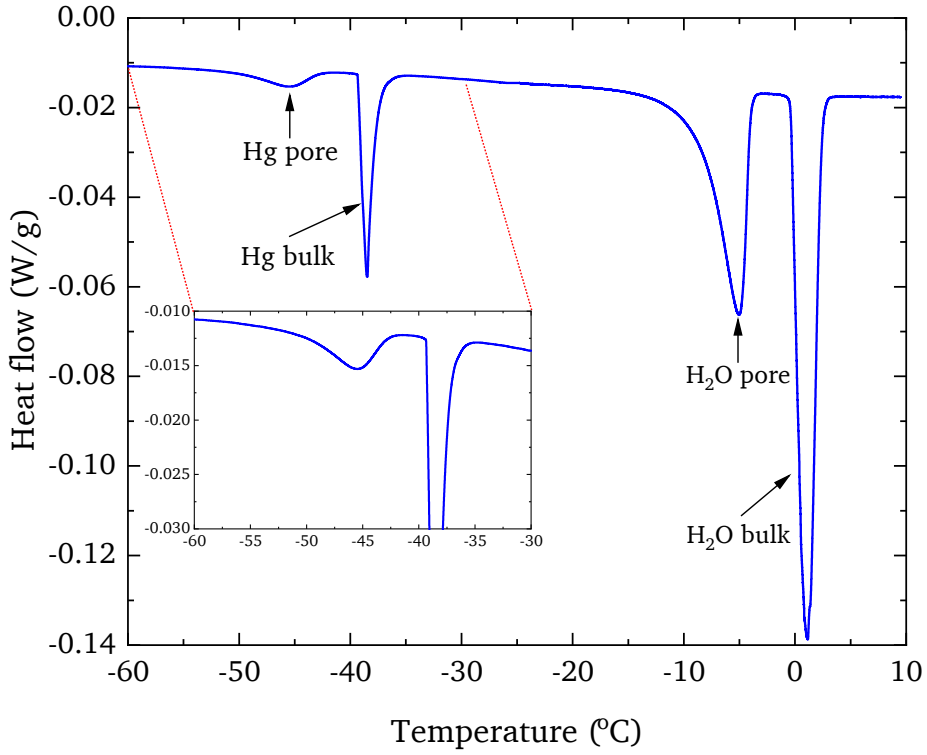


Figure 2.14: Example of DSC melting endotherm for a silica C10 pellet imbibed with dual-liquid, i.e. mercury and water. The sample was first entrapped with mercury using mercury porosimetry. Following this, the mercury-containing sample was then immersed in a bath of distilled water. The sample containing mercury and water was then frozen, and the melting curves were obtained.

2.7.3 Selecting the Probe Liquid

Many of the thermoporometry studies in literature have utilised a wide range of probe liquid, including cyclohexane,[227–229] water,[213,230–234] heptane,[229,234] benzene,[228,235] and mercury.[109] The choice of the probing fluid is crucial, especially when the experiment aims to find the whole pore size distribution for the sample's entire void space. In this case, the chosen liquid should wet the entire void space and remove all the air. If only certain pores are filled with liquid, the computed pore size distribution will not accurately represent the entire void space. Another key considera-

[223]R. Schmidt et al. *J. Am. Chem. Soc.*, **117**: 4049–4056, 1995.
[224]E. Hansen et al. *J. Phys. Chem. B*, **106**: 12396–12406, 2002.
[225]E. Perkins et al. *Chem. Eng. Sci.*, **63**: 1929–1940, 2008.
[226]O. Petrov and I. Furó. *Prog. Nucl. Magn. Reson. Spectrosc.*, **2**: 97–122, 2009.
[227]E. Shiko et al. *J. Colloid Interface Sci.*, **398**: 168–175, 2013.
[228]E. Hansen, R. Schmidt, and M. Stöcker. *J. Phys. Chem.*, **100**: 11396–11401, 1996.
[229]C. L. Jackson and G. B. McKenna. *J. Chem. Phys.*, **93**: 9002–9011, 1990.
[230]K. Morishige and K. Kawano. *J. Chem. Phys.*, **110**: 4867–4872, 1999.
[231]S. Jähnert et al. *Phys. Chem. Chem. Phys.*, **10**: 6039–6051, 2008.
[232]D. Majda et al. *J. Therm. Anal. Calorim.*, **127**: 207–220, 2017.
[233]T. Rottreau et al. *Microporous Mesoporous Mater.*, **264**: 265–271, 2018.
[234]D. Majda, W. Makowski, and M. Mańko. *J. Therm. Anal. Calorim.*, **109**: 663–669, 2012.
[235]G. Dosseh, Y. Xia, and C. Alba-Simionesco. *J. Phys. Chem.*, **107**: 6445–6453, 2003.

tion for choosing the correct probe liquids is the nature of the liquid-solid phase transition. It is recommended that the phase transition for the liquid be as abrupt as possible so that different pore sizes can be distinguished properly. This means that the probe liquid should transition from a well-defined solid phase to a clearly liquid phase over a small temperature range. For this reason, it is essential to consult with phase diagrams in order to pick a suitable probe fluid and check the likely complexity of the phase transition.[7] Probe liquids can also be chosen to have a sizeable Gibbs-Thomson constant as this will make it easier to observe when a given pore has frozen or molten. Additionally, large K_{GT} means that bigger pores can be probed using the thermoporometry method.

Two probe fluids can also be used simultaneously in the sample, for example, mercury and water or mercury and other hydrocarbons, such as cyclohexane, in what will be called a dual-liquid thermoporometry technique. In this technique, the sample is first entrapped with mercury using mercury porosimetry, and then the mercury-containing sample is immersed in a bath of a second probe fluid. The water could force the mercury out of the pore very quickly by capillary; however, if the sample is frozen to $-80\,^{\circ}\mathrm{C}$ (which took 4 minutes on the DSC machine used), it is possible to observe a DSC thermogram of the two probe fluids, as shown in Figure 2.14 for mercury and water in a silica C10 sample.[7] Because mercury melts at a lower temperature than water, the mercury melting curve can be measured while the water is still frozen. Once the mercury has melted, the melting curve for water at a higher temperature may be measured.

However, in thermoporometry experiments, water is the most widely utilised probe fluid. This is because it is non-hazardous, freely available, and has a high enthalpy of fusion, $\Delta H_f = 334$ $\mathrm{J/g}$. The high melting enthalpy is perhaps the most crucial characteristic of water since it boosts the experiment's sensitivity or allows for slower heating/cooling ramping rates or smaller sample masses to be used. Another advantage of using water is that the sample is not contaminated by water, which is readily adsorbed on the pore walls of hydrophilic materials from ambient air.[208]

2.7.4 Hysteresis in Thermoporometry

In thermoporometry, the melting and freezing curves of a mesoporous material are known to display hysteresis, which means that freezing occurs at lower temperatures than melting. Different theories have been proposed to explain the causes of melting-freezing hysteresis, including pore-blocking effects,[236] different shapes of solid-liquid interface,[216] and free energy barrier in melting and nucleation during freezing.[237] Denoyel et al.[238,239] studied the freeze-melting hysteresis process for a controlled pore glass (CPG) and MCM-41 samples and discovered similarities between hysteresis found in gas adsorption-desorption mechanisms and freeze-melting mechanisms in thermoporometry. These researchers, however, did not provide a precise thermodynamic explanation of hysteresis.

[236] K. Morishige, H. Yasunaga, and Y. Matsutani. *J. Phys. Chem. C*, **114**: 4028–4035, 2010.
[237] K. Morishige et al. *J. Phys. Chem. C*, **111**: 9488–9495, 2007.
[238] R. Pellenq et al. *Langmuir*, **25**: 1393–1402, 2009.
[239] I. Beurroies et al. *Thermochimi Acta*, **421**: 11–18, 2004.

Other theories proposed to account for thermoporometry hysteresis include that of Petrov and Furó,[226] where they have suggested that freezing-melting hysteresis is caused by a free energy barrier between metastable and stable states of pore-filling liquid. This theory suggests that the freezing process proceeds axially from the nucleation site to the pore while melting starts from the non-frozen layer at the pore surface to the pore centre. In this case, the melting process is delayed until the energy barrier required to commence melting is overcome. When the probe liquid is melted, the pore system returns to a local minimum energy state. However, an activation barrier must be overcome to reach the new minimum energy state, and it is this energy barrier that causes hysteresis. This is comparable to Cohan's[55] gas adsorption and desorption mechanism, in which the freezing process is mediated by a hemispherical meniscus, while a cylindrical sleeve type meniscus mediates the melting process.

Another theory proposes that the confined liquid gets super-cooled when there is no nucleation source to seed freezing at the equilibrium freezing temperature. Supercooling proceeds until homogenous nucleation eventually causes ice formation, similar to what happens with bulk liquids. On the other hand, the melting process can be sped up since the non-frozen liquid-like layer might commence melting.[226]

Another possible cause of hysteresis is heterogeneous nucleation, which occurs when the freezing is initiated by a solid ice phase that has already formed. However, if a narrower pore neck restricts the crystalline front's access to the pore, the pore may be prevented from freezing. As a result, the penetration of an outer crystalline front is delayed until the temperature drops to the threshold necessary for the narrow neck to freeze, according to the Gibbs-Thomson equation. This theory is similar to the pore-blocking mechanism explained in the gas adsorption sections. Based on the above description, Petrov and Furó[226] demonstrated that the following expression gives the freezing point depression:

$$\Delta T_{\mathrm{f}} \cong -\frac{\upsilon \gamma_{\mathrm{sl}} T^0}{\Delta H} \frac{S}{V} \tag{2.21}$$

whereas the melting point depression is given by:

$$\Delta T_{\mathrm{f}} \cong -\frac{\upsilon \gamma_{\mathrm{sl}} T^0}{\Delta H} \frac{S}{V} \tag{2.22}$$

where υ is the molar volume, γ_{sl} is the surface free energy, T_0 is the bulk liquid melting point, ΔH is the latent heat of melting, S is the surface area of the pore, and V is the volume of the pore. Petrov and Furó[226] used Steiner's[240] formula for equidistant surfaces to show that Equation (2.22) may be rewritten as:

$$\Delta T_{\mathrm{m}} \cong -\frac{\upsilon \gamma_{\mathrm{sl}} T^0}{\Delta H} 2\kappa = \Delta T_{\mathrm{f}} \frac{2\kappa V}{S} \tag{2.23}$$

[240] L. Parapatits and F. Schuster. *Adv. Math.*, **230**: 978–994, 2012.

where κ is the pore surface's integral mean curvature and is given by:

$$\kappa = \left(\frac{1}{2S}\right) \int_S \left(\frac{1}{r_1} + \frac{1}{r_2}\right) \mathrm{d}S \tag{2.24}$$

where r_1 and r_2 are the principal radii of curvature. For a cylindrical pore, $2\kappa V/S = 1/2$ (since for a cylinder, $\partial S/\partial V = 1/r$ and $S/V = 2/r$), and thus, this means the predicted numerical difference of a factor of 2 in ΔT_m and ΔT_f can be used to determine whether a pore is cylindrical or not.[7]

2.8 Conclusions

This chapter introduced the reader to some of the main techniques for porous materials characterisations, including mercury porosimetry, gas adsorption, computerised X-ray tomography (CXT), scanning electron microscopy (SEM), and thermoporometry. The next chapter will present the development and application of the hybrid method called integrated mercury porosimetry-gas sorption and imaging to characterise fresh methanol synthesis catalyst pellets to deliver a much better fundamental understanding of how specific pore subsets affect the mass transport through the pellet. The integrated technique allows one to selectively block a particular portion of the pore structure and determine the transport properties before and after their removal.

In Chapter 3, the reader will be introduced to fresh methanol synthesis catalyst pellets made from spray-dried and roll compacted feed materials.

Chapter 3

Integration of multi-scale porosimetry and multi-modal imaging in the study of structure-transport relationships in porous catalyst pellets

3.1 Abstract 52
3.2 Introduction 53
3.3 Theory 56
3.4 Materials and Method 59
3.5 Results 64
3.6 Discussion 91
3.7 Conclusion 98

3.1 Abstract

The forming process for heterogeneous catalyst pellets impacts on reactor performance. In order to intelligently optimise the product formulation and manufacturing procedure, the impact of fabrication options on the resultant pore structure and mass transfer properties must be fully understood. In this work, the more direct information possible from multi-modal imaging methods has been combined with the more statistically-representative, multi-scale data from porosimetry, including the rarely-used gas overcondensation technique, to characterise batches of methanol synthesis catalyst tablets made using different feed types. Despite the hierarchies of complexity of the porous pellets revealed by the computerised X-ray tomography and FIB-SEM images, the impact on mass transfer of controlled modifications to the void space, achieved through mercury porosimetry, could be modelled using a relatively simple random pore-bond network. The characteristic parameters for the model were obtained from a percolation theory-based analysis of the overcondensation data. A quantitative relationship was thereby obtained between the structural information contained within the overcondensation isotherms and the rate of mass uptake of gas into the porous pellets. This revealed the differential importance to mass transfer of particular sets of pores, associated with certain pellet structural features, and the impact on tortuosity of pellet fabrication parameters such as particle feed size.

3.2 Introduction

The ultimate, observed activity of many heterogeneous catalysts, such as methanol synthesis pellets, is limited by mass transport rates, rather than the intrinsic reaction rate. The reaction rate is said to be diffusion-limited. In such cases, the effectiveness factor of the catalyst pellets is well below unity. For many industrial processes the effectiveness factor can be in the region of 50-60%.[5] Hence, the performance efficiency of the catalytic process could be substantially improved by increasing catalyst effectiveness factor. This requires a deeper understanding of the pore structure-transport relationship within the catalyst pellets, and, also, how that pore structure depends upon the pellet fabrication method. In this work, we will study how different fabrication processes affect pore structure in the final pellet, and its impact on mass transport rates. In particular, how specific features of the void space are related to certain aspects of the fabrication process will be determined. This requires powerful pore structural characterisation methods that can deliver comprehensive and detailed analyses of the pellet void space.

In disordered porous media, heterogeneity often exists in the spatial distribution of porosity over different length scales. The void spaces themselves may also have varied characteristic sizes with different length scales. Various imaging modalities such as atomic force microscopy (AFM), computerized X-ray tomography (CXT), scanning electron microscopy (FIB-SEM) and electron tomography (3D-TEM) have been used to directly study porous materials.[7] However, for materials with hierarchical or multi-scale porosity, no single imaging modality alone can visualise pores across all the size scales from nanopores to micron-sized macropores or map macroscopic variation in nanoscopic properties.[241,242] Imaging modalities have limitations on the field-of-view (FOV) that they can image at a particular resolution. For example, a previous multi-scale imaging approach, used for studying fluid catalytic cracking particles (with $\sim$100 μm diameter), employed FIB-SEM that could image volumes of $2\times2\times2$ μm at a resolution of $20\times20\times20$ nm.[243] However, this voxel resolution is above the size of smaller mesopores and micropores, that can be probed with gas sorption. In addition, a typical catalyst pellet (5 mm diameter, 5 mm long) would contain 10^{10} such image volumes, each of which might be different in internal properties, and have some type and degree of spatial correlation, and thus may not be completely randomly distributed.[6] For imaging data to obtain the typical properties of a porous solid, then the FOV must encompass the representative volume or correlation length of the structure being imaged. For highly complex or fractal materials that may not be possible.[6] However, some other means to link together characterisation data may still be needed for highly heterogeneous materials. In this work it will be seen how indirect characterisation methods, that can span many orders of magnitude in pore sizes, like gas overcondensation and mercury porosimetry, can link together the various levels in the imaging hierarchy.

[5] M. V. Twigg. *Catalyst handbook*. CRC Press, 2018.
[7] S. P. Rigby. *Structural characterisation of natural and industrial porous materials: A manual*. Springer Nature, 2020.
[241] A. Muhammad et al. *Int. J. Coal Geol.*, **233**: 103641, 2021.
[242] M. Lin et al. *J. Energy*, **181**: 1285–1297, 2019.
[243] D. Winter, M. Florian, and B. Weckhuysen. *ACS Catal.*, **6**: 3158–3167, 2016.
[6] A. Nepryahin et al. *Chem. Eng. Sci.*, **152**: 663–673, 2016.

For hierarchical or multi-scale structures requiring imaging with multiple modalities, some sort of upscaling procedure is required to link together data acquired at different length-scales.[242,244,245] A variety of upscaling procedures have been adopted in the literature. One Such procedure involves identification of a set of different phases at a larger length-scale, such that regions that are considered as belonging to the same phase have similar properties at smaller length-scale. In rock structures these different phases might be identified with different types of mineral grains, where disparities in the mineralogy (e.g., quartz, illite etc.) leads to different phases with markedly different properties to each other.[242] However, some porous materials, such as industrial materials, are less discretely variegated such that useful identification of a limited set of such phases is impossible.[7] An alternative approach employs pore bond network models with separate bonds to represent microporosity in series or parallel with macroporosity. One such approach used an SEM image-based method to construct a multiscale pore network model that incorporates multi-scale pore structure spatial and statistical properties at different resolutions.[244,245] Other upscaling procedures rely upon random allocation of porosity and transport properties to individual lower length-scale regions in grids representing an upper length-scale.[243] However, many industrial materials have non-random distributions of lower length-scale properties over larger length-scales.[6] In such cases, an alternative strategy is required.

The indirect, mercury, or Wood's metal, intrusion methods have been combined with complementary SEM and/or CXT imaging to provide contrast agents to improve the image quality of the latter and/or to deshield pore size distributions of the former in order to obtain detailed void space characterisations.[246–248] However, an alternative strategy[6,112,249] for dealing with highly complex porous media, that has been proposed is to directly sift the various pore structural features for their importance to mass transport. This is achieved by progressively eliminating particular, chosen ranges of pore sizes from the transport network, via controlled pore-filling with an obstructing phase (e.g., mercury, ice, or water) using a porosimetric technique, and determining the subsequent impact on mass transport rates of a fluid. This approach is interventionist and experimental, and, thus, differs from modelling approaches in the past that have aimed at determining the importance of particular aspects of the pore structure to mass transport by computer simulation on model structures modified in various ways.[11–13] If a modelling approach is to be truly a priori predictive of mass transport, then it requires an exhaustive characterisation of the void space to ensure the structural model contains all the key features of the void space pertinent to mass transport to the requisite detail. The level of accuracy and comprehensiveness needed for the structural model may not be practicable, or even possible, with current computing power, for very complex

[244] J. Yao et al. *Int J Heat Mass Transf.*, **141**: 156–167, 2019.
[245] W. Song et al. *Transp. Porous Media*, 1–25, 2021.
[246] G. Cody and A. Davis. *Energy Fuels*, **5**: 776–781, 1991.
[247] J. Kaufmann. *Cem. Concr. Compos.*, **32**: 514–522, 2010.
[248] L. Ruffino et al. *Can. J Chem. Eng.*, **83**: 132–139, 2005.
[112] A. Nepryahin et al. *Adsorption (Boston)*, **22**: 993–1000, 2016.
[249] F. Hill et al. *Chem. Eng. J.*, **405**: 126750, 2021.
[11] S. Prachayawarakorn and R. Mann. *Catal. Today*, **128**: 88–99, 2007.
[12] C. Rieckmann and F. Keil. *Chem. Eng. Sci.*, **54**: 3485–3493, 1999.
[13] S. Gheorghiu and M. Coppens. *AlChE J.*, **50**: 812–820, 2004.

porous solids. Hence, statistical approaches based upon simplified pore structural models are often used.[7,14] However, it is then not clear how the supposed important feature of the simplified pore network model relates to the more complex, real network, or how to select the key aspects of the void space to incorporate into models.

In previous work using the sifting approach, entrapped mercury was used to obstruct pore structural features in tabletted methanol synthesis pellets, made using roll compacted (RC) feed, and compacted to two different densities.[6] It was found that mass transport was dominated by cracks through the pellet, and voids formed via the splintering of the edges of feed particles during compaction. However, the comprehensiveness of the pore characterisation was limited due to the use of only conventional gas sorption experiments to probe the void space left accessible following mercury entrapment, and the limitations on the resolution of the CXT imaging employed. Characterisation of macroporosity can be problematic, and the issues and potential solutions have been reviewed.[63] In this work, the gas overcondensation method will be used to expand the range of pore sizes that can be probed up to very large macropores. The gas overcondensation method used in this work, therefore, overcomes previous failings[6] with missing the largest macropores within the methanol catalyst pellets using both conventional adsorption, because capillary condensation was not achieved in these macropores, and also mercury porosimetry, because these macropores were shielded by very small necks for which intrusion would have required pressures in excess of the maximum possible for the apparatus used (414 MPa). Gas overcondensation, thus, makes available the full boundary desorption isotherm for use in percolation modelling not possible otherwise. In addition, multi-modal imaging, employing both high and low resolution CXT, together with FIB-SEM, will be used to improve interpretation of each other, as well as of the indirect pore characterisation methods, in addition to providing spatially-resolved information.

It is often suggested that model porous materials, such as MCM-48 or SBA-15, with controlled pore geometry, often achieved via templating or etching procedures, can inform interpretation of indirect pore characterisation methods.[7,250] These types of materials can aid the testing of fundamental theories for limited length-scale phenomena, such as the origins of single pore hysteresis in simple geometries.[7,250,251] However, these materials, necessarily, have limited unit cell sizes, and as will be seen here, the forms of characterisation data for disordered industrial materials are not just composites of that for model materials. Indeed, it will be seen here that characterisation data is dominated by pore-to-pore co-operative effects that are sample-spanning over macroscopic length-scales. Hence, the characterisation process must address the real, disordered material itself even in the first instance.

The main aim of the current work is to identify the critical pore structural features that impact mass transport due to the particular fabrication route employed and thereby inform potential future strategies for improved manufacturing of the tablets. It will be seen that, for the partic-

[14] B. Bukowski et al. *Adsorption (Boston)*, **27**: 683–760, 2021.
[63] J. Rouquerol et al. *Pure Appl. Chem.*, **84**: 107–136, 2011.
[250] A. V Neimark and P. Ravikovitch. *Microporous Mesoporous Mater.*, **44**: 697–707, 2001.
[251] J. Jagiello et al. *Carbon*, **178**: 113–124, 2021.

ular pellets studied here, these key features involve the macroscopic spatial distribution of the mesoporosity. In this chapter, methanol synthesis pellets made using two very different types of feed, produced by spray-drying or roll-compaction, will be studied. This is to examine how these different fabrication methods affect the finished pellet properties. Both the starting feed particles and the finished tablets will be studied. It will be seen how gas overcondensation can probe very small void spaces not accessible to mercury porosimetry and many imaging modalities, as well as probing very large macropores with the same technique. Multi-scale imaging, including lower resolution CXT (down to a few microns), higher resolution CXT (down to hundreds of nm), and FIB-SEM (down to a few nm), will be used to improve interpretation of the indirect methods and each other. It will be seen how this new combination of methods can be used to determine the key features of the void space that control gas-phase uptake into the porous pellets, and identify their relationship to the fabrication process and raw materials.

3.3 Theory

Mass transport properties can be characterised by kinetic gas uptake experiments. Kinetic mass uptake data, comprising amount adsorbed versus time, typically takes the mathematical form of an exponential growth, and, thus, is often fitted to the so-called Linear Driving Force (LDF) model.[7] The characteristic parameter of this process is the mass transfer coefficient, denoted k. The LDF *k*-value is defined by the function[7]:

$$M = M_0 \left(1 - e^{-kt}\right) \tag{3.1}$$

where M is the amount of nitrogen adsorbed at time t, M_0 is the ultimate total adsorbed amount of nitrogen for the adsorption pressure point, and k is the mass transfer coefficient. The apparent mass transfer coefficient, obtained from a fit to raw uptake data, must be corrected for the effect of concurrent adsorption using the slope of the isotherm at the relevant adsorption pressure point. In this way the actual mass transfer coefficient is obtained. For a porous sample, the mass transfer coefficient k depends upon the intrinsic effective diffusivity of the porous material, composed of the reference diffusivity D_A, the porosity (voidage fraction) and tortuosity of the medium, plus the diffusion penetration depth a, and a geometric factor, which is 15 for a spherical particle[7]:

$$k = \frac{15 D_A \frac{\varepsilon}{\tau}}{a^2} \tag{3.2}$$

The reference diffusivity will be the bulk molecular diffusivity in the molecular diffusion regime, and the Knudsen diffusivity for the critical pore size in the Knudsen regime. If a fraction of a porous network is removed in some manner, but the reference diffusivity and the particle overall size and geometry remain constant, then the ratio of the original tortuosity τ_0 to the subsequent tortuosity τ will be given by:

$$\frac{\tau_0}{\tau} = \frac{k}{k_0} \frac{\epsilon_0}{\epsilon} \tag{3.3}$$

where the subscript 0 denotes the parameter for the original porous network and the lack of subscript represents the general parameter for any modified network.

It has been proposed that, for multi-scale porous solids, that the total tortuosity τ has contributions from different length-scales, such that the total tortuosity is given by[252]:

$$\tau = \tau_a \tau_e \tau_i \tag{3.4}$$

where τ_a is the macroscopic tortuosity, describing the pore structure over length-scales of the whole pellet (mm), τ_e is the mesoscopic contribution to the tortuosity, which describes tortuosity measured over length-scales of a few pore diameters up to scales at which macroscopic heterogeneities become important, and τ_i characterises tortuosity over length-scales of up to a few pore diameters. Equation (3.4) has been found, via both computer modelling and experimental validation, to successfully relate the particular different tortuosities obtained from magnetic resonance imaging and pulsed-field gradient NMR methods that probed the total and meso-/micro-scale tortuosities, respectively.[252,253]

The macroscopic structure of the catalyst pellets studied in this work will be modelled by three-dimensional, random pore bond networks. Such networks consist of lattices of pore bond elements that meet at lattice node junctions. The typical number of pore bonds meeting at a node, averaged over the whole lattice, is called the connectivity Z. The overall size of the lattice measured in lattice bond units is denoted L. The parameters Z and L can be determined from percolation analysis of gas sorption data using a method based upon that developed by Seaton.[15] Percolation analysis is carried out in terms of percolation variables, the values of which are calculated from pore diameter distributions, and the branches of the hysteresis loop in gas sorption isotherms.

The Seaton[15] percolation analysis neglects single pore hysteresis, such that adsorption and desorption in a single lattice bond is considered reversible, and, thence, assumes that all hysteresis arises from network-based pore-blocking effects. This is considered reasonable if the pore units represented by model bonds are extensive, since adsorption in very long pores tends to that for the equilibrium mode, or dead-end pores.[7] Therefore, in the percolation analysis of gas sorption hysteresis, the bond occupation probability at a particular pressure is given by:

$$X = \frac{\text{The number of pores below their critical condensation pressure}}{\text{The total number of pores in the network}} \tag{3.5}$$

where X represents the number fraction of pores from which condensate would have evaporated in a perfectly connected network. Assuming that the pores have a cylindrical geometry, the pore number distribution as a function of pore diameter is calculated from the volume-weighted pore diameter distribution obtained from the adsorption isotherm. The number, n_i, of pores of diameter

[252] S. P. Rigby and L. F. Gladden. *J. Catal.*, **173**: 484–489, 1998.
[253] S. P. Rigby and L. F. Gladden. *Chem. Eng. Sci.*, **51**: 2263–2272, 1996.
[15] N. A. Seaton. *Chem. Eng. Sci.*, **46**: 1895–1909, 1991.

d_i is given by:

$$n_i = \frac{V_i}{\pi \frac{d_i^2}{4} l_i} \tag{3.6}$$

where V_i is the incremental volume of pores with diameter d_i, and l_i is the average pore length for such pores. It is assumed that pore length is always greater than diameter, and thus diameter is the characteristic pore dimension for adsorption. In the original Seaton method[15] it was assumed that the average pore length is the same in each pore size interval. However, here, as in previous work,[104] it will be allowed that the average pore length can depend upon diameter, such that:

$$l_i = m \cdot d_i^{\alpha} \tag{3.7}$$

where m and α are constants. The set of X values (one for each data point i on the adsorption isotherm) is then given by:

$$\boldsymbol{X_i} = \frac{\sum_{j=1}^{i} \boldsymbol{n_j}}{\sum_{\boldsymbol{j=1}}^{N} \boldsymbol{n_j}} \tag{3.8}$$

where N is the total number of pore size intervals.

The accessibility, X^A, is the number fraction of pores that are both below their critical pressure and have access to the surface, either directly or via a network of vapour-filled pores. Hence, in other words, it is the fraction of pores from which evaporation of condensate has actually occurred. The experimental values of X^A are calculated from the deviation between the separate pore-blocked desorption isotherm and unshielded adsorption isotherm according to the method described previously by Seaton.[15] The experimentally derived pairs of values of X and X^A are then fitted to a universal scaling relation G such that:

$$L^{\beta/v} Z X^A = G\left[(ZX - 3/2)L^{1/v}\right] \tag{3.9}$$

where β and v are critical exponents which take values of 0.41 and 0.88, respectively. The generalised scaling relation G was constructed using the simulation data of Kirkpatrick[254] for cubic lattices.

[104] S. P. Rigby, M. J. Watt-Smith, and R. S. Fletcher. *J. Catal.*, **227**: 68–76, 2004.

[254] S. Kirkpatrick et al. *Les Houches Summer School on Ill Condensed Matter*. Amsterdam: North-Holland, 1979. 321

Table 3.1: Characteristics of the whole pellet samples. Porosity values were obtained from mercury porosimetry. The bulk density was obtained from mercury porosimetry.

Sample	Porosity (%)	Bulk density (g/cm^3)	BET (m^2/g)	Cylinder dimension (diameter x height)
Fresh SD	47.10%	2.2	96.16 ± 2.56	5.5×3.4mm
Fresh RC	48.10%	2.3	88.13 ± 10.70	5.6×3.5mm

Table 3.2: Specific pore volumes and modal pore diameters of the samples determined by two different methods.

Sample	Hg pore volume (ml/g)	N_2 sorption pore volume (ml/g)	Hg modal pore diameter (nm)	N_2 modal pore diameter (nm)
Fresh SD	0.224± 0.006	0.226± 0.008	9.4	9.3
Fresh RC	0.217± 0.012	0.237± 0.021	10.9	10.4

3.4 Materials and Method

3.4.1 Samples studied

Fresh methanol synthesis catalyst pellets made using either spray dried (SD) or roll compacted (RC) feed materials were studied in this chapter. The Cu:Zn:Al molar ratio was 4.4:1.6:1 for both materials. The initial materials preparation used standard precipitation techniques employing metal nitrate precursor salts. The catalyst pellets were formed by a bi-directional axial compaction process. The SD and RC pellets are mesoporous cylindrical tablets with average dimensions of ∼5.5×3.5 mm (base diameter × height). The SD pellets had an average BET surface area of $96.2\,m^2g^{-1}$, and the RC pellets an average BET surface area of $88.1\,m^2g^{-1}$. Tables 3.1 to 3.2 contain further details and properties of the samples studied. The pellets were characterised by gas sorption both in their whole pellet and fragmented (∼53-73 microns powder particle size) forms. It is noted that the sample mean pore volumes obtained from gas overcondensation exceed those from mercury porosimetry. This is because the samples contain macropores that are shielded by narrow necks too small to intrude with the maximum pressure possible with the mercury porosimeter used.

3.4.2 Experimental Procedure

3.4.3 Integrated Mercury Porosimetry and Gas Sorption

The integrated mercury porosimetry and gas sorption technique consists of a series of experiments conducted on the same sample. Figure 3.1 shows the schematic representation of the gas-mercury-gas procedure used during the experiments. The nitrogen sorption isotherms were measured at liquid nitrogen temperature ($77\,K$) using a Micromeritics 3Flex physisorption analyser. Approximately $0.8\,g$ of the sample was weighed and placed into a pre-weighed standard physisorption sample tube with a sealing frit placed at the top to prevent the sample from being evacuated into the 3Flex manifold. The tube (with sample) was then loaded into the degassing station and

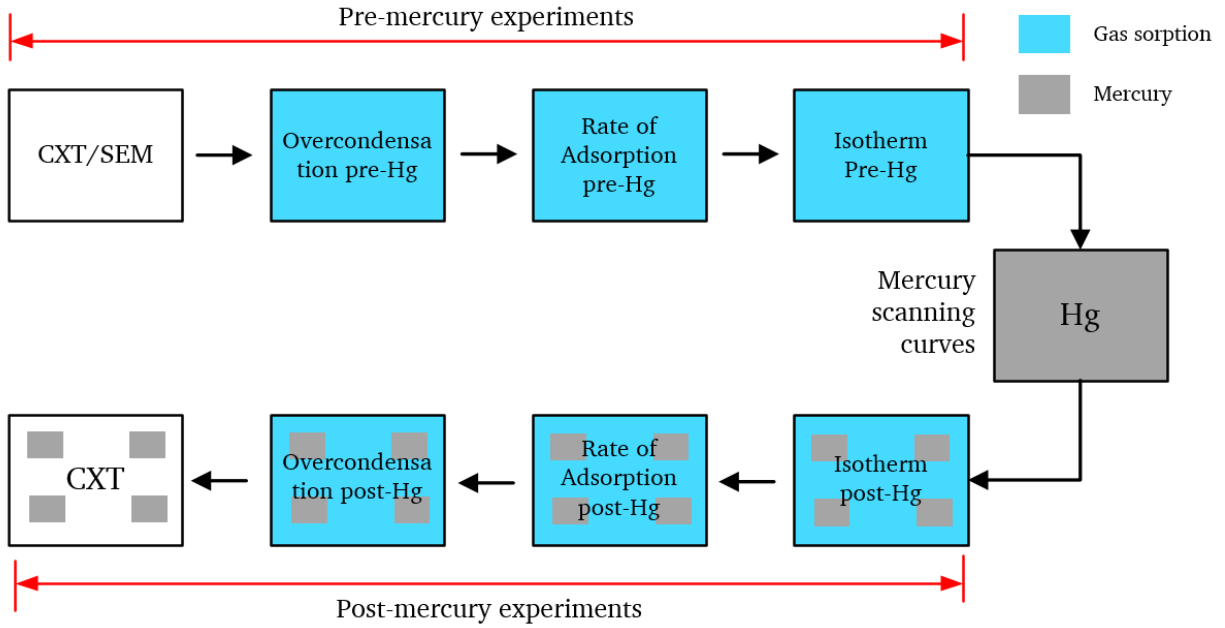


Figure 3.1: A schematic representation of the integrated mercury porosimetry-gas adsorption-imaging technique.

initially degassed at room temperature until a vacuum of $0.002\,\mathrm{mmHg}$ was reached. The temperature of the sample was then raised to $140\,^{\circ}\mathrm{C}$ by using a heating mantle, and the sample was left under a vacuum for $24\,\mathrm{h}$. The thermal pre-treatment drives off any physisorbed water on the sample but does not change the sample morphology. After the $24\,\mathrm{h}$ had passed, the heating mantle was removed, and the sample was allowed to cool down to room temperature. The sample tube and its contents were then re-weighed to obtain the dry weight of the sample. Isothermal jackets were then placed around the sample tubes before reattaching to the analysis port to begin the automated gas sorption analysis. The isothermal jacket ensures a constant thermal profile of $77\,\mathrm{K}$ along the length of the sample tube during the analysis stage. Nitrogen purity was 99.995%. The isotherms consisted of approximately 60 adsorption and 50 desorption points. Gas sorption was measured over the relative pressure (P/P_0) range of 0.01 to 0.995 for adsorption isotherm and 0.995 to 0.10 for desorption isotherm. The saturation pressure (P_0) was measured for each data point on the isotherm.

Once the first nitrogen gas sorption experiment was finished, the samples were allowed to reach room temperature ($\sim 295.15\,\mathrm{K}$) and then quickly transferred to a mercury intrusion porosimetry (MIP) machine to entrap mercury into the pores. Mercury intrusion and extrusion curves were measured using a Micromeritics Autopore IV 9500, which can generate a maximum pressure of $414\,\mathrm{MPa}$ (60,000 psia). Mercury intrusion data was generated for the range specified in the scanning curve pressure points, followed by retraction back down to atmospheric pressure. To do this, the sample was transferred into a penetrometer, and the weight of the penetrometer and sample was recorded. The penetrometer (with sample) is then placed in the low-pressure port of the instrument. During the low-pressure analysis, the sample is firstly evacuated up to

$50\,\mathrm{mmHg}$ to drive off any water vapour or atmospheric gases in the pore network. The sample bulb is then filled with mercury while the entire system is still under low pressure. Data collection begins at a pressure of $0.5\,\mathrm{psia}$, which is enough pressure to cause mercury to penetrate sample pores larger than $360\,\mu\mathrm{m}$ in diameter. After the low-pressure analysis was completed, the assembly weight (penetrometer + sample + mercury) was recorded, the penetrometer was transferred to the high-pressure port, and the chamber was closed tightly. The penetrometer is placed vertically in the high-pressure port, and it is surrounded by oil, which is the hydraulic fluid the instrument uses to generate high pressures. As the hydraulic fluid pressure rises, it is transmitted to the mercury in the penetrometer via its open capillary stem. An equilibration time of $15\,\mathrm{s}$ was used for each data point.

Once the mercury intrusion experiment was finished, the sample was immediately discharged from the penetrometer, recovered, and returned to the 3Flex sample tube, where the rate of adsorption and the conventional adsorption experiments were repeated. The sample was first cooled to $77\,\mathrm{K}$ by manually raising the Dewar flask, allowing the sample to freeze for approximately $30\,\mathrm{min}$. This part was important in the post mercury entrapment steps since it freezes the mercury in place to ensure that it all remains immobilised within the pellets. The warm and cold free space of blank tubes was first measured before analysis using helium pycnometry (skeletal density) and sample weight to subtract from the volume of the sample. This allows disabling the conventional warm and cold-free space method on low-pressure gas sorption instrumentation. The integrated rate of adsorption-mercury porosimetry aims to selectively block certain pore sizes and then study how important those pores were to the rate of mass transport before and after their removal. Previous experiments where the mercury was thawed and re-frozen after a week prior to a subsequent gas sorption have shown that the mercury ganglia did not move around over this timescale or due to the freezing, since the shapes of the gas sorption isotherms remained the same.[6]

3.4.4 Rate of Adsorption procedure

The sample preparation and the experimental setup for the rate of adsorption experiment are similar to that of other gas sorption experiments. The fresh SD and RC samples were degassed at $140\,^{\circ}\mathrm{C}$, and the samples were kept under vacuum for 24 hours to drive off any moisture or physisorbed gas on the pores. The rate of adsorption (ROA) technique works by dosing a known quantity of nitrogen gas onto the sample and then recording the amount of gas adsorbed, and the corresponding pressures over time. The dosing quantity was taken from the BET monolayer capacity (V_m). An additional $5\,\mathrm{cc(STP)/g}$ of gas was added to this amount to compensate for the initial expansion of the gas into the free space of the sample tube. This is because the gas first fills the sample tube before adsorbing onto the sample surface. The number of readings of pressure was set at 1000 readings per dose. The ROA data was collected at the lowest pressure point in the isotherm. In this region of the isotherm there is negligible obstruction from adsorbed phase and the diffusion is in the Knudsen regime and corresponds to the process conditions in the reactors in which the methanol synthesis pellets are used. The rate of uptake data was collected both before and after mercury entrapment.

3.4.5 Overcondensation gas sorption procedure

The nitrogen overcondensation (OC) experiment was carried out on a Micromeritics ASAP 2020 physisorption analyser. The OC experiment is explained further in previous work,[255] and uses a method similar to that described by Murray.[38] The OC experiment involves 'flooding' the sample chamber with condensed liquid nitrogen to submerge the sample in liquid nitrogen to investigate any porosity beyond the instrument upper limit for the conventional isotherm (P/P_0 >0.995). The conventional isotherms for these materials clearly show that porosity exists beyond the conventional instrument upper limit. Once the sample is fully submerged in liquid nitrogen and total pore filling is achieved, the pressure in the tube is lowered to just below saturated vapour pressure of nitrogen such that the bulk condensate vapourised completely while all the sample internal porosity is liquid-filled. Once this step has been achieved, the first data point on the overcondensation desorption isotherm can be measured. This point corresponds to the total pore volume of the sample. The pressure is then progressively lowered in small steps, and the rest of the desorption isotherm was obtained in the usual way. The reported raw data (relative pressure and volume adsorbed ($\mathrm{cc(STP)/g}$) is greatly offset to what would be expected due to the very large amount of gas (from the bulk liquid nitrogen) that must be removed before the onset of desorption from the sample porosity. The data was normalised to a quantity of gas on the adsorption isotherm below a relative pressure of 0.42 where, for the conventional isotherm, the desorption data coincides with the adsorption data. The OC data was collected for the samples both before and after mercury intrusion.

3.4.6 Computerised X-ray tomography and dual-beam electron microscopy

3.4.7 Low resolution computerised X-ray tomography (CXT)

For the low resolution CXT scans, the pellets were imaged before and after mercury entrapment using a Zeiss Xradia Versa XRM-500 to acquire 3D image stacks. The X-ray source for the Xradia 500 Versa instrument was set to $140\,\mathrm{kV}$ kV and power of $10\,\mathrm{W}$. The macro lens (0.4X) of the apparatus was used to image the full pellets with a diameter of $5.4\,\mathrm{mm}$ with $360°$ rotations. The average pixel size for empty pellets was $5.6\,\mu\mathrm{m}$, and the average pixel sizes for samples with mercury was $5.9\,\mu\mathrm{m}$. Image acquisition parameters were the same for all the empty samples and for the samples with entrapped mercury. The scan times were roughly $2\,\mathrm{h}$ and $2.5\,\mathrm{h}$ for empty and mercury filled pellets, respectively. Both samples were scanned with 1600 projections per $360°$ scan. Each 3D image stack contained 1016 slices with dimensions of 1024 x 1024 pixels and 24-bit depth. The 3D volume data sets were reconstructed using the filtered back projection (FBP) method.[128]

[255] S. Rigby et al. *Mater. Charact*, **167**: 110467, 2020.
[38] K. L. Murray, N. A. Seaton, and M. A. Day. *Langmuir*, **15**: 6728–6737, 1999.
[128] G. N. Ramachandran and A. V. Lakshminarayanan. *PNAS*, **68**: 2236–2240, 1971.

3.4.8 High resolution computerised X-ray tomography (CXT)

Multi-scale imaging of the feed materials was performed by X-ray tomography at the TOMCAT beamline (Swiss Light Source). High resolution microscope (Optique Peter) with 4x, 10x and 20x magnification and LuAG:Ce $20\,\mu\mathrm{m}$ scintillator was used in combination with Pco.Edge 5.5 detector, yielding an effective pixel size of 1.63, 0.65 and 0.325 $\mu\mathrm{m}$, respectively. Spray dried (SD) feed material was scanned with energy of 20 keV and 150 ms exposure time per projection. Monochromatic energy of 30 keV and exposure time of 500 ms was used to acquire images of bigger roll compacted (RC) particles. Both samples were scanned with 2500 projections per 180° scan. The 3D volume data sets were reconstructed using the propagation-based phase contrast method[256] and the gridrec algorithm.[257]

3.4.9 Focussed ion beam-scanning electron microscopy (FIB-SEM)

The serial milling images were acquired using a Crossbeam 550 (Carl 206 Zeiss Microscopy) instrument equipped with a cryo-stage and integrated VCT500 vacuum transfer system for FIB-SEM imaging. The samples were mounted onto a pre-tilted sample holder and was transferred into the Crossbeam 550 using the VCT500 shuttle. Once the samples were inside the instrument, an automated FIB milling algorithm was subsequently set up and executed. To ensure that the unsupervised automated FIB milling was successful, the equipment was properly aligned and calibrated on a weekly basis. The Crossbeam 550 was also calibrated to mill a cross-section with dimensions of 10 x 30 x 10 $\mu\mathrm{m}$ (*XYZ*) through the sample to acquire 3D image stack. A fixed voltage of 30 kV and current of 700 pA was used to generate the FIB images.

[256] D. Paganin et al. *J. Microsc.*, **206**: 33–40, 2002.
[257] F. Marone and M. Stampanoni. *J. Synchrotron Radiat.*, **19**: 1029–1037, 2012.

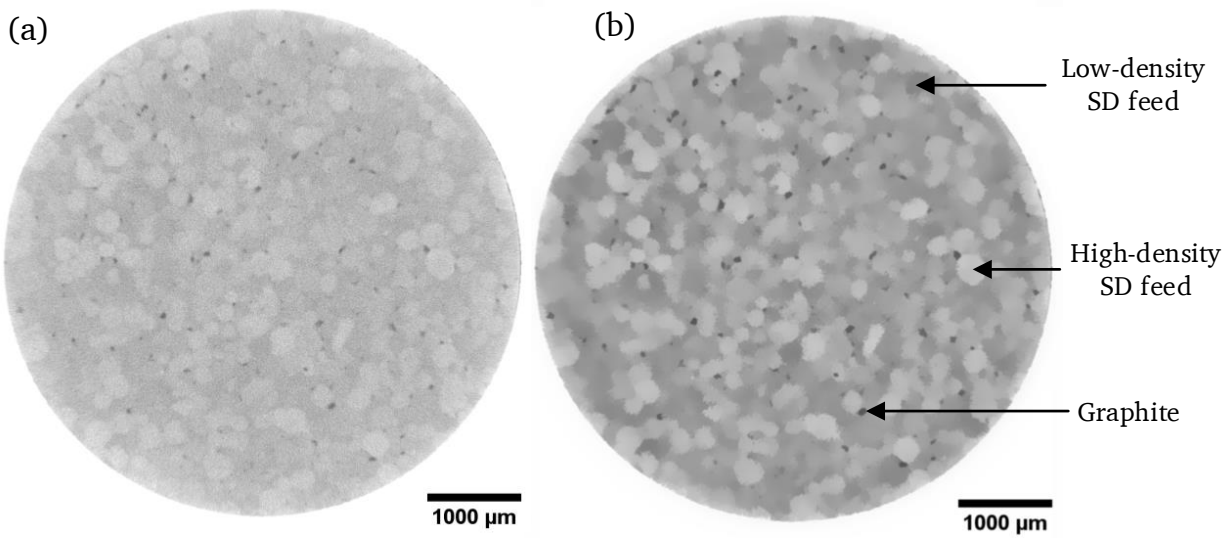


Figure 3.2: Typical examples of reconstructed 2D radial cross-section slice CXT images of the SD feed pellets.

3.5 Results

3.5.1 Imaging of empty spray-dried (SD) feed pellets

3.5.2 Low resolution CXT

Figure 3.2 shows typical examples of reconstructed 2D radial cross-section slice CXT images of the SD feed pellets. In Figure 3.2, the individual SD feed particles making up the pellet can be seen by virtue of a distribution in density in the particles evident from the variation in average pixel intensity in each SD feed particle. There are also many smaller, dark black spots, which correspond to the graphite lubricant particles. In addition, appendix A contains an intensity profile for a typical cross-section of a SD feed pellet. Since the pixel resolution is generally larger than the length-scale of variations in solid matrix density (except for carbon particles), the variations in the density profile are dominated by pellet voidage effects.

Figure 3.3 shows the 3D reconstruction and segmentation of the stack of the 2D slices for the SD feed pellet. The image has been segmented into three bins of intensity corresponding to the very low-density carbon particles, low density SD feed particles and high-density SD feed particles. From the segmentation of the three separate phases shown in Figure 3.3, it can be seen that their distributions are pervasive throughout the pellet and there are no signs of segregation by density.

3.5.3 High resolution CXT

Figure 3.4 shows a 3D reconstruction and 2D radial cross-section slice CXT images of the SD feed particles used to make the SD feed pellet. To aid the discernment of the relationship between the pellet and feed particles, a lower resolution 2D radial cross-section slice CXT image of the pellet has also been included. From Figure 3.4, it can be seen that the spherical SD feed particles that

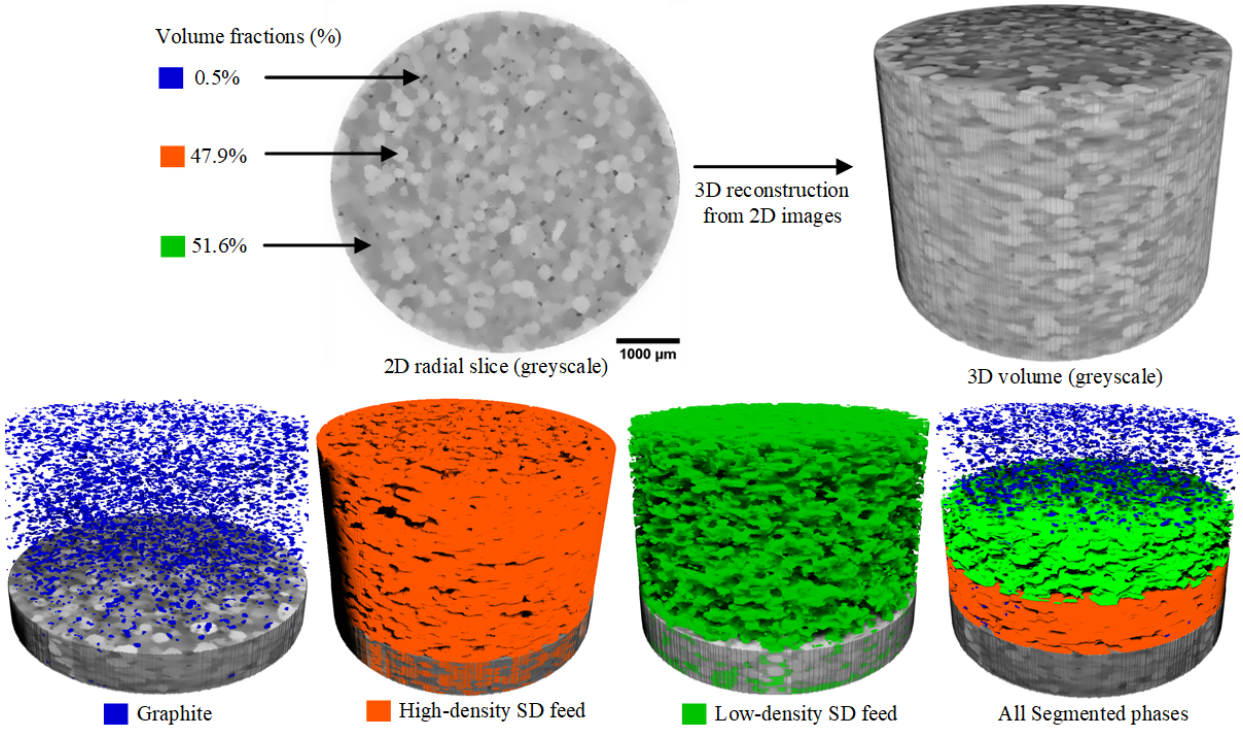


Figure 3.3: 3D reconstruction and segmentation of the stack of the 2D slices for the empty SD feed pellet. Dragonfly[258] software was used to reconstruct and process the images.

make up the pellet are themselves composite structures. The SD feed particles are themselves made up of a range of different types of smaller-scale ($\sim$1-10s µm) particles. Some smaller particles are solids of very high density, as shown by the bright white pixel intensity. Other particles consist of bright white shells surrounding large voids (denoted 'bubble pores'). There are also lower density particles. In between the smaller particles are some void spaces. The variation in the density of each individual SD feed particle in the lower resolution CXT image may be associated with variation in numbers of the high density solid smaller particles, and the shells, evident in the cross-sections of different smaller particles.

3.5.4 FIB-SEM imaging

Figure 3.5 shows an example of a FIB-SEM trench site, 2D slice SEM image and a 3D volume reconstruction from 510 slices. Also shown in Figure 3.5 is the results of segmentation of the reconstructed image into the three phases: pores, copper/zinc oxide and alumina. Table 3.3 shows the corresponding volume fractions of each of the three phases. Both the 2D slice and 3D volume show part of a rounded particle composed of dense copper/zinc oxide phase of size $\sim$5-10 µm. The size, shape, and composition (and thus electron density) of this round particle suggest it is an example of the particles that appear as rounded, bright white particles in the high resolution CXT image of the SD feed in Figure 3.4. It can also be seen that these rounded high-density particles have no macropores, as there is a gap in the distribution of macropores in the region of the particle

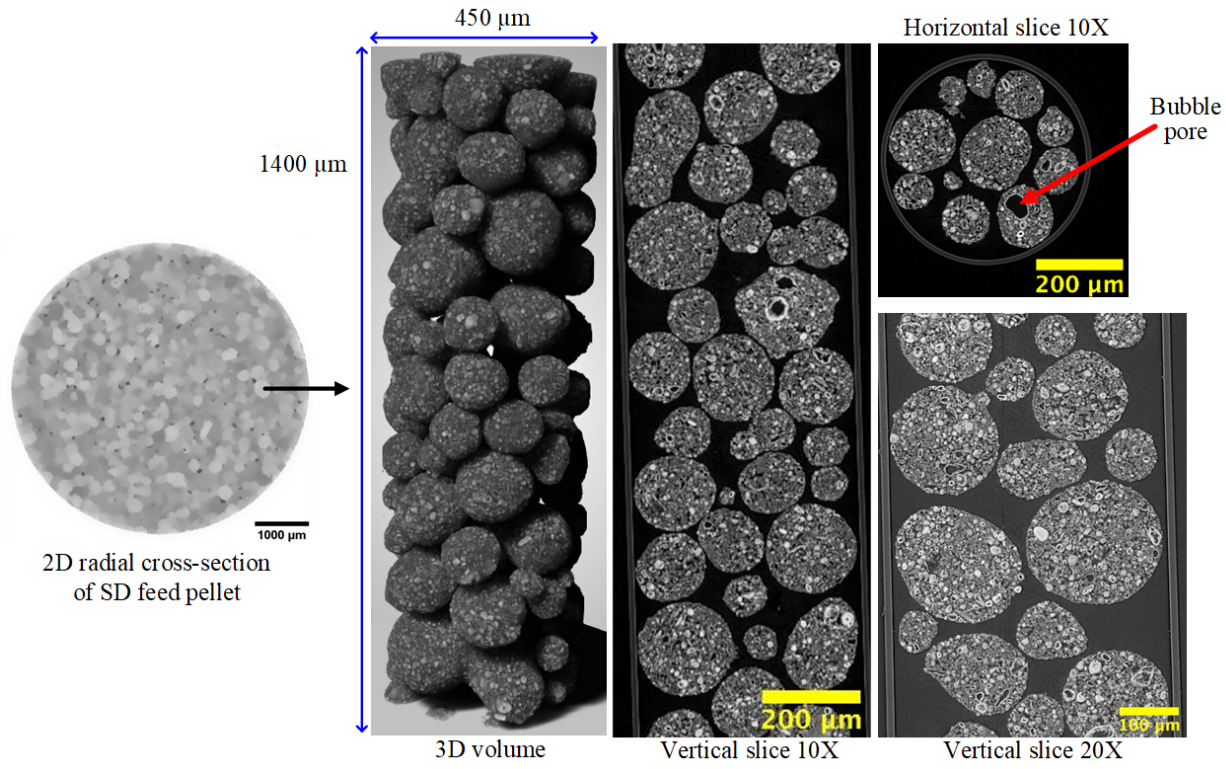


Figure 3.4: 2D radial cross-section and 3D reconstruction of high resolution CXT image of SD feed particle used to make the SD feed pellet. Also shown on the left side of the figure, for comparison purposes, is a low resolution image of a whole SD feed pellet with an arrow indicating a corresponding individual constituent feed particle.

Table 3.3: Volume fractions of each of the three phases in the 3D reconstruction FIB-SEM images of fresh spray dried and roll compacted feed pellets.

Phase	Fresh SD (%)	Fresh RC (%)
Pores	2.4%	2.1%
Alumina	36.0%	38.2%
CuO/ZnO	61.6%	59.8%

in the image.

It is noted that the field-of-view of the 3D volume reconstruction exceeds the correlation length of the visible underlying structure, since the voidage fractions reach a constant value measured over length-scales below that of the sampled volume. However, it can be seen that there is some variation in the macroporosity values detected in each trench of the SD feed pellet, which may reflect the spatial variation in density and porosity over much larger length-scales as seen in the CXT images, since the locations in pellets for FIB-SEM trenches were randomly chosen.

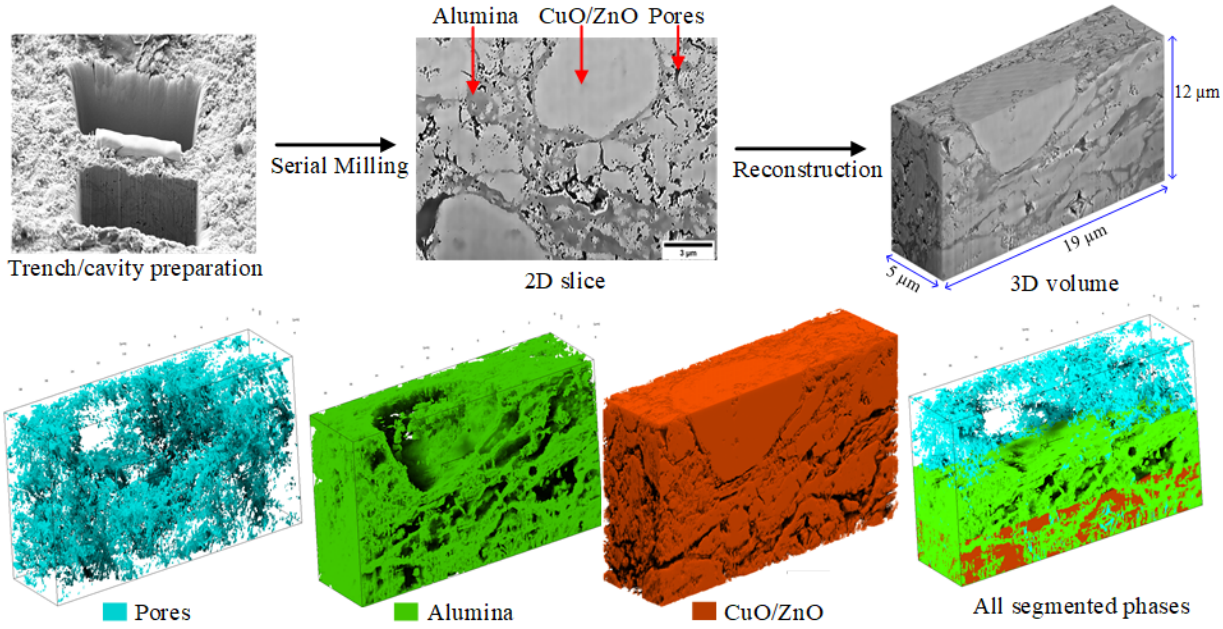


Figure 3.5: 2D and 3D reconstructed grayscale FIB-SEM images and segmentation result for fresh spray dried pellet. Also shown on the figure is the trench/cavity site. The scale bar corresponds to 2 µm.

3.5.5 Imaging of empty roll-compacted (RC) feed pellets

3.5.6 Low resolution CXT

Figure 3.6 shows typical examples of reconstructed 2D radial cross-section slice CXT images of the RC feed pellets. In Figure 3.6, it can be seen that there are many irregularly-shaped regions of varying size and density, as inferred from the pixel intensities. There is also some hint of density variation within the irregular shaped regions. The high-density regions are surrounded by darker lower density boundaries. In addition, appendix A contains an intensity profile for a typical cross-section of a RC feed pellet. The solid matrix is generally homogeneous (with the obvious exception of lubricant carbon particles) over the length-scales of the resolution in the CXT images in both Figure 3.2 and Figure 3.6 and thus variations in density are most probably the result of variations in porosity within a given voxel.

3.5.7 High Resolution CXT

Figure 3.7 shows a 3D reconstruction and 2D radial cross-section slice CXT images of the RC feed particles used to make the RC feed pellet. The 2D slice images contain regions of brighter intensity associated with higher density, and darker regions associated with lower density. To aid the discernment of the relationship between the pellet and feed particles, a lower resolution 2D radial cross-section slice CXT image of the pellet has also been included. From Figure 3.7 it can be seen that the irregular form of the RC feed particles matches that of the irregular regions seen in the low-resolution image, and thus the latter can be identified as the former. It can also be seen that, to the eye, the close-up views of the individual RC feed particle provided by the

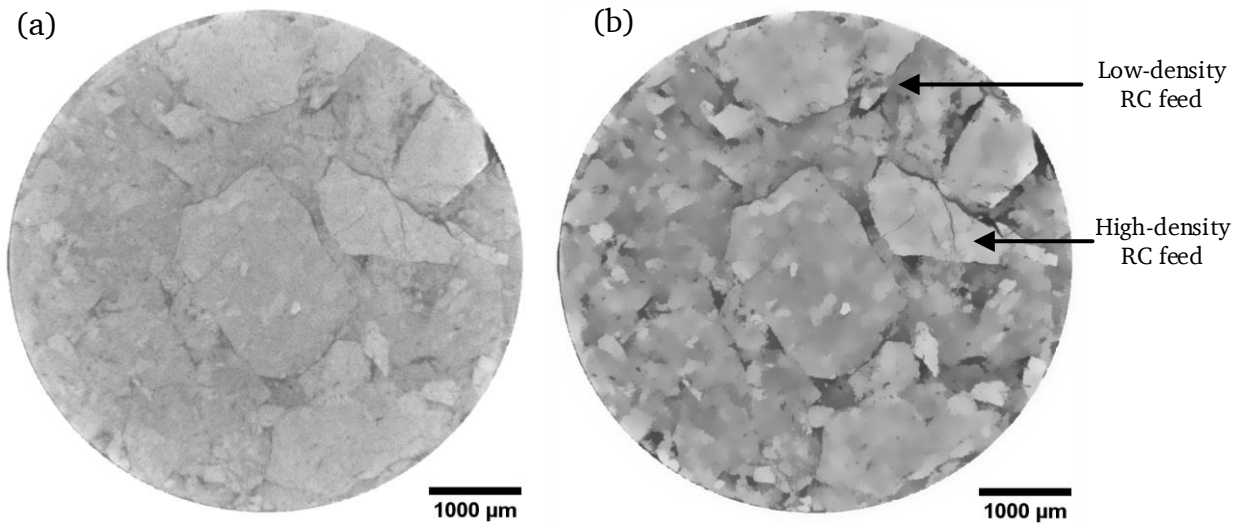


Figure 3.6: Lower resolution CXT 2D radial cross-section of whole pellet and showing schematically how it relates to higher resolution 3D reconstruction and 2D radial cross- section slice CXT images of the RC feed particles used to make the RC feed pellet.

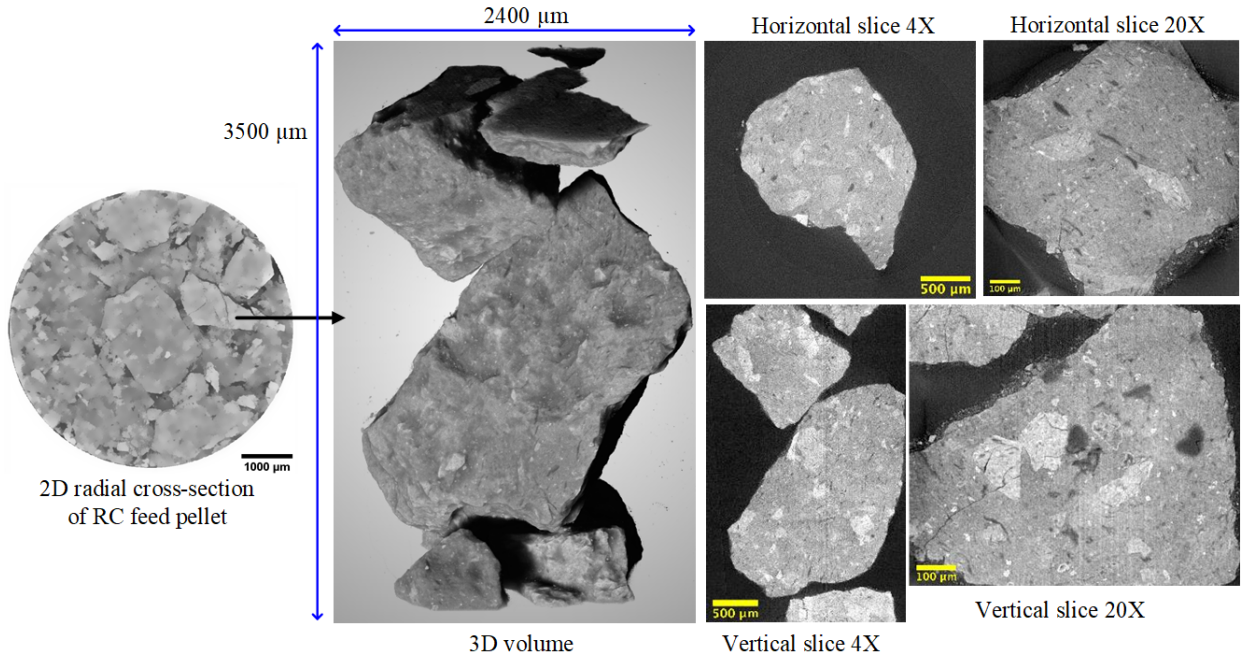


Figure 3.7: Lower resolution CXT 2D radial cross-section of whole pellet and showing schematically how it relates to higher resolution 3D reconstruction and 2D radial cross- section slice CXT images of the RC feed particles used to make the RC feed pellet.

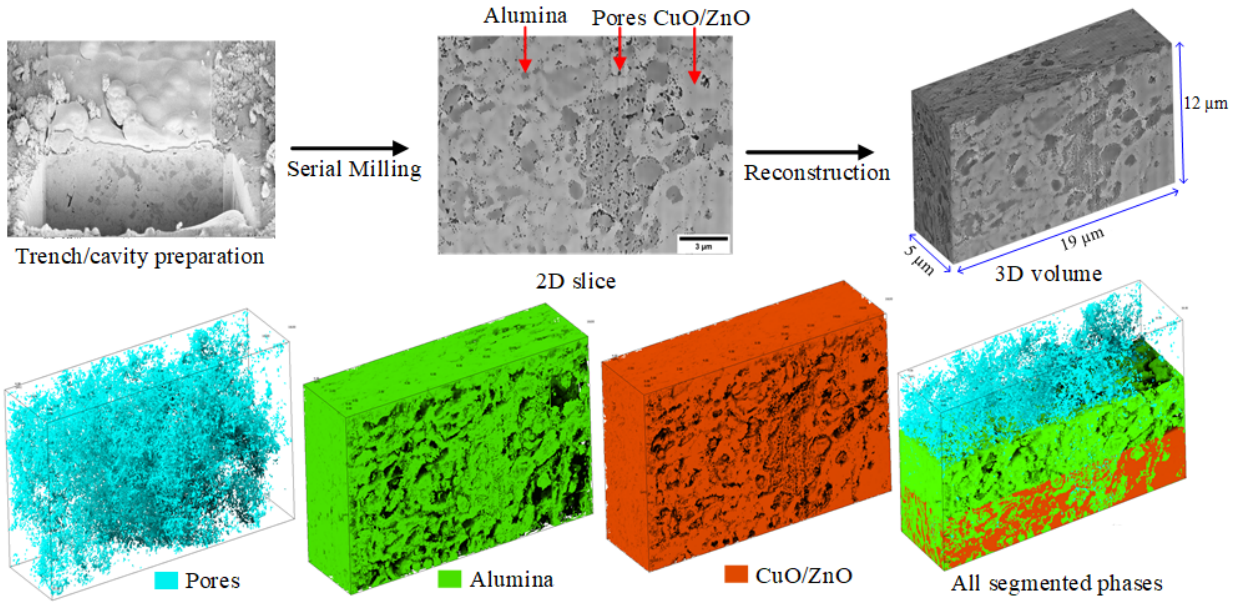


Figure 3.8: Fresh RC FIB-SEM trench site, and 2D and 3D reconstructed grayscale FIB-SEM images and segmentation result for fresh roll compacted pellet. The scale bar corresponds to 2 µm.

high resolution CXT look very similar to that of the lower resolution image of the whole RC feed pellet. Both the whole pellet and the feed particles have within them irregular regions of varying density. Hence, the RC feed pellet has the visual appearance of a fractal object, where increasing magnification, provided by the higher resolution CXT, reveals similar structures.

3.5.8 FIB-SEM imaging

Figure 3.8 shows an example of a FIB-SEM trench site, 2D slice SEM image, and a 3D volume reconstruction from 510 slices. Also shown in Figure 3.8 is the results of segmentation of the reconstructed image into the three phases: pores, CuO/ZnO and alumina. Table 3.3 shows the corresponding voidage fraction values for each of the three phases in the reconstructed 3D images that are detectable over the length-scales probed by the SEM. From Figure 3.8 it can be seen, in the volume sampled, that the texture of the RC feed pellet over length-scales ∼1-10s µm is very different to that of the SD feed pellet region seen in Figure 3.5.

3.5.9 Mercury porosimetry

Figure 3.9 shows the mercury porosimetry data for the SD and RC feed particles following analysis with the Kloubek[76] correlations. It can be seen that both show a small intrusion step at ∼100 µm that corresponds to the order of magnitude of the size of the individual feed particles, and thus corresponds to intrusion in gaps between them. While the intrusion curves for both types of feed particle have steps of similar volume at ∼10 nm, the SD feed particle intrusion curve has an

[76] J. Kloubek. *Powder Technol.*, **29**: 63–73, 1981.

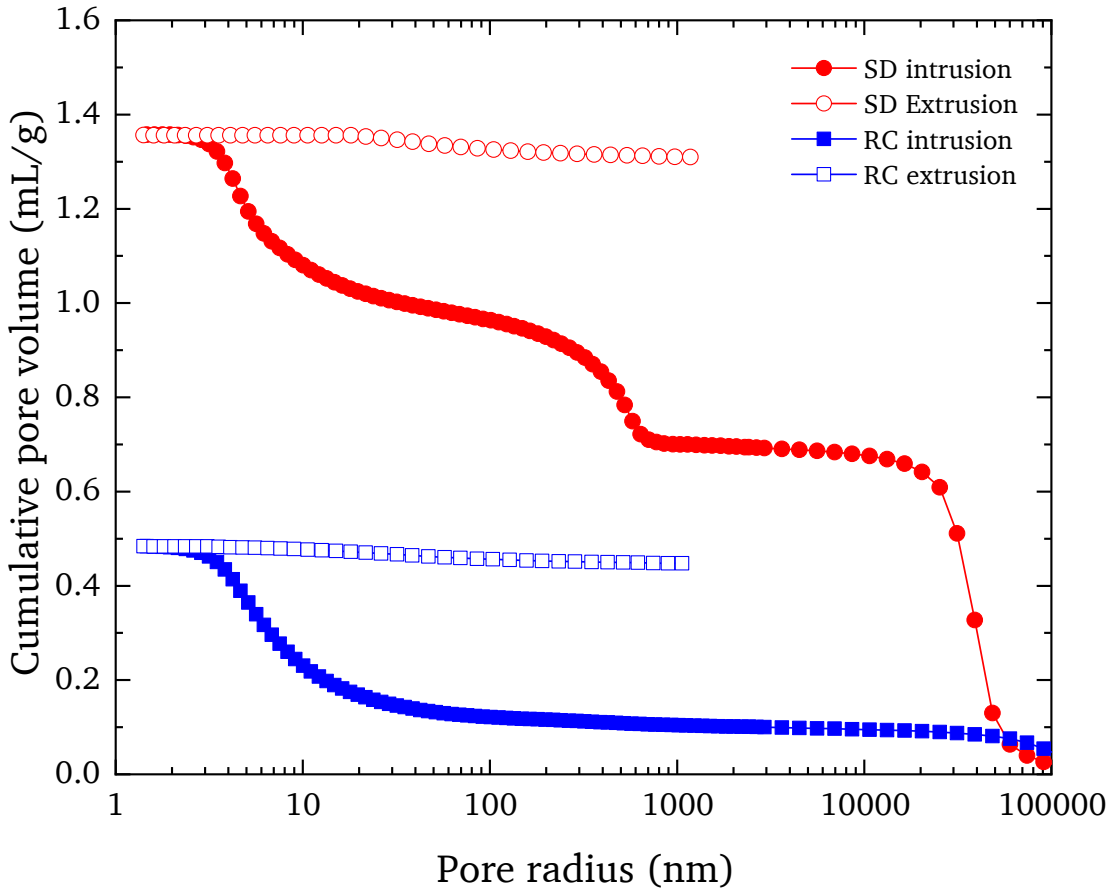


Figure 3.9: Mercury intrusion and extrusion porosimetry data for the SD and RC feed particles analysed using the Kloubek (1981) correlations.

additional step at ∼1 μm. From a consideration of the high resolution CXT data given in Figure 3.4 and Figure 3.7, it is likely that this additional step corresponds to intrusion into the bubble pores in the SD feed particle, which are not present in RC feed particles. The pore size at the additional step probably corresponds to pore sizes in the intact shells, or cracks in the shells, around the bubble pores in the SD feed.

Figure 3.10 shows mercury porosimetry scanning curves for whole pellets made with SD and RC feed. It can be seen that as the ultimate mercury pressure is increased, then, progressively, more intrusion occurs into ever smaller pore necks. From the mercury extrusion data, it can be seen that, typically, ∼75-100% of the intruded mercury becomes entrapped, depending upon the ultimate intrusion pressure, with fractionally less mercury becoming entrapped for higher ultimate intrusion pressures.

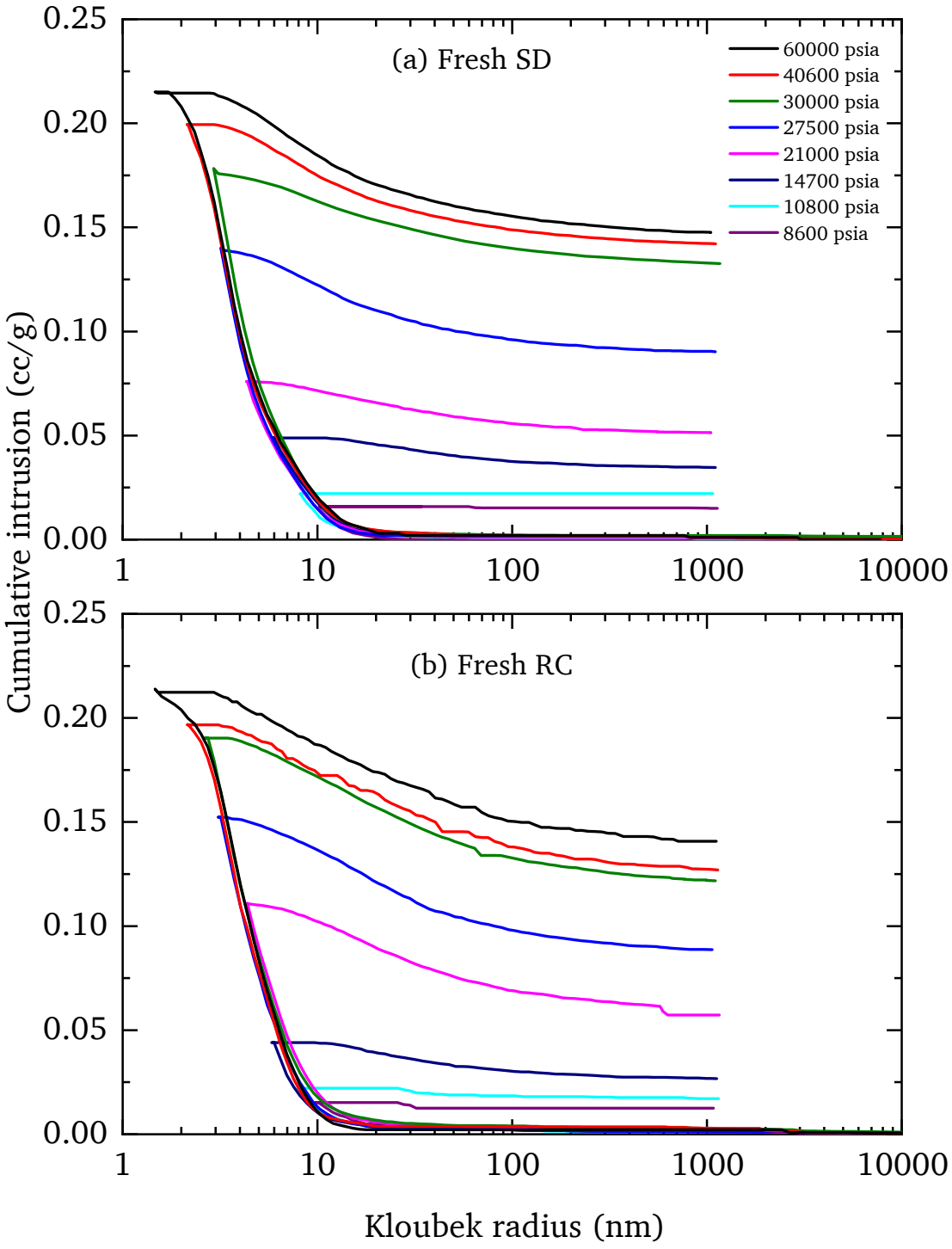


Figure 3.10: Mercury porosimetry scanning curve data for whole pellets made with (a) fresh spray dried feed and (b) roll compacted feed material analysed using the Kloubek (1981) correlations.

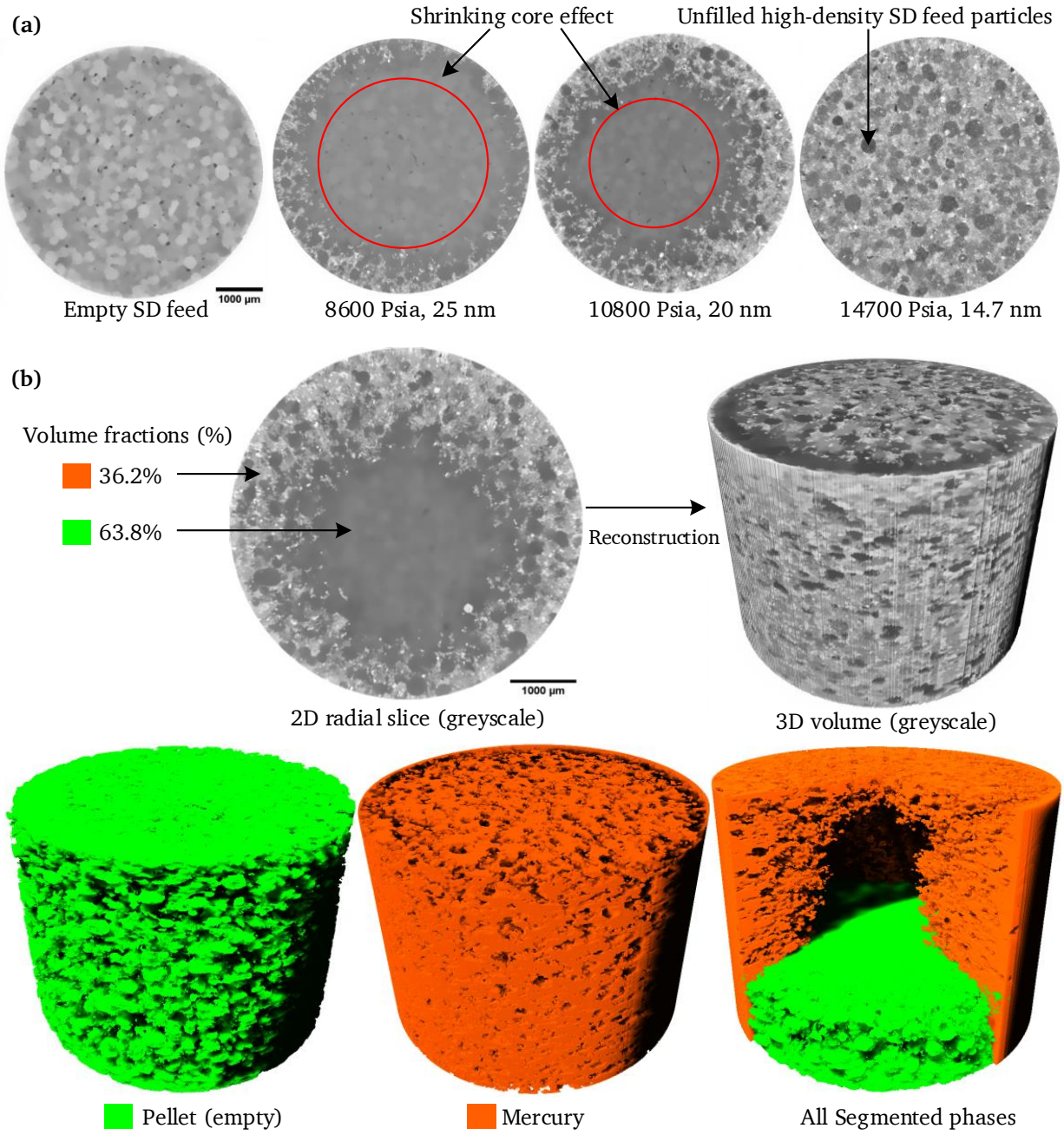


Figure 3.11: (a) 2D radial slice CXT images of whole fresh spray dried pellet following mercury intrusion to a range of pressures. (b) Segmented 3D reconstruction CXT images of a partially mercury intruded fresh SD feed pellet up to 10,800 Psia. The scale bar corresponds to 1000 µm.

3.5.10 Low resolution CXT imaging of pellets following mercury entrapment

Figure 3.11**(a)** shows typical reconstructed 2D radial slice CXT images of whole pellets following mercury intrusion to a range of pressures. Since mercury is a very electron dense element, the regions of the pellet containing entrapped mercury show up as bright white pixels, while the empty pellet matrix is in shades of grey. From Figure 3.11**(a)** it can be seen that the spatial patterns of mercury intrusion for the two types of pellets are very different. The series of images for the SD feed pellet show mercury intrusion occurs as a defined front that progressively migrates towards the centre of the pellet with increasing pressure. There is thus a 'shrinking core' effect for the remainder of the pellet unintruded with mercury. However, it is noted that behind the front, intrusion of all the void space is not complete, as some SD feed particles remain partly or fully without mercury even once the main intrusion front has moved past. Even once this front has reached the centre of the pellet, following intrusion to a pressure of 14,700 psia, unintruded SD feed particles are clearly evident, as dark circles, in the image.

In contrast, as seen in Figure 3.12**(a)**, for mercury intrusion of the RC feed pellet, once mercury has penetrated a band in the outer regions of the pellet at low pressure, further intrusion is more dendritic in form, with percolation achieved by 10,800 psia. The fractal dendritic form of the mercury intrusion path is more clearly evident in the 3D reconstruction CXT images of a partially-intruded RC feed pellet shown in Figure 3.12**(a)**. The image has been segmented to distinguish the regions with intruded mercury from the remaining pellet matrix. However, large zones of the pellet are left unintruded. The irregular polygonal form of the dark unintruded zones suggests that they are likely associated with particular RC feed particles within the pellet. Intrusion occurs via cracks, lower density RC feed particles, and the low-density regions surrounding high density feed particles. Eventually, at the very highest pressures, all of the regions of the pellet are intruded.

Figure 3.11**(b)** shows the segmentation results of the fresh SD pellet following mercury porosimetry up to 10,800 psia leading to entrapment filling 15% of the pore space. The figure depicts 3D renderings of the pellet showing entrapped mercury and the remaining empty pore spaces. The bright white pixels are associated with entrapped mercury as they represent largest X-ray absorbance, whereas the relatively grey regions represent empty void spaces without mercury. The volume fractions based on pixel intensity of mercury (orange colour) from the CXT images is 36.2%. The rest of the unfilled pore spaces in the pellet represented 63.8% of the volume fractions.

Figure 3.12**(b)** shows the segmentation results of the fresh RC pellet following mercury porosimetry up to 8,600 psia leading to entrapment filling 11% of the pore space. The mercury entrapment shows a similar pattern as the fresh spray dried pellet as it forms a shrinking core effect. The volume fractions of mercury and empty pore spaces are 33.2% and 66.8%, respectively.

3.5.11 Gas Sorption and Overcondensation Isotherms

As mentioned above, the overcondensation technique permits the obtaining of the full boundary desorption isotherm not possible with conventional adsorption. Figures 3.13 to 3.16 show the conventional gas sorption data, and also nitrogen overcondensation boundary desorption isotherms,

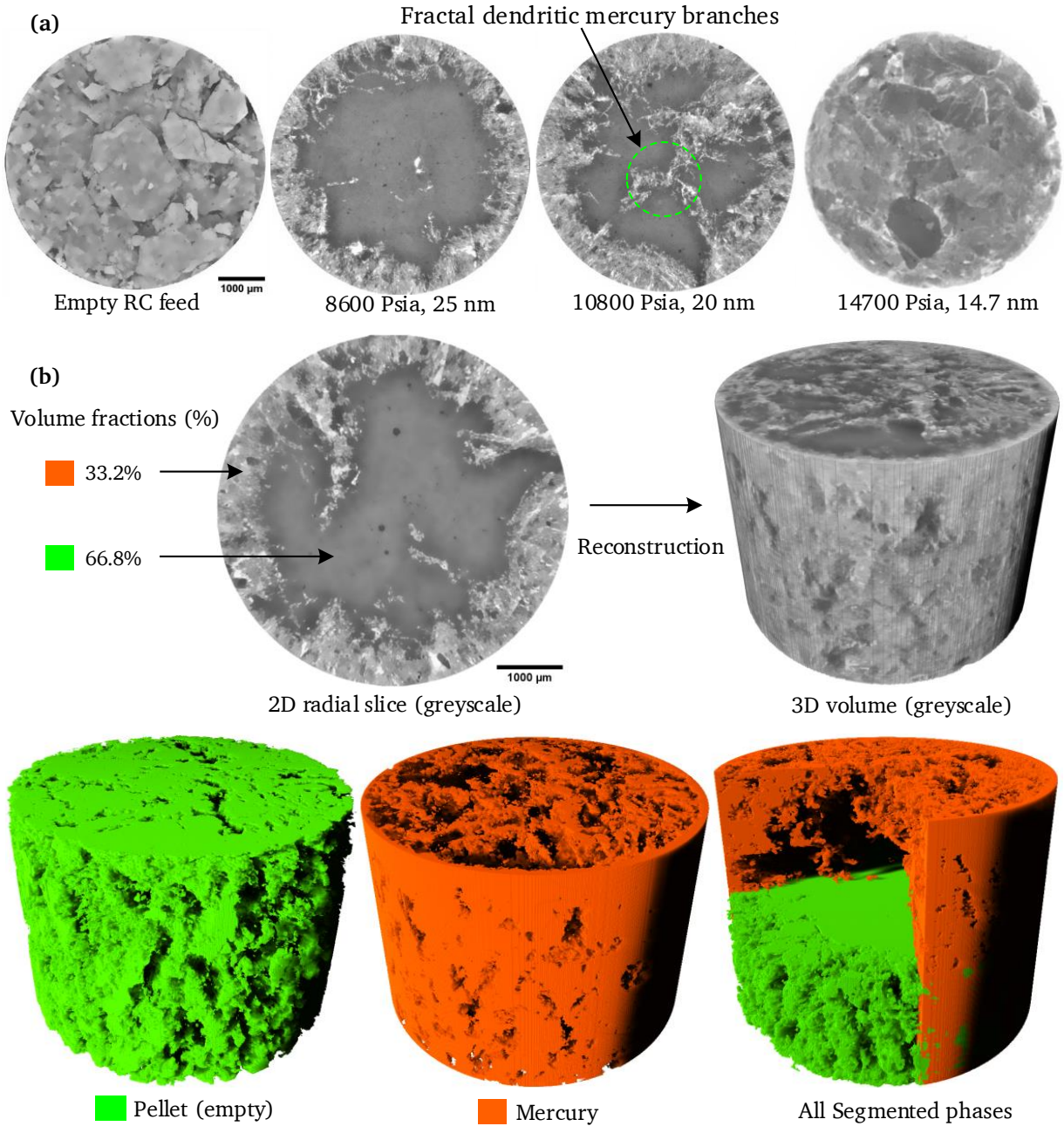


Figure 3.12: (a) 2D radial slice CXT images of whole fresh roll compacted pellet following mercury intrusion to a range of pressures. (b) Segmented 3D reconstruction CXT images of a partially mercury intruded fresh RC feed pellet up to 8,600 Psia. The scale bar corresponds to 1000 µm.

Table 3.4: Connectivity (Z) and lattice size (L) parameters from percolation analysis (Seaton, 1991) (a) Fresh SD pellets (b) Fresh RC pellets.

	(a) Fresh SD		(a) Fresh RC	
Sample	**Z**	**L**	**Z**	**L**
Powder (empty) (53-75 um)	3.19	2.89	3.03	2.99
Whole pellet (empty)	2.98	3.07	2.95	3.01
Whole post 8,600 psia	2.69	3.55	2.72	3.2
Whole post 10,800 psia	2.55	4.31	2.83	3.16
Whole post 14,700 psia	2.37	5.45	2.72	3.55

for empty SD and RC feed pellets, and also for these two types of pellets following mercury entrapment after intrusion to a range of different pressures. From Figure 3.13 and Figures 3.14 to 3.15, it can be seen that entrapment of mercury following intrusion to 10,800 and 14,700 psia has made the hysteresis loops wider for both the SD and RC feed pellets. This increase in hysteresis width has been made clearer for the RC feed pellet data by raising the isotherms obtained after mercury entrapment by 5.5 and 3.3 $\mathrm{cc(STP)/g}$, as seen in the insets in Figures 3.14 to 3.15, since entrapment also led to a more marked decrease in adsorption at lower relative pressures than for the SD feed pellet. In addition, percolation analysis[7,15] has been performed using the overcondensation desorption isotherm and the conventional adsorption isotherm for both the empty samples and those containing entrapped mercury, and the results are shown in Table 3.4. The analysis was repeatedly conducted assuming different values of the parameter α in Equation (3.7) of 0, -1, or -2 each time (see appendix A). It was found that the best fit of the experimental data, for both SD and RC feed pellets, to the universal scaling relation (Equation (3.9)) was obtained when the parameter α had a value of -1, suggesting pore bond lengths were inversely proportional to pore diameter. This suggests that, in the real material, the size of domains of similar pore diameter increases with diameter.

The connectivity parameter, Z, from the percolation analysis quantifies hysteresis width, because a narrow hysteresis loop is associated with a high connectivity, and vice-versa.[7] Further, the lattice size parameter also quantifies pore network accessibility because an (apparently) smaller lattice is more accessible. From Table 3.4, it can be seen, for both types of pellets, that the connectivity declines and the apparent lattice size increases, with increasing mercury entrapment as arises at higher intrusion pressures. The overall accessibility of the remaining open network is declining with increased mercury entrapment.

While the overall forms of the hysteresis loops for the conventional nitrogen sorption data for both types of pellet are relatively similar, in contrast, the overcondensation boundary desorption curves reveal some key differences. First, while the Gurvitch volumes for both types of pellet are higher for the overcondensation data, the pore volume missing from the conventional isotherm is larger for the SD feed pellets than for the RC feed pellets. Second, while the overcondensation boundary desorption isotherms show a much sharper percolation knee near the top of the hysteresis loop, not present in the conventional desorption isotherms, the overcondensation data for the

empty SD feed pellet also shows a second, more rounded, percolation knee at relative-pressures of ∼0.7-0.8, not evident in the overcondensation data for empty RC feed pellets, which have a much straighter, flatter desorption isotherm in this relative pressure region.

From Figure 3.13, it is noted that the sharp percolation knee near the top of the overcondensation isotherm for the SD feed pellet, first, remains sharp when shifted to lower relative pressure following mercury entrapment after intrusion to 10,800 psia, but then becomes very rounded following mercury entrapment after intrusion to 14,700 psia. In contrast, the second already more rounded percolation knee at relative pressures ∼0.7-0.8 remains unchanged until mercury is intruded to $\sim 21.000\,\mathrm{psia}$, when it disappears. It is noted that the conventional desorption isotherm for the SD feed pellet is effectively a desorption scanning curve. A *scanning curve* is defined as an isotherm whereby the progressive change in pressure is halted, and the direction of change is reversed before ultimately reaching one of either hysteresis closure points in the full boundary isotherms, which are the isotherms where complete pore-filling with condensate is achieved at the upper end in terms of amount adsorbed. From Figure 3.13 it can be seen that, while the conventional desorption isotherm descends slightly, it crosses to the overcondensation boundary isotherm well above the hysteresis closure point and also the more rounded percolation knee. The hysteresis loop was scanned further using a desorption scanning curve with the reversal in the direction of pressure change occurring at a relative pressure 0.85 on the boundary adsorption isotherm. These data are shown in Figure 3.17, where it can be seen that the lower pressure scanning curve exhibits different behaviour to the conventional desorption isotherm in that the former is converging on the lower hysteresis closure point.

Figure 3.18 compares the conventional nitrogen sorption isotherms for the empty SD feed pellet, with the equivalent data following mercury intrusion to 21,000 and 30,000 psia. From Figure 3.18, it is noted that the form of the conventional sorption isotherms following mercury intrusion to 21,000 psia shows a marked kink in the adsorption isotherm at a relative pressure just above 0.8, and a percolation knee at the same amount adsorbed in the desorption branch at a relative pressure of ∼0.7. This sharp knee at relative pressure ∼0.7 is also evident in the overcondensation boundary desorption isotherm in Figure 3.13. This formation of the kink in the sorption isotherms is what might be expected if there has been a greater loss of larger pores than smaller pores that fill below the kink. The parallel form of the branches of the hysteresis loop in the conventional sorption data following mercury intrusion to 30,000 psia (shown in Figure 3.18) may suggest a single pore origin for the hysteresis. The small step down, at a relative pressure of ∼0.4-0.5, in the conventional and overcondensation desorption isotherms, that closes the hysteresis, is, based on its position, probably due to cavitation, and suggests some larger pores are shielded by necks smaller than $\sim 4\,\mathrm{nm}$.

3.5.12 Fragmented Pellets

In order to further probe the impact of macroscopic heterogeneities, gas sorption experiments were conducted on powder samples of particle sizes 53-75 $\mu\mathrm{m}$ formed by fragmentation of whole pellets. This particular powder size fraction was chosen as it is similar to that for the original SD

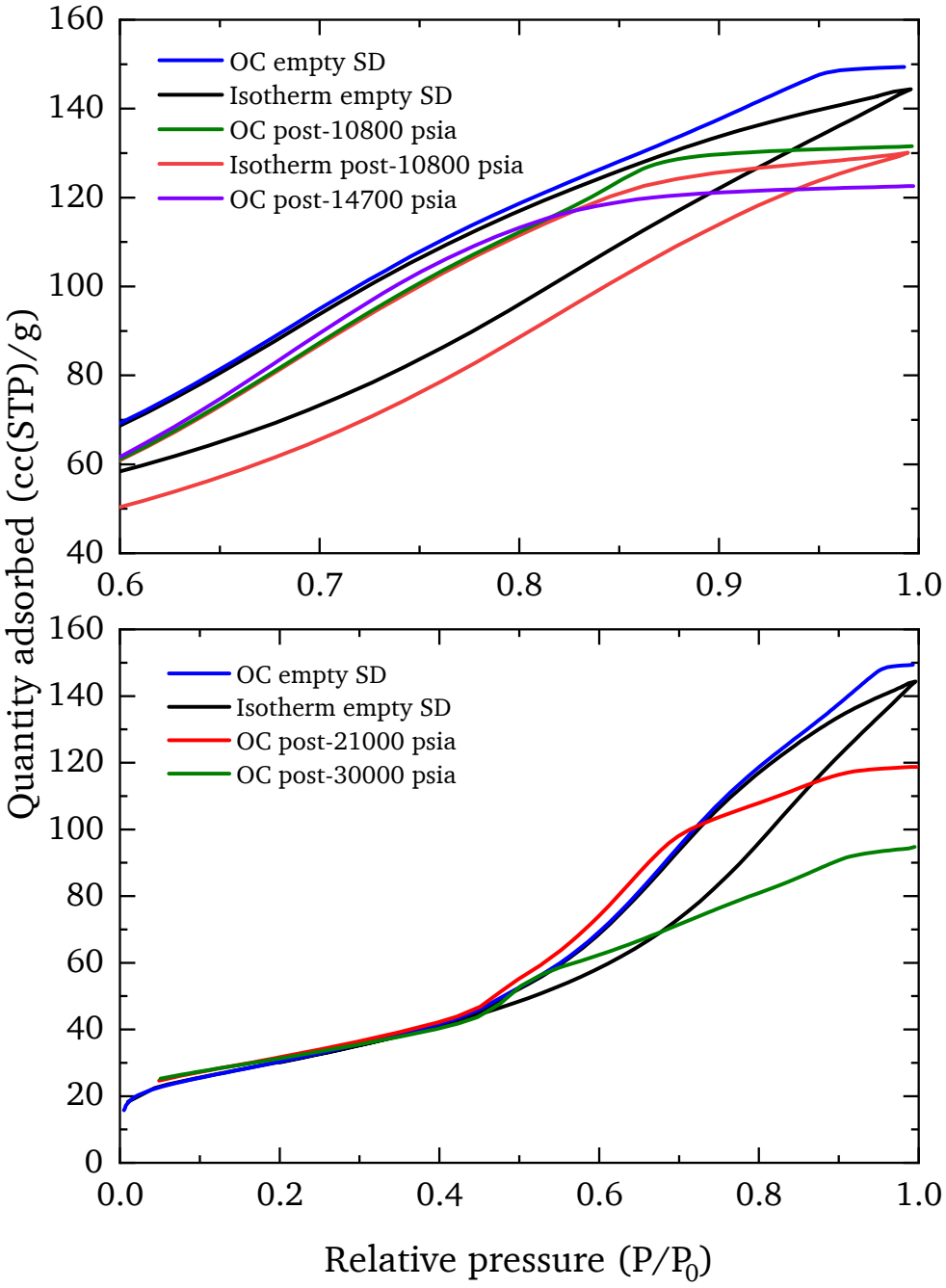


Figure 3.13: (a) Upper part of hysteresis loop region of conventional sorption isotherms for empty SD feed pellet sample and SD sample following mercury intrusion to 10,800 psia, together with overcondensation boundary desorption isotherms for empty SD sample, and SD samples following mercury intrusion to 10,800 and 14,700 psia. **(b)** Hysteresis loop region of conventional sorption isotherms for empty SD feed pellet sample and overcondensation boundary desorption isotherms for empty SD sample, and SD samples following mercury intrusion to 21,000 and 30,000 psia.

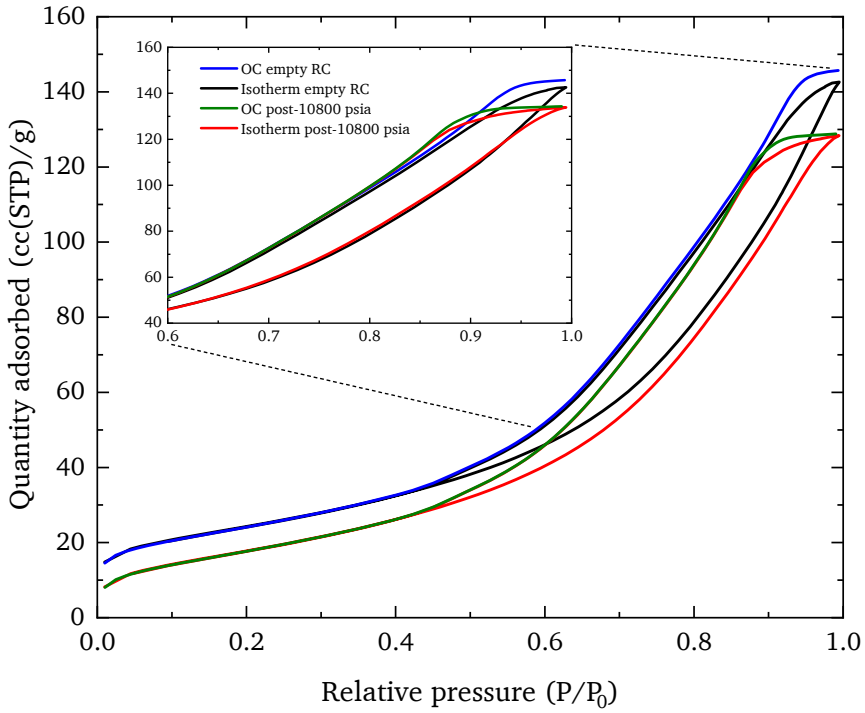


Figure 3.14: Conventional sorption isotherms and overcondensation boundary desorption isotherms for empty RC feed pellet sample, together with conventional sorption isotherms and overcondensation boundary desorption isotherms for RC samples following mercury intrusion to 10,800 psia. The inset shows the isotherms obtained after mercury entrapment adjusted upwards by 5.5 cc(STP)/g.

feed particles. Fragmented pellet samples were used, instead of original feed particles, as it is possible that the treatment of the pellet following forming of the feed into the tablet, as part of the overall fabrication procedure, may have impacted the mesopore structure, and only the effect of particle size of the final product sample material upon the gas sorption data was required. The data for the powder experiments demonstrate the impact of the bubble pores on conventional adsorption isotherms and the presence of advanced condensation effects.

Figure 3.19 show the conventional nitrogen sorption isotherms and overcondensation desorption boundary curve obtained for powdered samples of the SD and RC feed pellets. From the Figure 3.19**(a)**, it can be seen that desorption starts as soon as the direction of pressure changes is reversed for the SD feed powder, which contrasts with the whole pellet data shown in Figure 3.13. Further down the conventional desorption isotherm the hysteresis width increases, but the conventional desorption isotherm does not merge with the overcondensation curve until a relative pressure of ∼0.6-0.7, which is still above the hysteresis closure point, so the scanning curve is crossing but descending, rather than converging.[7] In contrast, the conventional desorption curve for the RC feed powder descends but crosses to join the overcondensation curve much higher up at relative pressures ∼0.8-0.9.

Percolation analysis was also performed on the nitrogen sorption data for the fragmented samples and the data is given in Table 3.4. From these data in Table 3.4, it can be seen for both

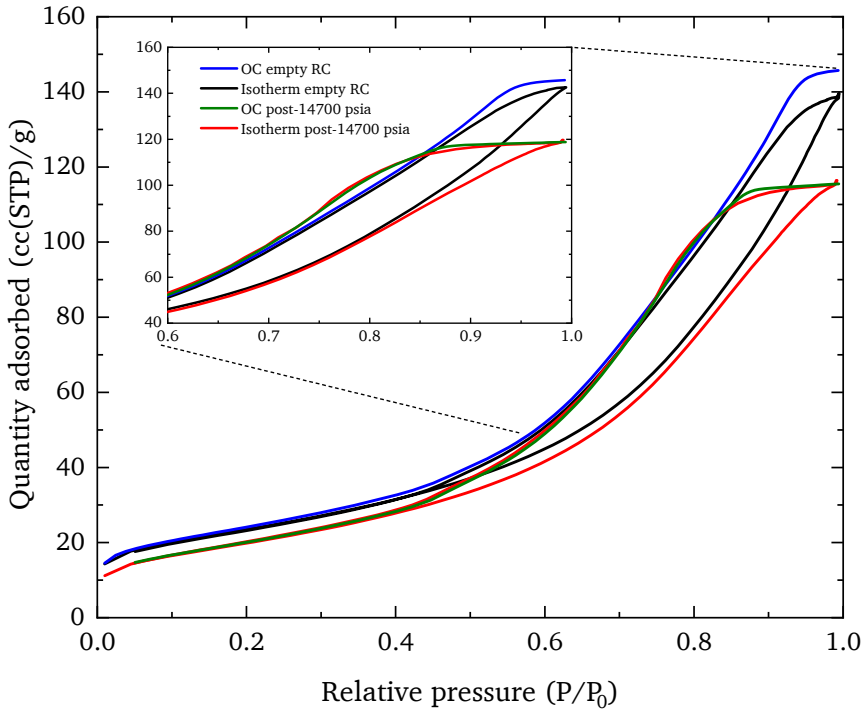


Figure 3.15: Conventional sorption isotherms and overcondensation boundary desorption isotherms for empty RC feed pellet sample, together with conventional sorption isotherms and overcondensation boundary desorption isotherms for RC samples following mercury intrusion to 14,700 psia. The inset shows the isotherms obtained after mercury entrapment adjusted upwards by 3.3 cc(STP)/g.

types of pellet, that the connectivity is higher, and the lattice size is lower for the fragmented samples compared with the empty whole pellet samples, though this difference is much less for the RC pellets. The overall difference in percolation parameters suggests that the pore network of the fragmented sample is more accessible than that of the whole pellet, as might be expected. However, the slim size of this difference for RC pellets may reflect the high degree of disorder also present at smaller length-scales in the feed particles themselves, as seen from the high-resolution CXT images.

Figure 3.20 shows, for the powdered pellet samples, nitrogen scanning loops initiated at relative pressures of 0.85, 0.72 and 0.6, from the conventional desorption isotherm which reach across to the boundary adsorption isotherm in each case. In each case, for both types of pellets, the scanning loops are crossing, but the loops for the RC feed material ascend higher, while crossing, than those for the SD feed. The narrow, almost horizontal crossing behaviour of the lower pressure scanning loops suggests hysteresis is dominated by single pore effects. It is noted that the width of the scanning loops increases with increasing relative pressure, and thus amount adsorbed, at their inception points. The very narrow, almost horizontal crossing behaviour of the lower pressure scanning loops suggests hysteresis is dominated by meniscus geometry effects. The increasing width of the scanning loops with increasing amount adsorbed is probably due to the decrease in percolation seeding effects from the lower prevalence of remaining vapour phase pockets.[7] The change

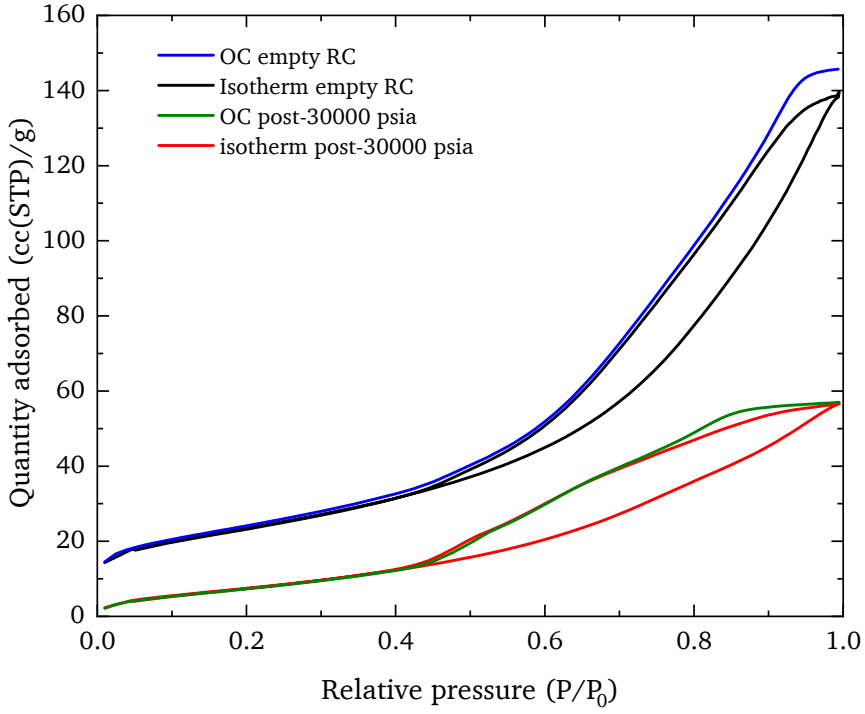


Figure 3.16: Conventional sorption isotherms and overcondensation boundary desorption isotherms for empty RC feed pellet sample, together with conventional sorption isotherms and overcondensation boundary desorption isotherms for RC samples following mercury intrusion to 30,000 psia.

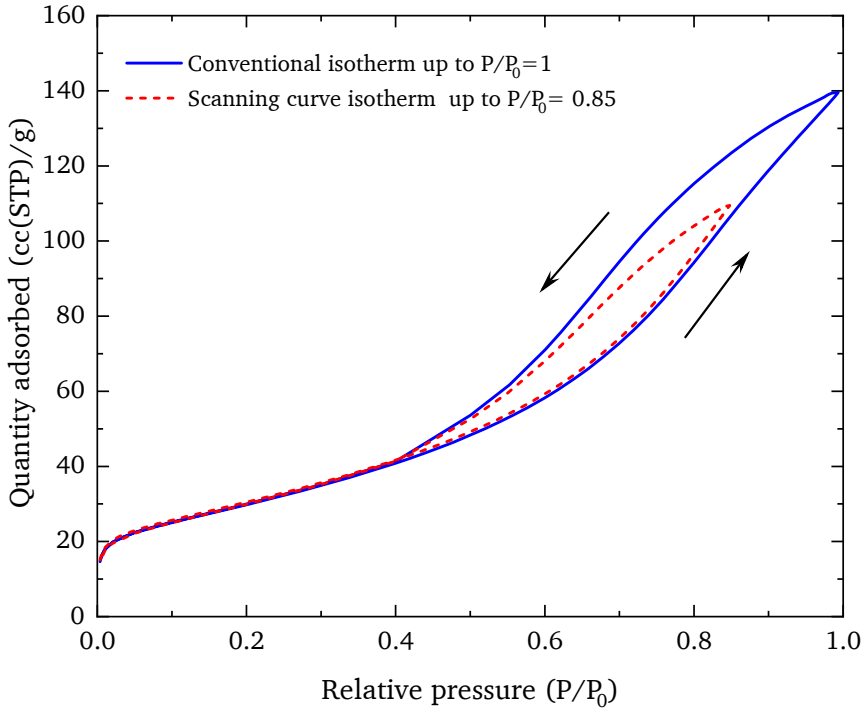


Figure 3.17: Conventional adsorption and desorption isotherms for an empty SD feed pellet and scanning curve with adsorption branch terminating at a relative pressure of 0.85, where desorption branch commenced.

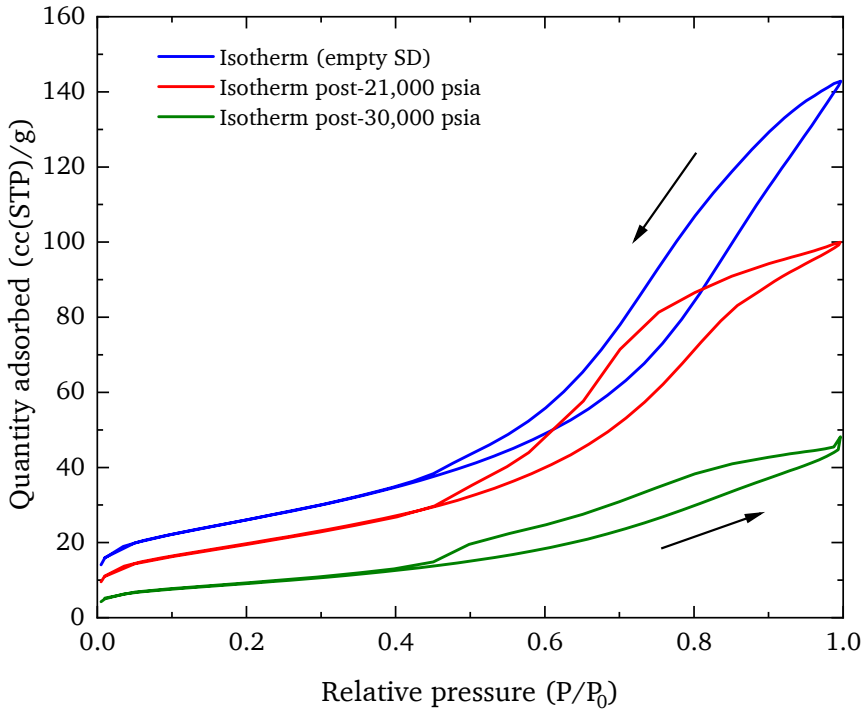


Figure 3.18: Comparison of the conventional nitrogen sorption isotherms for the empty SD feed pellet, with the equivalent data following mercury intrusion to 21,000 and 30,000 psia.

in width of scanning loop is thus a proxy measure of the spatial distribution of these pockets. It is noted that in Figure 3.20, for a given range of relative pressures covered by a scanning loop, the loop for the SD pellet is thinner than the corresponding loop for the RC feed pellet, suggesting a greater prevalence of percolation seed sites in the former.

Figure 3.21 compares the BJH pore size distributions (PSD) obtained (with Harkins-Jura *t*-layer correction) from the adsorption isotherms for the whole and fragmented samples of the RC and SD pellets. It can be seen that the PSDs for whole and powder match very well for smaller pore sizes, but beyond $\sim$12 nm for the SD samples, and beyond $\sim$17 nm for the RC samples, the powder PSDs are shifted to larger sizes than the whole pellet PSDs. This is probably due to advanced condensation (also known as the 'cascade effect') occurring in the whole pellets.[7]

3.5.13 Serial Sorption of Nitrogen and Water

Figure 3.22 shows the conventional nitrogen sorption isotherms for the empty SD and RC feed pellet, with the equivalent data following water adsorption up to 0.36, 0.497, 0.646 and 0.794 water relative pressures. The water adsorption scanning curves involved in suspending the samples over a large bath of sodium hydroxide solution of varying concentrations (to achieve each different relative humidity) for up to $\sim$7 days. From the nitrogen isotherms in Figure 3.22, it can be seen that as more water is adsorbed, the ultimate amount of gas adsorbed at the top of the isotherms decreases.

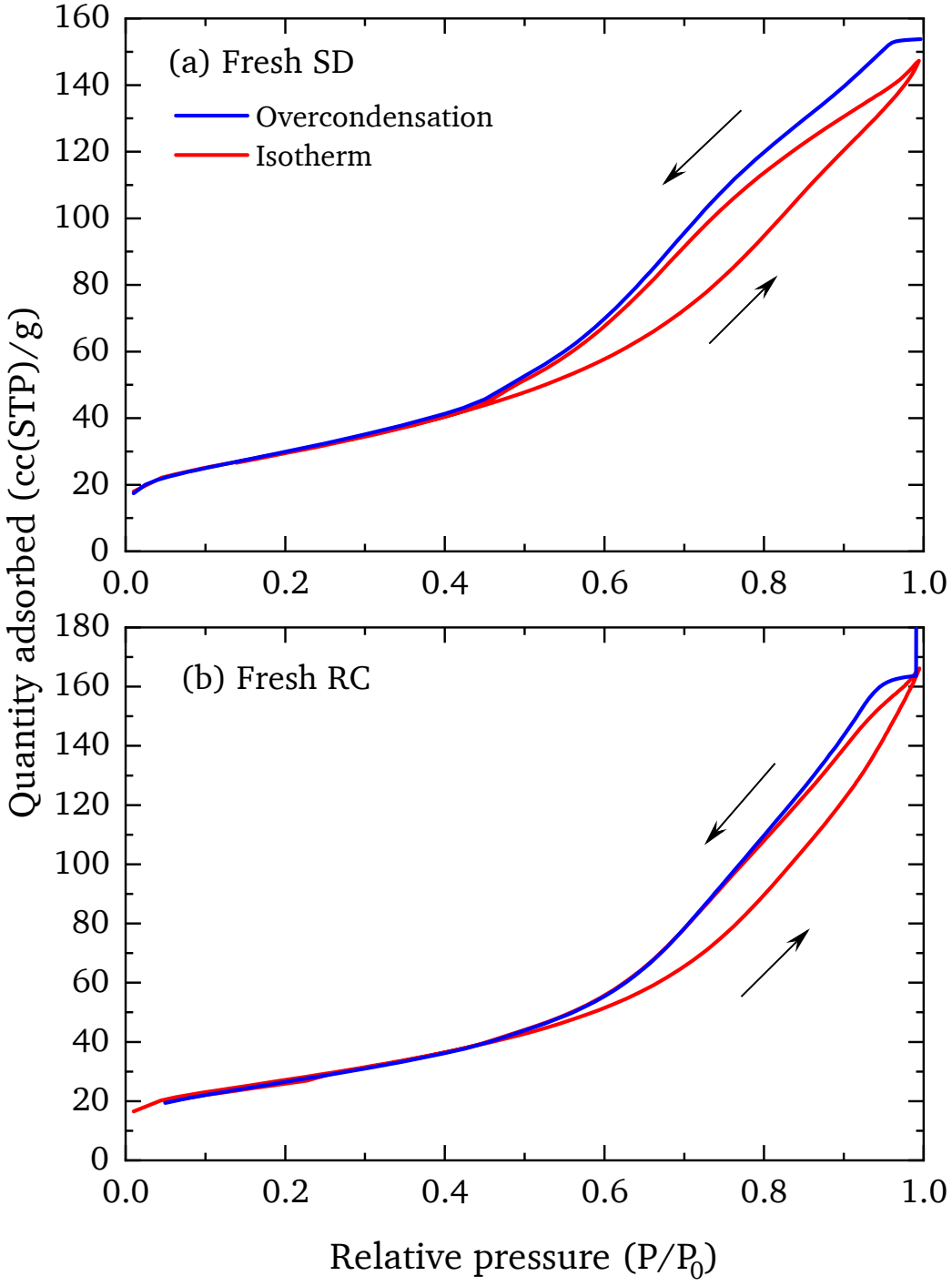


Figure 3.19: Conventional nitrogen sorption isotherms and overcondensation desorption boundary curve obtained for powdered samples of the fresh **(a)** spray dried and **(b)** roll compacted feed pellets.

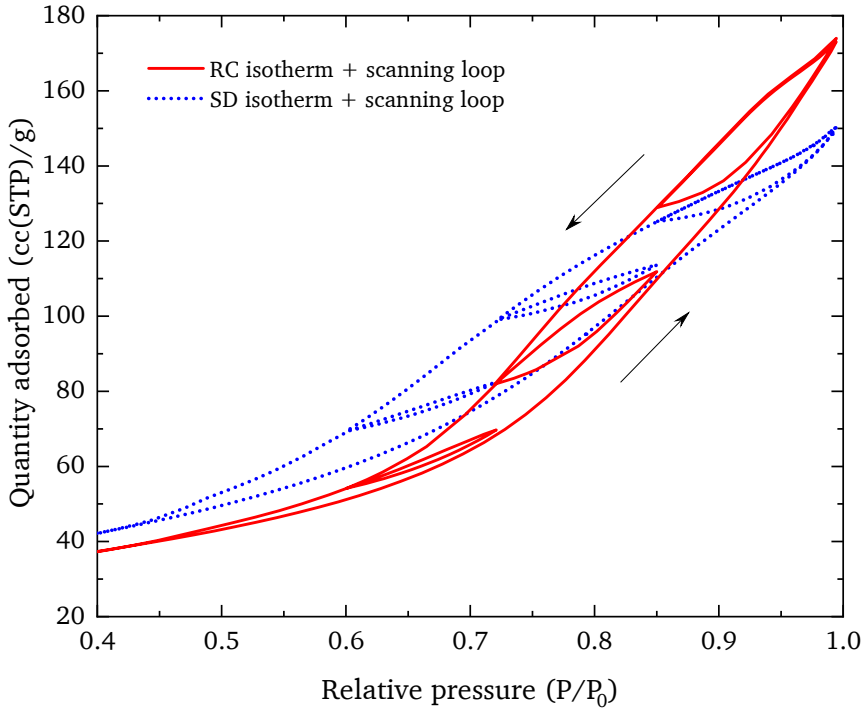


Figure 3.20: Nitrogen sorption scanning loops initiated at relative pressures of 0.85, 0.72 and 0.6, from the conventional desorption isotherms for fragmented samples of the SD feed pellet and RC feed pellet.

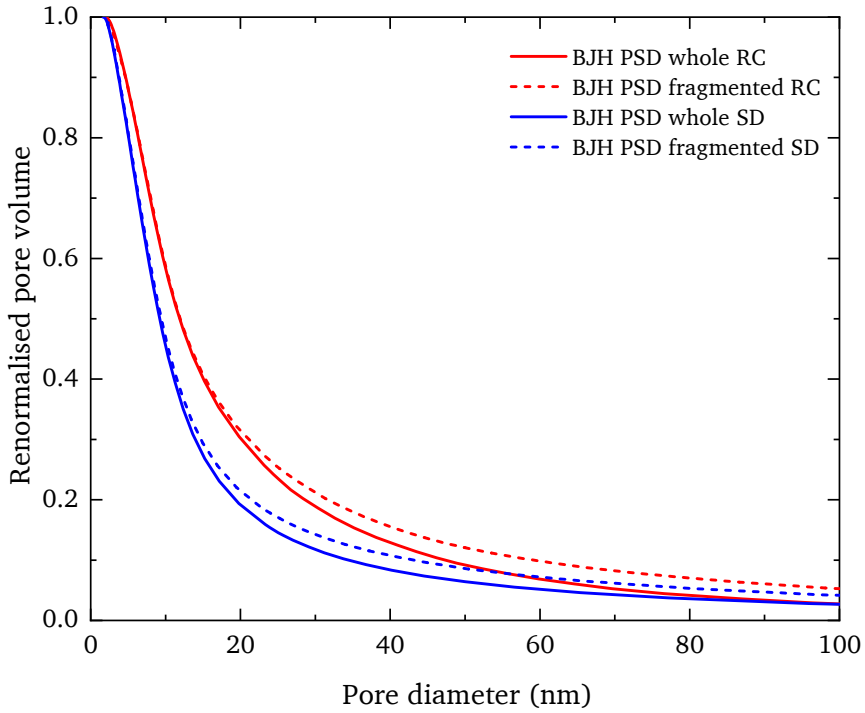


Figure 3.21: Comparison of the BJH PSDs obtained from the adsorption isotherms for the whole pellet and fragmented SD RC samples.

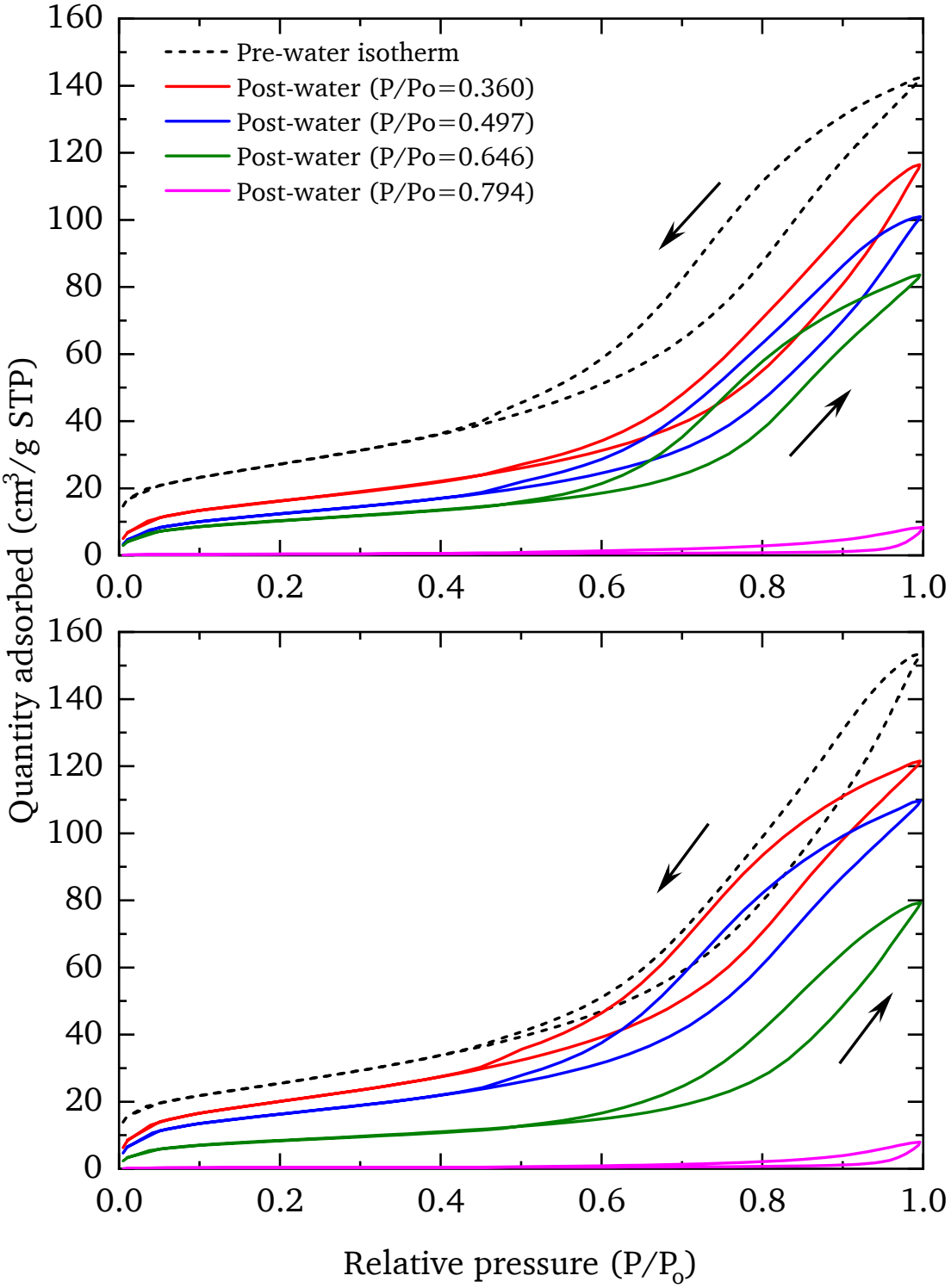


Figure 3.22: Typical examples of conventional nitrogen sorption isotherms for the empty SD feed pellet, with the equivalent data following water adsorption up to different water relative pressures.

3.5.14 Pore Size Distributions

Figure 3.23 shows the BJH PSDs of the sub-sets of pores that become inaccessible from the exterior, as the ultimate mercury intrusion pressure is increased to progressively higher pressure porosimetry scanning curves for the fresh SD and RC samples, respectively. These difference in PSD plots are obtained by subtracting the PSDs from isotherms for samples following successive mercury scanning curves. In general, a lower pressure scanning curves fills large and medium pores, while a higher-pressure scanning curve fills some of the remaining medium and smaller pores. Hence, access to ever smaller pores declines as the intrusion pressure is increased, as one might expect. It is also noted that the steep decline in incremental volume at the lowest pore size present in each distribution corresponds to the minimum penetrated radius for ultimate mercury intrusion pressures.

Figure 3.24 show the BJH PSDs of the sub-sets of pores that become inaccessible from the exterior, as the water partial pressure is increased to progressively higher for the fresh SD and RC samples, respectively. These differences in PSD plots were obtained by subtracting the PSDs from isotherms for samples following successive water scanning curves. In general, a lower pressure scanning curves fills smaller pores, while a higher-pressure scanning curve fills the medium and larger pores. Hence, access to ever larger pores declines as the water relative pressure is increased, as one might expect.

3.5.15 Rate of Adsorption

The rate of adsorption of nitrogen at very low pressure was measured for empty pellets and for pellets following mercury intrusion to various ultimate pressures. The mass uptake curves obtained were fitted to the linear driving force (LDF) model, and the mass transfer coefficients (MTCs) (denoted k) were corrected for adsorption using the slope of the equilibrium isotherm at the point where mass transport was measured.[7] The LDF fitting process is explained further in previous work[6] The MTCs so-obtained for SD feed and RC feed pellets are shown in Table 3.5 and Table 3.6, respectively. As can be seen from Table 3.5 and Table 3.6, the MTCs generally decline following mercury entrapment, and the drop increases with increased mercury entrapment, except between 14,700 and 21,000 psia for the RC feed pellets.

In order to examine further the impact of the entrapped mercury, the variation of MTC with increasing mercury intrusion pressure was compared with that predicted for a random distribution of entrapped mercury calculated from the Prager[259] model, as described in previous work.[7] The comparison of the observed fractional decline in the MTC following entrapment with that expected, for the same mercury saturation, from the Prager[259] model is shown in Figures 3.25 to 3.26. From Figures 3.25 to 3.26 it can be seen that, for both SD and RC feed pellets, the MTC is increasingly below that expected following mercury intrusion to 10,800 psia and then 14,700 psia. However, for intrusion to the highest pressures ($\geqslant$21,000 psia), the decline in MTC becomes the same as that expected for a random distribution of mercury. Figures 3.25 to 3.26 also show the variation in

[259] S. Prager. *J. Chem. Phys.*, **33**: 122–127, 1960.

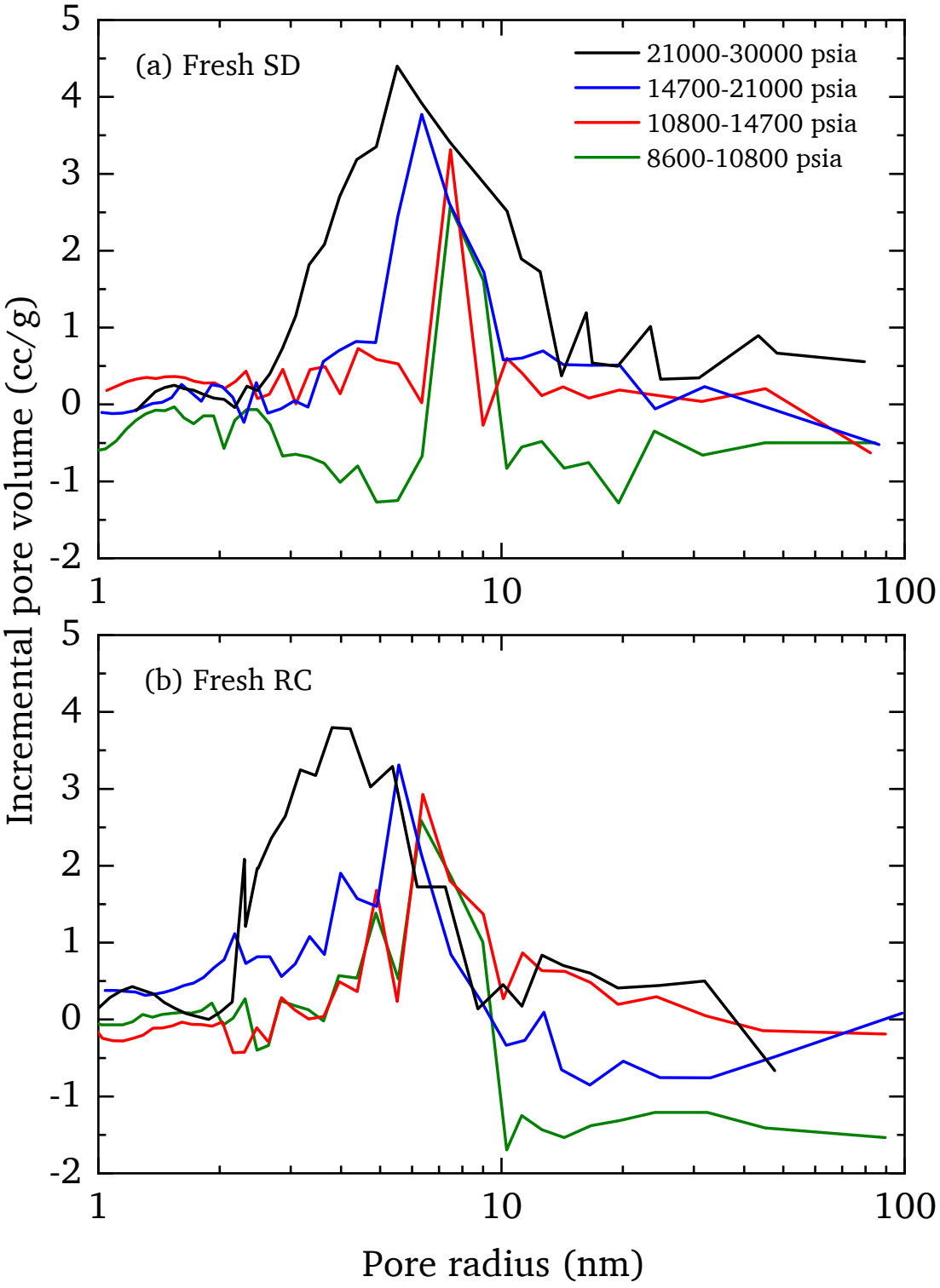


Figure 3.23: BJH pore size distributions for the sub-sets of pores that become inaccessible from the exterior as the mercury intrusion pressure is increased to progressively higher ultimate pressures (as indicated in legend) for scanning curves. (a) Fresh SD and (b) Fresh RC.

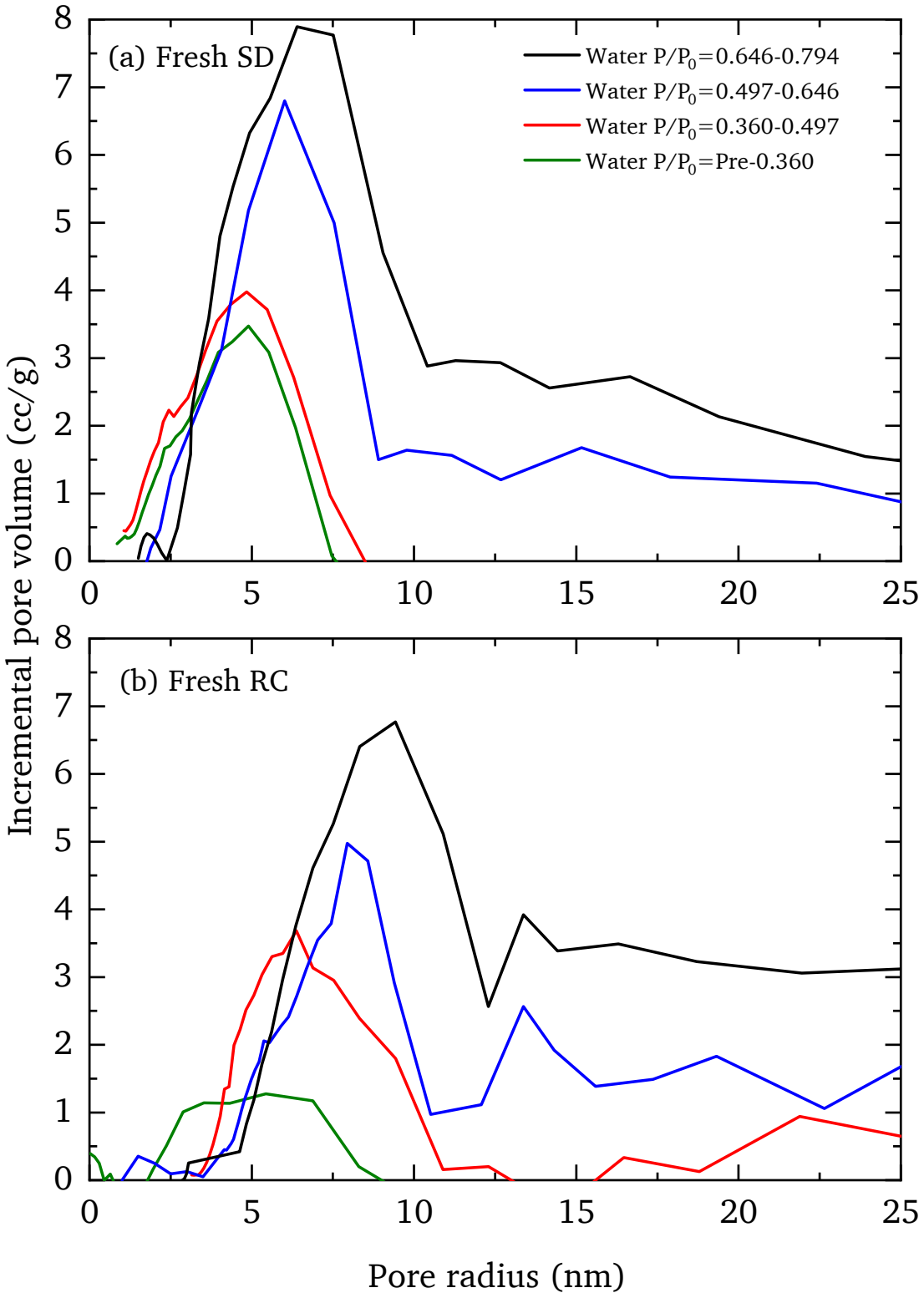


Figure 3.24: BJH pore size distributions for the sub-sets of pores that become inaccessible from the exterior as the water vapour pressure is increased to progressively higher pressures (as indicated in legend) for scanning curves. (a) Fresh SD and (b) Fresh RC.

Table 3.5: Variation in adsorption-corrected MTC, for nitrogen at low pressure, with increasing mercury saturation for whole SD feed pellets

MIP pressure(psia)	Minimum pore diameter penetrated (nm)	Fractional Hg saturation (%)	MTC for empty pellet, k_o(/s)	MTC for post Hg, k(/s)	Experimental k/k_o	Expected k/ko for random entrapment (Prager)
8,600	25.1	11.5	1.71	1.39	0.81	0.85
10,800	19.9	16.2	1.60	0.92	0.58	0.79
14,700	14.7	26.2	1.79	0.66	0.37	0.67
21,000	10.2	54.9	1.69	0.56	0.33	0.36
30,000	7.2	93.3	1.66	0.23	0.14	0.04

Table 3.6: Variation in adsorption-corrected MTC, for nitrogen at low pressure, with increasing mercury saturation for whole RC feed pellets

MIP pressure(psia)	Minimum pore diameter penetrated (nm)	Fractional Hg saturation (%)	MTC for empty pellet, k_o(/s)	MTC for post Hg, k(/s)	Experimental k/k_o	Expected k/ko for random entrapment (Prager)
8,600	25.1	11	1.91	1.37	0.72	0.86
10,800	19.9	15	1.73	1.10	0.64	0.81
14,700	14.7	19	1.66	0.28	0.17	0.76
21,000	10.2	58	1.72	0.43	0.25	0.34
30,000	7.2	91	1.86	0.30	0.16	0.05

adsorption-corrected MTC, for the SD and RC, with fraction of the pore volume occupied by water, and a comparison with that expected for a completely random arrangement of the blocking water phase, as predicted by the Prager[259] model. It can be seen that, for both SD and RC feed pellets, the MTC is much lower than would be expected for a random arrangement of water, thereby suggesting that, in an empty sample, the pores that subsequently are filled with water must have been making a significant, greater than expected, contribution to the mass transport.

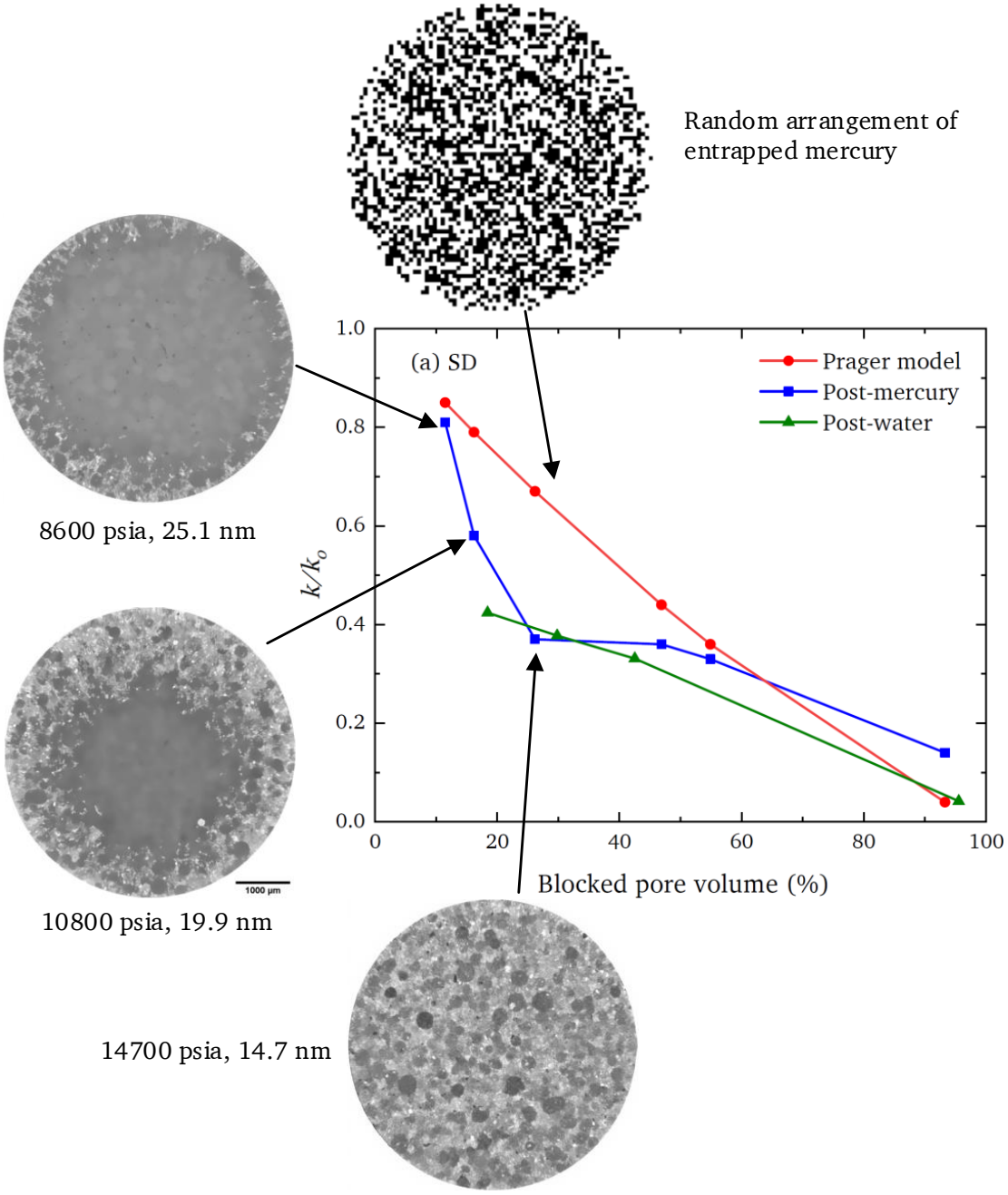


Figure 3.25: Comparisons of the observed fractional decline in the mass transfer coefficient following mercury entrapment and water adsorption and that expected for a random arrangement of entrapped of pore liquid from Prager model for fresh SD feed.

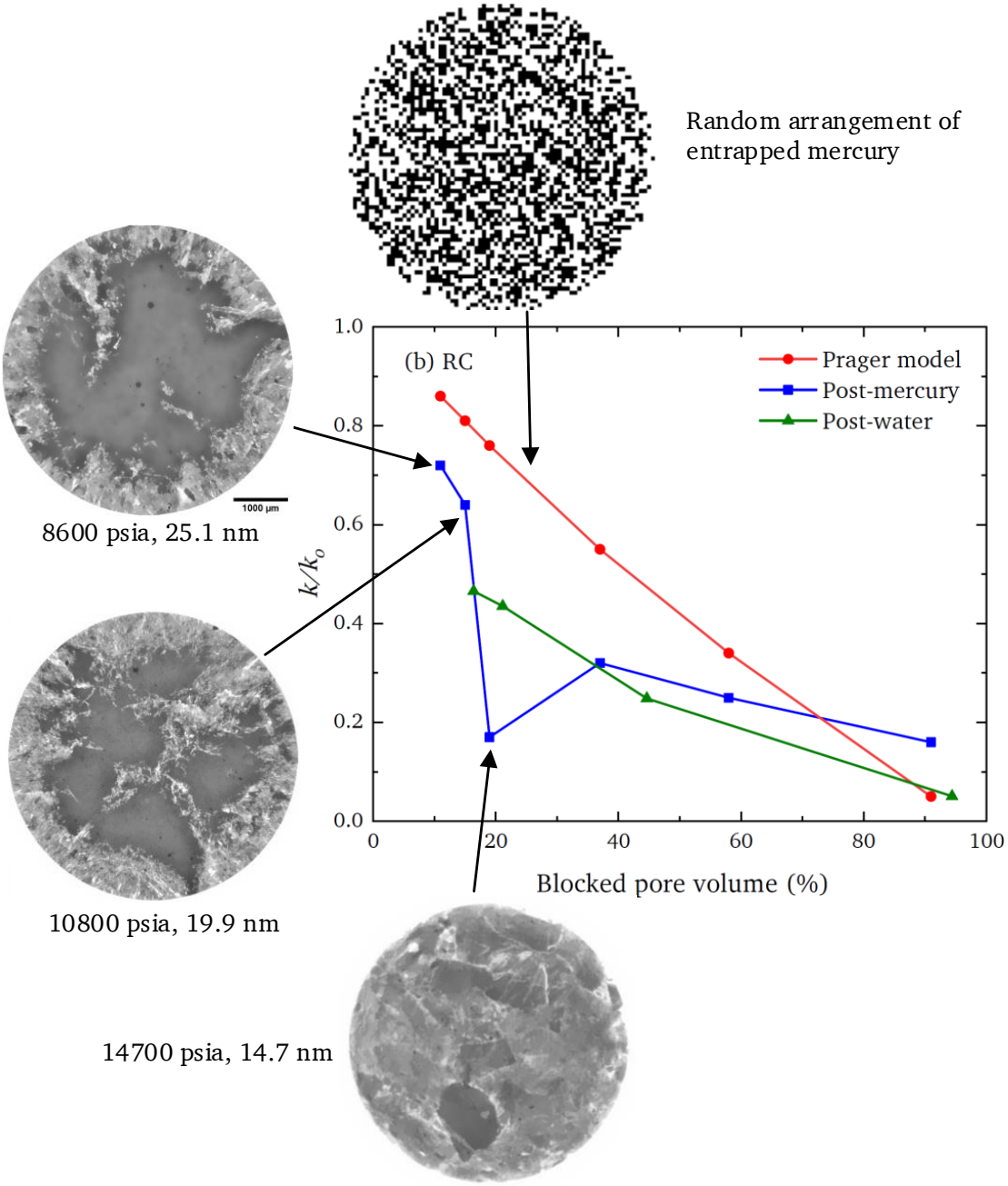


Figure 3.26: Comparisons of the observed fractional decline in the mass transfer coefficient following mercury entrapment and water adsorption and that expected for a random arrangement of entrapped of pore liquid from Prager model for fresh SD feed.

3.6 Discussion

The combination of the CXT with rate of adsorption studies following mercury entrapment allows the determination of the identity of features of the void space structure that are critical to mass transport. The rate of adsorption data for the SD and RC feed pellets showed that the MTC declined well below that expected, theoretically according to Prager[259] model, for a random distribution of mercury entrapped following intrusion to 10,800 and 14,700 psia. This suggests that the zones of the void space lost due to mercury entrapment following these intrusions are very important to mass transfer as their loss led to a greater than expected decline in MTC, relative to the benchmark random structure. From the CXT images of pellets following intrusion to these pressures, it can be seen, by eye, that the mercury is entrapped in a non- random pattern. In the case of the SD feed, the entrapped mercury advanced in a front towards the centre of the pellet, as amount entrapped increased with increased intrusion pressure. Given the barrier-like appearance of such a pattern of entrapment it seems clear why the loss of these pores is important. This pattern of entrapment implies that, when empty, there are pore pathways that, as they penetrate deeper into the pellet, are guarded by ever narrower necks. Hence, as diffusion penetration depth increases, the resistance to Knudsen diffusion will increase. In contrast, for the case of the RC feed pellet, mercury was entrapped in dendritic branches that traverse the pellet, thereby bypassing regions of high density. It is also clear that, for an empty pellet, these dendritic branches would provide diffusion pathways of lower resistance into the depths of the pellet. The slight increase in k/k_o for RC feed pellets between 14,700 and 20,200 psia is probably due to a decrease in the diffusion penetration depth, a, between these pressures, rather than a change in pore network diffusivity, as more mercury is entrapped. This rise in k/k_o is probably due to more mercury becoming entrapped in the core of the pellet as intrusion penetrates this region, thereby restricting gas uptake to only within the surrounding mantle region.

The multi-modal imaging at different resolutions aids the interpretation of the more indirect but multi-scale characterisation methods. This is shown schematically in Figure 3.27. From Figure 3.27, it can be seen that the additional, large pore size step in the mercury intrusion PSD for the SD feed particles is probably related to the 'bubble pores' seen in the high-resolution CXT images of the SD feed. The sizes in this step represent the pores in the shells that are seen to surround the bubble pores in the CXT images or the bubble pores more directly where this shell has been breached to the exterior. The gas overcondensation isotherms show these bubble pores are retained in the pellet made from the SD feed. This is because the typical size of many of the bubble pores, as seen in the higher resolution CXT images, of $\sim$10-100 µm is too large to achieve condensation during the conventional gas adsorption experiment. Hence, the gap between the top of the conventional adsorption isotherm and the overcondensation curve for the empty pellet is probably due to the existence of the bubble pores. The relative sharp desorption knee, at high relative pressures, that only arises in the overcondensation, and not the conventional, desorption probably represents the pore-blocking due to the smaller pores in the shells around the bubble pores. The bubble pores seen in the higher resolution CXT images are probably also responsible for the bright white dots seen in the lower-resolution CXT images of SD feed pellets following mercury entrapment. The distinct, circular, white dots are probably mercury that has become en-

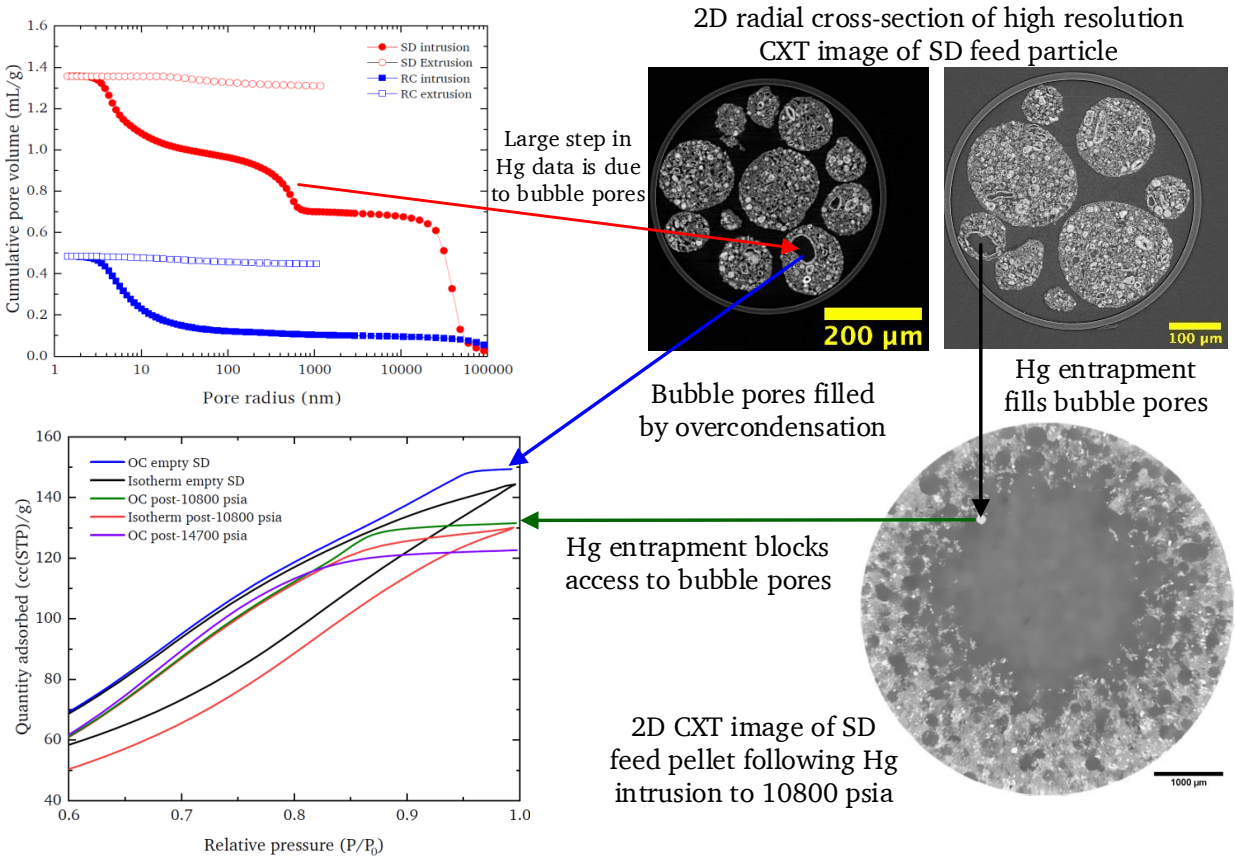


Figure 3.27: Schematic diagram showing how features of the pellet macroscopic structure, seen in the CXT images, impact the indirect data characterising the porosity, and how gas sorption and mercury porosimetry data inform the interpretation of aspects of the images.

trapped within the bubble pores. It is noted that some lower resolution CXT images even show white circular dots within darker round SD feed particles that have not been (much) intruded with mercury. This suggests that, while the shell of bubble pores near the margins of the individual SD feed particles is readily penetrated, the rest of the SD feed particle is shielded by narrower necks and thus is not penetrated at that pressure.

It has been seen that, for both types of pellet, the decreasing accessibility of the pore network due to mercury entrapment was made manifest in the overcondensation isotherms via the widening in the hysteresis with the conventional adsorption isotherms. However, this hysteresis widening arose from very different patterns in the spatial distribution of entrapped mercury in the two types of pellet, as seen in the lower resolution CXT images. In the case of the RC feed the higher resolution CXT images have revealed the fractal structure of the RC pellets. It is known[260] that fractal structures tend to lead to fractal processes within them. In this case the penetration pathways during quasi-equilibrium imbibition of mercury into the RC feed pellet are also fractal.

It has been found that the second, lower pressure, more rounded percolation knee, seen in

[260] D. Avnir. *Fractal approach to heterogeneous chemistry*. Wiley, 1989.

the overcondensation desorption isotherm for the SD feed pellets, has also been retained in the OC curve for the fragmented SD feed pellets. This suggests that this knee is mostly associated with the accessibility of the individual SD feed particles, since the powder particle sizes are of the same size or larger than the feed particles in the lower resolution CXT images. The lower (amount adsorbed) convergence point for the overcondensation and conventional desorption isotherms for the fragmented pellet compared to the corresponding whole pellet data is due to the lower accessibility to vapour phase for some of the SD feed particles buried within the whole pellet, when compared with the fragmented pellet. The difference in the BJH adsorption PSDs between whole and fragmented pellets shows that, in some places, the cascade of pore filling during individual advanced condensation events spans length-scales larger than the powder particle size of $\sim$53-75 $\mu\mathrm{m}$, and thus probably encompasses more than one SD feed particle. Since there is an upper limit (of $\sim$2 from classical theory[7]) on the critical ratio of adjacent pore sizes to enable advanced condensation to proceed, then this suggests given SD feed particles must, themselves, be adjacent to particles with similar (i.e., within the critical ratio) pore sizes in at least one direction. This is consistent with the segregated lower resolution CXT images that suggested that the low-and high-density tails of the distribution within SD feed particles are well-mixed, so the low density and high-density phases were each generally contiguous, and SD feed particles had neighbours of the same phase. This probably thus also explains why accessibility of the pellet interior to gas is maintained (as MTC value drops) despite the enveloping intrusion front seen in lower resolution CXT images of SD feed pellets following entrapment, albeit the open connections are only maintained by high density, lower pore size, SD feed particles.

The presence of advanced condensation effects, detected by comparing the adsorption PSDs for both whole and fragmented pellets, suggests that disordered porous materials are not just composites of the pore structures of the unit cells of templated, or otherwise controlled, pore size materials. The shift in the adsorption isotherm on fragmentation of the pellets shows that the juxtaposition of pore sizes over macroscopic scales is a critical feature of the overall porous structure. This suggests that the characteristic void space units for the capillary condensation process correspond to macroscopic regions of the network, rather than individual pores. The prevalence of network-scale, pore-to-pore co-operative effects in disordered materials can only be determined by studying the material itself.

The succession of overcondensation isotherms, following progressively increasing levels of mercury entrapment, have shown that the boundary desorption isotherm from overcondensation experiments on empty SD feed pellets bridges between the micron-sized bubble pores, that do not fill with condensate in conventional sorption experiments, and the pore necks with sizes below $4\,\mathrm{nm}$ that would not be intruded by mercury. The gas sorption data obtained following mercury intrusion to 30,000 psia that shows the cavitation step also implies that these narrow necks are directly accessible from the exterior via pathways that do not include the pores filled with mercury, such as the bubble pores and low-density SD feed particles. They are thus probably located in, relatively unintruded, high density SD feed particles, as might be expected.

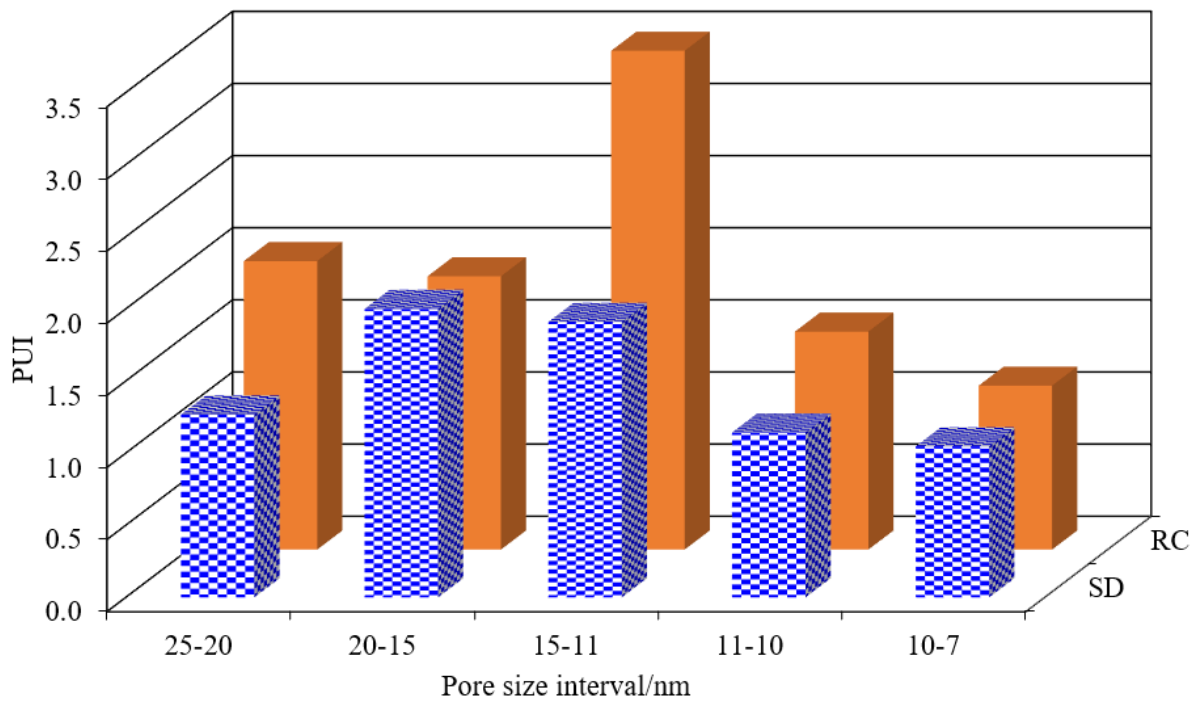


Figure 3.28: Measures of usefulness, to mass transport in SD and RC feed pellets, of pore size intervals, as indicated by PUI.

As discussed above, the studies of rate of adsorption for samples containing entrapped mercury have shown that some pores are more critical to mass transport than others. It is possible to define a pore utility index (PUI) that attempts to quantify the usefulness of a given pore size interval to overall mass transport, such that:

$$PUI = \frac{1 - \text{ experimental } (k/k_0)}{1 - \text{ expected } (k/k_0) \text{ for random structure}} \tag{3.10}$$

The PUI calculated for the SD and RC feed pellets from the ROA data in Tables 3.5 to 3.6 are shown in Figure 3.28. It can be seen that the pore intervals of 15-11 and 20-15 nm have the highest PUIs for the RC and SD feed pellets, respectively.

A measure of the relative accessibility of particular pores to the exterior can be obtained from a relationship between the roundedness of the percolation knee of the overcondensation isotherm and the tortuosity for mass transport, as will be described here. Given that tortuosity is a measure of the extension of the path length of the diffusional flux beyond that of the straight-line distance across the porous medium, then the relative change in tortuosity ($\Delta\tau = \tau - \tau o$) can be related to

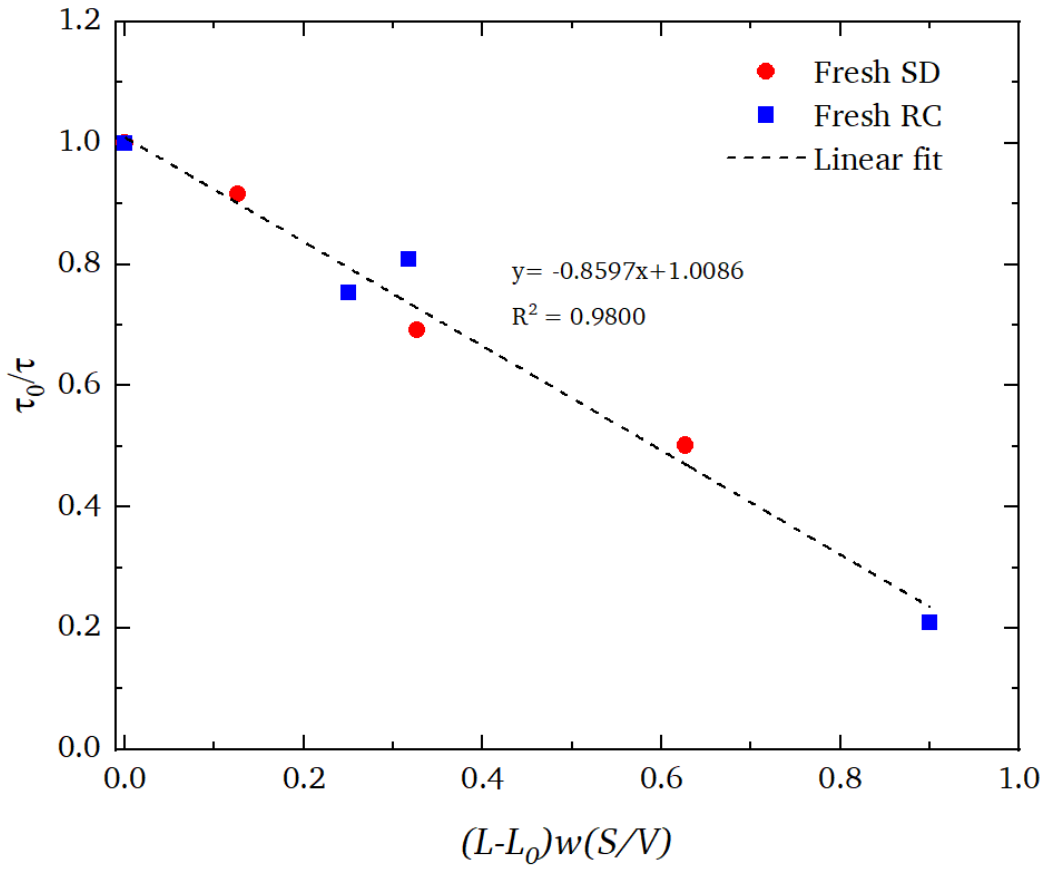


Figure 3.29: A plot of the tortuosity ratio (from Equation (3.3)) against percolation lattice size (from Table 3.4) for SD (red dots) and RC (blue squares) feed pellets following mercury entrapment to different intrusion pressures.

the relative change in effective network size,Λ, such that:

$$\frac{\Delta\tau}{\tau} = \frac{\Delta\Lambda}{\Lambda} \tag{3.11}$$

since, if the effective size of the network is increased, then the path length of the diffusive flux will correspondingly be increased.

The apparent, effective size of the network will be increased if the size of the underlying model percolation lattice, L, is increased. The aforementioned CXT images of the pellets following mercury porosimetry, in Figures 3.11 to 3.12, show that many feed particles remain free, or virtually free, of any entrapped mercury, while some others are completely, or nearly completely, filled with entrapped mercury. Hence, the individual feed particles tend to be either open or closed, respectively, following mercury porosimetry, and, thus, can be considered either present, or absent, respectively, from the model percolation network representing the macroscopic structure of the pellet. Therefore, the physical size of the underlying lattice unit in which L is measured can be considered as the size of a pellet feed particle, w. The characteristic physical size of the overall network would be proportional to the inverse of the surface-to-volume ratio $(S/V)_t$ of the tableted

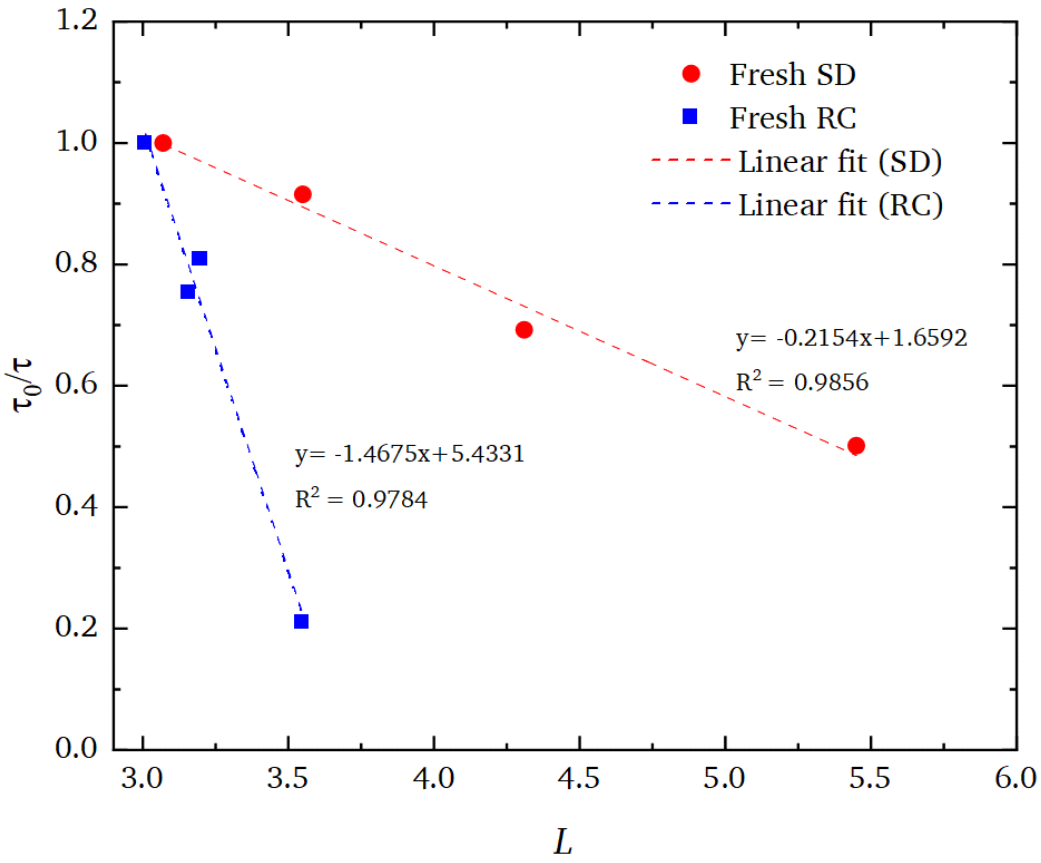


Figure 3.30: Plot of Equation (3.12) for experimental data for SD (red circles) and RC (blue squares) feed pellets.

pellet itself. The corresponding constant of proportionality would be a geometry factor characteristic of the shape of the pellet. The ratio of the geometry factors for the feed particles and whole pellet is denoted γ and would be equal to unity if the feed particles and pellet had the same geometrical shape. Hence, the macroscopic tortuosity for mass uptake into the pellet is related to the change in the size of the percolation model lattice (ΔL) following mercury entrapment according to:

$$\frac{\tau_{a0}}{\tau_a} = 1 - \gamma\,(L - L_0)\,w\left(\frac{S}{V}\right)_t \tag{3.12}$$

Hence, for a given pellet type, the ratio of the original experimental tortuosity to the tortuosity measured following pore structural modification via mercury entrapment should be a linear function of the lattice size obtained from percolation analysis of the corresponding overcondensation isotherm.

From the BJH difference PSDs in Figure 3.23, it can be seen that, as mercury is entrapped over pressure intervals 8600-10800 and 10800-14700 psia, the position of the peak in the pore sizes being filled stays the same for both the SD and RC feed pellets, and so the critical pore size for mass transport will remain the same. The remaining porosity following mercury entrapment is

one minus the fractional mercury saturation given in Tables 3.5 to 3.6. Hence, Equation (3.3) can be used to determine the ratio of tortuosities, since the critical reference Knudsen diffusivity is a constant over intrusion pressures up to 14700 psia. Equation (3.12) suggests that the tortuosity ratio will be a linear function of the percolation lattice size L, and, indeed, this is what is seen for both SD and RC feed pellets in Figure 25.

A universal plot for both pellet feed types can be obtained by plotting the data for each according to Equation (3.12) using the surface-to-volume ratio of the pellets calculated using the dimensions given in Table 3.1, and taking typical feed particle sizes of 200 and 1300 $\mu\mathrm{m}$ for the SD and RC feed particles. From Figure 3.30, it can be seen that the experimental data give rise to a good fit to Equation (3.12). The best-fit values for typical feed particle sizes from Equation (3.12) are consistent with what is observed in the CXT images of pellets, as seen from the similarity in grid size divisions and feed particle sizes in the images given in appendix A, and could be confirmed by directly measuring feed particle sizes in the CXT images (Figure 3.4 and Figure 3.7), and the average values thereby obtained for SD and RC feed were 205 and 1290 $\mu\mathrm{m}$, respectively.

The good fit of Equation (3.12) to the experimental data suggests that the macroscopic structure of the pellets is well-represented by a random bond network percolation lattice, where the feed particles relate to the individual lattice bonds. Hence, the percolation behaviour of the pellets is dominated by the macroscopic structural heterogeneities resulting from heterogeneity in the feed particles. The key difference in the pellet fabrication route relevant to mass transport is manifested in the different values of the parameter w in Equation (3.12), which corresponds to the feed particle size for the tableting process.

The reason that the key parameter of the model of macroscopic structure is the lattice size is that this parameter is a measure of the prevalence of surface clusters of larger pores important in an invasion percolation process like gas desorption or mercury intrusion. The roundedness of the percolation knee in gas desorption or mercury intrusion represents ‘premature’ penetration of the invading phase before the critical pressure for sample-spanning percolation is reached. In a completely random structure, the probability of formation of surface clusters is enhanced by the larger surface area-to-volume ratio of smaller lattices raising the probability of a given pore being located on the surface. When using a random lattice to represent a real heterogeneous material, an apparent small model lattice size represents a greater propensity for surface clusters than for a random structure. For example, the ‘shrinking core’ effect evident in the spatial pattern of the progressively encroaching front of entrapped mercury in the CXT images of the SD feed pellets reveals the particular creation of surface clusters of mercury penetration in this material. This is reflected in the steep growth in apparent model lattice size for this material as entrapped mercury fills up the surface clusters of larger pores with increasing intrusion pressure, so they are no longer available to facilitate nitrogen desorption. The model lattice size is thus a measure of the prevalence of surface clusters of larger pores, with apparently smaller lattice sizes indicating higher prevalence. These surface clusters of larger pores provide ‘super-highways’ giving easier access to the pellet interior to diffusing gas, and thus, when lacking with an apparently larger lattice size, mass transport is associated with higher tortuosity.

3.7 Conclusion

The above findings have shown how combining indirect characterisation methods, such as overcondensation and mercury porosimetry, can bridge several orders of magnitude in pore size, even down to molecular scale, with imaging methods that can provide detailed spatial information but for a limited range of resolution and/or field-of-view, can lead to a much more comprehensive and inter-linked characterisation of disordered hierarchical porous media. The hybrid characterisation methods, which integrate several techniques in one overall experiment, ensure that the characterisation data from different methods coheres and produces synergistic findings. The combination of overcondensation with multi-scale imaging identified the macropore structures missing from conventional isotherm data, namely the large 'bubble pores', and also allowed the specific sizes of the smaller pores shielding these structures to be measured.

It has been seen that the 'filtering' or 'sifting' strategy, involving combining characterisation techniques, described here can identify and spatially locate the particular pore sizes that most control mass transport in pore structures of different characters arising from different fabrication methods. As a result, different pore size intervals can be allocated a pore utility index value that quantifies their relative usefulness to mass transport. The characterisation methods also allow indication of how particular pore structural features relate to raw material properties and fabrication methods. Hence, the impact of the choices made in catalyst pellet manufacturing on mass transport can be identified and quantified.

It has been shown that a random pore bond network is a successful model for the macroscopic heterogeneity in pellet structure, as characterised by the percolation parameters, especially apparent lattice size. The percolation theory-based analysis of the overcondensation data has successfully, quantitatively predicted the relative change in tortuosity, from rate of adsorption experiments, as successively more of the pore structure is filled with entrapped mercury, thereby increasing the apparent lattice size. The model has demonstrated that the degree of heterogeneity in average pore sizes amongst individual feed particles, and their particle size relative to that of the pellet itself, greatly impact the accessibility of the pellet interior. While it has been seen that surface clusters of larger pores control access to the interior for both feed types, their particular geometric form has its origins in the feed type and fabrication process of the pellet. The differential importance, for mass transport, of particular pore size ranges within these surface clusters for each pellet type has been evaluated, and their location within the pellets has been visualised.

The next chapter discusses an image segmentation method based on deep learning neural network that can automatically segment CXT and FIB-SEM images of methanol synthesis pellets.

Chapter 4

Automated Segmentation of X-ray and FIB-SEM Images of Methanol Synthesis Catalyst using Deep Learning Neural Networks

4.1 Introduction 99
4.2 Materials and Image Acquisitions 104
4.3 Background on Artificial Neural Networks 107
4.4 Deep Learning Image Segmentation Strategy 112
4.5 Results and Discussion 116
4.6 Conclusion 127

4.1 Introduction

A typical methanol synthesis catalyst pellet comprises highly disordered and complex internal structures that are heterogeneous over a large length scale ranges. This type of catalyst can be characterised using standard indirect characterisation methods such as gas sorption and mercury porosimetry, as described in Chapter 3, because they are mostly cheap and can offer statistically representative information for the whole sample. The indirect characterisation methods can be further combined with modern imaging techniques such as computerised X-ray tomography (CXT), scanning electron microscopy (SEM) (or focused ion-beam, FIB-SEM), and transmission electron microscopy (TEM). The imaging could be obtained before and after imbibing the sample with electron-dense contrast agents such as mercury or Wood's metal. The imaging techniques can generate three-dimensional (3D) pictures of the internal structures of the catalyst and reveal the macroscopic spatial distribution of any entrapped contrast agent in the pore network. Both CXT and FIB-SEM serial milling can produce many contiguous slices that can be stacked together to obtain a 3D reconstruction of the imaged sample. The reconstructed 3D volume represents an accurate depiction of the geometry of the sample up to a particular resolution. The imaging techniques could themselves be combined together to create a multi-scale imaging system that images a tiny area of the original macroscopic CXT image at greater resolution using FIB-SEM or TEM to extract information at submicron resolutions (e.g., porosity or pore sizes). The resolution of a typical to-

mography is often limited to $\sim 1\,\mu\mathrm{m}$, but microscopy allows one to investigate objects down to the nanometre scale. Hence, the microporous features from higher resolution FIB-SEM images can be mapped onto the corresponding slice of the tomogram. Using these mapping features, the higher resolution information may then be propagated across the 3D volumetric tomographic data.[121]

In the past, the process of segmenting and extracting useful qualitative or quantitative information from CXT or FIB-SEM images was engineered manually, and, later, by using traditional computer vision algorithms such as thresholding,[261] watershed transformation[262] or a clustering method.[263] Segmentation is the process of assigning a label to each pixel in an image such that pixels with the same label are connected with respect to some visual or semantic property.[264] For tasks like image classification in traditional computer vision, a feature extraction process is used in which as many features as possible are retrieved from images, and these features create a definition (known as bag-of-words) for each object class present on the image. These definitions are searched for in other images during the deployment step. When a large number of features from one bag-of-words appear in another image, the image is identified as containing that particular object (e.g., mercury, graphite). The problem with this approach is that it requires deciding which features are essential in each image. On top of this, feature extraction becomes increasingly difficult as the number of classes to categorise increases. In order to determine which features best describe a distinct object class, the computer vision engineer must use their judgment and go through a lengthy trial and error process. Furthermore, each feature definition involves dealing with a plethora of parameters, all of which the computer vision engineer must fine-tune, which in part was an obstacle to the extraction of useful information from the images.[265]

Another issue with traditional image segmentation techniques, such as thresholding, is the assumption that images have a bimodal intensity histogram. Therefore, the required object can be extracted from the background by a simple operation that compares image values with a threshold value. This operation, however, is only possible if each phase on the image has a distinct, separate peak on the histogram plot. Intensity histogram plots were generated for the 2D CXT and FIB-SEM slices for the methanol synthesis catalyst pellets before and after applying noise reduction filters. For both image types, the noise reduction filters concentrated the peaks in the lower range of greyscale value, and a slightly better separation of the different phases was observed after applying the filter. However, there was still significant overlap between the intensities of the different phases on the CXT and FIB-SEM images; thus, a simple thresholding operation cannot be used to segment the methanol synthesis pellet images. As a result, segmentation of the different phases of interest necessitates using another technique, such as deep learning (DL) neural network.[266]

[121] V. Cnudde and M. Boone. *Earth Sci. Rev.*, **123**: 1–17, 2013.
[261] P. K. Sahoo, S. A. Soltani, and A. K. Wong. *Comput. graph*, **41**: 233–260, 1988.
[262] S. Beucher. *Scanning Microsc.*, **1992**: 28, 1993.
[263] D. Nameirakpam, M. Khumanthem, and J. Yambem. *Procedia Comput. Sci.*, **54**: 764–771, 2015.
[264] S. Ghosh et al. *ACM Comput. Surv.*, **52**: 1–35, 2019.
[265] N. O'Mahony, S. Campbell, and A. Carvalho. *Adv. Intell. Syst.*, **943**: 128–144, 2020.
[266] Y. Lecun, Y. Bengio, and G. Hinton. *Nature*, **521**: 436–444, 2015.

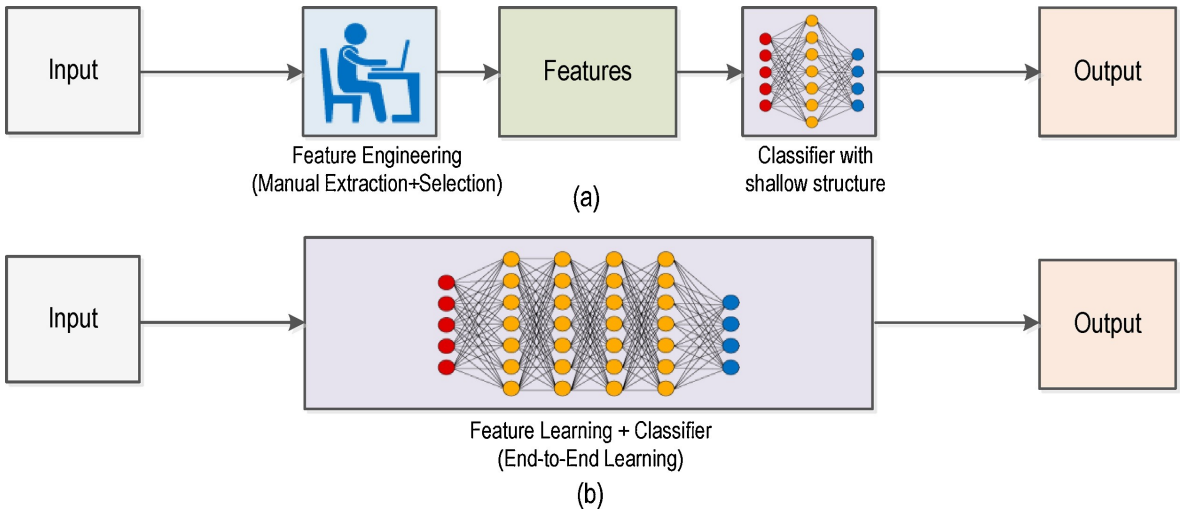
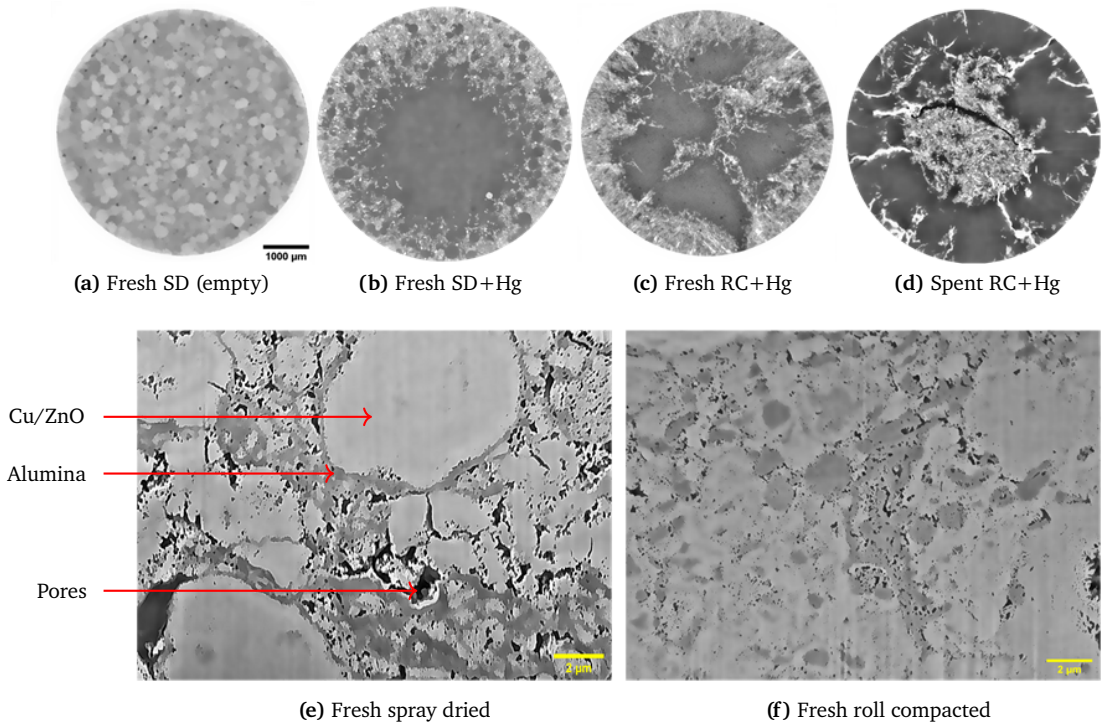


Figure 4.1: A schematic representation of the two different segmentation techniques using either (a) Traditional, (b) Deep learning [267].

In recent years, the emergence of deep learning,[266] a type of machine learning[268] and artificial intelligence (AI),[269] such as convolutional neural networks (CNN),[270] has had an enormous effect in the field of computer vision and are responsible for a significant increase in the ability to classify objects in an image. This surge in advancement has been made possible by increases in device capabilities such as processing power, memory capacity, power consumption, as well as the vast amounts of data available for training neural networks. Compared to traditional techniques, deep learning allowed computer vision engineers to achieve higher accuracy in tasks such as semantic segmentation, images classification, and object recognition. Because deep learning neural networks are trained rather than programmed, applications using this method frequently require less expert analysis and fine-tuning while utilising the massive quantity of image data accessible in today's devices. Additionally, deep learning algorithms have solved many of the problems associated with traditional image segmentation by introducing end-to-end learning where the neural network is trained on a dataset that has been manually delineated, and thereby, the network is asked to produce the correct labels on new, previously unseen images based on the underlying patterns or rules discovered in the training set.[265] On top of this, deep learning also offered computer vision engineers more flexibility since deep learning models can be re-trained using a new dataset for every use case, as opposed to traditional computer vision methods, which are often domain-specific. Figure 4.1 illustrates the differences between traditional and deep learning image segmentation workflow.

Several other studies have explored the application of deep learning to image segmentation in other research fields. Badran et al.[271] developed a deep learning neural network that is capable of segmenting fibre-reinforced ceramic composites that consist of fibre and matrix with identical im-

[268] S. Shalev-Shwartz and S. Ben-David. *Understanding Machine Learning*. Cambridge University press, 2014.
[269] M. H. Hassoun. *Fundamentals of Artificial Neural Networks*. MIT press, 1995.
[270] Y. LeCun, K. Kavukcuoglu, and C. Farabet. *IEEE Int. Symp. Circuits Syst.*, 253–256, 2010.
[271] A. Badran et al. *J. Mater. Sci.*, **55**: 16273–16289, 2020.



(a) Fresh SD (empty) **(b)** Fresh SD+Hg **(c)** Fresh RC+Hg **(d)** Spent RC+Hg

(e) Fresh spray dried **(f)** Fresh roll compacted

Figure 4.2: CXT (top row) and FIB-SEM (bottom row) images of cylindrical methanol synthesis catalyst pellets. **(a)** CXT image of empty fresh SD pellet, **(b)** Fresh SD pellet with mercury up to 10,800 psia, **(c)** Fresh RC pellet with mercury up to 10,800 psia, **(d)** Spent RC pellet with mercury up to 2,860 psia, **(e)** Fresh SD, and **(f)** Fresh RC. The scale bars correspond to 1,000 µm for CXT, and 2 µm for FIB-SEM images.

age intensities. Xiangyu et al.[272] have proposed an analysis program based on deep learning CNNs that can dramatically improve the throughput of CXT image analysis of pharmaceutical tablets while also achieving a highly robust quantitative analysis. Renata et al.[273] applied a deep learning segmentation method to microCT images of strain-hardening cement-based composites (SHCC) to accurately segment the polymer fibres and air voids from the cementitious matrices. Using the well-known U-Net[274] CNN architecture, Emanuella et al.[275] proposed a new deep learning CNN network that can easily discriminate between pores and cracks in an iron ore catalyst pellet imaged by microCT. Their study has shown that U-Net CNNs models could easily be applied to different types of materials containing pores and fissures, such as cementitious materials, rocks, sintered metals and ceramics. Deep learning applications are not limited only to image segmentation but have produced outstanding results, comparable to and in some cases surpassing human expert performance, in various other machine learning fields, including speech recognition,[276] driverless

[272] X. Ma et al. *J. Pharm. Sci.*, **109**: 1547–1557, 2020.
[273] R. Lorenzoni et al. *Cem. Concr. Compos.*, **108**: 103551, 2020.
[274] O. Ronneberger, P. Fischer, and T. Brox. *MICCAI*, **9351**: 234–241, 2015.
[275] E. Bezerra, K. Augusto, and S. Paciornik. *Int. J. Eng.*, **73**: 197–203, 2020.
[276] G. Hinton et al. *IEEE Sig. Proc.*, **29**: 82–97, 2012.

vehicles,[277] natural language processing,[278] healthcare,[279] fraud detection,[280] and board games.[281] This recent surge in machine learning applications is caused by the fact that deep learning algorithms are very successful when dealing with large amounts of unsupervised data since they learn data representations in a greedy layer-wise fashion.

In this chapter, an image segmentation method based on a deep learning neural network capable of automatically segmenting CXT and FIB-SEM images similar to those shown in Figure 4.2 was developed. The deep learning method utilised here is based on the software Dragonfly from ORS,[258] which uses the popular TensorFlow[282] deep learning engine in a user-friendly image processing environment. The software was run locally on a workstation equipped with Nvidia graphics RTX P6000 24Gb Quadro.

[277] J. Ni et al. *Appl. Sci.*, **10**: 2749, 2020.
[278] T. Young et al. *IEEE Comp. Intell.*, **13**: 55–75, 2018.
[279] A. Esteva et al. *Nat. Med.*, **25**: 24–29, 2019.
[280] A. Roy et al. , **4**: 129–134, 2018.
[281] S. Mesentier et al. , **10**: 1–10, 2017.
[258] R. Makovetsky, N. Piche, and M. Marsh. *Microsc. Microanal.*, **24**: 532–533, 2018.
[282] A. Martín et al. *CoRR*, 265–283, 2016.

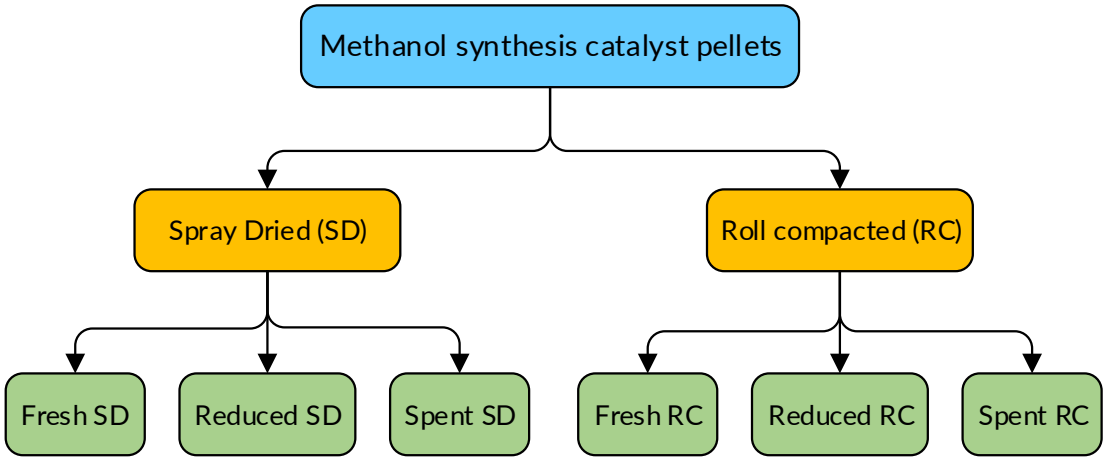


Figure 4.3: A simple flowchart showing the methanol synthesis catalyst pellets studied in this chapter.

Table 4.1: Properties of samples studied in this chapter **(a)** spray dried, and **(b)** roll compacted. The bulk density and porosity were obtained from mercury porosimetry.

(a) Spray dried feed material

Sample	Porosity (%)	Bulk Density (gcm^{-3})	BET (m^2/g)	Dimensions (bxh)
Fresh	47.1	2.2	113.8	5.5x3.4mm
Reduced	67.3	1.9	109.4	5.4x3.5mm
Spent	69.4	1.9	59.0	5.5x3.6mm

(b) Roll compacted feed material

Sample	Porosity (%)	Bulk Density (gcm^{-3})	BET (m^2/g)	Dimensions (bxh)
Fresh	48.1	2.2	122	5.6x3.6mm
Reduced	64.4	1.8	107.5	5.4x3.4mm
Spent	65.1	2.0	56.9	5.5x3.5mm

4.2 Materials and Image Acquisitions

4.2.1 Samples Studied

Methanol synthesis catalyst pellets manufactured using either spray-dried (SD) or roll compacted (RC) feed materials were studied in this chapter. The catalyst pellets from each batch came in either fresh, reduced or spent forms as shown in the simple flowchart in Figure 4.3. The fresh SD and RC pellets were studied in Chapter 3 using integrated gas sorption and mercury porosimetry. The reduced and spent SD and RC samples will be analysed further in Chapter 5. Table 4.1**(a)** and **(b)** contain further details and properties of the samples used in this chapter. The bulk density and porosity were obtained from mercury porosimetry. More information on mercury intrusion porosimetry can be found in Chapter 3.

4.2.2 Integrated Mercury Porosimetry and CXT Imaging

In this chapter, mercury metal was used as probe fluid for the X-ray imaging of the methanol synthesis catalyst pellet. The mercury was intruded into the sample pores using standard porosimetry experiment. The following section will describe how the mercury porosimetry experiment was conducted. Mercury intrusion and retraction curves were measured using a Micromeritics Autopore IV 9500, which can generate a maximum pressure of $414\,\mathrm{MPa}$ (60,000 psia). For each experiment, approximately $0.8\,\mathrm{g}$ of sample (4 pellets) were degassed at $140\,^{\circ}\mathrm{C}$, and the sample was kept under vacuum overnight ($24\,\mathrm{h}$). After 24 hours, the heating mantle was removed, and the sample was allowed to cool down to room temperature. The sample was then weighed to obtain the dry weight. The thermal pre-treatment drives off any physisorbed water vapour onto the sample but does not change the sample morphology.

Table 4.2: Mercury porosimetry scanning curve pressures used to control the amount of mercury in the sample pores

Sample	MIP pressure (psia)	Minimum pore diameter penetrated (nm)	Fractional Hg saturation(%)
Fresh SD	8600	25.1	11.5
Fresh RC	8600	25.1	10.8
Reduced SD	3800	56.7	8.5
Reduced RC	3800	56.7	5.4
Spent SD	2860	75.4	11.9
Spent RC	2860	75.4	9.6

The spatial extent and amount of information obtained from the CXT of mercury-containing samples depend upon the X-rays being able to penetrate the sample containing mercury. Because mercury is a particularly electron-dense element, X-ray may not be able to penetrate mercury to emerge with enough intensity to scan the sample if the sample contains a large amount of it. As a result, scanning curves must be used to control the quantity of mercury in the sample so that just a fraction of the pores are filled. Table 4.2 displays the scanning curve pressures used for each sample as well as the minimum pore diameter penetrated and the fractional mercury saturation in the sample pore network. The reduced and spent pellets, in general, have extensive fracture networks compared to the fresh pellets, as will be seen in the results section. The fracture network appears to be more complex near the pellet's top and bottom ends than the middle of the pellet. Hence, lower scanning curve pressures were required to fill the reduced and spent void spaces.

After the samples were degassed and weighed, the samples were then transferred into a penetrometer, and the weight of the penetrometer and sample was recorded. The penetrometer (with sample) is then placed in the low-pressure port of the instrument. During the low-pressure analysis, the sample is firstly evacuated up to $50\,\mathrm{mmHg}$ to drive off any water vapour or atmospheric gases in the pore network. The sample bulb is then filled with mercury while the entire system is still under low pressure. Data collection begins at a pressure of $0.5\,\mathrm{psia}$, which is enough pressure to cause mercury to penetrate sample pores larger than $360\,\mu\mathrm{m}$ in diameter. After the low-pressure analysis was completed, the assembly weight (penetrometer + sample + mercury) was recorded,

and the penetrometer was transferred to the high-pressure port, and the chamber was closed tightly. The penetrometer is placed vertically in the high-pressure port, and it is surrounded by oil, which is the hydraulic fluid the instrument uses to generate high pressures. As the hydraulic fluid pressure rises, it is transmitted to the mercury in the penetrometer via its open capillary stem. An equilibration time of $15\,\mathrm{s}$ was used for each data point.

One of the most important considerations while doing this type of experiment is that the sample must be transferred from the porosimeter tube to the CXT machine as fast and carefully as possible to avoid mercury migration or extrusion from the sample. In some instances, the sample might be frozen in liquid nitrogen to freeze the mercury in-pace upon discharge from the porosimeter quickly; however, this was not required for the methanol synthesis catalyst pellet as the mercury extrusion was relatively stable, and the distance travelled from the Autopore IV to the CXT machine was short. The stability of the entrapped mercury was tested by repeatedly collecting CXT images of the same sample at various intervals over a long period, such as a week, and comparing the spatial distribution of mercury between images.[6]

4.2.3 Low resolution computerised X-ray tomography (CXT)

For the low-resolution CXT scans, the pellets were imaged before and after mercury entrapment using a Zeiss Xradia Versa XRM-500 to acquire 3D image stacks. The X-ray source for the Xradia 500 Versa instrument was set to $140\,\mathrm{kV}$ kV and power of $10\,\mathrm{W}$. The macro lens (0.4X) of the apparatus was used to image the full pellets with a diameter of $5.4\,\mathrm{mm}$ with 360° rotations. The average pixel size for empty pellets was $5.6\,\mu\mathrm{m}$, and the average pixel size for samples with mercury was $5.9\,\mu\mathrm{m}$. Image acquisition parameters were the same for all the empty samples and the samples with entrapped mercury. The scan times were roughly $2\,\mathrm{h}$ and $2.5\,\mathrm{h}$ for empty and mercury-filled pellets, respectively. Both samples were scanned with 1600 projections per 360° scan. Each 3D image stack contained 1016 slices with dimensions of 1024 x 1024 pixels and 24-bit depth. The 3D volume data sets were reconstructed using the filtered back projection (FBP) method.[128]

4.2.4 Focussed ion beam-scanning electron microscopy (FIB-SEM)

The serial milling images were acquired using a Crossbeam 550 (Carl 206 Zeiss Microscopy) instrument equipped with a cryo-stage and integrated VCT500 vacuum transfer system for FIB-SEM imaging. The samples were only imaged before mercury intrusion. The samples were mounted onto a pre-tilted sample holder and was transferred into the Crossbeam 550 using the VCT500 shuttle. Once the samples were inside the instrument, an automated FIB milling algorithm was subsequently set up and executed. The equipment was properly aligned and calibrated weekly to ensure that the unsupervised automated FIB-SEM milling was successful. The Crossbeam 550 was also calibrated to mill a cross-section with dimensions of 10 x 30 x 10 $\mu\mathrm{m}$ (*XYZ*) through the sample to acquire a 3D image stack. A fixed voltage of 30 kV and current of 700 pA was used to generate the FIB images. The fresh SD and RC empty samples only were imaged using FIB-SEM.

[6] A. Nepryahin et al. *Chem. Eng. Sci.*, **152**: 663–673, 2016.
[128] G. N. Ramachandran and A. V. Lakshminarayanan. *PNAS*, **68**: 2236–2240, 1971.

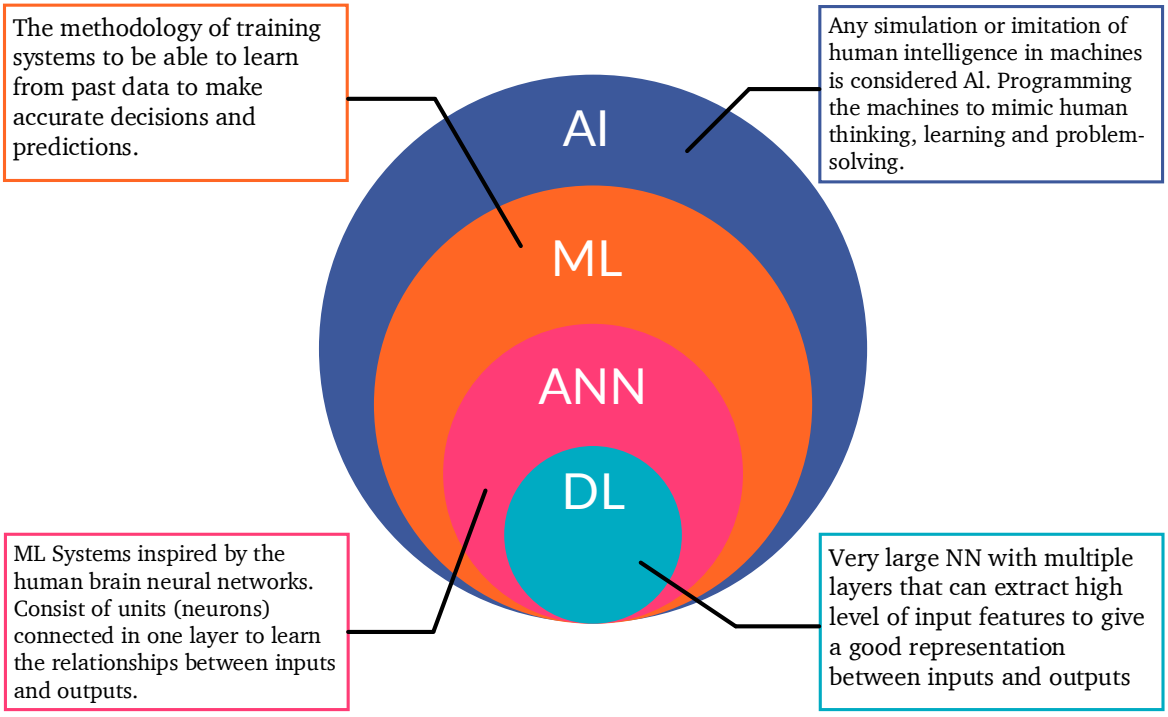


Figure 4.4: Relationship between artificial intelligence (AI), machine learning (ML), artificial neural networks (ANN), and deep learning (DL).

4.3 Background on Artificial Neural Networks

4.3.1 Deep Learning Neural Network Architecture

Deep learning (DL) is a subset of machine learning (ML)[268] and is based on Artificial Neural Networks (ANNs),[269] which is a computing model inspired by the organisation and workings of the neurons in the human brain. Figure 4.4 illustrates the relationships between the different subsets of AI. Artificial neural networks are composed of many computing nodes or 'neurons' that each performs a simple operation and interact with other neurons in the network to make decisions. The neurons can provide accurate answers to some complex issues such as image classification,[283] image segmentation,[284,285] and natural language processing.[286] Deep learning refers to the depth (or the number) of layers in a given ANN (>3 layers) and is widely accepted as a more advanced application of machine learning that is capable of doing more rigorous analysis.

Neurons are the basic working unit of the brain.[287] They are specialised cells designed to transmit information to other nerve cells, muscles or gland cells. The neuron can be thought of as a miniature self-contained information processor. It receives synaptic inputs, processes them, and

[283]T. Araújo et al. *PloS one*, **12**: e0177544, 2017.
[284]A. Garcia-Garcia et al. *Appl. Soft Comput.*, 1–23, 2017.
[285]A. Garcia-Garcia et al. *Appl. Soft Comput.*, **70**: 41–65, 2018.
[286]I. Sutskever, O. Vinyals, and Q. V. Le. *Adv. Neural Inf. Process. Syst.*, **4**: 3104–3112, 2014.
[287]H. B. Ferris. *Psychol. Bull.*, **15**: 257–263, 1918.

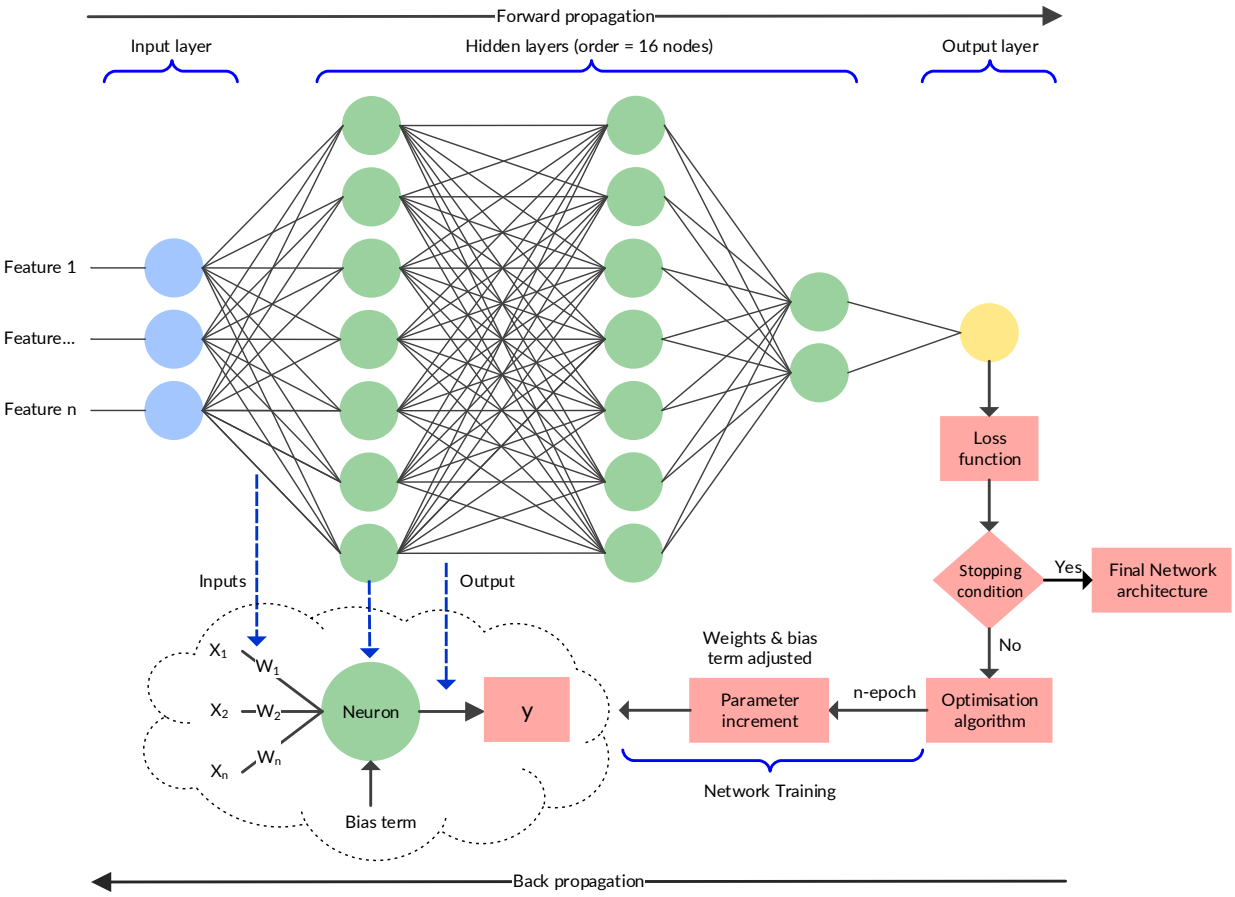


Figure 4.5: Schematic representation of an Artificial Neural Network (ANN) with a single row of input variables on the left, weighted synapses shown as arrows, neurons (green circles), and output value and actual values. This type of ANN is called a single-layer Feed forward Neural Network.

then generates an output. A neuron has three main parts: dendrites, a cell body (or soma) and an axon. The dendrites are structures primarily associated with receiving signals. The structure most associated with processing the signal is the cell body, while the axons are associated with the synaptic outputs.[287]

Figure 4.5 shows a schematic representation of a simple artificial neural network designed to mimic the connectivity pattern of a neuron. The network receives inputs(X_1, $X_{...}$, X_n), which are independent variables that travel down the synapses (connections), and into the neurons and then emerge from the other side as a single binary output. The network has an input layer, several hidden layers and an output layer. The hidden layers have multiple nodes creating depth (in this case, three hidden layers of 7, 7 and 2 nodes, respectively). Each connection on artificial neural network has *weight*[288] assigned to it. The weights (W_1, $W_{...}$, W_n) are important parameters in a neural network's functioning, and they are adjusted throughout the network training stage. Based on the weights, the neural network decides which signal gets passed along or not, or to what

[288]B. W. White and F. Rosenblatt. *AJP*, **76**: 705, 1963.

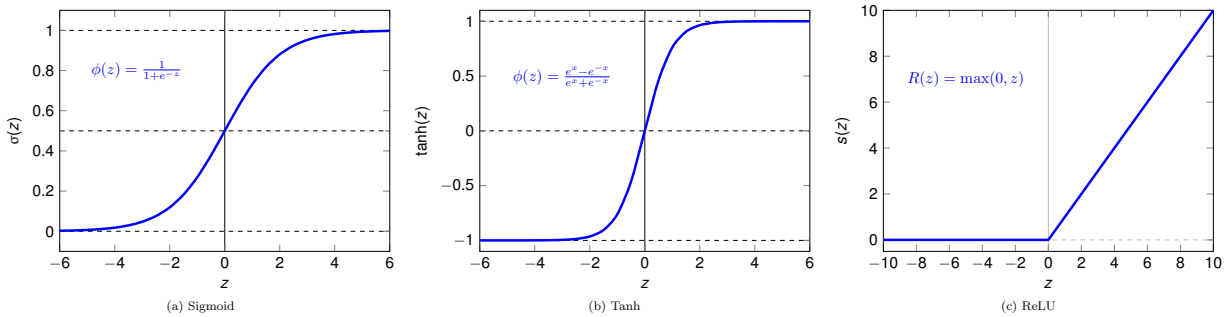


Figure 4.6: Typical examples of activation functions used in ANN. **(a)** Sigmoid function, **(b)** Tanh function, and **(c)** Rectified linear function.

extent a signal get passed along the network. The neurons in the ANN takes the weighted inputs (W_1*X_1, $W_{...}$*$X_{...}$, W_n*X_n), sums them all up and then applies an activation function.[289] Activation functions are usually non-linear functions that are attached to each node and determine whether a specific neuron should be activated (i.e., 'fired') or not, based on whether each neuron's input is relevant for the model's prediction. Common activation functions include Sigmoid, ReLU (Rectified Linear Unit) and TanH, and depending on the nature of data and segmentation tasks, these activation functions are selected accordingly. For example, ReLUs are known to have more biological representation (neurons in the brain either fire or they do not), and in modern neural networks, the default recommendation is to use the rectified linear unit defined by the activation function $R(z) = max(0, z)$.[290–292] Examples of common activation functions are shown in Figure 4.6.

To train and optimise any ANN, the predicted outputs from the network is compared with actual known values (for example, manually classified grounded truth images) by applying a loss function (or a cost function). The loss function shows the error in the predicted value from the network, and typically neural network seeks to minimise this function.[293] Once a loss function is found, a backward pass is performed through the entire network in a process known as backpropagation.[294] The backpropagation algorithm adjusts the weights and bias simultaneously in each iteration by keeping track of the derivates of the activation functions in each successive neuron in order to find the weights that brings the loss function to a minimum. This forward and backpropagation process is repeated for several iteration cycles, or epochs, until the disparity between the predicted and actual values are close to zero. An epoch corresponds to one forward and backward propagation through the network. The optimal input weights are found once the loss function does not change anymore, and the predicted and actual values are almost identical.

[289] P. Sibi, Allwyn J. S., and P. Siddarth. *J. Theor. Appl.*, **47**: 1344–1348, 2013.
[290] K. Jarrett et al. *Proc. IEEE Int. Conf. Comput. Vis.*, 2146–2153, 2009.
[291] H. Li et al. *J. Opt. Soc. Am. A:*, **34**: 1114–1118, 2017.
[292] M. J. Brown et al. *J. Appl. Biomech.*, **33**: 384–387, 2017.
[293] A. G. Roy et al. *Biomed. Opt. Express*, **8**: 3627, 2017.
[294] D. E. Rumelhart, G. E. Hinton, and R. J. Williams. *Nature*, **323**: 533–536, 1986.

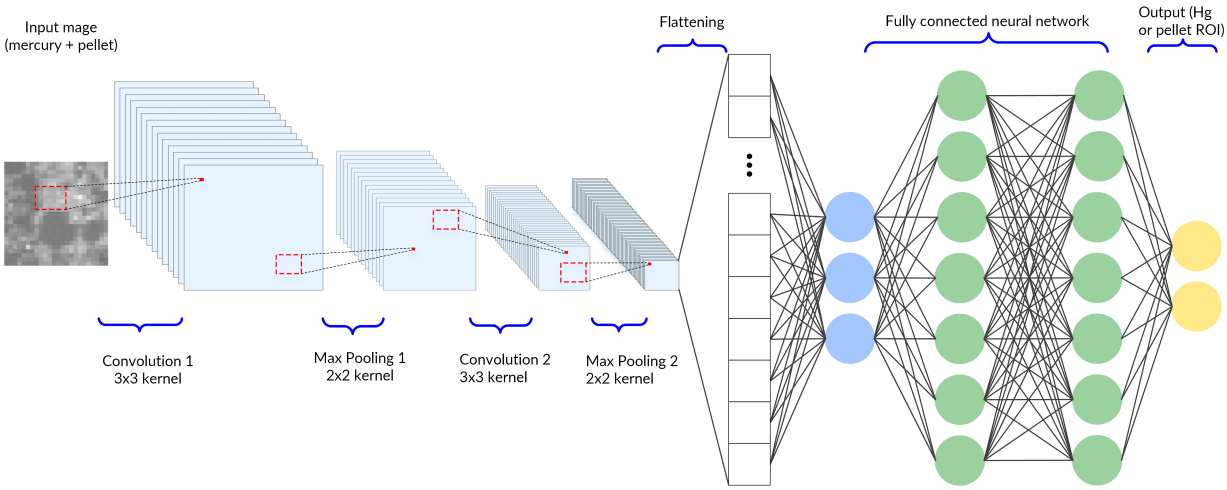


Figure 4.7: An example of a fully connected convolutional neural network architecture used in deep learning image segmentation.

4.3.2 Convolutional Neural Networks (CNNs) Architecture

A Convolutional Neural Network (CNN)[270,295–298] is a type of deep learning algorithm that can recognise and classify features in images for computer vision. A typical CNN has a multilayer neural network that can analyse visual inputs and perform different tasks such as image segmentation, classifications and detections. All deep learning convolutional neural network models follow a similar architecture as shown in Figure 4.7, and have two main parts: a *convolution* operation that splits the image into features for analysis, and a set of *fully connected layers* that takes the output from the convolution layer to predict the best label for the image.

In mathematics, convolution is an operation that takes two functions as input and produces a single output.[299] The output function describes how the shape of one function is modified by the other. Mathematically it has the form:

$$(f * g)(t) \stackrel{\text{def}}{=} \int_{-\infty}^{\infty} f(\tau)g(t-\tau)d\tau \tag{4.1}$$

In CNNs, however, convolution is the process of applying a feature detector (also known as kernel) to an input image with a predetermined stride step and extracting a feature map.[300] A kernel is essentially a matrix of values trained to detect specific features. The key concept behind CNNs is to spatially slide the kernel on a given input image to check if the feature it is supposed to detect is present. The network then carries out a convolution operation by calculating the dot product of the kernel and the input area where the kernel is overlapped (see Figure 4.8). Typically, multiple

[295]A. Krizhevsky, I. Sutskever, and G. E. Hinton. *Adv. Neural Inf. Process. Syst*, **25**: 1097–1105, 2012.
[296]Y. LeCun et al. *Proc. IEEE*, **86**: 2278–2323, 1998.
[297]H. Noh, S. Hong, and B. Han. *IEEE Int. Conf. Comput. Vis.*, **2015**: 1520–1528, 2015.
[298]K. Simonyan and A. Zisserman. *arXiv*, 1–14, 2014.
[299]S. Smith. *Digital signal processing: a practical guide for engineers and scientists*. Elsevier, 2013.
[300]I. Goodfellow, Y. Bengio, and A. Courville. *Deep Learning*. MIT press, 2016. 801

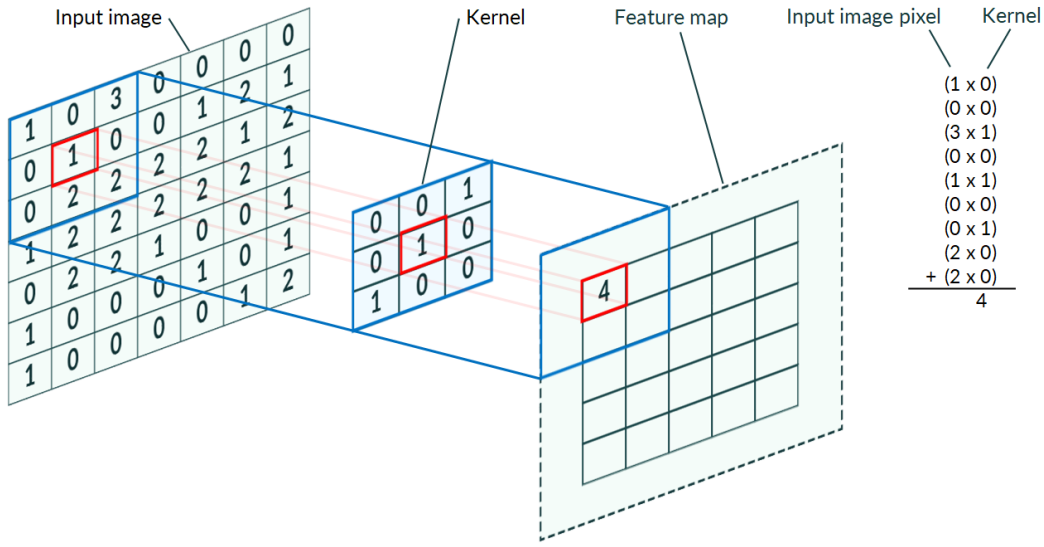


Figure 4.8: Example of convolution operation 2D showing **(a)** Input image **(b)** Kernel, and **(c)** a feature map. The convolution layers are the main building block of the CNN model. The convolution operation are usually performed in 3D as the image is represented by a 3D matrix with height, depth and width dimensions.

convolution operations are performed on a given input image using different filters, producing a distinct feature map each time. The feature maps are then all stacked together to make the final output of the convolution layer. The outputs from the convolution layers are summed up with a bias term and then fed to a non-linear *activation function* such as ReLU (Rectified Linear Unit), TanH or Sigmoid. Activation functions introduce non-linearity into the network. A downside of applying multiple convolution layers is the loss of pixels on the perimeter of the original input image, causing the shrinking of any interesting features on the boundaries after many successive convolutional layers. To overcome this issue and preserve the dimensionality of the feature maps, CNNs use *padding*,[300] which are a number of pixels (typically zeros) that are added to surround the input image.

The next step of CNN is called *pooling* or *downsampling*. Pooling refers to a small portion, and it is a process that scales down the amount of information the convolution layer generates for each feature and maintains only the most essential features.[300] The pooling process speeds up the model training time by reducing the amount of memory consumed by the network. There are different types of pooling operations, including max, average or sum pooling. Max pooling,[301,302] for example, slides a kernel over the input image and extracts the maximum values in that window, producing a *pooled feature map*, and hence effectively reducing to the most important pixels in an image. A deep convolutional neural network may have several convolutional and pooling layers. Figure 4.9 shows an example of max and average pooling operations using 2x2 kernel and stride step of 2. In CNNs, stride refers to the number of rows and columns traversed by the kernel per slide.[300]

[301] B. Graham. *arXiv*, 1–10, 2014.
[302] J. Nagi et al. *IEEE Signal Img. Proc.*, 342–347, 2011.

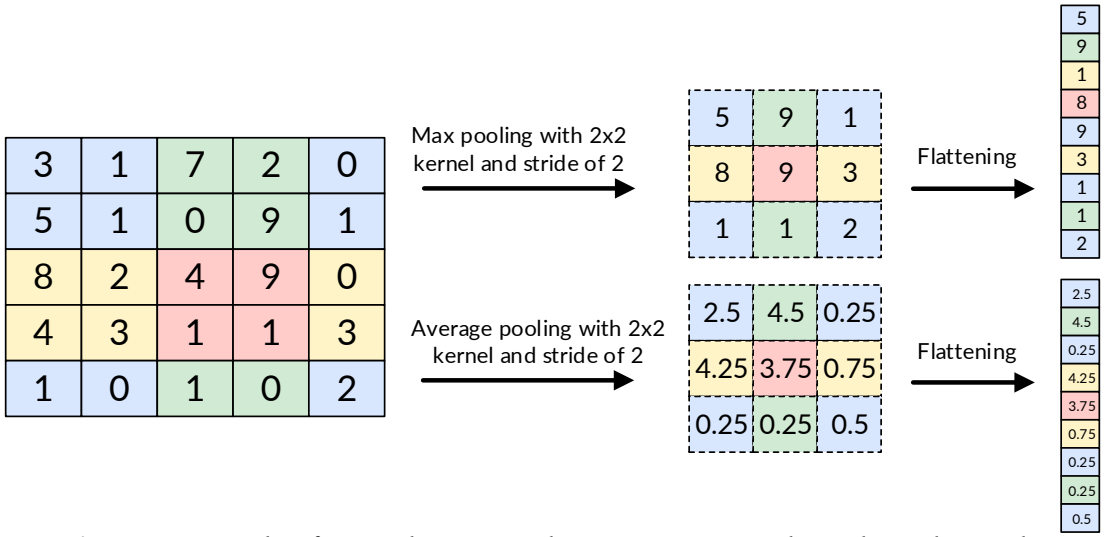


Figure 4.9: Examples of max and average pooling operation in convolutional neural networks.

The output from the convolution and pooling layers is then passed on to a *fully connected layers*. This section of the CNNs is essentially the same as the ANN architecture that was described in Section 4.3, and is composed of three layers: a fully connected input layer, a number of hidden layers and output layers. The fully connected input layer 'flattens' and transforms the output from the convolution + pooling layer into a single 1D array since the fully connected layer expects only 1D array data. This process is known as *flattening* as it converts the 3D volume of numbers from the convolution + pooling layers into a single 1D vector, which becomes the input for the *fully connected layer*.[300] The fully connected output layer generates the final probabilities to determine a class for the image (e.g., mercury or graphite).

4.4 Deep Learning Image Segmentation Strategy

4.4.1 Image Preprocessing

Figure 4.10 shows the overall image processing strategy and the software used in each step during the segmentation process. The main focus for this work is the deep learning segmentation technique; however, several preprocessing steps involving slice registration and various other filters were required for the raw CXT and FIB-SEM images to make the segmentation and phase-detection procedures easier. The filters reduced image noise and artefacts and were necessary for both the CXT and FIB-SEM images, and the deep learning segmentation models showed better results in the preprocessed images. The bulk of the preprocessing steps was performed in Fiji, which is a distribution of ImageJ[303] that bundles many open-source plugins and projects. The deep learning segmentation task was performed in Dragonfly,[258] an advanced 3D image visualisation and analysis software developed and licensed by Object Research Systems (ORS), Montreal, Canada.

First, the X-ray and SEM images were cropped to remove background and air pixels. The

[303] M. D. Abràmoff, P. J. Magalhães, and S. J. Ram. *Biophotonics Int.*, **11**: 36–41, 2004.

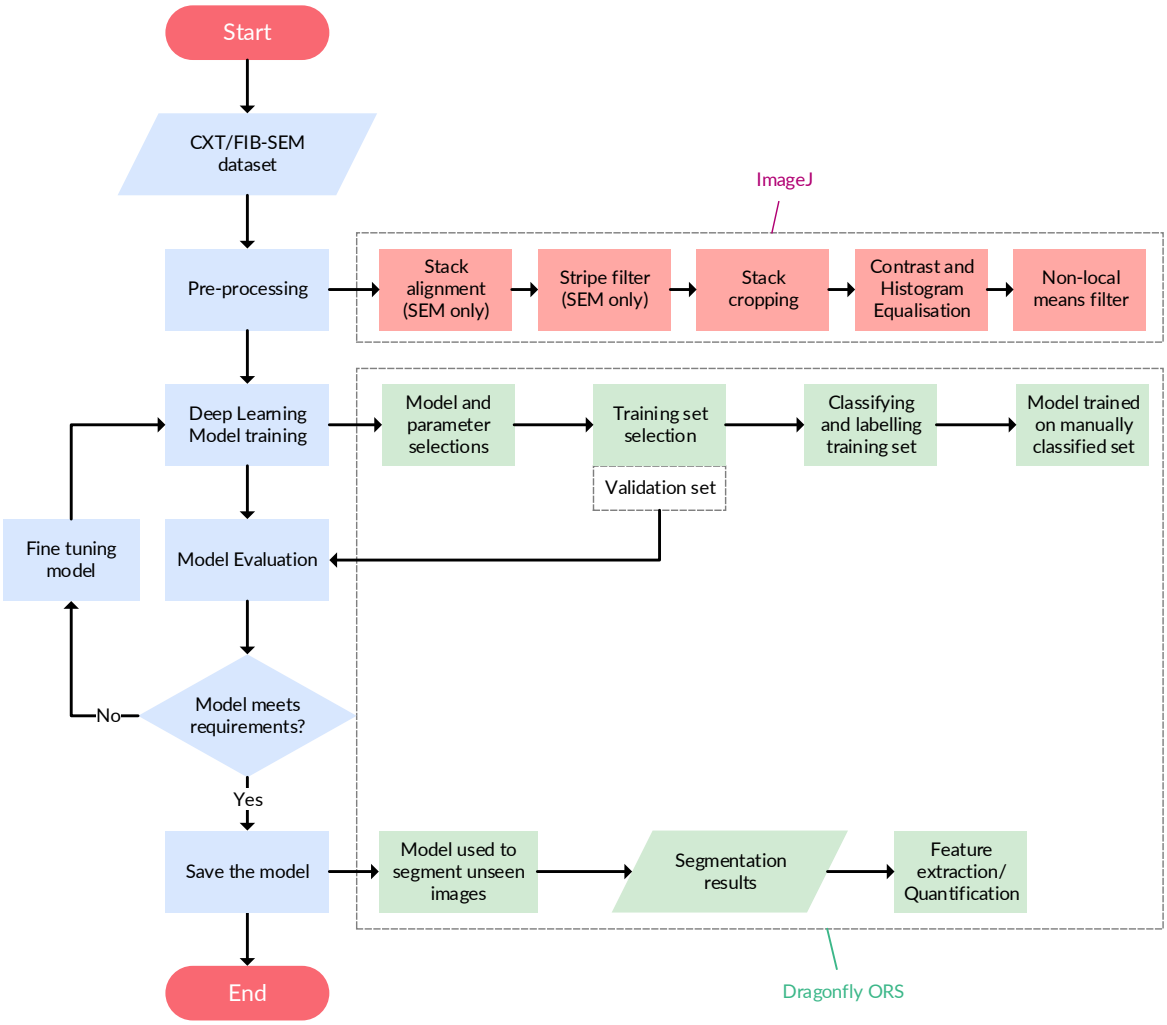
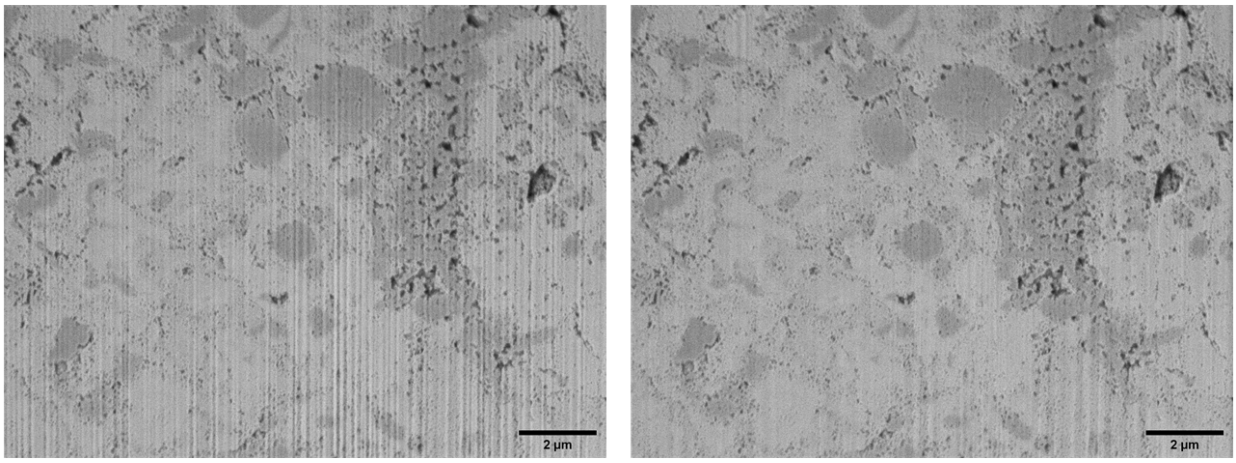


Figure 4.10: A flowchart showing the overall image processing steps.

images were then processed with automatic contrast and histogram equalisation filter by using the *Enhance Local Contrast* or CLAHE[304,305] plugin in Fiji. A non-local means filter with auto-sigma estimation option checked was also used to reduce the noise further and enhance image quality. The non-local means filter uses an edge-preserving low-pass algorithm; thus, the edges between different phases looked considerably sharper compared to the unfiltered images, making the manual segmentation of the training datasets tasks much easier.[306]

For the FIB-SEM images, stack alignment is an additional preprocessing step to produce a correct 3D volume and for proper visualisation and segmentation. This step involves the alignment of the image stack along the *Z*-axis (perpendicular to the milling direction). During serial milling, spatial drifts can occur due to displacement of the region of interest (ROI), loss of SEM

[304] A. M. Reza. *IJVSP*, **38**: 35–44, 2004.
[305] K. Zuiderveld. *J. Graphics Gems.*, 474–485, 1994.
[306] A. Buades, B. Coll, and J. Morel. *J. Image Proc.*, **1**: 208–212, 2011.



(a) Pre stripe filter **(b)** Post stripe filter

Figure 4.11: 2D FIB-SEM image of fresh RC sample pre and post stripe removal. **(a)** Before applying the striper filter. **(b)** After stripe filter. The scale bar corresponds to $2\,\mu\mathrm{m}$.

focus or irregular thickness of milled phase, and hence drift correction is required. Scale Invariant Feature Transform or SIFT[307] is the most commonly used algorithm to align a FIB-SEM stack where each slice is aligned to the previous one by applying a global translation, thus preserving the local morphological properties. The stack alignment procedure was performed in Dragonfly software, which uses several automatic slice matching processes such as SIFT, the sum of the square difference (SSD) and template matching algorithm.

Another artefact that appears on FIB-SEM images is the so-called curtaining effect. The curtaining effect occurs when a milled sample face shows horizontal or vertical lines that look like a theatre curtain or waterfall. The curtaining effect is detrimental for quantitative image analysis as it may obscure desired features and must be removed during the preprocessing stage. The vertical curtaining effect present in the FIB-SEM images was removed by applying a stripe filter;[308] a plugin in Fiji that uses a combination of wavelet and Fast Fourier transform. An example of before and after applying the stripe filter is shown in Figure 4.11.

4.4.2 Training Deep Learning CNNs

A total of three convolutional neural network (CNN) models were trained in Dragonfly. Details of the models and parameters used for each network are shown in Table 4.3. Segmentation of the CXT images with entrapped mercury was done using a neural network architecture FCDenseNet;[309,310] with a patch size of 64 x 64 pixels, stride ratio of 1 and batch size of 16. Mercury on the CXT images spanned over large areas, thus allowing the use of larger patch size pixels. The

[307] D. G. Lowe. *Int. J. Comput. Vis.*, **60**: 91–110, 2004.
[308] B. Münch et al. *EMPA Act.*, **17**: 34–35, 2009.
[309] F. Milletari, N. Navab, and S. Ahmadi. *Int. Conf. 3D Vis.*, 565–571, 2016.
[310] S. Jegou et al. *IEEE Comput. Soc.*, 11–19, 2017.

Table 4.3: Deep learning segmentation models used for CXT and SEM images and the training parameters.

DL Parameters	**U-Net A Model (Empty SD CXT)**	**FCDense-Net Model (Mercury filled CXT)**	**U-Net B Model (FIB-SEM)**
Patch size	32	64	32
Stride ratio	0.5	1	0.25
Batch size	32	16	8
Epochs number	100	100	100
Loss function	OrsDiceLoss	Categorical cross entropy	OrsDiceLoss
Optimisation algorithm	Adadelta	Adadelta	Adadelta

number of epochs was set to 100, with early termination of the training stage in 10 epochs if the loss function does not decrease further. The loss function and optimization algorithms were set to 'categorical-crossentropy' and 'Adadelta';[311] respectively. For the training dataset, 20 of the 1016 preprocessed 2D image slices were selected and manually delineated to identify each pixel with one of three phases: air, mercury and rest of the pellet. Dragonfly has tools that can be adjusted in size for the manual segmentation task, including brushes and erasers. These tools are found in the ROI painter function and can be customised accordingly. For each model, some of the different phases present in the training dataset were manually segmented (painted), diversifying according to their shape and size. The manually segmented images were subsequently used as input data for each network. Manual segmentation took around 1 to 3 hours for each sample.

To offer an unbiased evaluation of how precisely the trained model can segment the images correctly, the data from the image slices were separated into patches, with 80% of the patches being used for training and the remaining 20% being retained for validation. After 35 epochs, the trained model had 85% accuracy and 97% accuracy after 100 epochs (accuracy, in this case, is defined as the % of pixels with the material phase correctly identified). The amount of computer time required for training is determined by the number of training images, the complexity of deep learning network architecture, the number of epochs necessary to achieve an adequate accuracy for each training image, and computer performance. Each epoch in this study took 39 minutes to complete using a Workstation equipped with an Nvidia graphics RTX P6000 24Gb Quadro. In total, the model training took 65 hours. Once trained, the model was applied to all the slices and other images from samples with mercury, e.g. fresh roll compacted.

For the segmentation of high-and low-density SD CXT images, a U-Net;[274] convolutional neural network (U-net A) was used with a patch size of 32 x 32 pixels, stride to input ratio of 0.5, batch size of 32, loss function 'OrsDiceLoss', and optimisation algorithm of 'Adadelta'. For the FIB-SEM images, a U-Net model (U-Net B) with a patch size of 32 x 32 pixels proved adequate to capture the smaller image details. The stride ratio was set to 0.25, batch size of 8, loss function 'OrsDiceLoss', and optimisation algorithm of 'Adadelta'. To provide greater model controls, Dragonfly software includes an optional advanced parameters panel that contains additional fine-tuning functions (including TensorBoard controls), criteria for early training termination and conditions for the

[311] M. D. Zeiler. *CoRR*, **121**: , 2012.

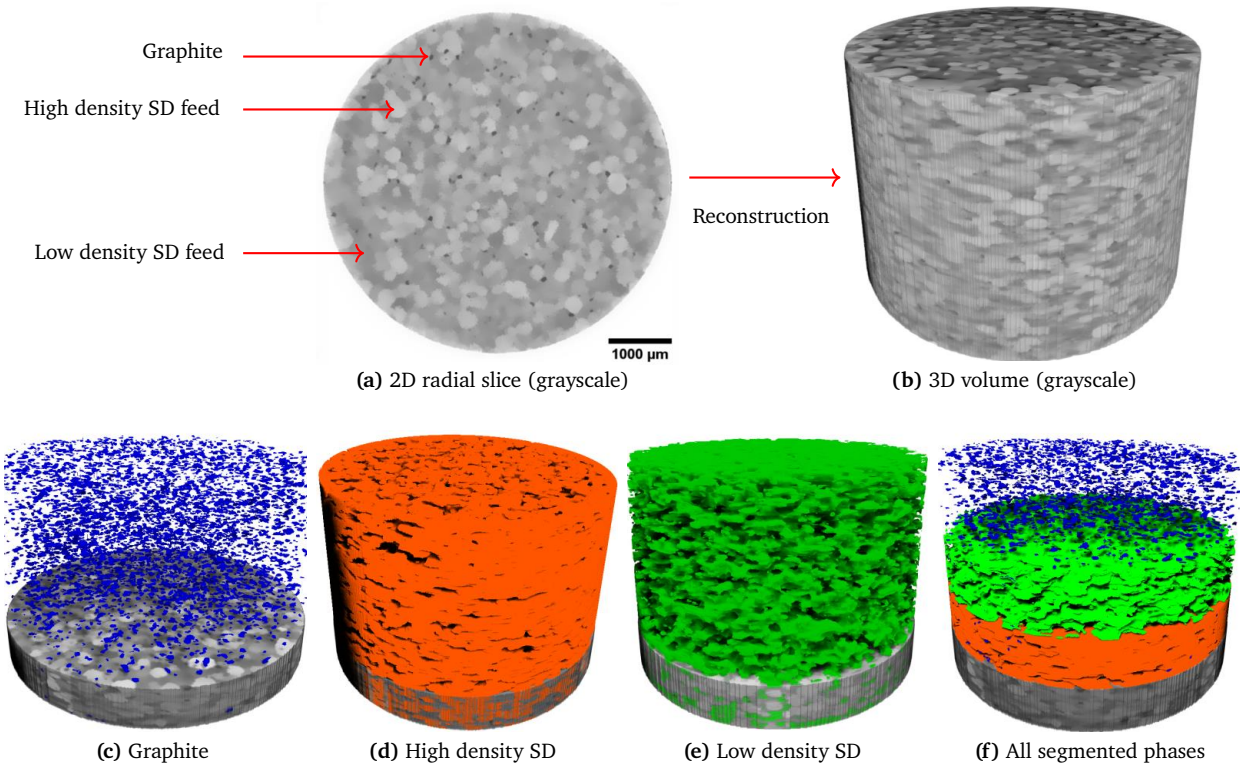


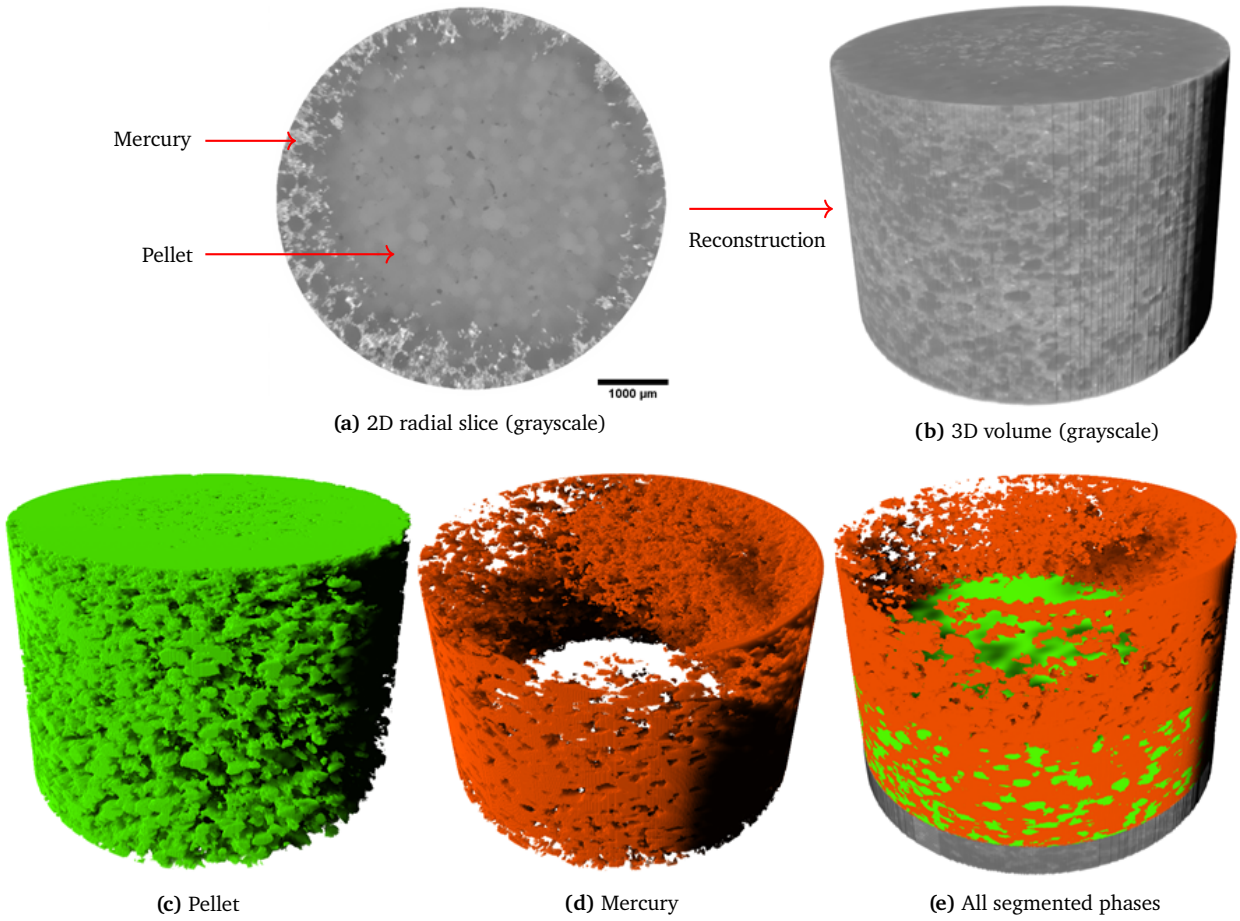
Figure 4.12: Raw and segmented CXT images of an empty fresh spray dried catalyst pellet. **(a)** Raw 2D radial slice, **(b)** 3D reconstructed grayscale volume of the pellet exterior, **(c)** Graphite (blue) representing 0.5% of the volume fraction, **(d)** High density spray dried feed material (orange) representing 47.9%, **(e)** Low density spray dried feed material (green) representing 51.6%, and **(f)** All the segmented phases. The scale bar corresponds to 1,000 µm.

learning rate reduction. However, these parameters are understood to be outside the capability of non-expert users as they correspond to many of the controls that professionals would have if they were directly programming their own solution with lower-level tools.

4.5 Results and Discussion

4.5.1 Fresh Pellets CXT Segmentation

After all the models were trained successfully, they were applied to segment the remaining unseen images from the same CXT or FIB-SEM batches, resulting in fully segmented image stacks. Figure 4.12 shows segmentation results for the empty fresh spray-dried CXT images. The U-Net[274] model (A) succeeded in segmenting all three phases (graphite, high-density, and low-density spray-dried feed) and took approximately 90 minutes to segment the complete image stack fully. From the segmentation of the three separate phases, it can be seen that their distributions are pervasive throughout the pellet, and there are no signs of segregation by density. The volume fractions for each phase were calculated from the images. The graphite from the CXT image represented 0.5%, while the low and high-density SD feed material represented 51.6% and 47.9%, respectively. The



(a) 2D radial slice (grayscale)

(b) 3D volume (grayscale)

(c) Pellet

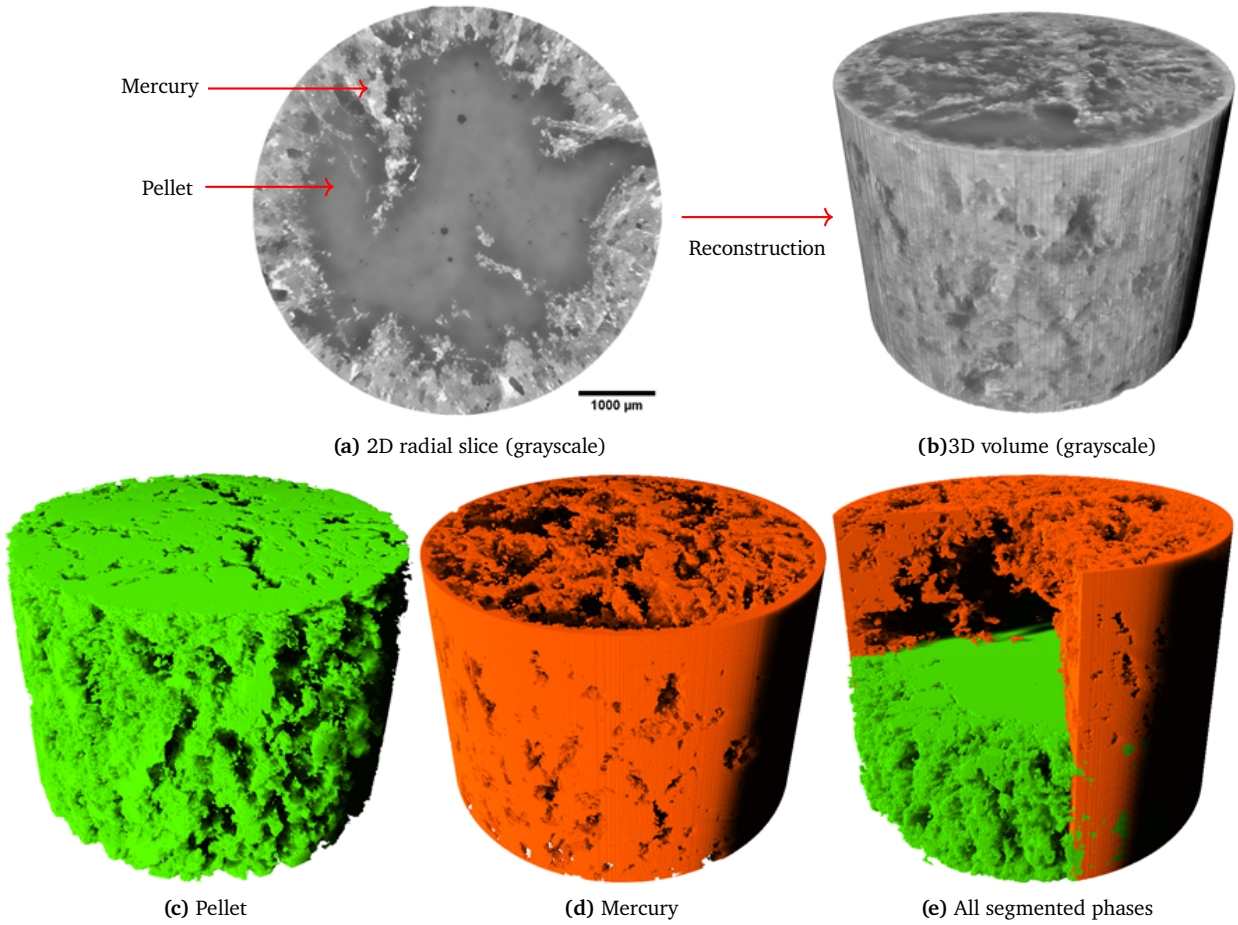
(d) Mercury

(e) All segmented phases

Figure 4.13: Raw and segmented CXT images of fresh spray dried catalyst pellet following mercury porosimetry up to 8,600 psia leading to entrapment filling 11.5% of the pore space. **(a)** Raw 2D radial slice. Bright white regions correspond to mercury, **(b)** 3D reconstructed grayscale volume of the pellet exterior, **(c)** Pellet regions with no entrapped mercury (green) representing 84.6% of the volume fraction, **(d)** Entrapped mercury in the void spaces (orange) representing 15.4%, and **(e)** All the segmented phases. The scale bar corresponds to 1,000 µm.

surface meshes and 3D renderings for each segmented phase are also displayed in Figure 4.12. The 3D surface rendering allows for quick visualisation of the spatial distribution of different phases in the catalyst pellet studied. A typical example of a reconstructed 2D radial cross-section slice and 3D rendered volume of the pellet exterior before segmentation, both in grayscale, are also displayed in the figure for comparison. From the 2D and 3D images, the individual feed particles making up the spray-dried pellet can be seen by virtue of the distribution in density in the particles evident from the variation in the average pixel intensity.

The U-Net model (A) accuracy reached 97%; however, this does not guarantee an error-free automated segmentation when the model is used on previously unseen images. Thus, some isolated clusters of inaccurately labelled pixels were sometimes found in the segmented images (e.g., low-density spray-dried regions were mistakenly labelled as high-density spray-dried feed). These errors were successfully corrected in the post-segmentation processing steps. Furthermore, the



(a) 2D radial slice (grayscale) **(b)**3D volume (grayscale)

(c) Pellet **(d)** Mercury **(e)** All segmented phases

Figure 4.14: Raw and segmented CXT images of fresh roll compacted catalyst pellet following mercury porosimetry up to 8,600 psia leading to entrapment filling 11.0% of the pore space. **(a)** Raw 2D radial slice. Bright white regions correspond to mercury, **(b)** 3D reconstructed grayscale volume of the pellet exterior, **(c)** Pellet regions with no entrapped mercury (green) representing 66.8% of the volume fraction, **(d)** Entrapped mercury in the void spaces (orange) representing 33.2%, and **(e)** All the segmented phases. The scale bar corresponds to 1,000 µm.

accuracy of the segmentation results was assessed visually by comparing randomly selected segmented slices with the corresponding original images.

Figure 4.13 shows the segmentation results of the fresh spray-dried pellet following mercury porosimetry up to 8,600 psia leading to entrapment filling 11.5% of the pore spaces. The figure depicts the 3D renderings of this pellet showing entrapped mercury and the remaining empty pore spaces. The bright white pixels on the 2D grayscale images are associated with entrapped mercury as they represent the largest X-ray absorbance, whereas the relatively grey regions represent empty void spaces without mercury. The mercury displays a shrinking core effect moving from all directions towards the centre of the pellets. It is also noted that behind the front, intrusion of all the void space is not complete, as some SD feed particles remain partly or fully without mercury even once the main intrusion front has moved past. The volume fraction based on mercury (orange colour) pixel intensity from the CXT images is 15.4%, which is slightly higher than the

11.5% obtained from mercury porosimetry data. The rest of the unfilled pore spaces in the pellet represented 84.6% of the volume fraction.

Figure 4.14 shows the segmented CXT images of fresh roll compacted catalyst pellet following mercury porosimetry up to 8,600 psia leading to entrapment filling 11% of the pore space. The FCDense-Net[309,310] model successfully isolated the mercury pixels from the rest of the empty pellet. The mercury entrapment shows a similar pattern as the fresh spray-dried pellet as it forms a shrinking core effect. However, some mercury gets intruded into the gaps between feed particles and forms a dendritic like branching. The irregular polygonal form of the dark unintruded zones suggests that they are likely associated with individual RC feed particles within the pellet. Intrusion occurs via cracks, lower density RC feed particles, and the low-density regions surrounding high-density feed particles. During the manufacturing phase, under-size or oversize particles from ribbon milling are frequently recycled back into the roll-compacted feed in the preparation of roll-compacted feed, and this can happen many times for some areas of the material resulting in changes in feed particle density. Some particles may not pack densely enough, resulting in spaces between them, or particles may splinter at regions of contact with other particles where stresses are higher, resulting in fractures between them.[7] The volume fractions of mercury and empty pore spaces are 33.2% and 66.8%, respectively. The volume fraction from the image is significantly higher than the true pore volume from mercury porosimetry data. This is probably due to mercury getting intruded into the large gaps between high-density roll compacted feed particles.

4.5.2 Reduced Pellets CXT Segmentation

Figure 4.15 shows the segmentation results for the empty reduced spray-dried pellet. The U-Net (A) model successfully segmented all the different phases on the images. The reduced SD pellets have the same feed particles composition as the fresh SD pellets (i.e. graphite, high and low-density SD feed material). However, the CXT imaging has revealed the presence of a splintering or cracking of the feed particles within the reduced SD pellet. The cracks might have developed due to the compaction forces acting on the points of contact on the pellet during the reduction process. The fracture network is thought to generate macroporosity that act as motorways for molecular diffusion, and provide quick access to the active sites in the pellet. This can be seen in the CXT images of the samples with entrapped mercury in the pores where the mercury tends to be associated with the cracks, as the crack network is feeding the mercury intrusion and is providing an entry point into the pellet.

4.5.3 Segmentation of Mercury in Cracks

Tracking the development and spatial distribution of large cracks in the pellets is essential to understanding the relationship between mechanical characteristics and microstructural properties of the pellets. The methanol synthesis catalyst pellets are used in reactors where the operating process conditions are such that the pore diffusion occurs in the Knudsen regime. One of the ways

[7] S. P. Rigby. *Structural characterisation of natural and industrial porous materials: A manual*. Springer Nature, 2020.

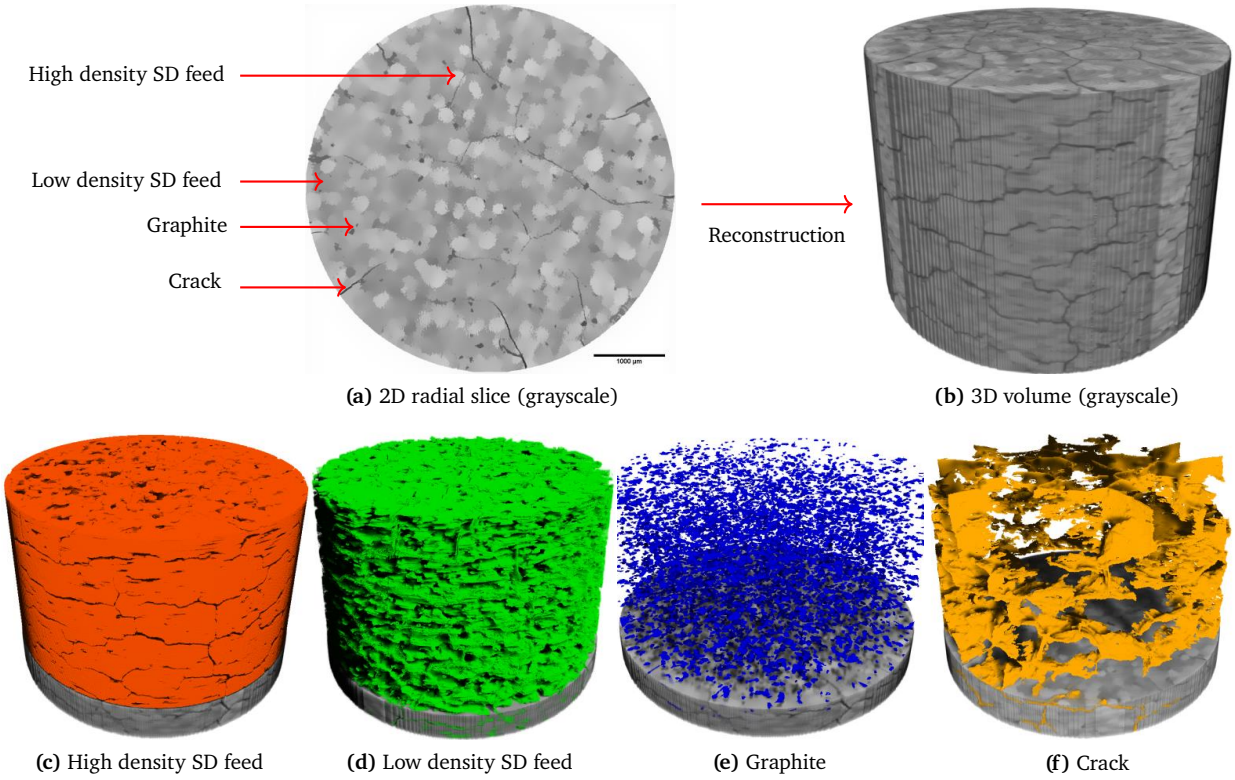
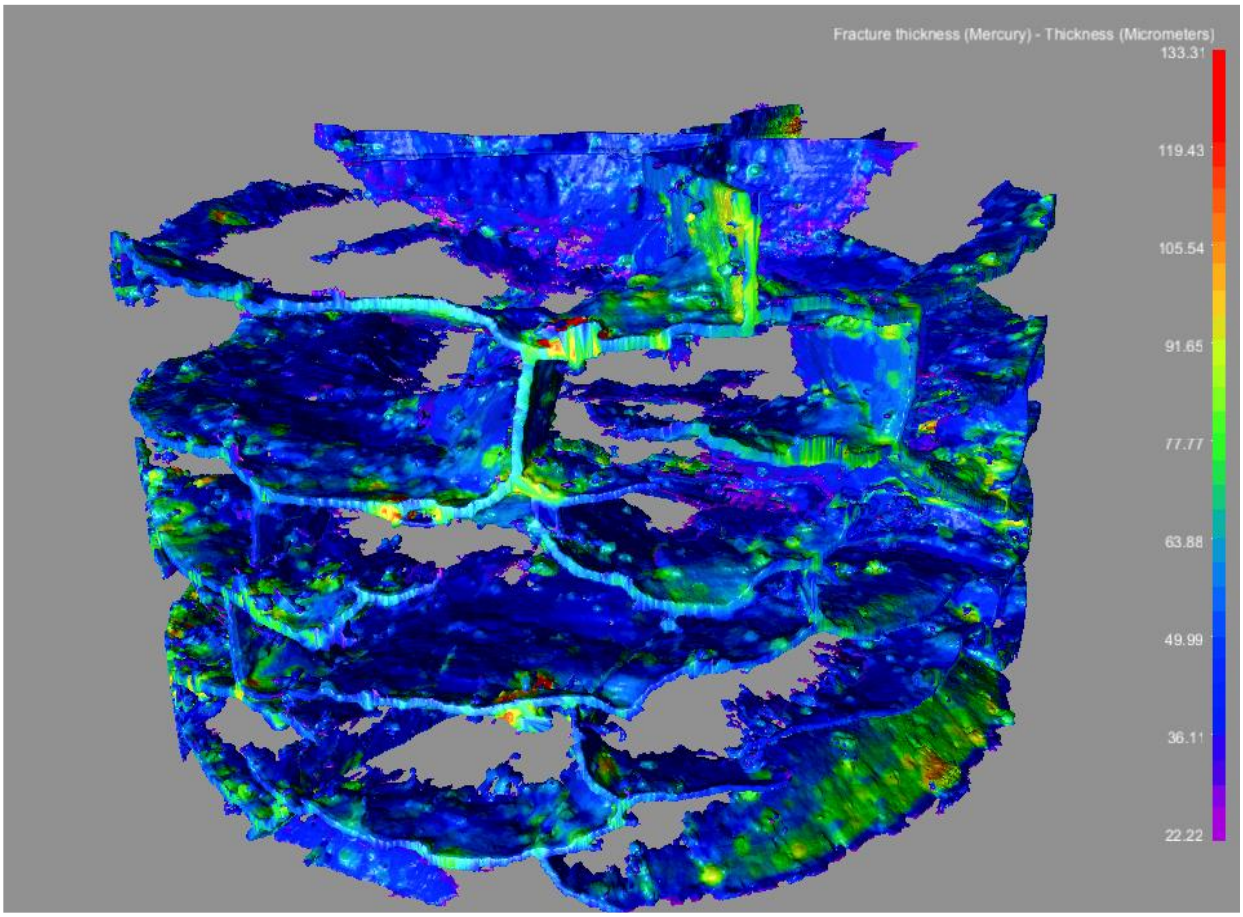


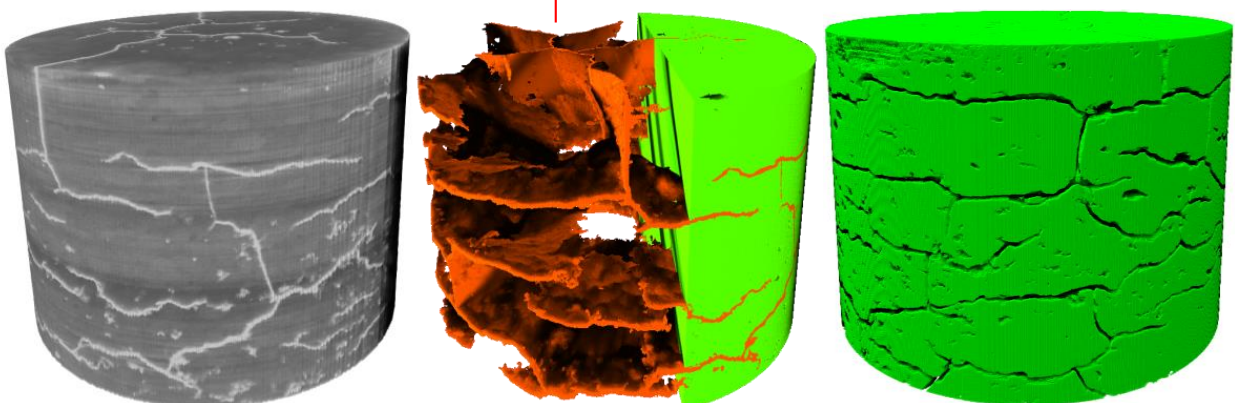
Figure 4.15: Raw and segmented CXT images of an empty reduced spray dried catalyst pellet. **(a)** Raw 2D radial slice, **(b)** 3D reconstructed grayscale volume of the pellet exterior, **(c)** High-density SD feed material (orange) representing 48.6% of the volume fraction, **(d)** Low-density SD feed material (green) representing 50.5%, **(e)** Graphite (blue) representing 0.9% of the volume fraction, and **(f)** All the segmented phases. The scale bar corresponds to 1,000 µm.

to lower the diffusional resistance, in such instances, is to introduce large pores into the structure to provide better access to the centre of the pellet where there are smaller pores providing active surface area. However, an increased number of pervasive large pores within the pellet might negatively impact pellet strength. Hence, the largest interconnected fracture network in the reduced SD pellets following mercury intrusion up to 3,800 psia leading to entrapment filling 3.6% of the pore space was isolated for further studies as shown in Figure 4.16. The fracture network was extracted during the post segmentation and quantification stages by refining the graphite ROI region. The crack network pixels have a similar intensity profile as the graphite and were initially segmented together as one multi-ROI. The "refine ROI" option was then used to isolate the largest interconnected fracture network in the pellet. A morphological thickness analysis was then performed on the mercury in the pores, which revealed that all fracture network thickness ranges from 22 to 130 µm. The crack thickness varies throughout the pellet; however, the thickest portion is generally at the beginning of the fracture. Additionally, the crack network does not seem to have a particular orientation and is varied across the 360° inside the pellet.

Figure 4.17 shows the segmentation results for the reduced roll compacted sample with mercury up to 3,800 psia leading to entrapment filling 5.4% of the pore space. The FCDense-Net[309,310]

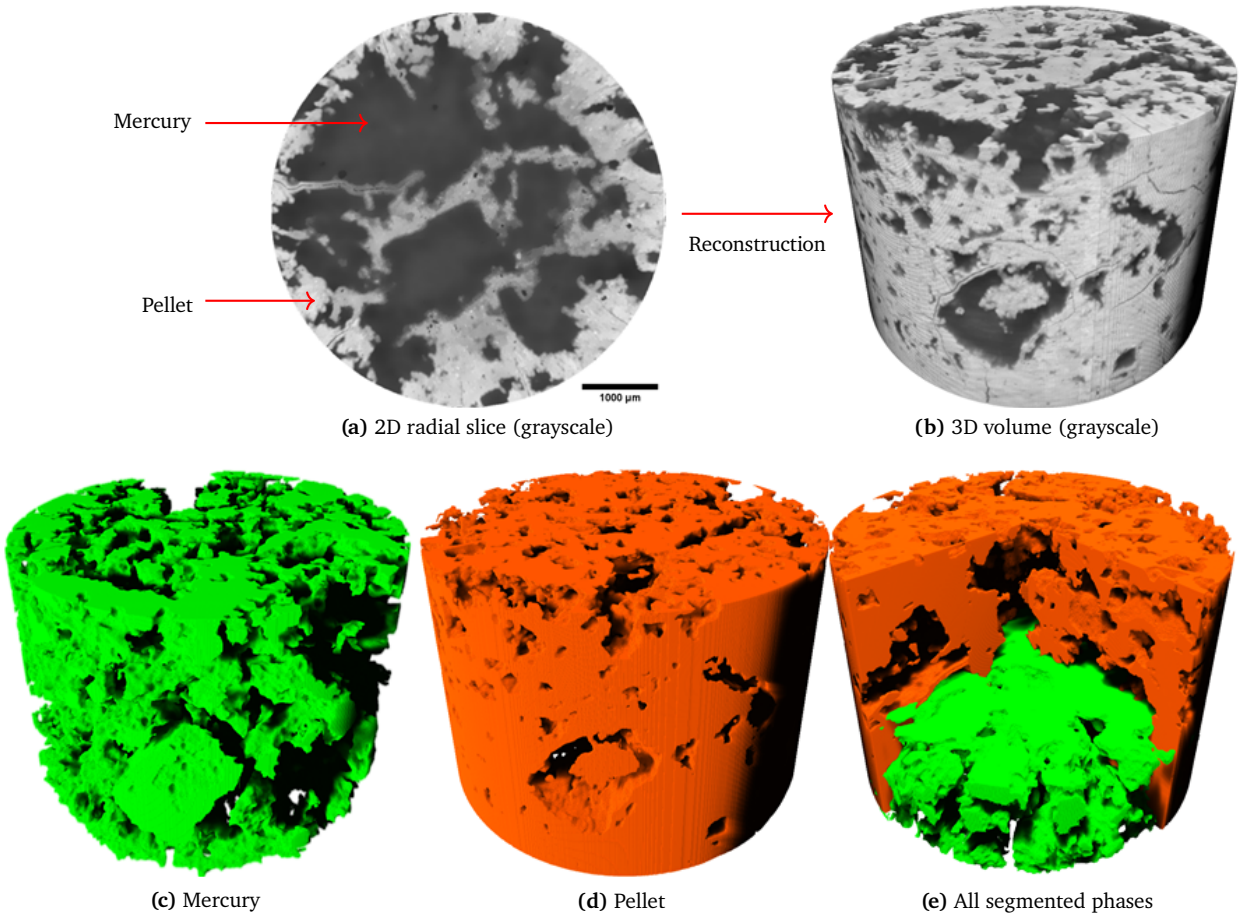


(a) Fracture thickness mesh



(b) 3D volume (grayscale) **(c)** All segmented phases **(d)** Pellet (no mercury)

Figure 4.16: Raw and segmented CXT images of reduced spray dried catalyst pellet following mercury porosimetry up to 3,800 psia leading to entrapment filling 8.5% of the pore space. **(a)** Largest interconnected fracture network in the pellet following mercury intrusion. The mesh depicts the thickness of the cracks in the pellet, **(b)** 3D reconstructed grayscale volume of the pellet exterior, **(c)** All the segmented phases, and **(d)** Pellet regions with no entrapped mercury (green) representing 96.3% of the volume fraction. The scale bar corresponds to 1,000 µm.



(a) 2D radial slice (grayscale) **(b)** 3D volume (grayscale)

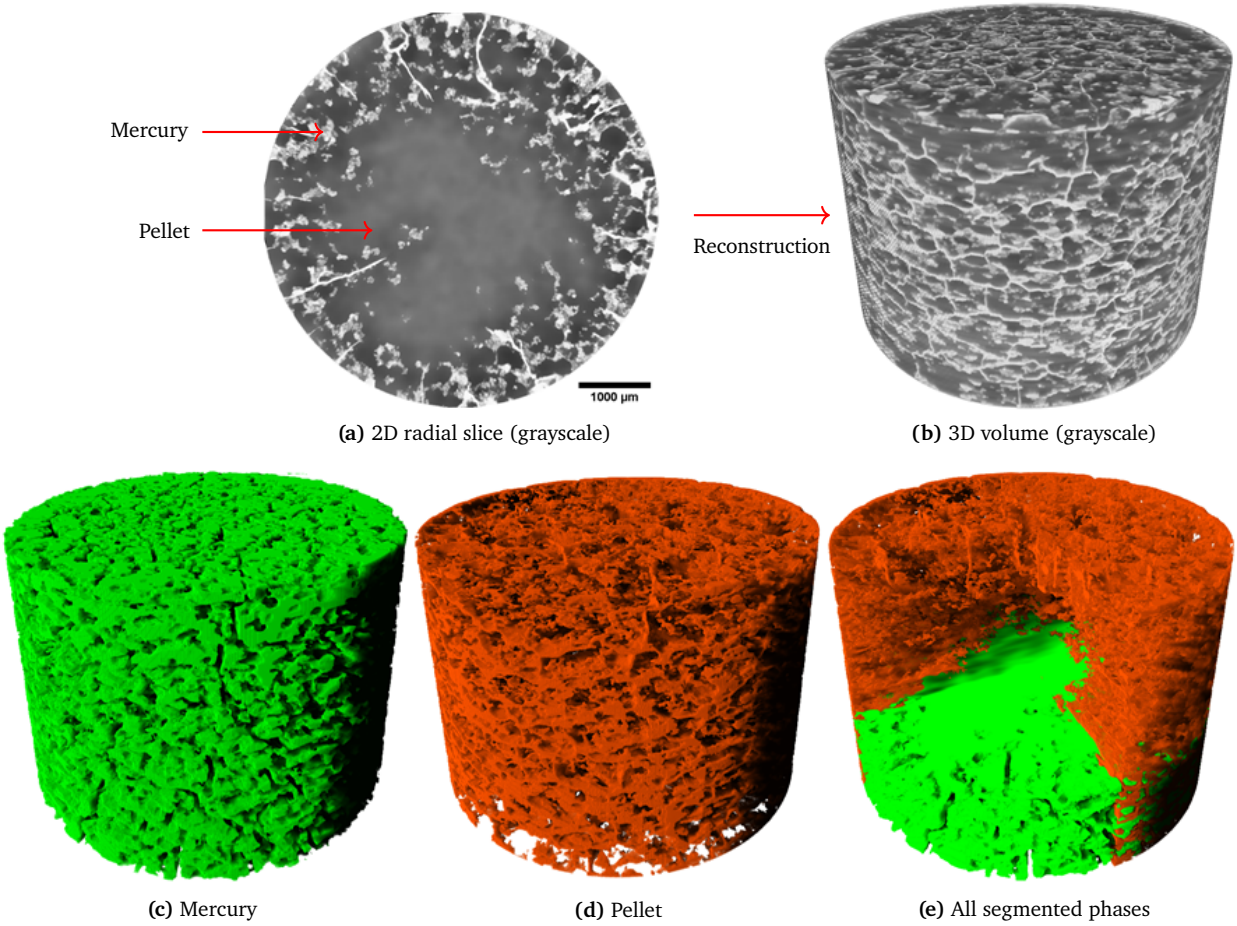
(c) Mercury **(d)** Pellet **(e)** All segmented phases

Figure 4.17: Raw and segmented CXT images of reduced roll compacted pellet following mercury porosimetry up to 3,800 psia leading to entrapment filling 5.4% of the pore space. **(a)** Raw 2D radial slice. Bright white regions correspond to mercury, **(b)** 3D reconstructed grayscale volume of the pellet exterior, **(c)** Entrapped mercury in the void spaces (orange) representing 36.2%, **(d)** Pellet regions with no entrapped mercury (green) representing 63.8% of the volume fraction, and **(e)** All the segmented phases. The scale bar corresponds to 1,000 µm.

model succeeded in segmenting all the different phases on the images. The mercury entrapment profile in the reduced RC sample follows a similar pattern as the fresh RC samples as it gets intruded into the gaps between feed particles and creates fractal dendritic branches. Additionally, large zones of pellet are left unintruded as they are probably thought to have a higher density than the rest of the feed material and are surrounded by pores with neck sizes smaller than ~56.7 nm, which is the minimum pore diameter penetrable at this scanning curve pressure. The volume fractions of the mercury and rest of the empty pellet as calculated from the CXT images are 36.2% and 63.8%, respectively.

4.5.4 Spent Pellet CXT Segmentation

Figure 4.18 displays the segmentation results for the spent spray-dried sample following mercury intrusion up to 2,860 psia leading to the entrapment filling 11.9% of the void space. The spent



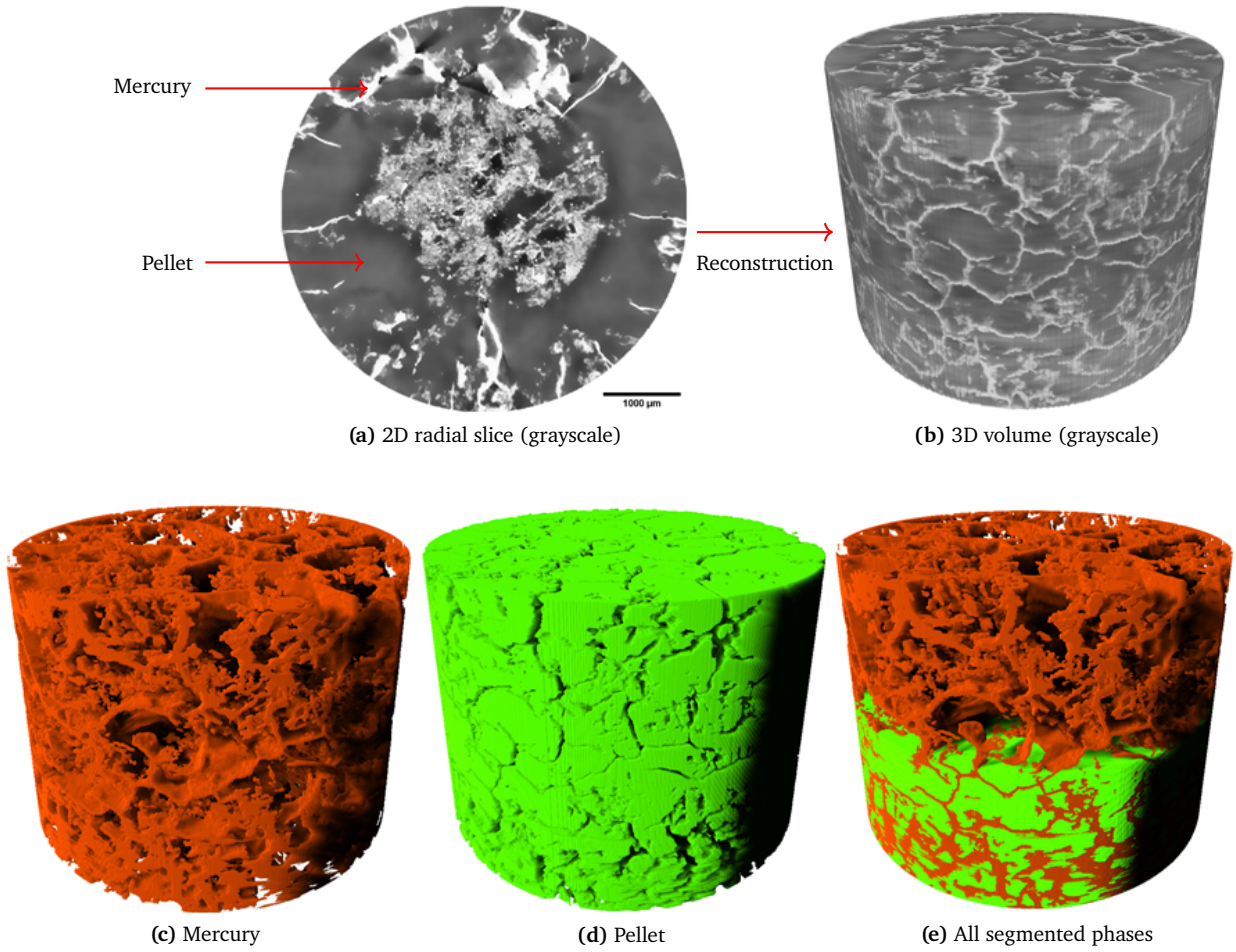
(a) 2D radial slice (grayscale) **(b)** 3D volume (grayscale)

(c) Mercury **(d)** Pellet **(e)** All segmented phases

Figure 4.18: Raw and segmented CXT images of spent roll compacted catalyst pellet following mercury porosimetry up to 2,860 psia leading to entrapment filling 11.9% of the pore space. **(a)** Raw 2D radial slice. Bright white regions correspond to mercury, **(b)** 3D reconstructed grayscale volume of the pellet exterior, **(c)** Entrapped mercury in the void spaces (orange) representing 20.8%, **(d)** Pellet regions with no entrapped mercury (green) representing 79.2% of the volume fraction, and **(e)** All the segmented phases. The scale bar corresponds to 1,000 µm.

pellets, in general, have more extensive fracture networks than the fresh and reduced pellets. The fracture network appears to be more complex near the top of the pellet and the bottom end than the middle of the pellet. As a result, lower scanning curve pressures were required to fill the void spaces in the spent pellets. As with the reduced SD, the entrapped mercury was associated with the cracks because the regions between the cracks that have no access to the crack network tended to be unintruded with mercury. Additionally, the outside mercury rims on the 2D radial cross-section images provide visual evidence of how far the mercury would have penetrated the sample without the presence of the fracture network. The volume fractions of the mercury and empty pore phases calculated from the CXT images are 20.8% and 79.2%, respectively.

Figure 4.19 displays the segmentation results of the spent roll compacted following mercury porosimetry up to 2,860 psia leading to entrapment filling 9.6% of the void space. As with the spent SD pellet, the spent RC required lower scanning curve pressure to fill up their pore spaces,



(a) 2D radial slice (grayscale) **(b)** 3D volume (grayscale)

(c) Mercury **(d)** Pellet **(e)** All segmented phases

Figure 4.19: Raw and segmented CXT images of spent roll compacted catalyst pellet following mercury porosimetry up to 2,860 psia leading to entrapment filling 27.2% of the pore space. **(a)** Raw 2D radial slice. Bright white regions correspond to mercury, **(b)** 3D reconstructed grayscale volume of the pellet exterior, **(c)** Entrapped mercury in the void spaces (orange) representing 23.2%, **(d)** Pellet regions with no entrapped mercury (green) representing 76.8% of the volume fraction, and **(e)** All the segmented phases. The scale bar corresponds to 1,000 µm.

but the mercury entrapment behaviours for the spent RC sample seem different from that of the spent SD. From Figure 4.19, it can be seen that mercury gets trapped around the middle of the pellet for the spent RC, whereas for the spent SD sample, the mercury gets stuck around the outside, showing structural differences between pellets. The volume fractions of the mercury and empty pore phases from the CXT images are 23.2% and 76.8%, respectively.

4.5.5 FIB-SEM Imaging Results

4.5.6 Fresh SD FIB-SEM

Figure 4.20 shows both the raw and segmented FIB-SEM serial milling images for the fresh spray-dried sample. The sample's surface morphology was studied using energy dispersive spectroscopy (EDS), which revealed that the darker areas are pores, the lighter grey areas are primarily alumina,

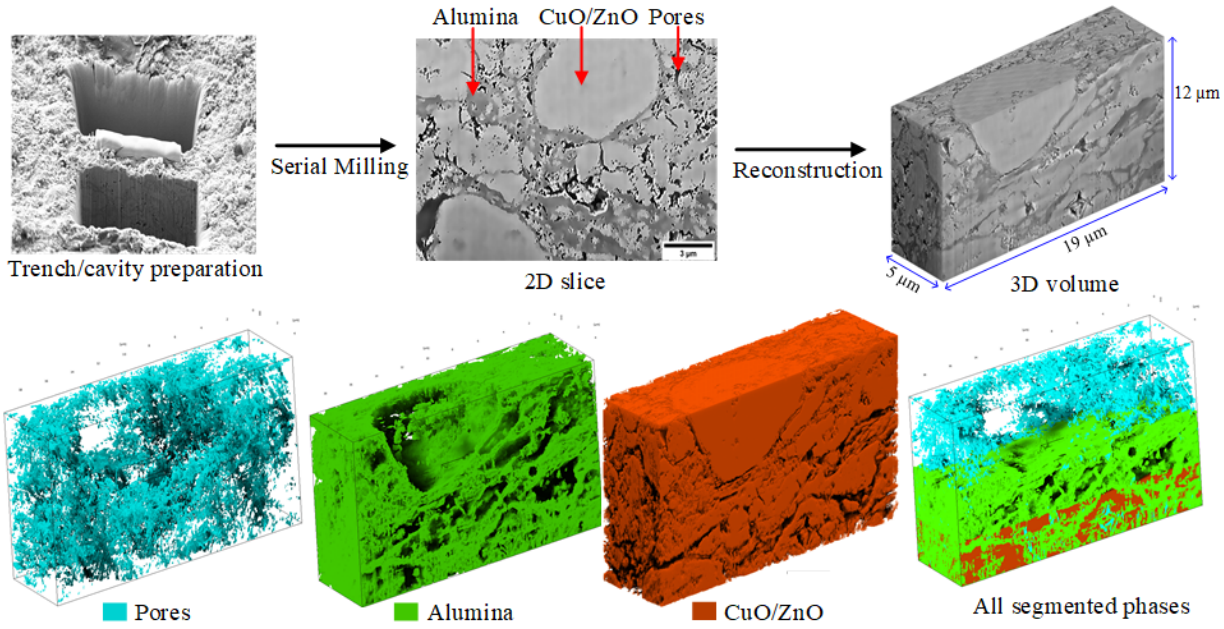


Figure 4.20: 2D and 3D reconstructed grayscale FIB-SEM images and segmentation for fresh spray dried pellet. **(a)** 2D grayscale image, **(b)** 3D reconstructed grayscale volume, **(c)** Pores representing 2.4% of the volume fraction, **(d)** Alumina representing 36.0% of the total volume fraction, **(e)** Copper/Zinc oxide representing 61.6% of the total volume fraction, and **(f)** All segmented phases. The scale bar corresponds to 2 µm.

and the brighter regions are Copper/Zinc oxide. Both the 2D slice and 3D volume show part of a rounded particle composed of dense CuO/ZnO phase of size ∼5-10 µm. The size, shape, and composition (and thus electron density) of this round particle suggest it is an example of the particles that appear as rounded, bright white particles in the high-resolution CXT image of the SD feed material in Chapter 3. It can also be seen that these rounded high-density particles have no macropores, as there is a gap in the distribution of macropores in the region of the particle in the image. The automatic segmentation of the 3 phases using the U-Net model (B) was successful in the case of the Cu/ZnO and alumina phases. However, the model was partially successful in segmenting the pores because the grey-values range of the pores heavily overlapped with the alumina. Comparison of the 2D slices of some of the spray-dried FIB-SEM images showed that some pores were incorrectly labelled as alumina in some isolated cases. However, The accuracy of the U-Net B model appeared qualitatively high. The volume fractions of each phase are 2.4% for pores, 36.0% for alumina, and 61.6% for CuZnO.

4.5.7 Fresh RC FIB-SEM

Figure 4.21 displays the raw and segmentation results for the fresh roll compacted pellet from 510 slices. As with the fresh SD, the roll compacted sample similarly shows three phases: pores, copper/Zinc oxide, and alumina. The three phases were subsequently segmented using the U-Net model (B), and the reconstructed images are also shown in Figure 4.21. From Figure 4.21 it can be seen, in the volume sampled, that the texture of the RC feed pellet over length-scales

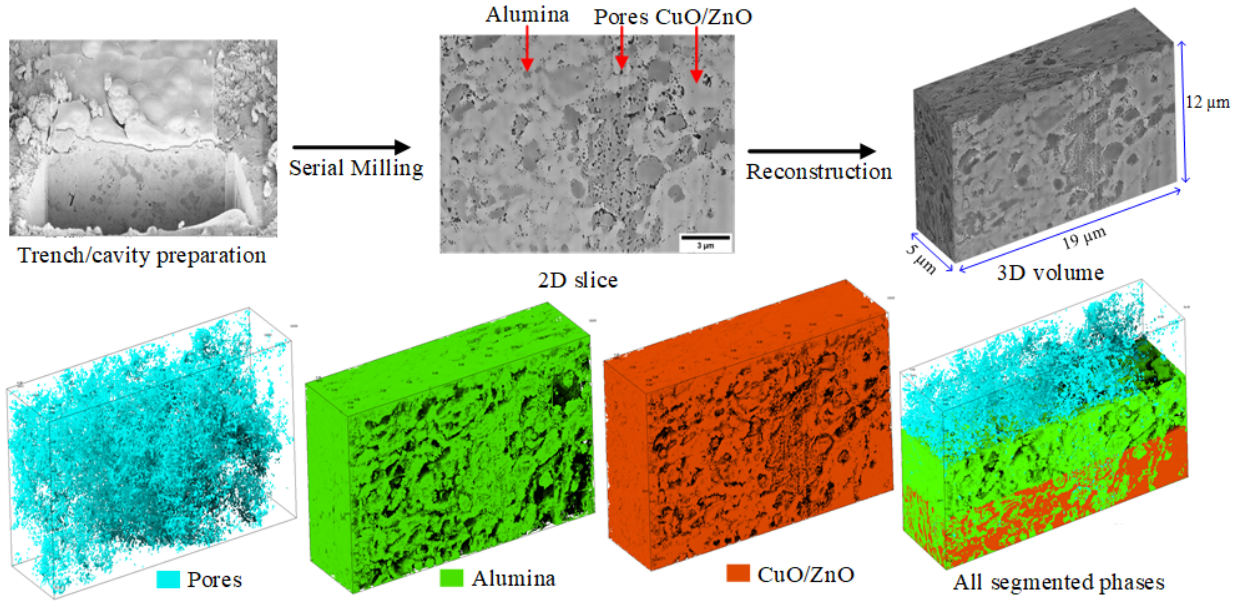


Figure 4.21: 2D and 3D reconstructed grayscale FIB-SEM images and segmentation result for fresh roll compacted pellet. **(a)** 2D grayscale image, **(b)** 3D reconstructed grayscale volume, **(c)** Pores representing 2.1% of the volume fraction, **(d)** Alumina representing 38.2% of the total volume fraction, **(e)** Copper/Zinc oxide representing 59.8% of the total volume fraction, and **(f)** All segmented phases. The scale bar corresponds to 2 µm.

∼1-10s µm is very different to that of the SD feed pellet region seen. The macropores in the roll compacted sample seem to be evenly distributed in the different regions of the pellets compared to the SD sample, where the macropores were found in only specific regions of the pellet. The volume fractions of the different phases are 2.1% pores, 59.8% Cu/ZnO and 38.2% alumina.

4.5.8 Post-segmentation Quantification and Model Validations

With the deep-learning model accuracies achieved in this segmentation work, the volume fractions of each phase could be calculated with great precision from the segmented image stack. Furthermore, the spatial distributions of the different phases were displayed with minimum noticeable inaccuracies. As a result, the segmented images would be suitable for various post-processing procedures for extracting other quantitative information, such as fracture thickness measurement and assessing if entrapped mercury's spatial distribution in the pores can be established. However, there are at least three other sources of inaccuracies that could affect the deep-learning segmentation approach used here. One is the quality of the original X-ray and FIB-SEM images, which is influenced by image resolution, near-field diffraction effects and the presence of noise or artefacts on the original image stack. In the present study, this source of error does not appear to be a limitation in the segmentation of CXT images of samples with mercury because of the filters used during the preprocessing stage. However, for the CXT and FIB-SEM images of the empty samples, some isolated clusters of inaccurately labelled pixels were sometimes found in the segmented images. These errors were successfully corrected in the post-segmentation processing steps.

The second source of the error is the manual segmentation procedure that must be used to create the training dataset. This is the most time-consuming stage, and there will most likely be some inadvertent labelling errors among the vast number of CXT (1004 x 1024) and FIB-SEM (2048 x 1536) pixels in each image slice, as well as judgment errors for pixels located at the boundaries of two phases. The manual segmentation errors are more likely to occur at single isolated pixels and have minimal impact on the final trained model. In contrast, judgment errors are more likely to affect only the exact location of the boundaries within a distance determined by pixel size or image resolution.

The third type of error is pixel mislabelling, which may occur during the inference step due to inaccuracies in the network model's coefficients. The accuracy of the segmentation model is governed by the parameters given during the training stage (i.e., number of training images, batch size, number of iterations and patch size). The error rate reduces typically as the number of training images and iterations increases to a certain point; hence, there is a trade-off between network accuracy and computer time required for training. However, an increased number of iterations may result in overfitting of the model's weights and could lead to poor segmentation of the previously unseen images. After each epoch, the error functions for both the training and validation patches were checked to confirm that both errors decreased in successive epochs, preventing the model from overfitting (an increase in the validation error indicates overfitting in this case). With 100 epochs and training parameters considered to be appropriate based on previously trained models, an error rate of 2.7% was achieved in the present image segmentation. However, a more comprehensive assessment is required to be undertaken to optimize the selection of training parameters and quantify the trade-off between computation time and error rate.

4.6 Conclusion

In this chapter, a deep learning image segmentation procedure was used to segment 3D CXT and FIB-SEM images from methanol synthesis catalyst pellets before and after mercury intrusion, in which the different phases on the pellets showed identical image intensities. Using a local workstation, this was accomplished within reasonable run times, proving a viable solution to the challenge of segmenting a large quantity of 3D CXT and FIB-SEM images and the associated barrier. Identifying the various phases in the segmented 2D slices of both the CXT and FIB-SEM images was consistent with the visual identification from the original slices. Additionally, the high and low-density phases on the empty SD samples could not be easily distinguished in the original CXT images, but they are readily differentiated in the segmented images. It was also demonstrated that the deep learning segmentation was successful in automating fracture network segmentation in the methanol pellets. Post-segmentation image processing allowed the distributions of phases and fractures networks to be rendered in forms that assisted in understanding their distributions in 3D space and extracting quantitative information on the microstructural properties.

The next chapter introduces freshly reduced and spent methanol synthesis catalyst pellets.

Chapter 5

Studies on the Effectiveness of Reduced and Spent Methanol Synthesis Catalyst

5.1 Introduction 128
5.2 Materials and Methods 129
5.3 Results 131
5.4 Discussion 147
5.5 Conclusion 151

5.1 Introduction

Chapter 3 introduced the reader to the concept of integrating multi-modal imaging with the more statistically-representative multi-scale methods to characterise fresh methanol synthesis pellets made using spray dried or roll compacted feed materials. The chapter looked at how different pellet fabrication processes affect pore structures in the final pellet and its impact on mass transport rate. In particular, how specific features of the void space are related to certain aspects of the fabrication process was determined. The results have shown that a combination of indirect characterisation methods, such as overcondensation and mercury porosimetry, and imaging techniques can provide detailed spatial information for a porous material. Additionally, it has been found that the degree of heterogeneity in average pore sizes between feed particles, and their particle size relative to that of the pellet itself, significantly impact the accessibility of the pellet interior.

This chapter will first introduce the reader to the reduced and spent methanol synthesis pellets, and will then test the effectiveness of reduced and spent pellets by using a combination of indirect characterisation methods, together with X-ray and SEM imaging, similar to that discussed in Chapter 3. The freshly reduced samples were reduced with a flowing gas mixture (20,000 l/hr/kg) containing 2 vol% hydrogen in balance nitrogen and held at a temperature of $225\,^{\circ}\mathrm{C}$ for 8 hours at ambient pressure. The resulting active catalyst is black in colour. The spent samples were aged by Johnson Matthey (JM) in a pilot-scale methanol synthesis reactor operating under conventional methanol synthesis conditions of T and P, and employing a realistic synthesis gas composition.

5.2 Materials and Methods

5.2.1 Samples studied

Freshly reduced and spent(aged) methanol synthesis catalyst pellets made using either spray-dried (SD) or roll compacted (RC) feed materials were studied in this work. The SD and RC pellets are mesoporous cylindrical tablets with dimension of ∼5.4×3.4 mm (base diameter × length)(see CXT images). The reduced SD and RC pellet have an average BET surface area of $118.1\,\mathrm{m^2 g^{-1}}$ and $112.9\,\mathrm{m^2 g^{-1}}$, respectively. The spent SD and RC pellets have an average BET surface area of $65.4\,\mathrm{m^2 g^{-1}}$ and $61.7\,\mathrm{m^2 g^{-1}}$, respectively. Tables 5.1 to 5.2 contain further details and properties of the samples studied.

Table 5.1: Characteristics of the freshly reduced and spent catalyst pellets. Porosity values were obtained from mercury porosimetry. The bulk density was obtained from helium pycnometry.

Sample	Porosity (%)	Bulk density ($\mathrm{g/cm^3}$)	BET ($\mathrm{m^2/g}$)	Cylinder dimension (diameter×height)
Reduced SD	67.3	1.91	118.070	5.5x3.4mm
Spent SD	69.4	1.92	65.395	5.4x3.4mm
Reduced RC	64.4	1.80	112.883	5.4x3.5mm
Spent RC	65.1	2.10	61.655	5.6x3.4mm

Table 5.2: Specific pore volumes and modal pore diameters of the samples as determined by two different methods

Sample	Hg pore volume (ml/g)	N_2 sorption pore volume (ml/g)	Hg modal pore diameter (nm)	N_2 modal pore diameter (nm)
Reduced SD	0.324	0.356	37.5	10.9
Spent SD	0.333	0.340	60.3	20.8
Reduced RC	0.322	0.332	35.9	11.7
Spent RC	0.315	0.321	51.0	19.1

5.2.2 Integrated mercury porosimetry and gas sorption

The integrated method or the 'sifting' strategy, which consists of a series of gas sorption and mercury porosimetry experiments conducted on the same sample, was used to analyse the reduced and spent catalyst pellets. The integrated method is explained in detail in Chapter 3, but the main steps of the experiment, as well as further aspects of the procedure that are unique to the samples tested in this chapter, will be discussed in this section. The integrated rate of adsorption-mercury porosimetry aims to selectively block specific pore sizes, and then study how important those pores were to the rate of mass transport before and after their removal. The reduced and spent samples were degassed at $140\,^{\circ}\mathrm{C}$, and the samples were kept under vacuum for 24 hours to drive off any physisorbed water on the pores.

Figure 5.1 shows a simplified block diagram representing the integrated mercury porosimetry and gas sorption techniques. First, an empty sample is imaged using both SEM and CXT. Next, the

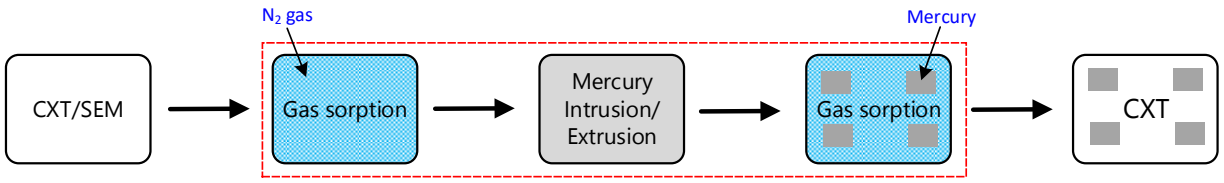


Figure 5.1: A schematic representation of the integrated mercury porosimetry-gas adsorption-imaging technique. The blue line shadings denote condensate, and the grey shadings denote mercury.

nitrogen gas sorption experiments, including conventional isotherms, rate of adsorption (ROA) and overcondensation, are conducted on the empty samples. After the first nitrogen gas sorption experiments, the sample is transferred to a mercury porosimetry (MIP) instrument to entrap mercury into the pores at different pressures. Once the mercury entrapment is finished, the sample is returned to the gas sorption rig, and the nitrogen adsorption experiments are repeated to obtain the post-mercury data. The samples were also imaged using X-ray before and after mercury entrapment.

5.2.3 Rate of Adsorption (ROA) procedure

The sample preparation and the experimental setup for the rate of adsorption experiment are similar to that of other gas sorption experiments. The reduced and spent samples were degassed at $140\,^{\circ}\mathrm{C}$, and the samples were kept under vacuum for 24 hours to drive off any moisture or physisorbed gas on the pores. The rate of adsorption (ROA) technique works by dosing a known quantity of nitrogen gas onto the sample and then recording the amount of gas adsorbed, and the corresponding pressures over time. The dosing quantity was taken from the BET monolayer capacity. An additional $5\,\mathrm{cc(STP)/g}$ of gas was added to this amount to compensate for the initial expansion of the gas into the free space of the sample tube.

5.2.4 Overcondensation gas sorption procedure

The overcondensation (OC) experiment is described in detail elsewhere in thesis in Chapter 3. The OC experiment is used to investigate any porosity beyond the instrument upper limit for the conventional isotherm (P/P_0 >0.995). The conventional isotherms for reduced and spent materials clearly showed that porosity exists beyond the conventional instrument upper limit, and therefore OC experiments were carried out on the samples to obtain the true pore volume and the correct pore size distribution of the sample.

5.2.5 Imaging using CXT and SEM

The reduced and spent catalyst pellets were imaged using low-resolution CXT and FIB-SEM. For the low-resolution CXT scans, the whole pellets were imaged before and after mercury entrapment using a Zeiss Xradia Versa XRM-500 to acquire 3D image stacks. A similar imaging technique as the fresh catalyst pellets were used for the reduced and spent pellets. The 3D volume data sets

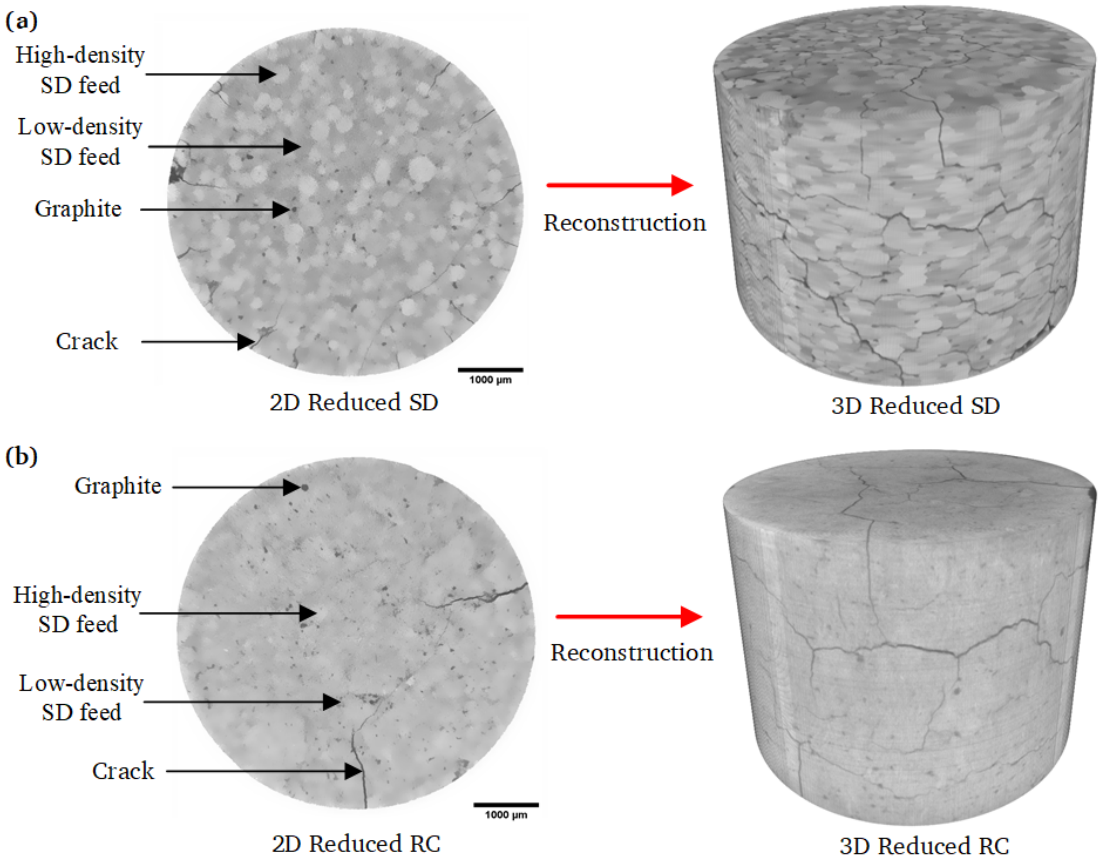


Figure 5.2: Raw 2D radial slice and 3D reconstructions for the **(a)** Empty reduced SD, and **(b)** Empty reduced RC feed pellet.

were reconstructed using the filtered back projection (FBP) method.[128] For the FIB-SEM imaging, a serial milling procedure was carried out using a Crossbeam 550 (Carl 206 Zeiss Microscopy) to acquire a series of 2D images and later stitched together to create a 3D volume stack.

5.3 Results

5.3.1 CXT Imaging

5.3.2 Imaging Empty Reduced SD and RC

Figure 5.2(a) and (b) shows typical example of 3D reconstruction and 2D radial cross-section slice CXT images of the empty reduced SD and RC feed pellets, respectively. The reduced SD and RC samples have the same feed particles composition as the fresh pellets, namely high-density and low-density feed particles. The samples also contain many smaller, dark black spots, which correspond to the graphite lubricant particles.

[128]G. N. Ramachandran and A. V. Lakshminarayanan. *PNAS*, **68**: 2236–2240, 1971.

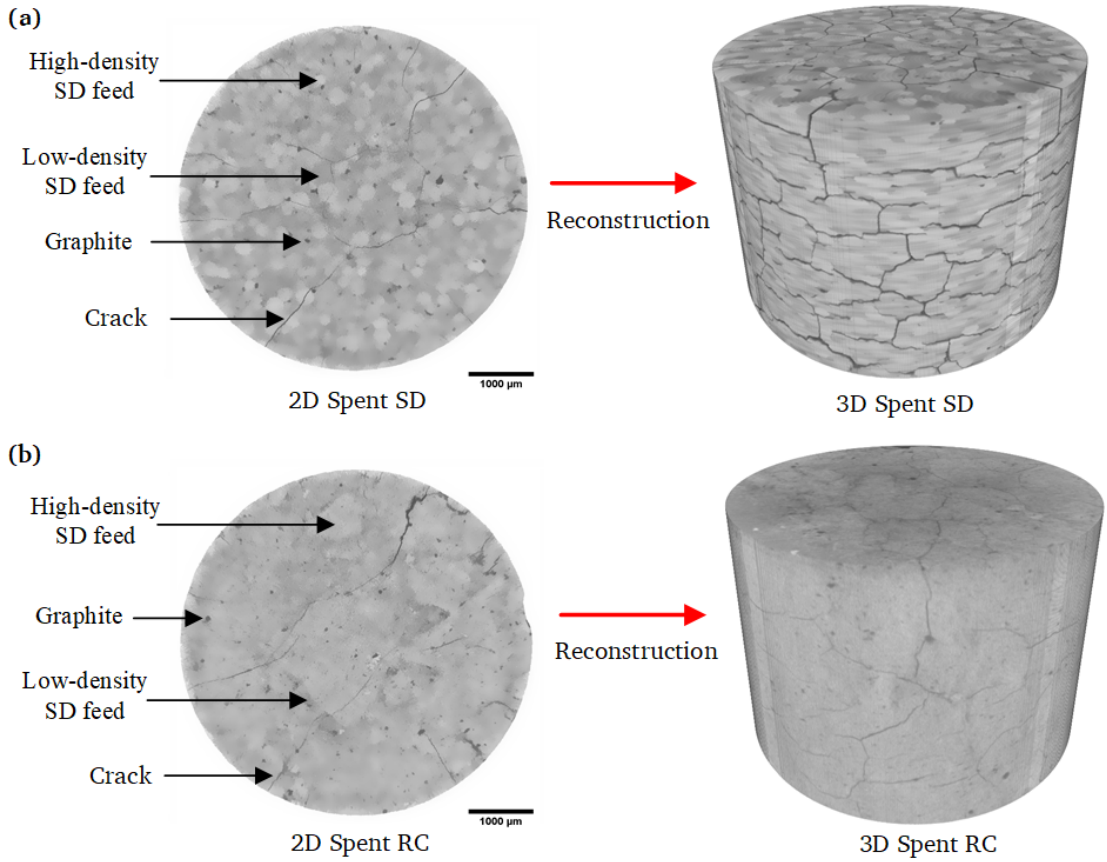


Figure 5.3: Raw 2D radial slice and 3D reconstructions for the **(a)** Empty spent SD, and **(b)** Empty spent RC feed pellet.

The CXT images of the freshly reduced and the spent pellet revealed the presence of a splintering or cracking of the feed particles that have not been seen in the fresh samples. The cracks might have developed during the reduction stage as the incidence of cracks have increased following the reduction. The reduction step results in some differential shrinkage of the pellet (as oxide is lost) which causes shear forces and cracking. The fracture network is thought to generate macroporosity that acts as motorways for molecular diffusion, and provide quick access to the active sites in the pellet. This can be seen in the CXT images of the samples with entrapped mercury in the pores where the mercury tends to be associated with the cracks, as the crack network is feeding the mercury intrusion and is providing an entry point into the pellet.

5.3.3 Imaging Empty Spent SD and RC

Figure 5.3(a) and (b) shows examples of 3D reconstruction and 2D radial cross-section slice CXT images of the empty spent SD and RC feed pellets, respectively. The spent SD pellet have more extensive fracture networks than the spent RC sample. The fracture network appears to be more complex near on the outer layer of the pellet as well as the top and bottom ends. The many irregularly-shaped regions of varying size and density seen in the fresh RC sample seems to slightly merged together in the spent RC pellets. However, there is still some hint of density segregation

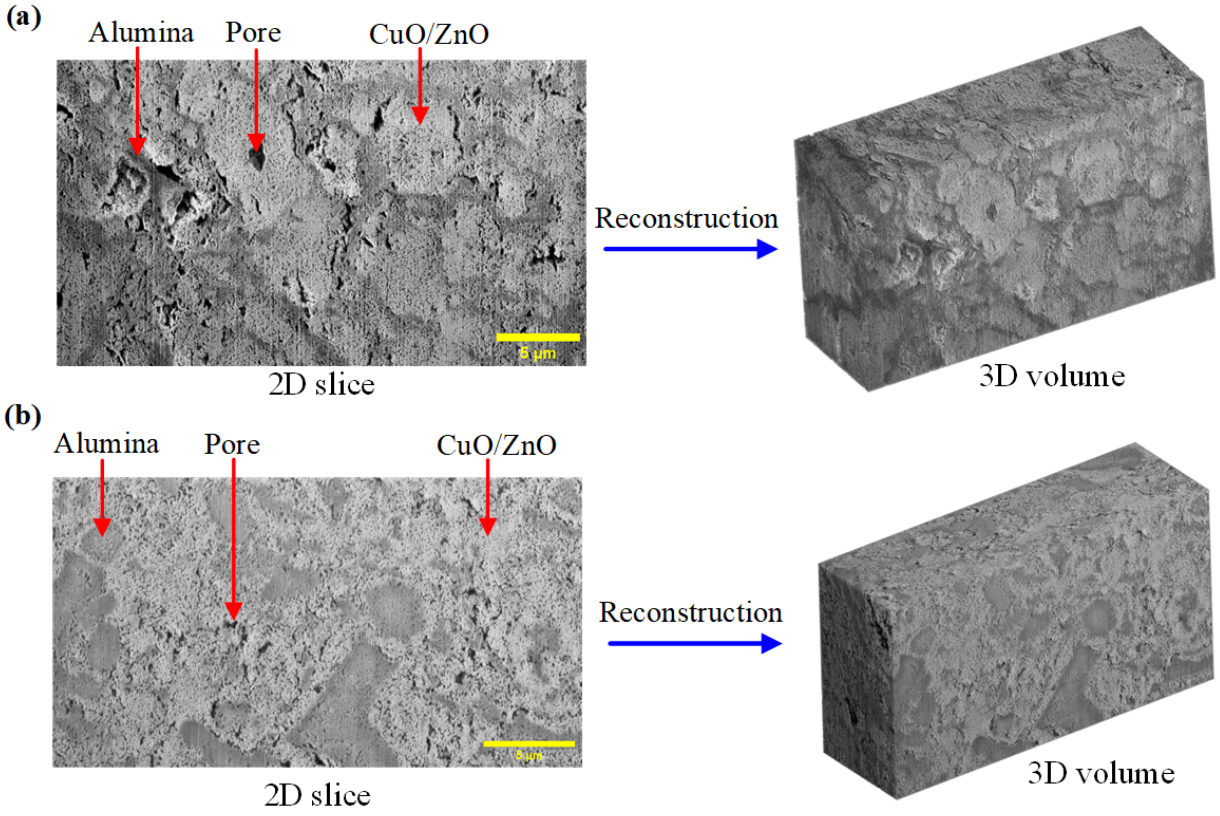


Figure 5.4: 2D and 3D reconstructed grayscale FIB-SEM images for the (a) Reduced SD and (b) Reduced RC. The scale bar corresponds to 5 µm.

within the irregular shaped regions on the RC pellet.

5.3.4 FIB-SEM Imaging

Figure 5.4(a) and (b) show a 2D slice SEM image and a 3D volume reconstruction from 300 slices for the reduced SD and RC pellets, respectively. For the reduced SD sample, the rounded, high-density particles found in the fresh SD samples have now much more macropores inside them. These high-density particles were similar to the particles that appeared as bright white particles in the high-resolution CXT images of the fresh SD feed that were seen in Chapter 3. The rounded particles in the fresh SD sample had no macropores, as there is a gap in the distribution of macropores in the region of the particles in the image. However, on the reduced SD sample, the number of pores on the dense Cu/O/ZnO phase has gone up, which leads to the creation of an additional porosity in the sample as the porosity has increased from 47.1% to 67.3% as can be seen in Table 5.1. The reduction process is thought to increase the number of macropores on the high-density regions of the reduced SD pellets, leading to an increase in pellet porosity. This is consistent with the changes in BET surface area measurements of the reduced samples shown in Table 5.1, where the surface area of the reduced samples has increased by more than $\sim$ 25% compared to the fresh catalyst pellets.

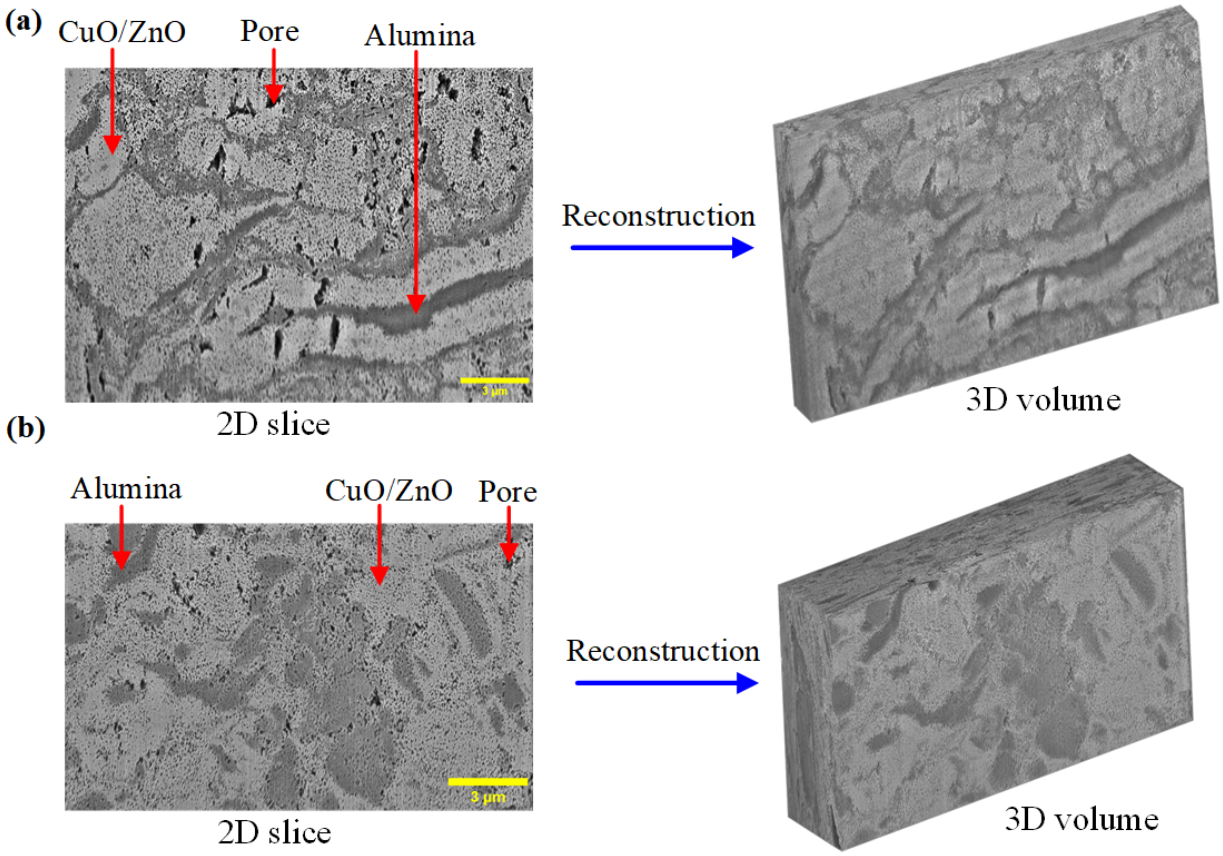


Figure 5.5: 2D and 3D reconstructed grayscale FIB-SEM images for the (a) Spent SD and (b) Spent RC. The scale bar corresponds to 5 µm.

Figure 5.5(a) and (b) show a 2D slice SEM image and a 3D volume reconstruction from 230 slices for the spent SD and RC pellets. The images show that the Cu/ZnO regions have grown in size, whereas the alumina particles have shrunk by agglomerating with their neighbouring particle. Additionally, many of the macropores in the alumina phase disappeared after the ageing process as there are not many large macropores found in the alumina phase. The shrinkage of the alumina phase contributes to the loss of the macropores in the pellet, which in turn leads to the loss of catalyst surface area, as can be seen in Table 5.1. The BET surface area of the spent samples fell by ∼30% compared to fresh samples and by more than ∼44% compared to the reduced samples. The loss of surface area for the spent pellets could also be attributed to catalyst deactivation due to sulphur poising, metal deposition onto the active sites, or sintering of the copper particles resulting in copper surface area loss.

5.3.5 Mercury Porosimetry Data

Figure 5.6(a)-(d) show the raw mercury porosimetry scanning curves for the whole reduced and spent SD and RC samples. Scanning curves up to different intrusion pressures were used during the mercury porosimetry experiments to 'filter-out' specific pores sizes by filling them with mercury.

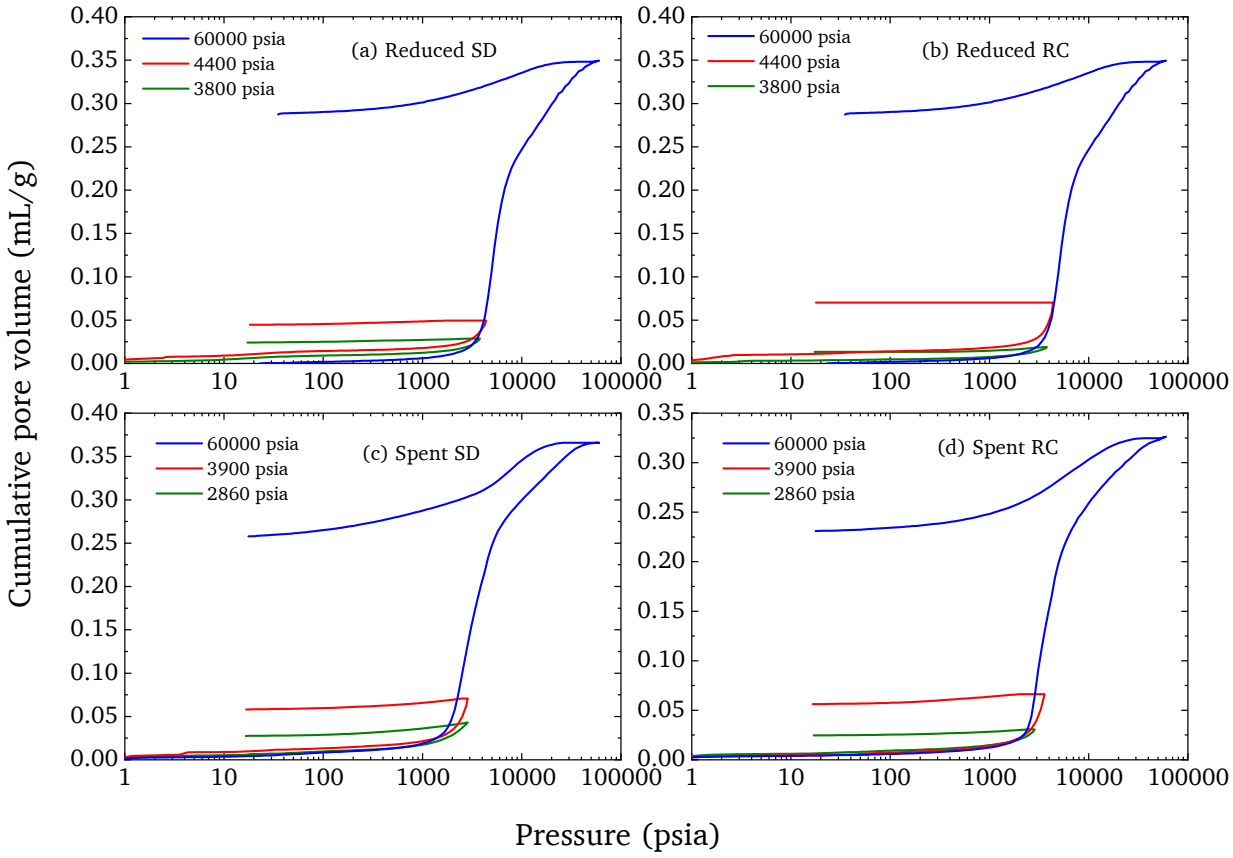


Figure 5.6: Mercury porosimetry scanning curve data for **(a)** Reduced SD, **(b)** Reduced RC, **(c)** Spent SD and **(d)** Spent RC. The mercury scanning curve pressures are indicated on the graph legends.

The top of each intrusion curve indicates which pore-necks have been penetrated and blocked out by mercury. The extrusion curves show what fraction of the pores that have been penetrated are still full of mercury. The scanning curves reveal the intra-batch variability amongst the pellets from the same batch. The spatial arrangement of each pellet is different from another due to the variation in the arrangement of the pre-compaction lumps. As a result of the intra-batch variability, the intrusion levels varied slightly from pellet to pellets at the same pressures. However, the overall intrusion curve shapes for each pellet followed similar patterns.

The raw data from the mercury porosimetry experiments were analysed using Kloubek[76], correlation which is a semi-empirical alternative to Washburn equation,[71] and the resulting curves are displayed in Figure 5.7 (a)-(d). The mercury intrusion data shows that as the ultimate mercury pressure is increased, then, progressively, more intrusion occurs into the ever-smaller pore necks. From the mercury extrusion data, it can be seen that, typically, ∼70-100% of the intruded mercury becomes entrapped, depending upon the ultimate intrusion pressure, with fractionally less mercury becoming entrapped for higher ultimate intrusion pressures. The Kloubek relationship

[76] J. Kloubek. *Powder Technol.*, **29**: 63–73, 1981.
[71] W. E. Washburn. *Phys. Rev.*, **18**: 206–209, 1921.

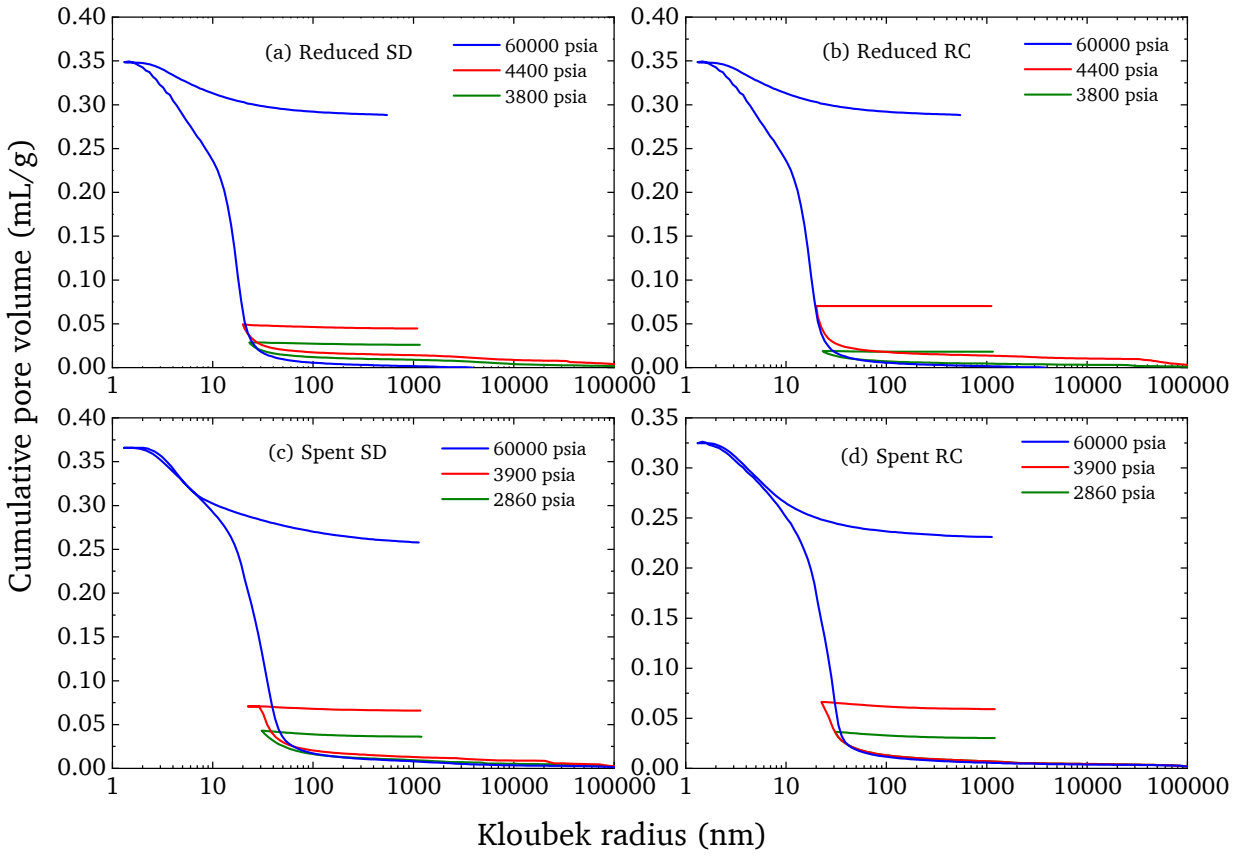


Figure 5.7: Mercury porosimetry scanning curve data analysed using the Kloubek correlation for **(a)** Reduced SD, **(b)** Reduced RC, **(c)** Spent SD and **(d)** Spent RC. The mercury scanning curve pressures are indicated on the graph legends.

is designed to remove the effects of contact angle hysteresis in mercury porosimetry data. The analysed data for the reduced and spent samples is shown in Figure 5.7, where the x-axis now represents the pore radius (nm). By applying this numerical relationship to the raw data for spent samples, a superposition of the intrusion and extrusion curves was achieved for smaller mesopore sizes (<10 nm for SD and <9 nm for RC). This creates 'swan-neck' like curves for the spent SD and RC sample. Furthermore, this indicates that for all the pore sizes below 10 nm, the cause of hysteresis was because of the different contact angles between the mercury and the pore walls for the advancing and retreating mercury menisci as described in previous work,[86,87] and therefore, only leaving structural hysteresis.

5.3.6 CXT imaging of pellets following mercury entrapment

Figure 5.8(a) and (b) shows typical reconstructed 2D radial slice CXT images of the reduced SD and RC samples following mercury intrusion up to 3800 psia. The regions of the pellet containing entrapped mercury appear as bright white pixels, while the empty pellet matrix appears in shades

[86]S. Rigby et al. *Appl. Catal., A*, **238**: 303–318, 2003.
[87]S. Rigby and K. Edler. *J. Colloid Interface Sci.*, **250**: 175–190, 2002.

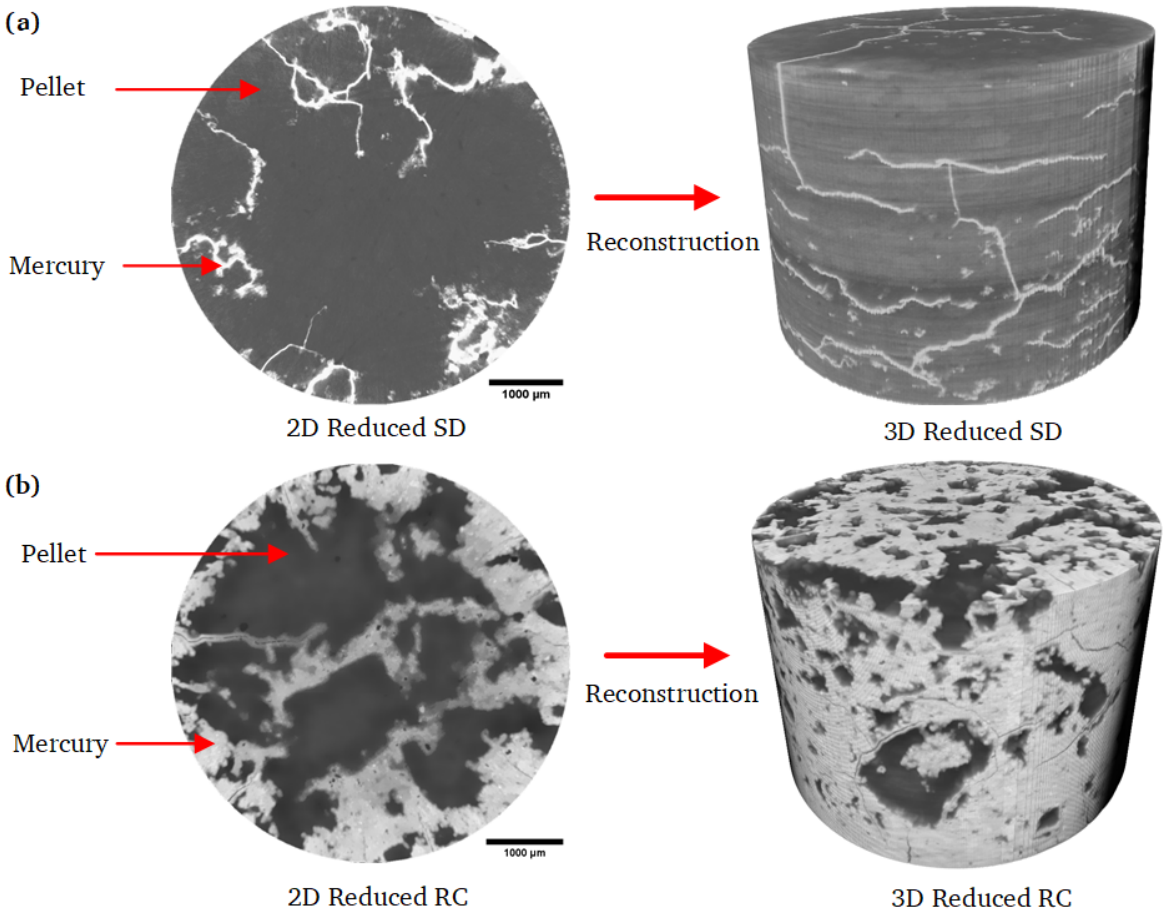


Figure 5.8: Raw CXT images of the reduced catalyst pellet following mercury intrusion up to 3800 psia (a) Reduced SD, and (b) Reduced RC. The white area represent entrapped mercury and the black regions unintruded matrix.

of grey. From Figure 5.8(a) and (b), it can be seen that mercury gets entrapped into the large macropores and the 'vein' like cracks in the pellets. Additionally, there are isolated mercury clusters within the pellet away from the cracks. This means there must be connecting paths of large meso-and-macropores that are accessible from the pellet's surface, leading to the centre of the pellet. One key finding made in the reduced pellets is that the reduction process produces cracking in the pellet structure, as can be seen the CXT image of the samples. The fracture network increases even more when the pellet has been used in the reactor. The fracture network is only found in the reduced and spent pellets and is thought to provide an entry point for the mercury into the samples. The fracture network is believed to provide macroporosity, act as molecular diffusion highways, and provide fast access to active sites inside the pellet. However, some of the cracks in the pellet are not completely saturated with mercury and therefore, during gas sorption experiments, the nitrogen gas will still be able to diffuse through the partially filled cracks and macropores.

The mercury entrapment profile in the reduced RC sample follows a similar pattern as the fresh RC samples as it gets intruded into the gaps between feed particles and creates fractal dendritic branches. Additionally, large zones of pellet are left unintruded as they are probably

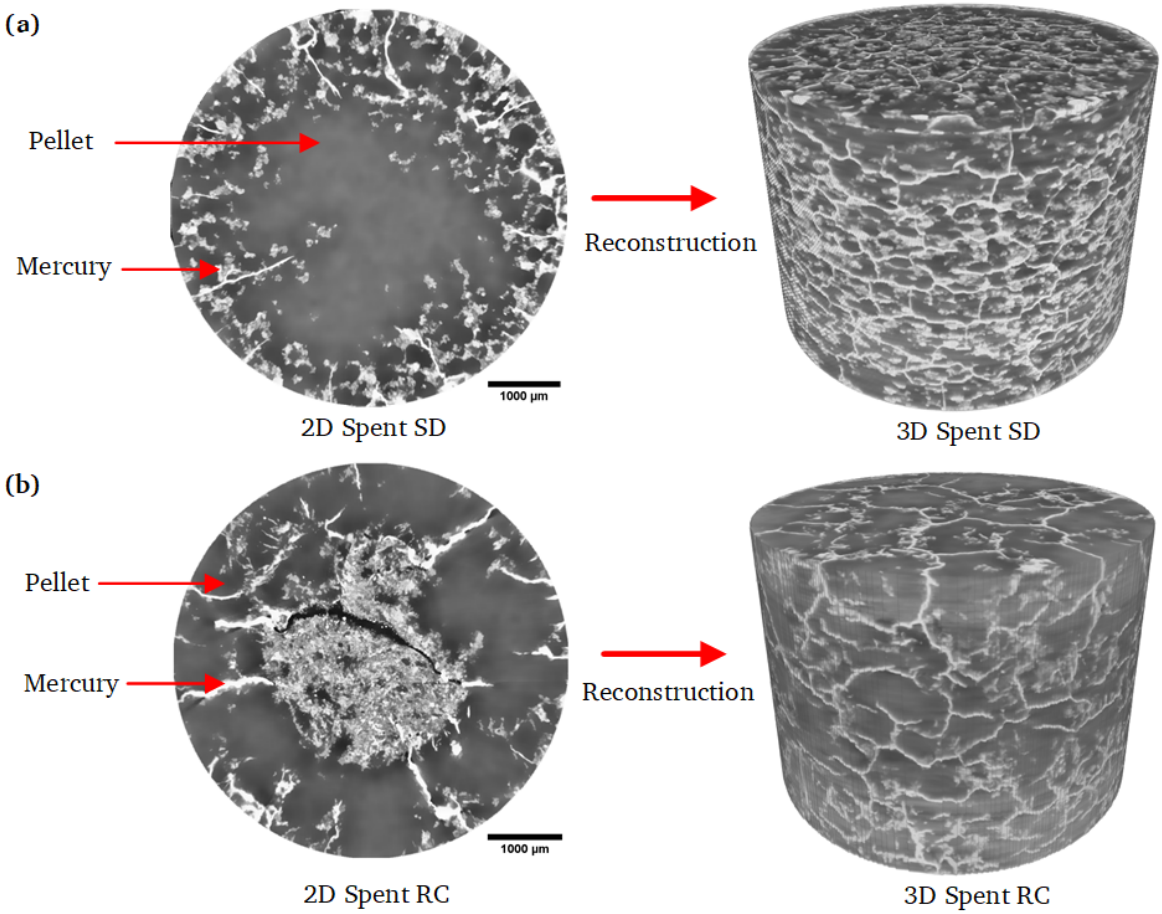


Figure 5.9: Raw CXT images of the spent catalyst pellet following mercury intrusion up to 2860 psia **(a)** Spent SD, and **(b)** Spent RC.

thought to have a higher density than the rest of the feed material and are surrounded by pores with neck sizes smaller than ~56.7 nm, which is the minimum pore diameter penetrable at this scanning curve pressure. The reduced and spent SD and RC samples were segmented using deep learning,[266] neural network in Dragonfly software.[258] The results of segmented images for the reduced and spent pellets with mercury are displayed in Chapter 4.

Figure 5.9(a) and (b) shows reconstructed 2D radial slice CXT images of the spent SD and RC pellets following mercury intrusion up to 2860 psia. The spent pellets, in general, have more extensive fracture networks than the reduced pellets. The fracture network appears to be more complex near the top and bottom ends of the pellet. Because of the large number of cracks present, lower scanning curve pressures were required to fill in the void spaces in the spent samples. The entrapped mercury was associated with the cracks, much the same as the reduced SD, because the regions between the cracks that do not have access to the crack network tended to remain mercury-free. Furthermore, the outer mercury rims on the 2D radial cross-section pictures show

[266]Y. Lecun, Y. Bengio, and G. Hinton. *Nature*, **521**: 436–444, 2015.
[258]R. Makovetsky, N. Piche, and M. Marsh. *Microsc. Microanal.*, **24**: 532–533, 2018.

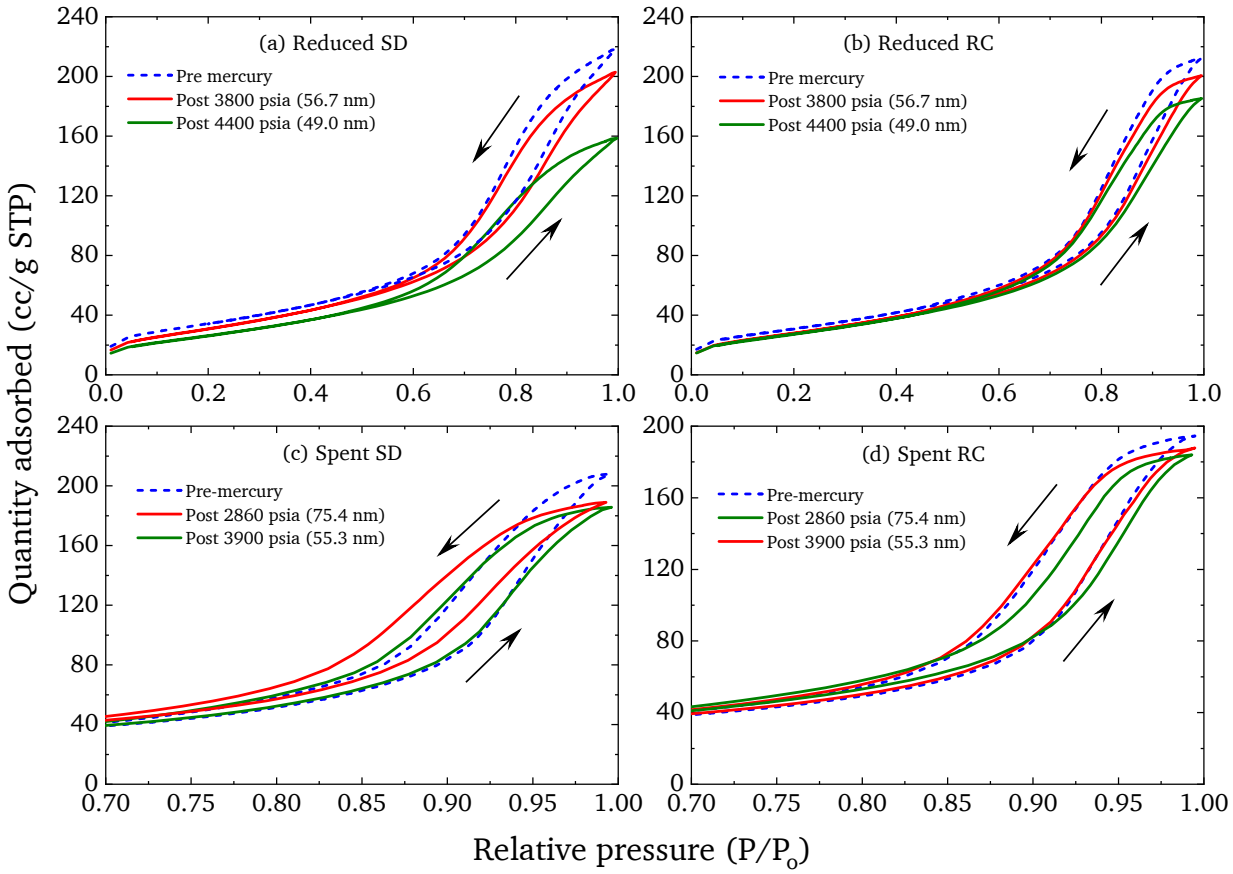


Figure 5.10: Typical examples of conventional nitrogen sorption isotherms before and after mercury intrusion up to different scanning curve pressure for the **(a)** Reduced SD, **(b)** Reduced RC, **(c)** Spent SD and **(d)** Spent RC. Arrows have been added to the plots to indicate the direction of the change in pressure for adsorption and desorption boundary curves.

how far the mercury would have penetrated the material if the fracture network had not been present.

The 2D radial cross-section images of the spent pellets reveal the structural differences in the mercury intrusion patterns between the SD and RC feed particles. For the spent SD sample, the mercury intrusion occurs as a defined front that progressively migrates towards the centre of the pellets. However, for the spent RC sample, the mercury first enters the cracks and is deposited in the centre of the pellets, and then it gradually spreads and fills in the centre of the pellets, like an inland river delta (e.g., the Okavango delta in Botswana).

5.3.7 Gas Sorption Data

5.3.8 Gas sorption scanning curve isotherms

Figure 5.10(a) to (b) show the conventional nitrogen sorption isotherms for the empty reduced and spent SD and RC samples (dashed lines), and for the samples following mercury entrapment after intrusion to a range of different pressures (solid lines). From the nitrogen isotherms, it can

be seen that as more mercury is added to the sample, the ultimate amount of gas adsorbed at the top of the isotherms decreases. The empty reduced samples generally have the highest pore volumes compared to the fresh and spent pellets. This is probably due to an increase in the pellet porosity post-reduction, as can be seen in the FIB-SEM images.

From Figure 5.10(a) to (b), it can also be seen that the shape of the isotherms is of Type IV according to the IUPAC classification,[63] without plateaus at relative pressures 1. The lack of plateaus at the highest relative pressure in the isotherm indicates that the sample's biggest void space is not completely filled with liquid nitrogen and some vapour pockets remain, which condensate can begin to evaporate. This makes the reduced and spent pellets suitable for conducting overcondensation isotherm, which is discussed in the following section. In addition, for both empty and entrapped mercury samples, percolation analysis[104] was carried out using the overcondensation desorption isotherm and the conventional adsorption isotherm. The percolation analysis was carried out similar to the fresh catalyst pellets described in Chapter 3, assuming a pore bond lengths were inversely proportional to the pore diameter since this relationship gave the least variation of coefficient of determination for fits of experimental gas sorption data to generalised scaling function in percolation analysis.

5.3.9 Overcondensation

The overcondensation method allows the determination of the whole boundary desorption isotherm, which is not achievable with conventional adsorption. Figure 5.11a shows the conventional gas sorption data and the nitrogen overcondensation boundary desorption isotherms for empty reduced SD and RC samples and the same samples following mercury entrapment after intrusion to 3800 and 4400 psia. From the reduced SD and RC figure, it can also be seen that mercury entrapment has made the hysteresis loops slighter wider compared to the before mercury OC curves implying reduced pore connectivity due to mercury blockage. The OC desorption boundary curves for the empty samples display smaller, more rounded percolation knees compared to the post-mercury knees. This means the condensate in the pores for the empty samples starts to evaporate quicker than in the post-mercury samples. There are two types of desorption hysteresis mechanisms: pore blocking or cavitation. When the relative pressure is reduced, the saturated liquid in the biggest pores should usually evaporate first before progressing in declining size order. Desorption by cavitation (or spontaneous nucleation of a bubble in a pore) can occur in hierarchical porous materials if the pore throat diameter is less than a specific threshold size. In this case, the pore cavity can empty whilst the surrounding pore throats remain filled with liquid. It is possible that the larger pores within the empty samples are closer to the surface and are not effected by the pore-blocking mechanism. Additionally, for smaller random lattice networks, there are more chances of having big pores on the surface of the network by chance alone. This means they can prematurely desorb before a percolation pathway is formed or before the percolation threshold is reached.

[63] J. Rouquerol et al. *Pure Appl. Chem.*, **84**: 107–136, 2011.
[104] S. P. Rigby, M. J. Watt-Smith, and R. S. Fletcher. *J. Catal.*, **227**: 68–76, 2004.

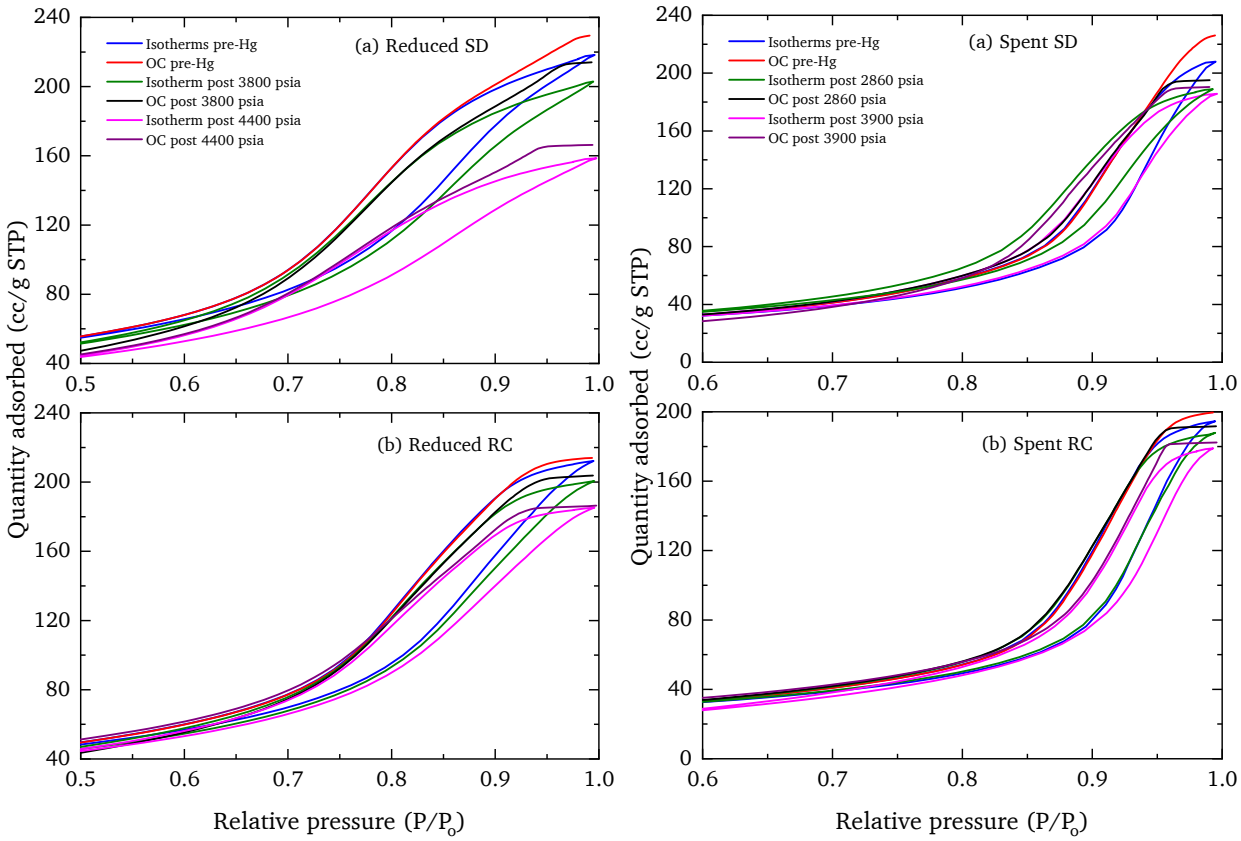


Figure 5.11: Hysteresis loop region of conventional sorption isotherms and overcondensation boundary desorption isotherms for empty samples, and the samples following mercury intrusion to up to different pressure. **(a)** Reduced SD and RC up to 3800 and 4400 psia, and **(b)** Spent SD and RC up to 2860 and 3900 psia.

On the other hand, the OC desorption curves for the post-mercury samples display a flat plateau at higher relative pressures and a sharper desorption knee that shifts towards lower relative pressure as more mercury is added to the sample. The flat plateau at high relative pressures indicates a complete pore filling during the OC experiment, and the sharp desorption knee indicates a pore-blocking effect. If small pores surround the bigger pores, no desorption will typically occur when the pressure is reduced because the surrounding narrow pores are still filled with liquid. This would allow the liquid in the bigger pores to become metastable and remain within the large pore cavities until the relative pressure is low enough to desorb the saturated liquid in the narrower pores, forming a connecting path from the pellet's centre to the surface. This type of behaviour is seen on the OC desorption branches for the reduced and spent sample post-mercury entrapment. This suggests that the larger macropore surrounding the smaller mesopores are filled with mercury, as seen on the X-ray images of the sample post mercury.

Seaton percolation analysis has also been performed on the overcondensation desorption isotherm, and Tables 5.3 to 5.4 show the corresponding data for the network model lattice and connectivity parameters obtained. From the tables, it can be seen that when mercury entrapment

increases at higher penetration pressures, the connectivity declines and the apparent lattice size increases for both the reduced and spent SD and RC pellets.

Figure 5.11b shows the conventional gas sorption data and the nitrogen overcondensation boundary desorption isotherms for empty spent SD and RC samples and the same samples following mercury entrapment after intrusion to 2860 and 3900 psia. From the spent SD and RC pellets, it can be seen that Gurvitch volumes are higher for the overcondensation data compared to the conventional isotherm data. However, the pore volume missing from the conventional isotherm is larger for the reduced pellets than for the spent pellets. Additionally, the spent SD and RC samples have much sharper percolation knees near the top of the hysteresis loop compared to the reduced samples. Furthermore, the overcondensation data for the reduced SD feed pellet still shows the second, more rounded, percolation knee at relative pressures of ~0.8-0.85, as seen in the fresh OC data. This second, more rounded percolation knee is not evident in the spent SD and RC or the reduced RC sample.

Table 5.3: Connectivity (Z) and lattice size (L) parameters from percolation analysis of gas sorption data for (a) Reduced SD pellet, (b) Reduced RC pellet following mercury intrusion to different stated pressures.

	(a) Reduced SD			**(b) Reduced RC**		
Sample	Empty pore Fraction (%)	Z	L	Empty pore Fraction (%)	Z	L
Pre-Hg	100.0	3.63	2.95	100.0	3.51	2.87
Post 3800 psia	91.5	3.05	4.21	94.6	2.98	4.9
Post 4400 psia	85.4	2.92	4.98	85.8	2.82	5.88

Table 5.4: Connectivity (Z) and lattice size (L) parameters from percolation analysis of gas sorption data for (a) Spent SD pellet, (b) Spent RC pellet following mercury intrusion to different stated pressures.

	(c) Spent SD			**(d) Spent RC**		
Sample	Empty pore Fraction (%)	Z	L	Empty pore Fraction (%)	Z	L
Pre-Hg	100.0	3.22	3.00	100.0	3.13	3.22
Post 2860 psia	88.1	3.05	4.62	90.4	3.01	4.52
Post 3900 psia	80.5	2.89	6.57	79.7	2.83	5.59

5.3.10 Pore Size Distribution

Figure 5.12(a)-(b) show the BJH PSDs of a sub-set of pores that become inaccessible from the exterior, for each stage in the series as the ultimate intrusion pressure is increased for progressively higher pressure porosimetry scanning curves for the reduced and spent samples. These pore size distribution (PSD) plot differences were created by subtracting PSDs from isotherms for samples collected after successive mercury scanning curves. In general, lower-pressure scanning curves fill large and medium pores, whereas higher-pressure scanning curves fill part of the remaining

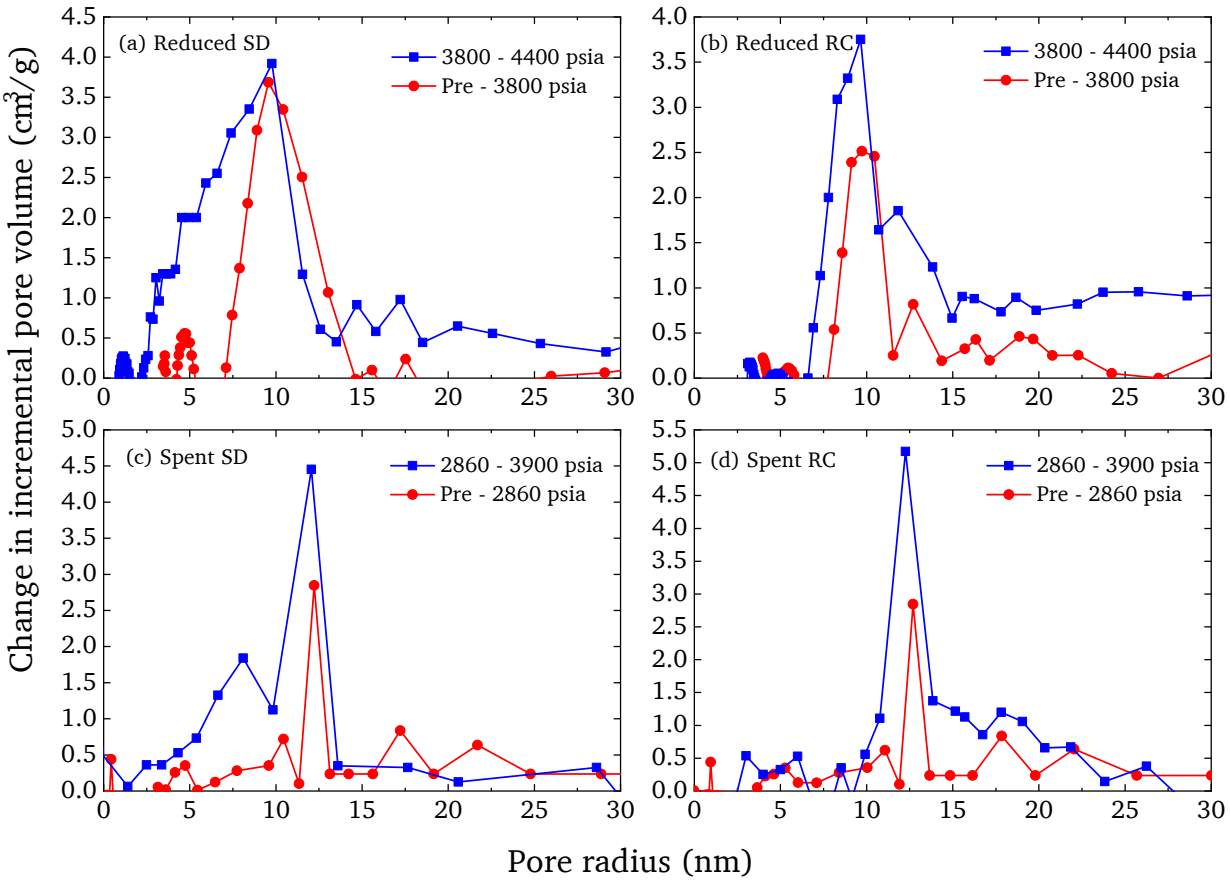


Figure 5.12: BJH pore size distributions for the sub-sets of pores that become inaccessible from the exterior as the mercury intrusion pressure is increased to progressively higher ultimate pressures (as indicated in legend) for each scanning curves. (a) Reduced SD, (b) Reduced RC, (c) Spent SD and (d) Spent RC.

medium and smaller pores. As a result, access to progressively smaller pores declines as the incursion pressure increases.

From the BJH difference PSDs in Figure 5.12, the position of the peak in the pore sizes being filled stays the same for reduced SD and RC feed pellets, and so the critical pore size for mass transport will remain the same. However, for the spent SD and RC samples, as mercury is entrapped over pressure intervals 2860-3900 psia, the position of the peak in the pore size being filled has shifted slightly to the smaller pores, and so the critical pore size for the mass transport will change.

5.3.11 Rate of Adsorption

The rate of adsorption of nitrogen at very low pressure was measured for empty reduced and spent pellets, and for pellets following mercury intrusion to various ultimate pressures. Mass transport properties can be characterised by kinetic gas uptake experiments. Kinetic mass uptake data, comprising amount adsorbed versus time, typically takes the mathematical form of an exponential

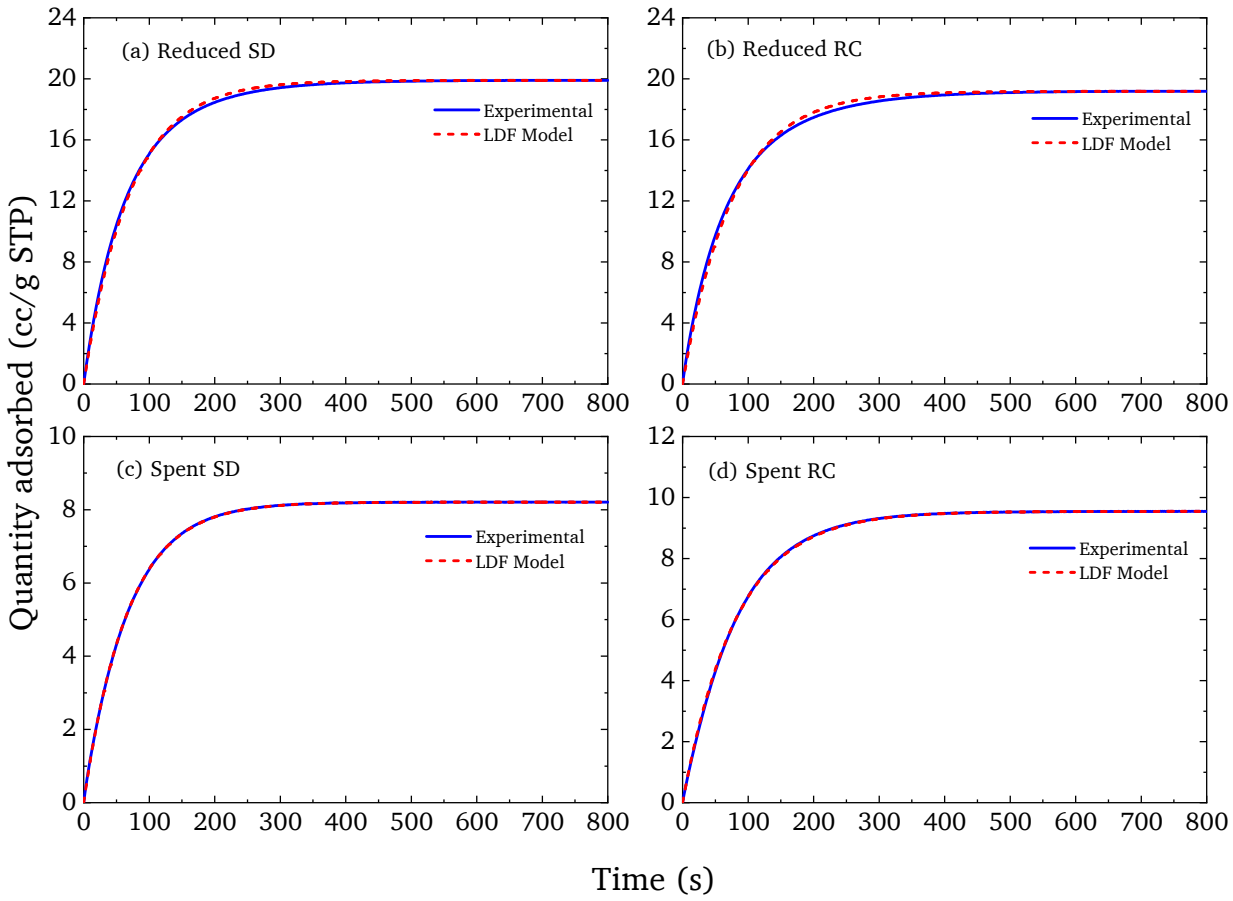
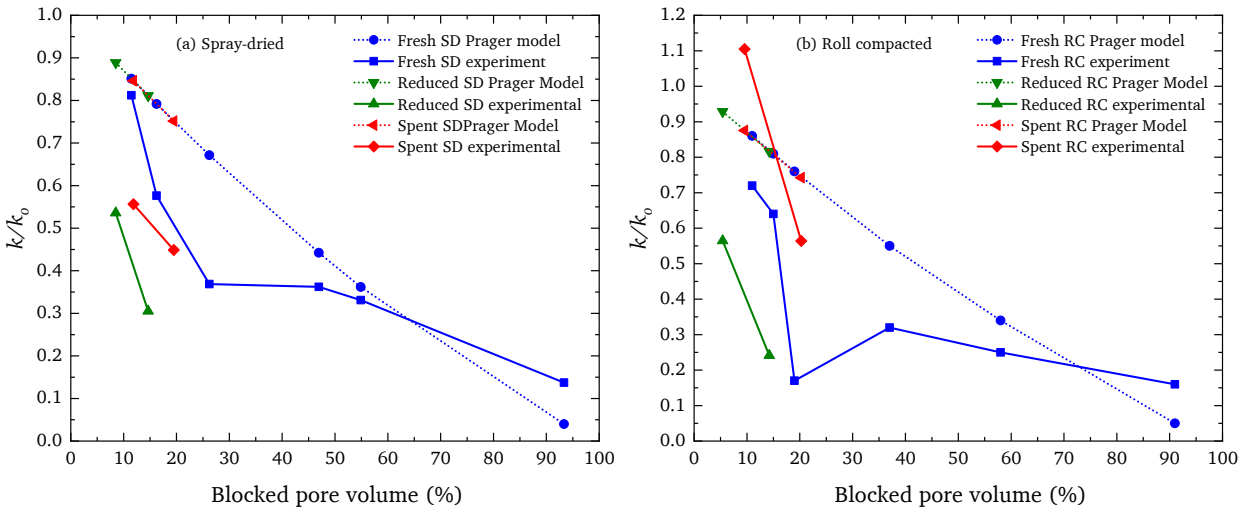


Figure 5.13: A comparison of the experimental nitrogen gas uptake data and the fits to the linear driving force (LDF) model for the empty reduced SD, reduced RC, Spent SD, and Spent RC pellets.

growth, and, thus, is often fitted to the so-called Linear Driving Force (LDF) model.[7] The LDF model is the simplest and most commonly applied intraparticle mass transfer model to calculate the effectiveness of a particular porous system.[7] Figure 5.13 shows examples of fits of the LDF to a typical set of experimental data for the empty reduced and spent SD and RC pellets. From the figures, it can be seen that the LDF gives a good fit to the experimental data with R^2 of >0.9952, and reaches equilibrium after 400 seconds. The best fits were obtained by changing the mass transfer coefficient until the 'sum of squared residuals' was as small as possible.

The gas uptake curves obtained for the reduced and spent pellets were fitted to the linear driving force (LDF) model, and the mass transfer coefficients (MTCs) (denoted k) were corrected for adsorption using the slope of the equilibrium isotherm at the point where the mass transport was measured.[7] Each MTC is expressed as a ratio to the MTC for the mercury-free sample (i.e. k_o). The MTCs so-obtained for reduced and spent pellets are shown in Tables 5.5 to 5.6, respectively. The tables also show the MTC expected for a completely random arrangement of entrapped mercury,

[7] S. P. Rigby. *Structural characterisation of natural and industrial porous materials: A manual*. Springer Nature, 2020.



(a) Spray-dried samples MTC change

(b) Roll-compacted samples MTC change

Figure 5.14: Comparisons of the observed fractional decline in the mass transfer coefficient (k/k_0) following mercury entrapment and that expected for a random arrangement of entrapped of pore liquid from Prager model for **(a)** Reduced SD feed, **(b)** Reduced RC feed, **(c)** Spent SD feed and **(d)** Spent RC feed pellets.

as predicted by the Prager model.[259]

As can be seen from Table 5.5, the MTCs generally decline following mercury entrapment for the reduced samples. However, for the spent SD sample, the MTC initially declines for the case with 11.9% of the pore volume filled with mercury but then drops significantly less than expected for the case with 19.5% of the pore volume filled with mercury. For the spent RC sample, the MTC following mercury intrusion up to 2860 psia, resulting in entrapment filling 9.6% of the pore space, is higher than the empty samples. The mass transfer coefficient is proportional to the D_e/a^2 for pure diffusion, where a is the effective characteristic particle size. If the core region of the sample was non-porous or encircled by an impermeable mercury boundary, as is the case for the spent RC sample, it is possible for the MTC to increase following mercury entrapment due to decreased effective characteristic particles size.

Figure 5.14 shows a comparison of the observed fractional drop in the MTC following mercury entrapment with that anticipated for the same mercury saturation from the Prager model. The figures compare the fresh, reduced and spent SD and RC sample, respectively. The variation of the MTC following mercury entrapment up to different pressures for the fresh samples has been discussed earlier in Chapter 3. From the spray-dried figure, Figure 5.14a, it can be seen that the observed MTC is significantly lower than would be predicted for a random arrangement of mercury for the reduced SD compared to the fresh SD for the same amount of mercury entrapment of ∼10% implying that in empty reduced SD samples, the pores that are subsequently filled with mercury must have made a greater-than-expected contribution to mass transfer compare to the empty fresh SD samples. Additionally, the observed MTC decline for spent SD samples with 11.9% of the void

[259]S. Prager. *J. Chem. Phys.*, **33**: 122–127, 1960.

volume filled with mercury is much lower than the fresh SD and that expected for a random arrangement of mercury as predicted by the Prager model, thereby suggesting that the pores filled with mercury must have been making a significant contribution to mass transport.

In contrast, the spent RC sample with 9.6% void volume filled with entrapped mercury display in Figure 5.14b, the observed MTC is larger than the fresh RC sample for the same amount of mercury entrapped (∼10%), and also for that expected for a random arrangement of mercury, suggesting that the pores filled with mercury are non-random and less important to the mass transport. In addition, a non-random arrangement may reduce the effective characteristic particle size. The figure also shows that the observed MTC for the reduced RC with 9.6% of the void volume of the pellet filled with mercury, the decline in the observed mtc was well predicted by the random Prager model, but the drop in the observed mtc was significantly lower than that of the fresh RC, suggesting that the pores filled with mercury in the reduced RC sample must be making a greater-than-expected contribution to the mass transfer compare to the fresh RC samples.

Table 5.5: Variation in adsorption-corrected MTC, for nitrogen at low pressure, with increasing mercury saturation for **(a)** Reduced SD, **(b)** Reduced RC.

(a) Reduced SD

MIP pressure (psia)	Minimum pore diameter penetrated (nm)	Fractional mercury saturation (%)	Experimental (k/ko)	Expected k/ko for random entrapment (Prager)
3800	56.7	8.5%	0.54	0.89
4400	49.0	14.6%	0.31	0.81

(b) Reduced RC

MIP pressure (psia)	Minimum pore diameter penetrated (nm)	Fractional mercury saturation (%)	Experimental (k/ko)	Expected k/ko for random entrapment (Prager)
3800	56.7	5.4%	0.56	0.93
4400	49.0	14.2%	0.24	0.82

Table 5.6: Variation in adsorption-corrected MTC, for nitrogen at low pressure, with increasing mercury saturation for **(a)** Spent SD and **(b)** Spent RC.

(a) Spent SD				
MIP pressure (psia)	Minimum pore diameter penetrated (nm)	Fractional mercury saturation (%)	Experimental (k/ko)	Expected k/ko for random entrapment (Prager)
2860	75.4	11.9%	0.56	0.85
3900	55.3	19.5%	0.45	0.75
(b) Spent RC				
MIP pressure (psia)	Minimum pore diameter penetrated (nm)	Fractional mercury saturation (%)	Experimental (k/ko)	Expected k/ko for random entrapment (Prager)
2860	75.4	9.6%	1.10	0.88
3900	55.3	20.3%	0.56	0.74

5.4 Discussion

The use of the CXT in conjunction with the rate of adsorption experiments after mercury entrapment allows for the identification of void space morphological characters that are important for mass transport. The rate of adsorption data for the reduced SD and RC, as well as the rate of adsorption data for spent SD pellets, revealed that the MTC decreased significantly less than what was expected according to the Prager model,[259] for a random distribution of mercury entrapped following intrusion to 3800, 4400, 2860, and 3900 psia. This shows that the pore spaces lost due to mercury entrapment following these intrusion pressures are critical for mass transfer since their loss resulted in a larger than predicted drop in MTC compared to the random benchmark structure. In contrast, the spent RC sample following mercury entrapment up to 2860 psia showed that MTC is larger than would be expected for a random arrangement of mercury, implying that the pores filled with mercury are less critical to the mass transport than they would have been if they were distributed more randomly. This would typically be seen if a substantial amount of mercury has been entrapped within the centre of the pellet to reduce the diffusive path length from the pellet surface.

The mass transfer coefficient is proportional to the D_e/a^2 for pure diffusion, where a is the effective characteristic particle size. The effective characteristic particle size refers to the maximum straight-line penetration depth that a molecule can access from the exterior rather than the actual tortuous route followed by the diffusive flux. If the core region of the sample was non-porous or encircled by an impermeable mercury boundary, as is the case for the spent RC sample, it is possible for the MTC to increase following mercury entrapment due to decreased effective characteristic particle size. Figure 5.15 shows a simple schematic representation of the relationship between the mass transport coefficient following mercury intrusion and the location of the entrapped mercury in the pellet. In the first case, mercury-filled pores are evenly distributed in the pellet, and it is

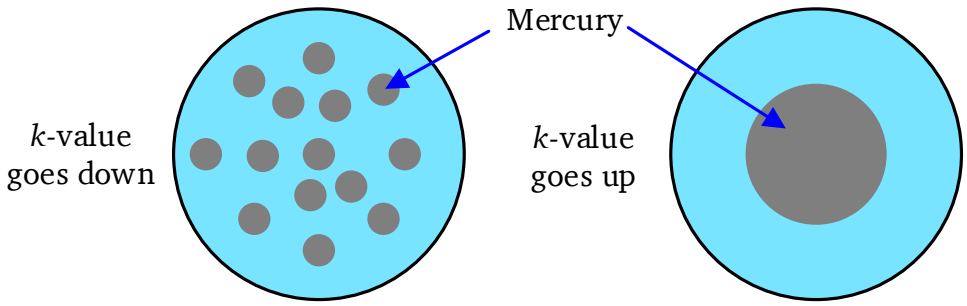
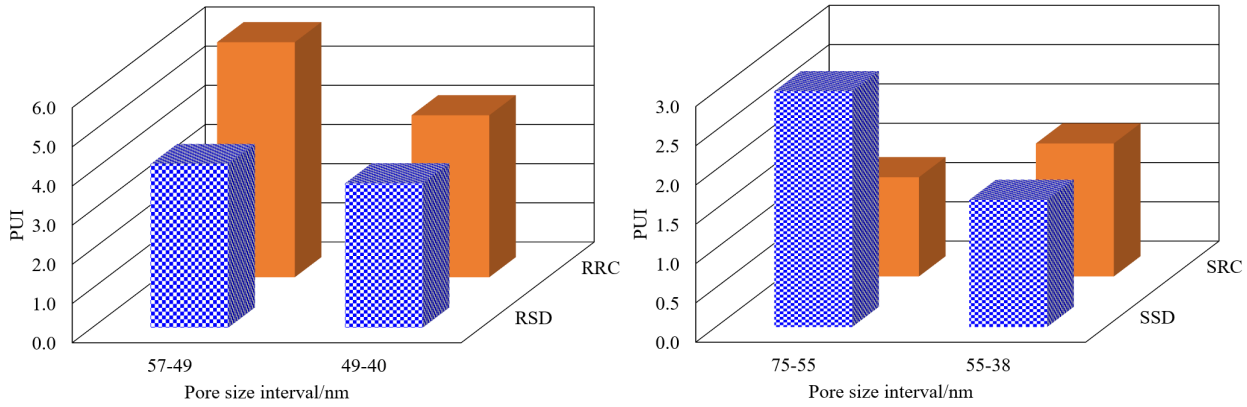


Figure 5.15: A schematic representation showing how the locations of entrapped mercury inside the pellet would affect the mass transport coefficient. The gray circles represents entrapped mercury and the light-blue shadings represents empty regions of the pellet where the gas is free to diffuse.



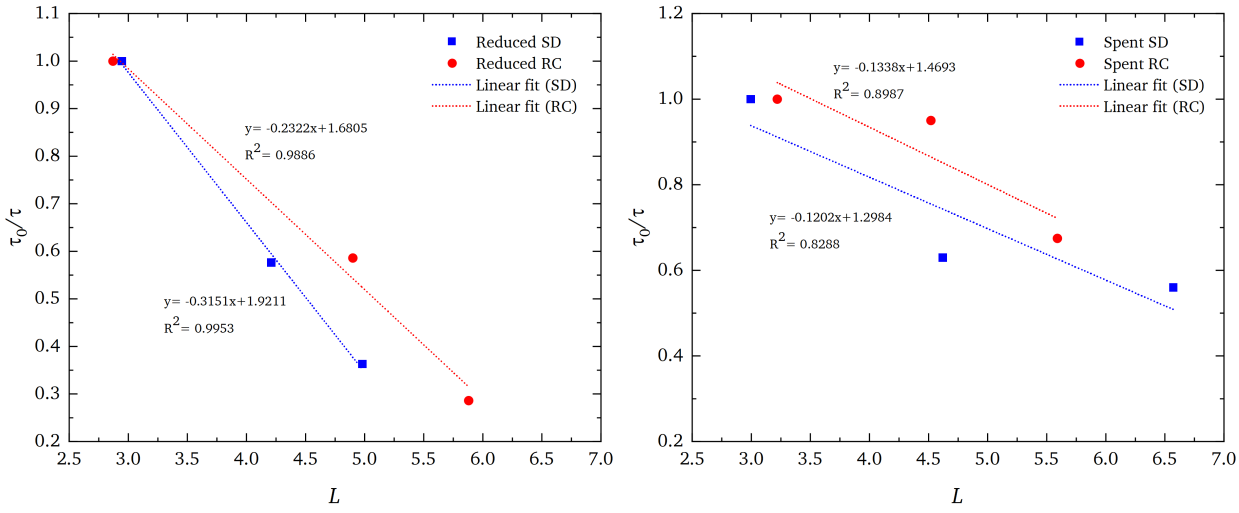
(a) Reduced SD and RC

(b) Spent SD and RC

Figure 5.16: Measures of usefulness, to mass transport in SD and RC feed pellets, of pore size intervals, as indicated by PUI for **(a)** Reduced SD and RC pellets, and **(b)** Spent SD and RC pellets.

expected that this type of mercury entrapment would decrease the mass transfer due to decreasing porosity and increased tortuosity. In the second type of pore spatial distribution, mass transfer is expected to go up after mercury entrapment due to the drop in the diffusive path length. From the CXT images of the spent RC sample following mercury intrusion up to 2860 psia, Figure 5.15, it can be seen that mercury fills in the large macropore network in the centre of the pellets, effectively, forming an impermeable core that is inaccessible from the exterior of the pellet. CXT image of the spent RC sample post-2860 psi confirms that the diffusive path length towards the centre has been reduced. This also leads to adsorption equilibrium being reached at a much quicker rate.

From the analysis of the rate of adsorption data for reduced and spent samples containing entrapped mercury, it can be seen that some particular pores are more critical to mass transfer than others. The usefulness of a given pore size interval to overall mass transport has been calculated by using the pore utility index (PUI), discussed in Chapter 3. The PUI calculated for the reduced and spent samples from the ROA data in Tables 5.5 to 5.6 are shown in Figure 5.16. From the figures, it can be seen that the first pore intervals (57-49 nm for reduced samples and 75-55 nm for spent SD) have the highest PUIs. However, for the spent RC sample, the second interval, 55-38 nm, has



(a) Reduced SD and RC

(b) Spent SD and RC

Figure 5.17: A plot of the tortuosity ratio against percolation lattice size following mercury entrapment to different intrusion pressures for **(a)** Reduced SD and RC pellets, and **(b)** Spent SD and RC pellets.

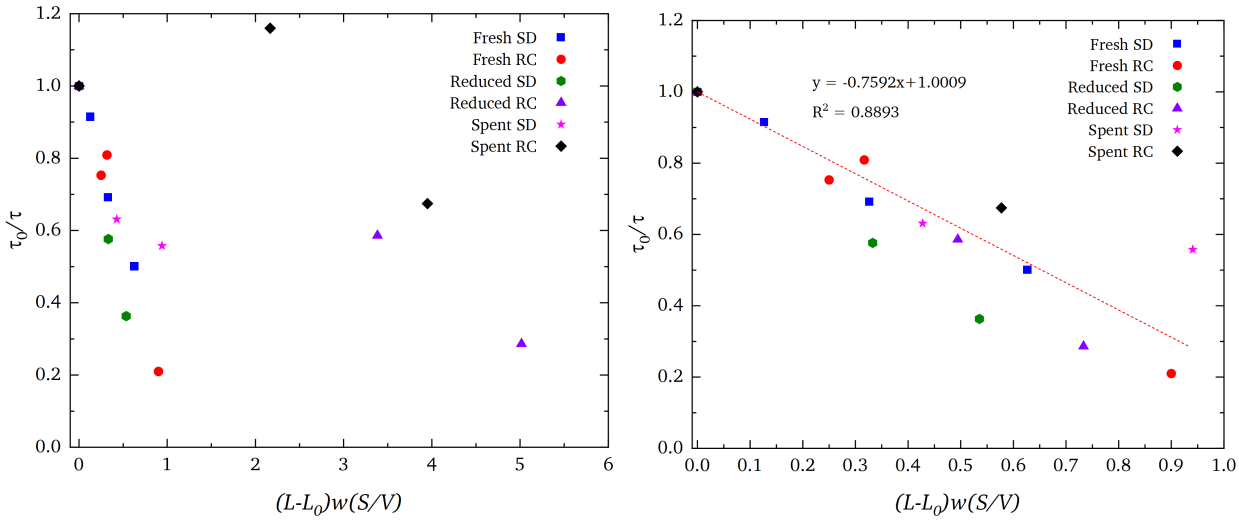
a higher PUI.

The macroscopic structure of the reduced and spent pellets can be modelled by a simple, 3D random pore bond network by using a similar analysis as the fresh catalyst pellets described in Chapter 3. The Random bond percolation modelling can capture key elements controlling mass transport and macroscopic heterogeneities in the pellet structure, as characterised by the percolation parameters. Using the Seaton[15] percolation method, the gas sorption data can be used as structural analysis to measure the connectivity and lattice size parameters for the real pellet. However, the lattice sizes are the most important parameter of the two as it measures how many surface pore clusters are found on the pellet. The surface clusters of big pores are the first set of pores that desorb nitrogen when the relative pressure is reversed. The prevalence of the surface clusters can be measured from the nitrogen overcondensation data for both before and after filling the pellet with mercury. The nitrogen overcondensation data could also be used to check how many surface clusters remain empty after mercury intrusion to different ultimate pressure and see what impact they have on mass transport. The random pore bond network model could then be used to predict the expected tortuosity change when the pellet is filled with mercury. A plot of the tortuosity changes against the lattice size, L, should be a linear function as predicted by Equation (5.1). This is indeed what is observed for the reduced and spent samples, as seen in Figure 5.17.

$$\frac{\tau_{a0}}{\tau_a} = 1 - \gamma\,(L - L_0)\,w\left(\frac{S}{V}\right)_t \tag{5.1}$$

The BJH difference PSDs in Figure 5.12 shows that as mercury is entrapped over the pressure intervals of pre-3800 and 3800-4400 psia for the reduced sample, pre-2860 and 2860-3900 psia for the spent samples, the position of the peak in the pore sizes being filled remains constant for

[15] N. A. Seaton. *Chem. Eng. Sci.*, **46**: 1895–1909, 1991.



(a) *w* value for RC = 1300 µm

(b) *w* value for RC = 195 µm

Figure 5.18: A plot comparing the experimental and predicted tortuosity changes for the fresh, reduced and spent methanol catalyst pellets. The pellet feed size, *w*, for the plot **(a)** uses a value of 1300 µm. The pellet feed size has been adjusted for plot **(b)** to superpose the reduced and spent RC pellets on the rest of the data. The new *w* value was found to be 195 µm.

both samples, and thus the critical pore size for mass transport remains constant. Figure 5.18 shows a universal plot for all the methanol (fresh, reduced and spent) pellets, which is obtained by using Equation (5.1) and the corresponding lattice size data. The feed particle sizes, *w*, for the fresh SD and RC methanol pellets were taken as 200 and 1300 µm, respectively, as seen reasonably from the corresponding CXT images. The experimental data for the fresh (SD and RC) samples and the reduced and spent SD samples gives an excellent fit to Equation (5.1), suggesting that the macroscopic structure of these pellets is well-represented by a random bond network percolation lattice using a w value mentioned above. However, the reduced RC and spent RC pellets are not well-represent by the random pore bond model when a w value of 1300 µm is used in Equation (5.1), as shown in Figure 5.18a. This is probably due to the wrong particle size, w, as the cracking creates new constituent feed particles by dividing the original feed particles into new, smaller feed particles. When the w value is reduced to ∼200 µm, the reduced and spent RC data superpose on the rest of the methanol data, as shown in Figure 5.18b.

This suggests that cracking seems to affect the roll compacted samples but does not impact the spray-dried samples as the size of the cracks are bigger than the spray-dried feed particles. The use of a new *w* value of ∼200 µm for the reduced RC and spent RC sample is supported by the CXT images of the reduced and spent RC sample, as can be seen in Figure 5.19, where the reduction processes produced significant cracking in the pellet structure, which seems to grow even more when the pellets are used in the reactors (aged material). The fracture network, in essence, fragments the pellet feed particles increasing porosity and accessibility. This also makes the reduced and spent pellets even more sensitive to smaller changes in the mercury intrusion pressure.

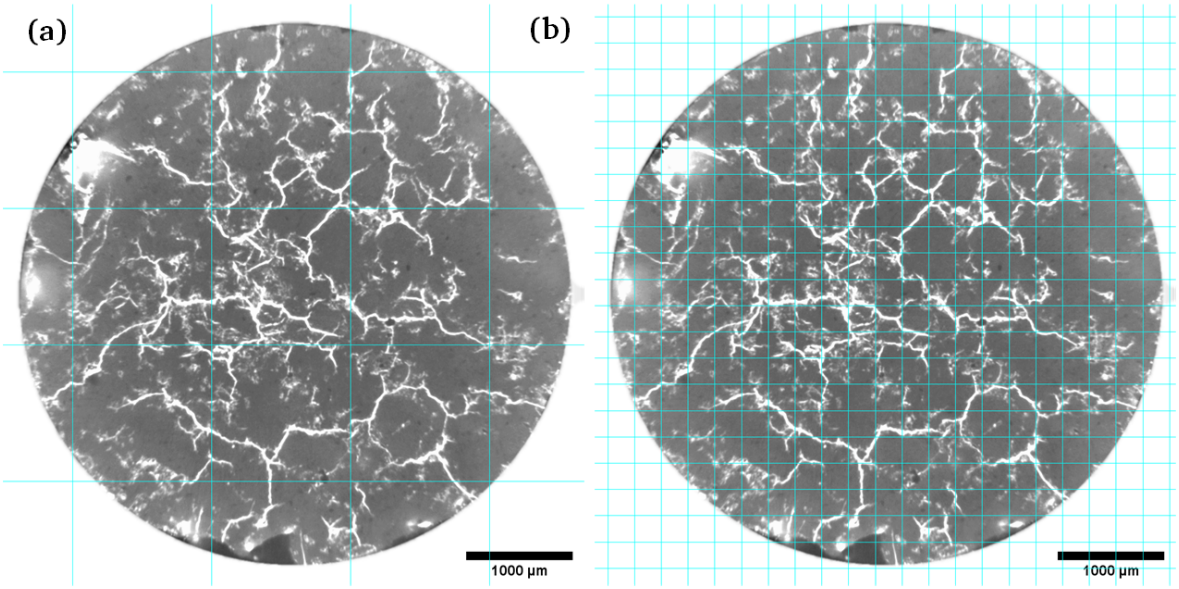


Figure 5.19: Spent roll compacted sample with mercury up to 2860 psia together with a grid of lines overlaid on the images. The grid length per square on each image is **(a)** 1300 um, and **(b)** 200 um.

5.5 Conclusion

This chapter presented the freshly reduced and spent methanol synthesis catalyst pellets made using spray-dried or roll compacted feed materials. It investigated how the various pellet fabrication methods affect the finished catalyst properties and the effects of the cracks on the pellet performance, diffusion and percolation processes. The integrated mercury porosimetry and nitrogen gas sorption, including rarely used overcondensation methods, was employed to expand the range of pore sizes that be examined up to very large macropores. Additionally, multi-modal imaging using low-resolution CXT and FIB-SEM was used to improve the interpretation of each other and that of the direct pore characterisation techniques. The impact on mass transfer of the controlled modifications to the void space, achieved through mercury porosimetry, was modelled with a random pore-bond network using characteristic parameters obtained from percolation analysis of the overcondensation data. It was found that a random pore-bond percolation model accurately captures the macroscopic structure of the reduced and spent SD pellets but not the reduced and spent RC pellets.

The following chapter will present a novel thermoporometry by the DSC method that uses three separate probe liquids to validate void-space characterisation obtained through indirect methods.

Chapter 6

Triangulation of Pore Structural Characterisation of Disordered Mesoporous Silica Using Novel Hybrid Methods Involving Dual-Probe Porosimetries

6.1 Abstract . . . 152
6.2 Introduction . . . 153
6.3 Theory . . . 157
6.4 Material and Methods . . . 160
6.5 Results . . . 164
6.6 Discussion . . . 176
6.7 Conclusion . . . 179

6.1 Abstract

The key issue, in applying indirect pore structure characterisation methods to disordered materials, is that usually some physical assumptions are necessary to probe pore size, such as concerning the mode of the phase transition used which determines meniscus geometry or kernel type. This issue often undermines the relative advantages of indirect methods, over direct methods like imaging, from both the wider range of pores sizes that can be probed in a single experiment and the much better statistical representativeness of the data, which are essential for highly heterogeneous disordered materials. This work introduces dual-liquid thermoporometry, and also dual-probe, serial water sorption and mercury intrusion, to complement multi-adsorbate, serial gas sorption, to overcome this issue by triangulating the data for three key probe molecules used in three different porosimetries, namely liquid intrusion, gas sorption, and thermoporometry. It has been found that augmenting one porosimetry, using just one probe molecule, to a dual-probe experiment removes the aforementioned, key drawback. The alternative, complementary dual-probe porosimetries can also cross-validate this approach for each other. This allows indirect methods to stand alone, without the need for direct imaging methods to inform or validate prior assumptions. Dual-liquid thermoporometry also allows the probing of the presence and nature of the advanced melting effect.

6.2 Introduction

A single method can never adequately shed light on a given natural phenomenon, and this is true for both direct and indirect pore structural characterisation methods. Indirect pore structural characterisation methods, such as mercury porosimetry, gas sorption, and thermoporometry, maintain many advantages over more direct methods, such as imaging.[7] Indirect methods can characterise a much broader range of pore sizes, from millimetres down to molecular scales, all in the same experiment, and quickly obtain data on nanoporosity for a more statistically-representative sample volume than the fields-of-view possible in all imaging modalities.[7] However, being indirect, the accuracy of void space descriptors obtained via these methods relies upon the validity of key parameters in the relationship between pore size and the relevant control variable, such as temperature in thermoporometry, and choices in the data analysis that reflect the basic geometry of the void space, such as pore shape. Further, the physical processes used for characterisation, such as capillary condensation in gas sorption, are more complex in disordered, amorphous materials than they are in templated, model materials, such as high-quality MCM-41 or SBA-15, with much simpler void space geometries.[7] In disordered networks, pore-to-pore co-operative processes, such as advanced condensation or advanced melting, can occur, and complicate data analysis. Hence, there is a need for experimental and data analysis procedures to address these issues. This chapter will present a triangulation procedure, involving three different probes, nitrogen, water and mercury, to validate pore space characterisations from different indirect methods.

Previous work has shown that the key parameters in the master equations relating control variables to pore sizes, such as the Gibbs-Thomson constant (K_{GT}) in thermoporometry, obtained from purported calibrations using model templated porous solids give rise to different values, depending upon the particular type of model, controlled pore size material used. For example, Gunko et al.[312] suggested K_{GT} for melting of water in silica pores was 67 $\mathrm{K\,\mu m}$, whereas Findenegg et al.[213] suggested it was 52 $\mathrm{K\,\mu m}$. A related issue is that indirect methods require an assumption of pore geometry, which implicitly makes assumptions about the meniscus geometry for the vapour/liquid or liquid/solid boundaries where one phase expands at the expense of the other during characterisation experiments. However, in the aforementioned case, the discrepancy (of $\sim$30%) in Gibbs-Thomson constant cannot be simply explained by suggesting melting occurs radially via a hemispherical meniscus in one case, but axially via a cylindrical sleeve meniscus in another, since then that difference in K_{GT} would be expected to be a factor of 2.[225,313,314] This discrepancy suggests that the calibration based upon model templated materials is not always generalisable, and, thence, must be performed each time for the exact material under test, including for difficult disordered materials. While an electron micrograph may reveal the particular pore geometry, even for micropores, for a small region of sample void space, this may not be representative of the whole sample volume, or of different pore sizes. The mode of phase transition,

[7] S. P. Rigby. *Structural characterisation of natural and industrial porous materials: A manual*. Springer Nature, 2020.
[312] V. Gun'ko et al. *Cent. Eur. J. Chem.*, **5**: 420–454, 2007.
[213] A. Schreiber, I. Ketelsen, and H. Findenegg. *Phys. Chem. Chem. Phys.*, **3**: 1185–1195, 2001.
[225] E. Perkins et al. *Chem. Eng. Sci.*, **63**: 1929–1940, 2008.
[313] O. Petrov and I. Furó. *Phys. Rev. E.*, **73**: 011608, 2006.
[314] I. Hitchcock et al. *Chem. Eng. Sci.*, **66**: 582–592, 2011.

relating to meniscus geometry for simple pore shapes, must be determined via a more generally applicable way.

Additional effects, other than single pore phenomena, occur during the phase transitions employed for indirect structural characterisation of disordered pore networks. While this adds to the complexity of data interpretation these additional effects can be used to obtain extra information about pore spaces. From a study using scanning curves, Everett[10] showed that gas desorption from disordered porous solids can involve a pore-to-pore co-operative effect known as 'pore-blocking' (or pore-shielding or pore shadowing), which has since widely been employed, together with percolation theory, to determine pore network connectivity.[15,315,316] While Gregg and Sing[8] explained why adsorption is not similarly affected by pore-blocking, it is affected by two other pore-to-pore co-operative effects, namely advanced condensation and (network) delayed condensation.[7,99]

The effect, now variously known as advanced condensation, advanced adsorption, or the cascade effect, was first published upon by de Boer.[317] The simplest operation of these effects occurs for a through ink-bottle pore geometry consisting of two relatively narrow cylindrical pore necks either side of, and co-axial with, a larger cylindrical pore body. In gas adsorption, capillary condensation in such a system is initiated in the pore necks via a cylindrical sleeve meniscus, which then completes a hemispherical meniscus at both ends of the pore body. If the diameter of the pore body is less than twice that of the pore necks, then the gas pressure needed to fill the necks also exceeds that to fill the pore body with condensate via axial expansion of the hemispherical menisci. Hence, necks and body will fill simultaneously at the same pressure. If the pore body diameter exceeds twice that of the neck, while the pore body does not fill at the same pressure as the necks, the pressure needed to fill it is then still lower than for if the pore body were part of a parallel pore bundle (a 'wine rack-type' structure). This bundle is the standard pore space model, for pore size distribution (PSD) derivation by gas sorption, used by both classical and DFT-based approaches.[9] Hence, PSDs for disordered materials obtained by standard methods are likely to be inaccurately skewed towards smaller pores.[7] It has also been found[110] that the width of single-pore hysteresis in gas sorption for cylindrical pores does not match the predictions of either the Cohan[55] equations or of non-local density functional theory (NLDFT).[250] This is an empirical indication that additional effects are at work than encompassed by these theories. The detection of the presence and extent of advanced adsorption effects is essential to obtain accurate PSDs, and this has been done in the past using NMR methods.[318]

[10] S. Lowell et al. *Characterization of porous solids and powders: surface area, pore size, and density.* Springer, 2005.
[15] N. A. Seaton. *Chem. Eng. Sci.*, **46**: 1895–1909, 1991.
[315] G. Mason. *J. Colloid Interface Sci.*, **95**: 277–278, 1983.
[316] M. Parlar and Y. Yortsos. *J. Colloid Interface Sci.*, **124**: 162–176, 1988.
[8] S. J. Gregg and K. S. Sing. *Adsorption, surface area and porosity.* 2nd. Academic Press, London, 1982.
[99] S. P. Rigby. *JM Techno. Review*, **62**: 296–312, 2018.
[317] J. H. De Boer and B. C. Lippens. *J. Catal.*, **3**: 38–43, 1964.
[9] F. Rouquerol et al. *Adsorption by powders and porous solids.* Academic Press, London, 1999.
[110] I. Hitchcock et al. *J. Phys. Chem. A.*, **118**: 20627–20638, 2014.
[55] L. H. Cohan. *J. Am. Chem. Soc.*, **60**: 433–435, 1938.
[250] A. V Neimark and P. Ravikovitch. *Microporous Mesoporous Mater.*, **44**: 697–707, 2001.
[318] I. Hitchcock et al. *Langmuir*, **26**: 18061–18070, 2010.

An analogous effect to advanced adsorption, known as advanced melting, has been proposed to occur in thermo-/cryo-porometry.[314] In a through ink-bottle pore full of probe fluid, the melting of solidified probe fluid within the pore necks occurs at the temperature required for the radial expansion of the cylindrical sleeve-shaped non-freezing layer, left at the pore-matrix interface, toward the centreline of the necks.[313] On completion, this then creates full hemispherical menisci between liquid and solid at both ends of the pore body. Melting can then occur at the same temperature in the pore body by axial advancement of these solid-liquid menisci if the pore body diameter is less than twice the pore neck diameter. The advanced melting effect has been observed in a range of disordered materials, including mesoporous catalysts[314] and cements.[319]

While, as mentioned above, the pore-to-pore co-operative effects in disordered networks potentially complicate data analysis and interpretation, their idiosyncratic features mean that their impact can be potentially deconvolved with the right datasets.[7,99] For example, while advanced adsorption and melting only conceals the presence of pore bodies for body sizes up to twice that of the neck (according to classical theory like the Kelvin equation), the pore-blocking effect can conceal pore bodies of any size behind the neck. Further, while advanced adsorption or advanced melting can occur in any direction, including inwards, the pore-blocking effect only acts in the direction of the percolation path to the exterior.

The aforementioned issues with gas sorption, mercury porosimetry and thermoporometry for amorphous materials, namely calibration, pore geometry, and pore-to-pore co-operative effects, only present problems with the conventional experiments as conducted with these techniques.[7,99] These conventional experiments are only run in parallel and typically only produce boundary adsorption/desorption isotherms, or boundary melting/freezing curves, or boundary intrusion or extrusion curves, for samples empty of anything but a single probe fluid. However, it is possible to combine these different techniques into hybridised methods consisting of serial experiments with different probes run on the same sample with little or no intermediate sample preparative treatment.[7,99] In this manner, the void space under test is modified in a controlled way, and this changes the results of applying a given technique with a particular probe fluid, and this change can elucidate the mechanisms involved in both the modification and probe processes. In this work we have greatly expanded the repertoire of hybrid methods run on the same sample and material from previous studies.[7,99] We have conducted novel thermoporometry experiments with multiple, immiscible probe liquids within the same sample. In addition, we have conducted the serial adsorption of water before mercury porosimetry, where the adsorbed water was retained during porosimetry, and then nitrogen adsorption afterwards on the same sample by freezing the pre-adsorbed water and entrapped mercury in-place. These have been augmented with serial adsorption of first nitrogen, second water, then nitrogen, and integrated nitrogen sorption and mercury porosimetry.[89] The hybrid experiments force the confrontation of the data from different techniques for the same sample, and enable parameter calibration and appropriate phase transition mode selection, even for amorphous solids.

[319] M. Wu et al. *Thermochim. Acta*, **665**: 11–19, 2018.
[89] S. Rigby, R. Fletcher, and S. Riley. *Chem. Eng. Sci.*, **59**: 41–51, 2004.

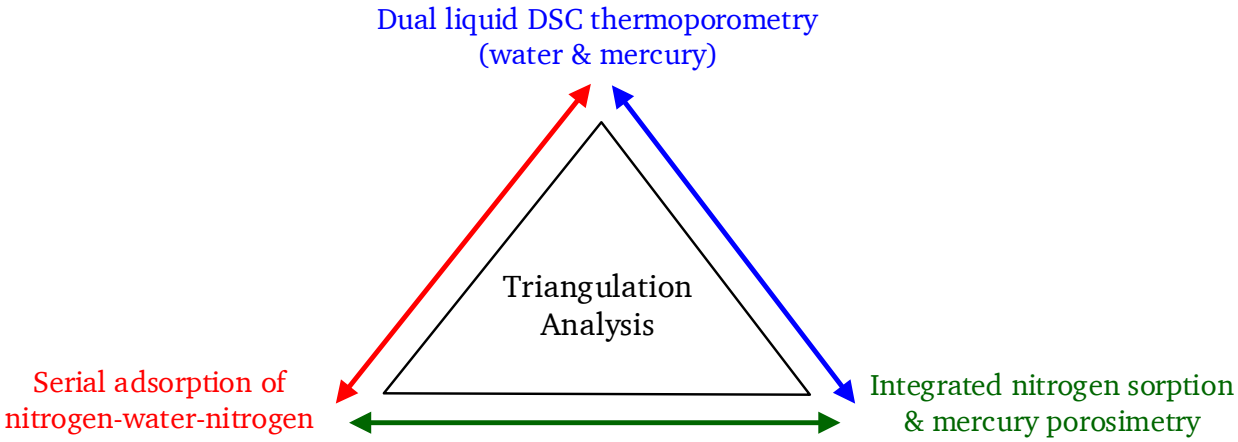


Figure 6.1: Schematic diagram illustrating the triangulation strategy adopted in this work.

Thermoporometry (or cryoporometry) with two different liquids has been performed previously but with the aim of studying the progress of liquid-liquid displacement or separation of miscible binary mixture components.[320–322] These studies focussed simply on the apparent relative pore sizes occupied by each of the two liquids involved, and, thus, did not consider the details of the phase transitions in the two liquids. In this work the mode of the phase transition in each liquid, and any interactions, will be considered in much more detail.

The new methods described here are trialled in a case study of a disordered, mesoporous, sol-gel silica material. Single-probe thermoporometry and gas sorption have been extensively used, in a solely parallel fashion, for pore structure characterisation of silica gel materials.[213,312,323,324] However, here, dual-liquid (water plus mercury) thermoporometry, serial water adsorption-and-mercury-porosimetry, serial nitrogen-and-water sorption, and integrated nitrogen sorption-and-mercury-porosimetry experiments were all conducted on the sol-gel silica material. The data from all these experiments were then analysed synergistically. This is shown schematically in Figure 6.1. Figure 6.1 shows the three probes used to triangulate findings, and the various hybrid experiments which use each probe. Given water is used as one of the three key probes in this work, it is important to properly understand its mode of adsorption in the type of material under study. Water sorption has the advantage that it can be used without extensive pre-drying for already partially water wet samples like cement pastes.[325] While water vapour sorption is widely used for pore structure characterisation of disordered materials,[325] the particular mode of water adsorption is sometimes suggested[8] to be as localised ganglia, rather than as a more pervasive multi-layer, on silicas. Hence, the structure of the adsorbed water film will be studied in detail using serial nitrogen adsorption.

[320] R. Valiullin and I. Furó. *Phys. Rev. E.*, **66**: 031508, 2002.
[321] R. Valiullin and I. Furó. *J. Chem. Phys.*, **116**: 1072–1076, 2002.
[322] J Mitchell, SC Stark, and JH Strange. *J. Phys. D: Appl. Phys*, **38**: 1950, 2005.
[323] K. Ishikiriyama, M. Todoki, and K. Motomura. *J. Colloid Interface Sci.*, **171**: 92–102, 1995.
[324] K. Ishikiriyama, M. Todoki, and K. Motomura. *J. Colloid Interface Sci.*, **171**: 103–111, 1995.
[325] M. Wu, B. Johannesson, and M. Geiker. *Constr. Build. Mater.*, **66**: 621–633, 2014.

6.3 Theory

6.3.1 Gas Sorption

6.3.2 Adsorbed Films on Fractally Rough Surfaces

The surface of amorphous silicas is known to be fractally rough.[326] The surface area A of an adsorbed film of general thickness z is related to the volume V of that film by[327]:

$$A(z) = \frac{dV}{dz} \tag{6.1}$$

In the special case where the surface of the solid is fractal, with surface fractal dimension D, then, $V(z)$ is proportional to z^{3-D} and therefore $A(z)$ is proportional to z^{2-D} by Equation (6.2). Hence, by eliminating z from these relations for V and A, then:

$$A \propto V^{(2-D)/(3-D)} \tag{6.2}$$

Hence, the film area on a fractal surface (D>2) will decrease with increasing film volume (and increasing z) as the film smooths out the roughness of the solid surface. Further, since the film itself and the residual pore volume, exterior to the film, share a mutual boundary, then the surface area of the residual pore space will correspondingly decrease with decreasing residual pore volume. Hence, the residual pore volume might be expected to follow a reciprocal relationship to Equation (6.2).

6.3.3 Capillary Condensation

Capillary condensation of the probe gas in isolated cylindrical meso-and macro-pores is predicted by the Kelvin equation[8,9]:

$$\ln\left(\frac{P}{P_0}\right) = -\frac{k\gamma V_M \cos\theta}{RT\,(r_p - t)} = \frac{-kF}{(r_p - t)} \tag{6.3}$$

where P/P_0 is the relative pressure at which capillary condensation occurs in a cylindrical pore of radius r_p, t is the multilayer film thickness, k is a geometrical parameter dependant on the pore and meniscus type (for adsorption within a cylindrical pore open at both ends $k = 1$; and for adsorption within a pore with one dead end, or for desorption from a hemi-spherical meniscus, $k = 2$), γ is the surface tension, V_m is the molar volume of the condensed adsorbed phase, θ is the contact angle with which the condensate meets the wall, and T is the absolute temperature. F is a property factor. The contact angle is generally assumed to be zero for wetting adsorbates. The two forms of the Kelvin equation, with different types of meniscus geometry on adsorption, are known as the Cohan[55] equations. The term $\gamma V_M/RT$ for nitrogen (component 1) at 77 K is 0.48 nm, while that for water (component 2) at 293 K is 0.54 nm. Hence, for adsorption in the same

[326] M. J. Watt-Smith, K. J. Edler, and S. P. Rigby. *Langmuir*, **21**: 2281–2292, 2005.
[327] P. Pfeifer et al. *Langmuir*, **7**: 2833–2843, 1991.

pore geometry the relative pressures for two different adsorbates are related by:

$$\ln\left(\frac{P}{P_0}\right)_1 = \frac{F_1}{F_2}\ln\left(\frac{P}{P_0}\right)_2 \tag{6.4}$$

For calculating the nitrogen pore size distributions (PSDs) used here, the Barrett-Joyner-Halenda[44] algorithm and the Harkins-Jura[42] *t*-layer equation were used.

6.3.4 Thermoporometry

Petrov and Furo[313] attributed freezing-melting hysteresis in cryoporometry to a free energy barrier between metastable and stable states of pore filling material. In a phenomenological description, these workers showed that freezing point depression is given by:

$$\Delta T_f \cong -\frac{v\gamma_{sl}T^0}{\Delta H}\frac{S}{V} \tag{6.5}$$

while the melting point depression is given by:

$$\Delta T_m \cong -\frac{v\gamma_{sl}T^0}{\Delta H}\frac{\partial S}{\partial V} \tag{6.6}$$

where v is the molar volume, γ_{sl} is the surface free energy, T^0 is the bulk melting point, ΔH is the latent heat of melting, S is the surface area of the pore and V is the volume of the pore. Using Steiner's formula for equidistant surfaces, Petrov and Furo[313] showed that Equation (6.6) can be rewritten as:

$$\Delta T_m \cong -\frac{v\gamma_{sl}T^0}{\Delta H}2\kappa = \Delta T_f\frac{2\kappa V}{S} = \frac{K_{GT}}{(d-2t)} \tag{6.7}$$

where κ is the integral mean curvature of the pore surface for a cylindrical pore of diameter d. $2\kappa V/S = 1/2$, and, hence, the numerical difference in ΔT_m and ΔT_f can be used to determine whether a pore has an open cylindrical geometry. Implicit in Equation (6.7), is the conception that, upon freezing, liquid solidifies in an axial direction initiated from the end where the liquid is in contact with bulk solid, while melting commences at the liquid film at the pore surface and propagates radially from the surface toward the pore bulk. However, for a dead-end cylindrical pore, melting can occur axially, since it would then be initiated from the hemispherical meniscus at the closed end of the pore. Similarly melting can be initiated from a hemispherical meniscus located at the interface between frozen and molten phases within co-axial, adjoining cylindrical pores of differing diameters.[7]

The non-freezing *t*-layer thickness was assumed to be a molecular monolayer. Given the modal size ($\sim$10 µm, so $\sim$33 times the size of 1 water molecule) of the pores of the material studied here, the variation in the *t*-layer thickness (with temperature and/or pore size) in thermoporometry ob-

[44] E. P. Barrett, L. G. Joyner, and P. P. Halenda. *J. Am. Chem. Soc.*, **73**: 373–380, 1951.
[42] W. Harkins and G. Jura. *J. Am. Chem. Soc.*, **66**: 1362–1366, 1944.

served in the literature[323] is much smaller than the impact of an axial versus radial mode for the phase transition. Similarly, the impact of the variation in supercooled water and ice densities, interfacial tension, and latent heats, with temperature are small;[323] compared to the phase transition mode effect.

6.3.5 Small Angle X-ray Scattering (SAXS)

The intensity of X-ray radiation scattered by a fractal surface is known to be proportional to a negative power of the q vector, such that[7,326]:

$$I(q) \propto q^{-\eta} \tag{6.8}$$

where $q = 4\pi\lambda^{-1}\sin(\varphi/2)$, λ is the wavelength of the radiation, and φ is the scattering angle. Normally this behaviour is only observed if q satisfies the inequality $\xi >> 1$ where ξ is the characteristic length-scale for the structure creating the scattering. From the value of η, the fractal nature of the system under investigation can be determined.[7,326] If the exponent is in the range $1<\eta<3$, then it describes the mass fractal of dimension $(D_m)_{\text{SAXS}}=\eta$, but if in the range $3<\eta<4$ then it describes surface fractals of dimension $(D_S)_{\text{SAXS}}=6-\eta$. For $\eta=4$, Equation (6.8) leads to Porod's law, where $(D_S)_{\text{SAXS}}=2$ and the surface is flat.

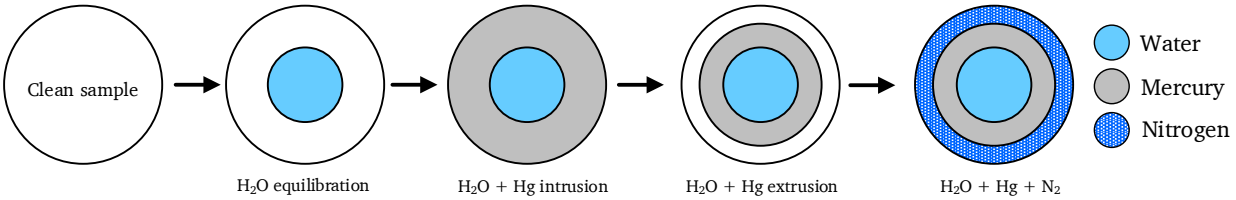


Figure 6.2: A schematic representation of the serial water pre-adsorption, mercury porosimetry and nitrogen adsorption experiment.

6.4 Material and Methods

6.4.1 Silica Materials

The sample studied in this work is a commercially-available, spherical, silica catalyst support, denoted G1, made by the sol-gel method. The sol-gel silica spheres have particle sizes in the range 2-7 mm, with the most common size being $\sim$3-4 mm.

6.4.2 Serial Water Pre-adsorption, Mercury Porosimetry, and Nitrogen Adsorption

The samples were heated to $90\,^{\circ}\mathrm{C}$ at $10\,^{\circ}\mathrm{C/min}$ and held for 60 minutes once the pressure had reduced to 100 mmHg. The temperature was then increased to $350\,^{\circ}\mathrm{C}$ at $10\,^{\circ}\mathrm{C/min}$ and the samples held under vacuum for 16 hrs. The samples were then cooled under vacuum and backfilled with dry nitrogen. Aliquots of the sample were then exposed to a water relative pressure of 0.85 using a saturated solution of potassium chloride. The samples were placed on a watch glass in a single layer next to a beaker of the saturated solution and enclosed within a small, sealed container for eight days. The watch glass was stored in an oven, and the oven temperature was kept at $20\,^{\circ}\mathrm{C}$. The samples were weighed before and after exposure.

Mercury intrusion/extrusion curves were measured on a Micromeritics AutoPore 9600 porosimeter between 0.0014 and 414 MPa for the intrusion followed by extrusion to 0.1034 MPa. Studies showed that, for samples containing pre-adsorbed water, an equilibration interval of 60 seconds was optimum. A prerequisite for a conventional mercury porosimetry experiment is for the sample to be dried to completely remove any adventitiously adsorbed species. The porosimeter evacuates the sample to less than 25 $\mu\mathrm{mHg}$ to facilitate filling of the sample cell with Hg prior to intrusion. For the samples containing pre-adsorbed water it was found that the evacuation stage would slow considerably and steady out at about 800 $\mu\mathrm{mHg}$. At this point the pre-adsorbed water is being slowly removed which is defeating the object of the study. For all runs using samples containing pre-adsorbed water the evacuation step was halted at 1000 $\mu\mathrm{mHg}$. This pressure ensured water was not removed from the sample porosity and still allowed the sample cell to fill correctly with mercury. Weight loss of the moisture equilibrated sample at 1000 $\mu\mathrm{mHg}$ was less than 1%. It is noted that water is considerably more wetting of the silica surfaces than mercury. Indeed, immersion of a silica-gel sphere containing entrapped mercury into a water bath leads to water displacing the mercury completely from the pores and out into the water bath.

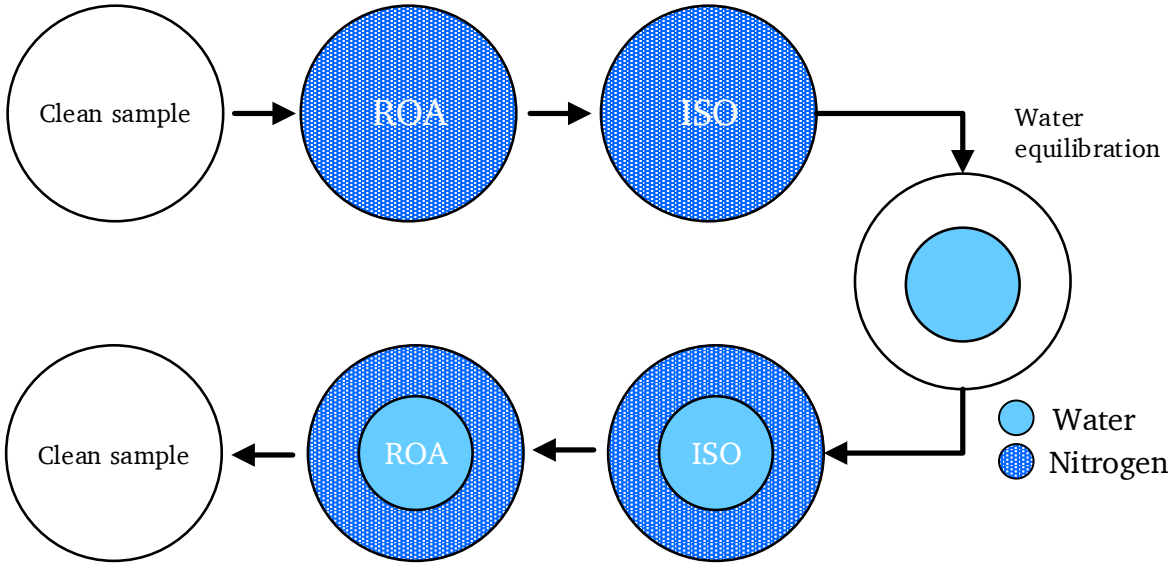


Figure 6.3: A schematic representation of the integrated nitrogen-water-nitrogen technique. ISO = isotherm,and ROA = rate of adsorption (not considered here).

Nitrogen adsorption-desorption isotherms were measured at liquid nitrogen temperature on a Micromeritics ASAP2420 physisorption analyser over the relative pressure range of 0.005 to 0.995 for adsorption and back down to 0.005 on the desorption. To measure the isotherms for samples containing pre-adsorbed water and post mercury porosimetry, the liquid nitrogen dewars were raised around the samples for 30 minutes to freeze the liquids inside the pores before opening the sample port to vacuum. Once the samples were fully evacuated the analysis was initiated. Backfilling of the sample at the start of the analysis was omitted, as was the lowering of the dewar post free space analysis, to prevent the samples warming and thawing the frozen water and/or mercury. This is a departure from normal operation. An equilibration interval of 60 seconds was used rather than the typical value of 10 seconds for a fully outgassed mesoporous material. Figure 6.2 shows the schematic representation of the serial water pre-adsorption, mercury porosimetry and nitrogen adsorption experiment.

6.4.3 Serial Adsorption of Nitrogen-Water-Nitrogen

The integrated water and nitrogen technique consists of a series of experiments conducted on the same sample. Figure 6.3 shows the schematic representation of the nitrogen-water-nitrogen procedure used during the experiments. The nitrogen sorption isotherms were measured at liquid nitrogen temperature (77 K) using a Micromeritics 3Flex physisorption analyser. Approximately 0.1 g of the sample was weighed and placed into a pre-weighed standard physisorption sample tube with a sealing frit placed at the top to prevent the sample from being evacuated into the 3Flex manifold. The tube (with sample) was then loaded into the degassing station and initially degassed at room temperature until a vacuum of 0.002 mmHg was reached. The sample temperature was then raised to 110 °C by using a heating mantle, and the sample was left under

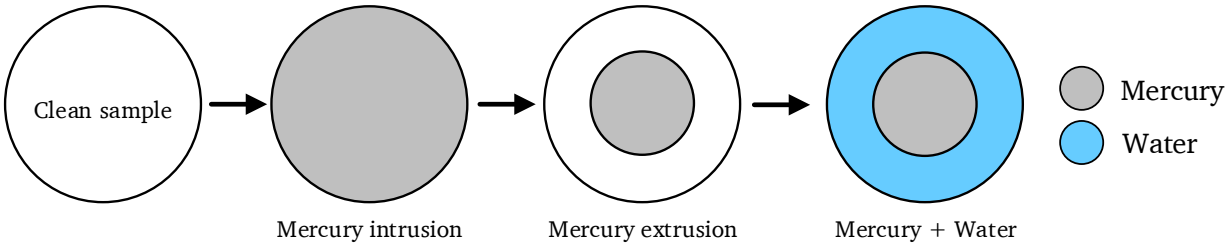


Figure 6.4: A schematic representation showing the dual-liquid DSC thermoporometry procedure.

vacuum for 24 hours. The thermal pre-treatment drives off any physisorbed water on the sample but does not change the sample morphology. After the 24 hours had passed, the heating mantle was removed, and the sample was allowed to cool down to room temperature. The sample tube and its contents were then re-weighed to obtain the dry weight of the sample. Isothermal jackets were then placed around the sample tubes before reattaching to the analysis port to begin the automated gas sorption analysis. The isothermal jacket ensures a constant thermal profile of 77 K along the length of the sample tube during the analysis stage. Nitrogen purity was 99.995%. Gas sorption was measured over the relative pressure (P/P_0) range of 0.01 to 0.995 for adsorption isotherm and 0.995 to 0.10 for desorption isotherm. The saturation pressure (P_0) was measured for each data point on the isotherm.

Once the first nitrogen gas sorption experiment was finished, the samples were allowed to reach room temperature ($\sim$295.15 K) and then suspended over a sodium hydroxide solution with a varying concentration for up to $\sim$7 days.

Once the water equilibration experiment was finished, the sample was immediately weighed and returned to the 3Flex sample tube, where the rate of adsorption and the conventional adsorption experiments were repeated. The sample was first cooled to 77 K by manually raising the Dewar flask, allowing the sample to freeze for approximately 30 minutes. This part was important in the post water entrapment steps since it freezes the water in-place to ensure that it all remains immobilised within the pellets. The integrated rate of adsorption-water aims to selectively block specific pore sizes and then study how important those pores were to the rate of mass transport before and after their removal.

6.4.4 Dual Liquid DSC Thermoporometry using Water and Mercury

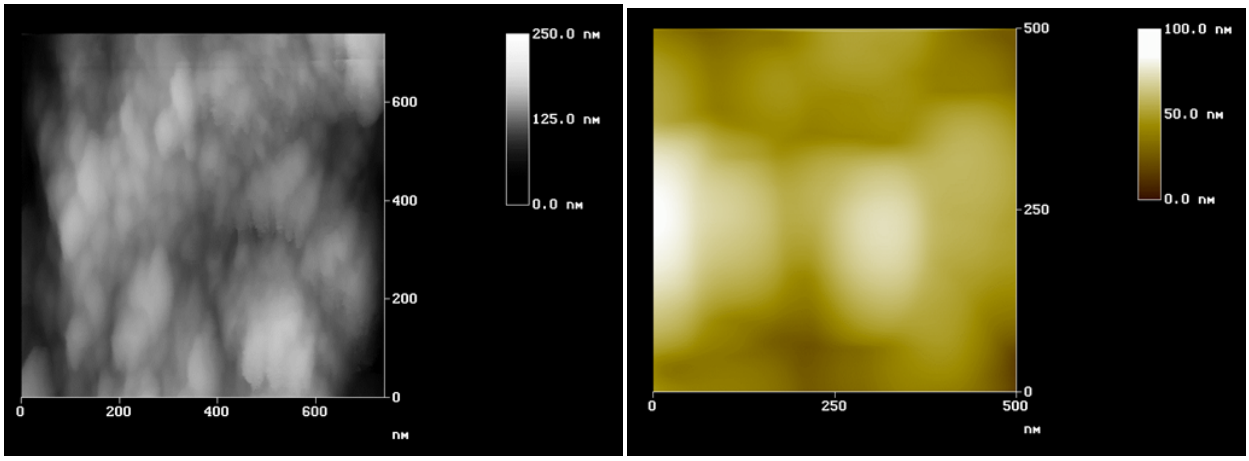
For the dual-liquid experiments, the samples were first entrapped with mercury using mercury porosimetry and the mercury containing samples were then immersed into a deionised water bath. Mercury intrusion and retraction curves were measured using a Micromeritics Autopore IV 9500, which can generate a maximum pressure of 414 MPa. The mercury intrusion data was generated for up to 60000 psia, followed by retraction down to atmospheric pressure. A clean sample was first transferred into a penetrometer, and the weight of the penetrometer and sample was recorded. The penetrometer (with sample) is then placed in the low-pressure port of the instrument. During the low-pressure analysis, the sample is firstly evacuated up to 50 mmHg to drive off any water

vapour or atmospheric gases in the pore network. The sample bulb is then filled with mercury while the entire system is still under low pressure. Data collection begins at a pressure of 0.5 psia, which is enough pressure to cause mercury to penetrate sample pores bigger than $\sim$360 $\mu\mathrm{m}$ in diameter. After the low-pressure analysis was completed, the assembly weight (penetrometer + sample + mercury) was recorded, the penetrometer was transferred to the high-pressure port, and the chamber was closed tightly. The penetrometer is placed vertically in the high-pressure port, and it is surrounded by oil, which is the hydraulic fluid the instrument uses to generate high pressures. As the hydraulic fluid pressure rises, it is transmitted to the mercury in the penetrometer via its open capillary stem. An equilibration time of 15 seconds was used for each data point.

Once the mercury porosimetry experiment was finished, the samples with mercury were immediately immersed into a deionised water bath for 5, 30 or 60 seconds. The samples were then placed inside a high-volume steel pan to run the DSC thermoporometry experiments. The DSC melting-freeze experiments were performed in TRIOS DSC2500 equipped with a cooling and data process system. A small drop of the probe liquids was also placed in the pans in every experiment. This droplet of liquid acts as a reference peak for the melting bulk liquid outside the sample pores. The pans with the samples were then loaded into the machine at room temperature ($\sim$295.15 K) and frozen to the required temperature of $-80\,^{\circ}\mathrm{C}$, immediately. To achieve temperature homogeneity and account for the differences between the actual temperature inside the pores and the sensor temperature, the samples were kept at this temperature for 30 minutes. After the samples reached thermal equilibration, the data points for the melting curves were measured over the range from $-80\,^{\circ}\mathrm{C}$ to $10\,^{\circ}\mathrm{C}$ at different ramping rates of $0.1\,^{\circ}\mathrm{C/min}$, $0.25\,^{\circ}\mathrm{C/min}$ and $0.5\,^{\circ}\mathrm{C/min}$. However, the increase in the ramping rate has caused a shift in the melting peak temperature towards the bulk peak, and therefore, only the first two ramping rates were used. Figure 6.4 shows a schematic representation of the novel dual liquid DSC experiment procedure. Multiple freeze-thaw cycles were used to check for any structural modification arising from mechanical damage during freezing, but none was observed.

6.4.5 Integrated Nitrogen Sorption and Mercury Porosimetry

The method consists of serial gas sorption and mercury porosimetry experiments conducted on the same sample. The method used here has been described previously in Rigby et al.[89]



(a) **(b)**

Figure 6.5: Larger **(a)** and smaller **(b)** length-scale AFM images of typical samples of G1 sol-gel silica showing the pore-scale morphology of the materials and the typical constituent particle size.

6.5 Results

6.5.1 Adsorbent Characteristics

Figure 6.5 shows an AFM image of a typical sample of G1. It can be seen that the basic structure consists of a partly sintered packing of sol spherical particles.

Table 6.1 shows the parameters obtained previously[326] from fits of the (fractal) Porod law (Equation (6.8)) to SAXS data for samples of pellet G1. It suggests that the average surface fractal dimension below $\sim$1 nm is equal to 2.1, while above $\sim$1 nm is 2.4.

Table 6.1: Parameters obtained previously from fits of the (fractal) Porod law to SAXS data for samples of pellet G1

Sample fractal dimension	q (n/m)	Length-scale cut-offs (nm)
1.977±0.004	0.626-3.23	0.31-1.60
2.246±0.004	1.0-3.54	0.28-1.0
2.34±0.04	0.566-0.997	1.0-1.768
2.51±0.05	0.503-0.998	1.0-1.988

6.5.2 Serial Nitrogen-Water-Nitrogen Adsorption

Figure 6.6 shows the nitrogen sorption isotherms obtained both before and after adsorbing water to relative pressures of 0.497, 0.646, 0.794, 0.871 and 0.914, and then freezing in-place. The nitrogen sorption isotherms obtained after water adsorption have been adjusted upwards in amount adsorbed, and it was found that they could be overlaid completely on top of the isotherms obtained for dry samples for the highest amounts adsorbed.

Figure 6.7 shows water sorption isotherms obtained for G1. Also shown is a fit of the fractal

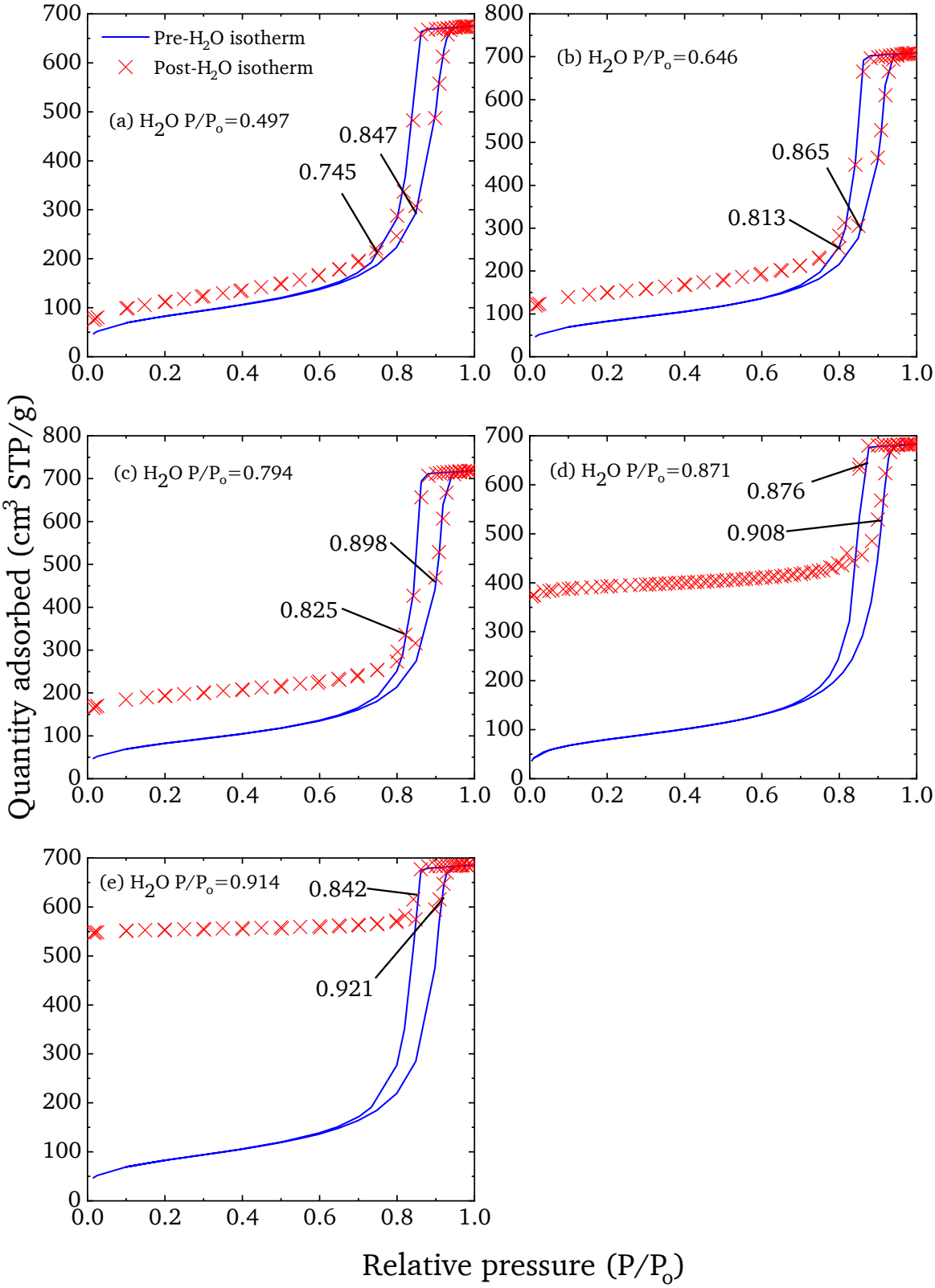


Figure 6.6: Nitrogen sorption isotherms obtained both before and after adsorbing water to relative pressures of **(a)** 0.497, **(b)** 0.646, **(c)** 0.794, **(d)** 0.871 and **(e)** 0.914, and then freezing in-place. The nitrogen sorption isotherms obtained after water adsorption have been adjusted upwards in amount adsorbed such that they overlay completely the top of the isotherms obtained for dry samples for the highest amounts adsorbed.

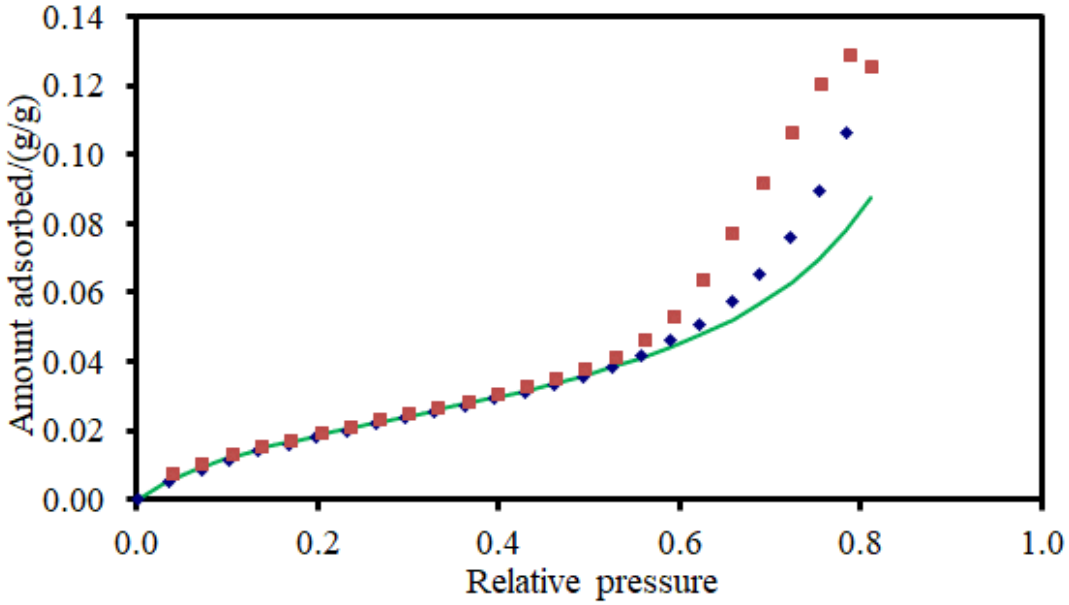


Figure 6.7: Water adsorption and desorption isotherms obtained at 283 K. Also shown (solid line) is a fit of the fractal BET isotherm for relative pressures <0.5.

BET isotherm for relative pressures less than 0.5, where the hysteresis starts indicating the possible onset of capillary condensation. In order to put the adsorption behaviour of nitrogen and water in a broader context, adsorption isotherms were also obtained for argon, propane, n-butane, n-hexane, and cyclohexane, and are given in appendix B. The isotherms for fresh G1 in Figure 6.6, together with those in appendix B, were all fitted to both the fractal BET and fractal FHH isotherms.[7,326] Examples (for fractal BET) of the results of these fits to the isotherms are given in appendix B, and the fitted parameters obtained for both models are given in Table 6.2. From Table 6.2, it is noted that the fractal dimensions from both the fractal BET and fractal FHH models are similar to those for short length-scales for SAXS for water, propane and n-butane, but significantly lower for n-hexane and cyclohexane.

It is noted that the fractal dimensions from the fractal FHH model in Table 6.2 are similar to that for length-scales <1 nm from SAXS (in Table 6.1) for propane, n-butane, and water, plus nitrogen at low pressures. However, the surface fractal dimension from the FHH model fit to the argon isotherm, and to higher pressures for the nitrogen isotherms, better matches the SAXS data for length-scales >1 nm.

The effective cross-sectional area for each adsorbate was calculated from the molar volume for a liquid at the conditions of the isotherm according to the method described by Gregg and Sing.[8] Figure 6.8 shows a plot of the logarithm of the monolayer capacities for each adsorbate on G1 against the logarithm of the molecular cross-sectional area. While it can be seen that the other adsorbates broadly follow a linear trend, water is a clear outlier where the monolayer capacity is significantly lower based upon its molar volume and the trend for the other adsorbates. The

Table 6.2: Fractal dimensions values obtained from the BET and fractal FHH isotherm fits

Adsorbate	Fractal BET surface fractal dimension	Length-scale range (nm)	Fractal FHH surface fractal dimension	Length-scale range (nm)
Argon	2.23	<0.98	2.42	0.36-1.60
n-Butane (C4)	2.27	<0.55	2.30	0.55-1.20
Cyclohexane (cC6)	2.00	<1.20	2.60	0.20-5.70
n-Hexane (nC6)	2.00	<1.30	1.96	0.85-1.50
Nitrogen	2.32	<0.95	(i) 2.20	<0.200
			(ii) 2.55	0.39-2.30
Propane (C3)	2.15	<1.00	2.26	0.64-1.10
Water	2.19	<0.52	2.28	0.31-0.62

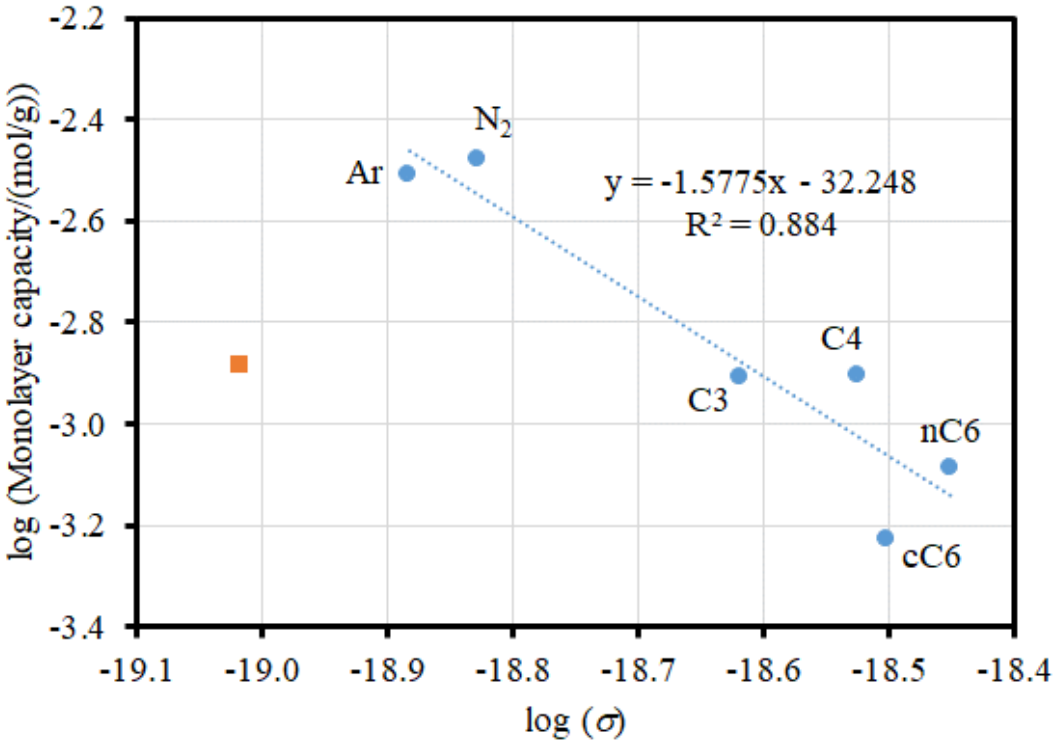


Figure 6.8: Plot of the logarithm of the monolayer capacities for water (square) and the other (labelled) adsorbates (circles) on G1 against the logarithm of the molecular cross-sectional area. The dashed line shows a straight-line fit to the data for the adsorbates other than water.

surface fractal dimension for G1 obtained from the best-fit straight line to the data-points for the adsorbates other than water was 3.15±0.57, where the unrealistically large value, and large error bar on that value (that does include the physically meaningful range of $2 \leqslant D \leqslant 3$), result from the scatter even for the adsorbates following the main trend. It is noted that argon and cyclohexane have apparent monolayer capacities lower than the trend line.

The nitrogen adsorption isotherms following water pre-adsorption were fitted to the fractal BET and fractal FHH isotherm equations, and the results are shown in Table 6.3. From Table 6.3, it can be seen that the fractal dimensions from both equations rise with increasing water saturation until a relative pressure of 0.794, and thereafter decline again, albeit less steeply.

Table 6.3: Fractal dimensions (±0.01) obtained from fits of the fractal BET and fractal FHH (high relative pressure) models to nitrogen adsorption isotherms before and after water adsorption to different relative pressures.

Water relative pressure	BET fractal dimension pre-H2O	BET fractal dimension post-H2O	FHH fractal dimension pre-H2O	FHH fractal dimension post-H2O
0.497	2.30	2.31	2.54	2.55
0.646	2.34	2.36	2.55	2.57
0.794	2.32	2.47	2.56	2.63
0.871	2.32	2.42	2.57	2.60
0.914	2.31	2.41	2.55	2.62

The ratio of the volumes of the total adsorbed nitrogen before and after addition of water to different relative pressures was obtained from the horizontal plateau values at the top of the nitrogen isotherms in Figure 6.6. This volume fraction was the maximum nitrogen saturation for each sample in the presence of water adsorbed to different pressures. As the total specific volume was the same, within a small intra-batch variation (∼1%), for each sample of G1 the nitrogen saturation was proportional to the volume of void space occupied by nitrogen at the top of the isotherm. The corresponding water saturation was estimated by subtracting the nitrogen saturation from unity. This latter calculation assumes that water did not block access to void space it did not actually occupy itself. Figure 6.9 shows plots of the logarithm of the saturation, for either water or nitrogen, against the logarithm of the ratio of nitrogen monolayer capacities for before and after water adsorption. It can be seen that the data for nitrogen fits well to a straight line for all values of water saturation, while that for water itself only fits well to a straight line for the data for water relative pressures 0.497-0.794. However, the overall form of the variation of the data for water itself is similar to that observed by Pfeifer et al.[327] on porous silica. The fractal dimension for the surface obtained, from the film equation (Equation (6.2)), for water is 2.14±0.02, while that obtained for nitrogen is 2.53±0.04. It is noted that the surface fractal dimension from the film equation for water is similar to that obtained from the fractal BET and fractal FHH models for water adsorption itself, and also from argon, propane or butane adsorption, and from SAXS for length-scales <1 nm. The fractal dimension from the film equation for nitrogen is similar to that also obtained for nitrogen using the fractal FHH isotherm fit for higher amounts adsorbed (at higher pressure) and for SAXS for length-scales >1 nm.

The relative pressures on the nitrogen isotherms where water adsorption causes deviations in the nitrogen data are revealed by the adjusted plots and are given in Table 6.4. It is noted that these deviations occur at pressures higher than the lower hysteresis closure point for nitrogen sorption. Also shown in Table 6.4 are the relative pressures (P2) calculated from Equation (6.3) for water adsorption into a pore with k=1, assuming that the relative pressure for water adsorp-

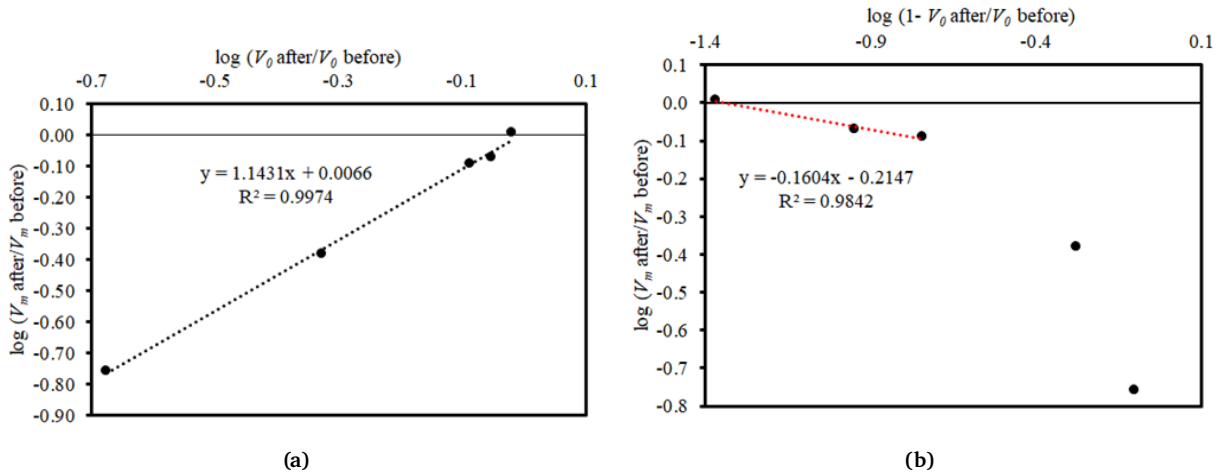


Figure 6.9: Fractal film plots for the nitrogen side **(a)** and water side **(b)** obtained from volumes of the ultimate total adsorbed nitrogen, and from the nitrogen monolayer capacities from the fractal BET equation, before and after addition of water. The dashed lines are fits of straight lines to the ranges of data shown.

tion experiment (P1) corresponded to k=2, and, from Equation (6.4), the corresponding relative pressure for nitrogen adsorption in the same pore with the same meniscus geometry. From Figure 6.6 and Table 6.4, it can be seen that water is condensing in pores that fill within the capillary condensation region for nitrogen but at relative pressures much lower than for nitrogen, though this discrepancy has decreased markedly at higher pressures. At higher pressures, the onset in the deviation between the nitrogen adsorption isotherms for before and after water adsorption at a relative pressure of 0.914 is that (∼0.921) expected simply from the difference in adsorbate property factor between the two adsorbates.

Table 6.4: Relative pressures for intermediate water adsorption in serial experiments. Also shown are the corresponding relative pressure for water adsorption if it had occurred instead via a cylindrical meniscus for pores that would fill by advanced condensation at the actual relative pressure.

H_2O adsorption relative pressure (assuming k=2), P1	Corresponding H_2O adsorption relative pressure (k=1), P2	N_2 adsorption relative pressure (P3) equivalent to P1	N_2 adsorption relative pressure (P4) equivalent to P2	Estimated relative pressure for deviation of N_2 desorption isotherms	Estimated relative pressure for deviation of N_2 adsorption isotherms
0.497	0.705	0.537	0.733	0.745	0.847
0.646	0.804	0.678	0.824	0.813	0.865
0.794	0.891	0.815	0.903	0.825	0.898
0.914	0.956	0.923	0.961	0.842	0.921

Figure 6.10 shows the cumulative BJH PSDs from the adsorption, obtained using a value of $k = 1$ in Equation (6.3), for sample of G1 before and after water adsorption to a relative pressure of 0.914. From a comparison of the two PSDs, it can be seen that the pore sizes left unfilled by

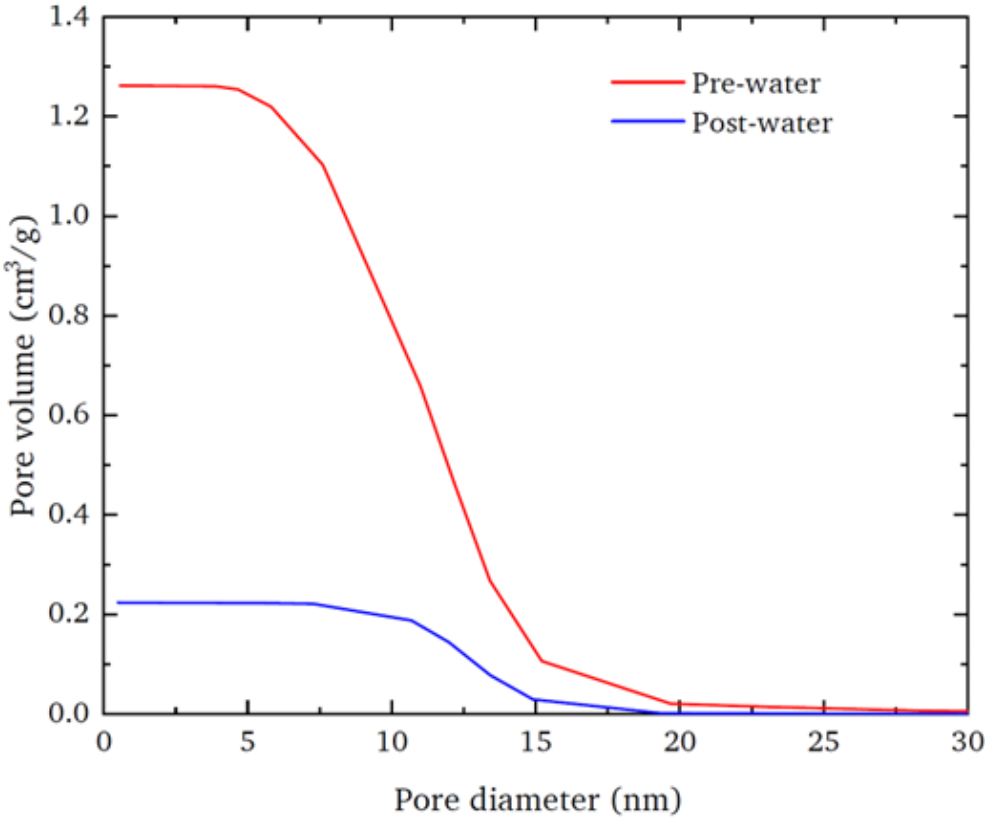
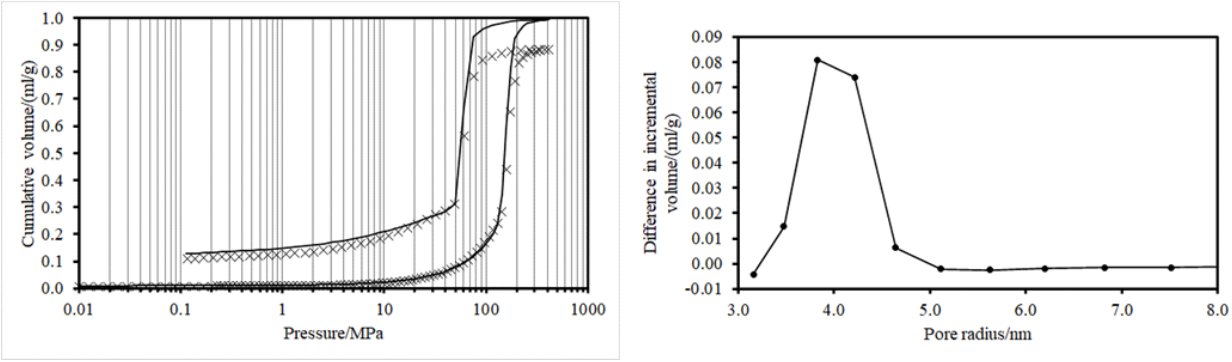


Figure 6.10: Cumulative BJH PSDs, obtained using a value of k=1 in equation (3), for sample of G1 before and after water adsorption to a relative pressure of 0.914.

water are in the range 10-15 nm. The relative pressure of 0.914 for water adsorption was chosen here as it gives rise to the same pore volume fraction left over without water saturation as the mercury saturation obtained by entrapment following porosimetry.

6.5.3 Serial Water Pre-adsorption, Mercury Porosimetry, and Nitrogen Adsorption

Figure 6.11a shows the raw mercury porosimetry data obtained for typical samples of G1 after the pellets had been initially dried at $350\,^{\circ}\mathrm{C}$ and following pre-adsorption of water to a relative humidity of 0.85 by suspension above a saturated KCl solution. Since it is not possible to completely remove entrapped mercury following porosimetry, then the experiments after water pre-adsorption were, necessarily, run on different samples from the same batch. In order to remove the small effects of intra-batch variability in pore volume between samples, the data obtained after water pre-adsorption was scaled such that a superposition of the lower part of the porosimetry curves was obtained. In the superposition process the sample mass for the curve after water adsorption was adjusted by a constant factor until the residuals with the data from before water adsorption were minimised. It can be seen from Figure 6.11a that an excellent superposition can be obtained for the curved regions in the initial intrusion, especially around the main percolation knee, and for the region where entrapment begins for extrusion when the extrusion curve deviates strongly



(a) (b)

Figure 6.11: Mercury intrusion and extrusion curves for G1 following drying at 350°C (solid line) and following pre-adsorption of water to a relative pressure of 0.85(x). (b) Variation with pore size, derived from Kloubek correlation, of difference in incremental volume intruded between samples with and without water pre-adsorption.

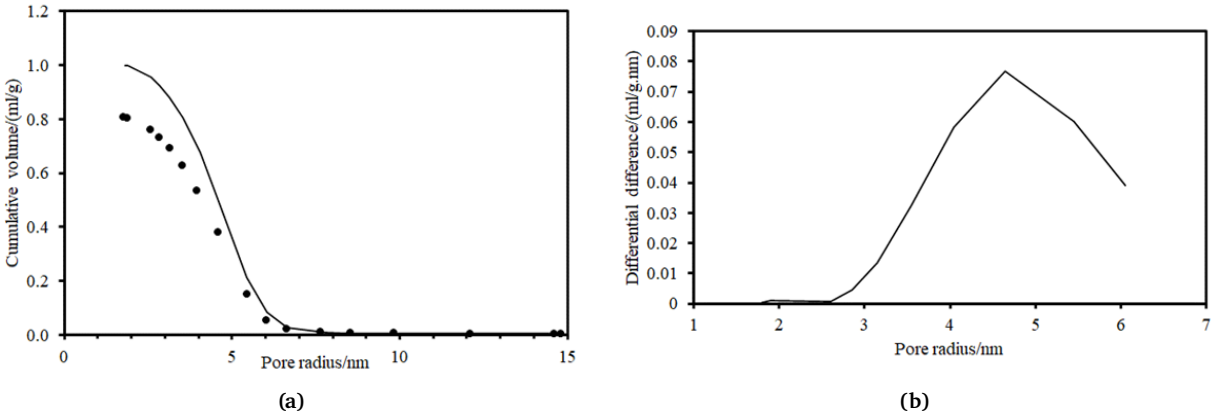
into a more horizontal path from the previous more vertical drop.

However, it is noted that, in contrast, a good superposition cannot be obtained for the porosimetry curves obtained with and without water pre-adsorption when the amount of intruded mercury is plotted as fractional saturation (as seen in Appendix B). This suggests that the shape of the top of the porosimetry curves is substantially altered by the water pre-adsorption. Figure 6.11a shows that the mercury entrapment for batch G1 declines only slightly following water pre-adsorption.

Figure 6.11b shows a plot of the variation with pore size of the differences in incremental intruded volume between before and after water pre-adsorption. The pore radius was obtained from the intrusion pressure using the Kloubek[76] correlations. Kloubek[76] developed calibrated versions of the Washburn equation[71] using mercury porosimetry data for model materials, namely a series of controlled pore glasses, for which the pore size of each had been independently determined from electron microscopy by Liabastre and Orr.[84] Given the Kloubek correlations are empirically calibrated, it is noted that pore sizes derived from these correlations have experimental errors of ∼4-5% associated with them. The results of analysing the raw mercury porosimetry data for G1, shown in Figure 6.11b, using the Kloubek correlations are given in the Appendix B. A good superposition was obtained for the main steps in the intrusion and extrusion curves for G1 using the Kloubek correlations. These correlations were designed to remove contact angle hysteresis, and the level of superposition achieved shows that the two materials have similar contact angles to each other, and to the CPGs originally used to obtain the Kloubek correlations. From Figure 6.11b, it can be seen that water adsorption to a relative pressure of 0.85 leads to a loss in intrusion of pores of sizes peaking around ~ 4 nm for G1.

Figure 6.12a shows the cumulative BJH PSD obtained from nitrogen adsorption isotherm, using a value of k=1 in Equation (6.3), for a typical sample of G1 after the pellets had been

[76] J. Kloubek. *Powder Technol.*, **29**: 63–73, 1981.
[71] W. E. Washburn. *Phys. Rev.*, **18**: 206–209, 1921.
[84] A. Liabastre and C. Orr. *J. Colloid Interface Sci.*, **64**: 1–18, 1978.



(a) (b)

Figure 6.12: (a) Cumulative BJH PSDs obtained from nitrogen adsorption isotherms, using a value of k=1 for typical samples of G1 following mercury porosimetry after the pellets had been initially dried at 350°C (solid line), and also following pre-adsorption of water to a relative humidity of 0.85 by suspension above a saturated KCl solution. **(b)** Differential difference plot obtained from the two PSDs shown in a.

initially dried at $350\,^{\circ}\mathrm{C}$, and also following pre-adsorption of water, to a relative humidity of 0.85, and mercury porosimetry. For consistency with the mercury porosimetry data, the nitrogen sorption data for the sample following water adsorption has been scaled by the same factor as for the corresponding mercury porosimetry data-set. It is noted that the difference in the cumulative nitrogen PSD pore volumes between before and after water adsorption is equal to the sum of the volumes lost to water (as shown by difference in ultimate intrusion volume in mercury intrusion curves) and entrapped mercury (taking account of the slightly less entrapment following water adsorption). This suggests that the mercury porosimetry and nitrogen sorption PSDs are a self-consistent set.

In order to further clarify the differences between the two PSDs shown in Figure 6.12a, Figure 6.12b shows a plot of the variation with pore radius of the difference in the differential of the PSDs shown in Figure 6.12a. In order to obtain the differentials, the cumulative PSDs were fitted to sixth-order polynomials up to the largest pore size data-points just before the cumulative plot became horizontal, and the equations for these fits were differentiated to obtain the differential PSD. It can be seen that the respective plots of the difference in the differential PSDs peak at a radius of $\sim$4.5 nm for G1. It is noted that the peak positions for the mercury and nitrogen data for G1 given in Figure 6.11b and Figure 6.12b are similar.

6.5.4 Dual Liquid Mercury-Water DSC Thermoporometry

Figure 6.13 shows the raw melting curve for sample of G1 containing both mercury and water following mercury entrapment during porosimetry and immersion in water afterwards. Small amounts of bulk liquids were added to sample to provide for internal references. It can be seen that both mercury and water within the sample pores show melting point depression relative to their respective bulk melting temperatures.

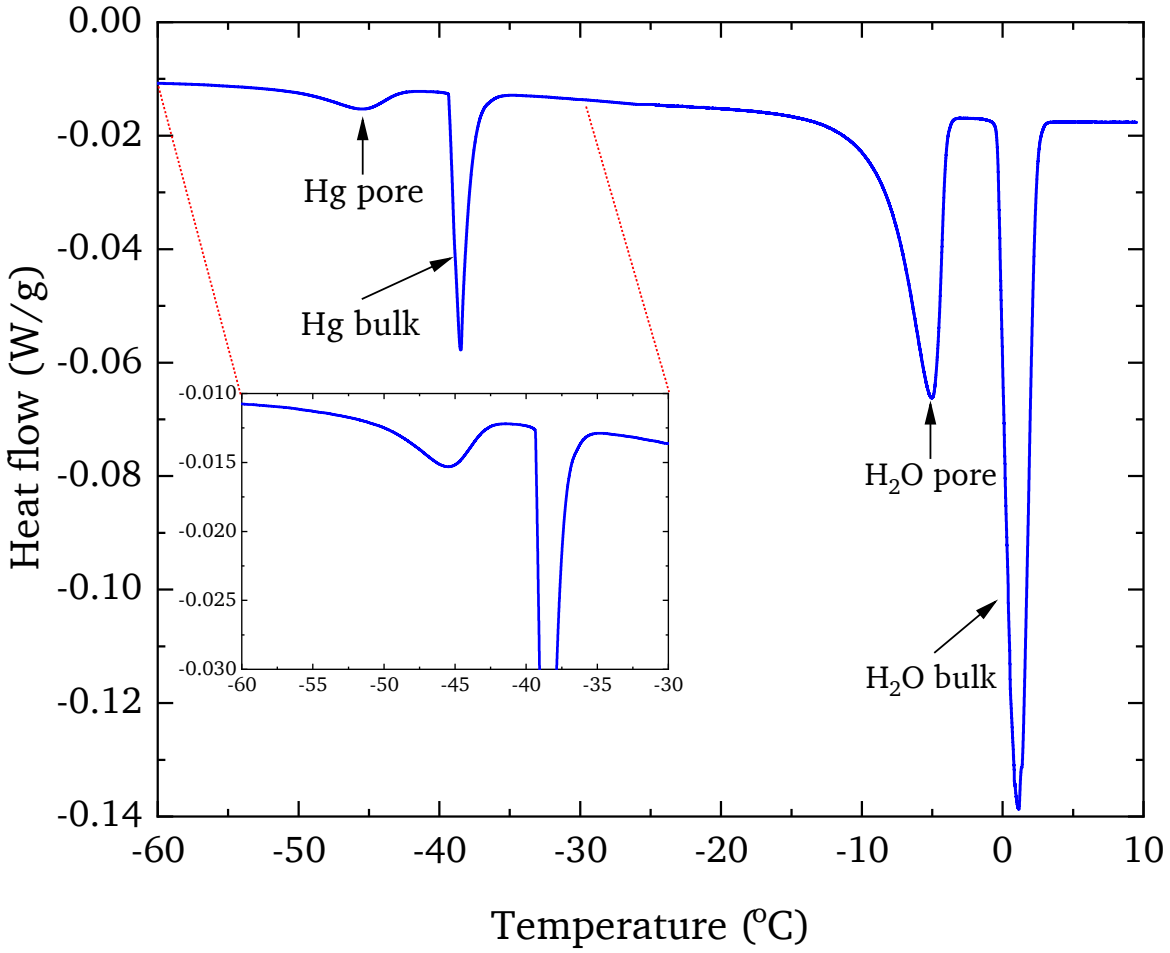


Figure 6.13: DSC melting curve for both mercury and water within the same sample of G1 following entrapment during porosimetry and immersion in water.

The melting temperatures in Figure 6.13 have been converted to pore sizes assuming values of k_{GT} in Equation (6.7) of $90\,\mathrm{K\,nm}$ and $52\,\mathrm{K\,nm}$, for mercury and water respectively. Figure 6.14 shows a comparison of the BJH PSD obtained from the nitrogen adsorption isotherm measured after water adsorption to P/P_0=0.914, shown in Figure 6.10, and the PSD from DSC thermoporometry for mercury entrapped in G1 shown in Figure 6.13. The modal volumes of each PSD have been renormalised to 1.0. From Figure 6.14, it can be seen that there is good agreement between the PSDs from nitrogen and mercury methods for the pore space left vacant after water adsorption to P/P_0=0.914.

Figure 6.15 shows the PSD for the region occupied by water adsorbed to a relative pressure of 0.914 obtained by subtracting the nitrogen adsorption BJH PSD (using $k = 1$ in Equation (6.3)) obtained after water adsorption from the corresponding PSD from nitrogen adsorption beforehand. The data for two separate suites of experiments on two different samples from batch G1 are shown to give an idea of inter-sample variability. In Figure 6.15, this difference PSD is also compared with the PSD for the adsorbed water itself using DSC thermoporometry with a K_{GT} value of $52\,\mathrm{K\,nm}$ in

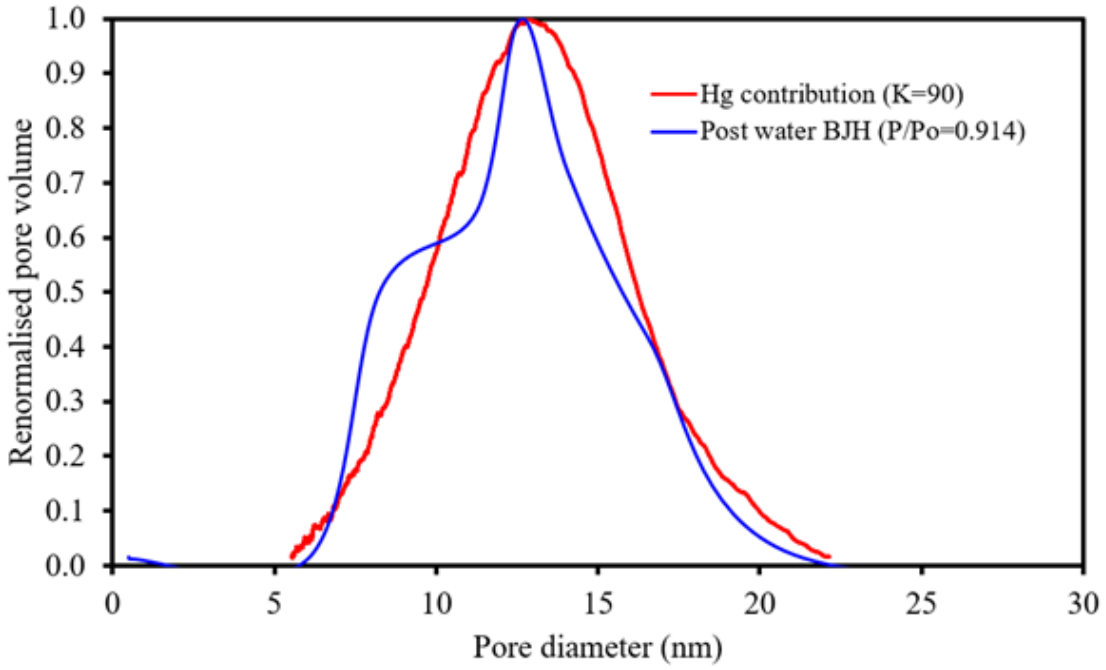
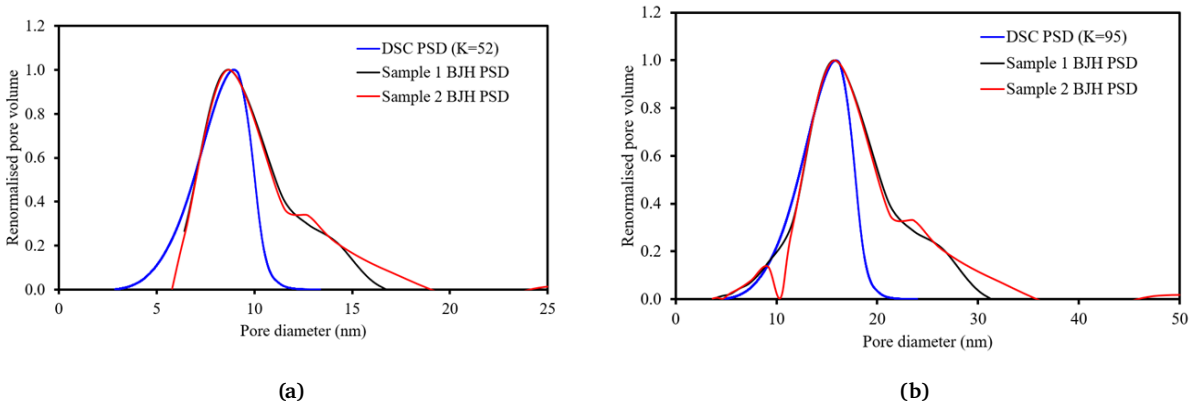


Figure 6.14: Comparison of the BJH PSD obtained from the nitrogen adsorption isotherm measured after water adsorption to P/P0=0.914, shown in Figure 10, and the PSD from DSC thermoporometry for mercury entrapped in G1 shown in Figure 13.

Equation (6.7). From a comparison of Figure 6.14 and Figure 6.15, it can be seen that, while the mercury occupies the largest pores in the sample, greater than $\sim$10 nm, the water occupies the smallest pores, less than $\sim$10 nm.

6.5.5 Integrated Nitrogen Sorption and Mercury Porosimetry

Figure 6.16 shows a comparison of the DSC thermoporometry PSD (using K_{GT}= 90 K nm in Equation (6.7)) for the void space occupied by entrapped mercury following porosimetry, with the PSD for that same void space estimated from the difference in the BJH PSDs (using k=1 in Equation (6.3)) obtained from nitrogen adsorption isotherms measured before and after mercury porosimetry. The volume of the modal pore size in each distribution has been renormalised to 1.0. It can be seen that there is good agreement between the modal pore sizes obtained by the two methods but the width of the mercury thermoporometry PSD is wider than the nitrogen difference PSD.



(a) **(b)**

Figure 6.15: PSD for the region occupied by water adsorbed to a relative pressure of 0.914 obtained by subtracting the nitrogen adsorption BJH PSD (using **(a)** k=1 or **(b)** k=2 in equation 3) obtained after water adsorption from the corresponding PSD from nitrogen adsorption beforehand. Data for experiments on two different samples (1 and 2) from batch G1 are shown to give an idea of inter-sample variability. Also shown is the PSD for the adsorbed water itself using DSC thermoporometry with a Gibbs-Thomson value of (a) 52 or (b) 95 K nm in equation 7.

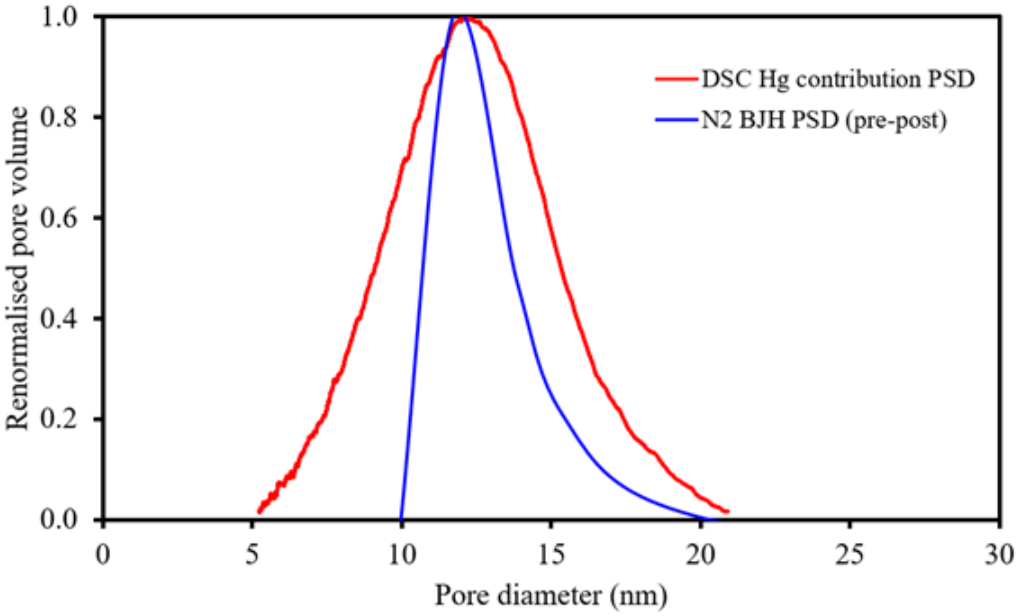


Figure 6.16: Comparison of the DSC thermoporometry PSD for the void space in G1 occupied by entrapped mercury following porosimetry, with the PSD for that same void space estimated from the difference in the BJH PSDs (using k=1 in equation 3) obtained from nitrogen adsorption isotherms measured before and after mercury porosimetry.

6.6 Discussion

The comparison of the adsorption behaviour of water with a range of different adsorbates has revealed its particular idiosyncratic behaviour for the test silica material. In the multi-layer region, the amount of adsorption of water, for the surface as a whole, is much lower than that which might be expected, for an adsorbate with its particular size, from the general trend for other, but less polar, adsorbates. However, the similarity between the surface fractal dimension from SAXS for shorter length-scales, and that from a fit of the fractal BET equation to the water isotherm, suggests that the growth of the multi-layer of water that does occur is in line with that expected from the BET model. This contrasts with the adsorption behaviour of n-hexane and cyclohexane which gives rise to apparent surface fractal dimensions higher than that for SAXS, as might be expected if adsorption was seeded only at a few sparsely distributed high energy sites and proceeded just by addition of adsorbate only to sites immediately adjacent to itself, to, maybe, form a radially-expanding 'dome-shape'. In that case the number of sites for adsorption would increase for each successive layer, leading to an under-estimate of fractal dimension, as seen for hexane molecules.

The structural analysis of the pre-adsorbed water phase by serial nitrogen adsorption is also consistent with adsorbed water forming a more dispersed film, rather than discrete ganglia. The variation of the water film volume with its surface area was found to be consistent with that expected for film growth on a surface with a fractal dimension the same as that obtained from SAXS (for length-scales $<1\ \mathrm{nm}$) according to the model of Pfeifer et al.[327]

In contrast, in the higher reaches of the adsorption isotherms, where the presence of hysteresis indicates non-reversible capillary condensation has commenced for both nitrogen and water, it was found that water adsorption at lower pressure affects the nitrogen adsorption at higher corresponding parts of its hysteresis loop region. This suggests water fills the smallest pores at lower pressures than expected compared to nitrogen, even after the differences in adsorbate property factor are taken into account. A possible explanation is that, despite the more limited overall adsorption of water in the multi-layer region, that adsorption is relatively localised within the smaller pores, thereby making the multi-layer thicker and the core volumes correspondingly smaller than for nitrogen, thereby leading to the earlier onset of capillary condensation there. At the uppermost reaches of the isotherms, the spatial disposition of water and nitrogen within the void space probably becomes more similar, since capillary condensation occurs at the expected corresponding relative pressures for pores of a certain size.

In contrast to water, the FHH plot for nitrogen suggests its adsorption only follows simple multi-layer build-up on the silica surface roughness for the very lowest pressure region of the isotherm. The similarity of the fractal dimension from FHH and SAXS over larger length-scales suggests that, thereafter, nitrogen adsorption follows the envelope surface of the packing of sol particles seen in the AFM images. This is a similar effect to that suggested by Tang et al.[328] for nitrogen adsorption on a close packing of smooth bovine serum albumin particles. As with this previous work, the change to an apparently larger fractal dimension, than for the silica particle

[328]Patricia Tang et al. *Langmuir*, **19**: 2632–2638, 2003.

surface roughness, may be due to the constraints on the occupancy numbers of successive upper layers of adsorbate that arise within the collars, or necks, formed at junctions between packing particles. A V-shaped profile collar region would have the same impact, of reducing the numbers of adsorption sites in successive layers, as the isolated pyramidal stacks of adsorbate envisaged in previous work on adsorption of nitrogen on flatter profile, but more chemically heterogeneous, silica surfaces.[326]

It has been seen that the cumulative intrusion and extrusion curves from mercury porosimetry for samples of G1, that are initially dried, diverge at the top of the curves from the corresponding data for the same samples which have water pre-adsorbed to a relative humidity of 0.85. The subsequent analysis of these curves suggests that pre-adsorption of water has filled-up, and thereby prevented mercury intrusion within, pores of sizes only up to $\sim$4 nm for G1. It is noted that the core pore sizes obtained from the Kelvin equation (Equation (6.3)) for capillary condensation of water, at 296 K and relative pressure of 0.85, with cylindrical sleeve ($k = 1$) and hemispherical ($k = 2$) meniscus geometries, are 3.2 nm and 6.4 nm, respectively. The BET coverage equation suggests that the statistical first layer coverage for G1 at a relative pressure of 0.85 is 95.3%, suggesting at least a monolayer had built up at condensation, giving rise to a *t*-layer correction of at least 0.6 nm. Hence, this suggests water is adsorbing with a cylindrical sleeve meniscus geometry for G1. Capillary condensation via a hemispherical meniscus can arise from the dead-ends in pores, or be initiated from filled neighbouring pores, or even from advanced condensation. In an inter-connected pore network, the filling of the smallest pore via a cylindrical sleeve meniscus will present a hemispherical meniscus to the adjoining pores, thereby potentially facilitating axial filling of such pores at lower pressure than otherwise. If the neighbouring larger pore diameter is less than twice the small pore, then it will also fill at the same pressure step via advanced condensation. If there is a significant spatial correlation in pore sizes, then these pore-pore co-operative effects will lead to more pores filling than would happen if the same pores were more widely dispersed within the network amidst larger pores. The aforementioned results thus suggest that the pores of sizes less than 5 nm in G1 are well-dispersed and only adjoined by much larger pore bodies that do not fill via either meniscus geometry at relative humidity of 0.85. This suggests a network of the type where narrow necks are interspersed between wide pore bodies. Indeed, G1 is a sol-gel silica formed by the agglomeration of tiny silica sol spheres, where wide pore bodies are formed in the central gaps between sol particles and these gaps are separated by narrow necks. This structure is evident in AFM images of samples of G1 shown in Figure 6.5

For sample G1, the loss of $\sim$10-15% of ultimate intruded volume in mercury porosimetry following water adsorption did not affect the level of mercury entrapment obtained very much at all. This is possible if that entrapment is arising from macroscopic structural heterogeneities whereby regions of large pores are surrounded by a 'sea' of small pores.[67] The loss of a sub-set of small pores in this sea will not affect entrapment in the larger pores. Light microscopy studies of pellets of G1 following entrapment have shown that the mercury ganglia have macroscopic dimensions.[88] The slight decline in entrapment for G1 following water adsorption may be because

[67] N. Wardlaw and M. McKellar. *Powder Technol.*, **29**: 127–143, 1981.
[88] S. Rigby, R. Fletcher, and S. Riley. *Appl. Catal., A*, **247**: 27–39, 2003.

the adsorbed water creates some more dead-ends with free mercury menisci from which retraction can be more easily initiated without the need for snap-off.

It is noted that the PSD from dual-liquid DSC thermoporometry for entrapped mercury in Figure 6.14 used a value of the mercury Gibbs-Thomson parameter of 90 $\mathrm{K\,nm}$. This is the value obtained previously by Bafarawa et al.[109] for melting of mercury via a hemispherical meniscus in a CPG. Hence, the value of K_{GT} cannot be any larger, and thus the pores filled with entrapped mercury cannot be any larger. According to Figure 6.14, the pores occupied by mercury are in the range $\sim$10-20 nm. However, according to Figure 6.15b, this is also the pore size range occupied by the complementary liquid, water, in the same dual-liquid DSC thermoporometry experiment. The two liquids cannot simultaneously occupy the same pores, and so one of the PSDs in Figure 6.14 and Figure 6.15b must be using incorrect key constants of proportionality in the master pore size equations. The fact that the sizes in the mercury DSC thermoporometry PSD cannot be made any larger suggests Figure 6.15b is the PSD in error. This means that the PSDs in Figure 6.15a must be the correct ones, because then water will be considered to occupy the complementary, smaller pores in G1, as might be expected as water is the wetting fluid. Further, the pore sizes occupied by water according to the PSD in Figure 6.15a, is more in line with the sizes ($<$10 nm) of the smallest 70% of pores in G1 according to the mercury intrusion PSD in Figure 6.11b, obtained using the Kloubek[76] correlations, than are those according to Figure 6.15b.

The water DSC thermoporometry PSD in Figure 6.15a used a value of K_{GT}=52 $\mathrm{K\,nm}$. This PSD was consistent, in terms of modal pore size, with that obtained by subtracting the BJH PSD, assuming capillary condensation occurred via a cylindrical sleeve meniscus, for nitrogen adsorption isotherms obtained after water adsorption from that obtained beforehand. It is noted that, in Figure 6.16, the modal pore size obtained from the difference between the PSDs, also obtained assuming nitrogen capillary condensation via a cylindrical sleeve meniscus, during adsorption either side of mercury entrapment from porosimetry on the same sample, coincides with the modal pore size containing the entrapped mercury from DSC thermoporometry. Hence, overall Figures 6.14 to 6.16 lead to a self-consistent set of PSDs assuming melting of mercury occurs via a hemispherical meniscus, while melting of water occurs via a cylindrical sleeve meniscus, and capillary condensation of nitrogen occurs via a cylindrical sleeve meniscus irrespective of whether complementary sets of pores are filled with frozen water or mercury, at the saturation levels of water and mercury tested (see Figure 6.6).

[109] B. Bafarawa et al. *J. Colloid Interface Sci.*, **426**: 72–79, 2014.

6.7 Conclusion

The multi-layer build-up of nitrogen and water both show idiosyncrasies compared to a basket of other adsorbates. Analysis of the surface area of the interface between, and complementary volumes of, a solid surface-adsorbed film and the residual pore space has shown that both water and nitrogen initially form multi-layer films on the silica. However, while that multi-layer build-up for water is concentrated in the smaller pores, in contrast, for nitrogen, it is more pervasive and rapidly becomes directed by the envelope surface of the packed bed of silica sol particles, rather than the surface roughness of individual constituent particles. Dual-probe thermoporometry or adsorption can be used to determine the correct mode of the phase transition used to characterise the pore structure of disordered mesoporous materials, without recourse to either model templated materials for calibration, or imaging methods.

In the next chapter, integrated nitrogen-mercury experiments and CXT imaging techniques will be used to study the pores that entrap mercury in high-temperature shift catalyst pellets.

Chapter 7

Study of the Entrapment of Non-wetting Fluid in High Temperature Shift Catalyst

7.1 Introduction 180
7.2 Materials and Method 181
7.3 Results 184
7.4 Discussion 203
7.5 Conclusion 204

7.1 Introduction

Hydrogen can be produced using electrolysis, but on a large industrial scale it is more cost-effective to liberate it from water using a chemical reducing agent or to generate it through partial oxidation of hydrocarbons in the presence of steam and oxygen. The most prevalent commercial method is steam reforming in which a hydrocarbon fuel is used as a reducing agent for the steam.[31] In modern plants, natural gas composed mainly of methane (CH_4) is most commonly used. Alternatively, petroleum naphtha could also be used depending on feedstock availability. Steam reforming of hydrocarbons involves six different catalytic process steps, including desulphurisation, primary steam reforming, secondary steam reforming, high-temperature water-gas-shift, low-temperature water-gas-shift and methanation.[31] Table 7.1 contains the corresponding reactions and typical catalysts for each step. In this chapter, we will mainly focus on the high-temperature shift catalyst pellet, which is composed of Fe_3O_4 and Cr_2O_3. This catalyst was originally developed by BASF in 1915 as part of the ammonia synthesis process.[21] However, the catalyst tested in this chapter was supplied by Johnson Matthey (JM), and the characterisation experiments were carried out here at the University of Nottingham. The low-temperature water-gas-shift reaction uses the high activity $CuO/ZnO/Al_2O_3$ that was analysed in detail in Chapters 3 to 5.

This chapter will study a high-temperature shift catalyst manufactured by precipitation. An integrated mercury porosimetry, nitrogen gas adsorption, and X-ray imaging strategy will be used

[31] C. H. Bartholomew and R. J. Farrauto. *Fundamentals of industrial catalytic processes*. John Wiley & Sons, 2011.
[21] A. Mittasch, M. Pier, and K. Winkler. *Germany Patent DE415686*, **24**: , 1923.

to identify and spatially locate the particular pore size ranges in the HTS pellet that entraps mercury. The work will also present the rate of adsorption technique to study the impact of the lost pores on mass transport. The X-ray imaging will be used to improve the interpretation of the data from the indirect methods and to study the spatial distribution of mercury within the void spaces of the material. It will be seen how this new combination of methods can be used to determine the critical features of the void space that entrap mercury and identify their impact on the mass transport of the materials.

Table 7.1: Process steps, reactions and catalyst used in steam reforming of hydrocarbons [31]

Process step	Reactions	Catalyst
Desulphurisation	R-S + H_2 → H_2S + R-H	$CoMo/Al_2O_3$
Primary steam reforming	HC + H_2O → H2 + CO + CO_2 + CH_4	Ni/MgO (naphtha) $Ni/CaAl_2O_4$ (methane)
Secondary steam reforming	$2CH_4$ + $3H_2O$ → $7H_2$ + CO + CO_2	$Ni/CaAl_2O_4$ Ni/α-Al_2O_3
HT Water gas shift	CO + H_2O → H_2 + CO_2	Fe_3O_4
LT Water gas shift	CO + H_2O → H_2 + CO_2	CuO
Methanation	CO + $3H_2$ → CH_4 + H_2O	Ni/Al_2O_3

7.2 Materials and Method

7.2.1 Samples studied

The material studied in this work were fresh, high-temperature shift (HTS) catalyst pellets denoted as H1, H2, H3 and H4. The HTS pellets are mesoporous cylindrical tables with dimensions of ∼7 x 4 mm (diameter x length) and are composed of iron, chromium and graphite lubricant particles. All the samples were manufactured by precipitation. H1 and H2 were calcined at $600\,^{\circ}\mathrm{C}$ and $650\,^{\circ}\mathrm{C}$, respectively. H3 sample is a low-density sample produced by applying lower pressures during the pelleting process. Finally, H4 sample is non-calcined and has a unimodal pore structure. H1 and H2 pellets have an average BET surface area of $28.3\,\mathrm{m^2g^{-1}}$ and $20.3\,\mathrm{m^2g^{-1}}$, respectively. The H3 and H4 samples have an average BET surface area of $27.1\,\mathrm{m^2g^{-1}}$ and $191.9\,\mathrm{m^2g^{-1}}$, respectively. Tables 7.2 to 7.3 contain further details and properties of the samples studied.

Table 7.2: Characteristics of the high temperature shift catalyst pellets. Porosity values were obtained from mercury porosimetry. The bulk density was obtained from helium pycnometry.

Sample	Sample porosity (%)	Bulk density ($\mathrm{g/cm^3}$)	BET ($\mathrm{m^2/g}$)	Cylindrical dimension (diameter x length)
H1	52.2	2.44	28.343	7.0x4.0 mm
H2	48.5	2.63	20.301	7.0x4.0 mm
H3	54.9	2.21	27.139	7.0x4.0 mm
H4	44.8	1.92	191.912	8.0x4.0 mm

Table 7.3: Specific pore volumes and modal pore diameters of the samples as determined by two different methods

Sample	Hg pore volume (ml/g)	N_2 sorption pore volume (ml/g)	Hg modal pore diameter (nm)	N_2 modal pore diameter (nm)
H1	0.214	0.156	29.5	26.4
H2	0.184	0.124	37.6	35.3
H3	0.248	0.160	29.9	30.4
H4	0.235	0.208	48.3	50.2

7.2.2 Integrated mercury porosimetry and gas sorption

The steps used in the integrated nitrogen sorption and mercury porosimetry techniques used to test the HTS pellets in this chapter closely follows that described in previous chapters. For a general description of the procedure, the reader is referred to this earlier work in Chapter 3. However, more specific aspects of the procedure that are unique to the experiments presented in this chapter will be described below. The 'filtering' strategy, which consists of a series of gas sorption and mercury porosimetry experiments conducted on the same sample, was used to analyse the high-temperature shift catalyst pellets. The samples were degassed at $110\,^{\circ}\mathrm{C}$ in the case of H1, H2, H3, and $140\,^{\circ}\mathrm{C}$ in the case of H4 before the initial nitrogen sorption experiment. The samples were kept under vacuum for 24 hours to drive off any physisorbed water onto the pores. Following the first nitrogen sorption experiment, the samples were allowed to cool to room temperature ($298.15\,\mathrm{K}$) before being transferred to the mercury porosimeter while still under nitrogen. The mercury porosimetry experiment were carried out using a Micromeritics Autopore IV 9500, which is capable of pressure up to 60,000 psia ($\sim$414 MPa). The contact angle and the surface tension values were taken as 140° and 0.485 N m^{-1}, respectively. Furthermore, because cleaning the entrapped mercury from a specific sample after an experiment for re-use in a subsequent mercury porosimetry experiment is difficult, each new experiment was instead performed on a new sample from the same batch.

Once the mercury porosimetry experiment was completed, the sample was then returned to the nitrogen sorption instrument. The sample was then cooled to 77 K to freeze the entrapped mercury. The sample were then evacuated to a vacuum following freezing, and the next nitrogen sorption experiment started. Each sample was re-weighed at the end of the integrated experiment to assess whether the change in mass was consistent with the extent of mercury entrapment reported by the porosimetry curves. This was proven to be true in each occasion (with in $\sim$5%). As a result, the apparent mercury retention shown in the porosimetry data (seen below) is due to true entrapment.

No overcondensation experiments were conducted on the HTS pellets as the samples showed a clear plateaus at relative pressure $\sim$1 using conventional isotherms. This behaviour is normally typical of sorption scanning curves where the void space is completely filled with liquid nitrogen at the top of the isotherms. The OC experiment is often used to investigate any porosity beyond the instrument's upper limit for the conventional isotherm ($P/P_0 > 0.995$).

7.2.3 Rate of Adsorption (ROA) procedure

The rate of adsorption (ROA) experiments was also conducted on the HTS pellets both before and after mercury entrapment. The rate of adsorption (ROA) technique works by dosing a known quantity of nitrogen gas onto the sample and recording the amount of gas adsorbed and the corresponding pressures over time. The dosing quantity was taken from the BET monolayer capacity. An additional $5\,\mathrm{cc(STP)/g}$ of gas was added to this amount to compensate for the initial expansion of the gas into the free space of the sample tube. This is because the gas first fills the sample tube before adsorbing onto the sample surface.

7.2.4 Imaging using CXT

The HTS catalyst pellets were imaged using low-resolution CXT before and after mercury entrapment to different intrusion pressures. For the low-resolution CXT scans, the whole pellets were imaged before and after mercury entrapment using a Zeiss Xradia Versa XRM-500 to acquire 3D image stacks. A similar imaging technique as the fresh catalyst pellets discussed in previous chapter was used for the HTS pellets. The X-ray source for the instrument was set to 140 kV and a power of 10 W. The apparatus's macro lens (0.4X) was used to image the full pellets with 360 degrees rotations. The average pixel size for empty pellets was 4.5 $\mu\mathrm{m}$, and the average pixel size for samples with mercury was 8.5 $\mu\mathrm{m}$ due to higher density of mercury-containing sample. Both samples were scanned with 1600 projections per 360 degrees scan. Each 3D image stack contained 1016 slices with dimensions of 2048 x 2048 and 1024×1024 image size for the empty and mercury-filled samples, respectively. The 3D volume data sets were reconstructed using the filtered back projection (FBP) method.[128]

[128] G. N. Ramachandran and A. V. Lakshminarayanan. *PNAS*, **68**: 2236–2240, 1971.

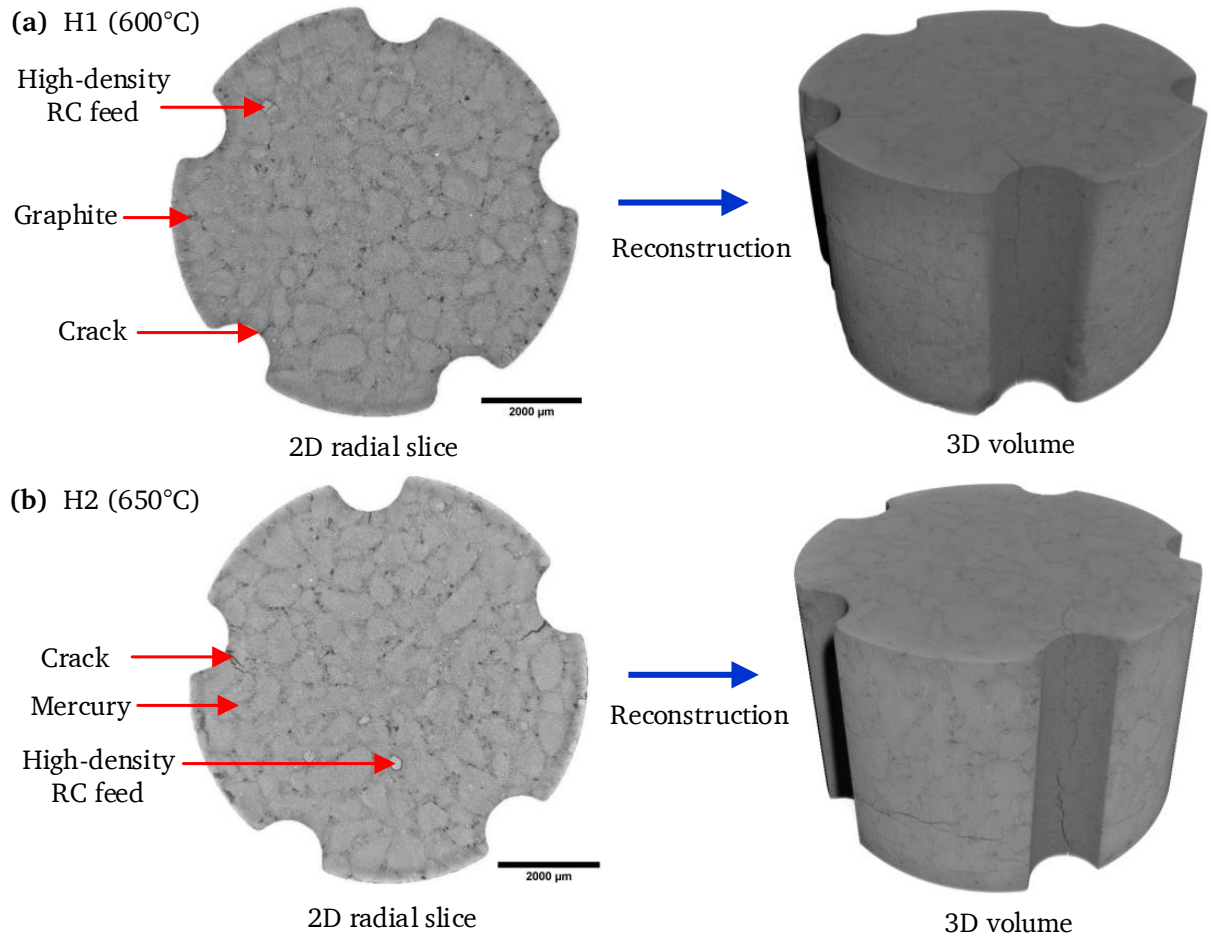


Figure 7.1: Raw 2D radial slices and 3D reconstructions for the empty HTS pellets **(a)** H1 pellet, and **(b)** H2 pellets.

7.3 Results

7.3.1 Imaging Empty Samples

Figure 7.1**(a)** and **(b)** show typical examples of the reconstructed 2D and 3D CXT images of the empty (no mercury in the pores) H1 and H2 samples, respectively. The Figure shows the individual feed particles that make up the pellets due to the density distribution in the particles seen from the variation in average pixel intensity in each feed particle. The pellets contain high-density and low-density feed particles and smaller, dark black spots that correspond to graphite lubricant particles. The pellets also display splintering or cracks, which are more evident in the 3D volume reconstructions.

Figure 7.2**(a)** and **(b)** show typical examples of reconstructed 2D and 3D CXT images of the empty H3 and H4 samples, respectively. For the H3 samples, it can be seen from the pixel intensities in (Figure 7.2**a**), there are several irregularly shaped particles of different sizes and densities. The H3 sample contains both low and high-density roll compacted feed particles. There

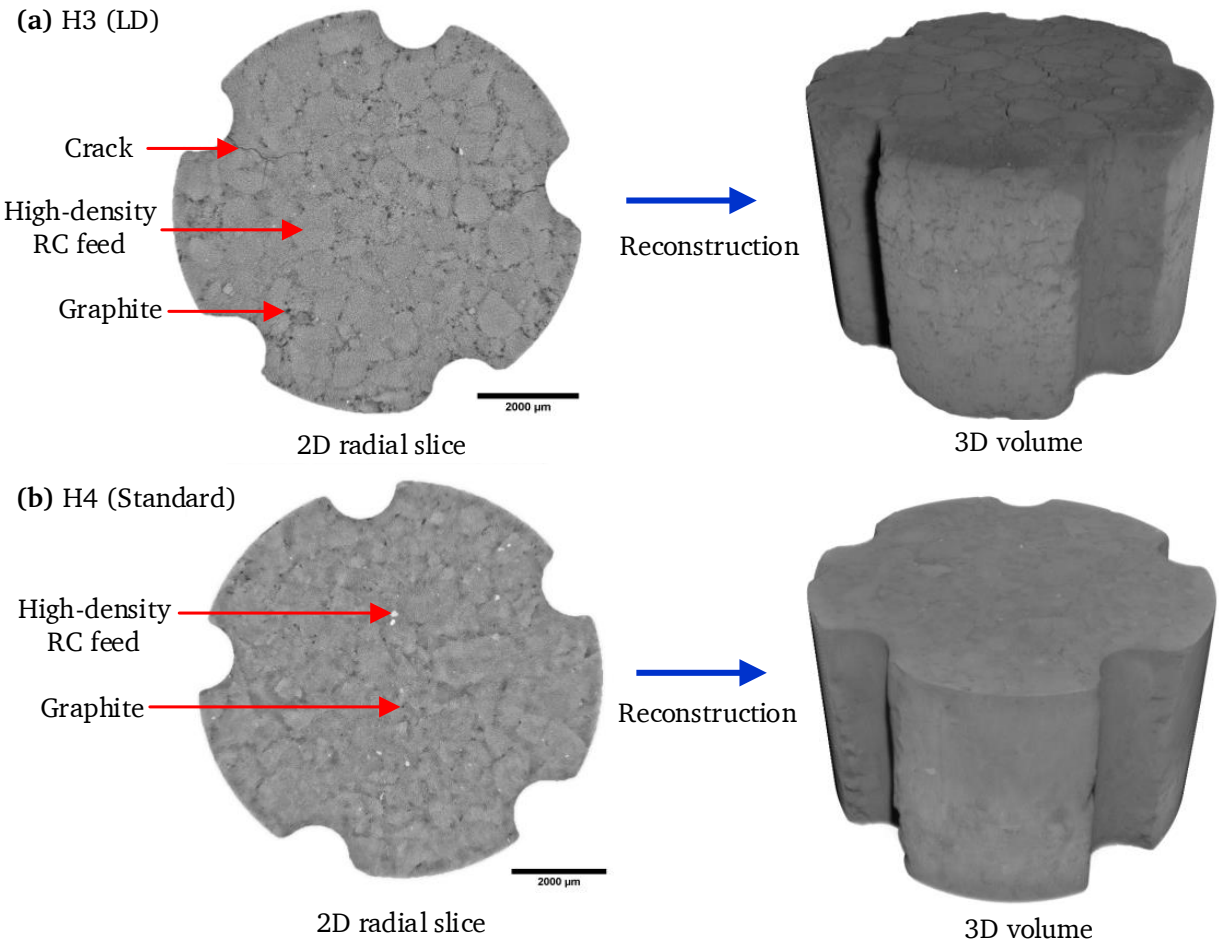


Figure 7.2: Raw 2D radial slice and 3D reconstructions for the empty HTS pellets **(a)** H1 pellet, and **(b)** H2 pellets.

are also graphite lubricant particles present on the images. The low-density H3 sample also has cracks, which look more extensive on the top and bottom ends of the sample. The H4 sample shown in Figure 7.2**b** displays both high density and low density roll compacted particles. There are also graphite lubricant particles, but no cracks on the H4 samples compared to other HTS pellets. The lack of cracks on the H4 sample could be attributed to the fact that this sample is not calcined, as cracking is widely considered to be as a result of the high-temperature calcination.[329]

7.3.2 Mercury Porosimetry Data

Figure 7.3 shows the raw data for mercury porosimetry experiment performed on whole pellets of HTS pellets. The raw data from the mercury porosimetry experiments were analysed using the Kloubek[69] correlation, which is a semi-empirical alternative to Washburn[71] equation, that is designed to remove the effects of contact hysteresis in mercury porosimetry data. All the samples

[329] J. Zhang et al. *Cryst. Res. Technol.*, **54**: 1800201, 2019.
[69] J. Kloubek. *Powder Technol.*, **29**: 89–97, 1981.
[71] W. E. Washburn. *Phys. Rev.*, **18**: 206–209, 1921.

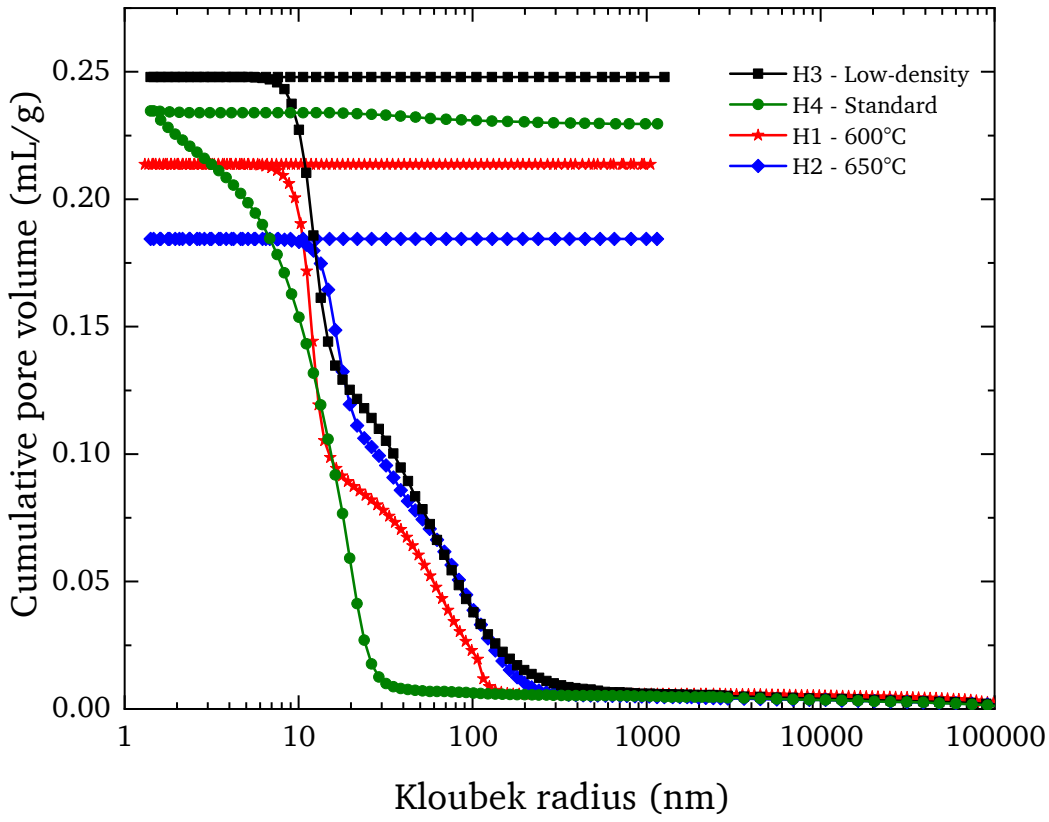


Figure 7.3: Comparison of typical examples of mercury porosimetry curves up to 60000 psia for the HTS pellets. The sample names are on the legends.

were subjected to a full intrusion up to 60000 psia, followed by a retraction back down to atmospheric pressure (14.7 psia). It can be seen from Figure 7.3 that the level of entrapment is very high for all the samples. Furthermore, the low-density sample (H3) shows the highest pore volume, whereas the H2 sample displays the lowest pore volume of all the samples.

As the mercury pressure starts to build up from low to high, the mercury starts to intrude into the gaps between the pellets, followed by long horizontal plateau before first significant intrusion starts at pressures of ∼500-600 psia for the H1 to H3 samples, and ∼3000 psia for the H4 sample. The first mercury intrusion leg for H1 to H3 samples fills in the biggest pores (>75 nm), and is followed by a second intrusion leg into smaller pore network starting at around ∼5000-6000 psia (∼55-75 nm). This suggests that H1, H2 and H3 samples have a bimodal pore structure sytem. This attribute is not observed in the H4 samples, indicating that H4 is a unimodal material. The H1 to H3 samples also display horizontal flat plateau at the highest pressure point, suggesting that all the pores are filled at this pressure (60000 psia), and no more mercury could be intruded into the sample.

The small initial intrusion of mercury at ∼0.01 MPa is due to the inter-pellet pentration, before intra-pellet intrusion begins at the pressure mentioned above for the different samples. As the pressure is lowered, there is a flat plateau for all the samples, which suggest that virtually all the

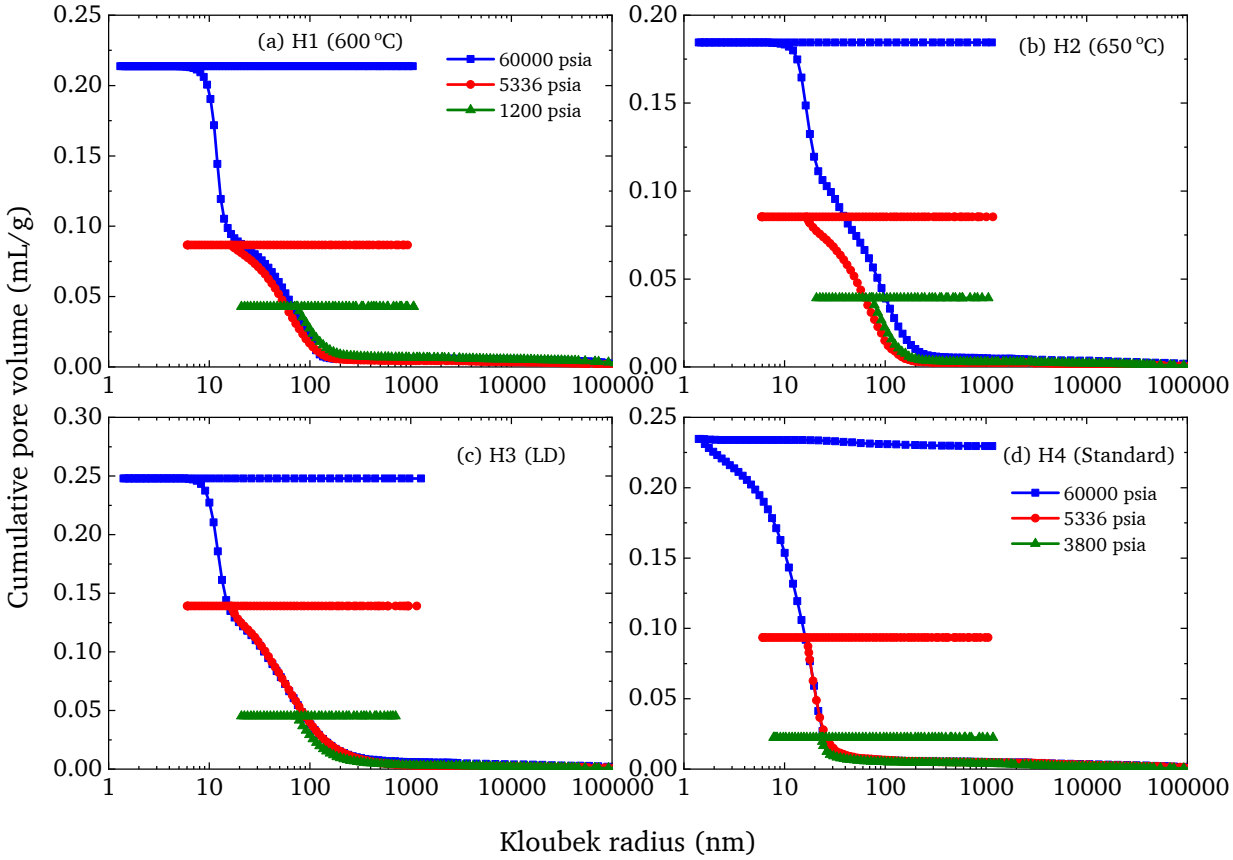


Figure 7.4: Mercury porosimetry scanning curves for the whole pellets analysed using the Kloubek correlation. **(a)** H1, **(b)** H2, **(c)** H3 and **(d)** H4. The mercury scanning curve pressures are indicated on the graph legends.

mercury that gets trapped in the pores remains trapped within the sample as no mercury leaves the sample, except for the H4 sample, where only <2% of the mercury leaves the pellet at 60000 psia.

Mercury scanning curve technique as well as powdering the samples were both employed in order to determine the cause of the mercury entrapment in the HTS pellets. The results of the mercury scanning curves analysed using the Kloubek[69] correlation are shown in Figure 7.4. As can be seen from the figures, no superposition is achieved with the Kloubek correlation for these samples, as the samples do not display mercury hysteresis. Mercury scanning pressure of up to 5336 psia was solely selected in order to separate the macro-and-mesopore pore structure networks seen in the H1 to H3 pellets (see Figure 7.7). From the mercury scanning curve figures for the HTS pellets, it can be seen that all the samples display up to 100% mercury entrapment for each mercury pressure used, suggesting that the mercury entrapment in the HTS pellets is independent of mercury scanning curves used.

The HTS samples were also powdered into particle sizes of ~50-75 μm, which is similar to the particle sizes of the starting feed particles of these pellets. The powdered samples were then subjected to full mercury intrusion up to 60000 psia, and the results were compared with that of

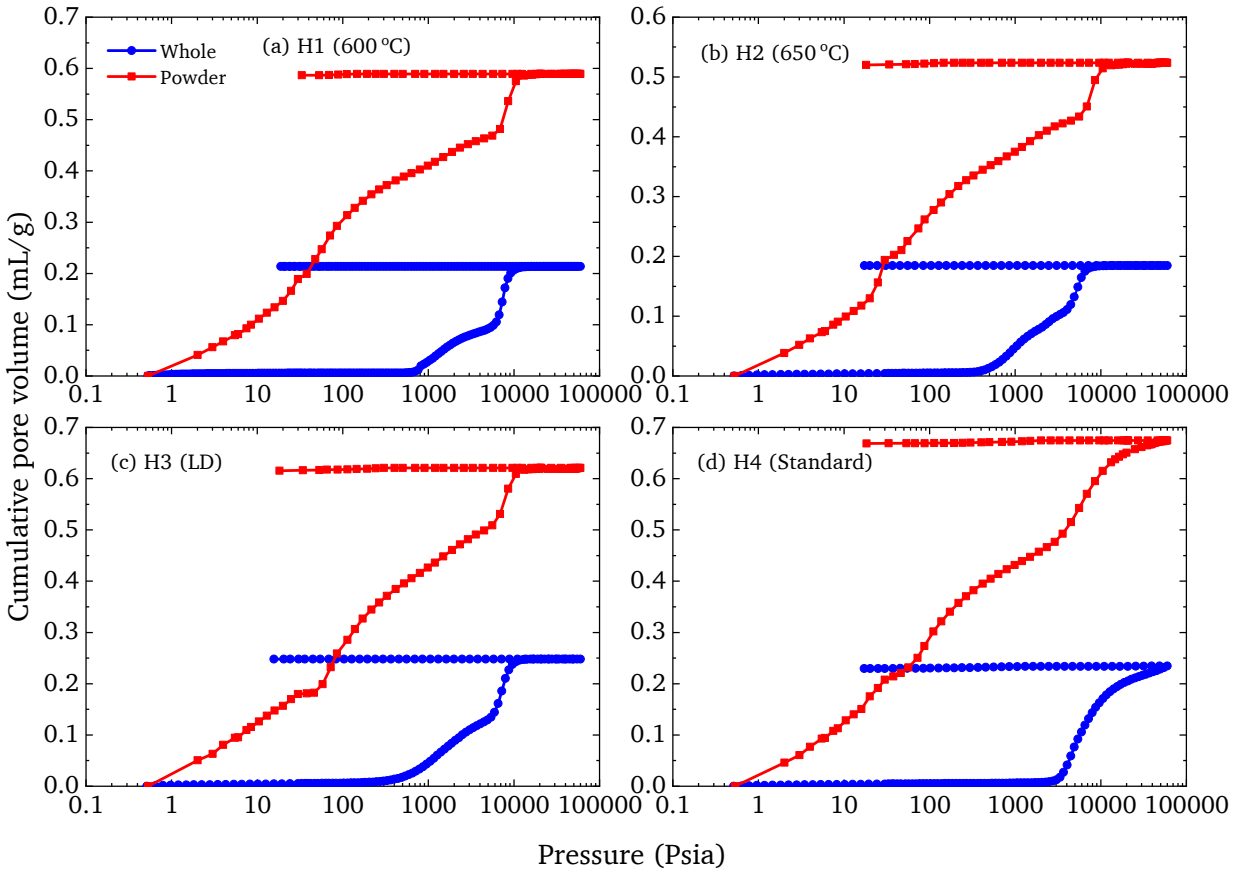


Figure 7.5: Mercury intrusion and extrusion comparison for the whole and powdered HTS pellets up to 60000 psia. The powdered pellet curves have not been adjusted. **(a)** H1, **(b)** H2, **(c)** H3 and **(d)** H4 pellet.

whole pellets from the same batch. The results for mercury intrusion and extrusion comparison for the whole and powdered HTS pellets are shown in Figure 7.5. The mercury intrusion data for the powdered sample shows a very high initial inter-particle intrusion, and therefore needed to be corrected for this rise, so that it could be compared with the data for the whole pellets. The powdered sample also displays a flat horizontal plateau at the highest mercury intrusion pressure and up to 100% mercury entrapment. The results of the adjusted powdered samples and the whole pellet comparisons are displayed in Figure 7.6. The figures show that the shapes of the powdered and whole pellets are similar after this adjustment, suggesting that the mercury entrapment in the powdered samples is independent of fragmenting the pellets into a powdered with sizes up to ∼50-75 µm.

Mechanically robust samples, such as HTS catalyst pellets, can be fractured to produce particles of varying sizes. In the past, it has been shown that the shape of the mercury intrusion curve and the quantity of entrapment change with particle size variation for catalyst pellets ranging from millimetres to ∼10−100s micrometres.[101] If the pellet is macroscopically patchwise heterogeneous, that is, if there is large-scale spatial correlation in pore size, fragmenting the pellet may

[101] S. P. Rigby. *J. Colloid Interface Sci.*, **224**: 382–396, 2000.

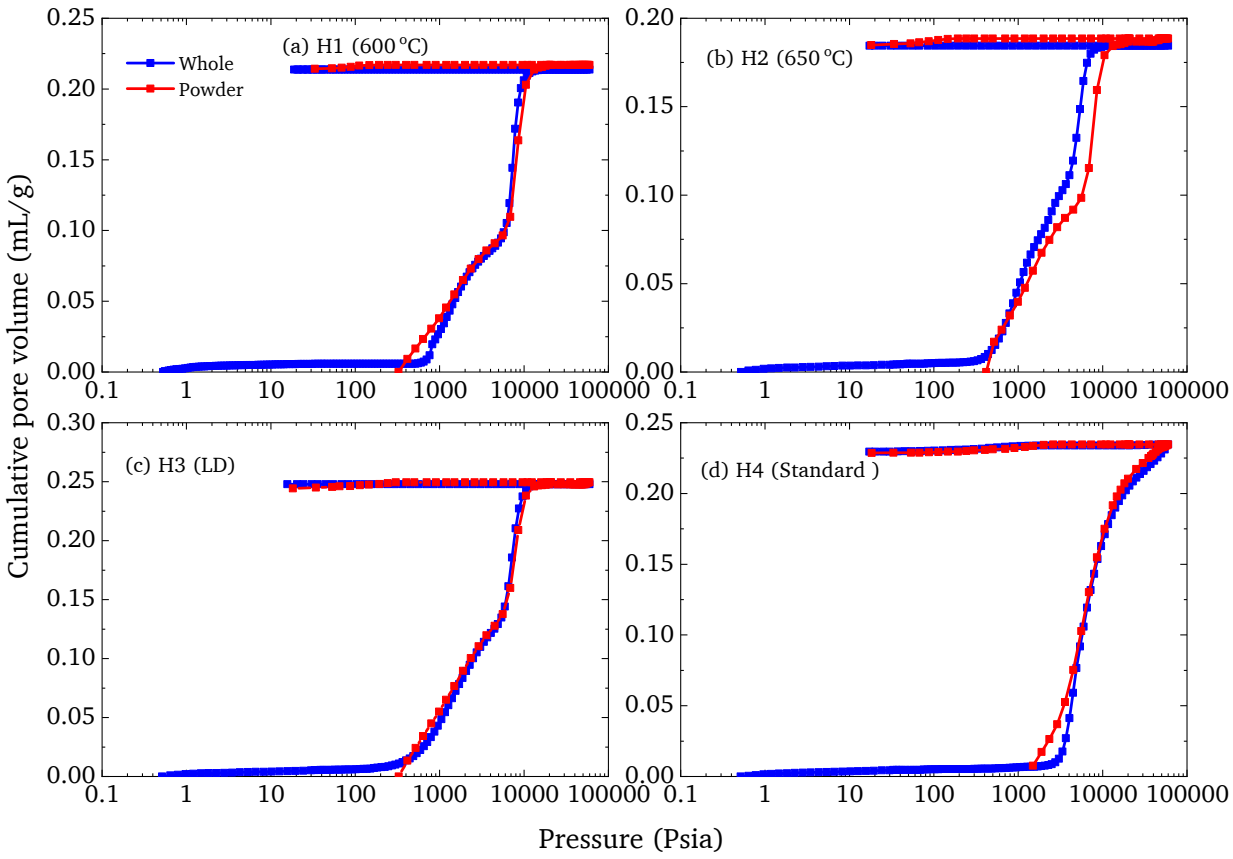


Figure 7.6: Mercury intrusion and extrusion comparison for the whole and powdered HTS pellets up to 60000 psia. The powdered pellet curves have been adjusted to match superpose the whole pellet data. **(a)** H1, **(b)** H2, **(c)** H3 and **(d)** H4 pellet.

de-shield a significant number of bigger pores, changing the shape of the percolation transition. On fragmentation of the sample, the mercury intrusion knee is expected to become more rounded and move toward bigger pore sizes.[7]

7.3.3 Mercury porosimetry Pore Size Distribution

Figure 7.7 shows the mercury porosimetry pore size distributions for the HTS following intrusion up to 5336 and 60000 psia. The differential distribution curve is obtained by differentiating the cumulative distribution curve and is essentially a plot of dV/d(log d) vs log d. This type of plot has the advantage of displaying a spectrum of pore sizes and is especially useful when the sample has two or more unique peak pore sizes (see H1-H3 plots). Furthermore, the area under the differential distribution curve can be used to estimate the pore volume in any pore range. The purpose of presenting data on a log differential plot is to cause an equal peak area on a plotted curve to represent equal pore volumes.

[7] S. P. Rigby. *Structural characterisation of natural and industrial porous materials: A manual*. Springer Nature, 2020.

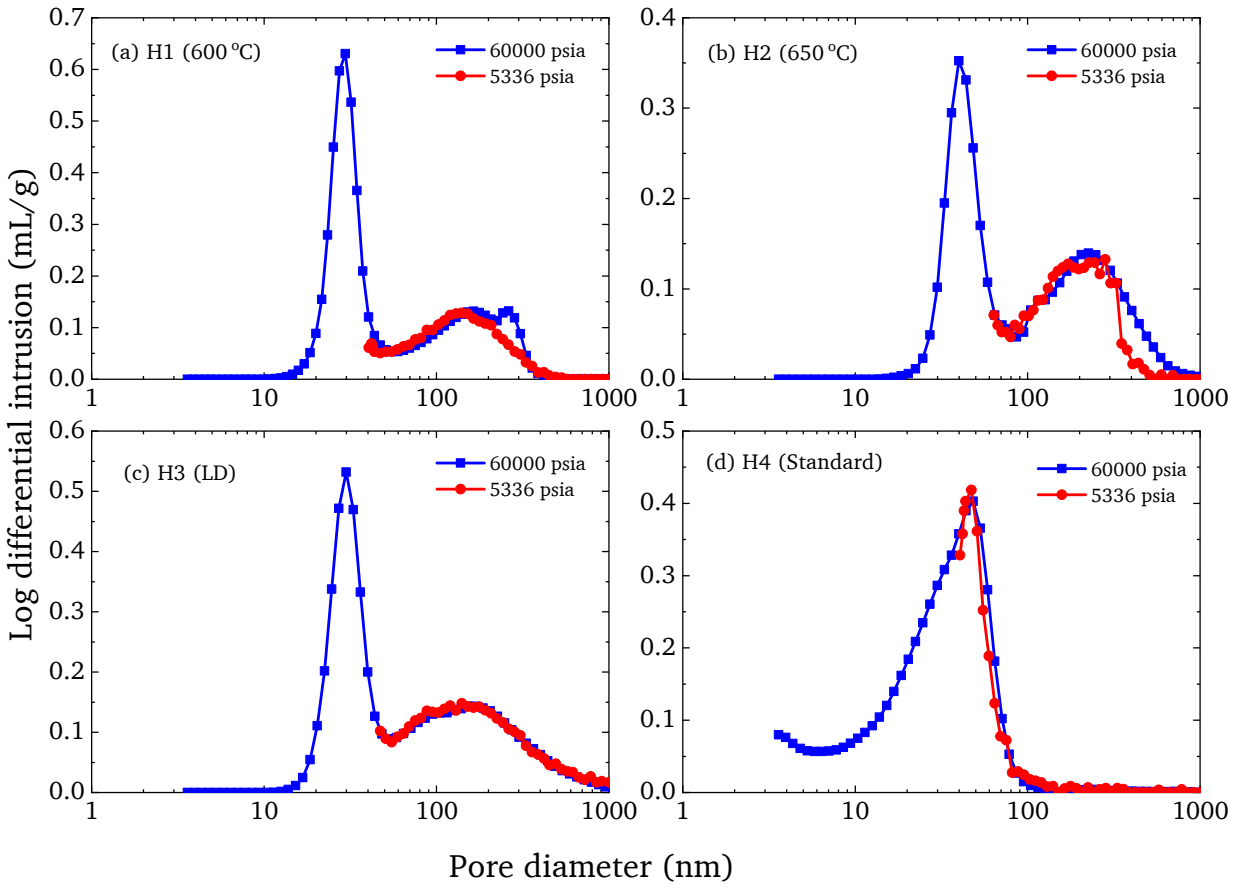


Figure 7.7: Mercury porosimetry pore size distributions for HTS pellets following intrusion up to 5336 and 60000 psia. **(a)** H1, **(b)** H2, **(c)** H3, and **(d)** H4 samples.

The log-differential pore volume curves for the H1 to H3 samples show a bimodal pore structure, where most of the lower pore ranges are below $\sim$30 nm. Additionally, the smaller pore size range of the plots contains a significant portion of the pore size distributions. The figure also clearly shows that the 5336 psia scanning pressure effectively divides the PSDs for H1-H3 samples into two segments, turning them from bimodal to a unimodal pore structure system as the mercury gets trapped in the bigger pore range (>35 nm). The H4 sample has a unimodal pore structure, with the most probable pore size being around $\sim$47 nm.

7.3.4 CXT Images of Pellets Following Mercury Porosimetry

Figure 7.8 shows a typical reconstructed 2D radial slice and 3D CXT image of the whole pellet for the H1 sample following mercury intrusion up to 1200 psia leading to entrapment filling up to 20.1% of the pore space. Because mercury has a high electron density, the regions of the pellet containing entrapped mercury appear as brilliant white pixels, whereas the empty pellet regions appear as grey in colour. From the image, it can be seen that mercury get intruded into the bigger pores and the cracks in the samples. Furthermore, a large portion of pellet are left unintruded by

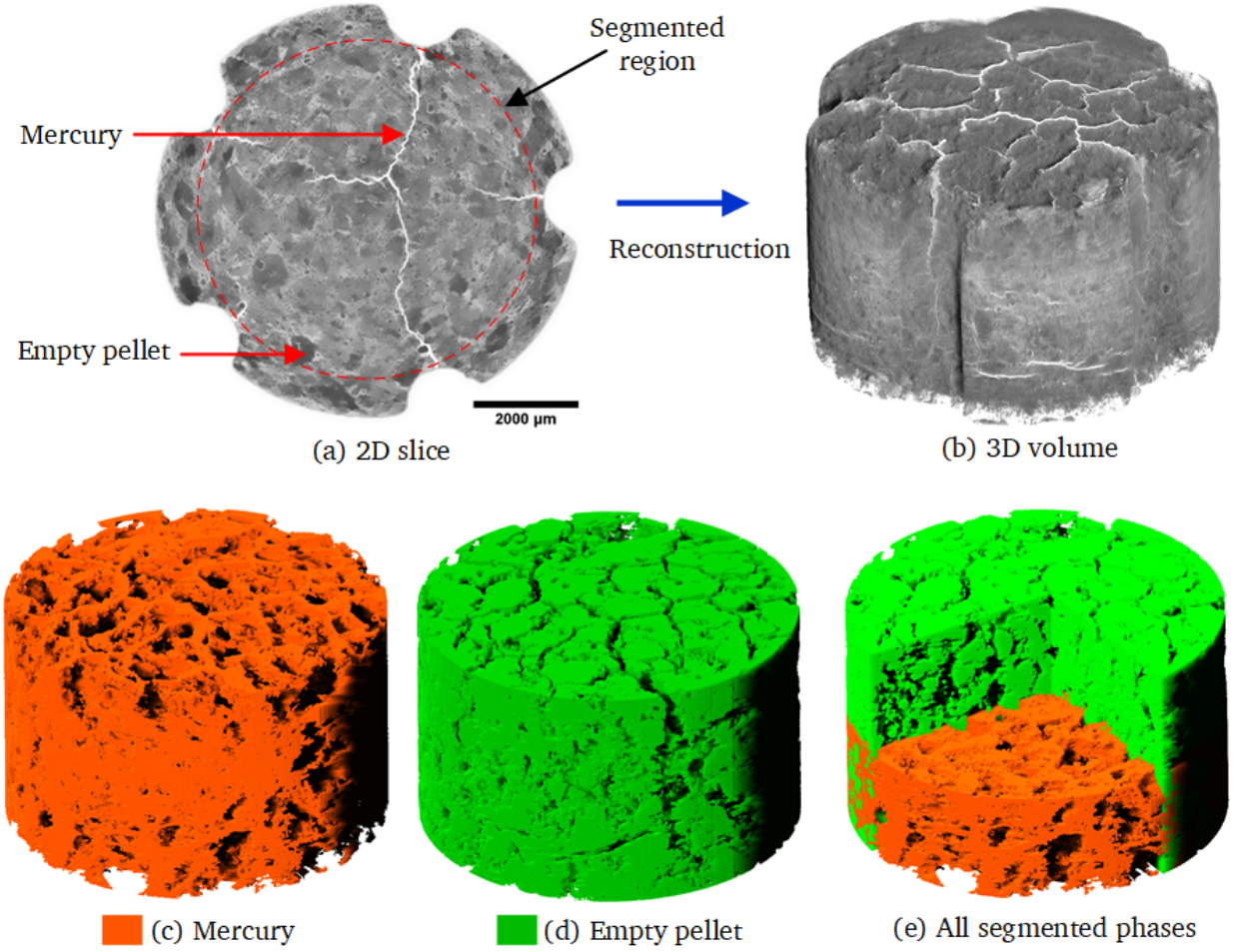


Figure 7.8: Raw and segmented CXT images of H1 pellet following mercury porosimetry up to 1200 psia leading to entrapment filling 20.1% of the pore space. **(a)** Raw 2D radial slice. Bright white regions correspond to mercury, **(b)** 3D reconstructed grayscale volume of the pellet exterior, **(c)** Entrapped mercury in the void spaces (orange) representing 42.8%, **(d)** Pellet regions with no entrapped mercury (green) representing 57.2% of the volume fraction, and **(e)** All the segmented phases. The scale bar corresponds to 2000 µm.

mercury since they are likely to have a higher density than the remainder of the feed particles, and are surrounded by pores with smaller neck sizes than the minimum pore diameter penetrable by the current mercury scanning curve pressure. The H1 samples have more extensive fracture networks than the rest of the HTS pellets. The fracture network appears to be more complex near the pellet's top and bottom ends than in the middle of the pellet.

Figure 7.8 also contains the segmentation results for the H1 sample. The image has been segmented into two bins of intensity corresponding to mercury containing and the empty regions of the pellets using deep learning[266] imaging segmentation. The deep learning method utilised here is based on the software Dragonfly from ORS,[258] which uses the popular TensorFlow[282] deep

[266]Y. Lecun, Y. Bengio, and G. Hinton. *Nature*, **521**: 436–444, 2015.
[258]R. Makovetsky, N. Piche, and M. Marsh. *Microsc. Microanal.*, **24**: 532–533, 2018.
[282]A. Martín et al. *CoRR*, 265–283, 2016.

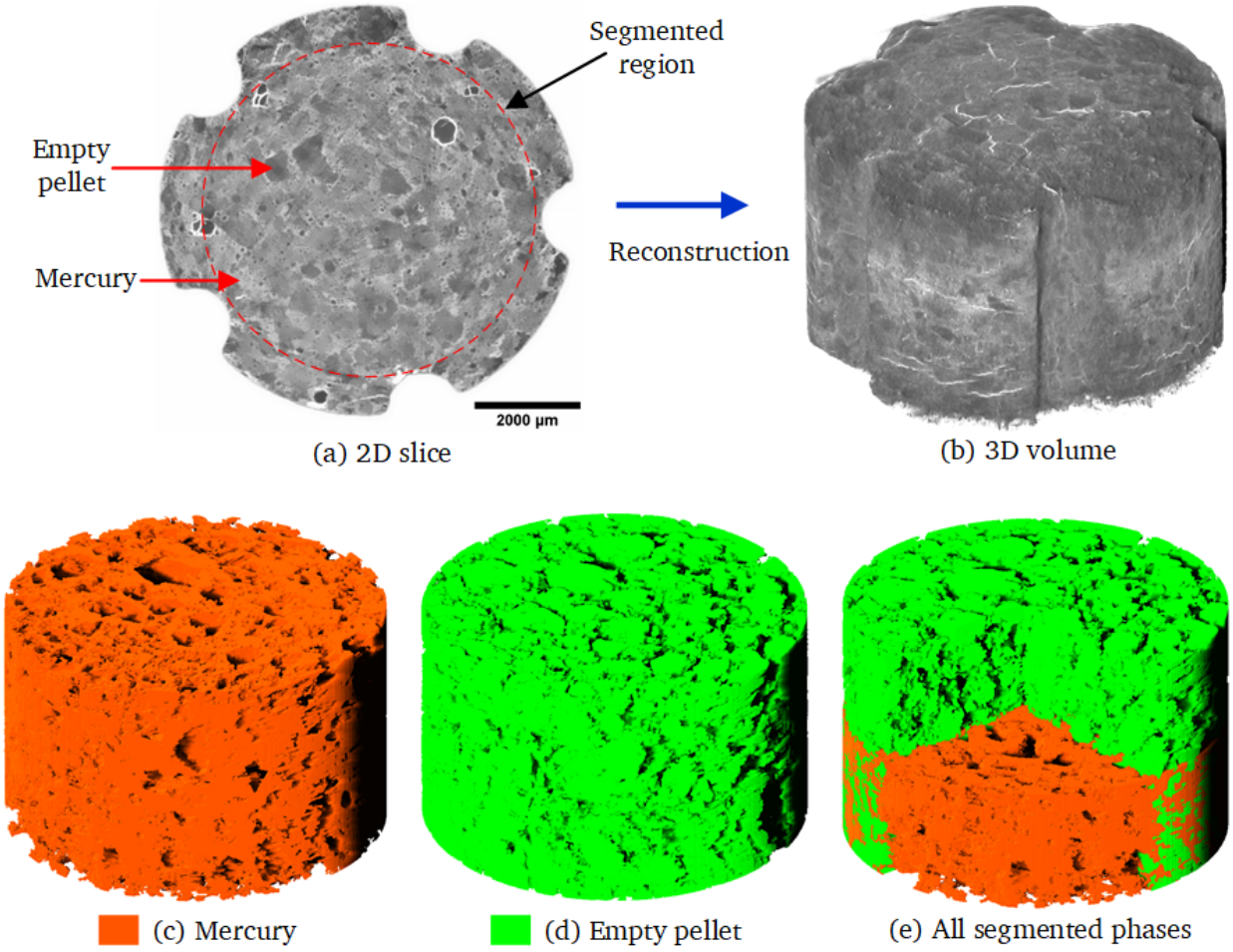


Figure 7.9: Raw and segmented CXT images of H2 pellet following mercury porosimetry up to 1200 psia leading to entrapment filling 21.2% of the pore space. **(a)** Raw 2D radial slice. Bright white regions correspond to mercury, **(b)** 3D reconstructed grayscale volume of the pellet exterior, **(c)** Entrapped mercury in the void spaces (orange) representing 51.7%, **(d)** Pellet regions with no entrapped mercury (green) representing 48.3% of the volume fraction, and **(e)** All the segmented phases. The scale bar corresponds to 2000 µm.

learning engine in a user-friendly image processing environment. Because of the shape of the HTS samples, it was not possible to carry out segmentation on the entire pellet image as it currently is; therefore, the CXT images of the HTS pellets were cropped to extract a cylindrical volume with a similar shape as the methanol catalyst pellet discussed in Chapters 3 to 5. The middle regions of the pellet chosen for the segmentation are highlighted with a circle (red dashed line) as shown in Figure 7.8. The volume fractions of the mercury and rest of the empty pellet as calculated from the CXT segmented images were 42.8% and 57.2%, respectively.

Figure 7.9 shows a typical reconstructed 2D radial slice and 3D CXT image of the whole pellet for the H2 sample following mercury intrusion up to 1200 psia leading to entrapment filling up to 21.2% of the pore space. The 3D surface rendering allows for quick visualisation of the spatial distribution of different phases in the catalyst pellet studied. As can be seen from the images, the mercury gets trapped preferentially in the larger pores and the fracture network on the

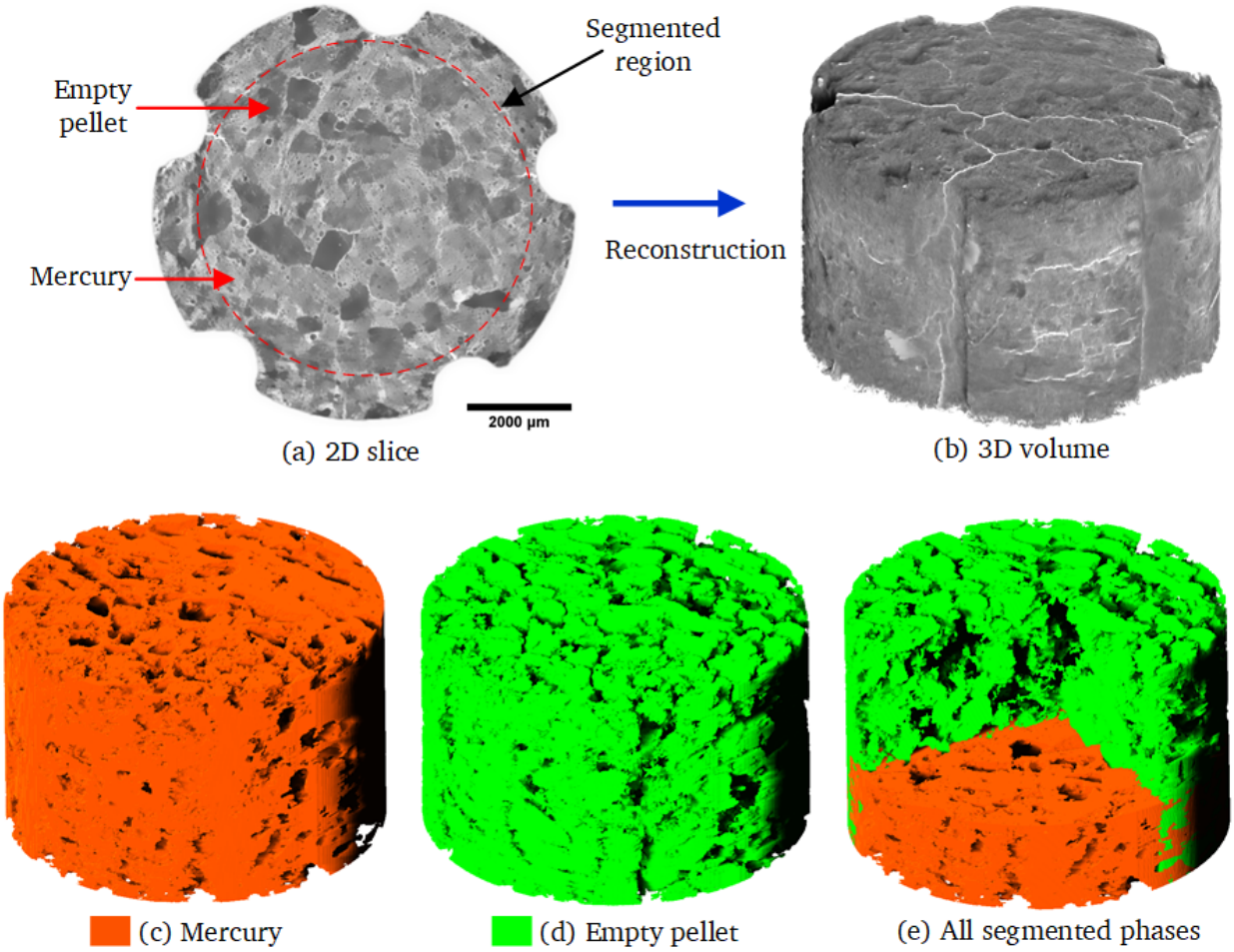


Figure 7.10: Raw and segmented CXT images of H3 pellet following mercury porosimetry up to 1200 psia leading to entrapment filling 18.2% of the pore space. **(a)** Raw 2D radial slice. Bright white regions correspond to mercury, **(b)** 3D reconstructed grayscale volume of the pellet exterior, **(c)** Entrapped mercury in the void spaces (orange) representing 60.3%, **(d)** Pellet regions with no entrapped mercury (green) representing 39.7% of the volume fraction, and **(e)** All the segmented phases. The scale bar corresponds to 2000 µm.

sample. The mercury intrusion pattern on the H2 sample forms what looks like a 'Sierpiński gasket' fractal shape.[330] The Sierpiński triangle is a fractal with the shape of an equilateral triangle, named after the Polish mathematician Wacław Sierpiński. The triangle can be subdivided indefinitely into smaller equilateral triangles that are identical to the original. As a result, the Sierpiński triangle looks much like a Christmas tree. Figure 7.9 also contains the segmentation results for the H2 sample. The selected region of the H2 sample has been segmented into two bins of intensity corresponding to mercury-containing and the empty regions of the pellets. The volume fraction based on mercury (orange colour) pixel intensity from the CXT images is 51.7%, and the rest of the unfilled pore spaces in the pellet represents 48.3% of the volume fraction.

Figure 7.10 shows a typical reconstructed 2D radial slice and 3D CXT image of the whole

[330]E. M. Anitas. *J. Nanomater.*, **10**: 925, 2020.

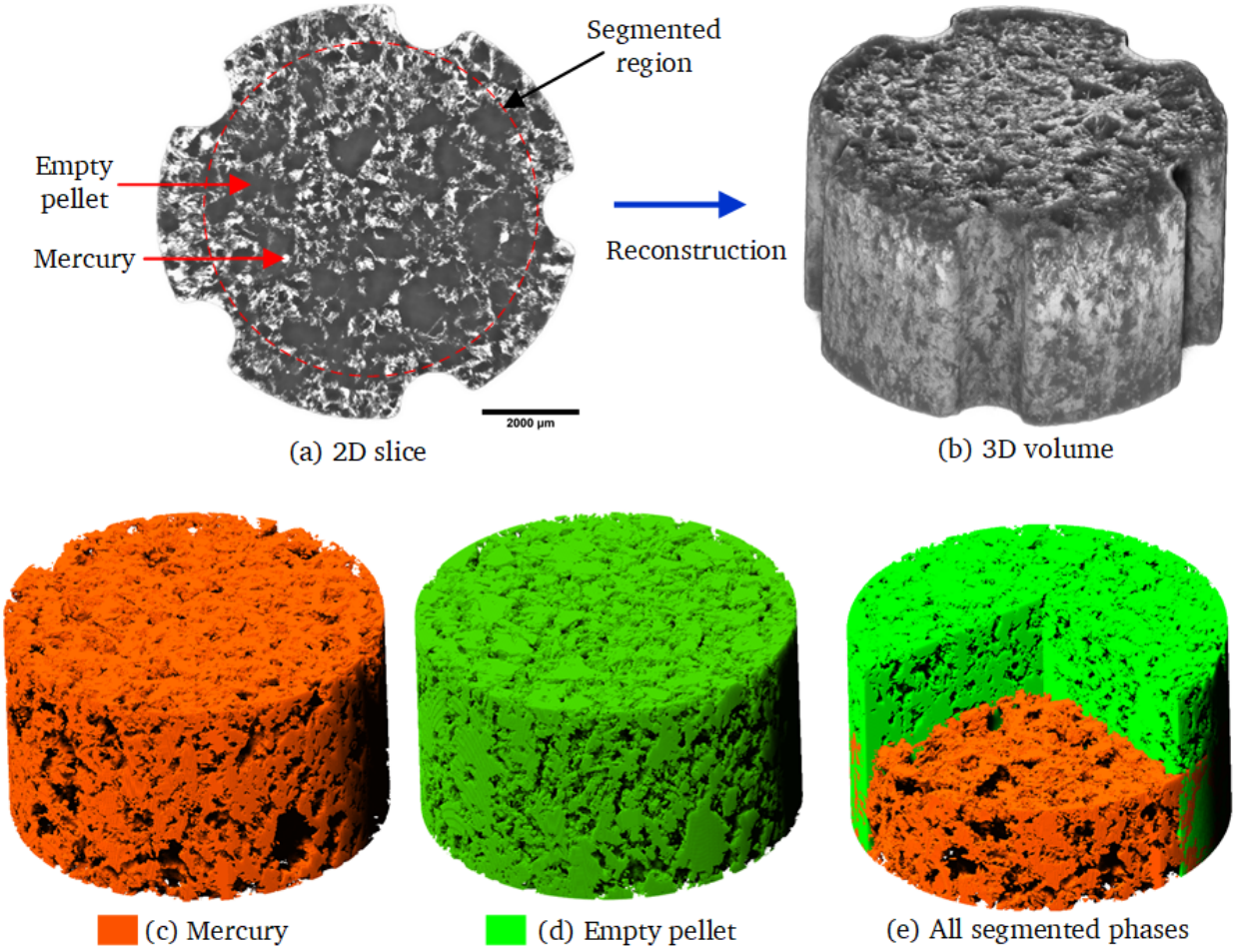


Figure 7.11: Raw and segmented CXT images of H3 pellet following mercury porosimetry up to 3800 psia leading to entrapment filling 9.6% of the pore space. **(a)** Raw 2D radial slice. Bright white regions correspond to mercury, **(b)** 3D reconstructed grayscale volume of the pellet exterior, **(c)** Entrapped mercury in the void spaces (orange) representing 37.5%, **(d)** Pellet regions with no entrapped mercury (green) representing 62.5% of the volume fraction, and **(e)** All the segmented phases. The scale bar corresponds to 2000 µm.

pellet for the H3 sample following mercury intrusion up to 1200 psia leading to entrapment filling up to 18.2% of the pore space. The H3 pellet, like the H1 and H2 samples, has a fracture network throughout the sample, which is visible due to the mercury filling the fractures. Furthermore, many areas of the pellet are mercury-free because they have a higher density than the rest of the feed particles or because the pores surrounding them have narrower neck diameters than the lowest pore diameter penetrable by the mercury scanning curve pressure. The selected region of the H3 sample has been segmented into two bins of intensity corresponding to mercury-containing and the empty regions of the pellets. The volume fraction based on mercury (orange colour) pixel intensity from the CXT images is 60.3%, and the rest of the unfilled pore spaces in the pellet represents 39.7% of the volume fraction.

Figure 7.11 shows a typical reconstructed 2D radial slice and 3D CXT image of the whole pellet for the H4 sample following mercury intrusion up to 3800 psia leading to entrapment filling up to

9.6% of the pore space. It can be observed from the images that after mercury has breached a band in the pellet's outer regions at low pressure, any further intrusion is more dendritic in form, with a percolation threshold being reached at this scanning curve pressure. The fractal dendritic form of the mercury intrusion path is more clearly evident in the 2D reconstruction CXT images of the H4 pellet shown in figure Figure 7.11. The image has been segmented to separate the mercury-intruded areas from the rest of the pellet matrix. Large sections of the pellet, however, remain unintruded. The volume fraction based on mercury (orange colour) pixel intensity from the CXT images is 37.5%, and the rest of the unfilled pore spaces in the pellet represents 62.5% of the volume fraction. The irregular polygonal shape of the dark unintruded zones indicates that they are most likely related to the high-density roll compacted feed particles contained within the pellet. The H4 pellet, unlike the H1-H3 samples, does not exhibit fracture network; therefore, intrusion occurs in the larger pores found in lower-density feed particles and low-density portions surrounding high-density feed particles. The absence of fractures in the H4 sample might be explained by the fact that it was not calcined, as cracking is commonly associated with high-temperature calcination.

7.3.5 Gas Sorption

Figure 7.12 shows the gas sorption isotherms for the HTS pellets before and after mercury entrapment up to different pressures (as shown in the captions). The figure also shows inset figures for samples H1 to H3 starting from a relative pressure of ∼0.8, as the region of interest is the capillary hysteresis region for these materials. The isotherms for the H1 to H3 samples before mercury porosimetry have similar shapes but different ultimate amounts of gas adsorbed. The quantity of gas adsorbed is relatively small until relative pressure of ∼0.8, representing the gas adsorbing onto the surface of these samples. However, at relative pressure ∼0.8-0.82, capillary condensation in the pores starts and continues up to a relative pressure of ∼1. The isotherms for the H1 to H4 samples have plateaued at relative pressure ∼1, suggesting that all the pores have been filled with condensate at the highest relative pressure possible in a conventional gas adsorption experiment. The largest pore size that can be probed with a gas adsorption experiment is ∼50 nm.[7] Since the isotherm for these sample reaches a plateau, H1-H3 samples do not possess pores greater than 50 nm for gas adsorption. When the direction of pressure is reversed on the desorption branch, the amount of adsorbed gas does not decrease immediately, and there is a flat plateau between ∼1-0.98. There is also a knee point at relative pressure ∼0.98, and the capillary evaporation then continues to a second percolation knee at relative pressure ∼0.9-0.92. After this second knee, the capillary evaporation continues to the hysteresis closure point at a relative pressure of ∼0.75.

Compared to H4, the adsorption and desorption isotherms for the H1 to H3 samples are not smooth curves. At relative pressure ∼0.952, for example, there is a prominent inflexion point on the desorption curve, indicating that the pore structure of the H1 to H3 sample is bimodal. H4 sample produces a type II isotherm with an H1-type hysteresis loop according to the IUPAC classifications.[36] The H4 sample produced a smooth curve with no inflexion point, with a similarly

[36] M. Thommes et al. *Pure Appl. Chem.*, **87**: 1051–1069, 2015.

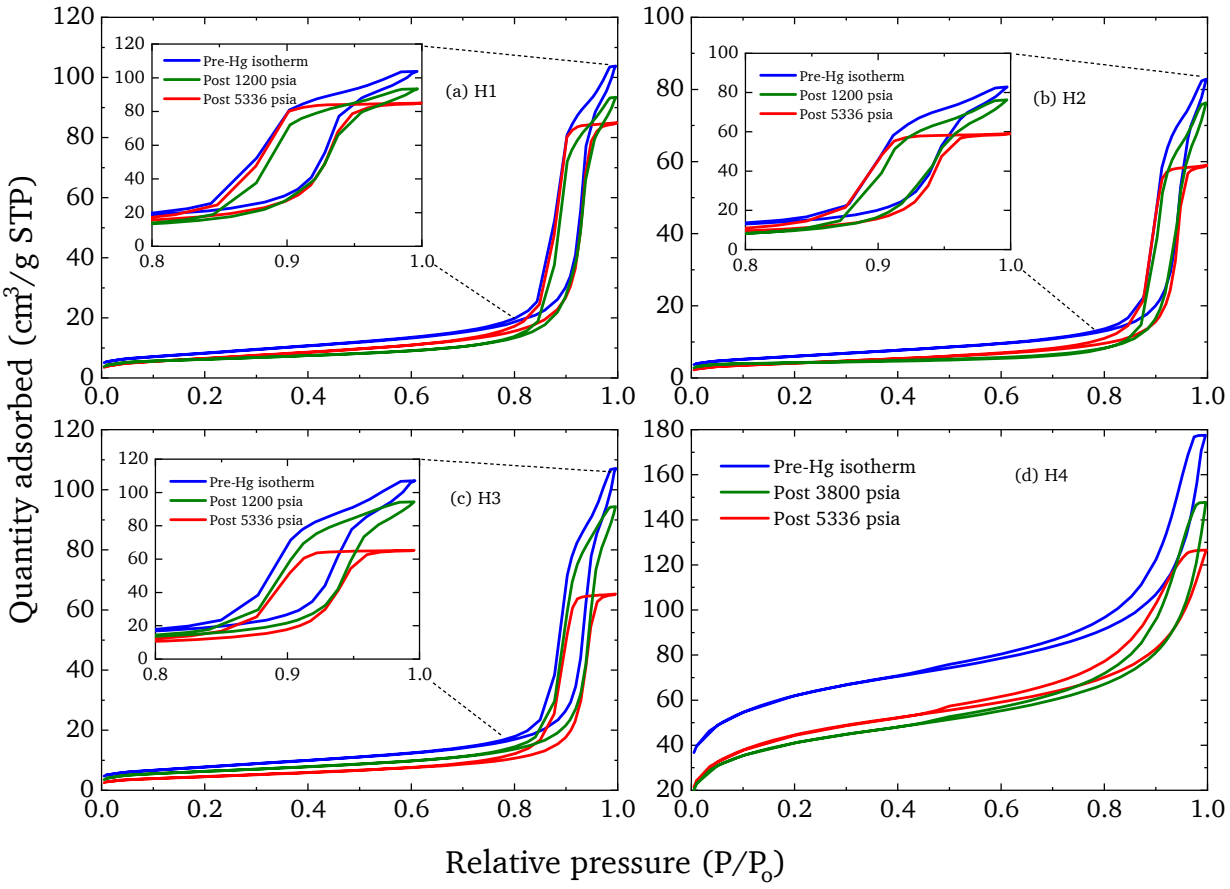


Figure 7.12: Gas sorption isotherms before and after mercury porosimetry up to different pressures for HTS pellets. **(a)** H1 before and after 5336 and 1200 psia, **(b)** H2 before and after 5336 and 1200 psia, **(c)** H3 before and after 5336 and 1200 psia, and **(d)** H4 before and after 5336 and 3800 psia.

shaped isotherms for before and after mercury porosimetry, suggesting that the pore structure of the H4 sample is unimodal. The nitrogen gas adsorption isotherm for the H4 sample shows the highest pore volume of all tested samples, with a pore volume of ∼178 cc/g STP. From the nitrogen isotherms for the H4 sample, it can be seen that the pore volume accessible to nitrogen decreases with higher mercury scanning curve pressures due to increased mercury entrapment.

Table 7.4: Summary of pore volume lost due to mercury entrapment for the HTS pellet.

Sample	Pore volume from N_2 sorption (Pre Hg) (cc/g)	Pore volume from N_2 sorption (Post Hg) (cc/g)	Entrapped Mercury pore (cc/g)
H1	0.164	0.132	0.032
H2	0.127	0.092	0.038
H3	0.154	0.102	0.055
H4	0.292	0.203	0.085

Figure 7.12 also contains the gas sorption isotherms for the HTS samples following the mercury porosimetry experiment up to different pressures. In order to compare the isotherms before

and after mercury porosimetry, the isotherm plots have been overlaid on the same figures. For H1 to H3, the isotherms following mercury intrusion up to 1200 psia display the same shape as the pre-mercury isotherms, and the isotherms do not exhibit a flat plateau at relative pressures ∼1. However, the pore volume has dropped by ∼10-12% due to mercury filling some of the larger pores in the sample. When the mercury intrusion pressure has been increased to 5336 psia, the shape of the isotherms for H1 to H3 samples has changed to type IV isotherm according to the IUPAC isotherm classifications;[36] with an apparent flat plateau at relative pressure ∼1, and the amount of adsorbed gas has reduced by ∼18-39%. The flat plateau indicates that all the pores accessible by nitrogen gas become filled with condensate. This suggests that the mercury has become entrapped, at least, in the biggest pores that could not previously be filled with condensate. Furthermore, when the direction of pressure change is reversed to commence the desorption process, the quantity adsorbed does not immediately decrease. Instead, there is a flat section of the isotherm that continues until relative pressure ∼0.922, and capillary evaporation begins at this pressure. This suggests that the mercury is either entrapped within the pores that desorption could occur from before mercury porosimetry and were responsible for creating the 'swan-neck ' like top parts of the isotherms. Alternatively, it is possible that the entrapped mercury is situated in such a way that it blocks quick evaporation from these pores when the direction of pressure change is reversed.

7.3.6 Incremental Pore Volume

To understand where the mercury is entrapped in the HTS pellets more clearly, 'change in incremental amount adsorbed graphs' have been calculated and plotted for the adsorption boundary curves, as shown in Figure 7.13. The change in the incremental amount of adsorbed plots has been generated based on the adsorption isotherm for before and after mercury intrusion up to 5336 psia only, as this is the more interesting result of the two scanning curves shown in Figure 7.12. These plots were obtained by subtracting the incremental amount adsorbed between each respective pair of pressure points for the isotherms before and after mercury entrapment. The nitrogen sorption isotherms measured before and after porosimetry were obtained using the same pressure table. Hence, it is possible to deconvolve the specific amounts of nitrogen adsorption and desorption that occurred prior to porosimetry within the particular pores that entrapped mercury by subtracting the isotherm obtained after porosimetry from the one obtained before porosimetry. Because the actual pressures recorded with the equipment for a particular pressure entered into the pressure table differed somewhat, linear interpolation between neighbouring data points was performed to calculate the quantity adsorbed for exactly the same pressures for both isotherms. For the HTS pellets, between relative pressures ∼0-0.85, there was very little difference between the incremental amounts adsorbed at a given relative pressure for before and after porosimetry; therefore, the plot is at approximately zero. This indicates that before and after mercury porosimetry, the isotherms are the same over this pressure region, and any small fluctuations in this pressure region have previously been explained as noise.[101] The relative pressures points between ∼0-0.85 are therefore not shown on the change in incremental amount adsorbed plots.

For the H1 and H2 samples, there is a positive signal around ∼0.925 relative pressure, which

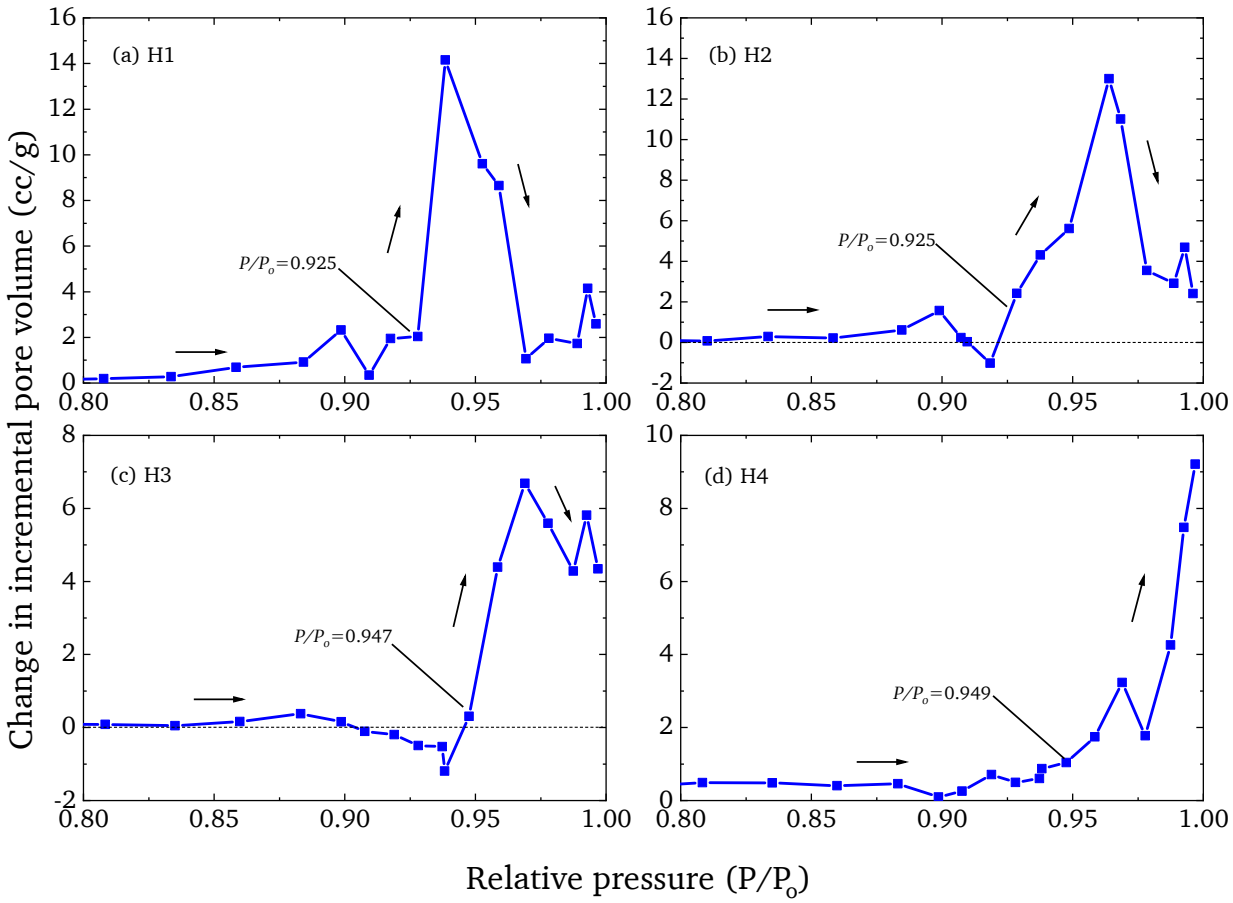


Figure 7.13: Change in incremental amount adsorbed plot for the HTS pellets based on adsorption branch. The incremental amount adsorbed was obtained by subtracting the isotherm obtained after porosimetry from that obtained beforehand. **(a)** H1, **(b)** H2, **(c)** H3, and **(d)** H4. Arrows have been added to indicate the direction of the change in pressure.

continues to ∼1. This positive signal shows that the gas sorption isotherm following mercury porosimetry adsorbs less gas than the equivalent isotherm that precedes mercury porosimetry due to mercury entrapment filling particular pores. From H1 and H2 figures, it can be seen that the smallest pores which entrap mercury fill at relative pressures ∼0.925 and continues to relative pressures 1, indicating that mercury is entrapped in pores that fill over this pressure range. For the H3 sample, there is a slight negative signal between ∼0.901-0.938, followed by a larger positive signal starting from 0.947. Again, it must be that the pores which entrap mercury fill in this relative pressure range. For H4 samples, the positive signal starts at around relative pressure of 0.949 and continues up to 1. Once more, it must be that the pores that entrap mercury are filled in this range of relative pressures.

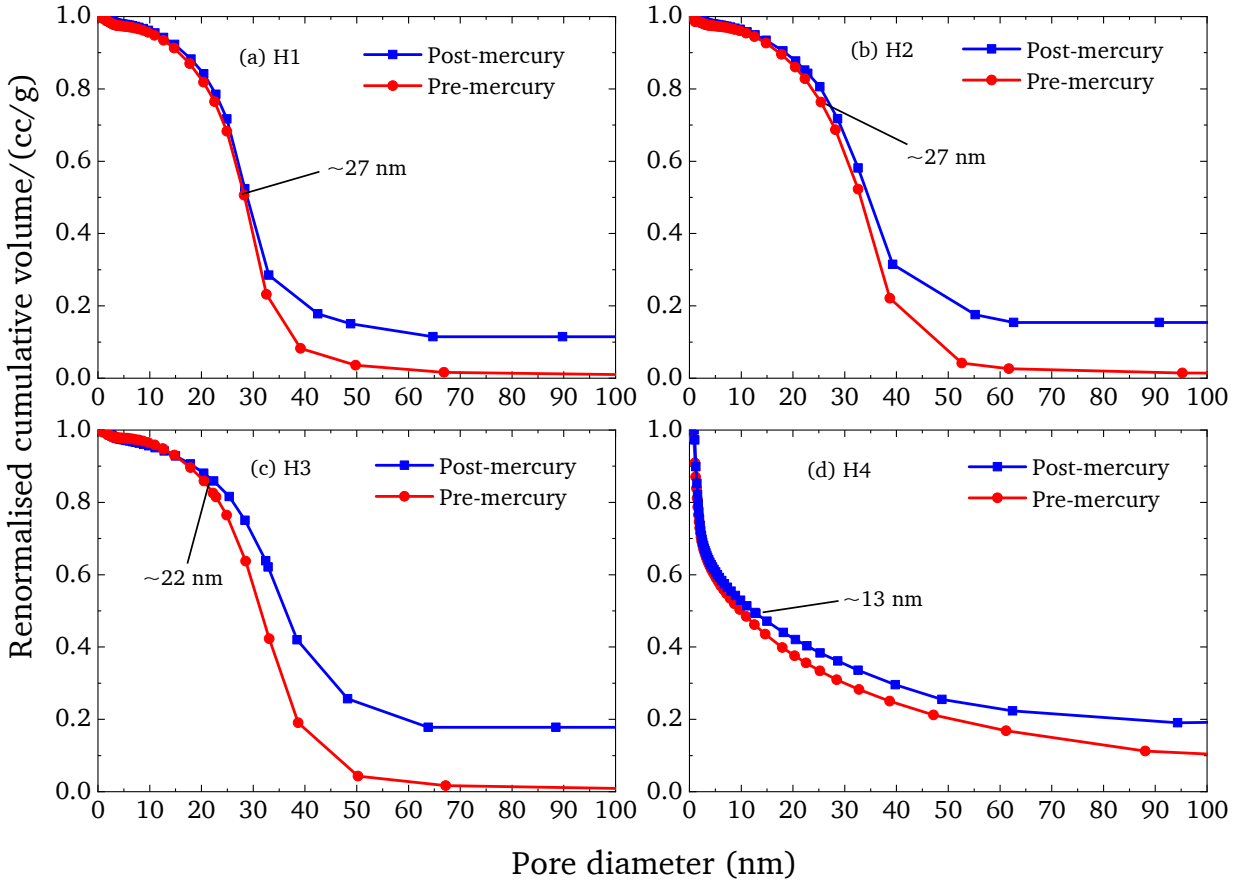


Figure 7.14: BJH cumulative PSDs derived from nitrogen adsorption isotherm obtained before and after mercury porosimetry up to 5336 psia for HTS pellets: **(a)** H1, **(b)** H2, **(c)** H3, and **(d)** H4. The ultimate pore volume of the cumulative distribution obtained after mercury has been renormalised such that it is the same as the before mercury.

7.3.7 Gas Sorption Pore Size Distribution

The pore size distribution (PSDs) obtained, using the BJH[44] algorithm, from the nitrogen adsorption isotherms obtained before and after mercury porosimetry for the HTS samples are shown in Figure 7.14. The ultimate pore volumes in the cumulative PSDs before and after mercury porosimetry has been renormalised to 1 to make the comparisons easier. This method of presenting the data demonstrates that the pore diameter distributions obtained after mercury entrapment are identical to that obtained before mercury porosimetry at smaller pore diameters but differ at larger pore diameters. Hence, the plots makes the loss of larger pores more apparent. As more mercury becomes entrapped, more larger pores become inaccessible to nitrogen. From the BJH PSD for the H1 and H2 samples, it can be seen that pores of sizes bigger than $\sim$27 nm are lost due to mercury entrapment within them. This is supported by the corresponding 'change in incremental amount adsorbed plots' for these samples shown in Figure 7.13, where there is a positive signal starting at relative pressure $\sim$0.925 ($\sim$27 nm) and continuing to 1, indicating that mercury is entrapped in pores that fill over this pressure range. Hence mercury porosimetry does not appear to have

[44] E. P. Barrett, L. G. Joyner, and P. P. Halenda. *J. Am. Chem. Soc.*, **73**: 373–380, 1951.

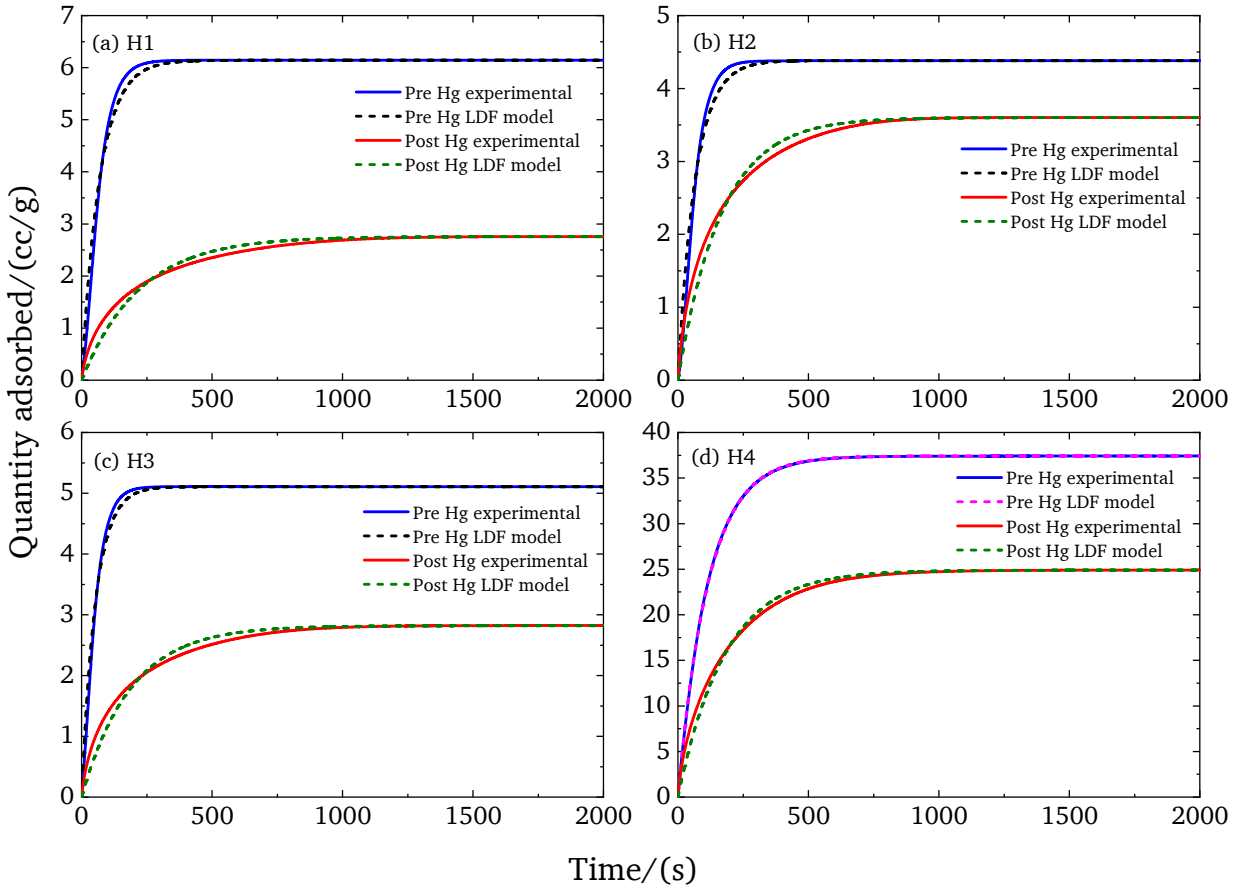


Figure 7.15: A comparison of the experimental nitrogen gas uptake data and the fits to the linear driving force (LDF) model for the HTS pellets before and after mercury porosimetry up to 5336 psia. **(a)** H1, **(b)** H2, **(c)** H3, and **(d)** H4 samples.

affected the accessibility of nitrogen to pores of radii less than $\sim$27 nm. The figure also shows that the lost pores for the H3 and H4 samples due to mercury entrapment up to 5336 psia are bigger than $\sim$22 and 13 nm, respectively.

7.3.8 Rate of Adsorption

Figure 7.15 shows the experimental gas uptake curves and the linear driving force (LDF) model fittings of the HTS sample before and after mercury porosimetry up to 5336 psia. Kinetic mass uptake data, comprising the amount adsorbed versus time, typically takes the mathematical form of exponential growth and, thus, is often fitted to the LDF model to extract the mass transfer coefficient (MTC)(denoted k).[7] The LDF model is the simplest and most commonly applied intraparticle mass transfer model to calculate the effectiveness of a particular porous system.[6] This model is found to give rise to good fits to the data with an R^2 of >0.9911. It is also found that most of the samples reach equilibrium after >1000 seconds. From the figures, it can be seen that the rate

[6]A. Nepryahin et al. *Chem. Eng. Sci.*, **152**: 663–673, 2016.

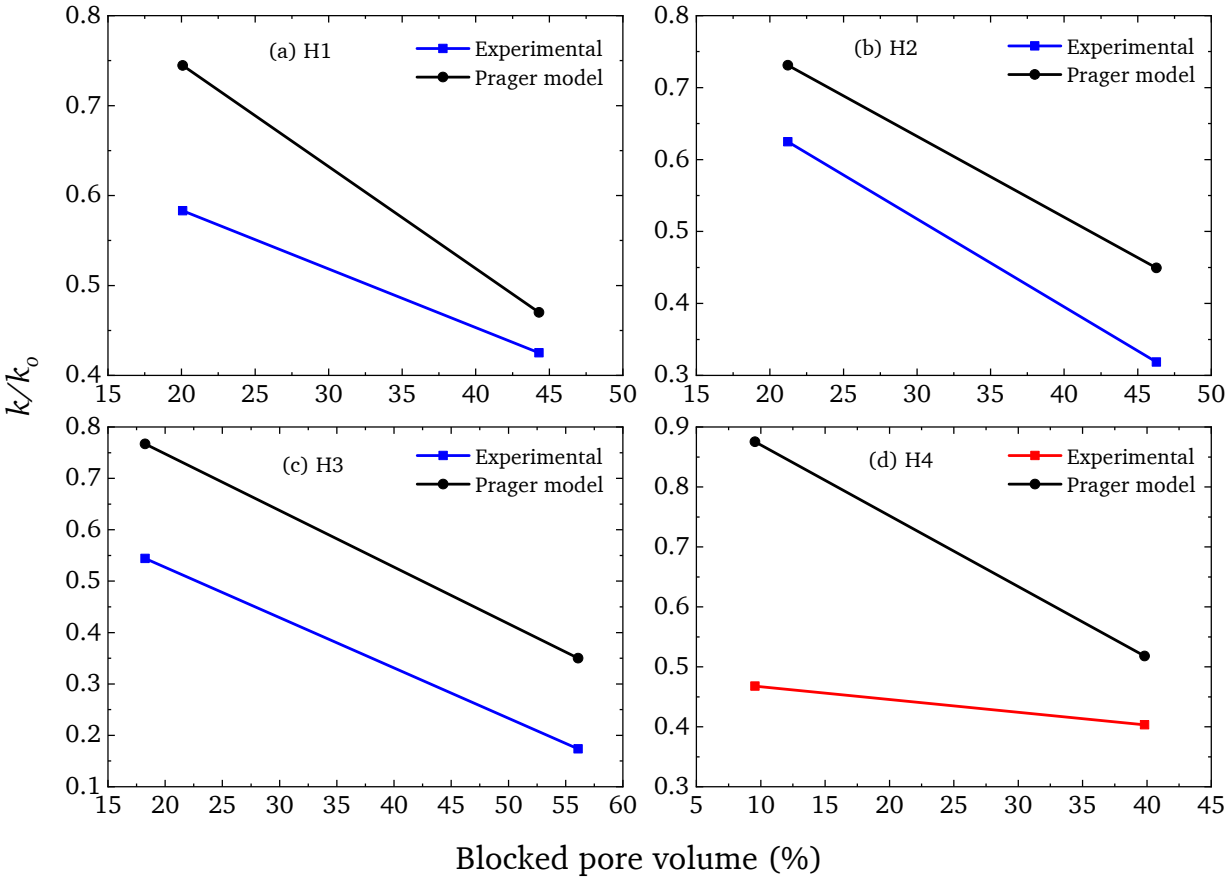


Figure 7.16: Comparisons of the observed fractional decline in the mass transfer coefficient (k/k_o) following mercury entrapment and that expected for a random arrangement of entrapped of pore liquid from Prager model for **(a)** H1, **(b)** H2, **(c)** H3 and **(d)** H4 pellets.

of uptake declines much more significantly following mercury entrapment. For example, for H1 samples, it was found that the adsorption corrected MTC were 0.842 s^{-1} before entrapment and 0.354 s^{-1} after entrapment. Hence, the MTC declined by a factor of >2 between before and after mercury entrapment.

Table 7.5 shows the mass transport coefficients obtained for HTS pellets before and after mercury up to 1200 psia and 5336 psia for the H1 to H3 samples, and 3800 and 5336 psia for the H4 sample. Each MTC is expressed as ratio to the MTC for the mercury-free sample (i.e. k_o). The tables also show the MTC drop expected for a completely random arrangement of entrapped mercury, as predicted by the Prager[259] model. As can be seen from the tables, the MTCs generally decline following mercury entrapment for the HTS pellets. The table also shows that the MTC dropped by a factor of >3 and >5 for the H2 and H3 samples between before and after mercury entrapments of up to 5336 psia. Whereas for the H4 samples, the MTC decline was ∼2 following mercury entrapment up to 5336 psia.

[259]S. Prager. *J. Chem. Phys.*, **33**: 122–127, 1960.

Table 7.5: Variation in adsorption-corrected MTC, for nitrogen at low pressure, with increasing mercury saturation for **(a)** H1, **(b)** H2 **(c)** H3 and **(d)** H4 samples, respectively.

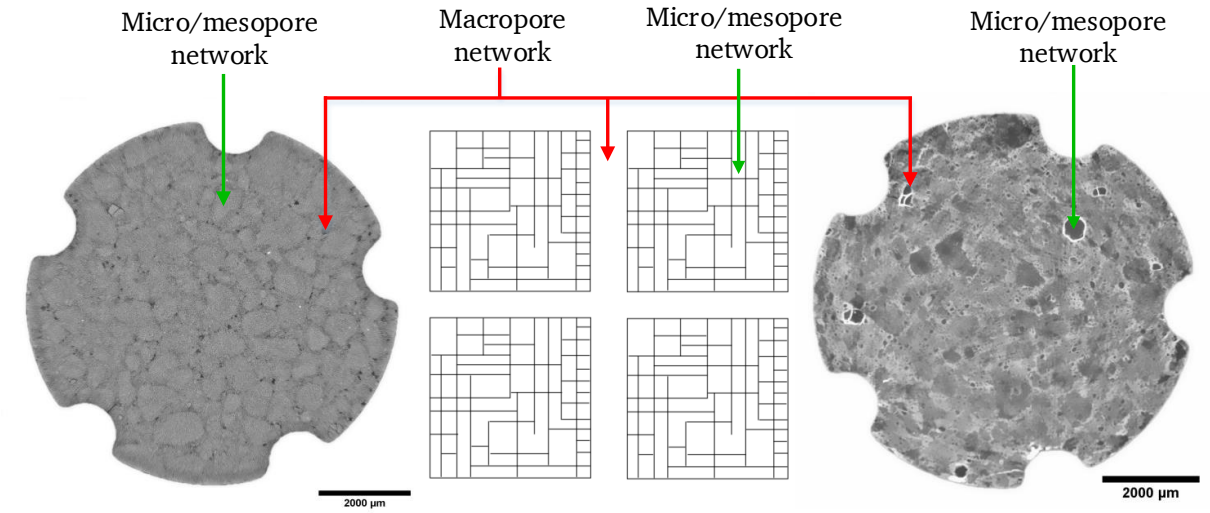
MIP pressure (psia)	Minimum pore diameter penetrated (nm)	Fractional mercury saturation (%)	Experimental (k/k_o)	Expected k/k_o for random entrapment (Prager)
1200	179.6	20.1	0.58	0.74
5336	40.4	44.3	0.43	0.47

MIP pressure (psia)	Minimum pore diameter penetrated (nm)	Fractional mercury saturation (%)	Experimental (k/k_o)	Expected k/k_o for random entrapment (Prager)
1200	179.6	21.2	0.62	0.73
5336	40.4	46.3	0.32	0.45

MIP pressure (psia)	Minimum pore diameter penetrated (nm)	Fractional mercury saturation (%)	Experimental (k/k_o)	Expected k/k_o for random entrapment (Prager)
1200	179.6	18.2	0.54	0.77
5336	40.4	56.1	0.17	0.35

MIP pressure (psia)	Minimum pore diameter penetrated (nm)	Fractional mercury saturation (%)	Experimental (k/k_o)	Expected k/k_o for random entrapment (Prager)
3800	56.7	9.6	0.47	0.88
5336	40.4	39.8	0.40	0.52

Figure 7.16 compares the observed fractional drop in the MTC following mercury entrapment with that anticipated for the same mercury saturation as predicted by the Prager[259] model. For the H1 samples, it can be seen that the observed MTC is significantly lower than would be predicted for a random arrangement of entrapment in the pores. This suggests that the mercury-filled pores must have been contributing to the mass transport significantly. The figure also shows that the observed MTC for the H4 sample with 10% of the void volume of the pellet filled with mercury, the decline in the observed MTC was well predicted by the random Prager model; however, the drop in the observed MTC was significantly larger than that predicted by the Prager[259] model, suggesting that the pores filled with mercury at 3800 psia must be making a greater-than-expected contribution to the mass transfer compare to the pores that are subsequently filled at 5336 psia.



(a) 2D radial cross-section CXT image of empty H2 sample.

(b) Schematic representation of pore structure network.

(c) 2D radial cross-section CXT image of H2 with mercury.

Figure 7.17: HTS pellet pore network structure representation for the macro/meso/micropores. **(a)** 2D radial cross-section slice CXT image for H2 sample, and **(b)** Schematic representation of pore structure network for H2 sample.

7.4 Discussion

The combination of the CXT imaging with the rate of adsorption studies after mercury entrapment allows for the classification of pore space structure features that are critical to mass transport for the HTS pellets. The rate of adsorption data for the HTS pellets demonstrated that the MTC declined well below that expected according to the Prager[259] model for a random distribution of mercury entrapment following intrusion to 1200, 3800 and 5336 psia. This shows that the pore spaces lost due to mercury entrapment following these intrusions are critical for mass transfer since their loss resulted in a larger than predicted drop in MTC compared to the random benchmark structure. A typical HTS catalyst pellet, which is only a few millimetres in size, is composed of an aggregate of microparticles that are several orders of magnitude smaller than the pellet itself. The gaps between the microparticles create a network of continuous macropores that spans the whole pellet. The macropore network is thought to be interconnected rather than distributed randomly among smaller pores. The pores in the microparticles, on the other hand, are typically in the mesopore (2-50 nm) size ranges, but they may contain larger pores up to a few hundred nm in diameter. Such a network of macro and microparticles is shown schematically in Figure 7.17.

The presence of a continuous network of macropores can be identified experimentally using mercury porosimetry, which produces a peak in the pore size range of the macropores if the network is continuous, as shown in Figure 7.7 for the HTS pellets. The macropore network is thought to act as a motorway for molecular diffusion and provide quick access to the active sites found in the micro/mesopore network. When the macropore network for the HTS samples was 'removed' from the pellet by filling them with frozen mercury, the MTC dropped by a factor of up to $\sim$5 following mercury entrapment, thereby signifying the importance of the macropore network in

the mass transport. Additionally, it was found that for the of H1-H3 samples, the mercury blocking the macropore at 5336 psia has effectively turned the pore structure of the pellet from bimodal to a unimodal pore size distribution.

The integrated mercury porosimetry and nitrogen gas adsorption technique has also been found to aid the identification of the pore sizes where mercury entrapment begins. By using the semi-empirical Kloubek[69] relationship, it is possible to remove the contact angle hysteresis from the mercury intrusion data, and the point where the intrusion and extrusion curves diverge will correspond to the pores where mercury entrapment begins. As the mercury porosimetry data for the HTS Pellets does not display hysteresis, and with 100% mercury entrapment, it is possible that the mercury wets the surface of the catalyst and thereby remains trapped inside the samples. The nitrogen gas adsorption was also found to help identify the pore sizes where mercury entrapment begins by using 'the change in incremental amount adsorbed plots'. The point where the mercury entrapment begins is indicated by the start of the positive signal in the plots. The relative pressures at these points can then be converted to pore size using, for example, the Kelvin[51] equations and the correct *t*-layer thickness methods.

7.5 Conclusion

The test presented in this chapter has demonstrated a technique to identify the set of pore sizes that entrap mercury in high-temperature shift catalyst pellets. It has been seen that the integrated mercury porosimetry, together with the X-ray imaging strategy described here, can identify and spatially locate the particular pore sizes that entrap mercury and study the importance of the sample-spanning macropores 'motorway' network to mass transport in the pellet using the rate of adsorption technique.

The last section of this thesis will summarise the key results of the work presented in this thesis.

[51] T. William. *Philos. Mag.*, **42**: 448–452, 1871.

Conclusions and Future Work

7.6 Conclusion

The work in this thesis investigated the structure-transport relationships in disordered porous materials such as methanol synthesis and high-temperature shift catalyst pellets. An experimental technique that employed multi-modal imaging methods, including high and low-resolution CXT and FIB-SEM, was combined with the more statistically-representative, multi-scale data from porosimetry, including the rarely-used gas overcondensation method. This combined characterisation method used mercury porosimetry scanning curves to gradually remove specific pore sizes from the transport network by filling them with mercury and then evaluating their relevance to mass transfer using nitrogen gas sorption. The multi-modal imaging permits the visualisation of the spatial distribution of the entrapped mercury and the location of the specific pore sizes in the pellet with entrapped mercury. This combined characterisation method can be used to inform both the design and optimisation of catalyst pellet manufacturing processes since the key features of the void space that control gas-phase uptake into the porous pellets can be determined, and their relationship to, for example, the fabrication process and raw materials can be identified.

Chapters 3 to 5 form the first part of the thesis. These chapters addressed the impacts of specific pore structural features on the properties of the finished tableted pellets for the fresh, reduced and spent methanol synthesis catalyst pellets. Fresh methanol synthesis pellets made using spray-dried or roll compacted feed materials were studied in Chapter 3. This chapter examined how the different fabrication methods affect the finished pellet properties by studying both the starting feed particles and the finished tablets. The results demonstrated that more thorough and interconnected information could be obtained by combining indirect characterisation methods, such as overcondensation and mercury porosimetry, compared to the standalone[9,65] characterisation method. The hybrid characterisation techniques presented in this chapter, which combined many techniques in a single experiment, ensured that characterisation data from various methods coheres and yields synergistic results. The combination of overcondensation with multi-scale imaging revealed the macropore structures missing from standard isotherm data, especially the large 'bubble pores' in the spray-dried feed material, and the exact sizes of the smaller pores shielding these structures.

[9] F. Rouquerol et al. *Adsorption by powders and porous solids.* Academic Press, London, 1999.
[65] H. Giesche. *Part. Part. Syst. Charact.*, **23**: 9–19, 2006.

The low and high-resolution CXT imaging and FIB-SEM serial milling provided detailed spatial information and bridged several orders of magnitude in pore size, even down to molecular scale. The imaging techniques revealed the hierarchical complexity of the methanol synthesis catalyst pellet. Despite the levels of complexity shown by CXT and FIB-SEM images, the impact on mass transfer of the controlled modifications to the void space, achieved through mercury porosimetry, was modelled with a random pore-bond network using characteristic parameters obtained from percolation analysis of the overcondensation data. The simple random pore-bond model established a quantitative relationship between the rate of mass uptake of gas into the porous pellets and the structural information included in the overcondensation isotherms. The finding from the model demonstrated the differential importance of specific pore sets associated with certain pellet structural features to the mass transfer rates and the influence of pellet fabrication parameters such as particle feed size on tortuosity.

In Chapter 4, an image segmentation method based on deep learning convolutional neuron networks (CNNs),[266,268,269] such as U-Net[274] and FCDense-Net,[309,310] was developed and used to successfully segment stacks of CXT and FIB-SEM images of methanol synthesis catalyst pellets. The deep learning models utilised were based on Dragonfly software from ORS,[258] which used the popular TensorFlow[282] deep learning engine in a user-friendly image processing environment. The segmentation was completed within reasonable run times and achieved a higher accuracy using a local workstation equipped with Nvidia graphics RTX P6000 24Gb Quadro. The segmentation method presented in this chapter demonstrated a possible solution to the difficulty of segmenting a large number of 3D CXT and FIB-SEM images using the traditional segmentation methods.

Chapter 5 studied the effectiveness of the freshly reduced and spent methanol synthesis catalyst pellets made using spray-dried and roll compacted feed materials. This chapter examined the impact of cracks on pellet performance and percolation processes and how different pellet manufacturing methods affect the final catalyst properties using the combined characterisation techniques. Mercury porosimetry allowed for controlled modifications to the void space, and the impact of the lost pores on the mass transport rates was probed with nitrogen gas uptake measurements. The effects on the mass transport of the controlled modifications to the void space were then modelled using a random pore-bond network and characteristic parameters from the percolation analysis of the overcondensation data. A random pore-bond percolation model was shown to accurately represent the macroscopic structure of the reduced and spent SD pellets but not the reduced and spent RC pellets. This was attributed to the fact that cracking seems to affect the roll compacted samples but does not impact the spray-dried pellet as the sizes of the cracks are larger than the average spray-dried feed particles.

[266]Y. Lecun, Y. Bengio, and G. Hinton. *Nature*, **521**: 436–444, 2015.
[268]S. Shalev-Shwartz and S. Ben-David. *Understanding Machine Learning*. Cambridge University press, 2014.
[269]M. H. Hassoun. *Fundamentals of Artificial Neural Networks*. MIT press, 1995.
[274]O. Ronneberger, P. Fischer, and T. Brox. *MICCAI*, **9351**: 234–241, 2015.
[309]F. Milletari, N. Navab, and S. Ahmadi. *Int. Conf. 3D Vis.*, 565–571, 2016.
[310]S. Jegou et al. *IEEE Comput. Soc.*, 11–19, 2017.
[258]R. Makovetsky, N. Piche, and M. Marsh. *Microsc. Microanal.*, **24**: 532–533, 2018.
[282]A. Martín et al. *CoRR*, 265–283, 2016.

Despite the benefits of the combined characterisation techniques mentioned above, the experiments can take a long time to complete for each sample (e.g., up to ∼3 days for single overcondensation experiment). However, the additional information gained offers previously unavailable and vital knowledge about porous materials without going through possibly inaccurate or intermediate simulation steps.

The second part of this thesis looked at High-temperature water-gas-shift (HT-WGS) catalyst and silica catalyst support material. In Chapter 6, a novel thermoporometry by DSC method that used three separate probe liquids (nitrogen, water, and mercury) was used to validate the pore space characterisations observation through various indirect methods. With this new method, we significantly increased the number of hybrid procedures that may be used with the same sample and research materials from previous studies.[7,99] In this work, new thermoporometry tests using several immiscible probe liquids were conducted on the same sample. Serial adsorption of water prior to mercury porosimetry, where the adsorbed water was kept during the porosimetry, and then nitrogen adsorption on the same sample by freezing the pre-adsorbed water and entrapped mercury in-place experiments were performed. Furthermore, serial adsorption of first nitrogen, then water, and finally nitrogen, as well as integrated nitrogen sorption and mercury porosimetry experiment, were also performed. These hybrid experiments allowed data comparisons from multiple techniques for the same sample, allowing parameter calibration and phase transition mode selections to be performed. This new method can be used to identify the correct, self-consistent set of Gibb-Thomson parameters for water and mercury and the correct meniscus geometry for nitrogen pore size distributions. The new methods described were trialled in a disordered mesoporous, sol-gel silica material.

The final chapter, (Chapter 7), studied high-temperature shift catalyst pellets manufactured via precipitation method using integrated mercury porosimetry, nitrogen gas adsorption and X-ray imaging to identify and spatially locate a particular pore size range that entraps mercury. The work also presented the rate of adsorption technique to probe the impact of the lost macropores on mass transport. The X-raying imaging was used to improve the interpretation of data from the indirect characterisation methods to study the spatial distribution of mercury within the void spaces of the samples. It was found that the integrated method and the X-ray imaging strategy can identify and spatially locate the particular pore sizes that entrap mercury and study the importance of the sample-spanning macropores motorway network to mass transport using the rate of adsorption technique. The macropore network in the pellets is thought to act as a motorway for molecular diffusion and provide quick access to the active sites in the centre of the pellets. By using the rate of adsorption, it was found that when the macropore network was 'removed' from the pellet by filling them with frozen mercury, the mass transport dropped by a factor of up to ∼5 following mercury entrapment, thereby signifying the importance of the macropore network for the pellet mass transport.

The experimental approach and modelling techniques proposed in this thesis can be applied

[7] S. P. Rigby. *Structural characterisation of natural and industrial porous materials: A manual*. Springer Nature, 2020.
[99] S. P. Rigby. *JM Techno. Review*, **62**: 296–312, 2018.

to a broad range of disordered porous materials, and we believe it represents a systematic path towards quantitative structure-transport relationships for highly disordered porous media, with implications for both industry and academia.

7.7 Future Work

In this thesis, new experimental methodologies were developed to understand the structure-transport properties of nanoporous materials, including heterogeneous catalysts. However, the development of such methodologies has revealed various other avenues for furthering the research. The current study on methanol synthesis catalyst pellets used only a conventional FIB-SEM instrument to image the distribution of the different phases and the pore morphology of the whole pellet. However, we recommend using Field Emission Gun-Scanning Electron Microscope (FEG-SEM) imaging as it can deliver more precise, less electrostatically distorted images with spatial resolutions down to 1.5 nm compared to conventional SEM. The use of FEG-SEM imaging is also recommended for both the spray-dried and the roll compacted feed particles themselves too.

Apart from using FEG-SEM, other research dimensions can be introduced so that the technique may be developed further. The integrated experiments and the theory-based percolation analysis of the overcondensation data using the random pore bond models presented in this thesis were only applied to two types of methanol synthesis catalyst pellet made using either spray-dried, or roll compacted feed materials. In order to further test the validity of the method, it is recommended that the method is applied to other types of catalyst pellets made in other ways, e.g., extrudates and granulated spheres. It is also recommended that the relative usefulness data of a given pore size interval to the overall mass transport coefficient is compared with the actual catalyst effectiveness factor data from Johnson Matthey (JM) to see how well they correlate.

Finally, creating a comprehensive image software that carries out both image processing and image analysis methods is recommended. This approach will be much more beneficial and is less time-consuming than the one used in this study. Creating and validating such software would take much effort; therefore, proficiency in a programming language would be pretty advantageous.

Appendix A: Fresh Methanol Synthesis Catalyst

Table 6: Variation of coefficient of determination (R^2) for fits of experimental gas sorption data to the generalised scaling relationship from percolation analysis depending upon the relation between pore diameter and pore length for the **(a)** fresh SD, and **(b)** fresh RC

	R^2			Z		
Pressure (psia)	**V/D**	**V/D^2**	**V**	**V/D**	**V/D$_2$**	**V**
8600	0.992	0.9571	0.8308	2.69	3.23	3.23
10800	0.9978	0.9202	0.8555	2.55	3.14	2.33
14700	0.9733	0.9398	0.8922	2.37	2.77	1.80

	R^2			Z		
Pressure (psia)	**V/D**	**V/D^2**	**V**	**V/D**	**V/D^2**	**V**
8600	0.9936	0.8907	0.8414	2.72	2.38	1.60
10800	0.9967	0.9167	0.8914	2.83	3.16	2.31
14700	0.9942	0.9235	0.9004	2.72	3.13	2.21

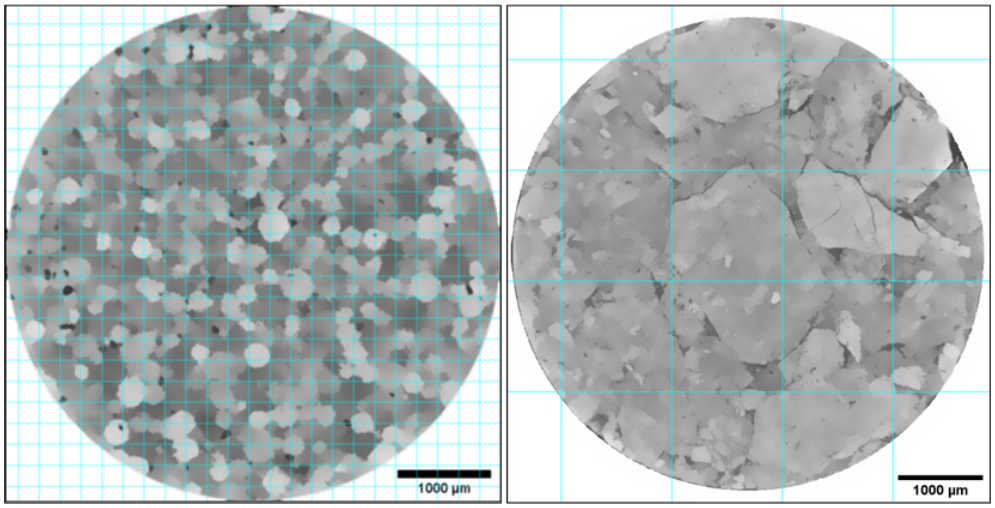
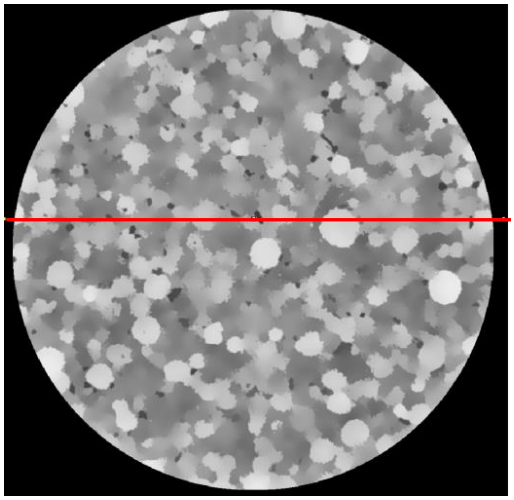
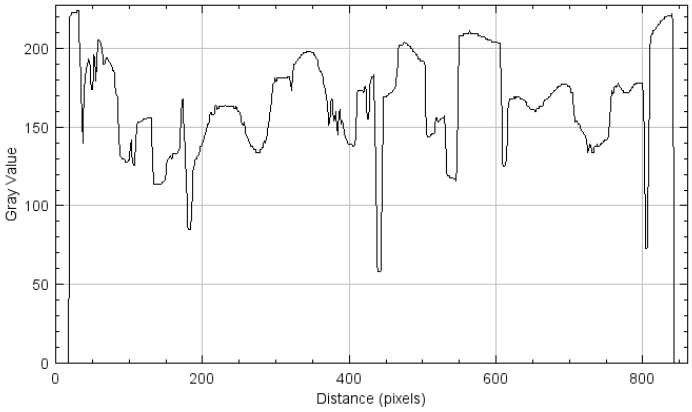


Figure 18: 2D radial cross-section CXT image of fresh methanol synthesis catalyst samples with line grid overlay for measuring the feed particle size, where **(a)** spray-dried grid division = 200 µm, and **(b)** roll-compacted grid division = 1300 µm.

(a) Fresh SD

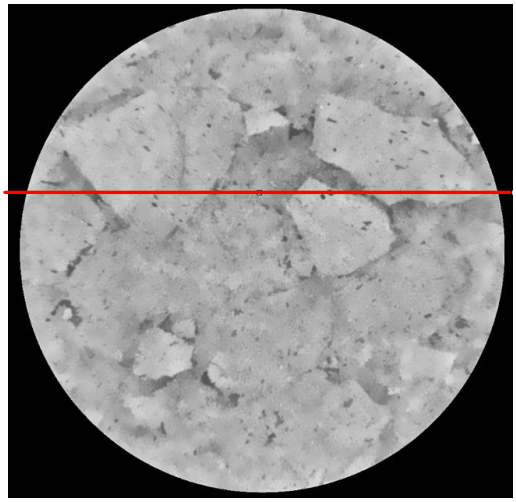


XY Plane

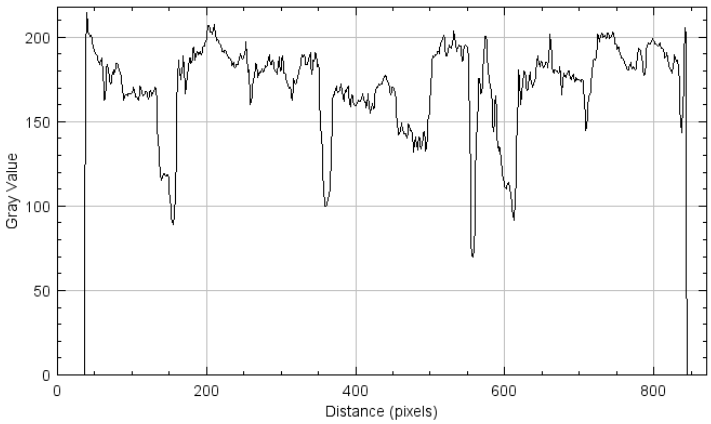


Fresh SD pellet XY profile

(b) Fresh RC



XY Plane



Fresh RC pellet XY profile

Figure 19: Low resolution CXT 2D reconstruction and the corresponding intensity profile plots for a chord shown (red) measured in ImageJ for whole **(a)** SD feed pellet, and **(b)** RC feed pellet.

Appendix B: Triangulation of Pore Structural Characterisation

This appendix contains isotherms for Silica C10 sample (G1) analysed in Chapter 6. The first section presents figures for the adsorption isotherms for G1 for different adsorbates. The second part contains serial mercury porosimetry and water adsorption plots.

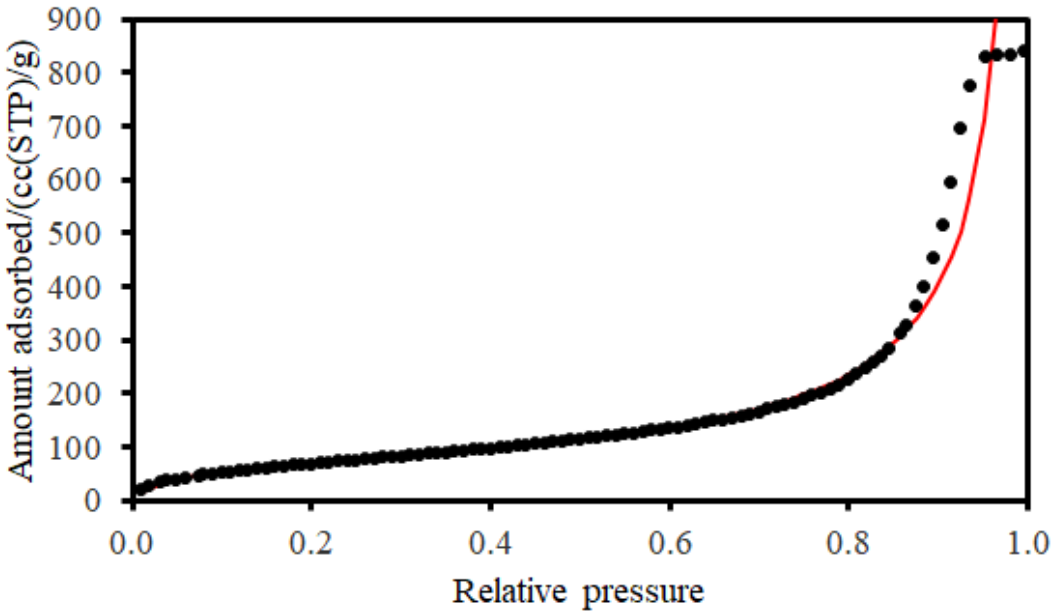


Figure 20: Adsorption isotherm for argon at 87 K. The solid line shown is a fit of the fractal BET equation for relative pressures <0.65.

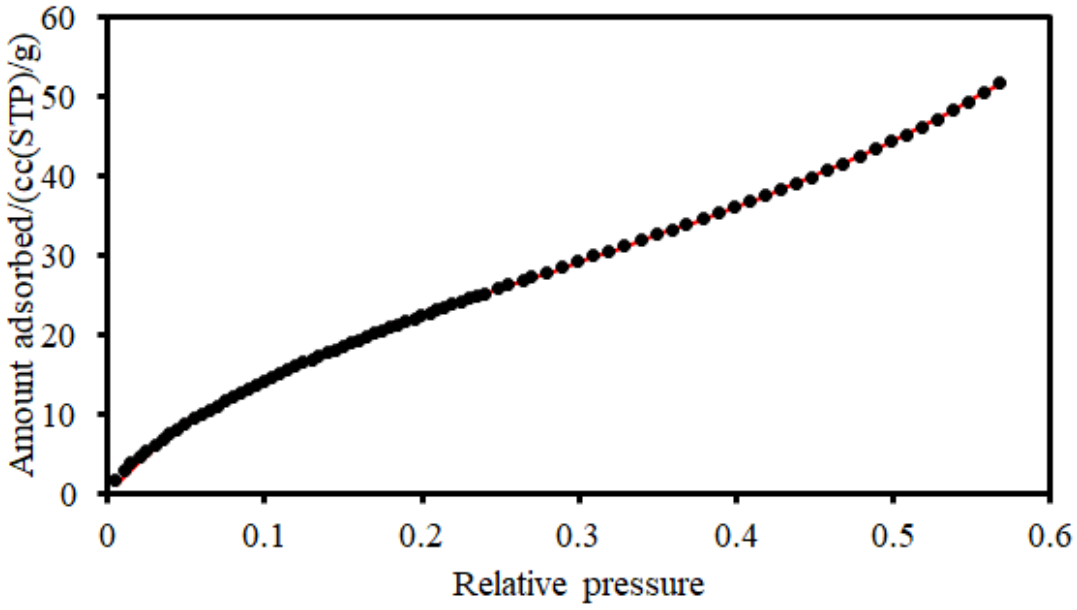


Figure 21: Adsorption isotherm for propane at 199 K. The solid line shown is a fit of the fractal BET equation for all isotherm.

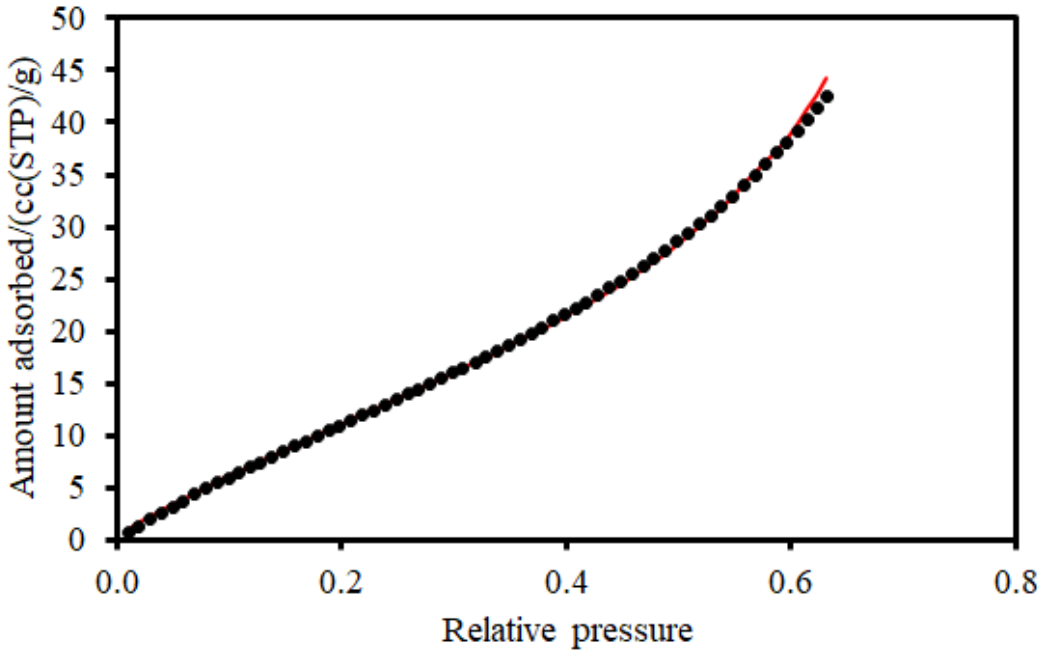


Figure 22: Adsorption isotherm for n-hexane at 273 K. The solid line shown is a fit of the fractal BET equation for relative pressures <0.6.

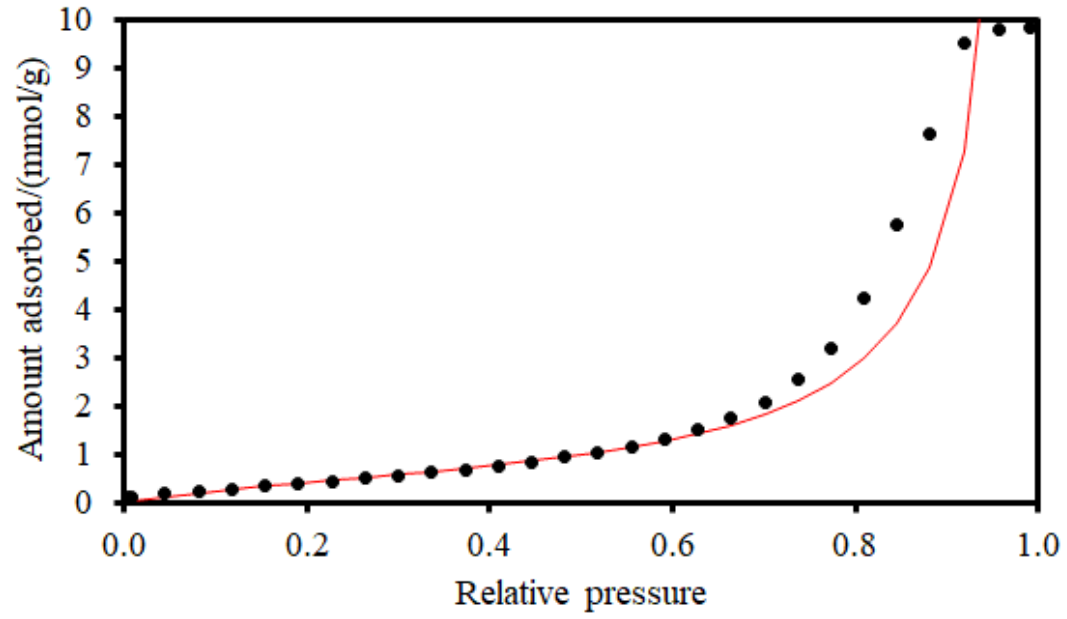


Figure 23: Adsorption isotherm for cyclohexane at 280 K. The solid line shown is a fit of the fractal BET equation for relative pressures <0.6.

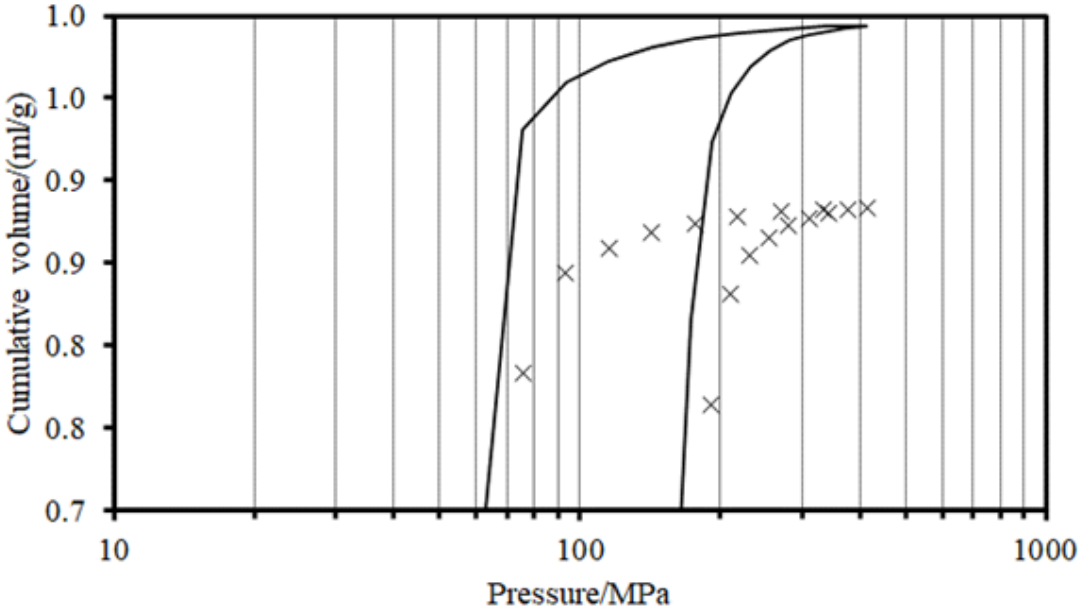


Figure 24: Close-up view of tops of mercury intrusion and extrusion curves for G1 following drying at 350°C (solid line) and following pre-adsorption of water to a relative pressure of 0.85 (x).

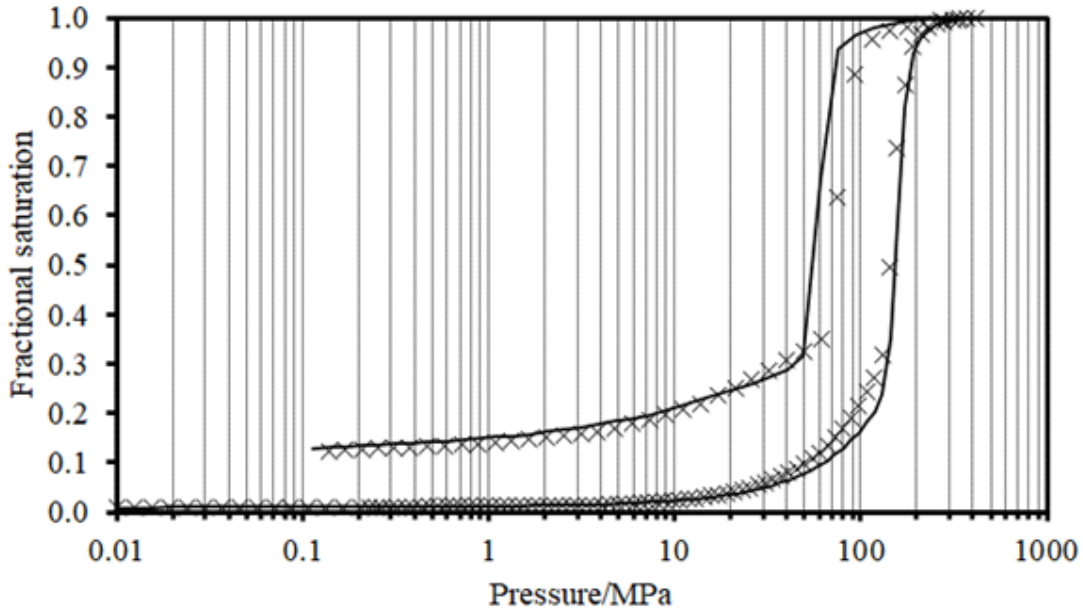


Figure 25: Fractional saturation (intruded volume at given pressure divided by ultimate intrusion volume) curves for mercury intrusion and extrusion for G1 following drying at 350°C (solid line) and following pre-adsorption of water to a relative pressure of 0.85 (x).

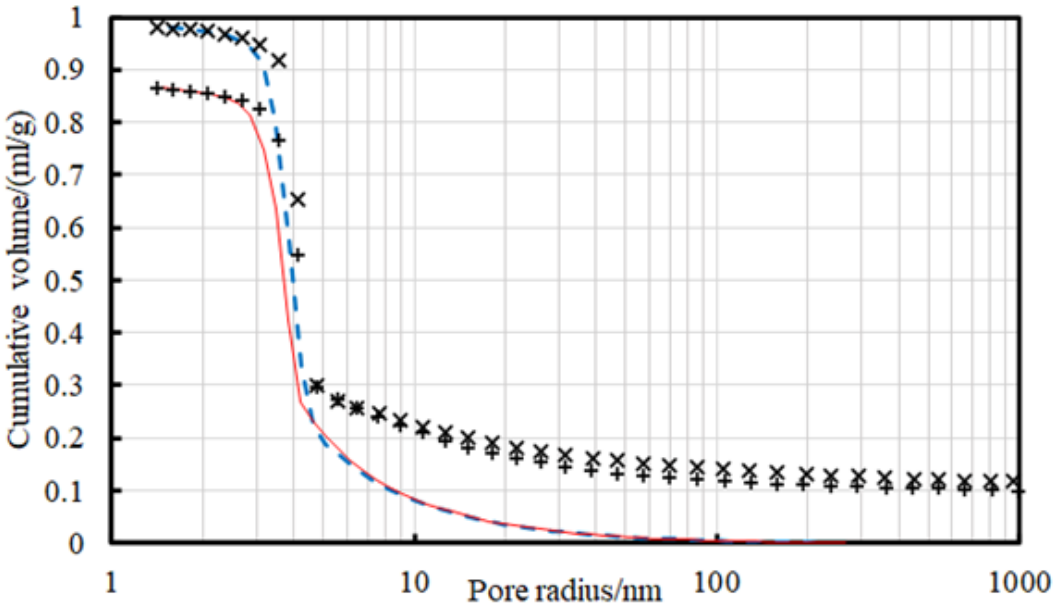


Figure 26: Mercury intrusion (lines) and extrusion (symbols) curves, analysed using the Kloubek correlations, for G1 following drying at 350°C (dashed line, x) and following pre-adsorption of water to a relative pressure of 0.85 (solid line, +).

Bibliography

[1] G. Q. LU and X. S. ZHAO. *Nanoporous materials: science and engineering*. World Scientific, 2004.

[2] J. N. ARMOR. New catalytic technology commercialized in USA during the 1990s. *Applied Catalysis A: General*, **222**: 407–426, 2001. doi: 10.1016/S0926-860X(01)00846-8

[3] J.M. THOMAS and W.J. THOMAS. Principles and practice of heterogeneous catalysis. *Applied Catalysis A: General*, 686, 1997. doi: 10.1002/bbpc.199700023

[4] I. CHORKENDORFF and J. NIEMANTSVERDRIET. *Concepts of modern catalysis and kinetics*. Wiley, 2003.

[5] M. V. TWIGG. *Catalyst handbook*. CRC Press, 2018.

[6] A. NEPRYAHIN, E. HOLT, R. FLETCHER, and S. RIGBY. Structure-transport relationships in disordered solids using integrated rate of gas sorption and mercury porosimetry. *Chemical Engineering Science*, **152**: 663–673, 2016. doi: 10.1016/j.ces.2016.06.057

[7] S. P. RIGBY. *Structural characterisation of natural and industrial porous materials: A manual*. Springer Nature, 2020.

[8] S. J. GREGG and K. S. SING. *Adsorption, surface area and porosity.* 2nd. Academic Press, London, 1982.

[9] F. ROUQUEROL, J. ROUQUEROL, K.S.W. SING, P. LLEWELLYN, and G. MAURIN. *Adsorption by powders and porous solids.* Academic Press, London, 1999.

[10] S. LOWELL, J. SHIELDS, M. THOMAS, and M. THOMMES. *Characterization of porous solids and powders: surface area, pore size, and density.* Springer, 2005.

[11] S. PRACHAYAWARAKORN and R. MANN. Effects of pore assembly architecture on catalyst particle tortuosity and reaction effectiveness. *Catalysis Today*, **128**: 88–99, 2007. doi: 10.1016/j.cattod.2007.06.036

[12] C. RIECKMANN and F. KEIL. Simulation and experiment of multicomponent diffusion and reaction in three-dimensional networks. *Chemical Engineering Science*, **54**: 3485–3493, 1999. doi: 10.1016/S0009-2509(98)00480-1

[13] S. GHEORGHIU and M. COPPENS. Optimal bimodal pore networks for heterogeneous catalysis. *AIChE journal*, **50**: 812–820, 2004. doi: 10.1002/aic.10076

[14] B. BUKOWSKI, F. KEIL, P. RAVIKOVITCH, G. SASTRE, R. SNURR, and M. COPPENS. Connecting theory and simulation with experiment for the study of diffusion in nanoporous solids. *Adsorption (Boston)*, **27**: 683–760, 2021. doi: 10.1007/s10450-021-00314-y

[15] N. A. SEATON. Determination of the connectivity of porous solids from nitrogen sorption measurements. *Chemical Engineering Science*, **46**: 1895–1909, 1991. doi: 10.1016/0009-2509(91)80151-N

[16] Z. ZHONG, U. ETIM, and Y. SONG. Improving the Cu/ZnO-based catalysts for carbon dioxide hydrogenation to methanol, and the use of methanol as a renewable energy storage media. *Frontiers in Energy Research*, 239, 2020. doi: 10.3389/fenrg.2020.545431

[17] M. BERTAU, H. OFFERMANNS, L. PLASS, F. SCHMIDT, and H. WERNICKE. *Methanol: the basic chemical and energy feedstock of the future*. vol. 1 Springer, 2014.

[18] A. SONTHALIA, N. KUMAR, M. TOMAR, V. EDWIN, and S. THIYAGARAJAN. Moving ahead from hydrogen to methanol economy: scope and challenges. *Clean Technologies and Environmental Policy*, 1–25, 2021. doi: 10.1007/s10098-021-02193-x

[19] T. VEZIROĞLU and S. ŞAHI. 21st Century's energy: Hydrogen energy system. *Energy conversion and management*, **49**: 1820–1831, 2008. doi: 10.1016/j.enconman.2007.08.015

[20] S. VERHELST, J. TURNER, L. SILEGHEM, and J. VANCOILLIE. Methanol as a fuel for internal combustion engines. *Progress in Energy and Combustion Science*, **70**: 43–88, 2019. doi: 10.1016/j.pecs.2018.10.001

[21] A. MITTASCH, M. PIER, and K. WINKLER. Execution of organic catalysis. *Germany Patent DE415686*, **24**: 1923.

[22] D. SHELDON. Methanol production: A technical history. *Johnson Matthey Technology Review*, **61**: 172–182, 2017.

[23] L. WADE, R. GENGELBACH, J. TRUMBLEY, and W. HALLBAUER. Methanol. *Kirk-Othmer Encyclopedia of Chemical Technology*, 16, 1981.

[24] M. ALVARADO. The changing face of the global methanol industry. *IHS Chemical Bulletin*, **3**: 10–11, 2016.

[25] K. KLIER. Methanol synthesis. *Advances in catalysis*, **31**: 243–313, 1982. doi: 10.1016/S0360-0564(08)60455-1

[26] J. YOSHIHARA, S. PARKER, A. SCHAFER, and C. CAMPBELL. Methanol synthesis and reverse water-gas shift kinetics over clean polycrystalline copper. *Catalysis letters*, **31**: 313–324, 1995. doi: 10.1007/BF00808595

[27] G.C. CHINCHEN, P. J. DENNY, D. G. PARKER, M. S. SPENCER, and D. A. WHAN. Mechanism of methanol synthesis from CO2/CO/H2 mixtures over copper/zinc oxide/alumina catalysts: use of14C-labelled reactants. *Applied Catalysis*, **30**: 333–338, 1987. doi: 10.1016/S0166-9834(00)84123-8

[28] J. YAO, J. YAN, Y. HUANG, Y. LI, S. XIAO, and J. XIAO. Preparation of ZnFe2O4/α-Fe2O3 nanocomposites from sulfuric acid leaching liquor of jarosite residue and their application in lithium-ion batteries. *Frontiers in chemistry*, 442, 2018. doi: 10.3389/fchem.2018.00446

[29] P. DAVIES, F. SNOWDON, G. BRIDGER, D. HUGHES, and P. YOUNG. Water-gas conversion and catalysts therefor. *UK Patent GB1010871*, 1965.

[30] G. ERTL, H. KNÖZINGER, and J. WEITKAMP. *Handbook of heterogeneous catalysis*. Wiley-VCH, 2008.

[31] C. H. BARTHOLOMEW and R. J. FARRAUTO. *Fundamentals of industrial catalytic processes*. John Wiley & Sons, 2011.

[32] C. RHODES, G. HUTCHINGS, and A. WARD. Water-gas shift reaction: finding the mechanistic boundary. *Catalysis Today*, **23**: 43–58, 1995. doi: 10.1016/0920-5861(94)00135-O

[33] R. KEISKI and T. SALMI. Deactivation of the high-temperature water-gas shift catalyst in nonisothermal conditions. *Applied Catalysis A: General*, **87**: 185–203, 1992. doi: 10.1016/0926-860X(92)80055-H

[34] F DOMKA, A BASINSKA, and R FIEDOROW. Porous structure of Fe2O3-Cr2O3 catalysts prepared from iron oxide-hydroxide systems. *Surface Technology*, **18**: 275–282, 1983.

[35] A. PEREIRA, Guillermo P. BERROCAL, G. MARCHETTI, A. ALBORNOZ, and M. CARMO. A comparison between the precipitation and impregnation methods for water gas shift catalysts. *Journal of Molecular Catalysis A: Chemical*, **281**: 66–72, 2008. doi: 10.1016/j.molcata.2007.07.042

[36] M. THOMMES, K. KANEKO, A. NEIMARK, J. OLIVIER, J. ROUQUEROL, and K. SING. Physisorption of gases, with special reference to the evaluation of surface area and pore size distribution (IUPAC technical report). *Pure and Applied Chemistry*, **87**: 1051–1069, 2015. doi: 10.1515/pac-2014-1117

[37] P. N. AUKETT and C. A. JESSOP. Assessment of connectivity in mixed meso/macroporous solids using nitrogen sorption. *Fundamentals of Adsorption*, 59–66, 1996. doi: 10.1007/978-1-4613-1375-5_6

[38] K. L. MURRAY, N. A. SEATON, and M. A. DAY. An adsorption-based method for the characterization of pore networks containing both mesopores and macropores. *Langmuir*, **15**: 6728–6737, 1999. doi: 10.1021/la990159t

[39] I. LANGMUIR. The adsorption of gases on plane surfaces of glass, mica and platinum. *Journal of the American Chemical society*, **40**: 1361–1403, 1918. doi: 10.1021/ja02242a004

[40] S. BRUNAUER, P. EMMET, and E. TELLER. Adsorption of gases in multi molecular layer. *Journal of the American Chemical Society*, **60**: 309, 1938. doi: 10.1021/ja01269a023

[41] G. HALSEY. Physical adsorption on non-uniform surfaces. *Journal of Chemical Physics*, **16**: 931–937, 1948. doi: 10.1063/1.1746689

[42] W. HARKINS and G. JURA. Surfaces of solids. XII. An absolute method for the determination of the area of a finely divided crystalline solid. *Journal of the American Chemical Society*, **66**: 1362–1366, 1944. doi: 10.1021/ja01236a047

[43] J. C. P. BROEKHOFF and J. H. de BOER. Studies on pore systems in catalysts: X. calculations of pore distributions from the adsorption branch of nitrogen sorption isotherms in the case of open cylindrical pores. *Journal of Catalysis*, **10**: 377–390, 1968. doi: 10.1016/0021-9517(67)90175-3

[44] E. P. BARRETT, L. G. JOYNER, and P. P. HALENDA. The determination of pore volume and area distributions in porous substances. I. computations from nitrogen isotherms. *Journal of the American Chemical Society*, **73**: 373–380, 1951. doi: 10.1021/ja01145a126

[45] K. K. ALIGIZAKI. *Pore structure of cement-based materials*. Taylor & Francis, 2006.

[46] J. H. de BOER, A. V. HEUVEL, and B. G. LINSEN. Studies on pore systems in catalysts IV. the two causes of reversible hysteresis. *Journal of Catalysis*, **3**: 268–273, 1964.

[47] G. H. FINDENEGG. Principles of adsorption at solid surfaces and their significance in gas/solid and liquid/solid chromatography. *Theoretical Advancement in Chromatography*, **383**: 1992. doi: 10.1007/978-94-011-2686-1_8

[48] M. THOMMES, R. KÖHN, and M. FRÖBA. Sorption and pore condensation behavior of pure fluids in mesoporous MCM-48 silica, MCM-41 silica, SBA-15 silica and controlled-pore glass at temperatures above and below the bulk triple point. *Applied Surface Science*, **196**: 239–249, 2002. doi: 10.1016/j.cis.2021.102529

[49] K. MORISHIGE and Y. NAKAMURA. Nature of adsorption and desorption branches in cylindrical pores. *Langmuir*, **20**: 4503–4506, 2004. doi: 10.1021/la030414g

[50] W. CRANSTON and A. INKLEY. *Determination of pore structures from nitrogen adsorption isotherms.* 1957. 143–154

[51] T. WILLIAM. On the equilibrium of vapour at a curved surface of liquid. *Philosophical Magazine*, **42**: 448–452, 1871.

[52] E. O. KRAEMER. On the equilibrium of vapour at a curved surface of liquid. *Treatise on Physical Chemistry*, **42**: 1661, 1931.

[53] J. W. MCBAIN. An explanation of hysteresis in the hydration and dehydration of gels. *Journal of the American Chemical Society*, **57**: 699–700, 1935. doi: 10.1021/ja01307a502

[54] A. G. FOSTER. The sorption of condensible vapours by porous solids. Part I. The applicability of the capillary theory. *Transactions of the Faraday Society*, **28**: 645, 1932. doi: 10.1039/tf9322800645

[55] L. H. COHAN. Sorption hysteresis and the vapor pressure of concave surfaces. *Journal of the American Chemical Society*, **60**: 433–435, 1938. doi: 10.1021/ja01269a058

[56] J. H. DE BOER, Van D. H., and B. G. LINSEN. Studies on pore systems in catalysts IV. The two causes of reversible hysteresis. *Journal of Catalysis*, **3**: 268–273, 1964. doi: 10.1016/0021-9517(64)90173-3

[57] D. H. EVERETT and W. I. WHITTON. A general approach to hysteresis. *Transactions of the Faraday Society*, **48**: 749–757, 1952. doi: 10.1039/TF9524800749

[58] D. H. EVERETT and F. W. SMITH. A general approach to hysteresis. Part 2: development of the domain theory. *Transactions of the Faraday Society*, **50**: 187–197, 1954. doi: 10.1039/TF9545000187

[59] D. H. EVERETT. A general approach to hysteresis. Part 3. A formal treatment of the independent domain model of hysteresis. *Transactions of the Faraday Society*, **50**: 1077–1096, 1954. doi: 10.1039/TF9545001077

[60] D. H. EVERETT. A general approach to hysteresis. Part 4. An alternative formulation of the domain model. *Transactions of the Faraday Society*, **51**: 1551–1557, 1955. doi: 10.1039/TF9555101551

[61] L. SLIWINSKA and H. DAVIS. The Gurvitsch rule: An example of a rule misnamed? *Ambix*, **34**: 81–88, 1987. doi: 10.1179/amb.1987.34.2.81

[62] J. C. BROEKHOFF. Mesopore determination from nitrogen sorption isotherms: fundamentals, scope, limitations. *Surface Science and Catalysis*, **3**: 663–684, 1979. doi: 10.1016/S0167-2991(09)60243-3

[63] J. ROUQUEROL, G. BARON, R. DENOYEL, H. GIESCHE, J. GROEN, P. KLOBES, P. LEVITZ, A. NEIMARK, S. RIGBY, and R. SKUDAS. Liquid intrusion and alternative methods for the characterization of macroporous materials (IUPAC technical report). *Pure and Applied Chemistry*, **84**: 107–136, 2011. doi: 10.1351/pac-rep-10-11-19

[64] J. ROUQUEROL, G. BARON, R. DENOYEL, H. GIESCHE, J. GROEN, P. KLOBES, P. LEVITZ, A. NEIMARK, S. RIGBY, and R. SKUDAS. The characterization of macroporous solids: An overview of the methodology. *Microporous and Mesoporous Materials*, **154**: 2–6, 2012. doi: 10.1016/j.micromeso.2011.09.031

[65] H. GIESCHE. Mercury porosimetry: A general (practical) overview. *Particle Systems Characterization*, **23**: 9–19, 2006. doi: 10.1002/ppsc.200601009

[66] J. VAN BRAKEL, S. MODRÝ, and M. SVATÁ. Mercury porosimetry: state of the art. *Powder Technology*, **29**: 1–12, 1981. doi: 10.1016/0032-5910(81)85001-2

[67] N. WARDLAW and M. MCKELLAR. Mercury porosimetry and the interpretation of pore geometry in sedimentary rocks and artificial models. *Powder Technology*, **29**: 127–143, 1981. doi: 10.1016/0032-5910(81)85011-5

[68] L. MOSCOU and S. LUB. Practical use of mercury porosimetry in the study of porous solids. *Powder Technology*, **29**: 45–52, 1981. doi: 10.1016/0032-5910(81)85003-6

[69] J. KLOUBEK. A new method for the investigation of porous structures using mercury porosimetry. *Powder Technology*, **29**: 89–97, 1981. doi: 10.1016/0032-5910(81)85007-3

[70] S. RIGBY, D. BARWICK, R. FLETCHER, and S. RILEY. Characterization of macroscopic structural disorder in porous media using mercury porosimetry. *Journal of Colloid and Interface Science*, **240**: 190–210, 2001. doi: 10.1006/jcis.2001.7636

[71] W. E. WASHBURN. The Dynamics of Capillary Flow. *Physical Review*, **18**: 206–209, 1921. doi: 10.1103/PhysRev.18.206

[72] L. C. DRAKE and H. L. RITTER. Macropore-size distributions in some typical porous substances. *Industrial and Engineering Chemistry*, **17**: 787–791, 1945. doi: 10.1021/i560148a014

[73] J. G. ROBERT and S. M. RAOUF. The contact angle in mercury intrusion porosimetry. *Powder Technology*, **29**: 53–62, 1981. doi: 10.1016/0032-5910(81)85004-8

[74] R. N. WENZEL. Surface roughness and contact angle. *Journal of Physical and Colloid Chemistry*, **53**: 1466–1467, 1949. doi: 10.1021/j150474a015

[75] J. KLOUBEK. A new method for the investigation of porous structures using mercury porosimetry. *Powder Technology*, **29**: 89–97, 1981. doi: 10.1016/0032-5910(81)85007-3

[76] J. KLOUBEK. Hysteresis in porosimetry. *Powder Technology*, **29**: 63–73, 1981. doi: 10.1016/0032-5910(81)85005-X

[77] L. S. MERRICK. Analysis of mercury porosimetry for the evaluation of pore shape and intrusion-extrusion hysteresis. *Journal of Pharmaceutical Sciences*, **80**: 376–379, 1991. doi: 10.1002/jps.2600800419

[78] N. WARDLAW, M. MCKELLAR, and L. YU. Pore and throat size distributions determined by mercury porosimetry and by direct observation. *Carbonates and Evaporites*, **3**: 1, 1988.

[79] S. LOWELL and J. SHIELDS. Theory of mercury porosimetry hysteresis. *Powder Technology*, **38**: 121–124, 1984. doi: 10.1016/0032-5910(84)80041-8

[80] S. LOWELL and S. JOAN. Influence of contact Angle on hysteresis in mercury porosimetry. *Journal of Colloid and Interface Science*, **80**: 192–196, 1981. doi: 10.1016/0021-9797(81)90175-2

[81] R. W. SMITHWICK and E. L. FULLER. A generalized analysis of hysteresis in mercury porosimetry. *Powder Technology*, **38**: 165–173, 1984. doi: 10.1016/0032-5910(84)80045-5

[82] S. P. RIGBY and P. I. CHIGADA. MF-DFT and experimental investigations of the origins of hysteresis in mercury porosimetry of silica materials. *Langmuir*, **26**: 241–248, 2010. doi: 10.1021/la902064y

[83] I. CHATZIS and F. DULLIEN. Mercury porosimetry curves of sandstones. Mechanisms of mercury penetration and withdrawal. *Powder Technology*, **29**: 117–125, 1981. doi: 10.1016/0032-5910(81)85010-3

[84] A. LIABASTRE and C. ORR. An evaluation of pore structure by mercury penetration. *Journal of Colloid and Interface Science*, **64**: 1–18, 1978. doi: 10.1016/0021-9797(78)90329-6

[85] S. P. RIGBY. New methodologies in mercury porosimetry. *Surface Science and Catalysis*, **144**: 185–192, 2002. doi: 10.1016/S0167-2991(02)80133-1

[86] S. RIGBY, D. BARWICK, R. FLETCHER, and S. RILEY. Interpreting mercury porosimetry data for catalyst supports using semi-empirical alternatives to the Washburn equation. *Applied Catalysis A: General*, **238**: 303–318, 2003. doi: 10.1016/S0926-860X(02)00348-4

[87] S. RIGBY and K. EDLER. The influence of mercury contact angle, surface tension, and retraction mechanism on the interpretation of mercury porosimetry data. *Journal of Colloid and Interface Science*, **250**: 175–190, 2002. doi: 10.1006/jcis.2002.8286

[88] S. RIGBY, R. FLETCHER, and S. RILEY. Determination of the cause of mercury entrapment during porosimetry experiments on sol–gel silica catalyst supports. *Applied Catalysis A: General*, **247**: 27–39, 2003. doi: 10.1016/S0926-860X(03)00059-0

[89] S. RIGBY, R. FLETCHER, and S. RILEY. Characterisation of porous solids using integrated nitrogen sorption and mercury porosimetry. *Chemical Engineering Science*, **59**: 41–51, 2004. doi: 10.1016/j.ces.2003.09.017

[90] S. RIGBY, M. WATT-SMITH, P. CHIGADA, J. CHUDEK, R. FLETCHER, J. WOOD, S. BAKALIS, and T. MIRI. Studies of the entrapment of non-wetting fluid within nanoporous media using a synergistic combination of MRI and micro-computed X-ray tomography. *Chemical Engineering Science*, **61**: 7579–7592, 2006. doi: 10.1016/j.ces.2006.08.068

[91] S. LOWELL and S. JOAN. Influence of pore potential on hysteresis and entrapment in mercury porosimetry: pore potential/hysteresis/porosimetry. *Journal of Colloid and Interface Science*, **90**: 203–211, 1982. doi: 10.1016/0021-9797(82)90413-1

[92] S. LOWELL and S. JOAN. Hysteresis, entrapment, and wetting angle in mercury porosimetry. *Journal of Colloid and Interface Science*, **83**: 273–278, 1981. doi: 10.1016/0021-9797(81)90032-1

[93] R. L. PORTSMOUTH and L. F. GLADDEN. Determination of pore connectivity by mercury porosimetry. *Chemical Engineering Science*, **46**: 3023–3036, 1991. doi: 10.1016/0009-2509(91)85006-J

[94] C. D. TSAKIROGLOU and A. C. PAYATAKES. A new simulator of mercury porosimetry for the characterization of porous materials. *Journal of Colloid And Interface Science*, **137**: 315–339, 1990. doi: 10.1016/0021-9797(90)90409-H

[95] C. SALMAS and G. ANDROUTSOPOULOS. Mercury porosimetry Contact angle hysteresis of materials with controlled pore structure. *Journal of Colloid and Interface Science*, **239**: 178–189, 2001. doi: 10.1006/jcis.2001.7531

[96] G. P. MATTHEWS, C. J. RIDGWAY, and M. C. SPEARING. Void space modeling of mercury intrusion hysteresis in sandstone, paper coating, and other porous media. *Journal of Colloid and Interface Science*, **171**: 8–27, 1995. doi: 10.1006/jcis.1995.1146

[97] S. RIGBY, P. CHIGADA, I. EVBUOMVAN, J. CHUDEK, T. MIRI, J. WOOD, and S. BAKALIS. Experimental and modelling studies of the kinetics of mercury retraction from highly confined geometries during porosimetry in the transport and the quasi-equilibrium regimes. *Chemical Engineering Science*, **63**: 5771–5788, 2008. doi: 10.1016/j.ces.2008.08.027

[98] S. RIGBY, M. HASAN, I. HITCHCOCK, and R. FLETCHER. Detection of the delayed condensation effect and determination of its impact on the accuracy of gas adsorption pore size distributions. *Colloids and Surfaces A: Physicochemical and Engineering Aspects*, **517**: 33–44, 2017. doi: 10.1016/j.colsurfa.2016.12.043

[99] S. P. RIGBY. Recent developments in the structural characterisation of disordered, mesoporous solids. *Johnson Matthey Technology Review*, **62**: 296–312, 2018. doi: 10.1595/205651318X696710

[100] S. P. RIGBY, R. S. FLETCHER, J. H. RAISTRICK, and S. N. RILEY. Characterisation of porous solids using a synergistic combination of nitrogen sorption, mercury porosimetry, electron microscopy and micro-focus X-ray imaging techniques. *Physical Chemistry Chemical Physics*, **4**: 3467–3481, 2002. doi: 10.1039/B110781J

[101] S. P. RIGBY. A hierarchical structural model for the interpretation of mercury porosimetry and nitrogen sorption. *Journal of Colloid and Interface Science*, **224**: 382–396, 2000. doi: 10.1006/jcis.1999.6707

[102] S. P. RIGBY and R. S. FLETCHER. Experimental evidence for pore blocking as the mechanism for nitrogen sorption hysteresis in a mesoporous material. *Journal of Physical Chemistry B.*, **108**: 4690–4695, 2004. doi: 10.1021/jp031253s

[103] S. P. RIGBY and R. S. FLETCHER. Interfacing mercury porosimetry with nitrogen sorption. *Particle & Particle Systems Characterization*, **21**: 138–148, 2004. doi: 10.1002/ppsc.200400925

[104] S. P. RIGBY, M. J. WATT-SMITH, and R. S. FLETCHER. Simultaneous determination of the pore-length distribution and pore connectivity for porous catalyst supports using integrated nitrogen sorption and mercury porosimetry. *Journal of Catalysis*, **227**: 68–76, 2004. doi: 10.1016/j.jcat.2004.06.025

[105] S. P. RIGBY, M. J. WATT-SMITH, and R. S. FLETCHER. Integrating gas sorption with mercury porosimetry. *Adsorption (Boston)*, **11**: 201–206, 2005. doi: 10.1007/s10450-005-5923-6

[106] S. P. RIGBY, I. O. EVBUOMWAN, M. J. WATT-SMITH, K. J. EDLER, and R. S. FLETCHER. Using nano-cast model porous media and integrated gas sorption to improve fundamental understanding and data interpretation in mercury porosimetry. *Particle & Particle Systems Characterization*, **23**: 82–93, 2006. doi: 10.1002/ppsc.200601012

[107] S. P. RIGBY, P. I. CHIGADA, E. L. PERKINS, M. J. WATT-SMITH, J. P. LOWE, and K. J. EDLER. Fundamental studies of gas sorption within mesopores situated amidst an inter-connected, irregular network. *Adsorption (Boston)*, **14**: 289–307, 2008. doi: 10.1007/s10450-007-9091-8

[108] S. P. RIGBY and P. I. CHIGADA. Interpretation of integrated gas sorption and mercury porosimetry studies of adsorption in disordered networks using mean-field DFT. *Adsorption (Boston)*, **15**: 31–41, 2009. doi: 10.1007/s10450-008-9147-4

[109] B. BAFARAWA, A. NEPRYAHIN, L. JI, E. HOLT, J. WANG, and S. RIGBY. Combining mercury thermoporometry with integrated gas sorption and mercury porosimetry to improve accuracy of pore-size distributions for disordered solids. *Journal of Colloid and Interface Science*, **426**: 72–79, 2014. doi: 10.1016/j.jcis.2014.03.053

[110] I. HITCHCOCK, SH. MALIK, E. HOLT, R. FLETCHER, and S. RIGBY. Impact of chemical heterogeneity on the accuracy of pore size distributions in disordered solids. *The Journal of Physical Chemistry A.*, **118**: 20627–20638, 2014. doi: 10.1021/jp505482p

[111] I. HITCHCOCK, M. LUNEL, S. BAKALIS, R. FLETCHER, E. HOLT, and S. RIGBY. Improving sensitivity and accuracy of pore structural characterisation using scanning curves in integrated gas sorption and mercury porosimetry experiments. *Journal of Colloid and Interface Science*, **417**: 88–99, 2014. doi: 10.1016/j.jcis.2013.11.025

[112] A. NEPRYAHIN, R. FLETCHER, E. HOLT, and S. RIGBY. Techniques for direct experimental evaluation of structure–transport relationships in disordered porous solids. *Adsorption (Boston)*, **22**: 993–1000, 2016. doi: 10.1007/s10450-016-9806-9

[113] S. RIGBY, M. HASAN, L. STEVENS, H. WILLIAMS, and R. FLETCHER. Determination of pore network accessibility in hierarchical porous solids. *Industrial & Engineering Chemistry Research*, **56**: 14822–14831, 2017. doi: 10.1021/acs.iecr.7b04659

[114] A. MIGUELEZ-MORAN, W. CHUAN-YU, H. DONG, and J. SEVILLE. Characterisation of density distributions in roller-compacted ribbons using micro-indentation and X-ray microcomputed tomography. *European Journal of Pharmaceutics and Biopharmaceutics*, **72**: 173–182, 2009. doi: 10.1016/j.ejpb.2008.12.005

[115] A. HESSENBRUCH. A brief History of X-rays. *Endeavour*, **26**: 137–141, 2002. doi: 10.1016/S0160-9327(02)01465-5

[116] J. AMBROSE. Computerized transverse axial scanning tomography: part 2. clinical application. *The British journal of radiology*, **46**: 1023–1047, 1973.

[117] D. CHIOIBASU, S. MIHAI, A. MAHMOOD, M. LUNGU, and I. POROSNICU. Use of X-ray computed tomography for assessing defects in Ti-Grade 5 parts produced by laser melting deposition. *Metals*, **10**: 2020. doi: 10.3390/met10111408

[118] J. KRUTH, M. BARTSCHER, S. CARMIGNATO, R. SCHMITT, L. DE CHIFFRE, and A. WECKENMANN. Computed tomography for dimensional metrology. *CIRP Annals*, **60**: 821–842, 2011. doi: 10.1016/j.cirp.2011.05.006

[119] G. N. HOUNSFIELD. Computerized transverse axial scanning tomography: Part 1. description of system. *The British Journal of Radiology*, **46**: 1016–1022, 1973. doi: 10.1259/0007-1285-46-552-1016

[120] G. N. HOUNSFIELD. Historical notes on computerized axial tomography. *Journal of the Canadian Association of Radiologists*, **27**: 135–142, 1976.

[121] V. CNUDDE and M. BOONE. High-resolution X-ray computed tomography in geosciences: A review of the current technology and applications. *Earth-Science Reviews*, **123**: 1–17, 2013. doi: 10.1016/j.earscirev.2013.04.003

[122] R. A. GEISE. *Computed tomography: physical principles, clinical applications, and quality control*. Elsevier, 1995.

[123] A. THOMPSON and R. LEACH. *Industrial X-Ray computed tomography*. Springer International Publishing, 2018.

[124] J. HSIEH. *Computed tomography: principles, design, artifacts, and recent advances*. SPIE PRESS, 2015.

[125] V. CNUDDE, B. MASSCHAELE, M. DIERICK, J. VLASSENBROECK, L. VAN HOOREBEKE, and P. JACOBS. Recent progress in X-ray CT as a geosciences tool. *Applied Geochemistry*, **21**: 826–832, 2006. doi: 10.1016/j.apgeochem.2006.02.010

[126] L. DE CHIFFRE, S. CARMIGNATO, J. P. KRUTH, R. SCHMITT, and A. WECKENMANN. Industrial applications of computed tomography. *CIRP Annals*, **63**: 655–677, 2014. doi: 10.1016/j.cirp.2014.05.011

[127] J. RADON. 1.1 über die bestimmung von funktionen durch ihre integralwerte längs gewisser mannigfaltigkeiten. *Classic papers in modern diagnostic radiology*, **5**: 21, 2005.

[128] G. N. RAMACHANDRAN and A. V. LAKSHMINARAYANAN. Three-dimensional reconstruction from radiographs and electron micrographs: application of convolutions instead of Fourier transforms. *Proceedings of the National Academy of Sciences*, **68**: 2236–2240, 1971. doi: 10.1073/pnas.68.9.2236

[129] L. A. FELDKAMP, L. C. DAVIS, and J. W. KRESS. Practical cone-beam algorithm. *Journal of the Optical Society of America A*, **1**: 612–619, 1984. doi: 10.1364/JOSAA.1.000612

[130] S. SCHLÜTER, A. SHEPPARD, K. BROWN, and D. WILDENSCHILD. Image processing of multiphase images obtained via X-ray microtomography: A review. *Water Resources Research*, **50**: 3615–3639, 2014. doi: 10.1002/2014WR015256

[131] T. HUANG, G. YANG, and G. TANG. A fast two-dimensional median filtering algorithm. *IEEE Transactions on Acoustics, Speech, and Signal Processing*, **27**: 13–18, 1979. doi: 10.1109/TASSP.1979.1163188

[132] P. PERONA and J. MALIK. Scale-space and edge detection using anisotropic diffusion. *IEEE Transactions on Pattern Analysis and Machine Intelligence*, **12**: 629–639, 1990. doi: 10.1109/34.56205

[133] A. BUADES, B. COLL, and J.-M. MOREL. A Non-local algorithm for image denoising. *IEEE Computer Vision and Pattern Recognition*, **2**: 60–65, 2005. doi: 10.1109/CVPR.2005.38

[134] R. M. HARALICK, S. R. STERNBERG, and X. ZHUANG. Image analysis using mathematical morphology. *IEEE Transactions on Pattern Analysis and Machine Intelligence*, **PAMI-9**: 532–550, 1987. doi: 10.1109/TPAMI.1987.4767941

[135] G. LITJENS, T. KOOI, B. BEJNORDI, A. SETIO, and F. CIOMPI. A Survey on deep learning in medical image analysis. *Medical Image Analysis*, **42**: 60–88, 2017. doi: 10.1016/j.media.2017.07.005

[136] S. FLENNER, M. STORM, A. KUBEC, E. LONGO, F. DÖRING, and D. PELT. Pushing the temporal resolution in absorption and Zernike phase contrast nanotomography: enabling fast in situ experiments. *Journal of synchrotron radiation*, **27**: 2020. doi: 10.1107/S1600577520007407

[137] A. M. PETROVIC, J. E. SIEBERT, and P. E. RIEKE. Soil bulk density analysis in three dimensions by computed tomographic scanning. *Soil Science Society of America Journal*, **46**: 445–450, 1982. doi: 10.2136/sssaj1982.03615995004600030001x

[138] J. M. HAINSWORTH and L. A. AYLMORE. The use of computer assisted tomography to determine spatial distribution of soil water content. *Soil Research*, **21**: 435–443, 1983. doi: 10.1071/SR9830435

[139] W. J. ANTON, J. LANGE, J. SCHOUTE, and J. BOUMA. Computed tomography as a tool for non-destructive analysis of flow patterns in macroporous clay soils. *Geoderma*, **64**: 183–196, 1995. doi: 10.1016/0016-7061(94)00020-B

[140] S. H. ANDERSON, C. J. GANTZER, J. M. BOONE, and R. J. TULLY. Rapid nondestructive bulk density and soil-water content determination by computed tomography. *Soil Science Society of America Journal*, **52**: 35–40, 1988. doi: 10.2136/sssaj1988.03615995005200010006x

[141] S. Y. WANG, S. F. AYRAL, and C. C. GRYTE. Reconstruction of oil saturation distribution histories during immiscible liquid-liquid displacement by computer-assisted tomography. *AIChE journal*, **30**: 642–646, 1984. doi: 10.1002/aic.690300418

[142] S. L. WELLINGTON and H. J. VINEGAR. X-ray computerized tomography. *Journal of Petroleum Technology*, **39**: 885–898, 1987. doi: 10.2118/16983-PA

[143] P. HUNT, P. ENGLER, and C. BAJSAROWICZ. Computed tomography as a core analysis tool: Applications, instrument evaluation, and image improvement techniques. *Journal of Petroleum Technology*, **40**: 1203–1210, 1988. doi: 10.2118/16952-PA

[144] H. J. VINEGAR and S. L. WELLINGTON. Tomographic imaging of three-phase flow experiments. *Review of Scientific Instruments*, **58**: 96–107, 1987. doi: 10.1063/1.1139522

[145] E. M. WITHJACK. Computed tomography for rock-property determination and fluid-flow visualization. *SPE formation evaluation*, **3**: 696–704, 1988.

[146] K. JASTI, G. JESION, and L. FELDKAMP. Microscopic imaging of porous media with X-Ray computer tomography. *SPE Formation Evaluation*, **8**: 189–193, 1993. doi: 10.2118/20495-PA

[147] V. CLAUSNITZER and J. HOPMANS. Pore-scale measurements of solute breakthrough using microfocus X-ray computed tomography. *Water Resources Research*, **36**: 2067–2079, 2000. doi: 10.1029/2000WR900076

[148] M. BETSON, J. BARKER, P. BARNES, T. ATKINSON, and A. JUPE. Porosity imaging in porous media using synchrotron tomographic techniques. *Transport in porous media*, **57**: 203–214, 2004. doi: 10.1023/B:TIPM.0000038264.33451.4a

[149] C. MILENA and V. JANA. CT derived porosity distribution and flow domains. *Journal of Hydrology*, **267**: 186–200, 2002. doi: 10.1016/S0022-1694(02)00149-X

[150] L. M. SCHWARTZ, F. AUZERAIS, J. DUNSMUIR, N. MARTYS, and S. BENTZ D. andTorquato. Transport and diffusion in three-dimensional composite media. *Physica A: Statistical Mechanics and its Applications*, **207**: 28–36, 1994. doi: 10.1016/0378-4371(94)90351-4

[151] M. SCHMITT, M. HALISCH, C. MÜLLER, and C. FERNANDES. Classification and quantification of pore shapes in sandstone reservoir rocks with 3-D X-ray micro-computed tomography. *Solid Earth*, **7**: 285–300, 2016. doi: 10.5194/se-7-285-2016

[152] L. DECKER, D. JEULIN, and I. TOVENA. 3D morphological analysis of the connectivity of a porous medium. *Acta Stereologica*, 1998. doi: 10.17632/6f36m26nx9.1

[153] J. ARNS, C. ARNS, A. SHEPPARD, R. SOK, M. KNACKSTEDT, and W. PINCZEWSKI. Relative permeability from tomographic images; effect of correlated heterogeneity. *Journal of Petroleum Science and Engineering*, **39**: 247–259, 2003. doi: 10.1016/S0920-4105(03)00066-4

[154] F. AUZERAIS, J. DUNSMUIR, B. FERREOL, N. MARTYS, J. OLSON, T. RAMAKRISHNAN, D. ROTHMAN, and L. SCHWARTZ. Transport in Sandstone: A Study based on three dimensional microtomography. *Geophysical Research Letters*, **23**: 705–708, 1996. doi: 10.1029/96GL00776

[155] D. COKER, S. TORQUATO, and J. DUNSMUIR. Morphology and physical properties of Fontainebleau sandstone via a tomographic analysis. *Geophysical Research: Solid Earth*, **101**: 17497–17506, 1996. doi: 10.1029/96JB00811

[156] S. SONG, K. JONES, B. LINDQUIST, B. DOWD, and D. SAHAGIAN. Synchrotron X-ray computed microtomography: studies on vesiculated basaltic rocks. *Bulletin of Volcanology*, **63**: 252–263, 2001. doi: 10.1007/s004450100141

[157] M. PRODANOVIC, W. LINDQUIST, and R. SERIGHT. 3D image-based characterization of fluid displacement in a Berea core. *Advances in Water Resources*, **30**: 214–226, 2007. doi: 10.1016/j.advwatres.2005.05.015

[158] Y. NAKASHIMA, Nakano T., Nakamura K., K. UESUGI, A. TSUCHIYAMA, and S. IKEDA. Three-dimensional diffusion of non-sorbing species in porous sandstone: computer simulation based on X-ray microtomography using synchrotron radiation. *Journal of Contaminant Hydrology*, **74**: 253–264, 2004. doi: 10.1016/j.jconhyd.2004.03.002

[159] C. H. ARNS, F. BAUGET, A. LIMAYE, A. SAKELLARIOU, T. J. SENDEN, and A. P. SHEPPARD. Pore-scale characterization of carbonates using X-Ray microtomography. *SPE Journal*, **10**: 475–484, 2005. doi: 10.2118/90368-PA

[160] P. LEHMANN, P. WYSS, A. FLISCH, E. LEHMANN, P. VONTOBEL, M. KRAFCZYK, A. KAESTNER, and F. BECKMANN. Tomographical imaging and mathematical description of porous media used for the prediction of fluid distribution. *Vadose Zone Journal*, **5**: 80–97, 2006. doi: 10.2136/vzj2004.0177

[161] M. REDWAN and D. RAMMLMAIR. Simultaneous monitoring of water saturation and fluid conductivity in unconsolidated sand columns. *Soil Science Society of America*, **74**: 1457–1468, 2010. doi: 10.2136/sssaj2009.0398

[162] R. AL-RAOUSH, K. THOMPSON, and C. WILLSON. Comparison of network generation techniques for unconsolidated porous media. *Soil Science Society of America Journal*, **67**: 1687–1700, 2003. doi: 10.2136/sssaj2003.1687

[163] R. I. AL-RAOUSH and C. S. WILLSON. Extraction of physically realistic pore network properties from three-dimensional synchrotron X-ray microtomography images of unconsolidated porous media systems. *Journal of Hydrology*, **300**: 44–64, 2005. doi: 10.1016/j.jhydrol.2004.05.005

[164] X. SHAN and H. CHEN. Lattice Boltzmann model for simulating flows with multiple phases and components. *Physical Review E.*, **47**: 1815–1819, 1993. doi: 10.1103/PhysRevE.47.1815

[165] B. FERREOL and D. ROTHMAN. *Multiphase flow in porous media*. Springer, 1995. 3–20

[166] R. D. HAZLETT, S. Y. CHEN, and W. E. SOLL. Wettability and rate effects on immiscible displacement: Lattice Boltzmann simulation in microtomographic images of reservoir rocks. *Journal of Petroleum Science and Engineering*, **20**: 167–175, 1998. doi: 10.1016/S0920-4105(98)00017-5

[167] H. VOGEL, J. TOLKE, V. SCHULZ, M. KRAFCZYK, and K. ROTH. Comparison of a lattice-Boltzmann model, a full-morphology model, and a pore network model for determining capillary pressure–saturation relationships. *Vadose Zone Journal*, **4**: 380–388, 2005. doi: 10.2136/vzj2004.0114

[168] B. AHRENHOLZ, J. TOLKE, P. LEHMANN, A. PETERS, and A. KAESTNER. Prediction of capillary hysteresis in a porous material using lattice-Boltzmann methods and comparison to experimental data and a morphological pore network model. *Advances in Water Resources*, **31**: 1151–1173, 2008. doi: 10.1016/j.advwatres.2008.03.009

[169] M. PORTER, M. SCHAAP, and D. WILDENSCHILD. Lattice-Boltzmann simulations of the capillary pressure–saturation–interfacial area relationship for porous media. *Advances in Water Resources*, **32**: 1632–1640, 2009. doi: 10.1016/j.advwatres.2009.08.009

[170] W. LINDQUIST, A. VENKATARANGAN, J. DUNSMUIR, and T. WONG. Pore and throat size distributions measured from synchrotron X-ray tomographic images of Fontainebleau sandstones. *Journal of Geophysical Research*, **105**: 21509–21527, 2000. doi: 10.1029/2000JB900208

[171] M. PRODANOVIĆ, W. LINDQUIST, and R. SERIGHT. Porous structure and fluid partitioning in polyethylene cores from 3D X-ray microtomographic imaging. *Journal of Colloid and Interface Science*, **298**: 282–297, 2006. doi: 10.1016/j.jcis.2005.11.053

[172] W. D. CARLSON. Three-dimensional imaging of earth and planetary materials. *Earth and Planetary Science Letters*, **249**: 133–147, 2006. doi: 10.1016/j.epsl.2006.06.020

[173] J. DEWANCKELE, M. BOONE, V. CNUDDE, L. BRABANT, M. BOONE, G. FRONTEAU, L. HOOREBEKE, and P. JACOBS. 4D imaging and quantification of pore structure modifications inside natural building stones by means of high resolution X-ray CT. *Science of the Total Environment*, **416**: 436–448, 2012. doi: 10.1016/j.scitotenv.2011.11.018

[174] C. PURCELL, W. HARBERT, Y. SOONG, R. MCLENDON, I. HALJASMAA, D. MCINTYRE, and J. JIKICH. Velocity measurements in reservoir rock samples from the SACROC unit using various pore fluids, and integration into a seismic survey taken before and after a CO2 sequestration flood. *Energy Procedia*, **1**: 2323–2331, 2009. doi: 10.1016/j.egypro.2009.01.302

[175] S. RIGBY, P. CHIGADA, J. WANG, H. BATEMAN, B. AL-DURI, and J. WOOD. Improving the interpretation of mercury porosimetry data using computerised X-ray tomography and mean-field DFT. *Chemical Engineering Science*, **66**: 2328–2339, 2011. doi: 10.1016/j.ces.2011.02.031

[176] S. RIGBY, H. JAHAN, L. STEVENS, C. UGUNA, C. SNAPE, D. LARGE, and R. FLETCHER. Pore structural evolution of shale following thermochemical treatment. *Marine and Petroleum Geology*, **112**: 104058, 2020. doi: 10.1016/j.marpetgeo.2019.104058

[177] E. P. PITCHER, D. J. LARGE, R. S. FLETCHER, and S. P. RIGBY. Multi-scale pore structural change across a paleodepositional transition in Utica shale probed by gas sorption overcondensation and scanning. *Marine and Petroleum Geology*, **134**: 105348, 2021. doi: 10.1016/j.marpetgeo.2021.105348

[178] A. PLESSIS and W. BOSHOFF. A review of X-ray computed tomography of concrete and asphalt construction materials. *Construction and Building Materials*, **199**: 637–651, 2019. doi: 10.1016/j.conbuildmat.2018.12.049

[179] J. SUMMERSCALES. *Microstructural characterisation of fibre-reinforced composites*. CRC Press, 1998.

[180] A. JONES, B. MILTHORPE, H. AVERDUNK, A. LIMAYE, T. SENDEN, A SAKELLARIOU, and A. SHEPPARD. Analysis of 3D bone ingrowth into polymer scaffolds via micro-computed tomography imaging. *Biomaterials Advances*, **25**: 4947–4954, 2004. doi: 10.1016/j.biomaterials.2004.01.047

[181] C. MASSARO, P. ROTOLO, F. RICCARDIS, E. MILELLA, A. NAPOLI, M. WIELAND, M. TEXTOR, and N. SPENCER. Comparative investigation of the surface properties of commercial titanium dental implants. Part I: chemical composition. *Journal of Materials Science: Materials in Medicine*, **13**: 535–548, 2002. doi: 10.1023/A:1015170625506

[182] E. RÖNKKÖ, T. TERPSTRA, and M. WALTON. *scientific studies of Egyptian mummy*. Block Museum of Art, 2019.

[183] R. AL-RAOUSH and A. PAPADOPOULOS. Representative elementary volume analysis of porous media using X-ray computed tomography. *Powder Technology*, **200**: 69–77, 2010. doi: 10.1016/j.powtec.2010.02.011

[184] J. BEAR. *Dynamics of fluids in porous media*. Courier Corporation, 1988.

[185] G. O. BROWN, H. T. HSIEH, and D. A. LUCERO. Evaluation of laboratory dolomite core sample size using representative elementary volume concepts. *Water Resources Research*, **36**: 1199–1207, 2000. doi: 10.1029/2000WR900017

[186] P. BAVEYE, H. ROGASIK, O. WENDROTH, I. ONASCH, and J. CRAWFORD. Effect of sampling volume on the measurement of soil physical properties: simulation with X-ray tomography data. *Measurement Science and Technology*, **13**: 775, 2002. doi: 10.1088/0957-0233/13/5/316

[187] M. RAZAVI, B. MUHUNTHAN, and O. HATTAMLEH. Representative elementary volume analysis of sands using X-ray computed tomography. *Geotechnical Testing Journal*, **30**: 212–219, 2007. doi: 10.1520/GTJ100164

[188] A. BOGNER, P. JOUNEAU, G. THOLLET, D. BASSET, and C. GAUTHIER. A history of scanning electron microscopy developments: Towards wet-STEM imaging. *Micron*, **38**: 390–401, 2007. doi: 10.1016/j.micron.2006.06.008

[189] M. KNOLL and E. RUSKA. Das elektronenmikroskop. *Journal Für Physik*, **78**: 318–339, 1932. doi: 10.1007/BF01342199

[190] I. UTKE, S. MOSHKALEV, and P. RUSSELL. *Nanofabrication using focused ion and electron beams: principles and applications*. Oxford University Press, 2012.

[191] R. LANGFORD and C. CLINTON. In situ lift-out using a FIB-SEM system. *Micron*, **35**: 607–611, 2004. doi: 10.1016/j.micron.2004.03.002

[192] L. GIANNUZZI, B. KEMPSHALL, S. SCHWARZ, J. LOMNESS, B. PRENITZER, and F. STEVIE. Springer, 2005.

[193] M. OVERWIJK, F. HEUVEL, and C. BULLE-LIEUWMA. Novel scheme for the preparation of transmission electron microscopy specimens with a focused ion beam. *Journal of Vacuum Science & Technology A*, **11**: 2021–2024, 1993. doi: 10.1116/1.586537

[194] A. LESLIE, K. PEY, K. SIM, M. BEH, and G. GOH. *TEM sample preparation using FIB: Practical problems and artifacts*. ASM International, 1995.

[195] L. GIANNUZZI, J. DROWN, S. BROWN, R. IRWIN, and F. STEVIE. Focused ion beam milling and micromanipulation lift-out for site specific cross-section TEM specimen preparation. *MRS Online Proceedings*, **480**: 1997. doi: 10.1557/PROC-480-19

[196] T. YAGUCHI, T. KAMINO, M. SASAKI, G. BARBEZAT, and R. URAO. Method for cross-sectional transmission electron microscopy specimen preparation of composite materials using a dedicated focused ion beam system. *Microscopy and Microanalysis*, **5**: 365–370, 1999. doi: 10.1007/s100059910019

[197] T. YAGUCHI, T. KAMINO, M. SASAKI, G. BARBEZAT, and R. URAO. Cross-sectional specimen preparation and observation of a plasma sprayed coating using a focused ion beam/transmission electron microscopy system. *Microscopy and Microanalysis*, **6**: 218–223, 2000. doi: 10.1007/s100059910019

[198] T. YAGUCHI, T. KAMINO, M. SASAKI, G. BARBEZAT, and R. URAO. A FIB micro-sampling technique and a site-specific TEM specimen preparation method for precision materials characterization. *MRS Online Proceedings*, **636**: D9.35.1, 2000. doi: 10.1557/PROC-636-D9.35.1

[199] S. ZAEFFERER, S. WRIGHT, and D. RAABE. Three-dimensional orientation microscopy in a focused ion beam–scanning electron microscope: A new dimension of microstructure characterization. *Metallurgical and Materials Transactions A*, **39**: 374–389, 2008. doi: 10.1007/s11661-007-9418-9

[200] L. VANDEWALLE. *Measuring, monitoring and modeling concrete properties*. Springer, 2006.

[201] L. HOLZER and B. MUENCH. *Advances in concrete through science and engineering*. RILEM, 2006.

[202] P. TRTIK, J. DUAL, B. MUENCH, and L. HOLZER. Limitation in obtainable surface roughness of hardened cement paste:'virtual'topographic experiment based on focussed ion beam nanotomography datasets. *Journal of microscopy*, **232**: 200–206, 2008. doi: 10.1111/j.1365-2818.2008.02090.x

[203] L. HOLZER, B. MUNCH, M. RIZZI, R. WEPF, P. MARSCHALL, and T. GRAULE. 3D-microstructure analysis of hydrated bentonite with cryo-stabilized pore water. *Applied Clay Science*, **47**: 330–342, 2010. doi: 10.1016/j.clay.2009.11.045

[204] G. DESBOIS, J. URAI, and P. KUKLA. Morphology of the pore space in claystones-evidence from BIB/FIB ion beam sectioning and cryo-SEM observations. *Earth Discussions*, **4**: 1–19, 2009. doi: 10.5194/ee-4-15-2009

[205] C. HOLZAPFEL, A. SCHAF, M. MARX, H. VEHOFF, and F. MUCKLICH. Interaction of cracks with precipitates and grain boundaries: Understanding crack growth mechanisms through focused ion beam tomography. *Scripta Materialia*, **56**: 697–700, 2007. doi: 10.1016/j.scriptamat.2006.12.025

[206] J. WILSON, W. KOBSIRIPHAT, R. MENDOZA, H. CHEN, J. HILLER, and D. MILLER. Three-dimensional reconstruction of a solid-oxide fuel-cell anode. *Nature Materials*, **5**: 541–544, 2006. doi: 10.1038/nmat1668

[207] N. DUYCKAERTS, M. BARTSCH, A. LORKE, F. SCHÜTH, and G. PRIETO. *FIB-SEM tomography imaging and 3D structure quantification of supported metal catalysts*. Wiley, 2016.

[208] J. RIIKONEN, J. SALONEN, and V. LEHTO. Utilising thermoporometry to obtain new insights into nanostructured materials: review part 1. *Journal of Thermal Analysis and Calorimetry*, **105**: 811–821, 2011. doi: 10.1007/s10973-010-1167-0

[209] M. R. LANDRY. Thermoporometry by differential scanning calorimetry: experimental considerations and applications. *Thermochimica acta*, **433**: 27–50, 2005. doi: 10.1016/j.tca.2005.02.015

[210] R. VALCKENBORG, L. PEL, and K. KOPINGA. Combined NMR cryoporometry and relaxometry. *Journal of Physics D: Applied Physics*, **35**: 249–256, 2002. doi: 10.1088/0022-3727/35/3/314

[211] G. P. JOHARI. The Gibbs-Thomson effect and intergranular melting in ice emulsions: Interpreting the anomalous heat capacity and volume of supercooled water. *Journal of Chemical Physics*, **107**: 10154–10165, 1997. doi: 10.1063/1.475322

[212] K. ISHIKIRIYAMA and M. TODOKI. Pore size distribution measurements of silica gels by means of differential scanning calorimetry: II. Thermoporosimetry. *Journal of colloid and interface science*, **171**: 103–111, 1995. doi: 10.1006/jcis.1995.1154

[213] A. SCHREIBER, I. KETELSEN, and H. FINDENEGG. Melting and freezing of water in ordered mesoporous silica materials. *Physical Chemistry Chemical Physics*, **3**: 1185–1195, 2001. doi: 10.1039/B010086M

[214] K. KLOETSTRA, H. ZANDBERGEN, M. KOTEN, and H. BEKKUM. Thermoporometry as a new tool in analyzing mesoporous MCM-41 materials. *Catalysis letters*, **33**: 145–156, 1995. doi: 10.1007/BF00817054

[215] T. YAMAMOTO, A. ENDO, Y. INAGI, T. OHMORI, and M. NAKAIWA. Evaluation of thermoporometry for characterization of mesoporous materials. *Journal of colloid and interface science*, **284**: 614–620, 2005. doi: 10.1016/j.jcis.2004.10.025

[216] M. BRUN, A. LALLEMAND, J. QUINSON, and C. EYRAUD. A new method for the simultaneous determination of the size and shape of pores: the thermoporometry. *Thermochimica acta*, **21**: 59–88, 1977. doi: 10.1016/0040-6031(77)85122-8

[217] C. A. JOHNSON. Generalization of the Gibbs-Thomson equation. *Surface Science*, **3**: 429–444, 1965. doi: 10.1016/0039-6028(65)90024-5

[218] J. W. GIBBS. On the equilibrium of heterogeneous substances. *American Journal of Science and Arts*, **16**: 441, 1869. doi: 10.11588/heidok.00013220

[219] W. THOMSON. On the equilibrium of vapour at a curved surface of liquid. *Proceedings of the Royal Society of Edinburgh*, **7**: 63–68, 1875. doi: 10.1017/S0370164600041729

[220] C. L. JACKSON and G. B. MCKENNA. Vitrification and crystallization of organic liquids confined to nanoscale pores. *Chemistry of Materials*, **8**: 2128–2137, 1996. doi: 10.1021/cm9601188

[221] K. OVERLOOP and L. VANGERVEN. Freezing phenomena in adsorbed water as studied by NMR. *Journal of Magnetic Resonance*, **101**: 179–187, 1993. doi: 10.1006/jmra.1993.1028

[222] J. STRANGE, M. RAHMAN, and E. SMITH. Characterization of porous solids by NMR. *Physical Review Letters*, **71**: 3589, 1993. doi: 10.1103/PhysRevLett.71.3589

[223] R. SCHMIDT, E. HANSEN, M. STÖCKER, D. AKPORIAYE, and O. ELLESTAD. Pore size determination of MCM-51 mesoporous materials by means of 1H NMR spectroscopy, N2 adsorption, and HREM. A preliminary study. *Journal of the American Chemical Society*, **117**: 4049–4056, 1995. doi: 10.1021/ja00119a021

[224] E. HANSEN, C. SIMON, R. HAUGSRUD, H. RAEDER, and R. BREDESEN. Probing pore size distribution by cryogenic and relaxation 2H-NMR. *The Journal of Physical Chemistry B*, **106**: 12396–12406, 2002. doi: 10.1021/jp0146420

[225] E. PERKINS, J. LOWE, K. EDLER, N. TANKO, and S. RIGBY. Determination of the percolation properties and pore connectivity for mesoporous solids using NMR cryodiffusometry. *Chemical Engineering Science*, **63**: 1929–1940, 2008. doi: 10.1016/j.ces.2007.12.022

[226] O. PETROV and I. FURÓ. NMR cryoporometry: Principles, applications and potential. *Progress in Nuclear Magnetic Resonance Spectroscopy*, **2**: 97–122, 2009. doi: 10.1016/j.pnmrs.2008.06.001

[227] E. SHIKO, K. EDLER, J. LOWE, and S. RIGBY. Probing hysteresis during sorption of cyclohexane within mesoporous silica using NMR cryoporometry and relaxometry. *Journal of colloid and interface science*, **398**: 168–175, 2013. doi: 10.1016/j.jcis.2013.02.002

[228] E. HANSEN, R. SCHMIDT, and M. STÖCKER. Pore structure characterization of porous silica by 1H NMR using water, benzene, and cyclohexane as probe molecules. *Journal of Physical Chemistry*, **100**: 11396–11401, 1996. doi: 10.1021/jp960305t

[229] C. L. JACKSON and G. B. MCKENNA. The melting behavior of organic materials confined in porous solids. *Journal of Chemical Physics*, **93**: 9002–9011, 1990. doi: 10.1063/1.459240

[230] K. MORISHIGE and K. KAWANO. Freezing and melting of water in a single cylindrical pore: The pore-size dependence of freezing and melting behavior. *Journal of chemical physics*, **110**: 4867–4872, 1999. doi: 10.1063/1.478372

[231] S. JÄHNERT, F. Vaca CHÁVEZ, S., A. SCHREIBER, M. SCHÖNHOFF, and G. FINDENEGG. Melting and freezing of water in cylindrical silica nanopores. *Physical Chemistry Chemical Physics*, **10**: 6039–6051, 2008. doi: 10.1039/B809438C

[232] D. MAJDA, M. ZIMOWSKA, K. TARACH, B. NAPRUSZEWSKA, and A. MICHALIK. Water thermoporosimetry as a tool of characterization of the textural parameters of mesoporous materials. *Journal of Thermal Analysis and Calorimetry*, **127**: 207–220, 2017. doi: 10.1007/s10973-016-5400-3

[233] T. ROTTREAU, C. PARLETT, A. LEE, and R. EVANS. NMR cryoporometric measurements of porous silica: A method for the determination of melting point depression parameters of probe liquids. *Microporous and Mesoporous Materials*, **264**: 265–271, 2018. doi: 10.1016/j.micromeso.2018.01.004

[234] D. MAJDA, W. MAKOWSKI, and M. MAŃKO. Pore size distribution of micelle-templated silicas studied by thermoporosimetry using water and n-heptane. *Journal of thermal analysis and calorimetry*, **109**: 663–669, 2012. doi: 10.1007/s10973-012-2372-9

[235] G. DOSSEH, Y. XIA, and C. ALBA-SIMIONESCO. Cyclohexane and benzene confined in MCM-41 and SBA-15: confinement effects on freezing and melting. *Journal of Physical Chemistry*, **107**: 6445–6453, 2003. doi: 10.1021/jp034003k

[236] K. MORISHIGE, H. YASUNAGA, and Y. MATSUTANI. Effect of pore shape on freezing and melting temperatures of water. *Journal of Physical Chemistry C*, **114**: 4028–4035, 2010. doi: 10.1021/jp910759n

[237] K. MORISHIGE, H. YASUNAGA, R. DENOYEL, and V. WERNERT. Pore-blocking-controlled freezing of water in cagelike pores of KIT-5. *Journal of Physical Chemistry C*, **111**: 9488–9495, 2007. doi: 10.1021/jp072022e

[238] R. PELLENQ, B. COASNE, R. DENOYEL, and O. COUSSY. Simple phenomenological model for phase transitions in confined geometry. 2. Capillary condensation/evaporation in cylindrical mesopores. *Langmuir*, **25**: 1393–1402, 2009. doi: 10.1021/la8020244

[239] I. BEURROIES, R. DENOYEL, P. LLEWELLYN, and J. ROUQUEROL. A comparison between melting-solidification and capillary condensation hysteresis in mesoporous materials: application to the interpretation of thermoporometry data. *Thermochimica Acta*, **421**: 11–18, 2004. doi: 10.1016/j.tca.2004.03.008

[240] L. PARAPATITS and F. SCHUSTER. The Steiner formula for Minkowski valuations. *Advances in mathematics*, **230**: 978–994, 2012. doi: 10.1016/j.aim.2012.03.024

[241] A. MUHAMMAD, M. MAHMOUD, Y. ZHANG, and S. IGLAUER. X-ray tomography imaging of shale microstructures: A review in the context of multiscale correlative imaging. *International Journal of Coal Geology*, **233**: 103641, 2021. doi: 10.1016/j.coal.2020.103641

[242] M. LIN, D. PATRICK, E. RUTTER, K. TAYLOR, and P. LEE. A novel upscaling procedure for characterising heterogeneous shale porosity from nanometer-to millimetre-scale in 3D. *Journal of Energy*, **181**: 1285–1297, 2019. doi: 10.1016/j.energy.2019.06.011

[243] D. WINTER, M. FLORIAN, and B. WECKHUYSEN. FIB-SEM Tomography Probes the Mesoscale Pore Space of an Individual Catalytic Cracking Particle. *ACS Catalysis*, **6**: 3158–3167, 2016. doi: 10.1021/acscatal.6b00302

[244] J. YAO, W. SONG, D. WANG, H. SUN, and Y. LI. Multi-scale pore network modelling of fluid mass transfer in nano-micro porous media. *International Journal of Heat and Mass Transfer*, **141**: 156–167, 2019. doi: 10.1016/j.ijheatmasstransfer.2019.06.077

[245] W. SONG, J. YAO, K. ZHANG, H. SUN, and Y. YANG. The impacts of pore structure and relative humidity on gas transport in shale: a numerical study by the image-based multi-scale pore network model. *Transport in Porous Media*, 1–25, 2021. doi: 10.1007/s11242-021-01663-6

[246] G. CODY and A. DAVIS. Direct imaging of coal pore space accessible to liquid metal. *Energy & fuels*, **5**: 776–781, 1991. doi: 10.1021/ef00030a001

[247] J. KAUFMANN. Pore space analysis of cement-based materials by combined Nitrogen sorption–Wood's metal impregnation and multi-cycle mercury intrusion. *Cement and Concrete Composites*, **32**: 514–522, 2010. doi: 10.1016/j.cemconcomp.2010.04.003

[248] L. RUFFINO, R. MANN, R. OLDMAN, E. STITT, E. BOLLER, and P. CLOETENS. Using X-Ray Microtomography for Characterisation of Catalyst Particle Pore Structure. *The Canadian Journal of Chemical Engineering*, **83**: 132–139, 2005. doi: 10.1002/cjce.5450830122

[249] F. HILL, T. HOTCHKISS, K. HARDSTONE, I. HITCHCOCK, V. NOVAK, and S. RIGBY. Hyperpolarised xenon MRI and time-resolved X-ray computed tomography studies of structure-transport relationships in hierarchical porous media. *Chemical Engineering Journal*, **405**: 126750, 2021. doi: 10.1016/j.cej.2020.126750

[250] A. V NEIMARK and P. RAVIKOVITCH. Capillary condensation in MMS and pore structure characterization. *Microporous and Mesoporous Materials*, **44**: 697–707, 2001. doi: 10.1016/S1387-1811(01)00251-7

[251] J. JAGIELLO, A. CHOJNACKA, S. POURHOSSEINI, Z. WANG, and F. BEGUIN. A dual shape pore model to analyze the gas adsorption data of hierarchical micro-mesoporous carbons. *Carbon*, **178**: 113–124, 2021. doi: 10.1016/j.carbon.2021.02.098

[252] S. P. RIGBY and L. F. GLADDEN. The use of magnetic resonance images in the simulation of diffusion in porous catalyst support pellets. *Journal of Catalysis*, **173**: 484–489, 1998. doi: 10.1006/jcat.1997.1940

[253] S. P. RIGBY and L. F. GLADDEN. NMR and fractal modelling studies of transport in porous media. *Chemical Engineering Science*, **51**: 2263–2272, 1996. doi: 10.1016/0009-2509(96)00083-8

[254] S. KIRKPATRICK, R. BALLIAN, R. MAYNARD, and G. TOULOUSE. *Les Houches Summer School on Ill Condensed Matter*. Amsterdam: North-Holland, 1979. 321

[255] S. RIGBY, L. STEVENS, T. MEERSMANN, G. PAVLOVSKAYA, G. REES, and R. FLETCHER. Structural and chemical heterogeneity in ancient glass probed using gas overcondensation, X-ray tomography, and solid-state NMR. *Materials Characterization*, **167**: 110467, 2020. doi: 10.1016/j.matchar.2020.110467

[256] D. PAGANIN, S. MAYO, T. GUREYEV, P. MILLER, and S. WILKINS. Simultaneous phase and amplitude extraction from a single defocused image of a homogeneous object. *Journal of Microscopy*, **206**: 33–40, 2002. doi: 10.1046/j.1365-2818.2002.01010.x

[257] F. MARONE and M. STAMPANONI. Regridding reconstruction algorithm for real-time tomographic imaging. *Journal of Synchrotron Radiation*, **19**: 1029–1037, 2012. doi: 10.1107/S0909049512032864

[258] R. MAKOVETSKY, N. PICHE, and M. MARSH. Dragonfly as a platform for easy image-based Deep Learning applications. *Microscopy and Microanalysis*, **24**: 532–533, 2018. doi: 10.1017/s143192761800315x

[259] S. PRAGER. Diffusion in inhomogeneous media. *Journal of Chemical Physics*, **33**: 122–127, 1960. doi: 10.1063/1.1731066

[260] D. AVNIR. *Fractal approach to heterogeneous chemistry*. Wiley, 1989.

[261] P. K. SAHOO, S. A. SOLTANI, and A. K. WONG. A survey of thresholding techniques. *Computer vision, graphics, and image processing*, **41**: 233–260, 1988.

[262] S. BEUCHER. The watershed transformation applied to image segmentation. *Scanning Microscopy*, **1992**: 28, 1993.

[263] D. NAMEIRAKPAM, M. KHUMANTHEM, and J. YAMBEM. Image segmentation using K-means clustering algorithm and subtractive clustering algorithm. *Procedia Computer Science*, **54**: 764–771, 2015. doi: 10.1016/j.procs.2015.06.090

[264] S. GHOSH, N. DAS, I. DAS, and U. MAULIK. Understanding deep learning techniques for image segmentation. *ACM Computing Surveys (CSUR)*, **52**: 1–35, 2019.

[265] N. O'MAHONY, S. CAMPBELL, and A. CARVALHO. Deep learning vs. traditional computer vision. *Advances in Intelligent Systems and Computing*, **943**: 128–144, 2020. doi: 10.1007/978-3-030-17795-9_10

[266] Y. LECUN, Y. BENGIO, and G. HINTON. Deep Learning. *Nature*, **521**: 436–444, 2015. doi: 10.1038/nature14539

[267] J. WANG, Y. MA, L. ZHANG, R. GAO, and D. WU. Deep Learning for smart manufacturing: methods and applications. *Journal of Manufacturing Systems*, **48**: 144–156, 2018. doi: 10.1016/j.jmsy.2018.01.003

[268] S. SHALEV-SHWARTZ and S. BEN-DAVID. *Understanding Machine Learning*. Cambridge University press, 2014.

[269] M. H. HASSOUN. *Fundamentals of Artificial Neural Networks*. MIT press, 1995.

[270] Y. LECUN, K. KAVUKCUOGLU, and C. FARABET. Convolutional networks and applications in vision. *IEEE International Symposium on Circuits and Systems*, 253–256, 2010. doi: 10.1109/ISCAS.2010.5537907

[271] A. BADRAN, D. MARSHALL, Z. LEGAULT, R. MAKOVETSKY, B. PROVENCHER, N. PICHÉ, and M. MARSH. Automated segmentation of computed tomography images of fiber-reinforced composites by Deep Learning. *Journal of Materials Science*, **55**: 16273–16289, 2020. doi: 10.1007/s10853-020-05148-7

[272] X. MA, N. KITTIKUNAKORN, B. SORMAN, H. XI, A. CHEN, M. MARSH, A. MONGEAU, N. PICHÉ, R. WILLIAMS, and D. SKOMSKI. Application of deep learning convolutional Neural Networks for internal tablet defect detection: high accuracy, throughput, and adaptability. *Journal of Pharmaceutical Sciences*, **109**: 1547–1557, 2020. doi: 10.1016/j.xphs.2020.01.014

[273] R. LORENZONI, I. CUROSU, S. PACIORNIK, V. MECHTCHERINE, M. OPPERMANN, and F. SILVA. Semantic segmentation of the micro-structure of strain-hardening cement-based composites (SHCC) by Applying Deep Learning on micro-computed tomography scans. *Cement and Concrete Composites*, **108**: 103551, 2020. doi: 10.1016/j.cemconcomp.2020.103551

[274] O. RONNEBERGER, P. FISCHER, and T. BROX. U-Net: Convolutional Networks for Biomedical Image Segmentation. *International Conference on Medical image*, **9351**: 234–241, 2015. doi: 10.1007/978-3-319-24574-4_28

[275] E. BEZERRA, K. AUGUSTO, and S. PACIORNIK. Discrimination of pores and cracks in iron ore pellets using Deep Learning Neural Networks. *REM - International Engineering Journal*, **73**: 197–203, 2020. doi: 10.1590/0370-44672019730119

[276] G. HINTON, L. DENG, D. YU, G. DAHL, and A. MOHAMED. Deep Neural Networks for acoustic modeling in speech recognition: the shared views of four research groups. *IEEE Signal Processing Magazine*, **29**: 82–97, 2012. doi: 10.1109/MSP.2012.2205597

[277] J. NI, Y. CHEN, Y. CHEN, J. ZHU, D. ALI, and W. CAO. A Survey on theories and applications for self-driving cars based on Deep Learning methods. *Applied Sciences*, **10**: 2749, 2020. doi: 10.3390/app10082749

[278] T. YOUNG, D. HAZARIKA, S. PORIA, and E. CAMBRIA. Recent trends in Deep Learning based natural language processing. *IEEE Computational Intelligence Magazine*, **13**: 55–75, 2018. doi: 10.1109/MCI.2018.2840738

[279] A. ESTEVA, A. ROBICQUET, B. RAMSUNDAR, V. KULESHOV, and M. DEPRISTO. A guide to Deep Learning in healthcare. *Nature Medicine*, **25**: 24–29, 2019. doi: 10.1038/s41591-018-0316-z

[280] A. ROY, J. SUN, R. MAHONEY, L. ALONZI, S. ADAMS, and P. BELING. Deep Learning detecting fraud in credit card transactions. **4**: 129–134, 2018. doi: 10.1109/SIEDS.2018.8374722

[281] S. MESENTIER, S. LEE, J. TOGELIUS, and A. NEALEN. AI-based playtesting of contemporary board games. **10**: 1–10, 2017. doi: 10.1145/3102071.3102105

[282] A. MARTÍN, B. PAUL, C. JIANMIN, C. ZHIFENG, D. ANDY, D. JEFFREY, and D. MATTHIEU. TensorFlow: a system for large-scale Machine Learning. *Computing Research Repository*, 265–283, 2016. doi: 10.5281/zenodo.4724125

[283] T. ARAÚJO, G. ARESTA, E. CASTRO, J. ROUCO, P. AGUIAR, C. ELOY, A. POLÓNIA, and A. CAMPILHO. Classification of breast cancer histology images using Convolutional Neural Networks. *PloS one*, **12**: e0177544, 2017.

[284] A. GARCIA-GARCIA, S. ORTS-ESCOLANO, S. OPREA, V. VILLENA-MARTINEZ, and J. GARCIA-RODRIGUEZ. A review on Deep Learning techniques applied to semantic segmentation. *Applied Soft Computing Journal*, 1–23, 2017.

[285] A. GARCIA-GARCIA, S. ORTS-ESCOLANO, S. OPREA, V. VILLENA-MARTINEZ, and J. GARCIA-RODRIGUEZ. A survey on Deep Learning techniques for image and video semantic segmentation. *Applied Soft Computing Journal*, **70**: 41–65, 2018. doi: 10.1016/j.asoc.2018.05.018

[286] I. SUTSKEVER, O. VINYALS, and Q. V. LE. Sequence to sequence learning with neural networks. *Advances in Neural Information Processing Systems*, **4**: 3104–3112, 2014. arXiv: 1409.3215

[287] H. B. FERRIS. The Neuron. *Psychological Bulletin*, **15**: 257–263, 1918. doi: 10.1037/h0072284

[288] B. W. WHITE and F. ROSENBLATT. Principles of neurodynamics: perceptrons and the theory of brain mechanisms. *American Journal of Psychology*, **76**: 705, 1963. doi: 10.2307/1419730

[289] P. SIBI, Allwyn J. S., and P. SIDDARTH. Analysis of different activation functions using back propagation neural networks. *Journal of Theoretical and Applied Information Technology*, **47**: 1344–1348, 2013.

[290] K. JARRETT, K. KAVUKCUOGLU, M. RANZATO, and Y. LECUN. What is the best multi-stage architecture for object recognition? *Proceedings of the IEEE International Conference on Computer Vision*, 2146–2153, 2009. doi: 10.1109/ICCV.2009.5459469

[291] H. LI, J. WANG, M. TANG, and X. LI. Polarization-dependent effects of an airy beam due to the spin-orbit coupling. *Journal of the Optical Society of America A*, **34**: 1114–1118, 2017. doi: 10.1002/ecs2.1832

[292] M. J. BROWN, L. A. HUTCHINSON, M. J. RAINBOW, K. J. DELUZIO, and A. R. DE ASHA. A Comparison of self-selected walking speeds and walking speed variability when data are collected during repeated discrete trials and during continuous walking. *Journal of Applied Biomechanics*, **33**: 384–387, 2017. doi: 10.1123/jab.2016-0355

[293] A. G. ROY, S. CONJETI, S. K. KARRI, D. SHEET, A. KATOUZIAN, C. WACHINGER, and N. NAVAB. ReLayNet: retinal layer and fluid segmentation of macular optical coherence tomography using fully convolutional networks. *Biomedical Optics Express*, **8**: 3627, 2017. doi: 10.1364/boe.8.003627

[294] D. E. RUMELHART, G. E. HINTON, and R. J. WILLIAMS. Learning representations by back-propagating errors. *Nature*, **323**: 533–536, 1986. doi: 10.1038/323533a0

[295] A. KRIZHEVSKY, I. SUTSKEVER, and G. E. HINTON. ImageNet classification with deep convolutional neural networks. *Advances in neural information processing systems*, **25**: 1097–1105, 2012.

[296] Y. LECUN, L. BOTTOU, Y. BENGIO, and P. HAFFNER. Gradient-based learning applied to document recognition. *Proceedings of the IEEE*, **86**: 2278–2323, 1998. doi: 10.1109/5.726791

[297] H. NOH, S. HONG, and B. HAN. Learning deconvolution network for semantic segmentation. *Proceedings of the IEEE International Conference on Computer Vision*, **2015**: 1520–1528, 2015. doi: 10.1109/ICCV.2015.178

[298] K. SIMONYAN and A. ZISSERMAN. Very deep convolutional networks for large-scale image recognition. *arXiv:1409.1556*, 1–14, 2014.

[299] S. SMITH. *Digital signal processing: a practical guide for engineers and scientists*. Elsevier, 2013.

[300] I. GOODFELLOW, Y. BENGIO, and A. COURVILLE. *Deep Learning*. MIT press, 2016. 801

[301] B. GRAHAM. Fractional max-pooling. *arXiv:1412.6071*, 1–10, 2014.

[302] J. NAGI, F. DUCATELLE, A. DI CARO, D. CIREŞAN, U. MEIER, A. GIUSTI, F NAGI, J. SCHMIDHUBER, and M. GAMBARDELLA. Max-pooling convolutional neural networks for vision-based hand gesture recognition. *IEEE International Conference on Signal and Image Processing Applications*, 342–347, 2011. doi: 10.1109/ICSIPA.2011.6144164

[303] M. D. ABRÀMOFF, P. J. MAGALHÃES, and S. J. RAM. Image processing with ImageJ. *Biophotonics International*, **11**: 36–41, 2004. doi: 10.1201/9781420005615.ax4

[304] A. M. REZA. Realization of the contrast limited adaptive histogram equalization (CLAHE) for real-time image enhancement. *Journal of VLSI Signal Processing Systems*, **38**: 35–44, 2004. doi: 10.1023/B:VLSI.0000028532.53893.82

[305] K. ZUIDERVELD. Contrast limited adaptive histogram equalization. *Graphics Gems*, 474–485, 1994. doi: 10.1016/b978-0-12-336156-1.50061-6

[306] A. BUADES, B. COLL, and J. MOREL. Non-local means denoising. *Image Processing*, **1**: 208–212, 2011. doi: 10.5201/ipol.2011.bcm_nlm

[307] D. G. LOWE. Distinctive image features from scale-invariant keypoints. *International Journal of Computer Vision*, **60**: 91–110, 2004. doi: 10.1023/B:VISI.0000029664.99615.94

[308] B. MÜNCH, P. TRTIK, F. MARONE, and M. STAMPANONI. Stripe and ring artifact removal with combined wavelet-fourier filtering. *EMPA Activities*, **17**: 34–35, 2009. doi: 10.1364/oe.17.008567

[309] F. MILLETARI, N. NAVAB, and S. AHMADI. V-Net: Fully convolutional neural networks for volumetric medical image segmentation. *International Conference on 3D Vision*, 565–571, 2016. doi: 10.1109/3DV.2016.79

[310] S. JEGOU, M. DROZDZAL, D. VAZQUEZ, A. ROMERO, and Y. BENGIO. The one hundred layers tiramisu: Fully convolutional DenseNets for semantic segmentation. *IEEE Computer Society*, 11–19, 2017. doi: 10.1109/CVPRW.2017.156

[311] M. D. ZEILER. Adadelta: an adaptive learning rate method. *Computing Research Repository*, **121**: 2012. doi: arxiv.org/abs/1212.5701

[312] V. GUN'KO, V. TUROV, A. TUROV, V. ZARKO, V. GERDA, and A. VALENTIN. Behaviour of pure water and water mixture with benzene or chloroform adsorbed onto ordered mesoporous silicas. *Central European Journal of Chemistry*, **5**: 420–454, 2007. doi: 10.2478/s11532-007-0010-3

[313] O. PETROV and I. FURÓ. Curvature-dependent metastability of the solid phase and the freezing-melting hysteresis in pores. *Physical Review E*, **73**: 011608, 2006. doi: 10.1103/PhysRevE.73.011608

[314] I. HITCHCOCK, E. HOLT, J. LOWE, and S. RIGBY. Studies of freezing–melting hysteresis in cryoporometry scanning loop experiments using NMR diffusometry and relaxometry. *Chemical Engineering Science*, **66**: 582–592, 2011. doi: 10.1016/j.ces.2010.10.027

[315] G. MASON. The effect of pore lattice structure on the pore size distributions calculated from sorption isotherms using percolation theory. *Journal of colloid and interface science*, **95**: 277–278, 1983. doi: 10.1016/0021-9797(83)90100-5

[316] M. PARLAR and Y. YORTSOS. Percolation theory of vapor adsorption—desorption processes in porous materials. *Journal of colloid and interface science*, **124**: 162–176, 1988. doi: 10.1016/0021-9797(88)90337-2

[317] J. H. DE BOER and B. C. LIPPENS. Studies on pore systems in catalysts II. The shapes of pores in aluminum oxide systems. *Journal of Catalysis*, **3**: 38–43, 1964. doi: 10.1016/0021-9517(64)90090-9

[318] I. HITCHCOCK, J. CHUDEK, E. HOLT, J. LOWE, and S. RIGBY. NMR studies of cooperative effects in adsorption. *Langmuir*, **26**: 18061–18070, 2010. doi: 10.1021/la103584k

[319] M. WU, K. FRIDH, B. JOHANNESSON, and M. GEIKER. Impact of sample crushing on porosity characterization of hardened cement pastes by low temperature calorimetry: comparison of powder and cylinder samples. *Thermochimica Acta*, **665**: 11–19, 2018. doi: 10.1016/j.tca.2018.05.002

[320] R. VALIULLIN and I. FURÓ. Low-temperature phase separation of a binary liquid mixture in porous materials studied by cryoporometry and pulsed-field-gradient NMR. *Physical Review E.*, **66**: 031508, 2002. doi: 10.1103/PhysRevE.66.031508

[321] R. VALIULLIN and I. FURÓ. Phase separation of a binary liquid mixture in porous media studied by nuclear magnetic resonance cryoporometry. *Journal of chemical physics*, **116**: 1072–1076, 2002. doi: 10.1063/1.1427706

[322] J MITCHELL, SC STARK, and JH STRANGE. Probing surface interactions by combining NMR cryoporometry and NMR relaxometry. *Journal of Physics D: Applied Physics*, **38**: 1950, 2005. doi: 10.1088/0022-3727/38/12/015

[323] K. ISHIKIRIYAMA, M. TODOKI, and K. MOTOMURA. Pore size distribution (PSD) measurements of silica gels by means of differential scanning calorimetry: I. Optimization for determination of PSD. *Journal of colloid and interface science*, **171**: 92–102, 1995. doi: 10.1006/jcis.1995.1154

[324] K. ISHIKIRIYAMA, M. TODOKI, and K. MOTOMURA. Pore size distribution measurements of silica gels by means of differential scanning calorimetry: II. Thermoporosimetry. *Journal of colloid and interface science*, **171**: 103–111, 1995. doi: 10.1006/jcis.1995.1155

[325] M. WU, B. JOHANNESSON, and M. GEIKER. Application of water vapor sorption measurements for porosity characterization of hardened cement pastes. *Construction and Building Materials*, **66**: 621–633, 2014. doi: 10.1016/j.conbuildmat.2014.06.004

[326] M. J. WATT-SMITH, K. J. EDLER, and S. P. RIGBY. An experimental study of gas adsorption on fractal surfaces. *Langmuir*, **21**: 2281–2292, 2005. doi: 10.1021/la048186t

[327] P. PFEIFER, G. JOHNSTON, R. DESHPANDE, D. SMITH, and A. HURD. Structure analysis of porous solids from preadsorbed films. *Langmuir*, **7**: 2833–2843, 1991. doi: 10.1021/la00059a069

[328] Patricia TANG, Nora YK CHEW, Hak-K CHAN, and Judy A RAPER. Limitation of determination of surface fractal dimension using N2 adsorption isotherms and modified Frenkel-Halsey- Hill theory. *Langmuir*, **19**: 2632–2638, 2003. doi: 10.1021/la00059a069

[329] J. ZHANG, L. GE, Z. CHEN, E. BOOM, and Z. ZHU. Cracking behavior and mechanism of gibbsite crystallites during calcination. *Crystal Research and Technology*, **54**: 1800201, 2019. doi: 10.1002/crat.201800201

[330] E. M. ANITAS. Structural properties of molecular sierpiński triangle fractals. *Nanomaterials*, **10**: 925, 2020. doi: 10.3390/nano10050925

